NMR | MRI

BIOLOGY | CHEMISTRY | MEDICINE | PHYSICS

RF COILS FOR MRI

Editors | J. Thomas Vaughan | John R. Griffiths

WILEY

RF Coils for MRI

EMR Handbooks

Based on the *Encyclopedia of Magnetic Resonance* (EMR), this monograph series focuses on hot topics and major developments in modern magnetic resonance and its many applications. Each volume in the series will have a specific focus in either general NMR or MRI, with coverage of applications in the key scientific disciplines of physics, chemistry, biology or medicine. All the material published in this series, plus additional content, will be available in the online version of EMR, although in a slightly different format.

Previous EMR Handbooks

NMR Crystallography
Edited by Robin K. Harris, Roderick E. Wasylishen, Melinda J. Duer
ISBN 978-0-470-69961-4

Multidimensional NMR Methods for the Solution State
Edited by Gareth A. Morris, James W. Emsley
ISBN 978-0-470-77075-7

Solid-State NMR Studies of Biopolymers
Edited by Ann E. McDermott, Tatyana Polenova
ISBN 978-0-470-72122-3

NMR of Quadrupolar Nuclei in Solid Materials
Edited by Roderick E. Wasylishen, Sharon E. Ashbrook, Stephen Wimperis
ISBN 978-0-470-97398-1

Forthcoming EMR Handbooks

MRI of Tissues with Short T_2 and T_2^*
Edited by Ian R. Young, Gary Fullerton and Graeme M. Bydder
ISBN 978-0-470-68835-9

Encyclopedia of Magnetic Resonance

Edited by Robin K. Harris, Roderick E. Wasylishen, Edwin D. Becker, John R. Griffiths, Vivian S. Lee, Ian R. Young, Ann E. McDermott, Tatyana Polenova, James W. Emsley, George A. Gray, Gareth A. Morris, Melinda J. Duer and Bernard C. Gerstein.

The *Encyclopedia of Magnetic Resonance* (EMR) is based on the original printed *Encyclopedia of Nuclear Magnetic Resonance*, which was first published in 1996 with an update volume added in 2000. EMR was launched online in 2007 with all the material that had previously appeared in print. New updates have since been and will be added on a regular basis throughout the year to keep the content up to date with current developments. Nuclear was dropped from the title to reflect the increasing prominence of MRI and other medical applications. This allows the editors to expand beyond the traditional borders of NMR to MRI and MRS, as well as to EPR and other modalities. EMR covers all aspects of magnetic resonance, with articles on the fundamental principles, the techniques and their applications in all areas of physics, chemistry, biology and medicine for both general NMR and MRI. Additionally, articles on the history of the subject are included.

For more information see: www.wileyonlinelibrary.com/ref/emr

RF Coils for MRI

Editors

J. Thomas Vaughan

University of Minnesota, Minneapolis, Minnesota, USA

John R. Griffiths

Cancer Research UK, Cambridge Research Institute, Cambridge, UK

A John Wiley and Sons, Ltd., Publication

This edition first published 2012

Registered office
John Wiley & Sons Ltd, The Atrium, Southern Gate, Chichester, West Sussex,
PO19 8SQ, United Kingdom

Front cover image credit:
Cover images were kindly supplied by Brandon Tramm and Jinfeng Tian.

Library of Congress Cataloging-in-Publication Data

RF coils for MRI / editors, J. Thomas Vaughan, John R. Griffiths.
p. ; cm.
Includes bibliographical references and index.
ISBN 978-0-470-77076-4 (cloth)
I. Vaughan, J. Thomas (John Thomas), 1957- II. Griffiths, John R., 1945-
III. Encyclopedia of magnetic resonance.
[DNLM: 1. Magnetic Resonance Imaging–methods. 2. Electromagnetic Fields.
3. Magnetic Resonance Spectroscopy–instrumentation. 4. Radio Waves.
5. Transducers. WN 185]
616.07'548–dc23

2012015267

A catalogue record for this book is available from the British Library.

ISBN-13: 978-0-470-77076-4

Set in 9.5/11.5 pt Times by Laserwords (Private) Limited, Chennai, India
Printed and bound in Singapore by Markono Print Media Pte Ltd

Encyclopedia of Magnetic Resonance

Editorial Board

Editors-in-Chief

Section Editors

SOLID-STATE NMR & PHYSICS

SOLUTION-STATE NMR & CHEMISTRY

BIOCHEMICAL NMR

MRI & MRS

HISTORICAL PERSPECTIVES

International Advisory Board

Contents

Contributors

Joseph J. H. Ackerman — *Department of Chemistry, Campus Box 1134, Washington University, Saint Louis, MO 63130, USA*
Chapter 1: An Historical Introduction to Surface Coils: The Early Days

Gregor Adriany — *Department of Radiology, Center for Magnetic Resonance Research, University of Minnesota, Minneapolis, MN 55455, USA*
Chapter 15: TEM Transceiver Head Array Coils for Ultra High Magnetic Fields

Can Eyup Akgun — *Center for Magnetic Resonance Research, University of Minnesota, Minneapolis, MN 55455, USA*
Chapter 30: Radiofrequency Fields and SAR for Transverse Electromagnetic (TEM) Surface Coils

Ergin Atalar — *Electrical & Electronics Engineering Department, Bilkent University, Ankara, TR-06800, Turkey*
Chapter 18: Catheter Coils

Nikolai I. Avdievich — *Department of Neurosurgery, Yale University, New Haven, CT 06520, USA*
Chapter 6: Quadrature Transverse Electromagnetic (TEM) Surface Coils
Chapter 16: Transverse Electromagnetic (TEM) Coils for Extremities

Barbara L. Beck — *McKnight Brain Institute, University of Florida, Gainesville, FL 32610, USA*
Chapter 4: Double-Tuned Surface Coils

C. A. T. van den Berg — *Department of Radiotherapy, University Medical Center Utrecht, Utrecht 3508GA, The Netherlands*
Chapter 17: Antennas as Surface Array Elements for Body Imaging at Ultra-high Field Strengths

Christopher M. Collins — *Department of Radiology, The Pennsylvania State University, College of Medicine, Hershey, PA 17033, USA*
Chapter 3: Quadrature Surface Coils

F. David Doty — *Doty Scientific Inc., Columbia, SC 29229, USA*
Chapter 21: Litz Coils for High Resolution and Animal Probes, Especially for Double Resonance

Randy Duensing *Invivo Corporation, Gainesville, FL 32608, USA*
Chapter 9: Transceiver Loop Arrays

George Entzminger Jr *Doty Scientific Inc., Columbia, SC 29229, USA*
Chapter 21: Litz Coils for High Resolution and Animal Probes, Especially for Double Resonance

Eiichi Fukushima *ABQMR, Albuquerque, NM 87106, USA*
Chapter 2: Radiofrequency Coils for NMR: A Peripatetic History of Their Twists and Turns

Mark A. Griswold *Department of Radiology, Case Western Reserve University, Cleveland, OH 44106, USA*
Chapter 10: Characterization of Multichannel Coil Arrays on the Benchtop

Rolf Gruetter *Laboratory of Functional and Metabolic Imaging, Ecole Polytechnique Federale de Lausanne, CH-1015 Lausanne, Switzerland*
Department of Radiology, University of Lausanne, CH-1015 Lausanne, Switzerland
Department of Radiology, University of Geneva, CH-1211 Geneva, Switzerland
Chapter 5: Nested Surface Coils for Multinuclear NMR

David I. Hoult *Institute for Biodiagnostics, National Research Council Canada, Winnipeg, Manitoba, MB R3B 1Y6, Canada*
Chapter 23: Receiver Design for MR

Tamer S. Ibrahim *Departments of Bioengineering and Radiology, University of Pittsburgh, Pittsburgh, PA 15213, USA*
Chapter 28: Radiofrequency Fields and SAR for Bird Cages

Jian-Ming Jin *Department of Electrical and Computer Engineering, University of Illinois, 1406 West Green Street, Urbana, IL 61801, USA*
Chapter 27: Practical Electromagnetic Modeling Methods

Sven Junge *Bruker Biospin MRI GmbH, Ettlingen 76275, Germany*
Chapter 20: Cryogenic and Superconducting Coils for MRI

Riccardo Lattanzi *New York University School of Medicine, New York, NY 10016, USA*
Chapter 8: Coil Array Design for Parallel Imaging: Theory and Applications

Rostislav A. Lemdiasov *Insight Neuroimaging Systems, 11 Canterbury St., Worcester, MA 01610, USA*
Chapter 26: Radiofrequency MRI Coil Analysis: A Standard Procedure

Wanzhan Liu *Medtronic Inc., Minneapolis, MN 55126, USA*
Chapter 29: RF Field Modeling for Double-Tuned Volume Coils

Reinhold Ludwig — *ECE Department, Worcester Polytechnic Institute, 100 Institute Road, Worcester, MA 01609, USA*
Chapter 26: Radiofrequency MRI Coil Analysis: A Standard Procedure

Arthur W. Magill — *Laboratory of Functional and Metabolic Imaging, Ecole Polytechnique Federale de Lausanne, CH-1015 Lausanne, Switzerland*
Department of Radiology, University of Lausanne, CH-1015 Lausanne, Switzerland
Department of Radiology, University of Geneva, CH-1211 Geneva, Switzerland
Chapter 5: Nested Surface Coils for Multinuclear NMR

Joseph Murphy-Boesch — *National Institutes of Health, Bethesda, MD 20892, USA*
Chapter 12: Double-Tuned Birdcage Coils: Construction and Tuning

Daniel P. Myer — *Communication Power Corporation (CPC), Hauppauge, NY 11788, USA*
Chapter 24: Radiofrequency Power Amplifiers for NMR and MRI

John Nyenhuis — *School of Electrical and Computer Engineering, Purdue University, West Lafayette, IN 47907, USA*
Chapter 32: RF Device Safety and Compatibility

Michael A. Ohliger — *University of California San Francisco, San Francisco, CA 94143, USA*
Chapter 8: Coil Array Design for Parallel Imaging: Theory and Applications

David M. Peterson — *McKnight Brain Institute, University of Florida, Gainesville, FL 32610, USA*
Chapter 25: Impedance Matching and Baluns

A. J. E. Raaijmakers — *Department of Radiotherapy, University Medical Center Utrecht, Utrecht 3508GA, The Netherlands*
Chapter 17: Antennas as Surface Array Elements for Body Imaging at Ultra-high Field Strengths

Devashish Shrivastava — *Center for Magnetic Resonance Research, University of Minnesota, Minneapolis, MN 55455, USA*
Chapter 33: Radiofrequency Heating Models and Measurements

Carl Snyder — *Department of Radiology, Center for Magnetic Resonance Research, University of Minnesota, Minneapolis, MN 55455, USA*
Chapter 14: TEM Arrays, Design and Implementation

Daniel K. Sodickson — *New York University School of Medicine, New York, NY 10016, USA*
Chapter 8: Coil Array Design for Parallel Imaging: Theory and Applications

Jinfeng Tian — *Center for Magnetic Resonance Research, University of Minnesota, Minneapolis, MN 55455, USA*
Chapter 31: TEM Coil Fields and SAR

J. Thomas Vaughan *Center for Magnetic Resonance Research, University of Minnesota, Minneapolis, MN 55455, USA*
Chapter 13: TEM Body Coils
Chapter 33: Radiofrequency Heating Models and Measurements

Andrew G. Webb *Department of Radiology, Leiden University Medical Center, Leiden 2333, The Netherlands*
Chapter 3: Quadrature Surface Coils
Chapter 19: Microcoils

Graham C. Wiggins *New York University School of Medicine, New York, NY 10016, USA*
Chapter 8: Coil Array Design for Parallel Imaging: Theory and Applications

Ernest W. H. Wong *Agilent Technologies, Santa Clara, CA 95051, USA*
Chapter 22: Millipede Coils

Steven M. Wright *Texas A&M University, College Station, TX 77845, USA*
Chapter 7: Receiver Loop Arrays

Nicola De Zanche *Alberta Health Services and University of Alberta, Edmonton, Alberta, AB T6G 1Z2, Canada*
Chapter 11: Birdcage Volume Coil Design

Series Preface

The *Encyclopedia of Nuclear Magnetic Resonance* was published in eight volumes in 1996, in part to celebrate the fiftieth anniversary of the first publications in NMR in January 1946. Volume 1 contained an historical overview and ca. 200 short personal articles by prominent NMR practitioners, while the remaining seven volumes comprise ca. 500 articles on a wide variety of topics in NMR (including MRI). Two "spin-off" volumes incorporating the articles on MRI and MRS (together with some new ones) were published in 2000 and a ninth volume was brought out in 2002. In 2006, the decision was taken to publish all the articles electronically (i.e. on the World Wide Web) and this was carried out in 2007. Since then, new articles have been placed on the web every three months and a number of the original articles have been updated. This process is continuing. The overall title has been changed to the *Encyclopedia of Magnetic Resonance* to allow for future articles on EPR and to accommodate the sensitivities of medical applications.

The existence of this large number of articles, written by experts in various fields, is enabling a new concept to be implemented, namely the publication of a series of printed handbooks on specific areas of NMR and MRI. The chapters of each of these handbooks will comprise a carefully chosen selection of Encyclopedia articles relevant to the area in question. In consultation with the Editorial Board, the handbooks are coherently planned in advance by specially selected editors. New articles are written and existing articles are updated to give appropriate complete coverage of the total area. The handbooks are intended to be of value and interest to research students, postdoctoral fellows, and other researchers learning about the topic in question and undertaking relevant experiments, whether in academia or industry.

Robin K. Harris
University of Durham, Durham, UK

Roderick E. Wasylishen
University of Alberta, Edmonton, Alberta, Canada

November 2009

Volume Preface

The RF coil is the component of the MRI system by which the MRI signal is stimulated and received or lost. Therefore informed specification, design, construction, evaluation, and application of properly selected RF coils are critical to a safe and successful MRI scan. Toward this goal, this handbook serves as an expository guide for engineers, scientists, medical physicists, radiographers, technologists, hands-on radiologists and other physicians, and for anyone with interests in building or selecting and using coils to achieve the best clinical or experimental results.

Since Purcell, Torrey, and Pound's re-entrant cavity resonator and Bloch, Hansen, and Packard's crossed transmit and receive coil pair (Physical Review, 1946), RF coils have evolved from the simple test-tube loaded, wire-wound solenoids and copper-tape resonators of chemistry laboratories to the complex multichannel transmitters and receivers of modern clinical and preclinical MRI systems. With deference to the literature already covering basic coil structures, this guide primarily addresses the dearth of reporting on modern coils for state-of-the-art MRI systems used in clinical diagnostics, biomedical research, and engineering R&D. Current RF coil designs and methods are covered across 33 chapters, divided into seven sections: surface coils, loop arrays, volume coils, special purpose coils, coil interface circuits, coil modeling and evaluation, and RF safety.

The first topic addressed is "surface coils," which are loosely defined as coils placed adjacent to a surface of a region of interest (ROI) in an NMR-active sample such as human anatomy. A surface coil is used for localizing a near-surface ROI, with high transmit efficiency and/or receive sensitivity. The first two chapters introduce surface coils by their history of development, design, and application. Chapters 3–6 include designs for quadrature surface coils, double-tuned surface coils, nested multinuclear surface coils, and surface coils built of transmission line (TEM) elements.

A loop array might be regarded as an array of surface coils. There are surface arrays to be applied to surfaces, and volume arrays to subtend sample volumes. Developed initially as a means of efficiently transmitting to and receiving from larger ROIs with the sensitivity and efficiency of a surface coil, receive, transmit, and transceiver arrays of loops or transmission line elements have found new and more powerful applications in parallel imaging and parallel transmit schemes to further improve imaging speed, quality, and safety. To address this important topic, four chapters are included covering receiver loop arrays, array design for parallel imaging, transceiver loop arrays, and bench top characterization of multichannel coil arrays.

Volume coils, as their name suggests, encompass a sample volume. Common clinical examples are head, limb, and body coils. While there are a number of volume coil technologies by various names, two popular designs are the birdcage and TEM coils and their many variants. The birdcage was originally developed and used as a transceiver head and body coil. It continues to be the most widely used body coil in clinical systems today for exciting a uniform field over a large ROI in the body. Chapters 11 and 12 cover birdcage, and double-tuned birdcage volume coil design. The TEM coil is essentially an array of transmission line elements surrounding a volume, or adjacent to a surface. This structure preserves the inherent field uniformity of a birdcage, but gains the benefits of an array with independent element operation. Accordingly, it is a popular option for parallel-transceiver and parallel-transmit applications. Chapters 13–16 give examples of TEM volume coil designs. Chapter 17 extends the topic further with antenna array elements.

A wide variety of coils offering significant solutions to problems in clinical diagnosis and preclinical science but not neatly fitting into the above categories have been classified as "special purpose coils."

Examples of five such coils are given in Chapters 18–22. Catheter coils for MRI-guided catheterization and high resolution vascular wall imaging is one example for clinical utility. Micro coils of sub-micrometer scale for nanoliter samples are an example of nanotechnology in coil design. Three popular approaches to preclinical probes are included with cryogenic and superconducting coils, single and double resonance litz probes, and millipede coils.

RF coils are of course not stand-alone devices. They must be designed within the context of the MRI system to which they interface. Receive coils must interface the system receiver(s). Transmit coils must interface the system power amplifier(s). Interfaces to the transmitter and receiver require close attention to impedance matching and baluns. The design, interface, and implementation of the receiver, transmitter, and impedance matching are covered in Chapters 23–25.

Coil design requires rigorous modeling and evaluation. The engineer must be familiar with these methods to design and build a safe and successful coil. Models are heavily relied upon by MRI technicians and physicians for predicting image quality and specific absorption rate (SAR) characteristics of a coil for a given application. This section lists six chapters dedicated to methods and examples of analytical and numerically based design and evaluation. A standard approach to RF coil analysis is given in Chapter 26. Chapter 27 reviews the analytical, finite difference time domain, finite element and moments methods of coil field modeling. Chapters 28–31 contribute specific examples of how to model fields and losses (SAR) for the birdcage and TEM coil designs.

The final section is reserved for the foremost concern for all coil designs and applications: "RF safety." Chapter 32 reviews the current SAR-based safety standards by which safety practices and procedures for coil design and use are regulated. SAR and how to calculate SAR in the body with different coils and implants are explained. Tissue heating is demonstrated adjacent to implants and lead wires due to RF–E-field coupling. Chapter 33 addresses the primary safety concern, RF heating, through design and validation of a more accurate bioheat equation. The electrodynamics (SAR) as well as thermodynamics (perfusion and convective heat transfer) and physiology (thermoregulatory reflex) must all be considered for an accurate prediction of temperature contours in the MRI subject. Phantom, animal, and human experimental models are described for measuring systemic and local RF-induced temperature rise.

Thirty nine outstanding authors contributed 33 chapters for this handbook on RF Coils for MRI. Authors were invited by the editors to contribute RF designs or design methods for which they are best known; in many cases they are the inventors and leading innovators of their respective technologies. In an effort analogous to collecting recipes for a community cookbook, authors were asked to contribute an expository account of their favorite RF recipes. Emphasis on the materials and methods sections was requested. This was an opportunity for the senior experts to teach the next generation of coil builders and users how to design, build, and use their most effective designs. Tricks of the trade and other "proprietary" information were called for, information that could not be found in the sparse and disparate literature on these topics. With little more than copyediting, the results are before the readers in the authors' own words. The personalities of the chapters therefore vary in style and content, but are preserved giving the reader an opportunity to meet the authors as well as to learn from them. Finally, Professor Vaughan wishes to thank his friend and colleague, Professor Griffiths whose steadfast patience, gentle prodding, and compensatory toil were necessary ingredients in baking this cake.

Above all else, we hope that engineers, scientists, technicians, and physicians will find "RF Coils for MRI" to be a useful addition to their laboratory benches and library shelves.

J. Thomas Vaughan
University of Minnesota, Minneapolis, Minnesota, USA

John R. Griffiths
Cancer Research UK, Cambridge Research Institute, Cambridge, UK

April 2012

PART A
Surface Coils

Chapter 1

An Historical Introduction to Surface Coils: The Early Days

Joseph J. H. Ackerman

Department of Chemistry, Campus Box 1134, Washington University, Saint Louis, MO 63130, USA

1.1 INTRODUCTION

Before the advent of modern magnetic resonance (MR) imaging scanners possessing superb magnetic-field-gradient systems and RF pulse shaping capabilities, it was common for objects that were to be examined by MR to be placed inside what are today known as *RF volume transmit/receive* coils. MR magnets "back in the day" had relatively narrow bores (few centimeters/inches) and similarly small samples, the most common sample-containing glass tube having an outer diameter of 5 mm. Small-diameter RF volume transmit/receive coils are highly sensitive on a per-unit-volume basis and provide quite homogeneous RF fields. The 5-mm MR probes now in use, common to all high-field, high-resolution analytical (structural chemistry/biology) magnetic resonance spectroscopy (MRS) systems, are highly evolved, offering extraordinary sensitivity, linewidth resolution, and multinuclide detection capabilities.

The introduction of larger bore superconducting magnets motivated the use of MRS for study of larger samples, in particular, intact biological systems, including small laboratory-animal models such as mice and rats. Volume coils had two disadvantages for studies such as these: they became increasingly insensitive with increasing sample size (receptivity scaling roughly as the inverse of the coil radius) and they offered no spatial selectivity (i.e., were unable to focus on a single organ or tissue of interest). Driven by a need for greater signal-to-noise sensitivity and spatial localization, surface coils were introduced, enabling numerous MRS studies of living systems and motivating additional engineering developments in concert with advances in magnet, magnetic-field-gradient, and RF technology.

1.2 BACKGROUND

Before their introduction for in vivo MRS, surface coils had been employed—and remain so today—in oil well logging. Oil well logging refers to the practice of interrogating the terra firma at various depths of and immediately surrounding an oil well borehole,

RF Coils for MRI
Edited by J. Thomas Vaughan and John R. Griffiths

ISBN: 978-0-470-77076-4

with the aim of inferring its oil carrying/producing characteristics. While well-logging tools employ a variety of technologies (e.g., electromagnetic, radioactive, and acoustic) to investigate geologic formations penetrated by a borehole, MR logging probes have played a prominent role.

In MR logging, a magnet designed to produce a relatively homogeneous field at a defined distance outside the borehole (sometimes referred to as an *inside-out* magnet) is inserted down into the borehole to the desired depth, polarizing the ^{1}H spin populations of fluid molecules (e.g., water and oil) in the surrounding rock. An RF receiver coil, which has been designed to detect ^{1}H spins precessing within the isocenter of the inside-out magnetic field, i.e., external to the coil and the borehole, monitors the ^{1}H MR response of fluid molecules external to the borehole. The well-logging MR procedure allows derivation of important geologic properties such as pore size and fluid permeability. While a far cry from the laboratory or clinical environment of in vivo surface coil measurements, the key underlying principle is the same—the MR signal is detected from a region remote from the interior of the coil, i.e., from outside the coil.[1,2]

Perhaps, the earliest in vivo MR implementation of the surface coil was reported by Morse and Singer in their now iconic *Science* report in which time-of-flight effects were employed to monitor blood flow in the arm of a volunteer human subject.[3] This early MR angiography demonstration employed two small surface coils separated by a distance of 1–3 cm and placed over a vein in the arm (Figure 1.1). The transmit RF from the upstream coil produced a perturbation (inversion via adiabatic fast passage) in the blood–water ^{1}H magnetization, a perturbation detected by the downstream receive RF coil at a timing dependent on the velocity of blood flow. This pioneering application did not exploit high-resolution MRS capabilities (i.e., narrow linewidth resonances). Indeed, the sample volume, a human volunteer's forearm, was substantially greater than the homogeneous magnetic field volume produced by the iron magnet (pole faces separated by ~10 cm). However, Morse and Singer did demonstrate the principle of localized excitation and detection of spin populations external to the surface coil with a living subject, one whose overall dimensions obviously far exceed that of the surface coil(s).

Figure 1.1. A copy of Figure 1.1 from the 1970 *Science* magazine article by O. C. Morse and J. R. Singer titled "Blood Velocity Measurements in Intact Subjects".[3] This figure shows a volunteer with her arm in the space between the pole faces of a 0.36 T (15.4 MHz) iron magnet. Two surface coils separated by 2.5 cm are visible, lying over a vein on top of the subject's forearm. The upstream coil served to perturb the flowing venous blood ^{1}H (water) magnetization via adiabatic fast passage. The downstream surface coil served to detect ^{1}H the magnetization as a function of time following upstream perturbation. This time-of-flight "angiography" demonstration is the earliest known (to this author) published use of surface coils in vivo. (Reproduced from Ref. 3. © American Association for the Advancement of Science, 1970.)

1.3 SURFACE COILS FOR MR SPECTROSCOPY IN VIVO

1.3.1 First Report

Superconducting, vertical bore, magnet diameters had become sufficiently large by the mid-1970s (e.g., 9–10 cm) that organs of small animals such as rat liver, heart, and kidney could carefully be excised, continuously perfused with media supplying oxygen and nutrients, placed within an RF coil, and sited

in an MR magnet such that the volume of homogeneous field was reasonably centered about the organ. This arrangement allowed high-resolution MRS studies of functioning, intact, mammalian organs to be performed. By the end of the decade, such procedures were being pursued to great advantage on both sides of the Atlantic.

It was recognized that organs supported on perfusion media, while valuable as model systems, were not entirely representative of the in situ blood-perfused in vivo state. Thus, in the latter part of the decade, an invasive strategy was introduced whereby, in a deeply anesthetized small animal, the organ of interest was surgically exposed while remaining fully connected to its vasculature, placed within an RF coil, and the living subject placed in the magnet such that the organ was in the homogeneous region of the field.[4] Although successful, such procedures were not without technical challenges. Indeed, it was during such attempts to monitor the high-resolution ^{31}P MRS signal from rat kidney in vivo that the presence of "contaminating" signal emanating from phosphocreatine in muscle tissue external to the kidney-containing RF coil suggested a new approach to MRS in vivo, the surface coil.[5,6]

Surface coils presented immediate and substantial advantages for MRS studies of small animals. Planar or slightly shaped/bent coils of a few turns and a few centimeters diameter allowed localized MRS interrogation of rat brain and leg muscle (Figures 1.2 and 1.3). They were also compatible with the tight space limitations imposed by vertical magnets with 9–10 cm bore diameters which, at the time, were common in laboratories pursuing MRS of intact

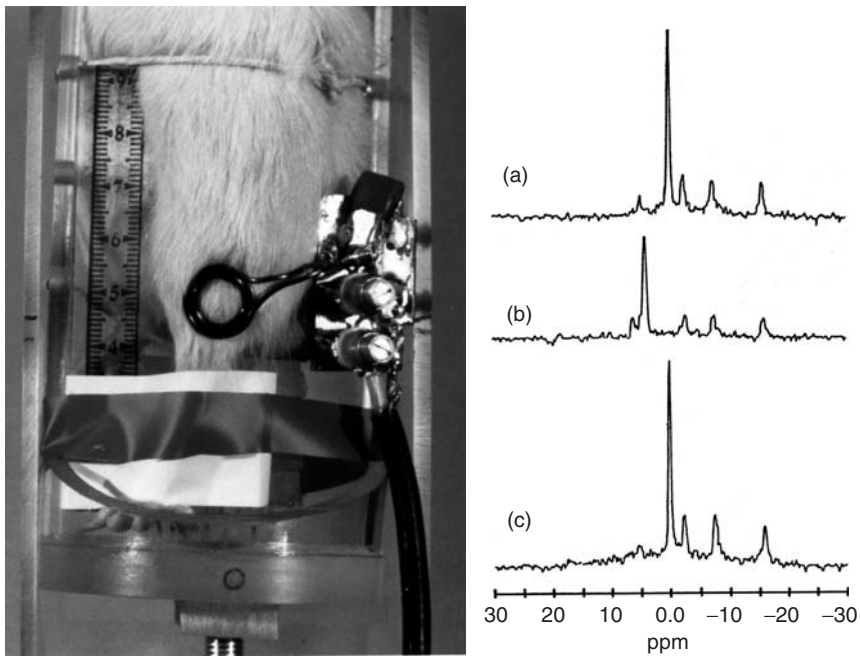

Figure 1.2. Photograph of early surface coil, circa 1980, designed to perform ^{31}P MRS for study of rat leg skeletal muscle, and resulting spectrum acquired in vivo. Subjects were oriented in a vertical position and secured in a clear, plastic, half-cylinder housing. This enabled placement of the entire apparatus with subject up into the vertical bore (~9 cm diameter) of the superconducting magnet. The reader's attention is drawn to the simplicity of coil design and of the frequency tuning and impedance matching circuit. These were important, robust attributes that led to rapid adoption by MR laboratories focused on studies of metabolism and physiology. Spectrum (a): nonischemic muscle below the knee joint; spectrum (b): ischemic muscle from the same area as in (a) after application of tourniquet above the knee; and spectrum (c): muscle above the tourniquet. Chemical shift assignments are β-phosphate of ATP, −16.1 ppm; α-phosphate of ATP, −7.5 ppm; γ-phosphate of ATP, −2.5 ppm; phosphocreatine, 0.0 ppm; and inorganic phosphate, 4.9 ppm. (Spectra adapted from Ref. 6. © Nature Publishing Group, 1980.)

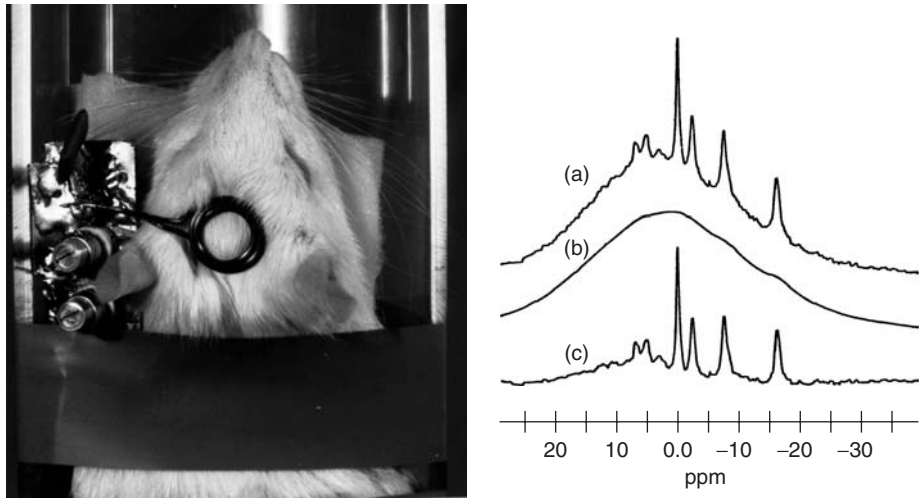

Figure 1.3. Photograph of early surface coil, circa 1980, designed to perform ^{31}P MRS for study of rat brain, and resulting spectrum acquired in vivo. Spectrum (a) original brain spectrum showing a broad baseline feature ("hump") due to bone and membrane ^{31}P resonances; spectrum (b) same spectral data as in (a) but following application of strong apodizing filter function; and spectrum (c) difference spectrum. Chemical shift assignments are the same as in Figure 1.2 with, in addition, phosphodiesters, 3.0 ppm and sugar phosphates, 6.7 ppm. (Spectra adapted from Ref. 6. © Nature Publishing Group, 1980.)

biological systems. Soon, the introduction of significantly larger diameter, horizontal bore magnets allowed surface coil experiments with larger subjects such as humans.

Surface coils also offered a variety of other advantages. It was quickly recognized that the strong, localized B_1 field of the surface coil yielded highly localized signal detection capability, while conferring immunity to coil loading (noise) from regions of the (electrically conducting) subject remote to, and thus not interrogated by, the coil. Further, given that most surface coils were relatively low-inductance devices and that tissue water is an enormously concentrated source of protons (~80 M), the strong ^{1}H MRS signal from tissue water provided a convenient means to shim the static magnetic field even with the coil tuning adjusted for other nuclides (e.g., ^{31}P, ^{13}C).[7] Finally, MR scanners with magnetic-field-gradient systems were rather a rarity in the early 1980s, precluding the use of localization schemes based on the use of field gradients, making surface coil localization much more practical. Laboratories interested in probing metabolism and physiology by high-resolution MRS were much more likely to possess strong expertise in biological science than in MR-related engineering. Thus, because the surface coil was truly simple in design and exceptionally robust to operate, it provided immediate entrée for biologically oriented laboratories to employ MRS in studies of small animal models.

1.3.2 Early Developments at Washington University in Saint Louis

Early development of surface coil techniques in our laboratory at Washington University in Saint Louis explored methods for making T_1 measurements,[8] determining absolute molar concentrations of detected species,[9] optimizing signal-to-noise and localization,[10] using a double-resonance tuning scheme to allow ^{1}H decoupling, while detecting ^{13}C-labeled substrates and their metabolic products,[11] selectively suppressing the large-amplitude, broad, underlying ^{31}P background resonance(s) from membrane and bone tissues when examining brain,[12] quantifying the consequences of using the surface coil as a receiver in the presence of homogeneous B_1 transmission,[13] electrically decoupling coaxial transmission and reception surface coils,[14] and enhancing surface coil spatial localization with an inhomogeneous surface gradient.[15–17] Reviews of these developments and their further extensions have been published.[18,19]

1.3.3 Advances in Pulse Sequences and Designs for Surface Coils

Other laboratories developed important pulse-sequence-related methods for leveraging the surface coil's inhomogeneous B_1 field to improve spatial selectivity. Depth pulses, a family of phase-cycled pulse sequences that provided improved spatial selectivity with surface coils, were described by Bendall and colleagues.[20] Bottomley *et al*. employed magnetic-field-gradient enabled slice-selective excitation parallel to the plane of the surface coil to improve localization at depth, a technique referred to as *depth-resolved surface coil spectroscopy* (*DRESS*).[21] Mike Garwood and coworkers introduced the Fourier series window (FSW) method,[22] a perceptive variation of the rotating-frame zeugmatography experiment,[23] to produce a localized region of detected signal intensity at a predefined depth from the coil plane. The FSW and depth-pulse methods shared complementary attributes, and the Garwood and Bendall teams collaborated to combine the FSW approach with depth-pulse procedures to improve performance for a number of important MRS experiments.[24] In a seminal advance, Garwood *et al*. demonstrated in 1989 that adiabatic pulses using a single surface coil for both B_1 transmission and signal reception (i.e., single-coil mode) could overcome many of the disadvantages of the surface coil's inhomogeneous B_1 profile, allowing uniform excitation, refocusing, and slice-selective inversion over a 10-fold or greater variation in B_1 magnitude.[25]

In concert with efforts to optimize surface coil pulse sequences, coil designs were modified to suit various applications. Presaging today's use of the surface coil as an element for construction of multi-coil arrays for parallel imaging, Hyde *et al*. published a series of insightful papers describing the design of noninteracting coil sets.[26,27] These efforts led the Hyde team to introduce the quadrature detection surface coil,[28] providing a 40% ($\sqrt{2}$) improvement in signal sensitivity.[29] In 1992, these and other advances in surface-coil-related hardware designs, pulse sequences, and applications to metabolic and physiologic research questions were reviewed in the three-volume Springer-Verlag compilation on the state of in vivo MRS, edited by M. Rudin and J. Seelig, to which the interested reader is referred.[30]

1.4 POSTSCRIPT

The early use of surface coils provided high signal sensitivity and localized detection in an era when MR laboratories did not have access to scanners with high-quality magnetic-field-gradient systems. With the introduction of modern, actively shielded magnetic-field-gradient assemblies, the role of the surface coil evolved to complement and take advantage of pulsed field-gradient methods. Today, surface coils continue to play an important role when spatially targeted, high-sensitivity MR detection is desired. They are especially well suited for high-field MRI and MRS applications with small laboratory animals (e.g., mice and rats), where they are often used in receive-only mode with a volume coil providing homogeneous transmit B_1. When surface coils are employed as elements of a large-scale receiver array, prior information, in the form of sensitivity profile maps for each array-element, allows undersampling of k-space with significant acceleration of image acquisition.

Morse and Singer would surely be pleased.

RELATED ARTICLES IN THE ENCYCLOPEDIA OF MAGNETIC RESONANCE

Ackerman, Joseph J. H.: Oxford Knights

Coils for Insertion into the Human Body

Gadian, David G.: From Brawn to Brain

Hoult, D. I.: Biomedical NMR Instrumentation—A Personal Viewpoint

Radda, George K.: The Development of In Vivo NMR in Oxford

Radiofrequency Systems and Coils for MRI and MRS

Shaw, Derek: From 5-mm Tubes to Man. The Objects Studied by NMR Continue to Grow

Surface and Other Local Coils for In Vivo Studies

Surface Coil NMR: Detection with Inhomogeneous Radiofrequency Field Antennas

Well Logging

Whole Body Machines: NMR Phased Array Coil Systems

REFERENCES

1. R. L. Kleinberg, Well logging, in *Encyclopedia of Nuclear Magnetic Resonance*, eds D. M. Grant and R. K. Harris, John Wiley & Sons, Ltd.: New York, Sussex, England, 1995, p. 4960.
2. R. L. Kleinberg, *The Industrial Physicist*, 1996, **2**, 18.
3. O. C. Morse and J. R. Singer, *Science*, 1970, **170**, 440.
4. T. H. Grove, J. J. H. Ackerman, G. K. Radda, and P. J. Bore, *Proc. Natl. Acad. Sci. U.S.A.*, 1980, **77**, 299.
5. J. J. H. Ackerman, Ackerman, Joseph J. H.: Oxford knights, in *Encyclopedia of Nuclear Magnetic Resonance, Historical Perspectives*, eds E. D. Becker, John Wiley and Sons, Ltd: Sussex, England, 1996, Vol. 1, p. 164.
6. J. J. H. Ackerman, T. H. Grove, G. G. Wong, D. G. Gadian, and G. K. Radda, *Nature*, 1980, **283**, 167.
7. J. J. H. Ackerman, D. G. Gadian, G. K. Radda, and G. G. Wong, *J. Magn. Reson.*, 1981, **42**, 498.
8. J. L. Evelhoch and J. J. H. Ackerman, *J. Magn. Reson.*, 1983, **53**, 52.
9. K. R. Thulborn and J. J. H. Ackerman, *J. Magn. Reson.*, 1983, **55**, 357.
10. J. L. Evelhoch, M. G. Crowley, and J. J. H. Ackerman, *J. Magn. Reson.*, 1984, **56**, 110.
11. N. V. Reo, C. S. Ewy, B. A. Siegfried, and J. J. H. Ackerman, *J. Magn. Reson.*, 1984, **58**, 76.
12. J. J. H. Ackerman, J. L. Evelhoch, B. A. Berkowitz, G. M. Kichura, R. K. Deuel, and K. S. Lown, *J. Magn. Reson.*, 1984, **56**, 318.
13. M. G. Crowley, J. L. Evelhoch, and J. J. H. Ackerman, *J. Magn. Reson.*, 1985, **64**, 20.
14. W. Chen and J. J. H. Ackerman, *J. Magn. Reson.*, 1992, **98**, 238.
15. M. G. Crowley and J. J. H. Ackerman, *J. Magn. Reson.*, 1985, **65**, 522.
16. W. Chen and J. J. H. Ackerman, *NMR Biomed.*, 1990, **3**, 147.
17. W. Chen and J. J. H. Ackerman, *NMR Biomed.*, 1990, **3**, 158.
18. C. S. E. Bosch and J. J. H. Ackerman, in *NMR Basic Principles and Progress, Vivo Magnetic Resonance Spectroscopy II: Localization and Spectral Editing*, eds P. Diehl, E. Fluck, H. Günther, R. Kosfeld, J. Seelig, M. Rudin, and J. Seelig, Springer-Verlag: Berlin and Heidelberg, Germany, 1992, Vol. 27, p. 3, Chapter 1.
19. C. S. Bosch and J. J. H. Ackerman, Surface coil NMR: Detection with inhomogeneous radiofrequency field antennas, in *Encyclopedia of Nuclear Magnetic Resonance*, eds D. M. Grant and R. K. Harris, John Wiley & Sons, Ltd.: New York, Sussex, England, 1996, Vol. 7, p. 4649.
20. M. R. Bendall and R. E. Gordon, *J. Magn. Reson.*, 1983, **53**, 365.
21. P. A. Bottomley, T. H. Foster, and R. D. Darrow, *J. Magn. Reson.*, 1984, **59**, 338.
22. M. Garwood, T. Schleich, B. D. Ross, G. B. Matson, and W. D. Winter, *J. Magn. Reson.*, 1985, **65**, 239.
23. D. I. Hoult, *J. Magn. Reson.*, 1979, **33**, 183.
24. M. Garwood, T. Schleich, M. R. Bendall, and D. T. Pegg, *J. Magn. Reson.*, 1985, **65**, 510.
25. M. Garwood, K. Ugurbil, A. R. Rath, M. R. Bendall, B. D. Ross, S. L. Mitchell, and H. Merkle, *Magn. Reson. Med.*, 1989, **9**, 25.
26. J. S. Hyde, A. Jesmanowicz, W. Froncisz, J. B. Kneeland, T. M. Grist, and N. F. Campagna, *J. Magn. Reson.*, 1986, **70**, 512.
27. W. Froncisz, A. Jesmanowicz, J. B. Kneeland, and J. S. Hyde, *Magn. Reson. Med.*, 1986, **3**, 590.
28. J. S. Hyde, A. Jesmanowicz, T. M. Grist, W. Froncisz, and J. B. Kneeland, *Magn. Reson. Med.*, 1987, **4**, 179.
29. C.-N. Chen, D. I. Hoult, and V. J. Sank, *J. Magn. Reson.*, 1983, **54**, 324.
30. M. Rudin and J. Seelig, eds., in *NMR: Basic Principles and Progress: In vivo Magnetic Resonance Spectroscopy I, II, & III*, eds P. Diehl, E. Fluck, H. Günther, R. Kosfeld, and J. Seelig, Springer-Verlag: Berlin and Heidelberg, Germany, 1992, Vol. 26, 27, & 28.

Chapter 2

Radiofrequency Coils for NMR: A Peripatetic History of Their Twists and Turns

Eiichi Fukushima

ABQMR, Albuquerque, NM 87106, USA

2.1 INTRODUCTION

Nuclear magnetic resonance (NMR) is now a mature field but shows no sign of slowing down in terms of new protocols. The associated hardware has also experienced huge strides, although much of that is due to the spectacular development of computer technology over the past half a century. Throughout these changes, the NMR detection coil has remained surprisingly unchanged, except for the new developments at the very high frequencies where the signal wavelengths are getting comparable to the physical size of the coils. This short review explores the various coils used over the years and, in particular, examines the reasons for the longevity of the solenoid for use at relatively low frequencies as well as other coils that offer particular advantages for special situations.

Because NMR deals with nuclear spins that precess in a magnetic field, the vast majority of experiments use coils for both detection and transmission. This presupposes a loose definition of coils; the dictionary definition of a coil being "a connected series of spirals ... into which a rope can be wound", which is consistent with a solenoid that we are all familiar with. Some modern coils, however, do not look anything like this definition. For the purpose of this short review, coils are taken to be the devices used to receive NMR signals, whatever their shapes may be. At the same time, some commonly used coils, especially those used at high frequencies, are not discussed for arbitrary reasons. This review is not so much history per se but a compilation of interesting ways to effect NMR detection. Most coils not specifically referenced here are described in the book by Lupu *et al*., listed under Further Reading.

2.2 HISTORY OF COILS

We start the list with a coil having the least likely geometry. It is known that a periodically varying electric field has a periodically oscillating magnetic field associated with it. Gersch and Lösch[1] demonstrated in 1957 that NMR signal can be detected from samples in an oscillating electric field of capacitors. The capacitor was placed between the pole pieces of an electromagnet in such a way that the RF electric field was parallel to the static magnetic field. To the author's knowledge, this experiment did not elicit much interest and remains an academic curiosity.

RF Coils for MRI
Edited by J. Thomas Vaughan and John R. Griffiths
 ISBN: 978-0-470-77076-4

The simplest geometry for an electric current that can generate a magnetic field is a straight line. The next simplest element may be that line bent into a loop. Both these geometries are used for NMR but do not represent the most straightforward applications due to the spatially inhomogeneous magnetic fields generated by them. In order for the generated magnetic field B_1 (and the sensitivity per spin—to be discussed later) to be uniform for a sample that has significant physical extent, there must be many wires so that they look the same, or at least similar, to the spins located at different parts of the sample. It will also turn out that the sensitivity per spin is enhanced, in general, if the spin is close to more wires carrying a certain current rather than fewer wires carrying the same current. For these and other reasons, the most common coil used in NMR is the solenoid, at least for reasonably low frequencies where the inductive reactance remains manageable.

The fact that solenoids perform extremely well is often taken for granted but it is worth considering in some detail. It would make sense to incorporate the features responsible for their good performance into other coil designs. The reciprocity theorem for NMR, as described by Hoult and Richards,[2] states that the sensitivity to NMR signal from a sample element is proportional to the intensity of the magnetic field at the position of the sample element due to a unit current in the coil. Because the magnetic field strength drops off with distance from any source, including coil wires, the sample needs to be close to the current elements by some measure in order to achieve the best signal-to-noise ratio (SNR). The solenoid works well compared to many other geometries because it does a good job of putting the current elements relatively close to all parts of an arbitrary sample placed within the coil, provided the coil has a reasonable ratio of length to diameter and its pitch is acceptably fine, i.e., the wire thickness is approximately equal to the gap between the wires. Another way to look at it is to realize that the magnetic field inside the solenoid is caused by currents flowing in all the turns of the solenoid, so the process is extremely efficient. By the same token, a small solenoid is much more efficient *per spin* than a large solenoid because an average spin will be closer to the wires in the small coil.

A counter-example would be a disproportionately short solenoid, the extreme case being a single loop of wire, the so-called surface coil. The surface coil, somewhat misnamed because there are other coil geometries that are equally or perhaps even more exclusively suited for surface use, is simple to make and it is likely that it was used in NMR since close to beginning of (NMR) time. It was formally introduced in the 1970s and 1980s primarily for in vivo biological applications in longitudinal fields of axial superconducting magnets for samples that are too large for the usual solenoid coil or where there is a need to spatially localize the signal source by the placement of the coil.

Despite the surface coil's simplicity and usefulness, the field is inhomogeneous compared to the solenoid; the relative magnetic field strength varies by a huge factor between a sample element at the center of the loop versus an element at the wire. This effect results in the most effective position of the "surface" coil not being at the surface against which the coil can be placed but at a distance that is comparable to the radius of the loop. At this separation, there is a balance between manageability of the inhomogeneity and making the distance from the coil not so great that it compromises the sensitivity. Thus, the usual "rule of thumb" is to make a coil with a radius approximately equal to the desired depth for the region of sensitivity.

This effect is used in an NMR application having an unusual scale: Earth's field NMR detection of underground water or other liquids. This application, pioneered in Siberia more than 25 years ago, uses a large circular or rectangular loop coil on the ground, with a typical dimension of 100 m, to detect NMR signals from depths comparable to the coil radius and, in favorable cases, even the diameter. Earth's field NMR is notoriously insensitive because of the weak static magnetic field of typically $\sim 5 \times 10^{-5}$ T, which leads to a relative sensitivity compared to 4.7 T of (10^{-5}) raised to, say, 3/2 power, or a factor of $\sim$30 million, although this estimate is likely to be inaccurate because of the immense range of extrapolation over five orders of magnitude in field strength. This deficit is recovered by having a sample that is larger than the usual sample in linear scale by the cube root of $\sim$30 million or $\sim$300. If the usual NMR sample is taken to be 1 cm across, an Earth's field NMR sample with large spin density, for example water, will have to be at least 30 m across so a loop coil that is $\sim$100 m across might be sufficient. This turns out to be true in many cases, and there are now commercial instruments by companies such as Iris in France (www.iris-instruments.com) and Vista Clara in the

United States (www.vista-clara.com) based on this principle for use in geophysical exploration without having to use expensive boreholes. Incidentally, this community calls its activity "surface NMR" which is a misnomer because it looks at samples quite far from the surface although it does make use of "surface coils".

This brings us back to the "surface coil" nomenclature. The usual surface coil is called so because it lies on a surface, not because it is good at looking at a surface. If it is desired to see NMR signals near a surface, i.e., a flat region that is close to the coil access, a big loop is inefficient because B_1 is acutely nonuniform across the loop coil and the tip angle varies wildly across the plane that the coil is placed against. The reciprocity theorem requires that the wires be close together, so that a good compromise will be to have wire spacings approximately equal to the distance from the coil to the region of interest. Depending on the relative orientation of the static field and the "surface" coil, one could think of using an array of small loops with currents alternating in adjacent loops, a meanderline coil (a zig-zag coil that is useful in nuclear quadrupole resonance (NQR) detection), or parallel wires with currents flowing in the same direction, all with characteristic dimensions approximately equal to the depth of the sample. However, arrays of loops with radii approximately equal to depth of interest have the problem that the components of the magnetic field vary on the scale of the separation of the loops so the filling factor is less than optimal. This is also true for the meanderline, which generates magnetic fields that alternate in direction from one wire to the next, so the field strength and orientation have a periodicity in the direction perpendicular to the wires.

The array of parallel wires, on the other hand, can generate quite a uniform magnetic field parallel to the plane of the coil and perpendicular to the wires at a distance equal to approximately the inter-rung spacing. Therefore, such a coil can be used in a static field that is perpendicular to the access direction, as you might find in old-fashioned electromagnets or permanent magnets with the static field perpendicular to the access direction. Another suitable situation would be Earth's field NMR experiments in which the static magnetic field is mainly perpendicular to a coil that is laid on the ground, as it is in much of the world, and it is desired to detect or characterize a sample that has a large extent at a shallow depth. An added feature of such coils is their ability to be used for rotating B_1 experiments by having two coplanar flat coils with one rotated 90° with respect to the other and driven in quadrature to attain an extra factor of $\sqrt{2}$ in SNR and more efficient transmitter operation (see Chapter 3).

Figure 2.1. A single-sided NMR magnet and coil built by Southwest Research Institute showing the "pancake" coil in the center and the electromagnet driven by the blue coils. (Photo supplied by Armando De Los Santos, Southwest Research Institute.)

As we have discussed, loop coils naturally lend themselves to unilateral NMR geometries. One of the earliest applications of such coils was for a unilateral device built by Southwest Research Institute, San Antonio, TX, USA, for examination of soil and moisture in concrete as shown in Figure 2.1. It was mounted behind a tractor to be dragged around a field, or mounted on wheels to be moved around on the concrete surface as measurements were made. These instruments were the forerunners of the commercially available NMR MOUSE.[3]

A saddle coil can be thought of as two loops on opposite sides of a cylinder that provides (or is sensitive to) a magnetic field that is perpendicular to the axis of the cylinder.[2] The pair of loops are, first, deformed into rectangles and, second, wrapped around the cylinder. Shaping them as rectangles allows the placement of the two coils on a relatively narrow cylinder and obtains good coverage in the axial direction. Wrapping the coil elements around the cylinder that serves as the coil form, of course, makes the coils compact and, more importantly, places the coil wires closer to the sample, thereby making the coil more sensitive to NMR signals.

As an aside, two single loop coils can be placed at right angle to each other for circularly polarized B_1 operation, i.e., the coils can be driven in quadrature

to be sensitive to circularly polarized magnetization rather than linearly polarized fields, enhancing transmit efficiency as well as for received SNR.[4] This is easy to do with flat coils such as loops but much harder (or impossible) with axial coils that surround the sample, e.g., solenoids, because they get in the way of each other. Besides the flat array mentioned above, Helmholtz coils, saddle coils, or birdcage-like coils can be driven in quadrature, as is commonly done these days for coils in standard superconducting magnets.

This is also true for a pair of coplanar but adjacent loop coils with currents opposed so the predominant field is in the plane of the loops. A typical application is that of "figure 8" coils used, for example, as large-scale surface coils for detection of underground water. In an early application, the author participated in setting up such a coil in Siberia. A 100 m diameter loop was twisted to form a "figure 8" with two opposed loops of diameter 50 m. Several of us placed ourselves around one loop and pulled on it to change its shape (and, therefore, its area) to change the far-field noise pickup as monitored by an operator at the console. This geometry, with the resulting useful field parallel to the plane of the coil, is ideal for making it into one-half of a quadrature transmit/receive coil by adding an identical pair of coils with their interloop axis rotated 90° from the first.

There are other situations in which a normal solenoid is not appropriate. An example is where the solenoidal geometry is inconsistent with geometrical constraints such as the shape of a magnet that restricts access. The best known examples are the use of transverse B_1 field coils in superconducting magnets that have static fields parallel to the bore. This has given rise to coils such as the saddle,[2] Alderman–Grant, and birdcage. Another novel solution is a tilted solenoid[5] in which each loop of wire is wound in a plane that is tilted approximately 45° from the axial direction. It works quite well—comparable to other nonsolenoidal coils—because the sacrifice in efficiency due to its tilt is compensated by the inherent superiority of the solenoid over other geometries such as birdcage and saddle, due to the high density of wires close to the sample, as mentioned repeatedly in this chapter.

A relatively new development is a family of extremely small coils that go by the label microcoils. Despite the range of sizes of coils called microcoils, we will arbitrarily define them as coils smaller than 1 mm in the largest dimension. The majority of such microcoils in use are for obtaining high-resolution spectra in strong magnetic fields of samples that are severely limited in volume.[6] Microcoils work well because they take advantage of the reciprocity relation, already mentioned, i.e., that the sensitivity per spin is proportional to the strength of the magnetic field generated at the site of the spin by a unit current in the receiver coil if it were to be used for transmitting, simply by being small. Although, sometimes thought of as a corollary to the filling factor, this effect is independent of it. It is simply a statement that the spin should be as close as possible to the wire in order that the sensitivity is maximized regardless of the filling factor. The simple fact that all parts of the sample inside the microcoil are very close to the coil wires guarantees good sensitivity per spin, which compensates for the relatively small size of the sample and relatively large resistance of the thin coil wire (see Chapter 19).

Microcoils, by their nature, have extremely small inductances, and this fact goes hand in hand with their uses at high frequencies where both capacitance and inductance of resonant circuits need to be small. Therefore, the recent development of microcoils for use at relatively weak fields[7] was not anticipated. In addition to the penalty of working in a weaker field, microcoils at low frequencies have a practical handicap of being difficult to tune/match because their inductances are so small. Resonating a small inductor in a resonant circuit at low frequencies requires a large capacitor that will, at best, make it inconvenient to tune because there are limits to the range of tuning variable capacitors. Furthermore, large capacitors tend to be more lossy compared to small capacitors because they usually use materials with higher dielectric constants in order to keep the volume compact and such materials happen to be lossy.

Low-inductance microcoils can be used at low frequencies if auxiliary inductors are used instead of the microcoil itself to define the resonant parameters.[8] The microcoil, say in series with the auxiliary coil, will represent only a small resistor and, provided the auxiliary coil has negligible resistance so that it does not contribute noise to the tank circuit, the SNR is surprisingly good. This is because the microcoil has favorable reciprocity parameters with only its resistance contributing to the degradation of the performance, i.e., the sample is close to the wire, which leads to excellent sensitivity. The presence of the auxiliary capacitor in the circuit has no effect on

the overall sensitivity provided it adds no noise to the received signal. The use of an auxiliary inductor has the added advantage of making the probe tuning insensitive to the sample coil's interaction with the surroundings, including the sample.

The low-field microcoil is an example of an adaptation of a standard technique, i.e., of a solenoid, to a case in which standard parameters could not be used and some modification was required. Specifically, the inductance was too small to be tuned in the usual manner at the required frequency. The opposite case is more common with the push toward stronger fields and larger samples, which results in the normal coils having inductances that are too large for the frequency. The solution to this problem is well known, i.e., to distribute the capacitances and reactances so that resonance frequency is determined not by the overall values of C and/or L but in smaller subsections of the coil.

One early example of distributed coil of this type was the pigtail coil.[9] It was a solenoidal coil in which the turns were periodically interrupted by capacitive connections between turns that were formed by twisting the free end of each turn with a free end of the next turn, resembling pigtails. The tightness of the twists of these insulated wires and the lengths of the pigtails determined the capacitance. Figure 2.2 shows a more recent adaptation of this idea for a coil under construction that was going to be too large to be resonated as a simple solenoid, i.e., a human wrist coil that works in a 1 T field in a permanent magnet where the field is transverse to the common access direction. In this case, it was sufficient to have each section of the resonant section be two turns of wire rather than one for the original Cook & Lowe coil. Such distributed reactance strategies, though not in the pigtail form, are now commonplace in clinical magnetic resonance imaging (MRI) where the coil needs to be large enough to accommodate humans in relatively strong magnetic fields.

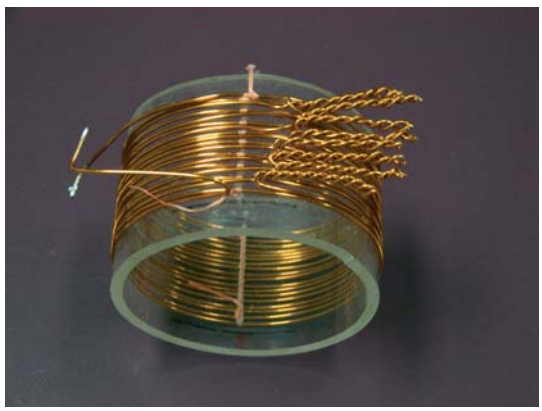

Figure 2.2. A partially finished pigtail coil for human wrist imaging. The solenoid was interrupted every two turns with a capacitor formed by the pigtails so the resonance condition was governed by two turns of wire resonating with the capacitance of a pigtail which could be adjusted by its length or tightness. The pigtails simplify the initial setup of the resonance condition and can be replaced by ordinary capacitors, if desired, after the capacitance values have been determined.

This scheme was also used in the late 1970s and early 1980s in what may have been the most powerful NMR experiment to that time or perhaps even now. Southwest Research Institute, San Antonio, TX, USA, had a contract with the Federal Aviation Administration to design and build a detector for dynamite in checked airline baggage. Their ingenious solution was to create a pulse proton NMR system, large enough for suitcases, to perform solid and Hahn echoes in order to pick out samples that had very long T_1 and very short T_2, characteristics nearly unique to dynamite. The apparatus had a solenoidal coil of rectangular cross section that was placed between the pole pieces of an electromagnet. In order to reduce the inductance to a manageable value, the coil was made in six sections, three sets each of a pair of coils wound in opposite senses, connected in parallel, and driven between the junction and the two ends in a way similar to the semi-toroid described later (see Figure 2.3). The entire coil, made of copper water tubing, was enclosed in a glass sleeve containing gaseous sulfur hexafluoride (SF_6) in order to suppress arcing when the 1.4 MW pulses were applied. (Even with a Faraday shield in addition to the SF_6 gas, putting one's hand along the inside surface of the sample space elicited sparks from the high-voltage sections of the coil to the hand. This made it simple to find the locations of the three high-voltage feed points.) The amplifier vacuum tube (Eimac 4CX35000C) for the transmitter's last stage dissipated 2 kW *just in its filaments*. That is equivalent to a major kitchen appliance such as an electric oven!

Other examples of a distributed component coil are the already mentioned Alderman–Grant coil and the birdcage coil. The latter can be thought of as a "ladder" of inductors and capacitors (which would be

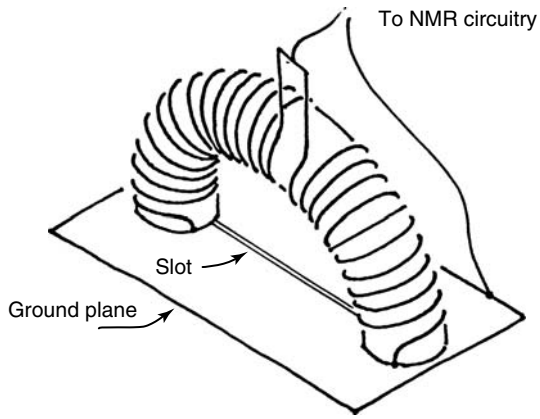

Figure 2.3. A semi-toroidal "surface" coil and the back side of the ground plane to which the two ends are electrically connected. A slot between the two holes eliminates the eddy currents that would otherwise attenuate the field past the ground plane. The useable field is on the front side of the ground plane and in an orientation that is parallel to the slot.

either a high- or low-pass filter depending on whether the rungs—of the ladder—were made of inductors or capacitors, respectively) that is closed onto itself in such a way that the time delay of the signal around the loop is one cycle of the RF field being applied to the coil. The uniform transverse magnetic field is generated by a longitudinal electric current density around the cylindrical surface that is a single cycle of a sinusoid. Thus the resonating elements are local rather than global, i.e., basically an inductor and a capacitor, so that the whole coil can be made much larger at the same resonance frequency than if the entire coil were made of one inductor to be resonated by a capacitor, as is done with a simple solenoid. An additional benefit of such distributed component coils is the reduction of capacitive (or dielectric) coupling to the sample. In short, this is due to the reduction of the largest potential difference generated within the coil by distributing the inductive and capacitive reactances.[10]

Over the years there have been a few coils designed and used wherein the transmit and/or receive "coils" were placed away from the actual sample space. The reasons for wanting to do such things include needing the space/clearance around the sample for optical or thermal access. The earliest such probe to the author's knowledge is due to Arnold in what was called the "race track" probe. His work is referenced by Halliday *et al*.[11] who published a later adaptation of Arnold's probe.

The downhole well-logging community uses some unusual coils, at least as far as the rest of the magnetic resonance community is concerned. These are some of the earliest examples of "inside-out" NMR for these geometries wherein the sample is not contained within the coil but outside the coil. One such coil used by Schlumberger as described by Kleinberg in a special issue of *Concepts in Magnetic Resonance*[12] is, perhaps, the simplest possible coil imaginable. It is topologically equivalent to a single wire plus suitable return paths that do not generate magnetic fields that counteract the primary field. Such a "coil" that runs longitudinally along the bore hole surface will generate an azimuthal field just outside the borehole. NMR signals can be generated from the surrounding strata containing oil or water in a radial static field that is generated by a suitably arranged permanent magnet blocks in the bore. Several such examples are described in Ref. 12.

We finish this review with another coil that has not found any practical applications but may be an instructive example.[13] The simple loop coil has already been described as a coil that is used for looking at a sample that is outside the coil. The field coming out of a solenoid's end has the same property except there is little or no gain over the simple loop because the increase in the number of turns is compensated by the volume of the solenoid in which there is no sample. (It would be more efficient to make a multiple turn loop with minimal volume inside the loop.) Some of that loss could be regained if both ends of the solenoid could be used and that led to the semi-toroid that is shown in Figure 2.3. (A toroid would be a terrific coil for a sample that fits in the coil because it can be considered to be a solenoid without end. However, its accessibility is a serious handicap for most applications.) This coil is topologically the same as the "figure 8" coil we described earlier but with a third dimension instead of it being a flat coil. An embellishment is the two halves of the coil being wound in opposite senses with the two ends of the coil connected to a ground plane that is presented to the sample. The electrical feed point is the junction of the two halves, far from the sample region. So, this coil also has minimal electrical interactions, i.e., it is not detuned by a dielectrically lossy sample that can come in contact with it. In addition, having the two halves connected

electrically in parallel raises the tuning frequency for its size. Finally, one could conceive of inserting some material inside the semi-toroid that will amplify the signal in an analogous fashion to what a ferrite would do at lower frequencies.

RELATED ARTICLES IN THE ENCYCLOPEDIA OF MAGNETIC RESONANCE

Birdcage Resonators: Highly Homogeneous Radiofrequency Coils for Magnetic Resonance

NMR Probes for Small Sample Volumes

Probe Design and Construction

Radiofrequency Systems and Coils for MRI and MRS

Sensitivity of the NMR Experiment

Solid State NMR Probe Design

Surface and Other Local Coils for In Vivo Studies

Surface Coil NMR: Detection with Inhomogeneous Radiofrequency Field Antennas

REFERENCES

1. V. U. Gersch and A. Lösch, *Ann. Phys.*, 1957, **20**, 167.
2. D. I. Hoult and R. E. Richards, *J. Magn. Reson.*, 1976, **24**, 71.
3. G. Eidmann, R. Savelsberg, P. Blümler, and B. Blümich, *J. Magn. Reson., Ser. A*, 1996, **122**, 104.
4. D. I. Hoult, C.-N. Chen, and V. J. Sank, *Magn. Reson. Med.*, 1984, **1**, 339.
5. E.-K. Jeong, D.-H. Kim, M.-J. Kim, S.-H. Lee, J.-S. Suh, and Y.-K. Kwon, *J. Magn. Reson.*, 1997, **127**, 73.
6. D. L. Olson, T. L. Peck, A. G. Webb, R. L. Magin, and J. V. Sweedler, *Science*, 1995, **270**, 1967.
7. L. O. Sillerud, A. F. McDowell, N. L. Adolphi, R. E. Serda, D. P. Adams, M. J. Vasile, and T. M. Alam, *J. Magn. Reson.*, 2006, **181**, 181.
8. A. F. McDowell, U.S. Pat. 7,405,567, (2008).
9. B. Cook and I. J. Lowe, *J. Magn. Reson.*, 1982, **49**, 346.
10. D. I. Hoult, Sensitivity of the NMR experiment, *Encyclopedia of Magnetic Resonance*, Published Online: 15 MAR, 2007. DOI: 10.1002/9780470034590.emrstm0490.
11. J. D. Halliday, H. D. W. Hill, and R. E. Richards, *J. Sci. Instrum.*, 1969, **2**, 29.
12. R. J. S. Brown, R. Chandler, J. A. Jackson, R. L. Kleinberg, M. N. Miller, Z. Paltiel, and M. G. Prammer, *Concepts Magn. Reson.*, 2001, **13**, 335. Special Thematic Issue: The History of NMR Well Logging.
13. R. A. Assink, E. Fukushima, A. A. V. Gibson, A. R. Rath, and S. B. W. Roeder, *J. Magn. Reson.*, 1986, **66**, 176.

FURTHER READING

C.-N. Chen and D. I. Hoult, *Biomedical Magnetic Resonance Technology*, Taylor & Francis, Adam Hilger, Bristol & New York, 1989.

M. Lupu, A. Briguet, and J. Mispelter, *NMR Probeheads: For Biophysical and Biomedical Experiments*, Imperial College, London, 2006.

Chapter 3
Quadrature Surface Coils

Christopher M. Collins[1] and Andrew G. Webb[2]

[1]*Department of Radiology, The Pennsylvania State University, College of Medicine, Hershey, PA 17033, USA*
[2]*Department of Radiology, Leiden University Medical Center, Leiden 2333, The Netherlands*

3.1 INTRODUCTION

The quadrature surface coil is a valuable tool for achieving high signal-to-noise ratio (SNR) in reception and low specific absorption rate (SAR) in transmission. As with a single linear surface coil, a single quadrature surface coil is typically used when the region of interest does not include an entire cross section through the subject, and is capable of being used on systems with only one transmit and receive channel. It is also possible to build an array of quadrature surface coils for improved performance over an array of single-channel coils with a given number of channels. Here we discuss the basic principles of quadrature operation, coil design, expected field, SNR, and SAR patterns, and then discuss some recent applications.

RF Coils for MRI
Edited by J. Thomas Vaughan and John R. Griffiths

ISBN: 978-0-470-77076-4

3.2 BACKGROUND

Two waveforms with a 90° difference in phase are said to be in quadrature. If these are used to drive two radiofrequency (RF) coils producing magnetic (B_1) fields that are equal in magnitude and orthogonal to each other in space, an RF magnetic field with circular polarization will result. Because the RF fields in NMR are intended to interact with precessing nuclei, this arrangement is more efficient than using a single coil producing a linearly polarized field, and, in principle, can result in half the RF power absorbed in tissue during transmission, and in a gain in SNR by a factor of $\sqrt{2}$ during reception.[1] The use of quadrature coils can also result in a substantial increase in B_1 field homogeneity over linear coils, especially at high frequency.

It is important to note that for a quadrature coil to function properly in both transmission and reception, the signal associated with the coil that leads by 90° during transmission must be made to lag by 90° during reception. An illustrated explanation for this is given in Figure 3.1.

Compared to a volume coil, a surface coil can provide relatively high SNR over a small region of interest. The ability to combine this with the advantages of quadrature transmission and/or reception makes quadrature surface coils among the most useful types of RF coils used in magnetic resonance imaging (MRI). Quadrature surface coils are used as

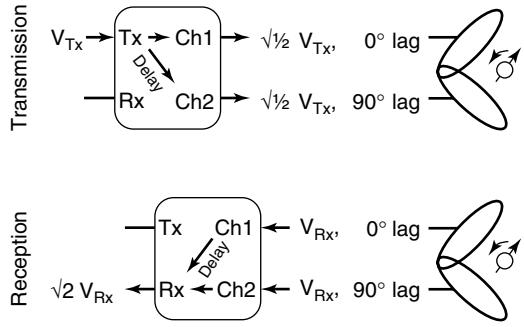

Figure 3.1. Illustration of quadrature hybrid coupler showing the need for delay on opposite channels during transmission and reception. Note that noise is neglected in this illustration.

receive-only coils in many applications, with the body coil being used for homogeneous RF transmission. At very high fields, since body coils are not yet commercially available, surface coils are often used in both transmit and receive mode. This is also true for many heteronuclear (e.g., ^{13}C and ^{31}P) spectroscopy experiments. Besides, when proton decoupling is used in local spectroscopy, the quadrature surface coil is very useful since it can achieve the necessary decoupling in the local region of interest with minimal sample heating over the rest of the body.

3.3 COIL CONSTRUCTION

3.3.1 Basic Coil Geometries

There are a number of different geometries that can be used as quadrature surface coils. The two coils usually lie in the same plane, although they can also be placed on a curved surface for imaging the back of the head or calf muscles, for example. Quadrature surface coils can be formed from circular/elliptical or square/rectangular loops, or can be combined with a different structure such as a stripline resonator. A selection of the most common geometries is shown in Figure 3.2. In each case, when the two different coils (represented by black and gray shapes) are driven with a 90° phase difference, a circularly or elliptically polarized field with the desired sense of rotation is created in a region either above or below the coil, where the sample is located. A shielding ground plane can be placed on the other side of the coils if desired.

The coils must be large enough to have adequate B_1 field strength throughout the region of interest and

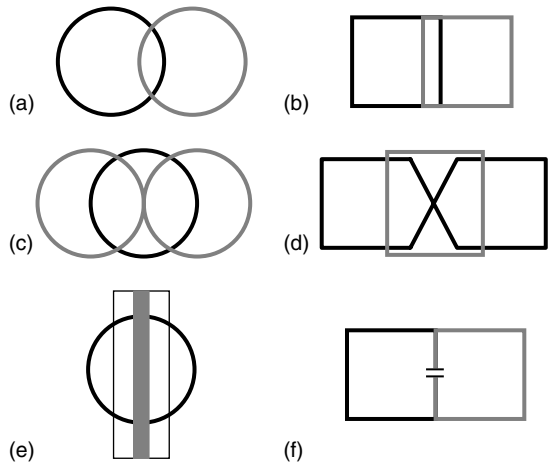

Figure 3.2. Different types of quadrature surface coils: (a) and (b) Two-loop structures with the overlap between the two coils chosen to minimize the mutual inductance. (c) and (d) Butterfly arrangements in which the intrinsic symmetry of the arrangement produces isolation between the coils. (e) A combination of single loop and stripline resonator. (f) Two loops with a single isolation capacitor between the two loops.

achieve the desired penetration depth, but if they are larger than necessary, they are sensitive to thermal noise from a larger portion of the sample, and so the SNR is degraded. For reference, the field along the axis of a single loop at low frequencies can be approximated as

$$B_y = \frac{\mu_0 I}{2} \frac{a^2}{(a^2 + y^2)^{1.5}} \tag{3.1}$$

for a circular loop where the coil axis is in the y-oriented direction, I is the coil current, a is the coil radius, and μ_0 is the magnetic susceptibility of free space. For a desired depth d within the tissue, the radius of the coil should be $d/\sqrt{5}$. For a butterfly coil, the radius of the loops in the figure-eight coil should be $0.6d$.[2]

For a rectangular loop, the corresponding equation for the magnetic field is

$$B_y = \frac{2\mu_0 I}{\pi} \frac{lw}{\sqrt{l^2 + w^2 + 4y^2}} \times \left(\frac{1}{l^2 + 4y^2} + \frac{1}{w^2 + 4y^2} \right) \tag{3.2}$$

where l and w are the length and width of the coil. Similar design criteria apply as for the circular loops,

in terms of the relationship between the values of d and r: in the crossover design shown in Figure 3.2(d) the angle between the crossover elements at the center of the coil should be greater than or equal to 150°.[2]

3.3.2 Coil Inductances

In order to determine the capacitance values necessary to resonate the RF coil at the desired frequency, the first step is to calculate the inductance of the coil. For example, the inductance of a circular loop of wire at low frequencies can be approximated as

$$L(nH) = \frac{\pi}{5} d_{\text{coil}} \left(\ln \left(\frac{8 d_{\text{coil}}}{d_{\text{wire}}} \right) - 2 \right) \tag{3.3}$$

where the coil and wire diameters, d_{coil} and d_{wire}, respectively, are measured in millimeters, and d_{coil} is measured from the center of the conductor. For a rectangular loop of round wire,

$$L(nH) = 0.4 \begin{bmatrix} (w+l)\ln\left(\frac{4lw}{d_{\text{wire}}}\right) - l\ln(a+t) \\ -w\ln(l+t) + 2\left(\frac{t+d_{\text{wire}}}{2}\right) - 2(w+l) \end{bmatrix} \tag{3.4}$$

where w and l are the width and length of the coil, respectively, and $t = \sqrt{(w^2 + l^2)}$.

3.3.3 Conductor Lengths

As is the case with all coil designs, the length of each conductor element has a major effect on the coil efficiency. Following the rule of thumb that individual segments of the coil should have a length less than 1/10 of the wavelength at the Larmor frequency ensures that phase shifts along the length of the coil are kept to a minimum. In principle, the use of several capacitors in series with these elements, rather than a single capacitor, means that the conservative electric field entering the patient is kept to a minimum, and frequency shifts between the unloaded and loaded coils are similarly minimized. If L is the inductance of the unsegmented loop, then the capacitance required to resonate it at the Larmor frequency is

$$C_{\text{seg}} = \frac{n_{\text{seg}}}{L_{\text{loop}}} \omega_0^2 \tag{3.5}$$

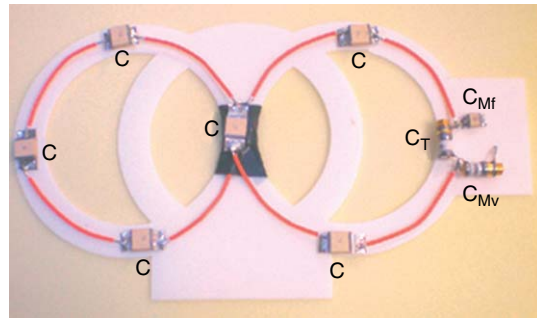

Figure 3.3. Photograph of the butterfly portion of a quadrature surface coil. Shown are the segmenting capacitors (C), variable tuning capacitor (C_T), and variable and fixed matching capacitors (C_{Mv} and C_{Mf}) arranged in a balanced configuration. The conductors are 2-mm diameter silver wires with a Teflon coating.

Balanced impedance matching should be used to maximize sensitivity and patient safety (Figure 3.3).[3] The use of cable traps and baluns also improve the performance of the coil, and are particularly important when the coil is used in receive mode only, since large currents can be induced in the coaxial cables when the volume coil transmits high-power pulses.

3.3.4 Quadrature Isolation

From simple electrical circuit theory, if two circuits resonating at the same frequency (f_0) are brought into close proximity, then the resonances will split, with one frequency being shifted above f_0 and the other below f_0. The coupling between the two resonators can be characterized by the coupling coefficient k. For MRI coils, this can often be approximated as

$$k = \frac{L_{12}}{L_1 L_1} \tag{3.6}$$

where the mutual inductance between the two coils, L_{12}, can be calculated as

$$L_{12} = \frac{1}{\mu} \int \mathbf{B}_{1,\text{coil1}} \cdot \mathbf{B}_{1,\text{coil2}} \mathrm{d}V \tag{3.7}$$

or with other standard equations and the self-inductance of the individual coils, L_1 and L_2, can be calculated from equations (3.3) and (3.4) or similar ones. To first order, the two shifted frequencies can

then be calculated as

$$f_{\text{upper}} = f_0(1 + k)$$
$$f_{\text{lower}} = f_0(1 - k) \quad (3.8)$$

Since neither circuit now resonates at f_0, the combined coil is highly inefficient. In addition, noise will be coupled from one circuit into the other. There are a variety of methods by which the coupling between the coils can be minimized. Since the coupling is predominantly due to the mutual inductance between the coils (L_{12}), this can be reduced by optimizing the overlap between the two coils. For two circular loops, the distance between the centers of the two loops at which the mutual inductance becomes zero is ~0.78 times the loop diameter. For two square loops, the distance is ~0.86 times the linear dimension in which the coils are overlapped. For a combination of a butterfly coil and a single loop or a single loop and a stripline element, in principle, the maximum decoupling will occur when the coil centers overlap exactly. Further decoupling can be accomplished with the use of decoupling capacitors between the coils or other approaches.[4,5]

3.3.5 Isolation of the Quadrature Surface Coil from the Transmit Coil

In most clinical applications, surface coils are used in receive-only mode, and must be decoupled from the transmit coil to ensure that no power enters the receive chain during transmission, potentially damaging sensitive electronic components. There are a number of different designs for such decoupling, all of which use active switching of PIN diodes. One very simple design, shown for only one element of the quadrature pair for simplicity, is shown in Figure 3.4. During the transmit phase, the diode is forward biased and forms a parallel circuit consisting of L and C_{m2}. This parallel circuit, in series with the circuit formed by the coil and C_t produces two resonances, each of which is shifted from f_0. During receive, the diode is reverse biased, thus being removed from the circuit, which resonates at the desired frequency with elements C_t, C_{m1}, and C_{m2}.

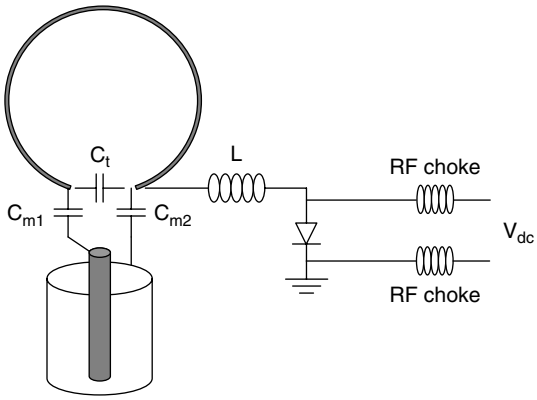

Figure 3.4. Simple circuit for decoupling a receive-only surface coil from a larger transmit coil using active PIN-diode switching. The dc current from the PIN-diode driver passes through two RF chokes (inductor) to isolate the high frequency and dc components of the circuit.

3.3.6 Predicted Field and SNR Patterns

Just as any 3D field can be separated into orthogonal components in a Cartesian coordinate system (i.e., x-, y-, and z-oriented components), so it can also be separated into a longitudinal component ($B_1{}^z$) and two circularly polarized components in the transverse plane with opposite directions of rotation ($B_1{}^+$ and $B_1{}^-$). It is customary in MRI to associate the term $B_1{}^+$ with the component that rotates in the same direction as nuclear precession and the term $B_1{}^-$ as the counterrotating component, rotating opposite to the direction of nuclear precession.[6] Since nuclear precession has a left-handed rotation about B_0,[7] however, this requires that $B_1{}^+$ and $B_1{}^-$ have unconventional definitions with respect to the direction of rotation when B_0 is oriented in the positive z-direction. For B_0 oriented antiparallel to the z-axis, $B_1{}^+ = (B_x + iB_y)/2$ and $B_1{}^- = (B_x - iB_y)^*/2$ where $B_1{}^+$, $B_1{}^-$, B_x, and B_y are all complex quantities having magnitude and phase, i is the imaginary unit, and the asterisk indicates the complex conjugate.

Since it rotates in the same direction as nuclear precession, $B_1{}^+$ interacts with the nuclei during excitation and is the pertinent component in producing a tip angle when driving the coil. It can be shown that applying the principle of reciprocity requires consideration of the $B_1{}^-$ field distribution when determining the receptivity distribution of the coil. While different mathematical derivations have been presented to explain this,[6,8,9] it is useful to consider the principle of reciprocity by driving the coil through the receive channel of the quadrature splitter (in which case a

primarily counterrotating field is created) or alternatively to consider that circularly polarized waves traveling to and from a given location must have opposite "handedness" (with the thumb indicating the direction of travel) in order to have magnetic fields with the same sense of rotation at the location of interest.

The field distribution pertinent for reception is the B_1^- field produced when the coils have opposite polarity than that used during transmission, or when the quadrature hybrid is driven through the receive port. Field distributions for pertinent and nonpertinent circularly polarized field components in transmission and reception have been described previously for a two-loop quadrature surface coil wrapped about a spherical sample at 300 MHz, where the sample was near a true dielectric resonance.[10] In Figure 3.5, distributions of these components are shown for a flat two-loop quadrature surface coil placed against a lossy slab of muscle tissue at 64 MHz. It is clear that when driving through either given channel of the quadrature splitter/combiner, only one field polarization is produced efficiently in the sample. At locations where the field is truly circularly polarized, there are voids in the counterrotating component. Thus, if images show significant signal voids, it is a strong indication that the cables connected to the RF coils must be switched to achieve the proper polarization.

As can be seen in Figure 3.5, the circularly polarized components of the RF magnetic field, B_1^+ and B_1^-, are typically shifted in opposite directions from each other in the presence of conductive samples.[11–13] The electrical currents induced in the sample by the changing magnetic fields are roughly 90° out of phase with the incident RF magnetic fields and thus (at least in the absence of significant wavelength effects) roughly 90° out of phase with the currents in the coil. These induced eddy currents in the sample produce a secondary magnetic field that is 90° out of phase with the primary field (produced by the coil in the absence of a conductive sample) and, in general, having a different orientation. When considering the vector nature and time dependence of these fields, it can be seen that the combination of the primary and secondary fields for a given single-channel coil will often cause a shift in opposite directions for B_1^+ and B_1^- (Figures 3.5 and 3.6). When the same coil is used for both transmission and reception, however, fairly symmetric images can still result, especially for low flip angles where the transverse magnetization is roughly proportional to B_1^+.

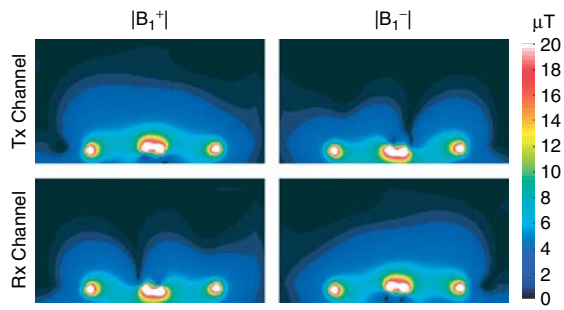

Figure 3.5. Distribution of pertinent and nonpertinent circularly polarized components of the B_1 field in transmission and in reception. Here B_1^+ is pertinent during transmission and B_1^- during reception. Distributions are calculated for a two-loop quadrature surface coil 1 cm from a slab of muscle tissue at 64 MHz. Each loop has a diameter of 17 cm, and is driven with 100 V. In simulation, results for transmit and receive channels are achieved by applying opposite polarity in each coil.

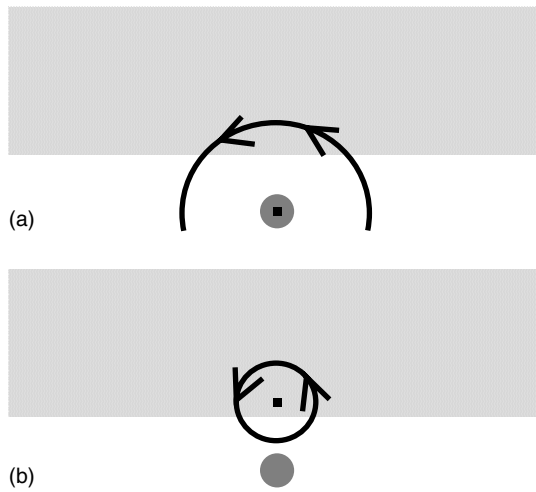

Figure 3.6. Conceptual diagram illustrating the source of asymmetry in B_1^+ and B_1^- despite symmetric current and sample. Magnetic flux density (solid black line and arrows) at a time (a) when the electrical current coming out of page (single black dot) is maximum in a current element (dark gray circle) and (b) when it is maximum in a nearby conductive sample (light gray box). The electrical current in the sample lags that in the coil by approximately 90° (neglecting wavelength effects), causing an elliptically polarized magnetic flux density with overall rotation in the clockwise direction to the right of center and in the counterclockwise direction to the left of center.

It is possible to calculate an intrinsic signal-to-noise ratio (ISNR) based on field distributions in the sample using a variety of different methods.[14–18] In general, the ISNR is proportional to the received signal intensity and inversely proportional to the square root of dissipated power. As an example, we calculate ISNR distributions for three quadrature surface coil geometries at 64 and 300 MHz using an equation for short-TR spoiled gradient-echo imaging[19]

$$\mathrm{ISNR} \propto \frac{\sin(\gamma|B_1^+|\tau)(1-e^{-\mathrm{TR}/T_1})|B_1^-|}{(1-e^{-\mathrm{TR}/T_1}\cos(\gamma|B_1^+|\tau))\sqrt{P_{\mathrm{diss}}}} \quad (3.9)$$

where γ is the gyromagnetic ratio for ^{1}H (42.58 MHz T^{-1}), τ is the effective pulse duration (3 ms), P_{diss} is the power dissipated in the sample (neglecting coil noise), and TR/T_1, the ratio of repetition time to longitudinal relaxation time, is 0.25. Figure 3.7 shows the ISNR distribution for both a receive-only case (with a homogeneous $B_1{}^+$ and flip angle of 30°), and for a transmit/receive case, using calculated $B_1{}^+$ and $B_1{}^-$ for the quadrature surface coil assuming a target flip angle ($\gamma|B_1{}^+|\tau$) of 30° at a depth of 5 cm into the sample on a line through the center of the coil, and the corresponding SAR distribution, all at 64 MHz. Figure 3.8 shows these same distributions at 300 MHz. In these simulations, the diameter of each circular loop is 17 cm, and the loop nearest the sample is 1 cm away from the surface of the sample.

The results in Figures 3.7 and 3.8 illustrate how different coil geometries can give very different SNR and SAR distributions. The butterfly/loop combination appears to have relatively homogeneous ISNR and SAR distributions, probably due to having the most widely distributed current and the largest overall size. The loop/stripline combination can achieve higher ISNR at some locations near the coil, but, due to its limited number of current elements and relatively small overall size, it has a less homogeneous ISNR distribution and requires stronger currents (inducing greater SAR) to achieve a given $B_1{}^+$ magnitude at 5 cm into the sample. Although quasi-static approximations would predict a 21.8-fold increase in absorbed power and SAR from 64 to 300 MHz, for the two-loop case, the actual absorbed power (and average SAR) increases by a factor of 28.9 while the maximum SAR in a 2-mm cubic

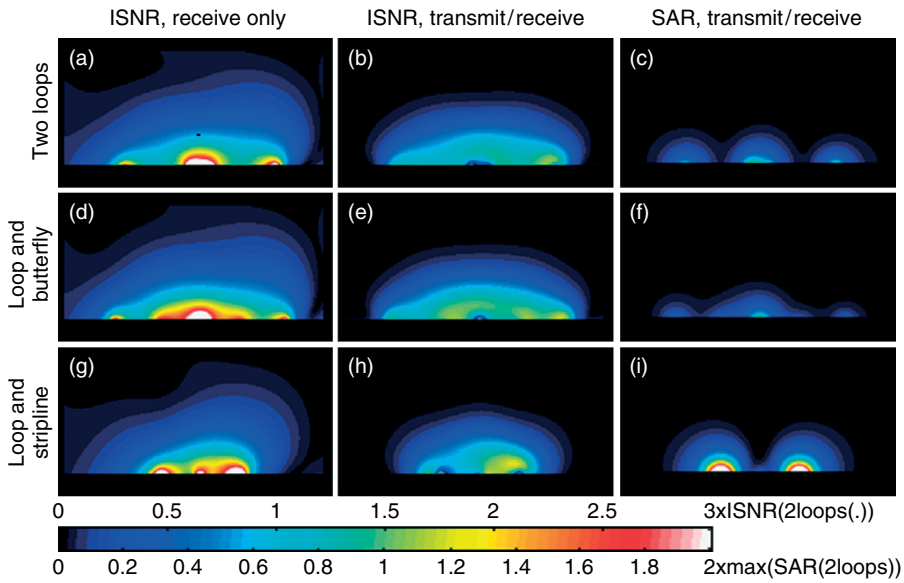

Figure 3.7. ISNR distribution for both a receive-only case (a,d,g) and for a transmit/receive case (b,e,h), and the transmit SAR distribution (c,f,i) for three different quadrature surface coil geometries, all on a transverse plane through the coil center at 64 MHz. Results for ISNR at each frequency are normalized to the value at 5-cm depth for the receive-only two-loop case (location of black dot in (a)), and results for SAR at each frequency are for achieving the same $B_1{}^+$ magnitude at the 5-cm location, normalized to the maximum value for the transmit/receive two-loop case.

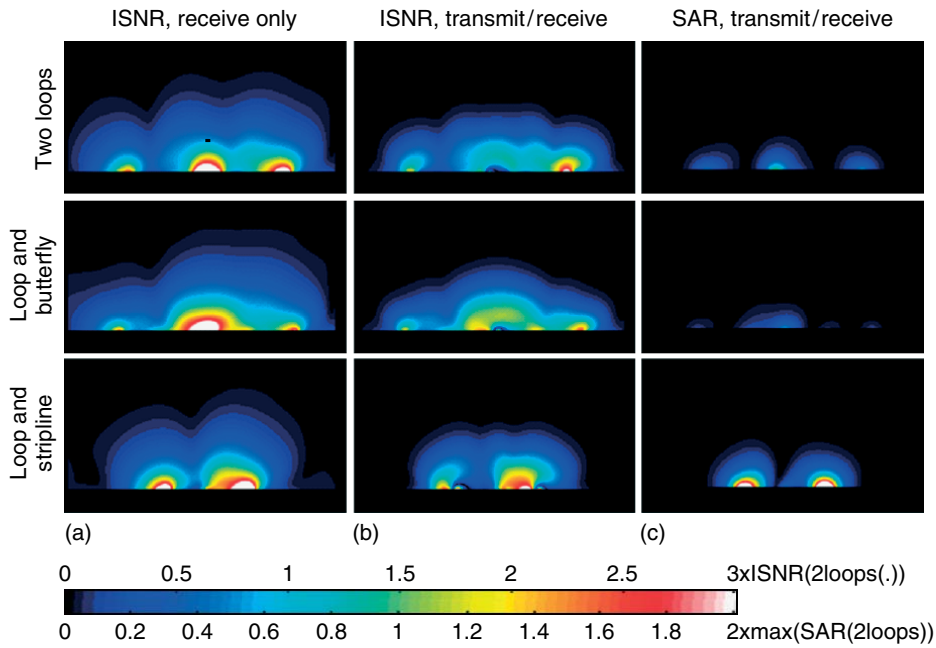

Figure 3.8. ISNR distribution for both a receive-only case (a) and for a transmit/receive case (b), and the transmit SAR distribution for three different quadrature surface coil geometries (c), all on a transverse plane through the coil center at 300 MHz. Results normalized as in Figure 3.7, but to values at 300 MHz. To compare with values for 64 MHz in Figure 3.8, multiply scale here by 4.67 for ISNR and by 59.9 for SAR.

region increases by a factor of 59.9. This indicates that the field distributions change from 64 to 300 MHz in such a way that decreasing penetration depths adversely affect possible gains. This effect is likely exaggerated here compared to that in the human body due to use of a slab of pure muscle tissue—one of the more conductive tissues of the human body—as a sample. A thorough analysis of these designs for receive-only configuration has been published recently.[2]

3.4 COIL TESTING AND EVALUATION

3.4.1 Network Analyzer Measurements

Either a human subject, or a loading phantom with size and dielectric properties similar to the particular part of the body to be imaged, should be used for optimizing the fine-tuning of the coil. The coil should not be placed directly next to the sample, since this produces heavy losses from the strong electric fields close to the coil, and also an input impedance that is highly dependent on very small changes in separation between the coil and the sample. Typically, a spacer of ~1/10 of the diameter of the loop should be used. Three measurements are made, the S_{11}, S_{22}, and S_{12}, the latter of which measures the isolation between the two channels. First, the S_{11} and S_{22} values for each individual coil should be less than -20 dB using variable tuning and matching capacitors. Then the overlap between the two coils should be optimized by positioning the two coils such that the S_{11} and S_{22} measurements both show single peaks at the original frequencies. In this case, the S_{12} should ideally be less than -20 dB. Results from a single loop/butterfly pair constructed for cardiac imaging at 7 T are shown in Figure 3.9.

After ensuring optimal operation under loaded conditions, another standard quantity to measure is the unloaded versus loaded Q-value. A high ratio indicates a relatively efficient coil, as most energy loss is due to the generation of the RF fields in the lossy

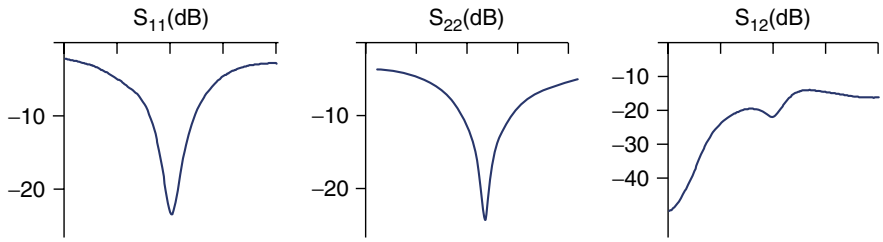

Figure 3.9. Example of *S*-parameter plots for the two channels of a quadrature surface coil placed on the chest of a human volunteer: 2 cm of foam padding was used as a spacer between the RF coils and the subject.

sample rather than to the source electrical currents in the resistive coil elements. Since surface coils couple tightly to the sample, a ratio of 10 : 1 or higher for the unloaded : loaded Q-value is usually realizable at field strengths of 3 T and above for proton resonators.

3.5 APPLICATIONS

The use of quadrature surface coils in standard clinical MRI setups has decreased significantly over the past decade with the introduction of multielement phased arrays. However, one can consider the quadrature surface coil to be the basic building block for such arrays, essentially forming a two-element array. Currently, the quadrature surface coil finds most use in more specialized applications, both in terms of heteronuclear spectroscopy and high-field proton imaging, where a body coil is not commercially available.

Single-tuned or double-tuned quadrature surface coils are widely used in localized ^{31}P spectroscopy of brain, muscle,[20] liver,[21] and heart.[22] To enable absolute quantitation, adiabatic RF pulses are used to obtain as homogeneous an excitation field as possible. Spectral localization techniques include multidimensional chemical shift imaging or the single-voxel image selection image-selected in vivo spectroscopy (ISIS) sequence.

These coils are also very useful for localized proton decoupling of ^{13}C spectra to keep the SAR limits within the International Electrotechnical Commission (IEC) and Food and Drug Administration (FDA) limits. An example is shown in Figure 3.10, in which a quadrature proton coil is used in combination with a linear ^{13}C coil for signal detection.[23]

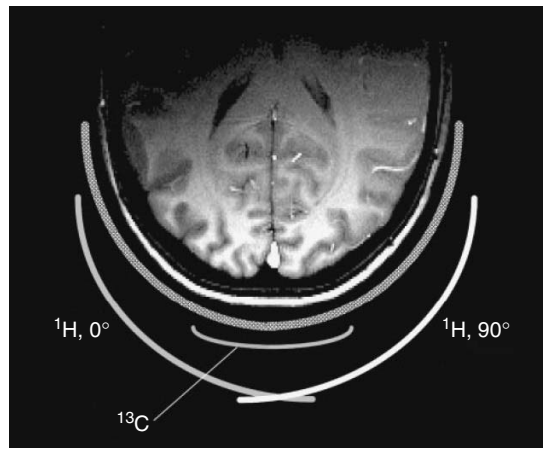

Figure 3.10. Cross-sectional view of a half-volume ^{13}C–^{1}H coil. The ^{1}H coil consists of two surface coil loops with distributed capacitance. The geometric arrangement of the two coils in conjunction with a quadrature hybrid generates a circularly polarized RF field over the field of view of the smaller ^{13}C surface coil which is placed above the intersection of the two ^{1}H coils. The ^{13}C coil overlaps partially with each of the ^{1}H coils, thereby minimizing the voltage induced by the ^{1}H coil in the ^{13}C coil. The T_1-weighted MDEFT image of a human head is shown to illustrate the excellent quality and relative homogeneity of the resulting ^{1}H RF field.

Finally, at very high fields, quadrature surface coils can be used as transmit/receive coils. An example is shown in Figure 3.11, in which images of the heart are obtained with a loop/butterfly configuration at 7 T, showing the improvements in B_1 homogeneity of the quadrature coil compared to a linear coil, and also the effects of connecting the coil up in the incorrect configuration.[24]

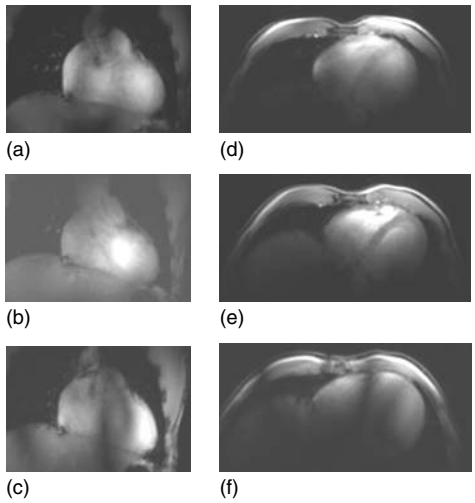

Figure 3.11. (a,b,c) Coronal and (d,e,f) axial low-resolution scout images acquired using different coil configurations. (a,d) Single loop coil; (b,e) loop/butterfly pair in quadrature configuration; (c,f) loop/butterfly pair in an antiquadrature configuration. Sequence parameters: turboFLASH sequence, TR/TR 4/1.82 ms, in-plane resolution 2.3 × 4.7 mm, slice thickness 10 mm.

3.6 TROUBLESHOOTING

The main challenges for successful quadrature surface coil compared to single-surface coil include achieving adequate decoupling (or isolation) and ensuring the correct polarization of the quadrature splitter–combiner.

If significant resonant splitting is observed between the two coils (i.e., they cannot successfully be tuned to the same frequency), better decoupling is necessary. Small adjustments in coil geometry may be adequate, but other approaches, especially the use of decoupling capacitors,[5] may also be used.

If, in an otherwise well-constructed coil, significant signal voids appear in the image, it is possible that the coil is not connected to the quadrature splitter/combiner with the proper polarization (it is in "antiquadrature"). If so, reversing the order in which the two coils are connected to the two quadrature channels may resolve the problem.

REFERENCES

1. D. I. Hoult, C.-N. Chen, and V. J. Sank, *Magn. Reson. Med.*, 1984, **1**, 339.
2. A. Kumar and P. A. Bottomley, *Magn. Reson. Mater. Phys.*, 2008, **21**, 41.
3. J. Muphy-Boesch and A. P. Koretsky, *J. Magn. Reson.*, 1983, **54**, 526.
4. H. T. Hui, B. K. Li, and S. Crozier, *IEEE Trans. Biomed. Eng.*, 2006, **53**, 317.
5. X. Z. Zhang and A. Webb, *J. Magn. Reson.*, 2004, **170**, 149.
6. D. I. Hoult, *Concepts Magn. Reson.*, 2000, **12**, 173.
7. E. M. Haacke, R. W. Brown, M. R. Thompson, and R. Venkatesan *Magnetic Resonance Imaging—Physical Principles and Sequence Design*, Wiley-Liss: New York, 1999, p 29.
8. R. Stollberger and P. Wach, In *Eighth Annual Meeting of the Society for Magnetic Resonance in Medicine*, August 12–18, Amsterdam, 1989, p 1174.
9. T. S. Ibrahim, *Magn. Reson. Med.*, 2005, **54**, 677.
10. J. H. Wang, Q. X. Yang, C. M. Collins, M. B. Smith, X. Zhang, H. Liu, X.-H. Zhu, G. Adriany, K. Ugurbil, and W. Chen, *Magn. Reson. Med.*, 2002, **48**, 362.
11. C. C. Hanstock, J. A. Lunt, and P. S. Allen, *Magn. Reson. Med.*, 1988, **7**, 204.
12. C. M. Collins, Q. X. Yang, J. H. Wang, X.-H. Zhu, G. Adriany, S. Michaeli, J. T. Vaughan, X. Zhang, H. Liu, P. Anderson, K. Ugurbil, M. B. Smith, and W. Chen, *Magn. Reson. Med.*, 2002, **47**, 1026.
13. P.-F. van de Moortele, C. Akgun, G. Adriany, S. Moeller, J. Ritter, C. M. Collins, M. B. Smith, J. T. Vaughan, and K. Ugurbil, *Magn. Reson. Med.*, 2005, **54**, 1503.
14. W. A. Edelstein, G. H. Glover, C. J. Hardy, and R. W. Redington, *Magn. Reson. Med.*, 1986, **3**, 604.
15. C. M. Collins and M. B. Smith, *Magn. Reson. Med.*, 2001, **45**, 692.
16. O. Ocali and E. Atalar, *Magn. Reson. Med.*, 1998, **39**, 462.
17. R. W. Singerman, T. J. Denison, H. Wen, and R. S. Balaban, *J. Magn. Reson.*, 1997, **125**, 72.
18. F. Wiesinger, P. Boesiger, and K. P. Pruessmann, *Magn. Reson. Med.*, 2004, **52**, 376.
19. E. M. Haacke, R. W. Brown, M. R. Thompson, and R. Venkatesan, *Magnetic Resonance Imaging—Physical Principles and Sequence Design*, Wiley-Liss: New York, 1999, p 455.
20. E. Mairiang, P. Hanpanicha, and P. Sriboonlue, *Magn. Reson. Imaging*, 2004, **22**, 715.

21. Z. Tosner, M. Dezortová, J. Tintera, and M. Hájek, *MAGMA*, 2007, **13**, 40.

22. A. M. El-Sharkawy, M. Schär, R. Ouwerkerk, R. G. Weiss, and P. A. Bottomley, *Magn. Reson. Med.*, 2009, **61**, 785.

23. G. Adriany and R. Gruetter, *J. Magn. Reson.*, 1997, **125**, 178.

24. M. J. Versluis, N. Tsekos, N. B. Smith, and A. G. Webb, *J. Magn. Reson.*, 2009, **200**, 161.

Chapter 4
Double-Tuned Surface Coils

Barbara L. Beck

McKnight Brain Institute, University of Florida, Gainesville, FL 32610, USA

4.1 INTRODUCTION

Magnetic resonance imaging and spectroscopy (MRI/S) are invaluable tools in the study and treatment of disease. MRI is a basic radiological tool used in the diagnosis of neurologic, orthopedic, cardiovascular, and oncologic disorders. MRS, the discipline out of which MRI developed, can be used for noninvasive detection and quantification of various metabolites in biological tissue. A continuing trend in magnetic resonance is the use of higher magnetic field strengths, with whole-body MRI scanners having static magnetic fields of 3–7 T and smaller bore animal MRI scanners with static magnetic fields up to 21 T. Since the available signal is proportional to the nuclear magnetization and the resonance frequency, these higher magnetic fields offer greater signal for any given nuclear species and has made in vivo MRS a mainstay of medical research. Typically, MRI and MRS are combined into one experiment where MRI is used to shim and obtain localized images and/or ^{1}H spectra and MRS is used to obtain metabolic information by acquiring spectra of ^{31}P, ^{23}Na, ^{13}C, or other nuclei. For the coil designer, this means tuning one coil to multiple frequencies, and various schemes have been introduced in the literature. These multiple frequency solutions can be implemented with surface coils, volume coils, or a combination of the two. This chapter focuses solely on the multiple frequency solutions as applied to surface coils. The earliest approaches to double-tuning surface coils involved quarter-wave transmission lines to tune and match[1–4] or variable length lines to displace tuning components outside the sample environment.[5,6] These transmission line schemes all suffered insertion losses that degraded the Q of the system. Later techniques circumvented transmission line losses by positioning all tuning components at the sample coil, although incurring losses elsewhere. These later techniques are the most commonly employed on surface coils today and can be grouped into two main categories; multiple pole circuits and transformer-coupled circuits. This chapter discusses the theory behind these two strategies, their equivalent forms, various implementations found in the literature, and impedance matching at multiple frequencies.

RF Coils for MRI
Edited by J. Thomas Vaughan and John R. Griffiths

ISBN: 978-0-470-77076-4

4.2 BACKGROUND

4.2.1 Multiple Pole Circuits

A surface coil is designed to be placed on top of a tissue of interest, and to fit such that the size of the coil generates a B_1 field that optimally covers the region of interest. The simplest visualization of the surface coil is that of a parallel resonant circuit whose frequency of operation is determined by the reactances of the loop inductor and the capacitor attached to it. To understand the multiple pole configurations, we must explore these reactance relationships. Figure 4.1(a) shows the reactances of an inductor and capacitor across a range of frequencies. The inductive reactance X_L varies as ω_L and the capacitive reactance X_C varies as $1/\omega_C$. The inductor and capacitor can be placed in a series or parallel configuration, with each configuration yielding a different reactance curve across frequency, shown in Figure 4.1(b), where the total reactance is given by

$$X_{T_{\text{series}}} = X_L + X_C \tag{4.1}$$

$$\frac{1}{X_{T_{\text{parallel}}}} = \frac{1}{X_L} + \frac{1}{X_C} \tag{4.2}$$

where $X_L = j\omega L$, $X_C = \frac{1}{j\omega C}$, and $j = \sqrt{-1}$.

A useful configuration of reactive components for a multiple-pole, double-resonant coil is a capacitor in series with a parallel combination of an inductor and capacitor.[7] This circuit and its reactance plot are shown in Figure 4.2(a). The reactance is at first capacitive, then becomes inductive as it passes through the pole of the parallel combination, and then is capacitive again.

If we plot the negative of the inductive reactance on top of this (Figure 4.2b), we will find points where the two traces intersect. These are the points where the capacitive and inductive reactances are equal and define the resonant frequencies of the circuit. We now have a circuit that is resonant at two frequencies consisting of the main coil inductor L_s and discrete components C_1, L_1, and C_s.

The multipole circuit described above has several equivalent circuits, shown in Figure 4.3. In addition, this technique has been applied to a quadruple resonant circuit.[8]

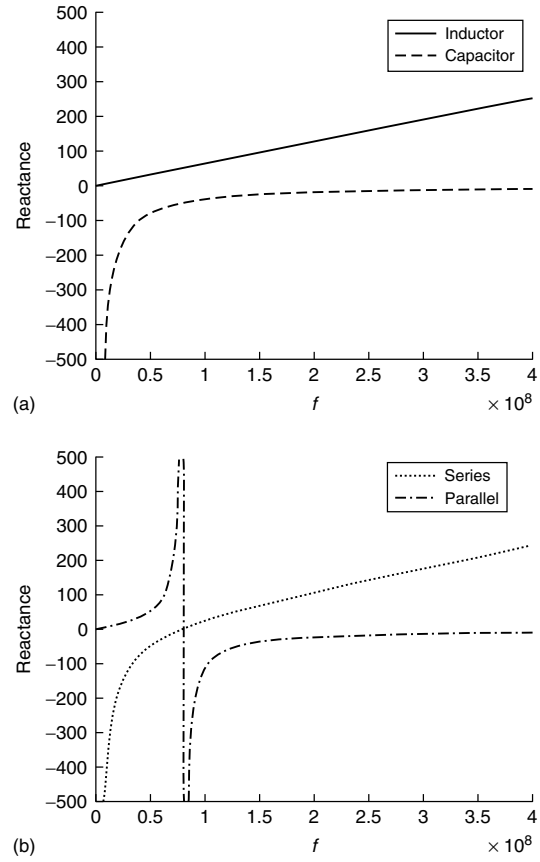

Figure 4.1. Plot of reactance across frequency of (a) a single inductor (__) or capacitor (- - -), and (b) series (. . .) and parallel (__.__) combinations of an inductor and capacitor.

4.2.2 Transformer-coupled Circuits

The transformer-coupled circuit is based on the principle of mutual inductance, in which two inductors share magnetic field and induce voltages in each other. In Figure 4.4, current I_1 circulating in L_1 generates flux Φ_{12}, which links with inductor L_2. The mutual inductance in terms of flux linkage[9] is

$$M_{12} = \frac{\text{Linkages in } L_2 \text{ produced by } I_1}{I_1} = \frac{N_2\Phi_{12}}{I_1} \tag{4.3}$$

where M_{12} is the mutual inductance between L_1 and L_2, and N_2 is the number of turns in L_2. Conversely, M_{21} is the ratio of the flux linkages in L_1 produced by a current I_2, to the current I_2. A changing current

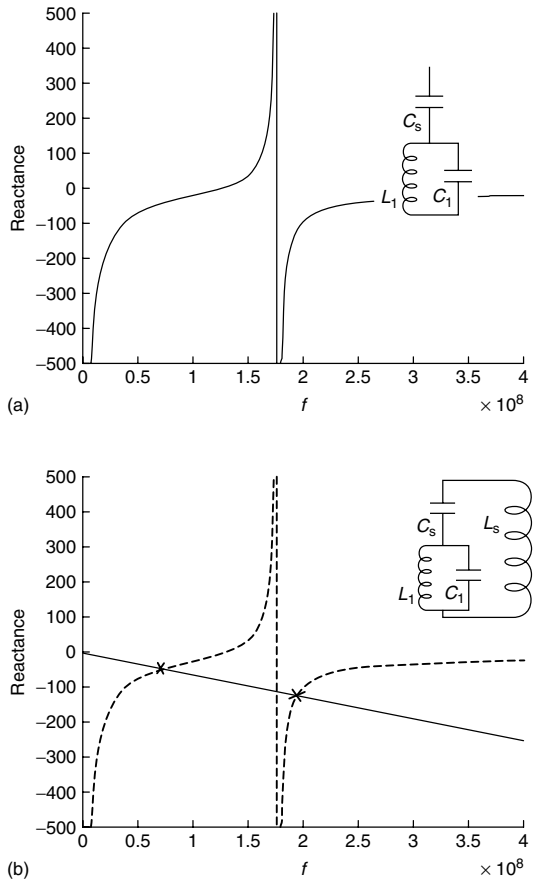

Figure 4.2. Plot of reactance across frequency of (a) a useful component combination for creating a pole, and (b) the negative of the inductive reactance superimposed on the pole plot and intersecting it twice (X).

in one coil will induce an open circuit voltage in the second coil and, if the current is sinusoidal, the voltage induced is

$$V_2 = -j\omega MI_1 \tag{4.4}$$

where $\omega = 2\pi f$ and f is the operating frequency. The voltage is negative because, according to Lenz's Law, the induced voltage is in a direction to oppose the change of current.

A coupling coefficient k with values between 0 and 1 is an indicator of the flux linkage between the two coils and is written as

$$k = \frac{M}{\sqrt{L_1 L_2}} \tag{4.5}$$

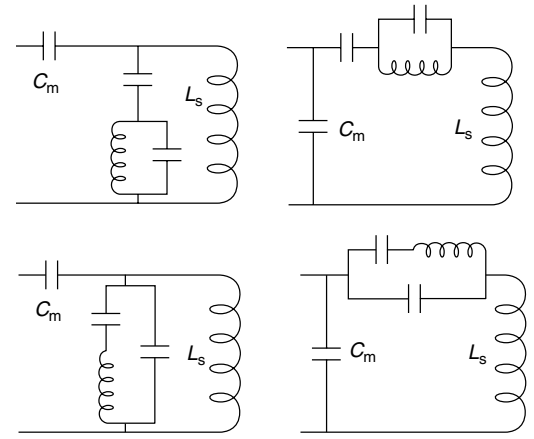

Figure 4.3. Equivalent configurations of the multiple pole circuits.

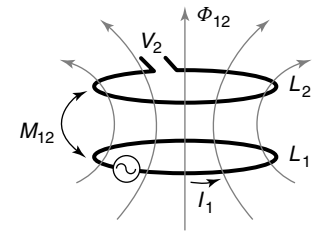

Figure 4.4. Flux linkage between adjacent loops of wire.

The idealized configuration above lends itself to the straightforward mathematical description given in equations (4.3–4.5). In reality, the variations on this simple circuit, such as differing radii, noncircular geometries, and varying distance between inductors, require special consideration for correct mathematical description. Indeed, entire textbooks have been written on inductance calculations.[10] But the above analysis sets the background for the following discussion.

For our investigation of double-tuned coils, we turn our focus to a tuned transformer-coupled circuit,[11] shown in Figure 4.5. The amount of coupling and the value of the primary and secondary reactive components determine the performance of the circuit.

Let us first assume that $L_s = L_p$ and $C_s = C_p$ such that the resonant frequencies of the primary and secondary are equal. We know from Figure 4.3 that there will be mutual inductance M because of flux linkage between the coils. However, we also know that the coupling coefficient k will depend on the value of the

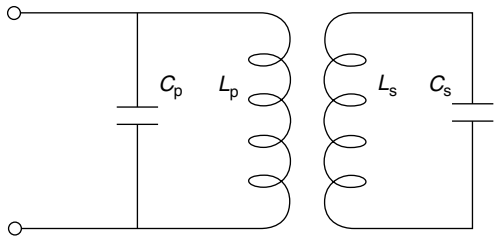

Figure 4.5. A tuned transformer coupled circuit.

inductances M, L_s, and L_p. The effect of k on the performance of the circuit of Figure 4.5 can be evaluated by PSpice simulation. Figure 4.6 shows the primary and secondary currents in L_p and L_s as k is varied.

Looking closely at the secondary current, a point is observed where the current is maximum, as shown in Figure 4.6(b). This is the point of critical coupling k_c, where the resistance of the secondary coupled into the primary is equal to the primary resistance.[12] When $k < k_c$, the coils are undercoupled and the primary and secondary currents occur at one frequency. Alternatively, when $k > k_c$, the coils are overcoupled and the currents are split between two frequencies. This is the coupling configuration utilized by a transformer-coupled double-tuned coil, except $C_s \neq C_p$ and L_s may or may not equal L_p.

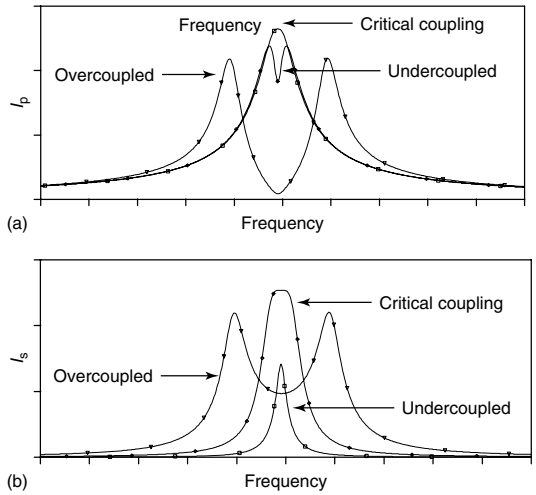

Figure 4.6. (a) Primary coil currents and (b) secondary coil currents of tuned, transformer-coupled circuits in three coupling conditions: undercoupled, critical coupling, and overcoupled.

Further exploration of the overcoupled case reveals that the phase of the currents in the primary and secondary are in phase, or co-rotating, at the lower frequency and 180° out of phase, or counter-rotating, at the upper frequency. The fields generated by the two overcoupled inductors will add at the lower frequency and subtract at the higher frequency. The particular geometric configuration of the two inductors will determine the resultant field and efficiency of the coil pair. For a coplanar pair,[11] the low-frequency, co-rotating currents generate a field slightly larger than a single coil alone. Conversely, at the higher frequency, the counter-rotating currents generate a field that is significantly lower than a single coil alone. As a result, the signal intensity at the low frequency is equivalent to or slightly higher than a single coil, but significantly lower (~50%) than a single coil at the high frequency.

4.3 CONSTRUCTION

4.3.1 Multiple Pole Circuits

Construction of a double-tuned coil based on the multiple pole technique (Figure 4.2b) requires special attention be given to the value of L_1 because it is a discrete inductor with a detectable resistive loss. This may be especially noticeable in the lower frequency circuit because it corresponds to the lower γ nuclei where the NMR sensitivity is inherently lower. At the higher frequency, the losses are dominated by the sample and the resistive loss in the inductor L_1 may be less noticeable. These losses can be understood by evaluating the efficiency of the circuit. In the simplest terms, it is a ratio of the power delivered to the coil inductor to the power dissipated in the tuning components, primarily the trap inductor. These efficiencies can be formulated as ratios of inductances. Assuming that the coil is loaded and that the resistances of the inductors are proportional to the inductances, the efficiency of the low- and high-frequency modes[7] can be written as

$$E_{\text{low}} = \sqrt{\frac{L_s}{L_1 + L_s}} \tag{4.6}$$

$$E_{\text{high}} = \sqrt{\frac{L_1}{L_1 + L_s}} \tag{4.7}$$

The low-frequency efficiency will be the best if the inductance L_1 is small compared to L_s. Conversely, the high-frequency efficiency will be the best if the inductance L_1 is large compared to L_s. Practical starting points for the ratio of L_s/L_1 are 4 or 5, yielding an efficiency of ~90% for the low frequency and ~45% for the high frequency. In the low frequency, the trap resonance is above the mode frequency and the reactance primarily inductive, with most of the trap current flowing through the trap inductor. L_1 and C_s are the controlling reactive components and C_s can be used to vary the low frequency. At the high frequency, the situation is reversed. The trap resonant frequency is below the mode frequency and the reactance primarily capacitive, with most of the current flowing through the trap capacitor. C_1 and C_s are now the controlling reactive components and C_1 can be used to vary the high frequency.

As an example, the circuit in Figure 4.7 can be implemented at 2 T for proton imaging at 85 MHz and phosphorus spectroscopy at 34 MHz with a circular loop of AWG 14 copper wire, a coil diameter of 4.5 cm (L_s), $C_s = 165$ pF, $C_1 = 180$ pF, and $L_1 = 22$ nH. L_1 is chosen to be approximately one-fifth of the inductance of L_s (110 nH). L_s can be determined by building a single-tune loop of the same size, resonating it with a single capacitor, and then computing the corresponding inductance using

$$f = \frac{1}{2\pi\sqrt{L_s C_s}} \tag{4.8}$$

$$\rightarrow L_s = \frac{1}{(2\pi f)^2 C_s} \tag{4.9}$$

The low-frequency circuit is tuned first with L_1 and C_s in the circuit and adjusting C_s. Then, C_1 is placed in the circuit and its value adjusted to tune the high-frequency circuit. There will be some interaction between these two adjustments, and an iterative procedure of going back to the dominant low-frequency component (C_s) and then the high-frequency component (C_1) may be required. However, there is usually a fair amount of independence between these two tuning adjustments. Matching this double-tuned circuit can be done inductively, capacitively, through a single port, or through two separate ports. Inductive matching, shown in Figure 4.7, is based on the mutual inductance.

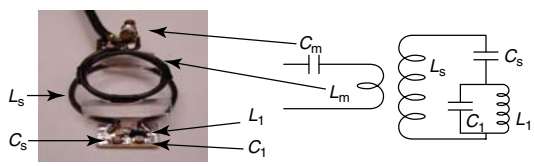

Figure 4.7. Photograph and schematic of multiple pole circuit. In this example, the circuit is inductively coupled. The two-turn matching inductor L_m is displaced coaxially by 1 cm. (See Appendix, Table A4.1).

If a matching coil L_m is placed near the sample coil L_s, the fields interact and the matching coil can be moved to adjust the amount of coupling. As the coupling changes, the impedance of the matching coil changes. The coil system is matched when the impedance looking into the matching coil has a real part equal to 50 Ω and the imaginary part equal to zero. For the circuit described above, L_m is a two-turn, 3.5 cm diameter inductor of AWG 14 copper wire and displaced 1 cm coaxially above the sample coil. A series capacitor in the matching inductor will improve the matching capability, and in this example C_m is 22 pF in parallel with a variable capacitor of value 1.5–19 pF. The low frequency is optimized when the variable is engaged ~12 turns (three-fourths of its total range) and the high frequency when engaged ~8 turns (one-half of its total range).

Note that the coupling constant k depends on the mutual inductance of the system as

$$k = \frac{M}{\sqrt{L_s L_m}} \tag{4.10}$$

where M is the mutual inductance, L_s is the inductance of the sample coil, and L_m is the inductance of the matching coil. M will change with Q and frequency[13] and require a different matching solution for each frequency, be it the physical displacement, axial or rotational between the two inductors, the size of the inductors, or the value of the series capacitor in the matching loop. The multipole circuit may also be matched with a series reactive component (most commonly a capacitor), as described in Section 4.3.2. In addition, the circuit may be driven with two ports (inductively coupled or series reactive); one port optimized for the low frequency and the other port optimized for the high frequency. The multipole circuit and its variations have been described extensively in the literature.[7,14–18]

4.3.2 Transformer-coupled Circuits

Construction of a double-tuned coil based on the transformer-coupled technique relies on the splitting of the current distribution in the overcoupled condition. Referring back to the circuit schematic of Figure 4.5, we can consider the case where $C_s \neq C_p$ and $L_s \approx L_p$ are circular loops of wire placed in a coplanar arrangement,[11] as shown in Figure 4.8. For this case, the resonant frequencies of the primary and secondary are not equal and are determined by the degree of coupling and the value of C_s and C_p.

In practice, one can consider the circuit as coupled inductors with a tuned secondary, where the secondary impedance coupled into the primary[12] appears inductive at the lower frequency and capacitive at the higher frequency. When the secondary impedance is added to the primary impedance, it requires that the capacitor C_p be chosen such that the noncoupled ($k = 0$) resonant frequency is slightly above the desired low frequency and that the capacitor C_s be chosen such that the noncoupled resonant frequency is slightly below the desired high frequency. When the two circuits are overcoupled, the primary shifts down to the desired low frequency and the secondary shifts up to the desired high frequency. For example, the circuit in Figure 4.8 can be implemented at 2 T for proton imaging at 85 MHz and phosphorus spectroscopy at 34 MHz with AWG 14 copper wire, an outer coil diameter of 4.8 cm, inner coil diameter of 4.3 cm, $C_s = 60$ pF, $C_p = 180$ pF, and C_m a variable capacitor with a range of 1.5–19 pF. The low-frequency circuit is tuned first (C_p), and then the high-frequency circuit (C_s). There will be some interaction between these two adjustments, and an iterative procedure of going back to the dominant low-frequency component (C_p), and then the high-frequency component (C_s), will be required.

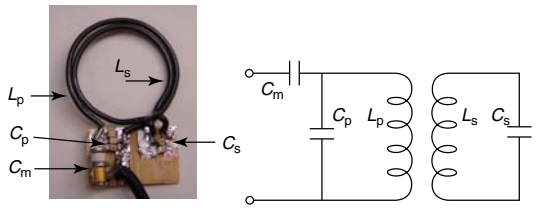

Figure 4.8. Photograph and schematic of transformer coupled circuit. In this example, the circuit is matched with a series capacitor C_m. L_s and L_p are coplanar. (See Appendix, Table A4.2).

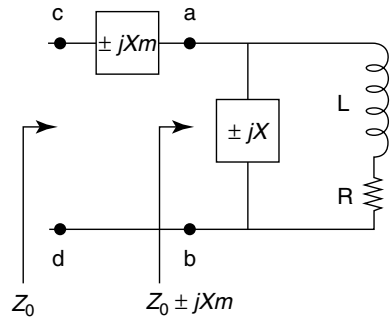

Figure 4.9. Schematic of L matching circuit. Shunt component between a–b is chosen such that the impedance looking into terminals a–b will be $Z_0 \pm jX$. The series reactance between a–c is chosen such that it is equal and opposite to the reactance between a–b resulting in an impedance looking into terminals c–d of Z_0. Z_0 is the characteristic impedance, usually 50 Ω.

A common matching method is to use a reactive component placed in series with the resonant coil, shown in Figure 4.9 as a single-tuned configuration for simplicity. The principle behind this matching method is that the component in the parallel, or shunt, connection to L is chosen such that the complex impedance looking into the parallel combination between ports a–b is,

$$Z_p = Z_0 \pm jX_m \tag{4.11}$$

where Z_0 is the characteristic impedance of the system, usually 50 Ω, and jX_m is a positive or negative reactance that results from picking the parallel component to yield the real part of Z_p equal to 50 Ω. The value of the series matching component can then be chosen to have the equal and opposite reactance of the jX_m in equation 4.11, so that the total impedance looking into the network between ports c–d is

$$Z_t = 50 + jX_m - jX_m = 50\ \Omega \tag{4.12}$$
(capacitor as series component)

or

$$Z_t = 50 - jX_m + jX_m = 50\ \Omega \tag{4.13}$$
(inductor as series component)

However, the complication for the double-tuned circuit is that this condition needs to be met at two

frequencies. The impedance coupled to the primary will be different at each frequency and require jX_m to change. In this example, C_m is a variable capacitor with range 1.5–19 pF, and optimized for the low frequency when engaged at ~4 turns (one-fourth of its total range) and the high frequency when fully engaged. In practice, the capacitor can be chosen to optimize the less sensitive nuclei at the lower frequency while maintaining sufficient, but suboptimal, match at the higher imaging frequency. Because of the mutual inductance, an iterative approach is required, returning to the low-frequency and high-frequency circuits to achieve the desired match.

As in the multiple pole circuits, the transformer-coupled circuits may be matched to system impedance using inductive coupling, but again, different impedances exist for each frequency and the inductive match must be adjusted for each. The tuned transformer-coupled circuit and its variations have been described extensively in the literature.[11,12,16,19–23]

4.4 COIL TESTING

Evaluation of any double-tuned circuit should be made in comparison to its single-tuned equivalent. That means the same materials are utilized, coil sizes are identical, and all coils are tuned and matched to the system impedance at their respective frequencies. Bench measurements of coil Q and magnetic field, and magnet measurements of the signal-to-noise ratio (SNR) and 90° power requirements should be made. Bench measurements of Q are made through direct coupling or by loose coupling of the circuit to a network analyzer.[24] Direct coupling refers to connecting the coil to the analyzer through a matching circuit (as in Figures 4.7 and 4.8). In this method, the coils must be well matched to 50 Ω to avoid reflection losses, and all cables roughly the same length so that insertion losses are equivalent. In the loose coupling method, two external probes are placed near the coil such that the field from the source probe excites the coil and the second probe senses the field from the excited coil. The probes can be placed on either side of the coil, or they can be an overlapped pair with zero mutual inductance placed on one side of the coil. In all cases, the Q is

$$Q = \frac{f_0}{BW} \tag{4.14}$$

where f_0 is the resonant frequency and BW is the frequency span between the −3 dB points.

The field may be measured utilizing a network analyzer, a thin saline phantom, and a field probe, as shown in Figure 4.10. The coil is attached to the reflection port on the analyzer, the phantom placed under the coil to provide physiologic loading (~150 mM saline), and the probe is placed approximately one radius under the coil. The field probe is attached to the transmission port of the analyzer and records the field intensity of the coil. The physical setup is held constant for all coil measurements. Again, the coils must be well matched to 50 Ω to avoid reflection losses, and all coil cables roughly the same length so that insertion losses are equivalent.

Magnet measurements can be made of optimized pulse powers and SNR of spectra or images from phantoms. A dual-chamber phantom of 150 mM saline in the outer chamber and a concentrated solution of the relevant spectroscopic nuclei in the inner chamber will allow suitable evaluation of SNR, pulse power, and B_1 field extent at both frequencies. The phantom should be thicker than that used for bench measurements, extending 2–3

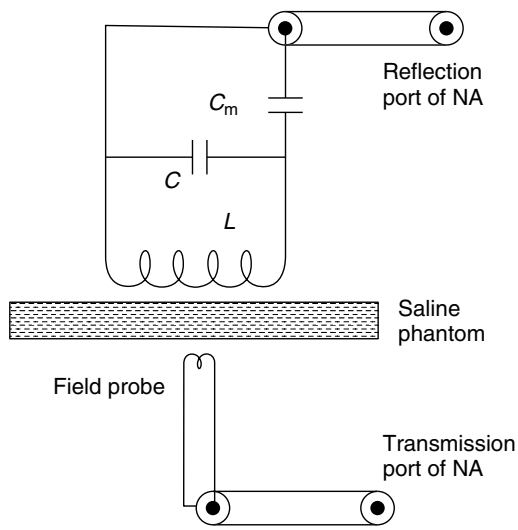

Figure 4.10. The bench evaluation set. The network analyzer supplies a small voltage to the RF coil. The magnetic field produced by the coil is coupled through the saline load to the field probe. The RF coil is tuned and matched to 50 Ω at the frequency of interest.

radii down the axis of the coil and extending beyond the coil conductors in the plane of the coil. Utilizing a single rectangular pulse of constant pulse width, spectra can be obtained from which the SNR is measured and power for a 90° tip angle recorded. Similarly, images can be acquired to measure SNR and pulse power, and should correlate with spectra results. Images can be used to evaluate the extent of B_1 coverage of the sample. This is especially important for the transformer-coupled, double-tuned coil because the countercurrents in the high-frequency mode reduce the B_1 with respect to a single-tuned coil.

4.5 COIL APPLICATION

Multiple frequency imaging and spectroscopy in vivo have been practiced for over 20 years. And as static magnetic fields have continually increased, the sensitivity of spectroscopy has increased, making the dual imaging/spectroscopy exam an important scientific tool in the study and treatment of disease. These techniques are currently being applied to many medical challenges such as multiple sclerosis, stroke, epilepsy, muscular dystrophy, cancer, congestive heart failure, and thyroid disease, among others, and to understanding the function and metabolism of multiple organs in the body. Common nuclei used in spectroscopy include ^{1}H, ^{31}P, ^{23}Na, ^{19}F, and ^{13}C. Numerous permutations of coil geometries and frequencies can be envisioned, but in the end, the particular disease under study will dictate the coil geometry and the nuclei, and the static field dictates the frequencies of operation.

4.6 TROUBLESHOOTING

The greatest advantage of a double-tuned coil is the ability to perform imaging and spectroscopy without changing coils, with shimming and localization of the area of interest achieved with the proton part of the coil and spectra of lower γ nuclei obtained with the lower frequency part of the coil. However, a complication can occur if the same tuning network is used for both imaging and spectroscopy because adjustment will be required at each frequency. The inductive match of Figure 4.7 requires either physical displacement of L_m, adjustment of C_m, or both. These adjustments are difficult to make when the coil is in the center of the magnet, and would require a long tuning wand attached to C_m or some elaborate apparatus attached to L_m to allow physical displacement. A similar argument applies to the capacitive match shown in Figure 4.8. The easiest solution to this problem is to optimize the matching for low-frequency operation and allow suboptimal matching at the imaging frequency. This is an acceptable solution if the proton coil is used for shimming and positioning. However, if the experiment requires high-resolution proton images or ^{1}H spectroscopy, the matching of the high-frequency circuit will need to be optimized as well. Some solutions to this problem have been proposed in the literature. Schnall *et al.*[7] suggests a parallel *LC* circuit in which *L* is utilized for the low-frequency match and the resultant parallel *LC* reactance utilized for the high-frequency circuit. Grist *et al.*[21] suggests a dual inductive match, with the matching loops placed orthogonally to minimize coupling between the two. Others[14,25,26] suggest a dual inductive match of fixed position and a series capacitor in the matching loops to adjust the match. Blocking traps may be needed in the matching loops to minimize coupling between the two frequencies.[22,27] In the series reactive matching technique (usually a capacitor), Viriot *et al.*[18] solves the dual-frequency matching requirements by using remote tuning boxes carefully placed at $\lambda/2$ distances from the coil. Others[19] suggest a dual-port capacitive match with blocking traps placed in the sample inductors to reduce coupling and allow independent operation of each channel. The matching scheme chosen by the coil designer will depend on the experimental requirements. If the proton channel is to be used for shimming and image placement, then a single port optimized for the low-frequency channel is the simplest implementation. However, if high-resolution images or proton spectroscopy is required, optimization of the match at both resonant frequencies will be necessary, at the cost of a more complicated physical setup or additional circuit components.

Finally, attention should be given to construction techniques because a poorly built coil can sabotage even the most exquisite theory. Soldering techniques are often overlooked by the novice when troubleshooting, but cold solder joints can cause intermittent connections that plague the proper

performance of the coil. Simple tutorials can be found online (search engine keywords "soldering tutorial" or "good soldering techniques") that demonstrate basic soldering skills. It is also advisable to spend some time planning the circuit board layout on which tuning and matching components are to be placed. If the components are placed far apart, which is the tendency for ease of physical placement, large loop areas may be created that become unwanted inductances added to the circuit. These can cause resistive losses or unwanted resonances. It is advisable to keep components as close to the sample coil as possible and minimize loop areas of current paths. High-frequency characteristics of discrete components, such as inductors, can cause unsuspected behavior. Large inductors can become self-resonant and exhibit a very high impedance or look capacitive: in short, not an inductor at all. Shield currents on cables[28] can interfere with tuning and compromise coil performance. Baluns[29,30] (see Chapter 25) and other balanced matching schemes[31] reduce voltage imbalances that can cause shield currents. Cable traps suppress shield currents that are present. These may be difficult to implement on a single-port, double-tuned coil because it would require a double-tuned balun and/or cable trap. However, a dual-port, double-tuned coil could easily implement both devices with low-frequency baluns/cable traps on one cable and high-frequency circuits on the other cable. Good construction techniques will go a long way in preventing the problems mentioned above. Awareness of these techniques will enable the coil designer to bring theory to practice.

4.7 CONCLUSION

Double-tuned surface coils make possible the acquisition of anatomic and metabolic information from a single MRI/S exam without disturbing the coil/patient setup. Such versatility enables good correlation between imaging and spectral locations. The most commonly used double-tuned circuits presented in the literature can be grouped into two categories: multiple pole and transformer-coupled. The multiple pole design inserts a discrete-component parallel resonant circuit into the sample coil, creating a pole in the reactance curve. This pole essentially creates a second capacitive reactance to resonate with the sample coil. The transformer-coupled design uses two mutually coupled, but tuned, coils with a large coupling constant to create two modes. The position of the two modes is controlled by the degree of coupling, the value of the capacitances, and the inductance of the coils. Both these double-tuning methods are very efficient in the low-frequency mode, but suffer losses in the high-frequency mode. Attention to design details and utilization of good construction techniques help minimize losses. The reader is encouraged to take advantage of the extensive reference list provided with this chapter to learn the many design permutations and subtleties already encountered by numerous researchers.

4.8 APPENDIX

See Tables A4.1 and A4.2 below.

Table A4.1. Bill of Materials for the multiple pole circuit of Figure 4.7

Component	Value	Part	Manufacturer
L_s	1 turn, 4.5 cm diameter	AWG 14 solid copper wire	Local hardware store
L_1	22 nH	B07T	Coil Craft, 1102 Silver Lake Road, Cary, IL 60013, (847) 639–6400
C_s	150 pF	ATC100B Series	American Technical Ceramics, One Norden Lane, Huntington Station, NY, 11746, (631) 622–4700
	15 pF	ATC100B Series	American Technical Ceramics (see above)
C_1	180 pF	ATC100B Series	American Technical Ceramics (see above)
C_m	22 pF	ATC100B Series	American Technical Ceramics (see above)
	1.5–19 pF	JMC55H01	Johanson Manufacturing Corporation, 301 Rockaway Valley Road, Boonton, NJ, 07005, (973) 334–2676
L_m	2 turns, 3 cm diameter		Local hardware store
Coax	RG-58 C/U	8 262	Belden Inc., 2200 U.S. Highway 27 South, Richmond, IN, 47374, 1-800-BELDEN1

Table A4.2. Bill of Materials for the transformer coupled circuit of Figure 4.8

Component	Value	Part	Manufacturer
L_p	1 turn, 4.8 cm diameter	AWG 14 solid copper wire	Local hardware store
L_s	1 turn, 4.3 cm diameter	AWG 14 solid copper wire	Local hardware store
C_p	150 pF	ATC100B Series	American Technical Ceramics, One Norden Lane, Huntington Station, NY, 11746, (631) 622–4700
	27 pF	ATC100B Series	American Technical Ceramics (see above)
	3.9 pF	ATC100B Series	American Technical Ceramics (see above)
C_s	56 pF	ATC100B Series	American Technical Ceramics (see above)
	4.3 pF	ATC100B Series	American Technical Ceramics (see above)
C_m	1.5–19 pF	JMC55H01	Johanson Manufacturing Corporation, 301 Rockaway Valley Road, Boonton, NJ, 07005, (973) 334–2676
Coax	RG-58 C/U	8 262	Belden Inc., 2200 U.S. Highway 27 South, Richmond, IN, 47374, 1-800-BELDEN1

REFERENCES

1. V. R. Cross, R. D. Hester, and J. S. Waugh, *Rev. Sci. Instrum.*, 1976, **47**, 1486–1489.
2. R. E. Gordon and W. E. Timms, *J. Magn. Reson.*, 1982, **46**, 322–324.
3. N. V. Reo, C. S. Ewy, B. A. Siegfried, and J. H. Ackerman, *J. Magn. Reson.*, 1984, **58**, 76–78.
4. A. Leroy-Willig, J. Bittoun, S. Kan, and P. Gonord, *Rev. Sci. Instrum.*, 1990, **61**, 799–801.
5. P. M. Joseph and J. E. Fishman, *Med. Phys.*, 1985, **12**, 679–681.
6. J. F. Martin and C. P. Daly, *Magn. Reson. Med.*, 1986, **3**, 346–348.
7. M. D. Schnall, V. H. Subramanian, J. S. Leigh, and B. Chance, *J. Magn. Reson.*, 1985, **65**, 122–129.
8. S. M. Eleff, M. D. Schnall, L. Ligetti, M. Osbakken, V. H. Subramanian, B. Chance, and J. S. Leigh, *Magn. Reson. Med.*, 1988, **7**, 412–424.
9. F. E. Terman, ed., *Radio Engineers' Handbook*, McGraw-Hill: New York, 1943, pp. 64–65, 154–164.
10. F. W. Grover, ed., *Inductance Calculations: Working Formulas and Tables*, D. Van Nostrand Company: New York, 1946.
11. J. R. Fitzsimmons, H. R. Brooker, and B. L. Beck, *Magn. Reson. Med.*, 1987, **5**, 471–477.
12. J. R. Fitzsimmons, B. L. Beck, and H. R. Brooker, *Magn. Reson. Med.*, 1993, **30**, 107–114.
13. D. I. Hoult and B. Tomanek, *Concept. Magn. Reson. B*, 2002, **15**, 262–285.
14. R. J. McNichols, S. M. Wright, J. S. Wasser, and G. L. Cote, *Rev. Sci. Instrum.*, 1999, **70**, 3454–3456.
15. S. S. Rajan, J. P. Wehrle, and J. D. Glickson, *J. Magn. Reson.*, 1987, **74**, 147–154.
16. M. D. Schnall, in *In Vivo Magnetic Resonance Spectroscopy I: Probehead and Radiofrequency Pulses Spectrum Analysis*, ed. M. Rudin, Springer-Verlag: New York, Berlin, Heidelberg, 1992, pp. 35–63.
17. M. O. Leach, A. Hind, R. Sauter, H. Requardt, and H. Weber, *Med. Phys.*, 1986, **13**, 510–513.
18. C. Viriot, S. Akoka, F. Seguin, and A. L. Pape, *Med. Biol. Eng. Comput.*, 1994, **32**, 427–431.
19. M. Alecci, S. Romanzetti, J. Kaffanke, A. Celik, H. P. Wegener, and N. J. Shah, *J. Magn. Reson.*, 2006, **181**, 203–211.
20. S. Kan and P. Gonord, *Rev. Sci. Instrum.*, 1991, **62**, 2427–2429.
21. T. M. Grist, A. Jesmanowicz, J. B. Kneeland, W. Froncisz, and J. S. Hyde, *Magn. Reson. Med.*, 1988, **6**, 253–264.
22. V. Volotovskyy, B. Tomanek, I. Corbin, R. Buist, U. I. Tuor, and J. Peeling, *Concept. Magn. Reson. B*, 2003, **17B**, 11–16.
23. J. R. Fitzsimmons, H. R. Brooker, and B. L. Beck, *Magn. Reson. Med.*, 1989, **10**, 302–309.
24. G. Jacobs, A. Assefa, and J. Willig-Onwuachi, In *16th Scientific Meeting of the ISMRM*, Toronto, 2008, p. 1082.
25. G. X. Shen, F. E. Boada, and K. R. Thulborn, *Magn. Reson. Med.*, 1997, **38**, 717–725.

26. T. Lanz, J. Ruff, A. Weisser, and A. Hasse, *Rev. Sci. Instrum.*, 2001, **72**, 2508–2510.

27. K. L. Zakian, J. A. Koutcher, and D. Ballon, *Magn. Reson. Med.*, 1999, **41**, 809–815.

28. D. M. Peterson, B. L. Beck, G. R. Duensing, and J. R. Fitzsimmons, *Concept. Magn. Reson. B*, 2003, **19**, 1–8.

29. C. N. Chen and D. I. Hoult, eds, in *Biomedical Magnetic Resonance Technology*, Adam Hilger: Bristol, 1989, p. 138.

30. T. Lanz, M. V. Kienlin, W. Beir, and A. Hasse, *MAGMA*, 1997, **5**, 253–246.

31. D. M. Peterson and G. R. Duensing, *RF Design*, 1997, January, 56–64.

Chapter 5
Nested Surface Coils for Multinuclear NMR

Arthur W. Magill and Rolf Gruetter

Laboratory of Functional and Metabolic Imaging, Ecole Polytechnique Federale de Lausanne, CH-1015 Lausanne, Switzerland
Department of Radiology, University of Lausanne, CH-1015 Lausanne, Switzerland
Department of Radiology, University of Geneva, CH-1211 Geneva, Switzerland

5.1 INTRODUCTION

A surface coil is any radiofrequency (RF) coil placed directly on the surface of the subject. Surface coils represent some of the simplest coil designs used in magnetic resonance, but are commonly used in experiments requiring the highest possible sensitivity.

In contrast to volume coils, which are designed to provide homogeneous sensitivity over the whole field-of-view, surface coils sacrifice field homogeneity to maximize the signal-to-noise ratio (SNR) over a limited region. Figure 5.1 shows an image of a mouse head, acquired with a volume and a surface coil. The volume coil gives a uniform image of the whole head—note that the brain occupies a relatively small part of that volume. While the NMR signal can be localized using field gradients, thermal noise cannot; coils are therefore sensitive to noise generated over their entire field-of-view. By designing a coil with a reduced field-of-view, for example covering only the brain, the noise level is immediately reduced without affecting the signal level. This is the principle by which a surface coil increases the SNR.

The image shown in Figure 5.1(b) is typical for a surface coil. It is bright close to the coil, but the intensity falls off rapidly with increasing depth into the sample. This is the main difficulty when using a surface coil—the RF transmit power that produces a 180° nutation at one location in the sample will give a much larger nutation closer to the coil and a lower nutation further from it, making it difficult to, for example, produce a spin echo. To overcome this problem, adiabatic RF pulses are routinely used with surface coils, which, above a certain B_1 threshold, produce the same nutation independent of B_1 amplitude.[1]

Surface coils are usually designed for a specific application, restricting the field-of-view to cover only the anatomy of interest (a particular brain region, liver, heart, etc.) to minimize the noise sensitivity. Surface coils can be used in receive-only mode, in combination with a suitable volume transmit coil, or as transmit-receive coils; the latter being more common in multinuclear applications.

Surface coils are regularly used for proton studies, but their main application is for non-proton

RF Coils for MRI
Edited by J. Thomas Vaughan and John R. Griffiths

 ISBN: 978-0-470-77076-4

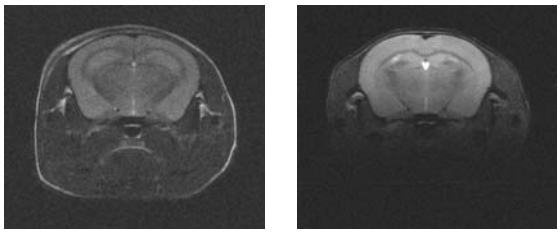

(a) (b)

Figure 5.1. Images of a mouse brain, acquired with (a) a volume coil and (b) a surface coil.

acquisitions, especially spectroscopy, where it is often not possible to achieve the required SNR with a volume coil. Indeed, the first reported use of a surface coil was to study ^{31}P, where the increased SNR allowed phosphorus to be investigated in vivo for the first time.[2]

5.2 MULTINUCLEAR MRI AND MRS

The vast majority of in vivo magnetic resonance experiments are performed using protons (^{1}H). Protons have a high gyromagnetic ratio (giving high NMR sensitivity), and are present in large quantities in the body, mostly in the form of water. However, other nuclei can be studied in vivo, potentially giving access to information not available from proton imaging or spectroscopy.

After protons, the most commonly investigated nuclei are phosphorus (^{31}P), carbon (^{13}C), and sodium (^{23}Na).[3] A comparison of the NMR properties of these nuclei is given in Table 5.1. Phosphorus magnetic resonance spectroscopy (MRS) is used to investigate tissue energy metabolism. Phosphorous-31 has a relatively large gyromagnetic ratio, and 100% natural abundance, so produces a reasonably large NMR signal. Carbon-13 is a more challenging nucleus, as it has a lower natural abundance (1.1%) and a lower gyromagnetic ratio. However, it can be used to investigate almost every metabolic pathway in the body. While phosphorus and carbon are commonly investigated via spectroscopy, sodium (^{23}Na) is usually imaged. Sodium-23 has 100% natural abundance, but is present in relatively low concentration in the body; however, its distribution is very inhomogeneous. Sodium is used to investigate tissue damage, such as that caused by stroke or cancer.

Table 5.1. Properties of some biologically interesting NMR active nuclei[3]

Nucleus	Spin	Gyromagnetic ratio MHz/T	γ_X/γ_{1H}	Relative sensitivity
^{1}H	1/2	42.58	1.00	100
^{13}C	1/2	10.71	0.25	1.6
^{23}Na	3/2	11.27	0.26	1.8
^{31}P	1/2	17.25	0.41	6.9

It is often useful to "double tune" a non-proton probe, enabling it to excite and detect an NMR signal at two (or more) frequencies—commonly that of the nucleus we wish to investigate and of proton. There are several reasons for wanting to add a proton channel to a non-proton coil. First, as the proton signal is always stronger than that from other nuclei, a proton channel is useful for quickly acquiring a scout image. The scout can then be used to plan the non-proton acquisition, based on the actual anatomy of the animal or volunteer. A proton channel is also useful for shimming the main field. A well-shimmed B_0 field is critical when attempting to detect a weak NMR signal, but it is difficult to set up the shim using a weak signal. As the shim is independent of the nucleus, adding a proton channel allows the magnet to be shimmed using the stronger proton signal, before switching to the non-proton channel (without moving the sample) to perform the actual experiment.

A second RF field, at the proton frequency, may also be used to enhance the signal on the X-channel, via nuclear Overhauser effect (NOE), polarization transfer, and/or J-decoupling (usually simply called *decoupling*, causing much confusion for the coil designer!). In heteronuclear spin systems, such as ^{13}C–^{1}H, the polarization of the observed nuclei can be significantly enhanced by saturating the higher γ nuclei, giving rise to the NOE.[1] The maximum enhancement available due to NOE for a particular pair of spin systems is $1 + \gamma_I/(2\gamma_S)$, where γ_I and γ_S are the respective gyromagnetic ratios. For ^{13}C–^{1}H, for example, the potential enhancement is almost a factor of three. Alternatively, polarization of the observed nuclei can be enhanced via J-coupling methods, such as INEPT, which transfer polarization from the coupled to the observed nuclei by simultaneously exciting both.[1] In this case, the maximum enhancement factor is γ_I/γ_S, giving almost a factor of four for ^{13}C–^{1}H. Heteronuclear spin systems couple (in a manner analogous to resonant circuits) producing a splitting of the resonance

peaks into multiplets whose type depends on spin multiplicity. This complicates the spectrum and reduces the peak height of already small resonances, making them harder to detect. The manifestation of J-coupling can be reduced or even eliminated by saturating the coupled spin partner during the acquisition with a second RF field $B_2 \gg 2\pi J/\gamma$, where J is the coupling between the two spin systems. The decoupling signal can be either continuous wave or, to increase the decoupling bandwidth, a series of composite pulses such as WALTZ or MLEV.[1]

When the proton channel is used only to acquire a scout image or shim the magnet, the RF coil can be switched between proton and non-proton mode, e.g., using PIN diodes, either to detune the inactive coil or to switch the resonance frequency of a single coil. NOE and polarization transfer, however, require simultaneous transmission on both the detected and decoupling channels; J-decoupling requires transmission on the decoupling channel while simultaneously acquiring the detected signal (Figure 5.2). These techniques place special requirements on the scanner hardware and the RF coil design. A scanner equipped for multinuclear studies is fitted with a complete second RF transmit and receive chain, often called the X-channel. Unlike the proton channel, which usually has a very narrow bandwidth, the X-channel is broadband, allowing it to be used for a range of different nuclei. The toughest demands on the RF system are from J-decoupling, where the decoupling transmit voltage is typically seven or more orders of magnitude larger than the detected NMR signal. Accurately recording this signal without interference from the decoupling is clearly an RF design challenge, requiring careful coil and system design.

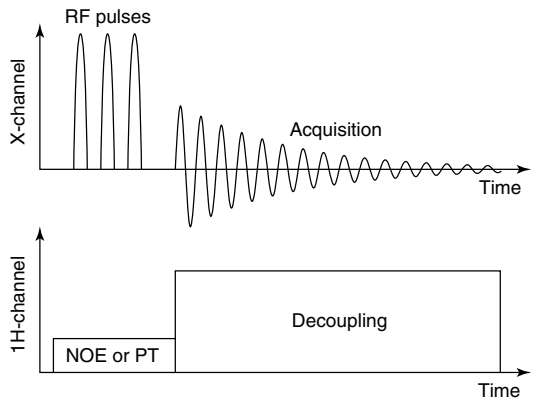

Figure 5.2. A typical multinuclear pulse sequence requires transmission on a second RF channel—for NOE or polarization transfer during transmission and J-decoupling during the acquisition.

5.3 BASIC SURFACE COILS

The simplest, and probably the most common, of all surface coils is a planar loop. The actual shape of a planar loop makes relatively little difference to the field it generates—circular and rectangular-shaped loops are both common. The magnetic field generated by a circular loop, oriented perpendicular to the y-axis, is shown as a map in the transverse plane in Figure 5.3(a). Surface coils are commonly curved to fit the surface of the sample, which helps to extend the magnetic field further into the sample. The circular loop in Figure 5.3(a) has been curved onto the surface of a z-oriented cylinder of twice the radius of the loop. All subsequent coil arrangements modeled in this chapter have been curved onto the same surface.

An alternative arrangement to a planar loop is a butterfly, or figure-of-eight, coil as shown in Figure 5.4(a). The generated field is concentrated closer to the coil than for a circular loop, and thus falls off more rapidly with increasing distance from the coil (Figure 5.3b). This can be useful if a very shallow field-of-view is required, for example, to avoid coupling to another nearby RF coil.

When designing a loop coil, the coil dimensions should be chosen to maximize the SNR of the signal detected from a given position, rather than the raw signal level. Consider a planar loop placed directly onto a semi-infinite conductive load, which is a good approximation when the load is much larger than the coil. The magnetic field on the loop axis, generated by the loop, is

$$B_1 = \frac{\mu_0 I}{2} \frac{R^2}{(y^2 + R^2)^{3/2}} \tag{5.1}$$

where R is the loop radius, and y is the distance into the sample. The signal voltage detected by the loop is

$$\xi = \omega_0 B_1 M_0 \Delta V \tag{5.2}$$

where M_0 is the sample magnetization, and ΔV is the voxel volume. The thermal noise voltage detected by

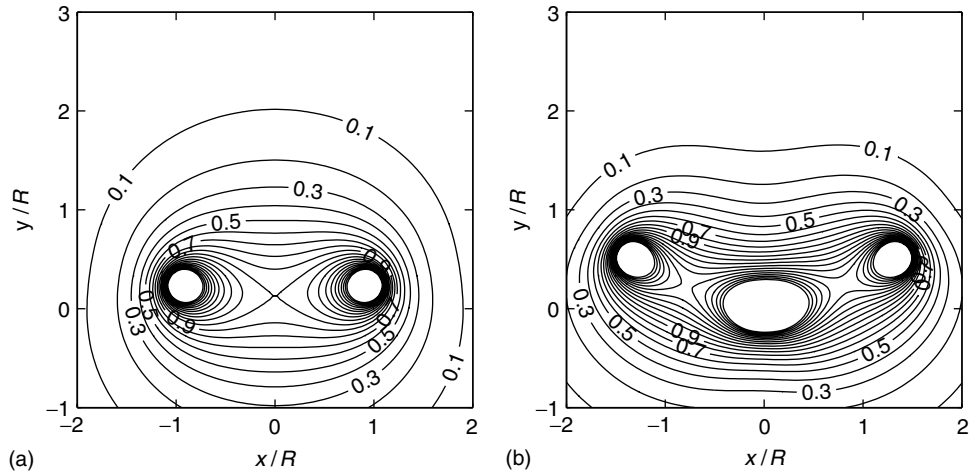

Figure 5.3. Transverse magnetic field B_{1xy} produced by (a) a circular loop and (b) a butterfly loop. Axes are normalized to the circular loop radius, and contour levels are relative to the field at the center of the circular loop. The butterfly loop was scaled to enclose the same area as the circular loop. The magnetic field in this and subsequent figures was numerically modeled using the Biot–Savart law.[4]

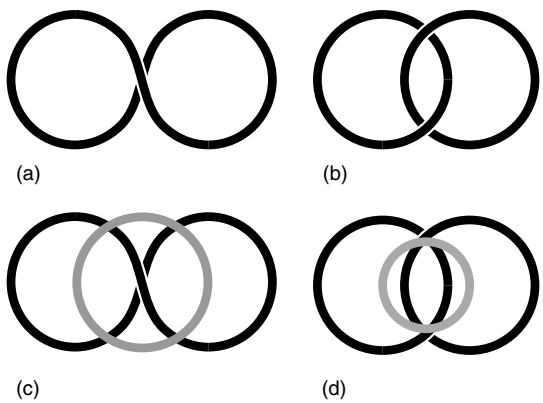

Figure 5.4. Coil designs: (a) a butterfly coil, (b) an optimally overlapped pair, (c) a quadrature butterfly, and (d) an Adriany–Gruetter coil.

the probe, which also depends on the field-of-view of the coil, is given by

$$N = \sqrt{4k_B T_s r_s \Delta f} \tag{5.3}$$

where k_B is Boltzmann's constant, T_s is the sample temperature, and Δf is the bandwidth of the measurement. The effective resistance of the sample r_s, as seen by the loop, is

$$r_s = \tfrac{1}{3}\mu_0^2\omega_0^2\sigma R^3 \tag{5.4}$$

where σ is the sample conductivity.[5] Finally, the SNR is given by

$$\psi = \frac{\xi}{N} \propto \sqrt{\frac{R}{\left(y^2 + R^2\right)^3}} \tag{5.5}$$

By differentiating equation (5.5) with respect to R, the depth of maximum SNR is found to be $R_0 = y/\sqrt{5}$. Equation (5.5) is the main design equation when planning a loop coil. A loop with a radius smaller than R_0 has insufficient sensitivity at the required depth, while a loop larger than R_0 is too sensitive to sample noise.

Plotting coil sensitivity and SNR (equations (5.1) and (5.5)) against loop radius clearly demonstrates that optimizing a loop coil to maximize B_1 intensity at a particular depth is not the same as optimizing the SNR at that depth (Figure 5.5). To stay within 90% of the optimum SNR, a loop coil should be designed such that $0.25 \leq R/y \leq 0.70$, where R is the coil radius and y is the depth of the target region.

The above analysis assumes that noise is generated only by the sample, and that the RF wavelength is large compared to the sample size. The proportion of noise generated by the sample, relative to that produced by the coil, may be determined by measuring the unloaded and loaded Q factors. For large coils, such as those used in human studies, sample noise in dominant (typically $Q_U/Q_L > 5$, indicating that more

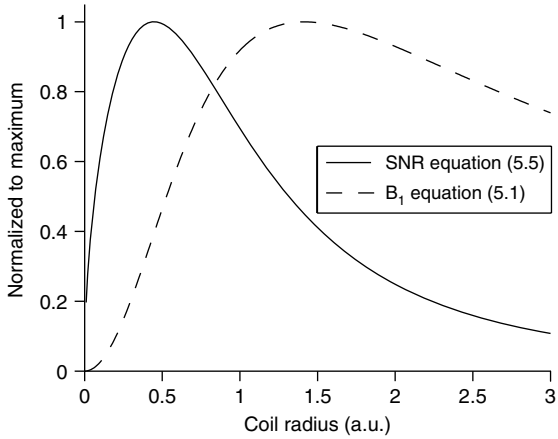

Figure 5.5. Variation in SNR and signal intensity, at unit depth, versus radius for a circular loop coil with a semi-infinite load.

than 80% of the total noise comes from the sample). With smaller coils, such as those used in small animal experiments, noise from the coil, due to losses in the conductor, capacitors and solder joints becomes more significant.[5] In this case, optimum SNR is achieved with a loop radius slightly larger than that predicted by equation (5.5).[6] At short wavelength, relative to the sample size, the sample has a significant influence on the B_1 field distribution, and full-wave electromagnetic simulations may be necessary to optimize the coil dimensions (see Chapter 27).

For lower frequency coils, it is sometimes necessary to add multiple turns to a coil, but it is important to realize that this does not improve the SNR. Consider, for example, adding a second turn to a circular loop to form a two-turn solenoid. The coil now "sees" twice as much signal from the sample. However, the noise level will also increase. There are two major sources of noise in an NMR experiment: thermal noise from the sample, and thermal noise from the coil. As the coil cannot distinguish between the NMR signal and thermal noise from the sample, increasing sensitivity to the signal also increases sensitivity to the noise by the same factor. At the same time, the coil now uses twice the length of wire as a single loop, doubling its resistance, and hence doubling its thermal noise contribution. The signal detected by the coil increases, but the noise increases by the same factor, and the SNR remains the same. Instead, the number of turns should be chosen to give a reasonable impedance at the resonance frequency, so that the loop can be resonated and matched to 50 Ω using achievable capacitor values.[7]

The opposite problem occurs at high frequency, as the RF wavelength approaches the conductor length of a single-turn loop. A significant phase shift is increasingly present along the length of the conductor, and the loop approaches transmission-line, rather than lumped-element, behavior. The current phase progression can be reduced by splitting the loop into two or more sections, separated by capacitors, such that each section is shorter than approximately a tenth of a wavelength. An added advantage of splitting the tuning capacitance in this manner is that it increases the required lumped capacitor values, which are otherwise often comparable to parasitic capacitances present around the loop, thus making the loop resonant frequency less sensitive to coil positioning with respect to the patient and other nearby conducting structures.

5.4 QUADRATURE

The NMR signal is generated by spins precessing about a magnetic field. This has an important consequence for the detected signal—it rotates in only one direction. When a single loop coil is used to detect the NMR signal, it operates in the linear mode. That is, it is sensitive to magnetic fields rotating in either direction about the static field. The main noise contribution comes in the form of thermal noise from the sample. Unlike the signal, the noise is not polarized, and is equally distributed between positive and negative rotating components. By making a coil insensitive to the counter-rotating field component, the noise power detected by the coil is halved without affecting the signal power. Because the measured NMR signal is a voltage, this increases the SNR by a factor of $\sqrt{2}$.[5,8]

Transmitting with a quadrature coil also offers significant benefit. Only the field component rotating in the same sense as spin precession produces a nutation. However, both the positive and negative rotating field components induce RF eddy currents in the sample, which cause Ohmic heating. An ideal quadrature coil generates no negative rotating field, and so halves the heating of the sample, while producing exactly the same spin nutation.

Production of a quadrature field requires two, ideally orthogonal, independently controllable magnetic fields. With surface coils, this is most commonly achieved by combining a pair of loop coils. When the

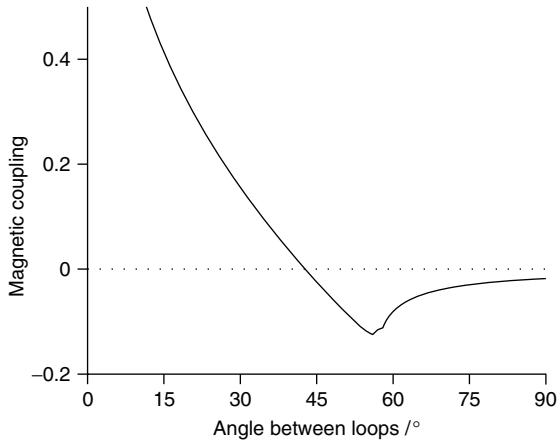

Figure 5.7. Inductive coupling between a pair of circular loops vs the angle between them. At approximately 43° overlap, the coupling is zero.

loops are positioned perpendicular to one another, the magnetic fields they generate are also approximately perpendicular, and the coupling between the loops is low. Figure 5.6 shows the positive and negative rotating fields generated by this arrangement. The pair generate a stronger positive than negative rotating field, but the efficiency is low, largely because the most sensitive region of one loop is in the periphery of the other.

To place the higher sensitivity regions closer together, the loops may be overlapped (Figure 5.4b). The loop fields are no longer perpendicular, causing the loops to inductively couple; the degree to which they couple depends on the size of the overlap. Outside the overlapped region, flux linkage between the loops creates a positive mutual inductance. Inside the overlapped region, the magnetic flux points in the opposite direction, and creates a negative mutual inductance. By carefully adjusting the overlap, the net mutual inductance can be minimized, at which point the loops are well decoupled.[9]

Figure 5.7 shows the mutual coupling between a pair of loops, wrapped onto a cylindrical surface, as a function of the angle between them. When the angle is small, i.e., close to a complete overlap, the coupling is very large. As the angle increases, the coupling reduces through zero to a negative minimum, and then increases back toward zero as the angle approaches 90°; in this particular case, the critical overlap is at approximately 43°. In practice, this overlap is best found by adjusting the loops at the bench, and monitoring the coupling between them with, e.g., a network analyzer. Figure 5.8 shows the positive and negative rotating fields generated by a pair of critically overlapped loops. In comparison to Figure 5.6, the intensity of the positive rotating field close to the loops is significantly increased, while the negative rotating field is decreased.

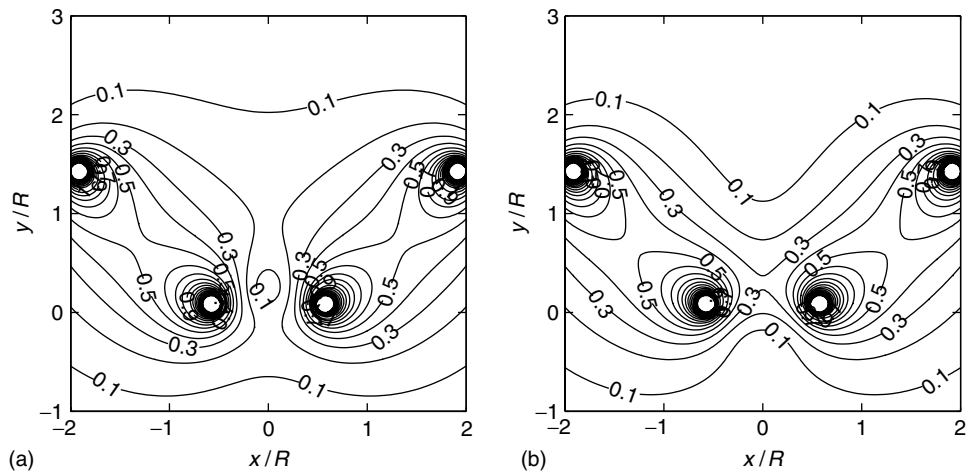

Figure 5.6. Transverse magnetic field B_{1xy} produced by a pair of perpendicular circular loops, rotating in the (a) positive and (b) negative direction. Field strength is relative to the field at the center of a single circular loop, and distances are given relative to the circular loop radius.

A quadrature pair can also be formed by combining a butterfly coil with a circular loop (Figure 5.4c). On one side of the pair, current flows in the same direction in the circular loop and the butterfly; on the opposite side, current in the butterfly opposes current flowing in the circular loop. Therefore, this arrangement is decoupled by symmetry, for any butterfly coil dimensions relative to the diameter of the circular loop.

It is clear from Figures 5.8 and 5.9 that surface coils do not produce a purely positive rotating B_1 field. The degree of polarization of the field may be characterized using

$$\beta = \frac{|\mathbf{B}_1^+|}{|\mathbf{B}_1^+| + |\mathbf{B}_1^-|} \tag{5.6}$$

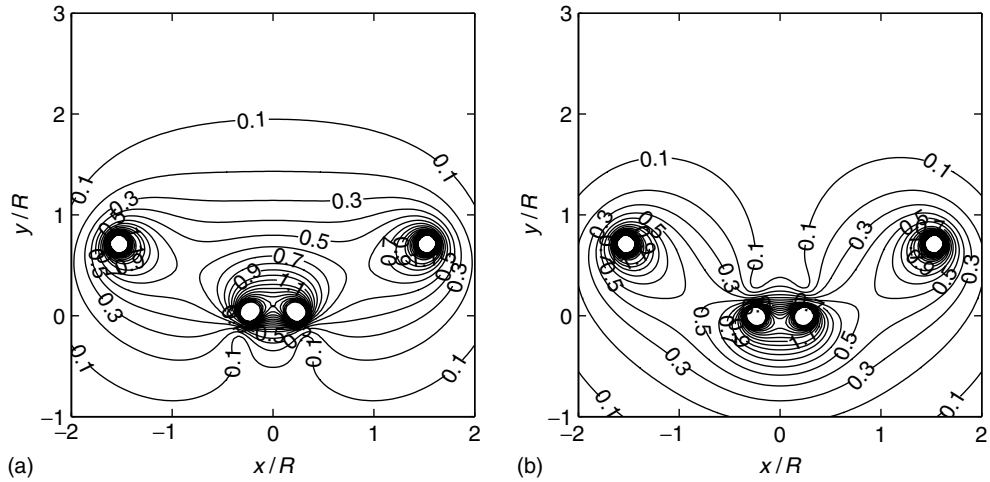

Figure 5.8. Transverse magnetic field B_{1xy} produced by a pair of optimally overlapped circular loops, rotating in the (a) positive and (b) negative direction. Field strength is relative to the field at the center of a single circular loop, and distances are given relative to the circular loop radius.

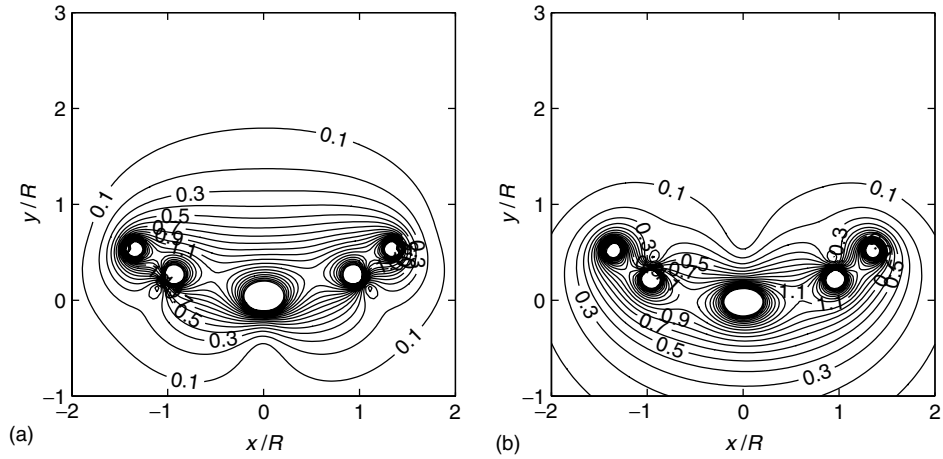

Figure 5.9. Transverse magnetic field B_{1xy} produced by a quadrature butterfly coil, rotating in the (a) positive and (b) negative direction. Field strength is relative to the field at the center of a single circular loop, and distances are given relative to the circular loop radius.

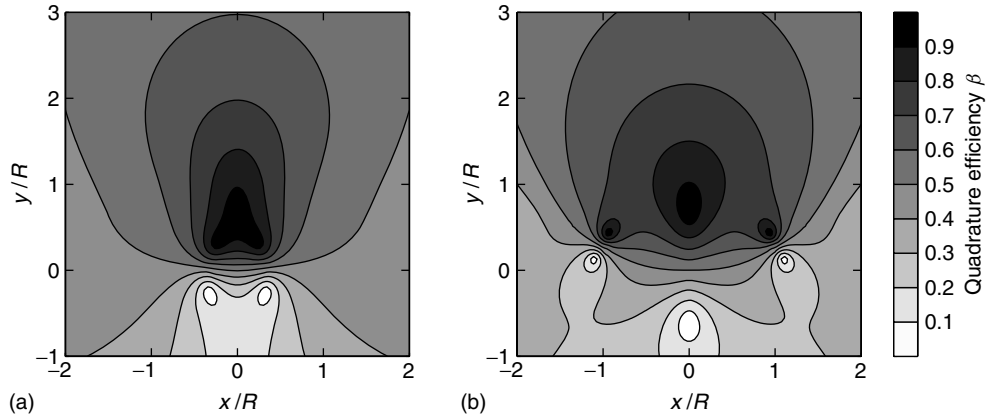

Figure 5.10. Maps showing the quadrature efficiency $\beta = |\mathbf{B}_1^+| / |\mathbf{B}_1^+| + |\mathbf{B}_1^-|$ of (a) an optimally overlapped pair, and (b) a quadrature butterfly coil.

where $\mathbf{B}_1^+$ and $\mathbf{B}_1^-$ are the positive and negative rotating field components.[10] A value of $\beta = 1$ indicates perfect quadrature, $\beta = 0$ is perfect antiquadrature (i.e., the field rotates in the wrong direction), and $\beta = 0.5$ indicates a linearly polarized field, with equal positive and negative rotating components. Over the region of optimum sensitivity, a surface coil should produce $0.5 \leq \beta \leq 1$. Figure 5.10 shows simulated β-maps for a pair of optimally overlapped loops, and for a quadrature butterfly coil. The butterfly pair produce a larger region of highly polarized field ($\beta > 0.7$) than the overlapped loops. However, Figure 5.10 has to be seen in combination with Figures 5.8 and 5.9. A highly polarized field offers little benefit if it is so weak that noise from other regions of the sample will dominate, as is increasingly the case with increasing distance from the butterfly pair.

Experimentally, the quality of a quadrature field may be assessed by reversing the connections to the RF coil, allowing us to detect the normally invisible counter-rotating field. An ideal quadrature coil will produce a bright image with the coil connected correctly, and no image with the connections reversed. In practice, there is usually some antiquadrature sensitivity toward the edge of the field-of-view, but there should be none at the center. The sensitivity profile of a coil can be assessed by acquiring images of a uniform phantom. This method works well for proton coils, but less well for coils tuned to a low-sensitivity nucleus where there is not enough signal to produce an image. One solution is to heavily dope the phantom, giving enough signal to produce an image. Alternatively, the coil can sometimes be retuned to another more sensitive nucleus with a similar gyromagnetic ratio. For example, a ^{13}C coil can often be retuned to ^{23}Na to perform this test, as $\gamma_{13C}/\gamma_{23Na} = 0.91$.

5.5 MULTINUCLEAR SURFACE COILS

The coils discussed so far are all designed to operate at a single frequency. This section introduces a selection of coils designed to operate at two frequencies, to enable the use of NOE and J-decoupling.

The key to a good multinuclear coil arrangement is high sensitivity on the X-channel, and good isolation between the different frequencies. There are essentially two ways to achieve this. The first is to tune a single coil to two frequencies.[11] A drawback of this type of design is the lack of freedom to individually optimize the RF fields at the two frequencies; the coil has the same field-of-view at both (this is no longer strictly true at high static field strength, as the wavelength at the ^{1}H frequency approaches the sample size; however, although the sensitivity profiles are different at the high and low frequencies, they still cannot be optimized separately). The second approach is to place two separate coils around the sample, tuned to different frequencies but having approximately the same field-of-view. This is the method examined in this chapter.

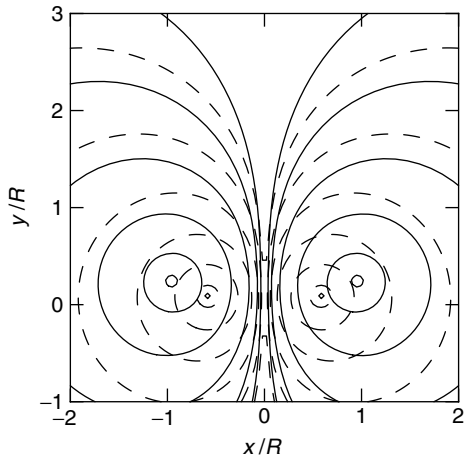

Figure 5.11. Flux line generated by a large loop (solid) placed concentrically around a smaller loop (dashed). The flux lines are almost parallel, producing high coupling between the loops.

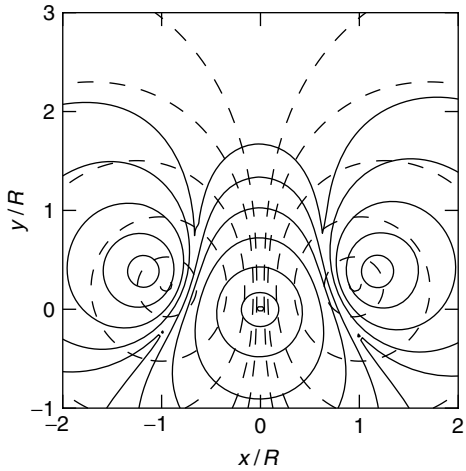

Figure 5.12. Magnetic flux lines between the butterfly (solid) and circular loop (dashed) are largely perpendicular.

A straightforward dual-coil design uses a large proton loop positioned concentrically around a smaller X-band loop, an arrangement which gives the proton coil a larger field-of-view than the X-coil.[12] This is often useful, as it is easier to plan the acquisition volume when more anatomy is visible, and the shimmed region should ideally be slightly larger than the acquired volume. It also ensures that the decoupling B_2 field completely covers the acquired volume. At the same time, the smaller size of the X-coil maximizes its sensitivity. The problem with this design becomes clear on examining the magnetic flux generated by the two loops (Figure 5.11); the flux lines are almost parallel, producing strong coupling between the coils. To decouple the coils, the flux lines generated by one coil should ideally be perpendicular to those generated by the other coil.

The butterfly coil, described in Section 5.4 (Figure 5.4c) as a single-frequency quadrature coil, can also be used as a dual-resonant linear coil.[13] Rather than using a symmetry argument, decoupling between a circular loop and a butterfly can be understood by considering the flux generated by the two loops (Figure 5.12). Flux generated by the butterfly is perpendicular to the flux generated by the circular loop, producing very low flux linkage between the pair, giving this coil design good separation between the two channels. Its disadvantages are a shallow sensitive volume, and that in terms of sensitivity and specific absorption rate (SAR), the benefit from operating the coil in quadrature mode is lost.

The Adriany–Gruetter design (Figure 5.4d) addresses this shortcoming by adding a third coil to the probe.[14] The design principle is similar to the double-resonant butterfly, but exchanges the butterfly loop for an optimally overlapped quadrature pair. Flux lines generated by the single loop, and each loop of the quadrature pair, are shown in Figure 5.13. In the center of the field-of-view, where the B1 intensity is strongest (Figures 5.3a and 5.8a), flux lines generated by each loop of the quadrature pair are largely perpendicular to those generated by the central loop (Figure 5.13), resulting in low coupling between quadrature pair and the single loop. The quadrature pair remain mutually decoupled as discussed in Section 5.4.

The overlapped pair are usually tuned to the proton frequency, with the smaller linear loop used for the X-band. This is important for human studies, as it halves the SAR deposited by the decoupler channel, which is the main SAR constraint in e.g. ^{13}C detection experiments. The loops of the quadrature pair are generally made slightly larger than the linear loop, to give a larger field-of-view at the proton frequency than the X-frequency, for the reasons described previously. The original design, built for human spectroscopy at 4 T, used 120 mm and 70 mm diameter loops, respectively. For small animal studies, where SAR is less of a concern, the overlapped pair

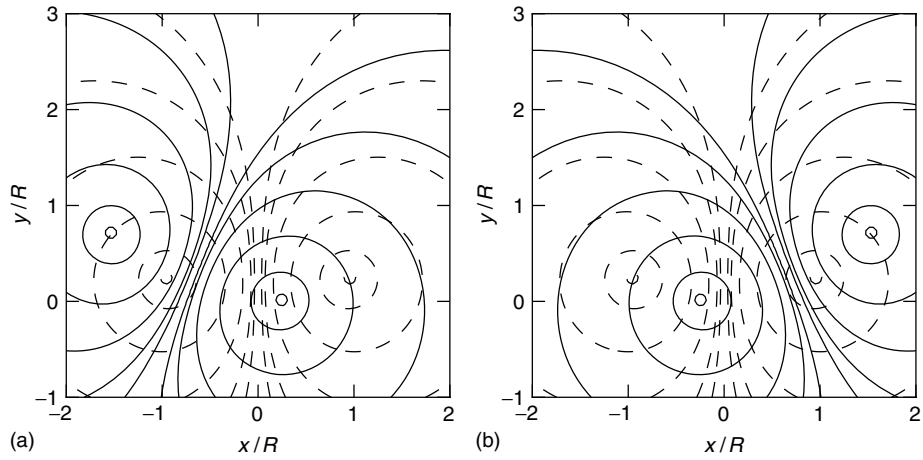

Figure 5.13. Magnetic flux lines generated by an Adriany–Gruetter coil. Flux lines generated by the (a) left and (b) right loops of the quadrature pair (solid) are almost perpendicular to the flux lines generated by the linear loop (dashed), resulting in low coupling between the ^{1}H and X coils.

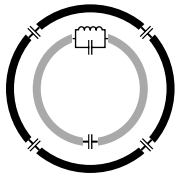

Figure 5.14. The lower frequency loop (inner) can be decoupled from the higher frequency loop (outer) by the addition of parallel-resonant trap circuit, tuned to the higher frequency. The loops are shown in a concentric arrangement, but as the decoupling does not depend upon geometry, any arrangement may be used.

can be tuned to the X-frequency, to attempt to take advantage of the $\sqrt{2}$ improvement in SNR, although the smaller field-of-view of the proton channel will give suboptimal J-decoupling.

Geometric decoupling of coils is very effective, but constrains the relative positions of the coils. An alternative approach to decoupling uses the fact that, in a multinuclear coil, different coil elements are tuned to different frequencies. Coupling is strongest at the higher frequency because, while the high frequency coil does not resonate below its fundamental frequency, the low-frequency coil can also resonate at higher harmonics. The problem is particularly acute for ^{13}C–^{1}H coils, as the proton frequency is almost exactly the forth harmonic of the ^{13}C coil.

Adding a parallel-resonant inductor–capacitor (LC) trap circuit to a coil splits the loop resonance into two peaks, an effect previously used to produce double-resonant coils.[11] More recently, the same circuit has been applied in a different manner, to prevent coupling at the higher frequency between a pair of loops tuned to two different frequencies (Figure 5.14).[15,16] The trap is tuned to the higher frequency, but inserted into the lower frequency loop. It blocks current flow at the higher frequency, preventing coupling between the two loops. At the low frequency, the trap presents a low inductive impedance, producing a slight shift in the loop resonance frequency, which can be corrected using the tuning capacitor. It is unfortunate that the trap must be added to the X-coil. While some sensitivity may be sacrificed on the ^{1}H channel, where the signal is stronger, the sensitivity of the X-channel is critical; care must be taken that the introduction of the trap circuit does not significantly reduce the performance at the X-frequency. However, with careful trap construction, SNR losses on the X-channel can be kept below 5%.[16]

Trap-decoupling provides an extra degree of freedom in multinuclear coil design, in that the arrangement of coil elements for the ^{1}H and X-channels can now be independently optimized. This opens up interesting possibilities such as an X-only surface coil combined with a ^{1}H volume coil,[17] or dual-frequency array coil design.

5.6 FILTERS

Although careful coil design can reduce interaction between the X- and ^{1}H-channels, further filtering is usually necessary to prevent significant noise injection from the decoupling channel into the observed channel.

RF power amplifiers are inherently noisy devices, typically having a noise figure above 10 dB, often generating noise over a far wider bandwidth than the amplifier's nominal operating range. In a homonuclear NMR experiment, the power amplifier output is usually gated off (disabled) during acquisition, to prevent noise from the amplifier entering the receiver. In a multinuclear experiment using J-decoupling, the decoupling power amplifier must be active during the acquisition. Placing a filter directly after the decoupling power amplifier, designed to block signal outside the transmit bandwidth, can reduce the noise level reaching the receive path. A bandpass filter is placed on the proton channel, while a low pass filter, which usually has a lower insertion loss, is preferred for the X-channel.

A second lower power filtering stage is often added between the receive coil and the preamplifier. Although the decoupling signal is generally outside the preamplifier bandwidth, a large out-of-band signal can saturate the preamplifier input, distorting the amplified signal. Placing a filter before the preamplifier can minimize this (Figure 5.15). The combination of coil decoupling and filtering should be strong enough to attenuate the decoupler signal down to the level of in-band thermal noise at the preamplifier input. Note that, as this filtering stage is placed before the preamplifier, its insertion loss is critical. A good filter can have an insertion loss as low as 0.1 dB, with 70 dB of attenuation in the stop-band.

5.7 SUMMARY

In vivo non-proton magnetic resonance is difficult because the signals are very small. However, the continued development of higher field systems makes non-proton magnetic resonance imaging and spectroscopy attractive. The RF design is further complicated by the need to transmit a proton signal, while receiving the nonproton signal. High sensitivity to the non-proton signal, and very strong decoupling between the proton and non-proton channels is key.

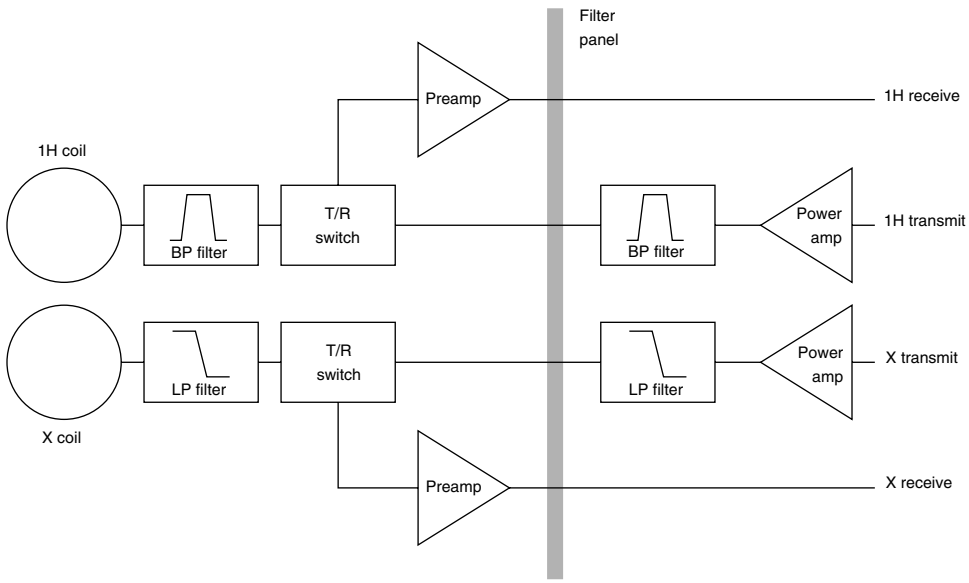

Figure 5.15. Filter placement for a multinuclear system. Filters directly after the power amplifiers prevent out-of-band noise from the amplifiers entering the RF chain. Filters between the coils and T/R-switches block the coupled signal, preventing saturation of the preamplifiers during J-decoupling.

Surface coils are ideal for non-proton magnetic resonance because they offer higher SNR than volume coils, albeit over a smaller field-of-view. Using separate coils for the different frequencies allows the field-of-view to be individually tailored at each frequency. However, careful design and construction is required to maintain the necessary decoupling between the different coils, using either a geometric or a trapped design. Finally, while good coil design is crucial to multinuclear magnetic resonance, system optimization is also important. In particular, filtering on both the observed and J-decoupling channels must be considered.

RELATED ARTICLES IN THE ENCYCLOPEDIA OF MAGNETIC RESONANCE

Brain MRS of Human Subjects

Decoupling Methods

Double Resonance in Liquids

Proton Decoupling During In Vivo Whole Body Phosphorus MRS

Radiofrequency Systems and Coils for MRI and MRS

Sensitivity of the NMR Experiment

Shimming of Superconducting Magnets

Sodium-23 Magnetic Resonance of Human Subjects

Surface and Other Local Coils for In Vivo Studies

Surface Coil NMR: Detection with Inhomogeneous Radiofrequency Field Antennas

REFERENCES

1. R. Freeman, *A Handbook of Nuclear Magnetic Resonance*, Longman Scientific & Technical: Harlow, 1988.
2. J. J. Ackerman, T. H. Grove, G. G. Wong, D. G. Gadian, and G. K. Radda, *Nature*, 1980, **283**, 167–170.
3. R. A. de Graaf, *NMR Spectroscopy: Principles and Techniques*, 2nd edn., John Wiley & Sons: Chichester, 2007.
4. J. Jin, *Electromagnetic Analysis and Design in Magnetic Resonance Imaging*, CRC Press: London, 1998.
5. C.-N. Chen and D. I. Hoult, *Biomedical Magnetic Resonance Technology*, IOP Publishing: Bristol, 1989.
6. A. Kumar, W. A. Edelstein, and P. A. Bottomley, *Magn. Reson. Med.*, 2009, **61**(5), 1201–1209.
7. J. Mispelter, M. Lupu, and A. Briguet, *NMR Probeheads: for Biophysical and Biomedical Experiments*, Imperial College Press: London, 2006.
8. D. I. Hoult, C.-N. Chen, and V. J. Sank, *Magn. Reson. Med.*, 1984, **1**(3), 339–353.
9. P. B. Roemer, W. A. Edelstein, C. E. Hayes, S. P. Souza, and O. M. Mueller, *Magn. Reson. Med.*, 1990, **16**, 192–225.
10. J. Wang, Q. X. Yang, X. Zhang, C. M. Collins, M. B. Smith, X. H. Zhu, G. Adriany, K. Ugurbil, and W. Chen, *Magn. Reson. Med.*, 2002, **48**(2), 362–369.
11. J. R. Fitzsimmons, H. R. Brooker, and B. Beck, *Magn. Reson. Med.*, 1989, **10**(3), 302–309.
12. J. Mispelter, B. Tiffon, E. Quiniou, and J. M. Loste, *J. Magn. Reson.*, 1989, **82**(3), 622–628.
13. P. A. Bottomley, C. J. Hardy, P. B. Roemer, and O. M. Mueller, *Magn. Reson. Med.*, 1989, **12**(3), 348–363.
14. G. Adriany and R. Gruetter, *J. Magn. Reson.*, 1997, **125**(1), 178–184.
15. M. Alecci, S. Romanzetti, J. Kaffanke, A. Celik, H. P. Wegener, and N. J. Shah, *J. Magn. Reson.*, 2006, **181**(2), 203–211.
16. A. Dabirzadeh and M. P. McDougall, *Concepts Magn. Reson.*, 2009, **35B**(3), 121–132.
17. D. W. Klomp, W. K. Renema, M. van der Graaf, B. E. de Galan, A. P. Kentgens, and A. Heerschap, *Magn. Reson. Med.*, 2006, **55**(2), 271–278.

Chapter 6

Quadrature Transverse Electromagnetic (TEM) Surface Coils

Nikolai I. Avdievich

Department of Neurosurgery, Yale University, New Haven, CT 06520, USA

6.1 INTRODUCTION

High-field imaging (>4 T), while advantageous for increased signal-to-noise ratio (SNR), is a challenging task that requires special instrumentation. Constructing efficient volume coils for high-field human imaging of sufficiently large objects (body, head, etc.,) is difficult because of low SNR and significant power deposition associated with the large excitation volume (sample volume "seen by the coil") of these devices. With increasing magnetic field strength B_0, the issue of radiofrequency (RF) power deposition becomes severe. For example, as reported by Vaughan, the power required to achieve an equivalent RF magnetic field B_1 was ~4 times higher for a head-sized transverse electromagnetic (TEM) volume coil at 7 T in comparison to 4 T (see Chapter 26).[1]

RF Coils for MRI
Edited by J. Thomas Vaughan and John R. Griffiths

ISBN: 978-0-470-77076-4

On the other hand, surface coils, which have restricted excitation volume and, therefore, higher efficiency (greater $B_1/(P)^{1/2}$), have a strongly inhomogeneous B_1 field. Thus there is considerable interest in the development of alternative RF coil structures that can reduce total power deposition while preserving sensitivity and some homogeneity, such as open or half-volume coils. A number of imaging applications with a restricted field of view (FOV) (smaller than the size of the object) can benefit greatly from the use of open volume coils. The large coil opening provides a closer fit, improving the coil's filling factor. This, together with the reduced excitation volume, can provide a substantial increase in transmission efficiency (reduction of the total power deposition), as well as improvement in receiver sensitivity, as compared to closed full-volume coils. At the same time, these devices provide a sufficiently large relatively homogeneous B_1 field region so as to be used as transmit coils. They also improve patient comfort and accessibility, features that are especially important in functional magnetic resonance imaging (fMRI), where additional stimulation equipment is frequently used inside the volume coil.

For SNR and transmission efficiency purposes, it is desirable to operate RF volume coils in quadrature (see Chapter 3) due to the $(2)^{1/2}$ factor of improvement.[2] At high field strengths, an additional benefit of quadrature operation is the reduction of the RF penetration artifact due

to stimulation of the eddy currents in the large conducting objects.[3–7] This effect distorts the RF magnetic field profile inside large (comparable with the RF wavelength) objects (such as a human body or head) and thus alters the image intensity. These effects are most pronounced when linear devices are used.[3,5,6] Quadrature operation is easily achieved in a conventional full-volume coil by driving a naturally occurring degenerate pair of modes simultaneously.[8] However, for an open half-volume coil (TEM or birdcage) no frequency-degenerate modes naturally exist. Therefore, to achieve quadrature operation in an open half-volume coil, two orthogonal modes must be selected, made explicitly degenerate, and driven independently.

The use of half-volume open transmit/receive MRI coils for imaging of large objects, such as human breast and shoulder, has been explored previously for experiments at 1.5 T.[9–12] Various designs of open head coils have also been reported for experiments at higher (up to 7 T) field.[13–18] TEM volume coils have become a well-established alternative to conventional birdcage designs for imaging at high fields for a number of advantages. Different TEM structures based on stripline,[19,20] coaxial elements,[1,8,21,22] and other types[23–25] have been reported. Because the inductances of the elements comprising birdcage coils increase with the coils' overall sizes, capacitors of unreasonably low value are required to resonate the large (i.e., body or head sized) birdcage coils. Size-scaling of TEM coils is much easier, since the area of the elements comprising a TEM coil can be controlled by adjusting the distance between the coil's legs and its shield. Additional advantages of the TEM coils include absence of the end ring currents producing component of B_1 parallel to B_0 and not contributing to magnetic resonance.[1,8]

The design concepts for open and partially open TEM coils were first described by Adriany *et al*.[14] and Vaughan *et al*.[15,16] and further developed by Peshkovsky *et al*.[18] In this chapter, we describe the design and construction of a quadrature half-volume TEM head transmit/receive coil. This coil demonstrates improved sensitivity and transmit efficiency, as compared to full-volume coils, and can potentially provide an alternative to high-frequency full-volume body coils in imaging applications with restricted FOV.

6.2 BACKGROUND

6.2.1 Comparison of Full-volume and Half-volume Coils

Open half-volume coils, as compared with the closed full-volume devices, can provide significantly higher transmission efficiency because their excitation (sample) volume V_S is decreased approximately by half. The value of the RF magnetic field B_1 per unit of applied power can be obtained according to[26]

$$\frac{B_1}{\sqrt{P}} \sim \sqrt{\frac{Q \cdot \eta}{\omega \cdot V_s}} \tag{6.1a}$$

$$\eta = \frac{\int_S B_1^2 dV}{\int_C B_1^2 dV} \tag{6.1b}$$

where P is the input power, Q is the coil's quality factor, ω is the resonance frequency, η is the magnetic field filling factor, and indexes S and C imply integration over the sample and total coil volume, respectively. Thus, a decrease in the V_S leads to an increase in the transmit efficiency. Additionally, since the open coils may be constructed to more closely fit the objects to be imaged, their magnetic field filling factors η are higher, leading to a further increase in the B_1 value [equation (6.1)]. Since the noise is reduced and the reception strength is increased, substantial SNR improvements can also be achieved with these coils. The increase in reception strength can be understood if one considers the reciprocity principle,[27] which states that the amount of signal picked up by the coil is proportional to the amount of the B_1 field produced per unit of the input current in the transmit mode. The reduction in noise is a consequence of the smaller V_S of the open coil relative to a conventional closed volume coil, which, when operated in receive mode, collects noise from the areas outside of the region of interest for the study.

A TEM coil consists of a number of identical coupled resonant elements producing several modes resonating at different frequencies. The number of modes in a chain of coupled elements is equal to the number of elements. In a closed TEM coil,[8] some of the modes become degenerate and the number of distinct resonant frequencies is reduced. The second lowest resonance frequency of the TEM coil corresponds to a frequency-degenerate pair of modes with the relative current flowing in an element m is given by $\sin(2\pi m/N)$ for one mode and $\cos(2\pi m/N)$

for the other mode, where N is the total number of elements. This distribution of current has been shown to create a homogeneous B_1 field inside the volume coil.[28] In a closed TEM coil, quadrature operation is achieved by simultaneously driving these two orthogonal degenerate modes by connecting to two or four resonant elements separated by 90°, producing a circularly polarized homogeneous B_1 field.[8]

A partially open TEM volume coil configuration can be constructed by removing a single element from a closed volume coil.[15,16] This type of coil, however, cannot be considered a truly open coil for the following reason: the orientation of the elements in a TEM coil is such that the through-space inductive coupling is still effective when one element of a closed, densely spaced TEM coil is removed.[29] In contrast, in a birdcage coil with one mesh removed, the coupling between the open ends practically disappears.[29] Therefore, this coil's operation is in principle the same as that of a regular closed TEM coil, where the current distribution patterns become somewhat distorted by the removal of an element. That distortion can be compensated by appropriate adjustments of other elements to restore the closed full-volume coil quadrature operation, and a quadrature driving of two (or four) resonant elements separated by 90° can still be applied (see Chapter 16).[15,16] However, removal of more than one element substantially decreases the inductive coupling between the two terminal elements and changes the boundary conditions dramatically, altering the resulting resonant modes and therefore requiring a different approach.

Analogous to a typical closed TEM, an open half-volume TEM can also be viewed as a resonator in which a standing wave is formed in the radial direction. However, the mode current distributions in the elements forming these two types of coils are very different. In a closed TEM coil, the current distributions are modulated sinusoidally, such that an integral number of full periods fit for one complete revolution. In an open TEM coil, no coupling exists between the first and the last elements in the chain, so this boundary condition changes, requiring that an integral number of half-periods fit between the first and the last element. Modes are formed at different frequencies according to the number of half-periods. Thus, the lowest frequency corresponds to zero half-periods; i.e., the current in all elements is in phase. The second lowest mode (surface mode) corresponds to one half-period, while the third lowest mode (butterfly mode) corresponds to two half-periods or one full period. Figure 6.1 shows the theoretical current distributions and B_1 patterns for the surface and the butterfly modes of a seven-element half-volume coil. In a half-volume TEM coil, no frequency-degenerate modes naturally exist. Therefore, to achieve quadrature operation, the most homogeneous orthogonal B_1 fields appearing at neighboring frequencies (the surface and the butterfly modes) must be made degenerate and independently driven.

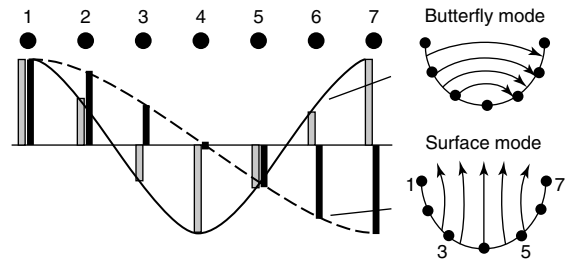

Figure 6.1. Theoretical current distributions for the surface (black bars) and butterfly (gray bars) modes of the seven-element half-volume coil and the corresponding B_1 field patterns.

6.2.2 Quadrature Driving and Tuning

In the open half-volume coil, Figure 6.1, no current flows through the central element (element 4) for the surface mode, while for the butterfly mode the current in this element is large. Therefore, any adjustments made to this element will only shift the frequency of the butterfly mode, leaving the surface mode unperturbed. At the same time, frequencies of both modes are affected when symmetrical elements on the left and the right sides are adjusted simultaneously, since both modes support currents in those elements (Figure 6.1). Using these two procedures allows the frequencies of these modes to be made degenerate while keeping them decoupled. Similarly, connecting of the RF source to the central element drives only the butterfly mode and does not affect the surface mode. The surface mode can be driven by splitting the RF signal and connecting it to the symmetrical pair of elements (elements 1 and 7, 2 and 5, 3 and 6) with a 180° phase shift between them. Connecting to elements 1 and 7, which carry the maximum current, is recommended since it produces the largest

coupling. Again, this type of connection drives only the surface mode, which carries 180°-shifted currents in the these two elements (Figure 6.1).

6.3 COIL CONSTRUCTION

6.3.1 Coil Design and Materials

As an example, we consider a 4 T (170 MHz ^{1}H frequency), seven-element, half-volume quadrature TEM coil previously described by Peshkovsky *et al*.[18] and shown in Figure 6.2(a). In this work, the term *half-volume* refers to a semicircular coil design of 180° of an arc. The coil measured 20 cm in length with 20 cm inside diameter (ID) (diameter measured at the centers of resonant elements) and 26 cm shield diameter. The diameter measurements correspond to the distance between legs 1 and 7, which would be the opposite legs in a closed 12-element coil of this size. Capacitive coaxial elements similar to those described by Vaughan *et al*.[8] were used to build the coil. Copper tubes of 12.5 and 6.4 mm outside diameter (OD) (wall thickness 0.6 mm) were used to construct the outer shell and central conductor of the TEM elements, respectively. The shield for the coil was constructed from a 50 μm polyamide film with a 5 μm copper layer laminated on top of it (Gould Electronics, Eastlake, OH). The thickness of the copper is approximately equal to the skin depth at 170 MHz. This preserves a high unloaded Q-factor for the TEM resonator while suppressing gradient eddy currents.[8] The surface mode was driven using a symmetrical matching network[18] connected to the elements 1 and 7, as shown in Figure 6.2(b). To ensure 180° phase shift between the currents in these elements, a virtual ground was created at the center point between the connections by using a balun (50 Ω lumped-element λ/4 transformer) comprised of two capacitors C and two inductors L (see Chapter 25). The 50 Ω impedance is ensured by satisfying the conditions $1/\omega C = \omega L = 50\ \Omega$. It is also helpful to distribute the matching capacitance by introducing fixed capacitors C_2 in addition to the variable capacitor C_1. A detailed description of how to choose values for these capacitors can be found elsewhere.[30] The butterfly mode was driven capacitively at the central leg in a manner used in closed TEM coils,[18] using a variable capacitor C_3 (Figure 6.2b). This type of matching provided an isolation of better than −23 dB between the two

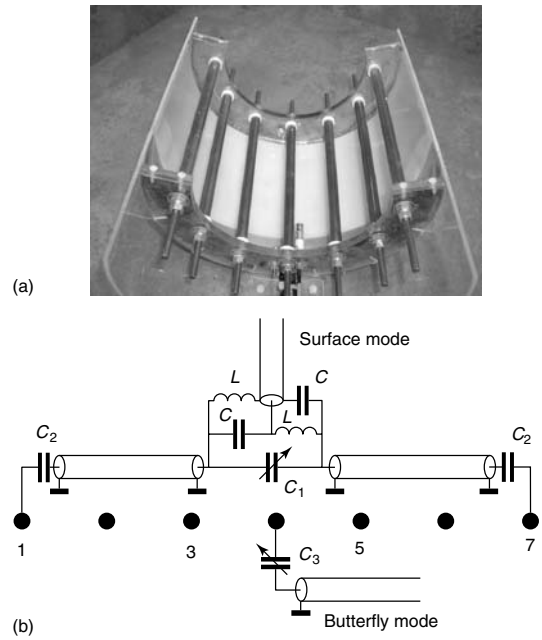

Figure 6.2. (a) A picture of the seven-element open half-volume quadrature TEM coil. (b) Coil's driving schematic. Driving of the surface mode is realized using λ/4 transformer and capacitors C_1 and C_2. Quarter-wavelength transformer providing 180° phase shift is comprised of two capacitors C and two inductors L. Driving of the butterfly mode is provided using the variable capacitor C_3.

quadrature modes. High-voltage variable and fixed capacitors for matching the coil were purchased from Voltronics (Denville, NJ) and ATC (100 C series, American Technical Ceramics, Huntington Station, NY), respectively.

The coil's performance was compared with a full-volume TEM coil (27 cm ID, 20 cm length, 33 cm shield diameter) operating in the transmit/receive mode.[31] The smaller diameter of the half-volume TEM coil was made possible by tighter fit and improved access, (i.e., the patient lies directly on the coil), whereas the full-volume coil required a larger diameter so that it could be slid over the patient's head, accommodating the subject's face and nose. The comparison between the half-volume and full-volume coils of different diameter is given to demonstrate the optimal SNR achievable with each configuration. The transmit/receive half-volume TEM coil performance was also compared with the full-volume TEM coil

transmit/surface coil array-receive system, which is an optimal configuration in terms of its SNR.[21] The four-coil array was constructed using a 6.4 mm wide copper tape. Each coil measured 8×7.5 cm in size and had four capacitors equally distributed over it. When placed on an acrylic former of 26.5 cm ID, the array covered an arc of 110°. Further details of the four-coil array have been described elsewhere.[21]

6.3.2 Bench Tuning Procedure

First, all the resonant TEM elements were adjusted (by pulling the central conductors out) such that the frequency of the surface mode was ~170 MHz. Next, the frequency of the butterfly mode was brought to the same value by increasing the capacitance in the central element (by moving the central conductors of the elements in). In cases when the intrinsic capacitance of the element is insufficient, additional fixed capacitors can be placed at one or both ends of the central element. Since isolation between the modes depends on the relative capacitances in the symmetric elements, it was optimized by asymmetrical adjustments in the element pairs 1 and 7, 2 and 6, and 3 and 5. This procedure was combined with bench measurements of the distribution of RF currents in the TEM elements, which allowed us to minimize distortions due to element adjustments and compare experimentally measured current distribution with the theoretically expected values (Figure 6.1). Visualizing the current distribution also provides an easy way to identify the correct resonance modes. Figure 6.3 shows the measured RF currents in the TEM elements for both modes after they were made degenerate in frequency. Measurements were performed using the device previously described by Avdievich *et al*.[31] The method provides only the amplitude measurements and is not sensitive to the current phase.[31] As seen from Figure 6.3, the theoretical current distribution patterns became somewhat perturbed because of the adjustments made to bring the mode frequencies to the same value. The distribution for the surface mode roughly follows the theoretical pattern, while for the butterfly mode the current in the central leg was relatively amplified.

Thus, the coil tuning procedure included three iterative steps: (i) matching two resonance frequencies, (ii) adjusting isolation between the modes, and (iii) correcting distribution of currents (symmetry). In a nine-element coil, as opposed to the seven-element coil used here, adjusting the elements 3 and 7, which carry no currents in the butterfly mode, would affect only the surface mode, which would simplify the tuning procedure.

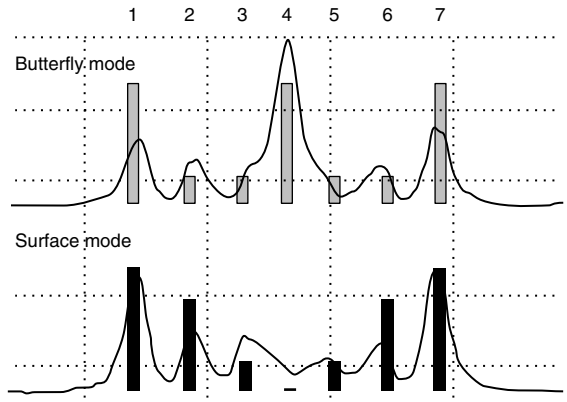

Figure 6.3. Measured values of currents squared in the elements for both modes after they were made degenerate in frequency. Superimposed are the theoretical current squared distributions for the surface (black bars) and butterfly (gray bars) modes.

Both linear mode Q-factors were measured from the S_{11} reflection coefficient as a doubled ratio of the resonance frequency over the 3 dB bandwidth for an unloaded coil as well as for the coil loaded with a 16 cm head-mimicking spherical phantom filled with 50 mM KCl. Ratios of unloaded to loaded Q-factors (Q_U/Q_L) measured 520/130 and 570/50 for the butterfly and the surface modes, respectively. While unloaded Q-factors of both modes were similar, the loaded values substantially differed as a result of the more peripheral distribution of the butterfly mode magnetic field profile.

6.4 COIL TESTING AND EVALUATION

6.4.1 Imaging Procedure

Imaging measurements were performed on a 4 T Varian Inova system (Varian Associates, Inc., Palo Alto, CA). RF field transmission profiles (B_1 maps) were recorded using the technique described by Pan *et al*.[32] The power corresponding to 90° flip angles produced by the half-volume TEM coil was determined by maximizing the signal obtained from the 1 cm coronal

slices near the bottom of the phantom where the signal was expected to be the strongest. A similar procedure using a central transverse slice through the phantom was used to determine the 90° flip angle power settings for the full-volume TEM coil. The transmission power was then set to 60° to obtain the B_1 maps and to 90° to record the images. Imaging parameters were as follows: repetition time = 2 s, FOV = 20 × 20 cm with a 3 mm slice thickness, and an in-plane resolution of 128 × 128 voxels.

For in vivo comparison, anatomic brain images were taken using both the volume and the half-volume TEM coils. An inversion recovery T_1-weighted gradient-echo sequence was used with the following imaging parameters; TE (echo time) = 5 ms, TR (repetition time) = 2.4 s, TIR (inversion recovery time) = 0.8 s, with 1.5 mm isotropic voxels at a resolution of 128 × 128. For the IR preparation, a hyperbolic secant inversion pulse was used. In addition, B_1 maps were evaluated for the half-volume TEM coil as described previously.[32]

6.4.2 Testing Results

Figure 6.4 presents the B_1 maps obtained with the half-volume TEM coil in a spherical phantom for the surface, butterfly, and quadrature modes. The B_1 maps for the two linear modes are distorted because of the RF penetration artifact, which is observed in conducting objects imaged at high frequencies.[3–7] The distortions are complementary to each other, leading to an effective self-compensation of the artifact when the coil is operated in quadrature, as can be seen from the symmetrical B_1 pattern of the quadrature mode presented in Figure 6.4(c).

Figure 6.5 shows gradient-echo images collected with the full-volume transmit/receive TEM coil (Figure 6.5a), transmit/receive half-volume TEM coil operating in the quadrature mode (Figure 6.5b), and the full-volume TEM-transmit/surface four-coil array receive-only system (Figure 6.5c). In addition, images collected with the surface (Figure 6.5d) and the butterfly (Figure 6.5e) modes of the half-volume TEM coil are provided to illustrate the RF penetration artifact, which alters the image intensity. As in the case of the B_1 maps, there are "hot" and "cold" spots in the linear surface and butterfly mode images, which are complementary to each other. Consequentially, the artifact is suppressed when the modes are combined during quadrature operation

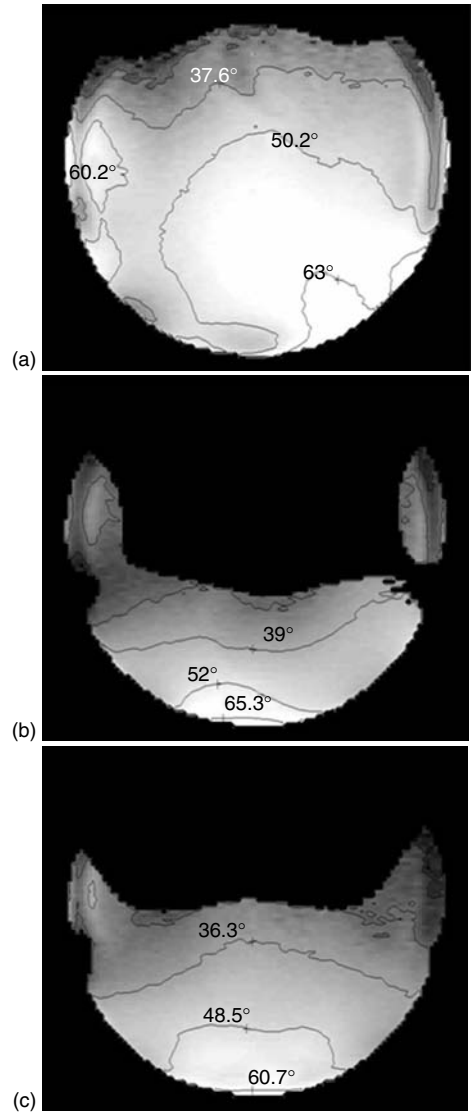

Figure 6.4. B_1 maps obtained with the (a) surface, (b) butterfly, and (c) quadrature modes of the half-volume TEM coil.

of the coil. It should be noted that the "hot" and "cold" spots in the images and the B_1 maps taken with either linear mode do not coincide, but are rather formed on the opposite sides. This relates to the fact that, while the B_1 maps follow transmission profiles of the devices, the images collected at high flip angles are functionally dependent on both the receive and transmission profiles. A detailed

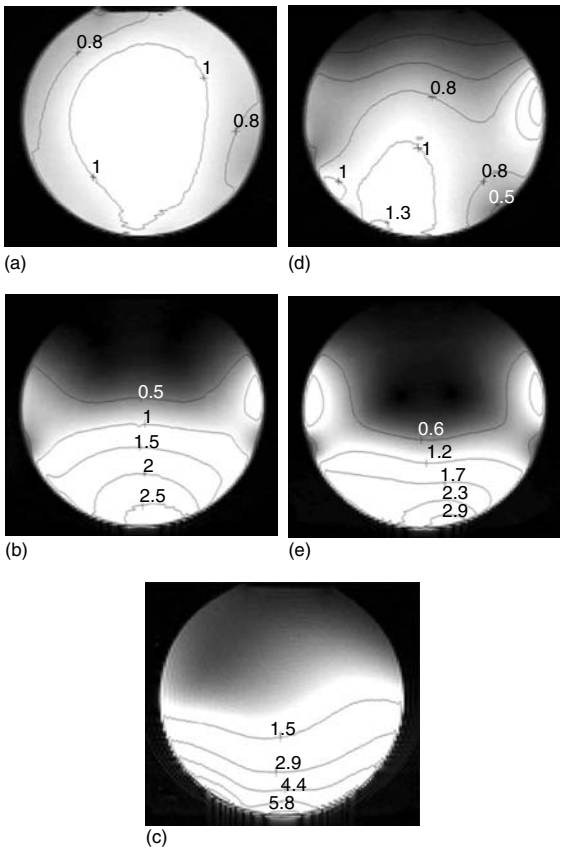

Figure 6.5. Gradient-echo images recorded with (a) the full-volume TEM coil operating in the transmit/receive mode, (b) the half-volume transmit/receive TEM coil, and (c) the full-volume TEM-transmit/surface array-receive system, as well as the images recorded with (d) the surface and (e) the butterfly linear modes of the half-volume TEM coil.

explanation of this effect is beyond the scope of this chapter and is given elsewhere.[3–7]

The sensitivity levels given in Figure 6.5 are normalized to the maximum level for the volume TEM coil. To further illustrate the sensitivity differences of the three devices, the central slice profiles through the images, shown in Figure 6.5(a–c), are plotted in Figure 6.6. The plots represent the sensitivities as a function of the distance from the coils, with the origin at the edge of the phantom (the spacers between the phantom and the coils were approximately 1.5 cm in each case). For the depths less than ∼5 cm (∼half of the coil's radius), the half-volume TEM coil shows significant advantages

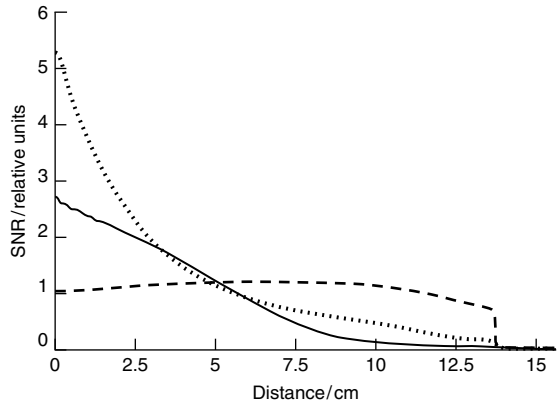

Figure 6.6. Plots of the central slice profiles through the images recorded with the half-volume transmit/receive TEM coil (solid line), the full-volume TEM-transmit/surface array-receive system (dotted line), and the full-volume transmit/receive TEM coil (dashed line), representing the sensitivities of the devices as a function of the distance from the edge of the phantom.

over the full-volume coil. The surface receiver array also shows improved sensitivity with respect to the half-volume TEM coil for depths of ∼3 cm. Thus, significant improvement in the SNR can be achieved by using the half-volume TEM without the need to use separate, actively decoupled devices for transmission and reception and multiple receivers, as in the volume-transmit/array-receive combination. This illustrates the capacity of the half-open volume TEM coil to improve the SNR by both reducing the excitation volume and increasing the magnetic field filling factor relative to a closed full-volume TEM coil. The homogeneous region of the device is sufficiently large for it to be used as an efficient "local" volume coil, while many of the conveniences and sensitivity advantages of the surface coils are retained. Additionally, the half-volume TEM coil achieved the 90° flip angle excitation at 7 dB lower power than the full-volume TEM coil. This drastically reduces total power deposition into the scanned objects, which is especially problematic for body coils at high frequencies.

Figure 6.7 illustrates a gradient-echo human brain image obtained with the half-volume TEM coil together with the B_1 map, obtained at the same anatomic location. The figure shows the applicability of the device as an efficient transmit/receive volume coil, which provides significant RF penetration

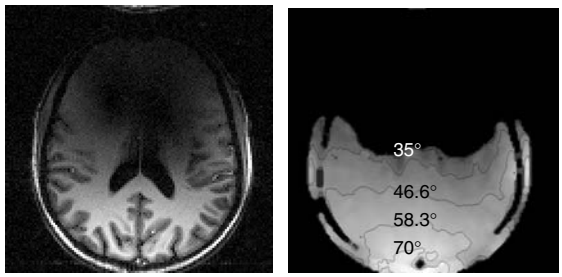

Figure 6.7. (a) Inversion recovery T_1-weighted image in brain using half-volume TEM coil. (b) Corresponding B_1 map at the same imaging slice.

from the cortex well into deeper structures such as the thalamus. Both the image and the B_1 map maintain sufficient left–right symmetry.

6.5 APPLICATIONS

6.5.1 Functional Magnetic Resonance Imaging (fMRI)

One of the potential applications of the open TEM volume coil is functional imaging. Figure 6.8 demonstrates results of a visual fMRI study obtained with the half-volume TEM coil.[18] Figure 6.8(a) shows the anatomic location imaged with the conventional TEM coil, and Figure 6.8(b) demonstrates the fMRI results for approximately the same slice obtained with the half-volume TEM coil. In these experiments, visual stimulation at 4 Hz was delivered by LED goggles (Grass telefactor). Gradient-echo planar imaging (EPI) images were collected from four axial slices intersecting the calcarine fissure, which defines the visual cortex. Imaging parameters were as follows: echo time = 30 ms, repetition time = 400 ms, FOV = 19.2 × 19.2 cm with a 3 mm slice thickness, and in-plane resolution 64 × 64 voxels (3 mm isotropic voxels). The stimulus paradigm consisted of two repetitions of 40 s stimulus duration followed by 40 s of rest. Images were Gaussian-filtered with linear baseline correction. Activation maps were generated using a paired Students t-test with a Bonferroni-corrected activation threshold at a significance level of $p < 0.01$.[33] It is clear that significant activation can be seen throughout the primary visual cortex V1 both at the surface and well into deeper cortical structures. For example, significant activation is also observed in the middle temporal gyrus of the visual cortex V5, which is located several centimeters from the cortical surface and is responsible for higher level processing of motion in the visual system. The ability to detect activation from such distinct areas of the visual system would be difficult to achieve with a standard surface coil. This demonstrates the unique capability of the half-volume TEM coil to obtain high SNR images in a more open environment with significant spatial coverage.

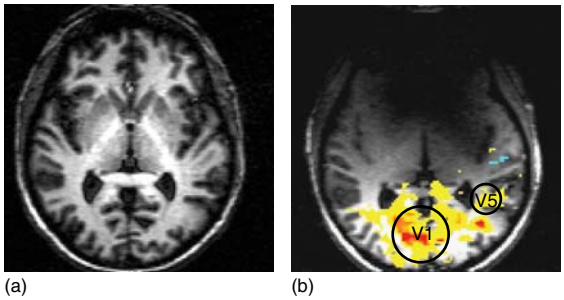

Figure 6.8. Functional MRI results for visual activation. (a) Anatomic image using conventional TEM coil. (b) Thresholded t-map (Bonferroni-corrected statistical significance of $p < 0.01$) from echo planar fMRI acquisition with half-volume TEM coil overlaid on corresponding anatomic image. Activation in primary visual cortex V1 and middle temporal visual cortex V5 are shown.

6.5.2 Parallel Imaging (SENSE)

Another example of half-volume TEM coil applications includes sensitivity encoding (SENSE) parallel imaging. Typically, SENSE parallel imaging[34] of large objects, such as the human torso, is performed using receive-only arrays of multiple decoupled surface coils[35,36] or microstrip detectors.[37] Transmission is commonly provided by a larger body coil. To optimize SNR for SENSE imaging, the spatial distributions of the receive coils must not only have minimal noise correlation but also differ substantially in both amplitude and phase.[35] Alternatively, the same transmit/receive volume coil can provide multiple receive channels if the signals from two or more of its degenerate modes are digitized separately.[38,39] However, certain limitations still apply. For example, two intrinsically degenerate homogeneous modes of

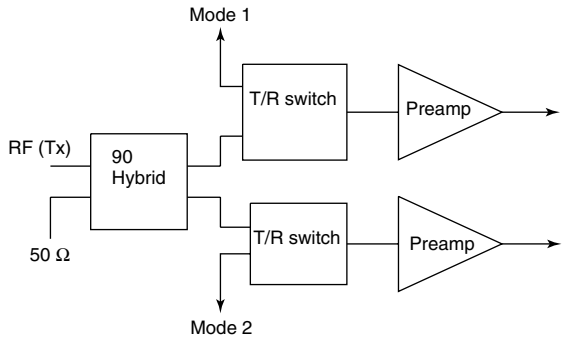

Figure 6.9. Schematic of SENSE parallel imaging using linear modes of the half-volume TEM coil as independent receive channels.

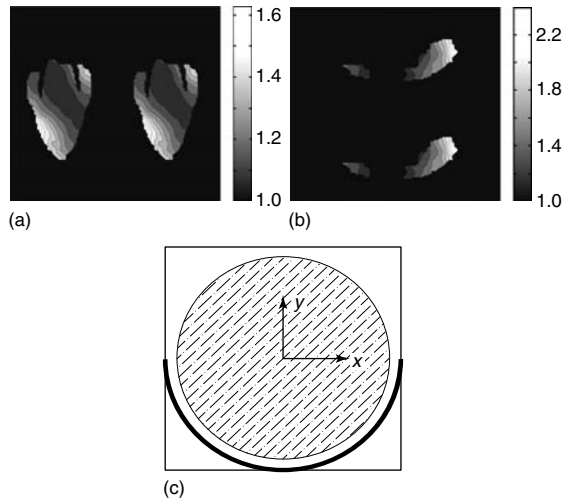

Figure 6.10. G-factor maps with reduction ($R = 2$) of FOV in (a) x- and (b) y-directions using mode sensitivity profiles obtained experimentally from human head gradient-echo images. (c) The geometry of the SENSE experiments.

a full-volume coil do not provide sufficient difference in amplitudes for g-factor minimization. On the other hand, the modes of the half-volume coil have very different spatial profiles[18] and, consequently, can be utilized for SENSE parallel imaging.[39] By eliminating the need for additional hardware (a separate set of receive coils), the coil design and the SENSE experimental setup is substantially simplified. Figure 6.9 shows a block diagram of the setup. During transmission, the circularly polarized RF field was generated using the two modes of the coil by combining them in quadrature. For SENSE imaging, the signals from each mode were acquired simultaneously but through separate independent receive channels (Figure 6.9).

Figure 6.10a and b show the g-factor maps obtained using the measured sensitivity profiles for a human head with $R = 2$ and the FOV reduced in the x- and the y-directions, respectively. Human head images recorded with the linear modes of the coil were used to calculate the g-factor maps. Table 6.1 summarizes these results as well as data from the phantom. The noise correlation measured for a human head and a head-mimicking phantom was less than 5% due to intrinsic isolation of two orthogonal modes of the half-volume coil. The spatially averaged g-factor values obtained for the FOV reduction in the x- and the y-directions were very similar (Table 6.1). Although the average g-value with the FOV reduced in the y-dimension was slightly higher, the reduction of the FOV in this direction may be preferable because of the better peripheral g-factor distribution.

SENSE images with $R = 2$ for both the x- and the y-directions of FOV were acquired from a 2.0 L phantom and a human head. As an example, Figure 6.11, which was acquired with a T_1-weighted gradient-echo inversion recovery sequence, shows human brain image obtained using the half-volume TEM coil in the transmit/receive quadrature mode (Figure 6.11a), images with FOV reduced in x-dimension recorded by each receive channel (Figure 6.11b and c), and a final SENSE reconstructed image (Figure 6.11d). On the basis of the experimental evaluation of the g-factor distribution (see Table 6.1 and Figure 6.10), no significant difference in the SNR was observed between the full FOV image (Figure 6.11a) and

Table 6.1. g-Values obtained at an acceleration factor $R = 2$, using experimentally measured sensitivity profiles for a spherical phantom and a human head

Direction of the FOV reduction	Phantom		Head	
	(Average)	(Maximum)	(Average)	(Maximum)
x	1.03	1.78	1.04	1.69
y	1.04	6.60	1.04	2.54

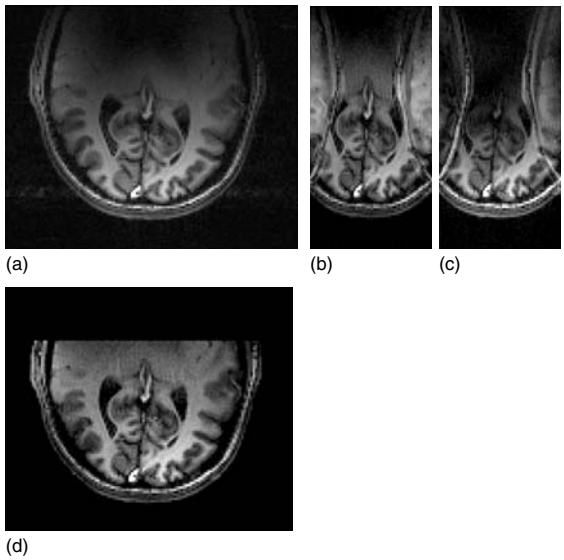

Figure 6.11. Axial brain images obtained using half-volume TEM in (a) conventional quadrature transmit/receive mode. (b) and (c) Twofold reduced FOV images recorded using surface and butterfly modes, respectively. SENSE-reconstructed images with reduction factor $R = 2$ and FOV reduced in (d) x-direction. T_1-weighted inversion recovery gradient-echo sequence were collected with TR = 2500 ms, TIR = 900 ms, a 90° excitation pulse, and a slice thickness of 1.5 mm with 128 × 128 resolution over a FOV of 19.2 × 19.2 cm.

the SENSE reconstructed image (Figure 6.11d) after correction for the difference in scan time. The SENSE reconstructed image with $R = 2$ in the y-direction (not shown) did not reveal any difference in the scan-corrected SNR as well.

To increase the acceleration rate above 2, the number of the degenerate modes could be increased. Decoupling elements from each other and separate driving of each individual element can potentially provide a way of producing a half-volume TEM resonator with a larger number of degenerate modes. Alternately, a combination of two half-volume coils could be used, which would increase the number of available channels to four and extend the coverage to the full-volume. Thus SENSE acquisitions using half-volume coils can be useful in rapid imaging applications, such as EPI-fMRI, allowing increased spatial resolution to be achieved without an increase in readout times. Finally, patient access for stimulus presentation can also be improved.

RELATED ARTICLES IN THE ENCYCLOPEDIA OF MAGNETIC RESONANCE

Birdcage Resonators: Highly Homogeneous Radiofrequency Coils for Magnetic Resonance

High-Field Whole Body Systems

Probe Design and Construction

Spatial Encoding Using Multiple rf Coils: SMASH Imaging and Parallel MRI

Surface Coil NMR: Detection with Inhomogeneous Radiofrequency Field Antennas

REFERENCES

1. J. T. Vaughan, M. Garwood, C. M. Collins, W. Liu, L. DelaBarre, G. Adriany, G. P. Andersen, H. Merkle, R. Goebel, M. B. Smith, and K. Ugurbil, *Magn. Reson. Med.*, 2001, **46**, 24.
2. C.-N. Chen, D. I. Hoult, and V. J. Sank, *J. Magn. Reson.*, 1983, **54**, 324.
3. G. H. Glover, C. E. Hayes, N. J. Pelc, W. A. Edelstein, O. M. Mueller, H. R. Hart, C. J. Hardy, M. O'Donnell, and W. D. Barber, *J. Magn. Reson.*, 1985, **64**, 255.
4. J. R. Keltner, J. W. Carlson, M. S. Roos, S. T. S. Wong, T. L. Wong, and T. F. Budinger, *Magn. Reson. Med.*, 1991, **22**, 467.
5. D. I. Hoult, *J. Magn. Reson. Imaging*, 2000, **12**, 46.
6. J. Wang, Q. X. Yang, X. Zhang, C. M. Collins, M. B. Smith, X. H. Zhu, G. Adriany, K. Ugurbil, and W. Chen, *Magn. Reson. Med.*, 2002, **48**, 362.
7. C. M. Collins, Q. X. Yang, J. Wang, X. Zhang, H. Liu, S. Michaeli, X. H. Zhu, G. Adriany, J. T. Vaughan, P. Anderson, H. Merkle, K. Ugurbil, M. B. Smith, and W. Chen, *Magn. Reson. Med.*, 2002, **47**, 1026.
8. J. T. Vaughan, H. P. Hetherington, J. O. Otu, J. W. Pan, and G. M. Pohost, *Magn. Reson. Med.*, 1994, **32**, 206.
9. D. Ballon, M. C. Graham, S. Miodovnik, and J. A. Koutcher, *J. Magn. Reson.*, 1990, **90**, 131.
10. C. H. Oh, S. K. Kim, Y. J. Yang, and C. B. Ahn, In *Proceedings of the 6th Annual Meeting of ISMRM*, Sydney (NSW), 1998, p. 2025.
11. H. Fujita, W. O. Braum, S. M. Shvartsman, R. W. Brown, T. J. Reisker, D. A. Molyneaux, and M. A. Morich, In *Proceedings of the 6th Annual Meeting of ISMRM*, Sydney (NSW), 1998, p. 645.

12. J. Jin, in *Electromagnetic Analysis and Design in Magnetic Resonance Imaging*, ed M. R. Neuman, CRC Press: Boca Raton, FL, 1999.
13. J. T. Vaughan, H. P. Hetherington, and G. M. Pohost, In *Proceedings of the 3rd Annual Meeting of ISMRM*, France, 1995, p. 996.
14. G. Adriany, E. Yacoub, I. Tkac, P. Anderson, H. Merkle, and J. T. Vaughan, In *Proceedings of the 8th Annual Meeting of ISMRM*, Denver, CO, 2000, p. 563.
15. J. T. Vaughan, In *Proceedings of the 9th Annual Meeting of ISMRM*, Glasgow, Scotland, 2001, p. 15.
16. J. T. Vaughan, M. Garwood, and K. Ugurbil, In *Transactions 2001 Antenna and Propagation Society International Symposium*, 2001, 1, p. 378.
17. G. Adriany, P.-F. Van de Moortele, P. M. Andersen, J. P. Strupp, J. B. Ritter, C. J. Snyder, S. Moeller, J. T. Vaughan, and K. Ugurbil, In *Proceedings of the 12th Annual Meeting of ISMRM*, Kyoto, Japan, 2004, p. 1604.
18. A. Peshkovsky, R. P. Kennan, M. E. Fabry, and N. I. Avdievich, *Magn. Reson. Med.*, 2005, **53**, 937.
19. X. Zhang, K. Ugurbil, and W. Chen, *J. Magn. Reson.*, 2003, **161**, 242.
20. G. Bogdanov and R. Ludwig, *Magn. Reson. Med.*, 2002, **47**, 579.
21. N. I. Avdievich and H. P. Hetherington, *Magn. Reson. Med.*, 2004, **52**, 1459.
22. J. T. Vaughan, G. Adriany, C. J. Snyder, J. Tian, T. Thiel, L. Bolinger, H. Liu, L. DelaBarre, and K. Ugurbil, *Magn. Reson. Imaging*, 2004, **52**, 851.
23. J. F. Bridges, U.S. Pat. 4 751 464. (1988).
24. W. Dür and S. Rauch, *Magn. Reson. Med.*, 1991, **19**, 446.
25. H. Wen, A. S. Chesnick, and R. S. Balaban, *Magn. Reson. Med.*, 1994, **32**, 492.
26. C. P. J. Poole, *Electron Spin Resonance: A Comprehensive Treatise On Experimental Techniques*, Wiley: New York, 1983.
27. D. I. Hoult, *Concepts Magn. Reson.*, 2000, **12**, 173.
28. C. E. Hayes, W. A. Edelstein, J. F. Schenck, O. M. Mueller, and M. Eash, *J. Magn. Reson.*, 1985, **63**, 622.
29. J. Tropp, *J. Magn. Reson.*, 1997, **126**, 9.
30. A. R. Rath, *Magn. Reson. Med.*, 1990, **13**, 370.
31. N. I. Avdievich, V. N. Krymov, and H. P. Hetherington, *Magn. Reson. Med.*, 2003, **50**, 13.
32. J. W. Pan, D. B. Twieg, and H. P. Hetherington, *Magn. Reson. Med.*, 1998, **40**, 363.
33. P. Jezzard and N. F. Ramsey, in *Quantitative MRI of the Brain: Measuring Changes Caused by Disease*, ed P. S. Tofts, Wiley: Chichester, 2003, p. 413.
34. K. P. Pruessmann, M. Weiger, M. B. Scheidegger, and P. Boesiger, *Magn. Reson. Med.*, 1999, **42**, 952.
35. M. Weiger, K. P. Pruessmann, and P. Boesinger, *Magn. Reson. Med.*, 2001, **45**, 495.
36. M. A. Ohliger, R. L. Greenman, R. Giaquinto, C. A. McKenzie, G. Wiggins, and D. K. Sodickson, *Magn. Reson. Med.*, 2005, **54**, 1248.
37. R. F. Lee, C. J. Hardy, D. K. Sodickson, and P. A. Bottomley, *Magn. Reson. Med.*, 2004, **51**, 172.
38. F.-H. Lin, K. K. Kwong, I.-J. Huang, J. W. Belliveau, and L. Wald, *Magn. Reson. Med.*, 2003, **50**, 1107.
39. N. I. Avdievich, A. Peshkovsky, R. P. Kennan, and H. P. Hetherington, *J. Magn. Reson. Imaging*, 2006, **24**, 934.

PART B
Loop Arrays

Chapter 7
Receiver Loop Arrays

Steven M. Wright

Texas A&M University, College Station, TX 77845, USA

7.1 INTRODUCTION

From the earliest days of MRI, researchers have sought ways to improve the signal-to-noise ratio (SNR) of the experiment. For any given MRI sequence, the SNR is fundamentally determined at the output of the receiver "coil", which detects the time-varying magnetic field produced by the sample. Evolving from magnetic resonance spectroscopy (MRS) in which the sample was placed inside a coil that encompassed the sample, early MRI was similarly done using a "volume" coil that essentially viewed the entire sample. A significant breakthrough occurred when Ackerman demonstrated that improved SNR could be obtained by placing a small coil on the surface of the sample, close to the region of interest.[1] Two somewhat parallel paths toward improving the efficiency of the MRI experiment followed: one focusing on manipulating gradients to make MRI faster, and the other attempting to optimize RF technology. Improved gradient technology and pulse sequence design have brought dramatic advances in efficiency and methodology, and RF coil technology has similarly brought significant improvements in SNR, enabling the use of faster imaging methods.

A convergence of sorts is taking place in the field today. As resolution is pushed toward theoretical limits, the SNR provided by coil arrays becomes of increasing importance. Similarly, as imaging speed is pushed toward hundreds of frames per second, the localization provided by coil arrays is playing a key role in advancing dynamic imaging. Research in RF coil array technology should continue unabated for many years, as high-field magnets continue to bring challenges for which RF coil arrays will play a significant role.

Interestingly, arrays of loops were first suggested as a means of reducing imaging time by using their ability to spatially localize the MR signal.[2–5] A number of early researchers proposed using arrays of switched loop elements to adjust the sensitivity pattern of an array of loop coils, optimizing the array configuration for use with a single receiver.[6–9] Soon, Roemer used multiple receivers, each responsible for a single loop element, and demonstrated that array coils could obtain an "optimal" SNR over the entire

RF Coils for MRI
Edited by J. Thomas Vaughan and John R. Griffiths

ISBN: 978-0-470-77076-4

region covered by the loop array.[10] This demonstration generated tremendous interest in RF loop arrays, which has only increased over the subsequent years. This chapter is intended for researchers interested in understanding the basic principles of loop arrays and how they can be used to provide improved SNR. For those interested in the analysis of arrays, basic methods of estimating the sensitivity patterns of loops and how to combine the signals for "optimal" SNR will be reviewed. Practical issues, such as the implementation of the arrays and matching networks, are left for other chapter.

7.2 SIGNAL-TO-NOISE RATIO IN LOOP ARRAYS

7.2.1 Signal-to-noise Ratio from a Uniform Sample

The derivation of the SNR for a uniform sample is widely available,[11–16] and will only be summarized here for convenience in what follows. Hoult and Richards introduced the use of reciprocity to include the sensitivity of the coil explicitly in the expression for the SNR of an MRI experiment.[11] The electromotive force (EMF) produced at the terminals of a coil is found through reciprocity as

$$v(t) = -\frac{\partial}{\partial t}\int_v \vec{B}_1 \cdot \vec{M}_{xy}\, \mathrm{d}v \tag{7.1}$$

where $\vec{B}_1$ is the magnetic flux density produced by the coil by 1 A of current at a reference point defined as the coil terminals, and $\vec{M}_{xy} = M_{xy}(\hat{a}_x \cos\omega t - \hat{a}_y \sin\omega t)$ is the transverse magnetization per unit volume producing the signal being detected, which is obviously dependent upon the pulse sequence, the magnetic field strength, and the properties of the material. With rare exceptions,[17] we can consider the polarization of the coil to be constant and the time variation of the magnetization to be dominated by the rotation around the static magnetic field and the gradients. Thus, for purposes of analyzing the detected voltage we can ignore the relaxation effects when taking the derivatives. This in turn allows us to use phasor notation for convenience, and write the "steady state" detected signal as

$$V_{\text{signal}} = -j\omega\int_v \vec{B}_1 \cdot \vec{M}_{xy}\, \mathrm{d}v \tag{7.2}$$

We recover the time form of the voltage by $v(t) = \mathrm{Re}\{V_{\text{signal}} e^{+j\omega t}\}$, and the time derivative has been replaced by $j\omega$, where $\omega = \gamma B$. While more general derivations are available, to simplify we consider the SNR at a single voxel with volume ΔV. Assuming that the fields of the coil and the magnet are constant over this voxel, we can write $\vec{M}_{xy} = \sqrt{2} M_{xy} \cdot \hat{p}$, where $\hat{p} = (\hat{a}_x + j\hat{a}_y)/\sqrt{2}$. In this equation, M_{xy} remains complex to allow for the phase imparted by the pulse sequence, magnetic field inhomogeneity, or other causes. Thus, equation (7.2) becomes:

$$V_{\text{signal}} = \sqrt{2}\omega \Delta V M_{xy} B_t \tag{7.3}$$

B_t is the "effective coil sensitivity", $B_t = \vec{B}_1 \cdot \hat{p}$. The effective coil sensitivity is different for the coil as a receiver or transmitter due to the conjugation required in the two cases.[18] This can be achieved by conjugating the sign of the magnetization vector $\hat{p}$ depending on whether optimizing a transmit or receive array.

The noise output by the coil scaled to the bandwidth used in detecting the signal, Δf, is characterized by R_{in}, the resistance of the coil at the terminals where the 1 A is specified in equation (7.1):

$$V_{\text{noise}} = \sqrt{4kT\,\Delta f\, R_{\text{in}}} \tag{7.4}$$

where T is the effective temperature, ordinarily but not always room temperature, and k is Boltzman's constant. Thus, the detected SNR, i.e., SNR_k, of a free induction decay (FID) or echo, expressed as the ratio of the peak detected signal voltage to the rms noise level is

$$SNR_k = \frac{\sqrt{2}\omega \Delta V M_{xy} |B_t|}{\sqrt{4kT\,\Delta f\, R_{\text{in}}}} \tag{7.5}$$

We can use equation (7.5) to determine the minimum detectable volume of water for a given coil and field strength given the details of a particular experiment. The symbol SNR_k is used to distinguish this quantification of SNR from that of the image or the "coil" SNR, SNR_c, to be described below.

7.2.2 Coil SNR, SNR_c

While a great many factors determine the SNR available in an MR experiment, two can be optimized independently of the particular imaging parameters. The properties of the coil and sample contribute to determining the SNR through the sensitivity pattern

of the coil, $B_1(\vec{r})$, and the resistance seen at the coil terminals, R_{in}. It is useful to separate from equation (7.5) the "coil SNR or coil efficiency", i.e.,

$$SNR_{\text{c}} = \frac{\sqrt{2}|B_t|}{\sqrt{R_{\text{in}}}} \tag{7.6}$$

The coil SNR makes it clear that we can improve the SNR of the MR experiment either by increasing the flux density produced by the coil or reducing the resistance, or noise, produced by the coil.

7.2.3 SNR Improvement with Surface Coils

Early work in MR imaging and spectroscopy relied on coils that encompassed the sample, or at least some part of the sample—such as a coil surrounding the head or abdomen. While gradient methods can be used to localize the source of the signal to a desired slice, or, if desired even a region contained within a slice, the noise comes from the entire region within the sensitive region of the coil. In most MR experiments, the noise is predominantly contributed by broadband thermal radiation from the sample, unaffected by image localization. Researchers quickly recognized that, if the region of interest was known, say a left kidney, a small RF coil could be designed to fit over the region of interest. The "local" or "surface" coil acts as a spatial filter, eliminating noise detected from outside the region of interest. Ackerman may have been the first to use a surface coil, using one to improve the SNR in ^{31}P spectroscopy of a rat.[1] An early, perhaps the first, surface coil is shown in Figure 7.1. In its simplest form, a surface coil is simply a loop of wire placed as close as possible to the region of interest in the object to be studied. Figure 7.2(a) and (b) illustrates a simple loop coil, and its spatially variant magnetic field.

The immediate difficulty in designing a surface coil is optimizing the loop size and shape. Defining the "optimal" coil has remained an active area of research, as the interplay between the signal and noise can be quite complex when designing a coil. As an example, Figure 7.3 shows the SNR along a line at $z = 0$, $y = 1$ cm, over a set of four concentric rectangular coils in the xz plane ($y = 0$). The "spatial filter" nature of the coil is evident, with the 1.5 cm coil giving a significantly higher SNR directly in front of the coils at this height. However, at a greater height, or even simply further off axis at the same height, the larger coil will provide the higher SNR. Figure 7.4 compares the SNR for the same four coils at a distance of 12 cm from the coil plane, showing that the smallest coil now suffers a significant SNR loss in comparison to the larger coils. Figure 7.5 compares the relative SNR of the four coils on axis, and demonstrates that, at any particular distance, one would choose a different "optimal" coil size. This optimization is discussed further below, but requires knowledge of the coil resistance and sensitivity maps.

Figure 7.1. An early surface coil experiment by Ackerman *et al*. The surface coil, placed over the brain of a rat, acts as a spatial filter, preventing noise contribution from outside the area of interest immediately beneath the coil.[1]

7.3 SNR IMPROVEMENT WITH LOOP ARRAYS

A single surface coil improves the SNR only over a limited region. Additionally, with few exceptions, a simple loop surface coil is sensitive to only one component of the rotating magnetization. Stated another way, a simple loop has a linear polarization. It is clear that adding a second loop to detect the other component of magnetization, properly combined, could improve the SNR, a technique called *quadrature detection*.[19] Adding additional elements, properly configured to form an array, can improve the SNR even further. Each loop provides a high relative SNR over a small region, but properly combined, the signal from the array provides high SNR over the entire field of view covered by all eight individual elements. There are a number of methods to combine the signals from the loop array. While in practice hardware combiners may be used for subsets of elements, we can consider each element to have its own

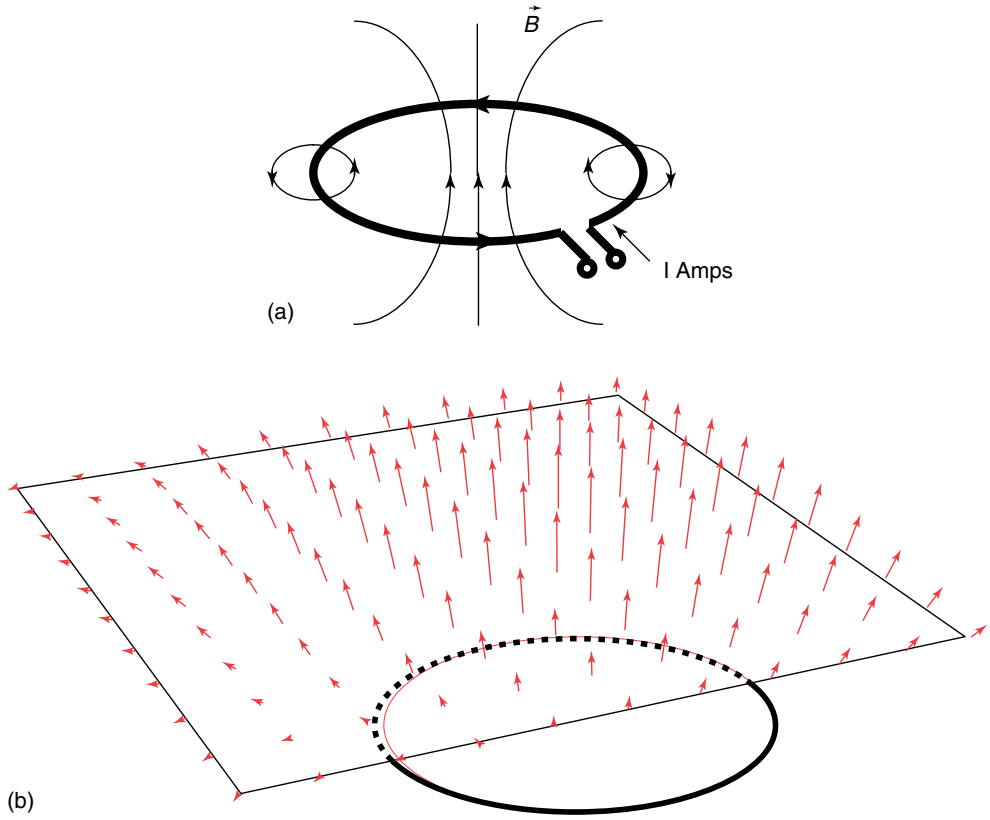

Figure 7.2. (a) Magnetic flux due to a simple loop element. The magnitude and direction of the magnetic flux line determine the magnitude and phase of the signal received by a surface coil at each point. (b) A vector field plot indicating the relative magnitude and direction of the magnetic flux on a grid of 11×11 points in a plane parallel to and above a simple loop. In a straightforward reconstruction of an image detected by this coil in this plane, this would result in a slowly varying modulation of the brightness and phase.

receiver, which digitizes the complex signal and the associated noise. Then our challenge becomes one of properly "weighting" the signals from each coil for optimal SNR at each point. This chapter only addresses the optimization of SNR in conventional imaging. To illustrate the problem of determining the optimal combination of signals, Figure 7.6(a) depicts the relative direction and intensity of the flux density from two coils at three points in a plane perpendicular to the coil plane, and Figure 7.6(b) depicts the intensity of the two coils over a plane parallel to the coils. The intensity of the detected signal is proportional to the magnitude of the flux density, and the phase proportional to the direction of the flux density in the *xy* plane. Clearly, to obtain maximal SNR at each point the signals from each coil would have to be weighted differently at each point. For example, at a point where only one coil contributes significant flux density, the other coil will still contribute noise and should not be included in the reconstruction. At points where both contribute, the signals need to be brought back in phase (to first order). The amplitude and phase corrections required are referred to as *weighting coefficients*. There are a number of methods to obtain these weighting coefficients. The simplest is a rather intuitive technique called *sum of squares* (*SOS*), which can easily be applied to a set of magnitude images with no knowledge of field patterns or noise levels from the coils. However, Roemer and others have derived the general solution for the optimal currents, or weighting functions, in

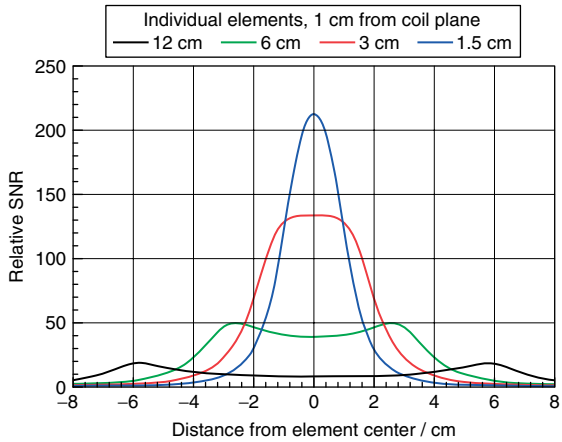

Figure 7.3. Relative SNR of four concentric square coils along a line parallel to the coil plane and 1 cm above the coils. The line is at $z = 0$ cm, $y = 1$ cm; the coils are in the xz plane at $y = 0$. The 1.5 cm coil provides the highest SNR at the center of the FOV, but suffers reduced SNR in comparison to the other coils several centimeters off axis. The coils have lengths of 12, 6, 3, and 1.5 cm (center to center), modeled as constructed from a 0.375 cm copper tape. Coils are modeled using quasistatics at 63.5 MHz, and are located 1 cm from a load with conductivity 0.72 S m^{-1}, with dimensions 30 × 30 cm in x and z, and 10 cm in y.

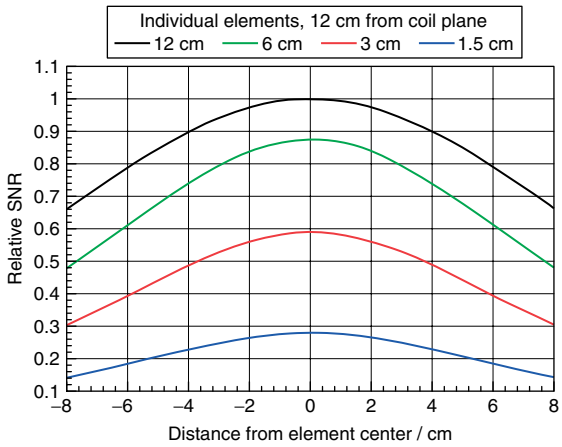

Figure 7.4. Relative SNR of the four concentric square coils from Figure 7.3 along a line parallel to the coil plane and 12 cm above the coils. At this distance from the coils, the SNR of the 1.5 cm coil is the lowest due to the small field of view of that coil. The 12 cm coil provides the highest SNR.

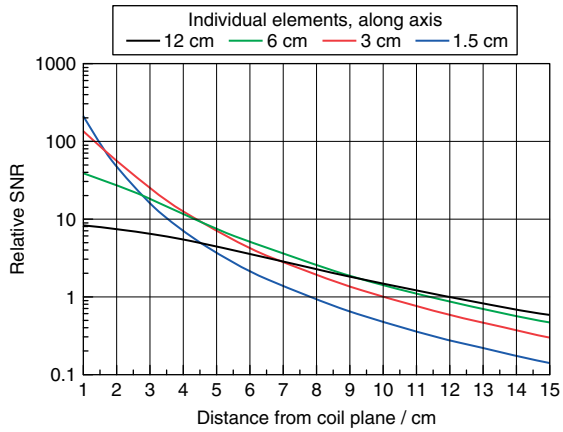

Figure 7.5. Relative SNR vs distance (on coil axis) from a plane containing the four surface coils described in Figure 7.3. The optimal coil size is a function of the imaging depth, with the smallest coil providing the highest SNR close to the coil and the largest coil providing the highest SNR far from the coil.

an MRI array problem, and it will be summarized first.[10,20]

7.3.1 Expression for Loop Array Efficiency

Equation (7.6) described the voltage SNR of a receive coil in terms of the flux density it would produce as a transmit coil. This is consistent with a well-known principle that the relative SNR of two coils can be compared by finding the input power required to create a given tip angle, essentially a measure of the efficiency of a coil. The transmit coil efficiency is, of course, closely related to equation (7.6). One can define the "coil efficiency" as the ratio of the effective power density delivered to the observation point to the total power absorbed by the coil, P_{abs}. Noting that only the transverse power density is of importance in MRI and MRS, and once again ignoring fixed constants, the coil efficiency can be defined as

$$\eta_c = \frac{|B_t|^2}{P_{\text{abs}}} = \frac{B_t^* B_t}{\frac{1}{2}|I|^2 R_{\text{in}}} \tag{7.7}$$

As the transverse magnetization B_t was defined with $I = 1$ A, equations (7.6) and (7.7) provide the link between the coil efficiency as a transmitter and

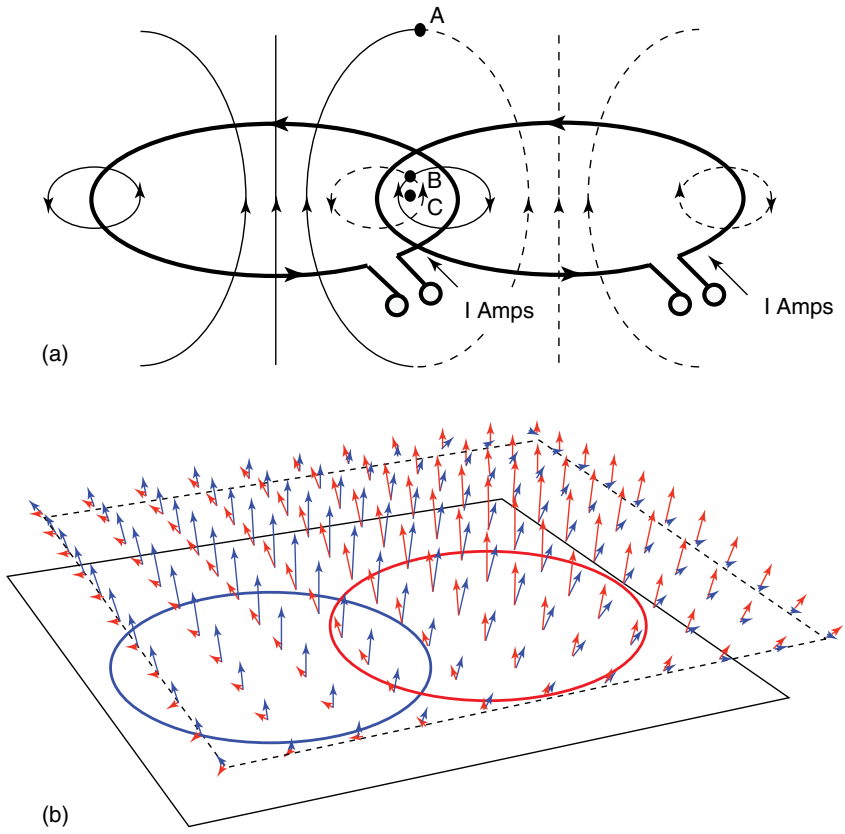

Figure 7.6. (a) Two overlapped loop coils depicting the flux lines from each. At points A, B, and C, along a line perpendicular to the array, the flux lines would be approximately opposed (A), 90° apart (B), or aligned (C). In order to "combine" the signals from these two loops for optimal SNR, the appropriate phase shifts would be different at each point. (b) A vector field plot indicating the relative magnitude and direction of the magnetic flux from two loops, on an 11×11 grid in a plane parallel to and above the two loops. Red vectors correspond to the red coil, blue to the blue coil. At each point, different "weightings" would be required in a combination for optimal SNR.

the SNR it produces as a receiver: i.e.,

$$\eta_c = SNR_c^2 = \frac{|B_t|^2}{P_{abs}} \tag{7.8}$$

This is particularly useful in trying to analyze different array coil configurations. Consider a simple array of loop coils. In practice, one would connect each element to an independent receiver channel. Conceptually, however, for every voxel we need to find properly the weight of the signals from the different elements before combining them. The weighting coefficients would be implemented with variable gain amplifiers and phase delays, as illustrated in Figure 7.7(a). For the analysis here, we consider the reciprocal problem, i.e., finding the weights to create the maximum coil efficiency, as defined by equation (7.7) and illustrated in Figure 7.7(b).

To find the coil efficiency, we need the effective flux density of the array, $B_{t,\text{array}}$. This is obtained by a summation of the effective flux density of each coil, B_{ti}, weighted by the current into each coil:

$$B_{t,\text{array}} = \sum_{i=1}^{N_{\text{coils}}} B_{ti} I_i = \langle B_t I \rangle \tag{7.9}$$

To evaluate the coil efficiency, we need the squared magnitude, $|B_{t,\text{array}}|^2$:

$$|B_{t,\text{array}}|^2 = B_{t,\text{array}}^* B_{t,\text{array}} = \langle I^* B I \rangle \tag{7.10}$$

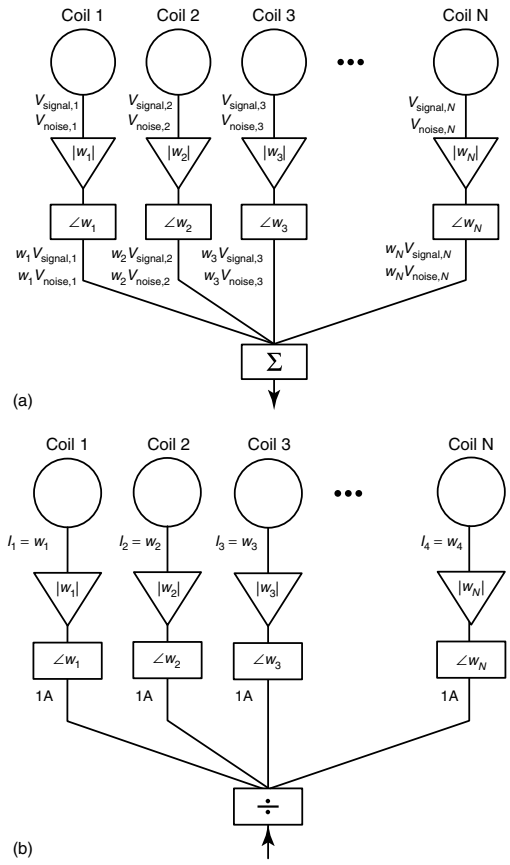

Figure 7.7. (a) Illustration of an N element loop "phased" array, with weighting functions represented by amplifiers followed by N phase delay units. In reality, this is implemented in software because the amplitudes and phases required for optimal SNR at each point are different. (b) An alternative view for optimizing the weighting coefficients of the array by maximizing array efficiency. Just as the SNR of two coils can be compared by measuring the power required for a 90° tip, we can optimize an array coil by determining the weighting factors that create the highest effective flux density for a given input power. Just as in receive mode, the weighting functions are represented by N amplifiers and N phase delay units. Assuming 1 A out of the divider, the weighting factor for each coil is simply the desired current.

where $I\rangle$ is a column vector of the array currents, $\langle I^*$ is a row vector (the conjugate-transpose of $I\rangle$), and $\mathbf{B}$ is a square matrix obtained as the outer product of the column and row vectors with the effective fields of each coil at the observation point:

$$I\rangle = \begin{bmatrix} I_1 \\ I_2 \\ \vdots \\ I_N \end{bmatrix} \mathbf{B} = B_t^*\rangle\langle B_t$$

$$= \begin{bmatrix} B_{t1}^* B_{t1} & B_{t1}^* B_{t2} & \cdots & B_{t1}^* B_{tN} \\ B_{t2}^* B_{t1} & B_{t1}^* B_{t2} & & \\ \vdots & & \ddots & \\ B_{tN}^* B_{t1} & & & B_{tN}^* B_{tN} \end{bmatrix}$$

$$\langle I^* = [I_1^* \quad I_2^* \quad \cdots \quad I_N^*] \tag{7.11a–c}$$

The real power absorbed by a two port circuit is easily found to be

$$P_{\text{abs}} = \frac{1}{2}(|I_1|^2 R_{11} + |I_2|^2 R_{22} + (I_1^* I_2 + I_2^* I_1) R_{12}) \tag{7.12}$$

which can also be expressed in matrix form as

$$P_{\text{abs}} = \frac{1}{2}\langle I^* R I\rangle \tag{7.13}$$

where R is the matrix comprised of the real components of the impedance matrix Z, with elements.

$$\mathbf{R} = \begin{bmatrix} R_{11} & R_{12} & \cdots & R_{1N} \\ R_{21} & R_{22} & & \\ \vdots & & \ddots & \\ R_{N1} & & & R_{NN} \end{bmatrix} \tag{7.14}$$

As with R_{in}, the elements of the $\mathbf{R}$ are referenced to the same terminals at which the current for B_{ti} is 1 A. In the absence of coupling between coils, R_{ii} is the same as the input resistance of the ith coil, $R_{\text{in},i}$. These values are used for the analysis and design of the coil arrays, but in practice, as they represent the noise levels and noise correlation, $\mathbf{R}$ is often determined by measuring noise statistics from data obtained from the scanner with the transmitter blanked.

Equations (7.10) and (7.13) give the effective flux density and the power absorbed by the array. Substitution into equation (7.8) obtains the efficiency of a coil array, or equivalently, the square of the array SNR:

$$\eta_{\text{c}} = \frac{\langle I^* B I\rangle}{\frac{1}{2}\langle I^* R I\rangle} \tag{7.15}$$

Equation (7.15) is a ratio of quadratic Hermitian forms, commonly found in optimization problems.[21] The solution is the eigenvector (the set of currents, $[I]$) that maximizes the coil efficiency. Equivalently, with no loss of generality, we can assume that the splitter provides 1 A to each coil so that the currents input to the coils simply become the applied gain and phase shifts, or "weighting functions", $[w]$, where $[w] = [I]$, as is commonly used in the literature.

Solving equation (7.15) for the currents that maximize the coil efficiency at any spot requires the effective flux density for each coil as well as information on the self- and mutual resistances from each coil (or the noise statistics as discussed above). For purposes of analysis, we can calculate these quantities with a variety of methods, as is discussed below. In practice, however, there are a number of approaches that can simplify the solution that are commonly used.

7.3.2 Optimization of Array Signal-to-noise Ratio or Efficiency in MRI

We need to optimize the coil efficiency, which we can write as

$$\eta_c = \frac{P_{del}}{P_{abs}} \tag{7.16}$$

where

$$\begin{aligned} P_{del} &= \langle I^* B I \rangle \\ \text{and} \\ P_{abs} &= \langle I^* R I \rangle \end{aligned} \tag{7.17}$$

The current vector that optimizes η_c can be obtained by writing the quadratic forms as double sums and taking the derivatives explicitly.

$$\eta_c = \frac{\sum_{i,j}^{N} I_i^* B_{ij} I_j}{\sum_{i,j}^{N} I_i^* R_{ij} I_j} \tag{7.18}$$

Taking the derivative with respect to each of I_i^* leads to a set of N equations:

$$\frac{\partial \eta_c}{\partial I_i^*} = \frac{1}{P_{abs}^2}\left[P_{abs}\sum_j B_{ij} I_j - P_{rec}\sum_j R_{ij} I_j\right] i = 1, N \tag{7.19}$$

Setting each equation to zero and rewriting the equations, we have

$$B I\rangle = \eta_c R I\rangle \tag{7.20}$$

Substituting for η_c from equation (7.15) above, we have

$$B I\rangle = \frac{\langle I^* B I\rangle}{\langle I^* R I\rangle} R I\rangle \tag{7.21}$$

But, since

$$B = B_t^*\rangle\langle B_t \tag{7.22}$$

the scalar $\langle B_t I\rangle$ is eliminated, and this can be simplified to

$$B_t^*\rangle = \left\{\frac{\langle I^* B_t^*\rangle}{\langle I^* R I\rangle}\right\} R I\rangle \tag{7.23}$$

The term in the braces is also a scalar, and does not impact the overall efficiency, as discussed below. Denoting this quantity as $1/\lambda$, as done by Roemer, we have an expression that can be solved for the optimal current vector:

$$B_t^*\rangle = \frac{1}{\lambda} R I\rangle \tag{7.24}$$

The excitation currents needed for optimal antenna efficiency, or SNRs, are

$$I\rangle = \lambda R^{-1} B_t^*\rangle \tag{7.25}$$

The scalar λ does not affect the SNR, as it is applied to each element of the current vector. However, it can be selected to maintain constant absorbed power for all observation points (equivalent to constant noise power in the reconstructed image) or, alternatively, to maintain a constant effective flux density at all observation points (equivalent to normalizing the array sensitivity pattern to be uniform over the image). Constant noise power is the approach generally used, and is achieved by substituting the current vector given by equation (7.25) into equation (7.13), differentiating the expression, and setting the result to zero. This results in

$$\lambda_{noise} = \{\langle B_t R^{-1} B_t^*\rangle\}^{-\frac{1}{2}} \tag{7.26}$$

which is denoted λ_{noise} because it forces the denominator of the SNR expression to be constant. Alternatively, solving for constant effective flux density in equation (7.10) results in

$$\lambda_{signal} = \{\langle B_t R^{-1} B_t^*\}^{-1} \tag{7.27}$$

Given the optimal current vector from equation (7.25) and the vector of pixel values from each coil, the combined data at each pixel, P_c, is

$$P_c = \langle PI \rangle \tag{7.28}$$

Many practical questions remain, such as decoupling the coils to enable them to operate independently (maintaining the sensitivity pattern of each loop element), computing or measuring the sensitivity pattern matrix **B**, and computing or measuring the noise correlation matrix **R**. The latter two are discussed in Section 7.4. First, it is worth pointing out a simplified reconstruction technique that remains commonly used, the SOS technique.

7.3.3 Signal Combination with the "Sum-of-squares" Technique

For designing a loop array, the generalized method above is quite straightforward to use. In practice, one generally measures the noise correlation matrix, **R**, by obtaining noise measurements from each channel with the RF transmitter off or set to transmit zero power. A number of techniques are available to measure the coil sensitivity patterns, and, as these may be required for parallel imaging, a number of techniques are available, often built into the software on clinical scanners. For older systems, or animal scanners, however, accurate sensitivity patterns may not be readily available. In this case, a simplified combination method known as the SOS technique can be used. In most cases, this method will not result in significant SNR loss, as compared to the more general technique. Taking the magnitude of the image effectively aligns the signals at each point. Thus, no phasing is required. As to the relative magnitude of the weighting functions for each image, it should be clear that, if there is no signal at that point, either there is no information at that point (air) or the loop provides no signal. A reasonable approach is to simply weight the data from each coil at each pixel by the pixel value. Denoting the pixel value from the elements as P_i, the reconstructed voxel, P_c, becomes

$$P_c = \sqrt{\sum_i P_i^2} \tag{7.29}$$

The square root is taken to maintain the original intensity (consider a point at which only one coil contributes signal).

Obviously, the SOS method should follow from the generalized approach. If we assume that there is no noise correlation and all the noise levels are equal, then **R** becomes the identity matrix (any constant affects only the overall image intensity and can be ignored). If we assume that the image intensity is proportional to the sensitivity pattern, then equation (7.25) becomes

$$I\rangle = \lambda R^{-1} B_t^* \rangle = \lambda P\rangle \tag{7.30}$$

Using a constant noise approach,

$$\lambda_{\text{noise}} = \{\langle B_t R^{-1} B_t^* \rangle\}^{-\frac{1}{2}} = \{\langle PP \rangle\}^{-\frac{1}{2}} \tag{7.31}$$

Using these values, a combined data point becomes simply

$$P_c = \langle PI \rangle = \frac{\langle PP \rangle}{\{\langle PP \rangle\}^{-\frac{1}{2}}} \tag{7.32}$$

which agrees with equation (7.29) above, which was arrived at heuristically.

7.4 QUASISTATIC ANALYSIS OF LOOP ARRAY ELEMENTS

Many methods are available to model coils and coils systems. In theory, the calculation of mutual impedances and flux densities of coil arrays over lossy samples is mildly complex. A highly accurate calculation would need to include the inhomogeneities and physical extent of the sample, the current distribution on the coils and their perturbations by the presence of the other coils and the load, and of course the shielding effects on the electric and magnetic fields due to eddy currents introduced in the lossy sample. Several approaches are available that can include some or all of these complications. Examples include analytical solutions for canonical geometries, finite element approaches, integral equation solvers, and finite-difference time-domain approaches.

For a great many applications, a simple approach based on quasistatics will provide good results. The quasistatic method uses statics to compute the magnetic flux density and the magnetic vector potential, but then assumes a time-varying magnetic field (simply adding an $e^{+j\omega t}$ time variation) to allow one to obtain an electric field. The losses in the sample are computed from the electric field. The impedance matrix for the array can then be approximated, as

described below. While this is an approximate technique that does not enforce all boundary conditions on the fields, it is considered to be a good approximation for many cases of interest in MRI and MRS, where dimensions of the coil (or at least individual copper segments) and sample dimensions are generally small compared to the wavelength. Additionally, the method can be extended to handle multiply connected structures, such as birdcage coils, and even RF shields. An excellent discussion of the basic approach can be found in the text by Smythe,[22] particularly Chapters 6 and 16, or nearly any introductory electromagnetics text. Obviously, the technique can break down for high-field magnets, where more accurate methods may be required.

7.4.1 Fields, Fluxes, and Vector Potentials

The quasistatic form of Maxwells' equations are obtained by setting the frequency variation $\omega = 0$ in Ampere's law, but leaving it nonzero in Faraday's law. This gives the following set of equations:

$$\begin{aligned} \nabla \times \vec{B} &= \mu \vec{J} \\ \nabla \times \vec{E} &= -j\omega \vec{B} \\ \nabla \cdot \vec{B} &= 0 \end{aligned} \tag{7.33a–c}$$

Assuming a known current distribution, the magnetic vector potential $\vec{A}(\vec{r})$ and the magnetic flux density $\vec{B}(\vec{r})$ produced by a known current distribution $I(\vec{r})$ can be obtained in a straightforward manner:

$$\vec{A}(\vec{r}) = \frac{\mu}{4\pi} \int_{\text{coil}} \frac{\vec{J}(\vec{r}')\mathrm{d}v'}{R} \tag{7.34}$$

$$\vec{B}(\vec{r}) = \frac{\mu}{4\pi} \int_{l} \frac{I(\vec{r}')\mathrm{d}\vec{l} \times \hat{a}_R}{R^2} \tag{7.35}$$

where r' is the magnitude of the vector $\vec{r}'$, the vector from the integration point on the conductor to the observation point $\vec{r}$, $\mathrm{d}\vec{l}$ is the differential path length along the conductor at the point of integration, and $\hat{a}_R$ is a unit vector in the direction of the vector $\vec{R} = \vec{r} - \vec{r}'$, which is the vector from the source point to the observation point. R is the magnitude of the vector $\vec{R}$, as illustrated in Figure 7.8. The current distribution $I(\vec{r})$ is generally known to a high degree of accuracy for practical well-performing coils, such as simple loops, planar pairs, and birdcage designs.

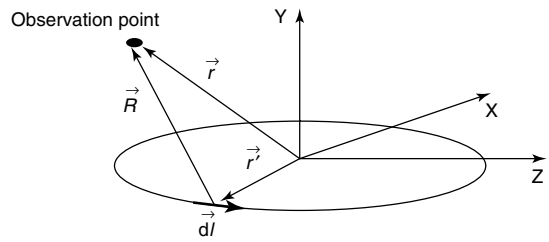

Figure 7.8. A loop in the xz array, with the vectors discussed in the text depicted.

Once the current begins to substantially diverge from being constant over a given segment, performance of the coil, as well as this model, begins to suffer. The flux density and the magnetic vector potential are related by the fact that the divergence of the flux density must be zero (Gauss's law for the magnetic field), which leads to the following equation:

$$\vec{B} = \nabla \times \vec{A} \tag{7.36}$$

We obtain an approximation for the electric fields by assuming that the static magnetic flux density is time varying with an $e^{j\omega t}$ time variation. Then, we use Faraday's law

$$\nabla \times \vec{E} = -j\omega \vec{B} \tag{7.37}$$

and equation (7.2) to obtain

$$\nabla \times \vec{E} = -j\omega \nabla \times \vec{A} \tag{7.38}$$

from which we can conclude (approximately, since we have assumed a static vector potential)

$$\vec{E}(\vec{r}) = -j\omega \vec{A}(\vec{r}) \tag{7.39}$$

7.4.2 Coil Self- and Mutual Impedances

One can show using the reaction theorem that the port open-circuit impedance parameters can be expressed in terms of the electric fields and currents as[23]

$$Z_{ij} = \frac{-1}{I_i I_j} \int_{v} \vec{E}^{\,j}(\vec{r}) \cdot \vec{J}^{\,i}_{\text{coil}}(\vec{r})\mathrm{d}v \tag{7.40}$$

where $\vec{E}^{\,j}(\vec{r})$ is the electric field due to the assumed constant current distribution on coil j, and $\vec{J}^{\,i}_{\text{coil}}$ is the assumed current distribution on coil i. The vector $\vec{r}$ is from the origin to the integration point. Both the self-impedances Z_{ii} and the mutual impedances Z_{ij}

are obtained from equation (7.40), which is exact if the current distributions are known and the proper Green's function for the media is used. In this case, the actual current on coil i is complex, due to the loss from the coil and the sample. However, one can obtain approximate results by using equivalent sources $\vec{J}_s^i(\vec{r})$ to account for the lossy medium. The equivalent sources are the currents induced in the sample by the electric field of the coil:

$$\vec{J}_s^i(\vec{r}) = \sigma(\vec{r})\vec{E}^i(\vec{r}) \tag{7.41}$$

We obtain the electric field from equations (7.34) and (7.39). Additionally, with a single simply connected conductor, such as a loop, equation (7.34) becomes

$$\vec{A}(\vec{r}) = \frac{\mu}{4\pi}\int_{\text{coil}} \frac{I(\vec{r}')\mathrm{d}\vec{l}}{|\vec{r}-\vec{r}'|} \tag{7.42}$$

At this point, the integral in equation (7.40) can be expressed in two parts, one forming the reaction of the electric fields of coil j with the equivalent sources representing the lossy sample, and the other the reaction between the fields of coil j and the assumed current on coil i.

$$Z_{ij} = \frac{-1}{I_i I_j}\left\{\int_{\text{sample}} \vec{E}^j(\vec{r})\cdot\vec{J}_s^i(\vec{r})\mathrm{d}v + \int_{\text{coil}} \vec{E}^j(\vec{r})\cdot\vec{J}_{\text{coil}}^i(\vec{r})\mathrm{d}v\right\} \tag{7.43}$$

Using equations (7.39) and (7.41), and noting that one can assume an input current in both coils of 1 A, leads to the expressions for the resistive and reactive coupling terms:

$$\begin{aligned} R_{ij} &= \mathrm{Re}\{Z_{ij}\} \approx \mathrm{Re}\int_{\text{sample}} \vec{E}^j(\vec{r})\cdot J_s^i(\vec{r})\mathrm{d}v \\ &= \sigma\omega^2\int_{\text{sample}} \vec{A}^j(\vec{r})\cdot\vec{A}_s^i(\vec{r})\mathrm{d}v \\ X_{ij} &= \mathrm{Im}\{Z_{ij}\} \approx \mathrm{Im}\int_{\text{coil}i} \vec{E}^j(\vec{r})\cdot J_s^i(\vec{r})\mathrm{d}v \\ &= \omega\int_{\text{coil}i} \vec{A}^j(\vec{r})\cdot J_s^i(\vec{r})\mathrm{d}v \end{aligned} \tag{7.44a, b}$$

Note that the copper loss has been ignored. For coils systems that are not heavily dominated by sample loss, one would need to include the copper loss terms, which are widely available. Additionally, any perturbation in the inductive coupling due to the sample is ignored. Sample effects will always be present, but are essentially impossible to include analytically due to the variation from study to study.

Only in a very few cases can these quantities be evaluated analytically, such as in the case of the flux on the axis of a circular loop or solenoid, each of which is discussed below. In general, the integral is performed numerically, by discretizing the loop into a number of straight segments and summing the flux densities created by each straight segment. Fortunately, a great many experiments are done with variations of three simple coils, the circular loop, solenoids, and "birdcage" coils. Approximate formulas exist for the fields and impedances of these coils. Although not accurate in all cases, particularly as the coil dimensions approach a significant fraction of a wavelength, these formulas are accurate enough for most applications.

7.5 EXAMPLES AND DISCUSSION

Three examples will be considered to illustrate the performance improvement possible by the use of loop arrays: a two-loop quadrature coil, a set of arrays of decreasing loop size but constant overall dimension, and a 16-channel volume coil array. Quadrature coils may be the earliest form of array coils.[19,24] In the simplest form, a quadrature coil is an array of two identical coils, one rotated by 90° about the static field axis (z). If the coils are volume coils, with uniform fields throughout the sample, and ignoring asymmetries in the load, the two coils provide equal sensitivity but with magnetic fields rotated by 90°. A quadrature combiner recovers a $\sqrt{2}$ improvement in SNR. The quadrature combiner is equivalent to weighting the two coil signals by $w_1 = 1\angle 0^\circ$ and $w_2 = 1\angle 90^\circ$. If the quadrature coil does not provide uniform fields, but a quadrature combiner does not provide optimal weights at all locations. For example, consider the case illustrated in Figure 7.9, where two 6 cm loop elements are centered and 1 cm away from two faces of a cubic phantom centered at the origin and 6 cm on a side. Despite a commercial program rendering, each coil was modeled with the quasistatics techniques described above. All modeling in this section assume a Larmor frequency of 63.5 MHz. Figure 7.10 displays the ratio of the SNR obtained by a true array combination to that obtained using a

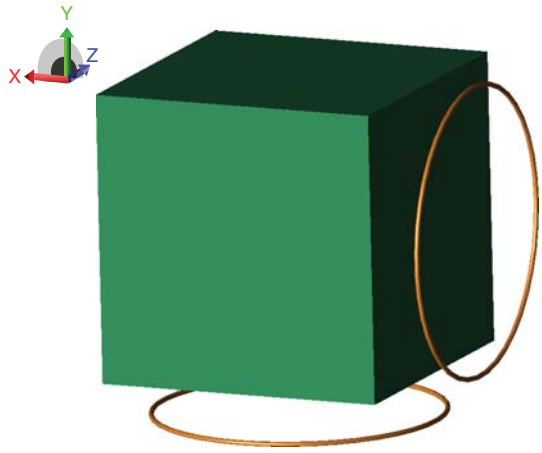

Figure 7.9. Two 6 cm diameter loops positioned at 90° around a 6 × 6 × 6 cm phantom. The loops are 1 cm away from the phantom face, with the axis crossing the origin. In this case, at the origin (center of the phantom), the SNR gain should be 1.4 for the quadrature combiner and for an array, but using the two loops as a true array with two receivers would provide improved SNR at all other locations.

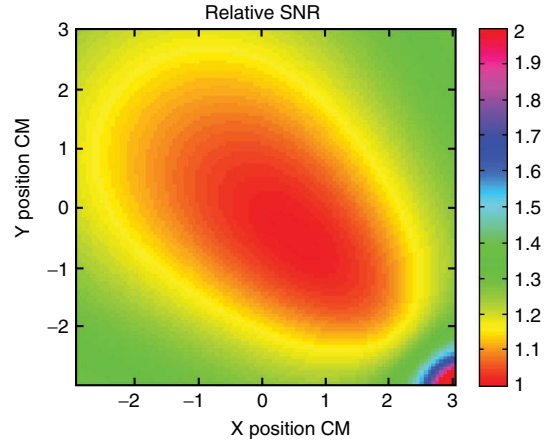

Figure 7.10. Relative SNR between a true array combination (general method) and using a quadrature combiner with the array illustrated in Figure 7.9. In the center, the two methods provide equal SNR. Close to either coil, adding signal from the other coil adds predominantly noise, and therefore the true array combination provides a $\sqrt{2}$ improvement in SNR over the quadrature combiner. In the corner close to both elements, the quadrature combiner does not work well because of the phases of the coils at those points, so the array combination provides significant improvement.

simple quadrature combiner. The data is shown for an axial slice (*xy* plane) at $z = 0$. In the center, where the fields of the two coils are expected to be equal in amplitude but oriented 90° apart, the quadrature combiner works as well as the array combination. Away from the center, the SNR of the array combination is better. In particular, near each element there is a 30–40% improvement—essentially the more remote element is providing only noise. At the corner of the plot, near both coils, the orientation of the coil flux lines is not favorable for the use of a quadrature combiner, and the array combination provides even more SNR improvement. For display purposes, the plot has been truncated at 2.0 in Figure 7.10. This example illustrates that even with a simple two element array, unless they are volume coils with very close to homogeneous fields, the array combination is worthwhile.

As a second example, a single 12 cm square loop is compared to 2 × 2, 4 × 4, and 8 × 8 element arrays all with the same overall (12 cm) outer dimension. The dimension 12 cm is measured from the center of the conductors, which is modeled as 0.375 cm wide. The 12 cm coil and one element of the 2 × 2, 4 × 4,

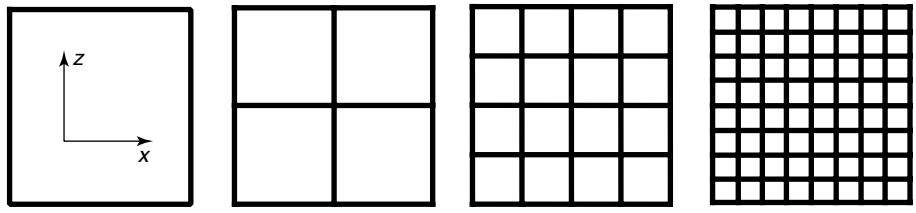

Figure 7.11. A single square element, 12 cm on a side (center to center of conductors), and three arrays with the same outer dimensions as the 12 cm coil. All conductors are modeled as 0.375 cm copper strip (copper losses are included in the model). A single element from each case corresponds to the elements used in Figures 7.3–7.5. The coils were considered to be perfectly decoupled using ideal noiseless isolating preamplifiers.

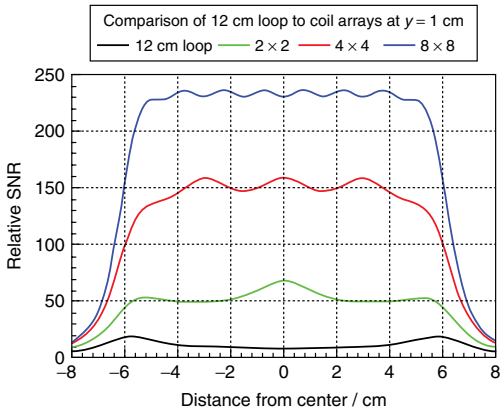

Figure 7.12. Relative SNR of a single 12 cm square loop compared to three arrays with the same overall dimension as the 12 cm loop, along a line parallel to the coil plane and 1 cm above the coils. The line is at $y = 1$ cm, $z = 0.75$ cm to avoid proximity to array element conductors. The coils are in the xz plane at $y = 0$. The 8×8 element array, consisting of 64 1.5 cm coil elements, provides the highest SNR over the entire 12 cm, not suffering the limited field of view of the isolated element. The coils have lengths of 12, 6, 3, and 1.5 cm (center to center). Coils are modeled using quasistatics at 63.5 MHz, and are located 1 cm from a load with conductivity 0.72 S m^{-1}, with dimensions 30×30 cm in x and z, and 10 cm in y.

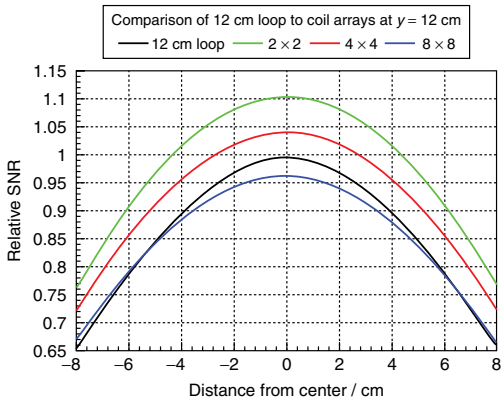

Figure 7.13. Relative SNR of a single 12 cm square loop compared to three arrays with the same overall dimension as the 12 cm loop, along a line parallel to the coil plane and 12 cm above the coils. The line is at $y = 12$ cm, $z = 0.75$ cm. All cases provide essentially the same SNR, with the SNR provided by the 8×8 element array reduced by less than 5% from that of the single 12 cm loop, due to copper losses in the 64 element array.

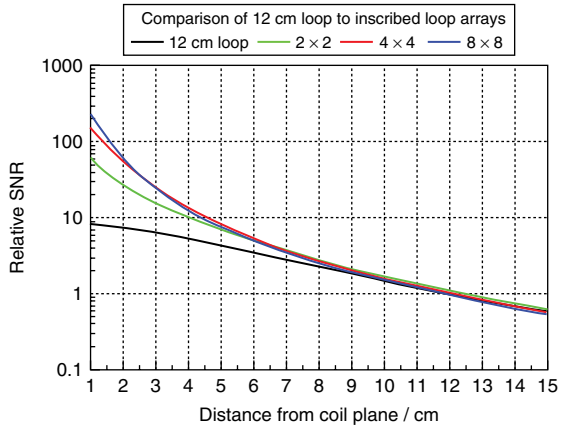

Figure 7.14. Relative SNR of a single 12 cm square loop compared to three arrays with the same overall dimension as the 12 cm loop, along a line normal to the arrays and parallel to the axis of the 12 cm loop. The line is at $z = 0.75$ cm, to avoid conductors. Unlike the case with individual elements, the SNR using small elements does not suffer, as the array "synthesizes" the large loop far from the array. Hence, the array obtains the benefit of the small elements close to the array and retains the advantage of the larger elements at distance.

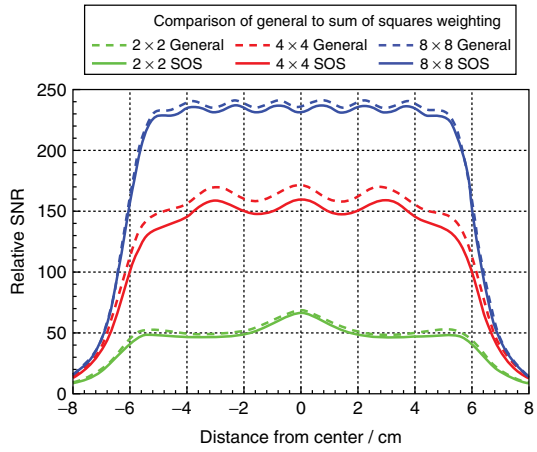

Figure 7.15. Comparison of the relative SNR for the array coils in Figure 7.12 using two different combination techniques, the general method and the "sum-of-squares" method. Solid lines are using the "sum-of-squares" method, and are identical to the results in Figure 7.12. The dashed lines use the general method, requiring the complex coil sensitivity patterns and the **R** matrix for the array. In this case, relatively little improvement is obtained using the general method.

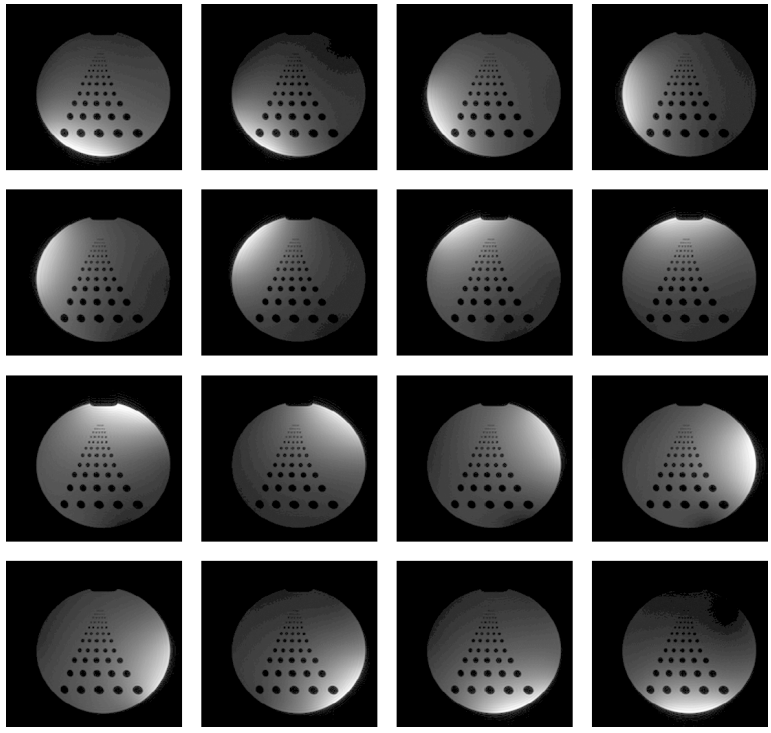

Figure 7.16. Individual element patterns from a 16 channel head coil array described in detail elsewhere.[27] The individual elements have very little sensitivity at the center, yet the combined image (not shown) has an SNR comparable to that of a conventional quadrature volume coil in the center.

and 8×8 arrays are identical to the coils used for Figures 7.3–7.5. For purposes of modeling, all elements were located 1 cm from the bottom surface of a 30 cm $\times$ 30 cm (x and z), 10 cm high (y) phantom with conductivity = 0.72. The array plane was at $y = 0$. Figure 7.11 illustrates the single 12 cm loop and the three arrays. Noise correlation from the sample and the copper loss was included, but no preamplifier noise was included in the model. Additionally, the coils were considered to be perfectly decoupled, or operating as ideal isolating preamplifiers. In the array, the conductors overlapped one another. As stated before, all conductors, even in the 8×8 array, were 0.375 cm wide. Thus the individual elements for the 2×2, 4×4, and 8×8 arrays were square loops of 6, 3, and 1.5 cm width, as measured from the center of the conductors. These loops match the elements used in Figures 7.3–7.5. Figure 7.12, which corresponds to Figure 7.3, shows that along a line parallel to the array face (at $z = 0.75$ cm, $y = 1.0$ cm), the arrays obtain the SNR benefit of the individual smaller elements, but there is no loss in field of view as was the case with the individual elements (Figure 7.3.) Importantly, Figure 7.13 shows that, even remote from the element, at a distance of 12 cm, the SNR of the array matches or exceeds that of the large 12 cm loop. For the 8×8 element array, the SNR is reduced marginally from that of the other arrays simply due to the increased copper loss in the 64 elements. Figure 7.14, which compares directly to Figure 7.5 for the single elements, illustrates that the array coil SNR exceeds or matches that of the individual coil at all depths, even when using the 1.5 cm loops in the 8×8 array. The data is offset along a vertical line from the origin by 0.75 cm in both x and z, in order to avoid the conductors in the array, as was done in Figures 7.12 and 7.13. One can understand these results by considering that the weighting functions are all very nearly 1 for a spot far from the elements. In this case, all the elements would have nearly identical currents (again, returning to the transmit case for physical intuition). The current on all "inside"

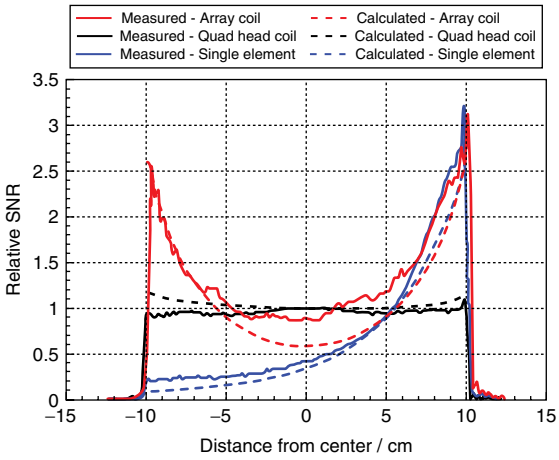

Figure 7.17. Comparison of measured (solid) and calculated (dashed) relative SNR from a 16 channel array coil,[27] a conventional quadrature volume coil, and a single element of the array coil. The array was optimized for SNR at the outside of the head by making the overall array shorter than the volume coil, resulting in somewhat smaller SNR in the center of the volume. The array combination provides nearly a factor of three improvement at the outer region, and recovers nearly the same SNR as the volume coil in the center. The measured and calculated SNR were both normalized so that the volume coil had an SNR of 1 at the center for purposes of comparison.

conductors would be canceled by the current on the adjacent loop element, leaving the only effective currents being those on the outside of the array. Thus, for positions far from the array, the optimized currents form, in effect, the original 12 cm loop. Even though the "inner" conductors do not radiate because of this cancellation, they would still dissipate heat and lower the coil efficiency (and reciprocally, SNR). However, for a coil dominated by sample loss, this effect is small. All the array combinations used in Figures 7.12–7.14 used the simple SOS combination, where only the magnitude of the sensitivity patterns is required. It is interesting to compare the results from a general combination, requiring the magnitude and phase (direction) of the sensitivity patterns and the resistance or noise correlation matrix are required. Figure 7.15, which repeats the SNR calculations of Figure 7.12, 7.1 cm above the array, shows that in this case there is relatively little improvement obtained by the more complicated general reconstruction. However, since the sensitivity maps and noise matrices are often obtained directly from the scanner, there is little reason not to use the general approach. In certain special cases, there may be far greater gains to be made by using the general method.[25,26]

A final example reinforces the principle that the array synthesizes the "optimal array", even far from the array where the optimal coil may be a single large element or volume coil. In this example, described in detail in Ref. 27, a 16 channel array of rectangular loops was designed and constructed for comparison with a conventional quadrature head coil. The overall length of the array was smaller than that of the head coil to provide higher SNR at the periphery, potentially sacrificing some SNR in the center of the volume. Figure 7.16 shows the individual receive patterns from the 16 elements in a phantom, showing the highly localized patterns, with each element detecting a little signal from the center of the volume. Figure 7.17 compares the measured and calculated relative SNR from the array, the quadrature volume coil, and a single element. The measured and calculated datasets were each normalized to the SNR of the quad volume coil at the center of the volume to allow direct comparison. As expected, the individual element shows significant SNR boost at the periphery but very little SNR at the center of the volume. The array, although designed to sacrifice SNR in the middle by making it shorter, as shown in the calculated data, does a bit better than expected in the middle, nearly equaling the volume coil. At the periphery, the array SNR is nearly a factor of three higher than the volume coil SNR.

REFERENCES

1. J. J. Ackerman, T. H. Grove, G. G. Wong, D. G. Gadian, G. K. Radda, *Nature*, 1980, **283**, 167–170.
2. J. W. Carlson, *J. Magn. Reson.*, 1987, **74**, 376–380.
3. D. Kwiat, S. Einav, G. Navon, *Med. Phys.*, 1991, **18**, 251–265.
4. M. Hutchinson and U. Raff, *Magn. Reson. Med.*, 1988, **6**, 87–91.
5. J. R. Kelton, R. L. Magin, S. M. Wright, In *Proceedings of SMRM, 8th Annual Meeting*, 1989.
6. E. B. Boskamp, In *Proceedings of the 6th Annual Meeting of the Society of Magnetic Resonance in Medicine*, 1987, 405.

7. S. M. Wright, R. L. Magin, J. R. Kelton, In *Proceedings of the 6th Annual Meeting of the Society of Magnetic Resonance in Medicine*, 1987, 96.
8. S. M. Wright, R. L. Magin, J. R. Kelton, *Magn. Reson. Med.*, 1991, **17**, 252–268.
9. H. Requardt, J. Offermann, H. Kess, N. Krause, H. Weber, *Radiology*, 1987, **165**, 574–575.
10. P. B. Roemer, W. A. Edelstein, C. E. Hayes, S. P. Souza, O. M. Mueller, *Magn. Reson. Med.*, 1990, **16**, 192–225.
11. D. I. Hoult and R. E. Richards, *J. Magn. Reson.*, 1976, **24**, 71–85.
12. A. Macovski, *Magn. Reson. Med.*, 1996, **36**, 494–497.
13. M. Ohliger, A. Grant, D. Sodickson, *Magn. Reson. Med.*, 2003, **50**, 1018–1030.
14. T. Redpath and C. Wiggins, *Phys. Med. Biol.*, 2000, **45**, 217–227.
15. C. N. Chen, V. J. Sank, S. M. Cohen, D. I. Hoult, *Magn. Reson. Med.*, 1986, **3**, 722–729.
16. D. I. Hoult and P. C. Lauterbur, *J. Magn. Reson. (1969)*, 1979, **34**, 425–433.
17. A. Trakic, H. Wang, E. Weber, B. K. Li, M. Poole, F. Liu, S. Crozier, *J. Magn. Reson.*, 2009, **201**, 186–198.
18. D. I. Hoult, *Concepts Magn. Reson.*, 2000, **12**, 173–187.
19. D. Hoult, C. Chen, V. Sank, *Magn. Reson. Med.*, 1984, **1**, 339–353.
20. S. M. Wright and L. L. Wald, *NMR Biomed.*, 1997, **10**, 394–410.
21. R. F. Harrington, *Field Computation by Moment Methods*, Krieger Publishing: Malabar (FL), 1982.
22. W. R. Smythe, *Static and Dynamic Electricity*, 3rd edn., McGraw-Hill: New York, 1968.
23. R. F. Harrington, *Time-Harmonic Electromagnetic Fields*, McGraw-Hill: New York, 1961.
24. J. S. Hyde, A. Jesmanowicz, T. M. Grist, W. Froncisz, J. B. Kneeland, *Magn. Reson. Med.*, 1987, **4**, 179–184.
25. A. Jesmanowicz, J. Hyde, W. Froncisz, J. Kneeland, *Magn. Reson. Med.*, 1991, **20**, 36–47.
26. A. Reykowski, Theory and Design of Synthesis Array Coils for MRI, Ph.D. thesis, Texas A&M University: College Station (TX), 1997.
27. J. R. Porter, S. M. Wright, A. Reykowski, *Magn. Reson. Med.*, 1998, **40**, 272–279.

Chapter 8

Coil Array Design for Parallel Imaging: Theory and Applications

Daniel K. Sodickson[1], **Michael A. Ohliger**[2], **Riccardo Lattanzi**[1], **and Graham C. Wiggins**[1]

[1]*New York University School of Medicine, New York, NY 10016, USA*
[2]*University of California San Francisco, San Francisco, CA 94143, USA*

8.1 INTRODUCTION

Parallel MRI techniques accelerate image acquisitions by extracting spatial information from the sensitivity patterns of radiofrequency (RF) coil arrays and using that information to substitute for a portion of the data that would normally be acquired using sequentially applied magnetic field gradients.[1–3] These strategies have been embraced clinically and exploited in order to reduce the duration of lengthy imaging examinations, increase temporal resolution in time-critical studies, enhance spatial resolution, expand anatomical coverage, reduce image artifacts, and increase patient comfort. The effectiveness of any parallel image reconstruction technique is fundamentally limited by the amount and distinctiveness of spatial information contained within a coil array. Therefore, a careful choice of coil array design is critical for the effective use of parallel MRI. This review is intended to provide an introduction to the basic principles of coil array design for parallel MRI.

Even when accelerated imaging is not required, detector arrays are ubiquitous tools in MRI because they provide images with a high signal-to-noise ratio (SNR) across a large field of view (FoV).[4] This SNR advantage arises because each detector in an array responds to magnetization from local regions while ignoring magnetization (and noise) from the rest of the sample. Parallel MRI methods similarly take advantage of the local nature of each coil's reception pattern in order to extract additional spatial information about the sample.

The use of coil arrays for spatial encoding leads to design considerations not present for sequential, gradient-based applications. One manifestation of these new considerations has been an expansion of the number of coil elements found in a typical array. Largely as a result of developments in parallel MRI, commercial MR systems with 32 or more independent receiver channels have become

RF Coils for MRI
Edited by J. Thomas Vaughan and John R. Griffiths
 ISBN: 978-0-470-77076-4

routinely available, and prototypes with as many as 128 receiver channels are poised to enter the market. Moreover, a similar trend toward parallelism in the transmit chain is now under way, and the development of techniques and technologies for parallel RF transmission[5,6] is on the rise.

Accompanying the expansion in the number of available receiver (and transmitter) channels on many systems, there has been a remarkable diversity in the coil arrays that have been created specifically for parallel MRI. In an effort to tailor coil arrays' spatial encoding properties, researchers have sought new ways of customizing the sensitivity profiles of individual detectors, and they have also explored novel geometrical arrangements for those coil array elements. The present review is not intended as an enumeration of all of the coil arrays that have been proposed for parallel MRI to date, nor does it presume to make pronouncements about "good" or "bad" design ideas. Rather, a group of basic principles and intuitive tools is introduced that coil array designers can apply to new designs. These principles and tools are illustrated with practical examples of many-element head coil arrays. Details of the construction and evaluation of these sample arrays are provided, along with some troubleshooting tips, in order to highlight the kinds of concrete decisions that a designer of coil arrays for parallel MRI may be called upon to make. Additional general design examples and elaboration on certain basic principles may be found in a review article from 2006,[7] which we have distilled, reorganized, amplified, and updated here.

8.2 BACKGROUND

8.2.1 Principles of Spatial Encoding with Coil Arrays

The goal of parallel imaging is simple: to replace sequential spatial encoding steps traditionally performed using magnetic field gradients with spatial information derived from the simultaneous operation of arrays of RF coils. This general definition is broad enough to cover parallel transmission as well as parallel reception. However, while many tantalizing analogies and related principles connect these two domains, we will focus in the remainder of this chapter upon parallel reception. From time to time, we will briefly address challenges related to RF transmission, otherwise leaving questions of parallel transmit coil array design for a more dedicated treatment elsewhere.

The mechanisms of spatial encoding with RF coil arrays may be viewed from several complementary perspectives, each of which offers potentially valuable insights for coil array design. Many of these perspectives have been embodied in distinct algorithms used to reconstruct parallel MR image data.

8.2.1.1 Emulation of Spatial Harmonics

Coil arrays can provide spatial information about a sample by emulating the spatial modulations produced by the magnetic field gradients. This idea is the basis of the SMASH (SiMultaneous Acquisition of Spatial Harmonics) technique.[1] From this perspective, one approach to designing coil arrays is to choose detectors that have linear combinations that approximate spatial harmonics as well as possible. This procedure is illustrated schematically in Figure 8.1(a) for a coil array with three component coils. In this example, the array is placed parallel to and above a coronal image plane. The top panel of Figure 8.1(a) shows the real and imaginary parts of each coil sensitivity, calculated along the central frequency-encoding line. The bottom panel shows how these coil sensitivities may be combined to approximate the real and imaginary parts of the first spatial harmonic.

8.2.1.2 Unfolding of Aliased Data

When data are acquired on a Cartesian k-space grid and then undersampled by a factor R, the reconstructed image is aliased. Each reconstructed voxel represents the sum of R equally spaced voxels across the FoV. The process of aliasing is shown schematically in Figure 8.1(b), where two pixels from each of three component coil images (top row) are folded into a single pixel within the aliased images (bottom row). It is possible to reconstruct a fully sampled image from the aliased data because each coil is differentially sensitive to distinct aliased pixels. The image-domain formulation of Cartesian SENSE (sensitivity encoding)[2] operates using an unfolding principle in image coordinate space. When the parallel MR image reconstruction is viewed as an unfolding of aliased pixels, it is clear that coil arrays with component coil sensitivities that are spatially selective for different aliased regions will be effective at reconstructing undersampled data.

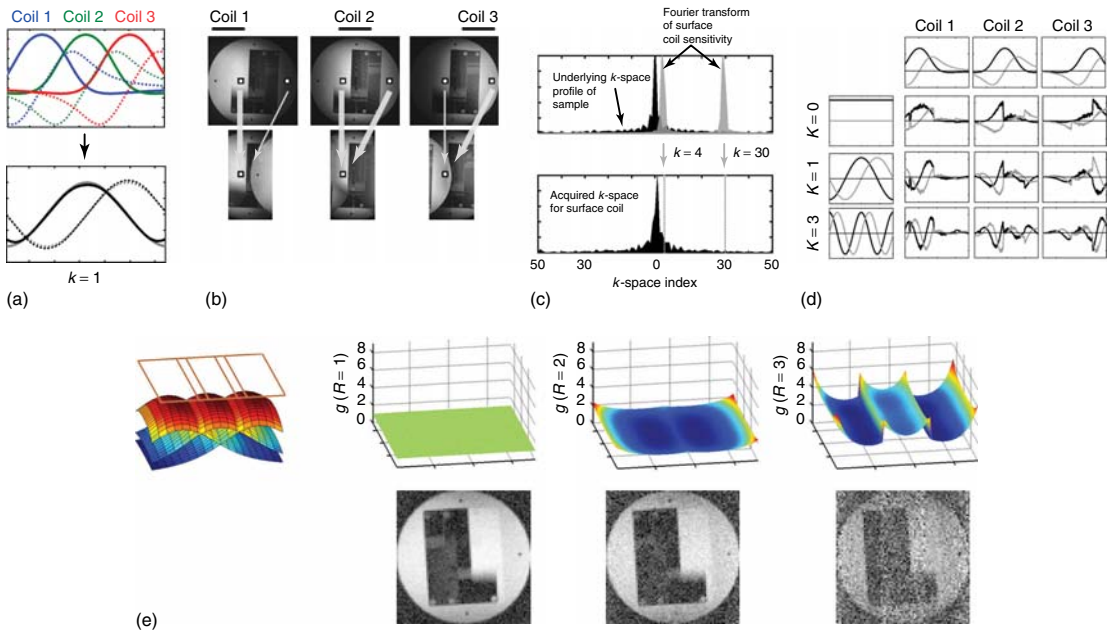

Figure 8.1. Schematic illustrations of several useful perspectives on coil array spatial encoding (a–d), and examples of noise amplification in parallel image reconstruction (e). Each illustration was generated by simulating a three-coil linear array located parallel to and above a coronal image plane. (a) The real (solid lines) and imaginary (dotted lines) parts of coil sensitivities along the central frequency-encoding line are shown in the top plot, color-coded by coil number. The bottom plot illustrates the least-squares fits of the real (solid black line) and imaginary (dotted black line) parts of the coil sensitivities to the first spatial harmonic over the field of view (solid and dotted gray lines). (b) Three simulated component-coil images (top row) are undersampled to generate three aliased images (bottom row). Two pixels in the fully encoded images fold onto a single pixel in the aliased images. Spatial information is available because each component coil sees the two aliased pixels with different relative signal intensities (indicated by the widths of the arrows). (c) Convolution of the sample's underlying k-space distribution (top graph, black curve) by a single component coil's spatial frequency response function (gray curves). In this figure, the convolution process is explicitly shown at the $k = 4$ and $k = 30$ lines. Each point in the acquired component coil k-space (bottom curve) is a weighted sum of several surrounding frequency components from the sample magnetization. (d) Each acquired k-space point from each component coil gives a generalized projection through the sample, which is known as an *encoding function*. The real (dark curves) and imaginary (light curves) parts of nine illustrative projections through the central line of simulated sample are shown. (e) Noise amplification with increasing acceleration. The three-element array is shown at the left with its component coil sensitivities. Surface plots of g-factor for acceleration factors $R = 1–3$ using this array are shown above simulated images. Peaks in the g-factor map correspond to areas of increased noise, and hence decreased SNR, in the images. The particular location and shape of noise peaks and valleys are influenced by the choice of coil array geometry, image plane, and acceleration factor.

8.2.1.3 Broadening of the Acquired k-Space Data

The Fourier transform of the product of a coil sensitivity distribution and a magnetization distribution can be written as the convolution of the two functions' Fourier transforms. This process is shown graphically in Figure 8.1(c) for one coil element within a three-coil array. Because of the convolution by the coil array frequency-response function, each spectral component of the surface coil data contains information about several surrounding spatial frequencies within the sample magnetization. Combination of multiple component coil signals may therefore be used to fill in missing spatial frequency information (as was already demonstrated for the case of spatial harmonic generation). Since the spectral width of typically smooth coil sensitivities tends to be rather

limited, the contribution of distant k-space positions to any given missing k-space position is small. A number of parallel imaging techniques,[8–10] including the frequently used GRAPPA (generalized autocalibrating partially parallel acquisitions) technique,[3] take advantage of this k-space locality to limit the reconstruction to a modest kernel around each missing k-space position, in an approach which may be viewed as a hybrid between SMASH and SENSE.[10]

8.2.1.4 Generalized Spatial Projections

Instead of privileging either the image domain or the k-space domain, one may treat coil sensitivities and gradient-induced harmonic modulations on an equal footing, considering both as components of generalized modulations against which objects are projected in the generation of MR signals. From this perspective, each acquired datapoint represents a distinct "generalized projection" through the sample.[2,10] Examples of these projections for a three-coil array are plotted in Figure 8.1(d). Coil array sensitivities can be tailored for parallel imaging such that they lead to overall projection functions that are as spatially orthogonal as possible. This perspective on spatial encoding is particularly powerful because it is easily adapted to various encoding schemes. Indeed, while much focus is placed on designing coil sensitivities to complement the gradient-encoded Fourier harmonics, it is also possible to implement non-Fourier gradient encoding techniques that complement the coil sensitivities.

While a more detailed discussion of particular parallel MR image reconstruction techniques is beyond the scope of this chapter, we briefly review a general formalism for parallel image reconstruction which is useful for the understanding of key concepts in coil design and evaluation. The most important design principle for parallel MRI detectors is based on the recognition that, while gradient-induced spatial harmonic functions are orthogonal to each other over a chosen FoV, the sensitivity-modulated harmonics, also called "encoding functions", generally are not orthogonal. This lack of orthogonality is responsible for amplified noise in the final reconstructed image, and an analysis of these noise amplifications forms the basis for most quantitative assessments of array performance. In a general parallel MR image reconstruction, the MR signal received from coil l at k-space position $\mathbf{k}_m$, in response to precessing transverse magnetization that has density $M(\mathbf{r})$, is discretized and written as[2,10]

$$S_l(\mathbf{k}_m) = \sum_{\text{voxel } j} C_l(\mathbf{r}_j) M(\mathbf{r}_j) e^{i\mathbf{k}_m \cdot \mathbf{r}_j} + n_l(\mathbf{k}_m) \tag{8.1}$$

In equation (8.1), $C_l(\mathbf{r}_j)$ represents the spatial sensitivity of the lth detector at the position $\mathbf{r}_j$ of the jth voxel, $i = \sqrt{-1}$ is the imaginary unit, and $n_l(\mathbf{k}_m)$ is the noise that is recorded along with the signal in the lth detector at the mth k-space point. If the acquired signal and noise, together with the magnetization density, are written as column vectors, then the signal equation becomes

$$\mathbf{S} = \mathbf{E}\mathbf{M} + \mathbf{n} \tag{8.2}$$

where the encoding matrix $\mathbf{E}$ is given by

$$E_{(lm),j} \equiv C_l(\mathbf{r}_j) e^{i\mathbf{k}_m \cdot \mathbf{r}_j} \tag{8.3}$$

Within this formalism, reconstructing an image amounts to finding a matrix $\mathbf{F}$ such that $\mathbf{FE}$ is equal to the identity matrix. In general, $\mathbf{E}$ is a rectangular matrix, and there are many possible choices for $\mathbf{F}$. It has been shown[2] that the minimum-norm solution of equation (8.2) that leads to a reconstructed image with the least possible noise is given by

$$\mathbf{F}_{\text{min norm}} = (\mathbf{E}^H \boldsymbol{\Psi}^{-1} \mathbf{E})^{-1} \mathbf{E}^H \boldsymbol{\Psi}^{-1} \tag{8.4}$$

Here, the superscript H indicates a Hermitian conjugate or conjugate transpose operation, and $\boldsymbol{\Psi}$ is the coil array's noise covariance matrix, which describes the noise statistics of the ensemble of coil elements. Formally, $\boldsymbol{\Psi}$ can be written as

$$\boldsymbol{\Psi} \equiv \langle (\mathbf{n} - \bar{\mathbf{n}})(\mathbf{n} - \bar{\mathbf{n}})^{\dagger} \rangle_{\text{time}} \tag{8.5}$$

where the angled brackets indicate a temporal average, and $\bar{\mathbf{n}}$ is a vector containing the time-average of each noise channel (for white noise, this is generally zero). We can also define a noise *correlation* matrix, which is a normalized version of $\boldsymbol{\Psi}$:

$$\Psi_{ll'}^{\text{corr}} = \frac{\Psi_{ll'}}{\sqrt{\Psi_{ll}\,\Psi_{l'l'}}} \tag{8.6}$$

Here, the matrix indices l and l' identify the coils whose noise correlation or covariance is specified. The noise correlation matrix is useful because it represents intrinsic correlations between the noise signals of various coils, and is independent of both the overall amplifier gain in each channel and the absolute amount of coil loading. It is important to note, however, that for the purposes of image

reconstruction [equation (8.4)], the unnormalized noise covariance matrix is the relevant quantity.

Because noise from separately acquired points in k-space is generally independent, $\boldsymbol{\Psi}$ is block-diagonal. The diagonal elements of $\boldsymbol{\Psi}$ are equal to the total noise power received by a given coil, and the off-diagonal elements of $\boldsymbol{\Psi}$ represent correlations in noise between multiple coils. The mere presence of correlated noise does not, by itself, reflect poorly on a given coil array. In fact, for any array with a nonsingular noise covariance matrix, a linear transformation may always be found such that the noise from all of the combined channels is uncorrelated.[11] The predominant criterion for judging a coil array is the SNR of the final image.

8.2.2 Noise Propagation and SNR Behavior in Parallel MRI

As mentioned earlier, one of the chief distinctions between parallel MRI and fully gradient encoded Fourier imaging is that the encoding functions used for parallel imaging [equation (8.3)] are generally not spatially orthogonal. As a consequence, the reconstruction matrix [equation (8.4)] is typically not unitary, and there is a spatially varying increase in noise throughout the image.[2,12] The total amount of noise amplification that is introduced by the reconstruction is strongly dependent on the choice of array design. Because the image reconstruction used in equation (8.4) is a linear transformation, the noise power of an R-fold accelerated reconstruction can be calculated from the encoding matrix[2]

$$(\sigma_j^R)^2 \propto [(\mathbf{E}_R^H \boldsymbol{\Psi}^{-1} \mathbf{E}_R)^{-1}]_{j,j} \tag{8.7}$$

where $\mathbf{E}_R$ is the encoding matrix corresponding to an R-fold accelerated acquisition. Using the same array in the absence of parallel imaging, the encoding matrix is $\mathbf{E}_{\text{full}}$ and the noise power is given by

$$(\sigma_j^{\text{FULL}})^2 \propto [(\mathbf{E}_{\text{full}}^H \boldsymbol{\Psi}^{-1} \mathbf{E}_{\text{full}})^{-1}]_{j,j} \tag{8.8}$$

The SNR at any given voxel position j is defined as the ratio of the reconstructed signal $(\mathbf{FS})_j$ to the noise standard deviation σ_j. Therefore, the change in SNR that occurs as a consequence of parallel imaging can be written formally as

$$\left(\frac{SNR_j^R}{SNR_j^{\text{FULL}}}\right)^2 = \left(\frac{\sigma_j^{\text{FULL}}}{\sigma_j^R}\right)^2 = \frac{\left[(\mathbf{E}_{\text{full}}^H \boldsymbol{\Psi}^{-1} \mathbf{E}_{\text{full}})^{-1}\right]_{j,j}}{\left[(\mathbf{E}_R^H \boldsymbol{\Psi}^{-1} \mathbf{E}_R)^{-1}\right]_{j,j}} \tag{8.9}$$

In the special case of an image with uniform Cartesian sampling, equation (8.9) can be written in the compact form

$$SNR^R = \frac{SNR^{\text{FULL}}}{\sqrt{R[(\mathbf{E}_R^H \Psi^{-1} \mathbf{E}_R)]_{j,j}[(\mathbf{E}_R^H \Psi^{-1} \mathbf{E}_R)^{-1}]_{j,j}}} \tag{8.10}$$

The factor of $\sqrt{R}$ in the denominator of equation (8.10) reflects the fact that, for Fourier sampling, $[\mathbf{E}_{\text{full}}^H \boldsymbol{\Psi}^{-1} \mathbf{E}_{\text{full}}]_{j,j} = R[(\mathbf{E}_R^H \boldsymbol{\Psi}^{-1} \mathbf{E}_R)]_{j,j}$. This factor represents an overall loss in SNR that occurs simply because there are fewer acquired k-space points. Changes in coil array design have very little impact on this effect. The second term in equation (8.10) describes a spatially dependent amplification of noise, which has become known as the geometry factor, or the "g-factor"[2]:

$$g_j \equiv \sqrt{[(\mathbf{E}_R^H \boldsymbol{\Psi}^{-1} \mathbf{E}_R)]_{j,j}[(\mathbf{E}_R^H \boldsymbol{\Psi}^{-1} \mathbf{E}_R)^{-1}]_{j,j}} \tag{8.11}$$

The g-factor is (by definition) always greater than or equal to 1, and it quantifies the fractional loss in SNR that occurs due to the non-orthogonality of the array coil sensitivities. While the compact expression for the g-factor in equation (8.11) applies strictly to images with uniform Cartesian k-space sampling patterns, the more general expression in equation (8.9) can still be used for arbitrary sampling patterns.

In Figure 8.1(e), the g-factor maps for a range of accelerations using a simulated three-element array placed parallel to and above a coronal image plane are shown. The locations of the coil array elements and their corresponding sensitivity patterns are shown at the left. Note the increase both in the mean value and in spatial heterogeneity of the g-factor with increasing acceleration. SENSE-reconstructed images in which noise has been added to simulated component-coil data are shown below the g-factor maps, confirming that SNR decreases wherever g-factor increases.

When evaluating coil arrays for image reconstructions other than SENSE, it is straightforward to derive an analytical formula for the geometry-related SNR changes that is analogous to equation (8.9), as long as the overall reconstruction procedure represents a linear transformation. Analytical SNR formulas are more complicated, however, for reconstructions that involve nonlinear transformations such as sum-of-squares coil combinations, or for combined reconstructions that include expressly

nonlinear algorithms such as compressed sensing.[13] An alternative method for predicting the SNR effects of using a particular coil array in a parallel reconstruction involves adding simulated noise to a sample image, and measuring the pixel-by-pixel SNR of the reconstructed data. This simulation-based technique is particularly valuable for parallel reconstruction methods for which analytic SNR formulations are cumbersome, or for reconstructions that require iterative matrix inversions.

Because many of the sequence-dependent determinants of SNR have been removed from the expression for the g-factor in equation (8.11), this parameter has become an attractive figure of merit for assessing the performance of coil arrays for parallel MRI. While the g-factor is a generally useful measure, it does have several limitations. For example, changes in coil geometry will likely alter a coil array's baseline SNR [equation (8.8)] together with that array's g-factor. Naturally, improvements in g-factor are not valuable when they come at the cost of severe degradations in the overall performance of an array. In addition, the g-factor is a function of *both* the coil sensitivities and the pattern of acquired k-space lines. Therefore, the g-factor will, in general, be different for different undersampling factors, object sizes, phase-encoding directions, and image planes. Finally, it is important to recognize that, while the g-factor is predominantly dependent on the acquisition pattern and the coil sensitivities, there is still a second-order dependence of g on the noise covariance matrix $\boldsymbol{\Psi}$. Drastic changes in an array's baseline noise power can also affect the array's g-factor.

8.2.3 Computational Analysis of Prospective Coil Array Designs

Equations (8.9–8.11) are analytical tools for evaluating coil array performance for parallel MRI. In order to make use of these expressions, it is necessary to know (i) the coil sensitivities $C_l(\mathbf{r})$, (ii) the noise covariance matrix $\boldsymbol{\Psi}$, and (iii) the pattern of the k-space acquisition. The k-space acquisition pattern is determined by the desired image plane geometry and pulse sequence. The coil sensitivities and noise covariance matrix can, of course, be measured empirically at the time of imaging. However, for understanding and designing coil arrays, it is useful to have methods for predicting $C_l(\mathbf{r})$ and $\boldsymbol{\Psi}$ computationally.

The spatial sensitivity pattern $C_l(\mathbf{r})$ of each coil within an array can be calculated using the well-known principle of reciprocity.[14–17] The principle of reciprocity states that the magnetic flux induced through a coil by precessing magnetization can be written in terms of $\hat{\mathbf{B}}^{\text{coil}}$, which is the magnetic field that would be generated by a unit current flowing around that coil. Accordingly, the complex spatial sensitivity function can be written in terms of the two transverse components of $\hat{\mathbf{B}}^{\text{coil}}$:

$$C_l(\mathbf{r}) = [\hat{B}_x^{\text{coil}}(\mathbf{r})]_l - i[\hat{B}_y^{\text{coil}}(\mathbf{r})]_l \qquad (8.12)$$

The noise covariance matrix can similarly be computed in terms of $\hat{\mathbf{E}}^{\text{coil}}$, which is the electric field created by a unit current flowing around the conductor path of the coil[4,18,19]

$$\boldsymbol{\Psi}_{ll'} = 4kT\Delta f \int \sigma(\mathbf{r})\hat{\mathbf{E}}_l(\mathbf{r}) \cdot \hat{\mathbf{E}}_{l'}^*(\mathbf{r})\mathrm{d}^3\mathbf{r} \qquad (8.13)$$

In this expression, $\sigma(\mathbf{r})$ is the sample conductivity, T is the absolute temperature, k is Boltzmann's constant, and Δf is the receiver bandwidth.

The field definitions of $C_l(\mathbf{r})$ and $\boldsymbol{\Psi}$ permit the theoretical evaluation of any prospective coil array design. For sufficiently low magnetic field strength and Larmor frequency, the Biot–Savart law may be used to derive field patterns. At higher frequencies, full-wave solutions, such as multipole expansions, dyadic Green's function techniques, or finite difference/finite element approaches, are required. Systematic and detailed coil array design examples that illustrate these principles have been presented for cardiac[20] as well as for head[21,22] and abdominal[23] imaging, among other applications.

8.2.4 Limits of Performance: Ultimate Intrinsic SNR

Though the general fitness of a prospective coil array design for parallel imaging applications may be evaluated using the computation techniques just described, in order to assess the true impact of a prospective design it is often desirable to compare its performance to that of a known reference design. In view of the vast range of coil array designs that have been explored for parallel MRI, however, the choice of a suitable reference design can be challenging. Furthermore, even a time-consuming comparative evaluation of multiple designs does not give a solid indication of exactly how much further

room for improvement there may be. It would be advantageous, therefore, to compare against an absolute reference representing the best possible coil performance.

Fortunately, such an absolute reference exists, in the form of the ultimate intrinsic SNR ratio (uiSNR). This quantity is defined as the highest SNR compatible with the constraints of Maxwell's equations on one hand (i.e., fields/currents must be physically realizable) and spatial encoding on the other (i.e., the reconstructed image must achieve a desired level of accuracy). The behavior of uiSNR for parallel MRI in particular has been studied using various computational approaches.[24–26] In each approach, a basis set of coil sensitivities (and corresponding noise correlations) is derived from a complete basis of either field[24,25] or current[26] modes for a defined object geometry, and the optimum SNR linear combination is determined from this basis set. Any prospective new coil sensitivity distribution that might be hypothesized to improve SNR must be able to be represented as a superposition of these modes, and must therefore fall short of or at best match the optimum. Analogous studies of ultimate transmit performance have also been performed using related techniques.[27]

Figure 8.2 summarizes some of the lessons that may be learned from a study of ultimate intrinsic limits of performance. The top row of the figure illustrates numerically and graphically the approach to the uiSNR as the number of coils surrounding a spherical volume is increased. For an 8-element and a 64-element array, the ratio of computed SNR to uiSNR at the center of the sphere at 7 T is shown above a depiction of the SNR-optimizing current pattern in each array. The ideal current pattern corresponding to the uiSNR, computed using a dyadic Green's function approach,[26,28] is shown at right. (A single temporal snapshot is displayed—the pattern precesses at the Larmor frequency over time.) The plot at the bottom left of Figure 8.2 compares central SNR for the same 8- and 64-element arrays with uiSNR as a function of field strength. Even in the presence of simulated coil-derived noise contributions (curves labeled with diamond and triangle), central SNR increases with increasing number of coils, even as the size of individual coils decreases below the expected optimum diameter for single-coil SNR. Baseline SNR increases as field strength increases, but at the same time the approach to ultimate performance is slower at the higher field, with a larger number of component coils and/or more complex current patterns required to reach the limiting SNR value. At the bottom right of Figure 8.2, plots of $1/g$ (i.e., geometry-related SNR decrease, neglecting the square root of acceleration factor due to undersampling) as a function of acceleration along a single phase-encoding dimension are shown for various magnetic field strengths. $1/g$ falls off more slowly with acceleration at higher field strengths, demonstrating an improved capability for spatial encoding with increasing Larmor frequency and decreasing wavelength. Although the results shown in Figure 8.2 are all derived from simulations, coil performance evaluation as compared with ultimate limits may be carried out experimentally as well.[26] Ultimate current patterns such as those shown in Figure 8.2, moreover, may be used as a guide for intuition about which classes of coil designs might be expected to be most effective, and, eventually, as concrete targets for new coil designs.[28] Given that any particular value of uiSNR will apply only for a fixed object geometry and composition, not to mention a particular spatial region and in some cases a particular k-space trajectory, translation of ultimate current or field patterns into concrete array designs remains a nontrivial proposition. However, certain general insights may be gleaned immediately, for example regarding the increasing contribution to ideal array performance of electric as opposed to magnetic dipole components as field strength increases.[28]

8.3 COIL CONSTRUCTION

8.3.1 Essential Principles of Good Coil Array Design for Parallel Imaging

As is evident from the preceding theoretical discussion, coil arrays designed with parallel imaging in mind must combine at least two key features: (i) good baseline SNR and (ii) effective encoding capability. In meeting the second requirement, it is important not to forget the first. Although certain aspects of parallel imaging arrays set them apart from arrays not designed for acceleration, most of the venerable principles of good coil array design continue to apply (see Chapter 7). In other words, the loaded-to-unloaded Q of each element must be considered, as must the coupling of signal and noise between elements, the match circuitry, the preamplifier behavior, etc. The additional requirements of

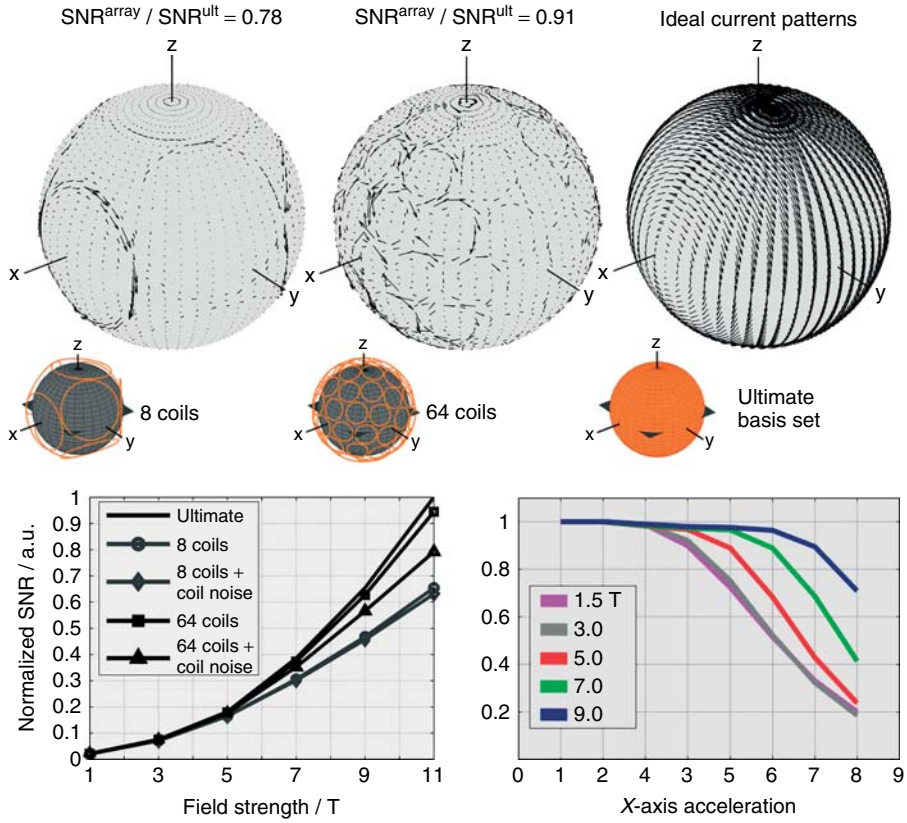

Figure 8.2. Lessons from ultimate intrinsic SNR. Top row: Approach to ultimate SNR as the number of coils surrounding a spherical volume is increased. Ideal surface current patterns associated with the best possible SNR at a voxel in the center of the sphere are compared, at 7 T, with SNR-optimized current patterns for an 8-element and a 64-element array at a single time-point. The corresponding SNR, normalized to the ultimate intrinsic SNR, is reported for both coils above the current plots. Bottom left: Central SNR as a function of magnetic field strength for the same 8- and 64-element arrays, computed both with and without coil-derived noise contributions, as compared with the ultimate limits. Note the increased baseline SNR as well as the slower approach to ultimate performance as field strength increases. Bottom right: Central SNR behavior as a function of acceleration (along a single phase-encoding dimension) for various magnetic field strengths. Plots of $1/g$ (i.e., geometry-related SNR decrease with acceleration, neglecting the square root of acceleration factor due to undersampling) demonstrate a slower reduction and therefore improved spatial encoding capability at higher field strength.

spatial encoding amount to tailoring the shape and distribution of coil sensitivities to maximize acceleration while minimizing the corresponding noise amplification. Note that the result may depend strongly upon the target application. Note also that the stringency of the constraints of spatial encoding may also vary with the number and distribution of elements. For example, at low channel count, careful attention must generally be paid to g-factor optimization and to questions such as the detailed spacing between elements, whereas a sufficient number of channels may allow performance that begins to converge toward ultimate limits independent of some of the fine details of element geometry and placement.

8.3.1.1 Element Composition and Arrangement

Some of the first decisions facing any coil designer involve what basic geometries and materials to use for array elements, and where to place elements with respect to one other. These decisions take on additional importance when one is designing

arrays for parallel imaging. Generally speaking (and ignoring certain perturbations at high field strength), the element geometry determines the shape of individual coil sensitivity patterns, and the element arrangement determines the mutual information content of those sensitivities. While it is not practical to survey each parallel imaging array design that has appeared in the literature or that has been developed for routine use, we will identify certain basic classes of designs in order to highlight the degrees of freedom that are available to coil designers when developing a new coil array.

Conducting loops are still most commonly used as fundamental element geometries, but effective parallel imaging arrays may also be constructed from striplines,[29–33] or even from encircling coupled structures such as birdcages[34] or transverse electromagnetic (TEM) coils. In terms of coil arrangement, loop or strip elements can be arranged in straight lines,[35,36] 2D grids,[37,38] or wrap-around arrays[21,22] that surround the sample axially. One of the basic principles of coil array design for parallel MRI is that the coil elements should be arranged so that they have sensitivity variations that are principally aligned with the direction of undersampling. From the perspective of emulating spatial harmonics, elements must be aligned so that they can reproduce the missing *k*-space lines. From the perspective of resolving aliased pixels, coils must be located so that they can be sensitive to different aliased regions of the image. For a fixed number of array elements, linear arrays provide for the maximum amount of spatial information in a single direction. Grid-type arrays and wrap-around arrays provide fewer elements in any specific direction, but their multidimensional character allows simultaneous undersampling in several directions at once. The ability to encode spatial information in multiple directions is important for several reasons. First, many imaging protocols require the acquisition of multiple studies with different image plane orientations, and it is clearly not desirable to use a different coil array every time the image plane orientation changes. Furthermore, there are applications such as cardiac imaging where oblique image planes are chosen to match the patient's anatomy, and it is impossible to predict the exact image plane orientation beforehand. Finally, it has been shown that simultaneous undersampling along two (or more) dimensions at once leads to a smaller geometry factor than would an equivalent amount of net acceleration along one dimension.[24,39] The preceding discussion highlights one of the most significant differences between coil array design for parallel MRI and coil array design for conventional gradient-encoded MRI. In conventional gradient-encoded MRI, coil array design is largely independent of the choice of acquisition strategy. In parallel MRI, on the other hand, the direction of sensitivity variation needs to be carefully coordinated with the direction of *k*-space undersampling.

In considering the optimal placement of elements, it is important to remember that coil sensitivities are complex-valued functions of position, and the phase as well as the magnitude of the sensitivities can play an important role in spatial encoding. One common attribute of simple loop-based array designs is that spatial encoding is largely accomplished by having surface coil sensitivities with varying magnitudes across the FoV. However, concentric looping structures such as a crossed butterfly coil and a loop coil can be used effectively as independent elements.[40,41] Even though the magnitudes of these coils' sensitivities have similar basic shapes, the phase distributions are quite different, and thus the two coils can be used effectively to encode spatial information. Various other crossed coil designs taking advantage of the phase of coil sensitivities have also been proposed.

Even more complex element structures and coil sensitivity patterns may be achieved through hardware-based combination of multiple individual coils. Generally speaking, when a sufficient number of receiver channels are available, the greatest flexibility is attained by maximizing the number of independent elements and performing all combinations in software following data acquisition. However, for a number of reasons it may be desirable to allow hardware combinations to smaller effective numbers of elements. For example, some coil array designers have sought to develop scalable arrays that work well on different MR platforms with varying numbers of receivers, allowing combinations of array elements in certain fixed ratios when fewer receiver channels are available. Adaptive combinations of coil array elements are also useful when multiple anatomical regions are to be imaged with the same coil array.[42] Perhaps, somewhat paradoxically, rapid growth in the number of commercially available receive channels has also led to the investigation of various adaptive "array compression" approaches, which seek to limit the raw data load by finding coil combinations that pack

the greatest possible encoding information into a reduced number of physical channels.[43,44]

8.3.1.2 *The Impact of Coil Coupling, and Decoupling Strategies*

For a long time, the elimination of inductive coupling has been considered an important part of designing RF coil arrays for MRI. When coils couple inductively, they resonate as a single structure, and it can be very difficult to match the impedance of each element simultaneously to the input impedance of the receiver circuitry. When this match is non-optimal, the preamplifier noise figure can be seriously degraded, leading to an image with a poor SNR. The development of parallel MRI techniques has led to renewed emphasis on removing coupling and maintaining coil isolation. As mentioned earlier, parallel MRI techniques require a coil array's component-coil sensitivity profiles to be as distinct as possible in order to encode spatial information. When coils couple inductively, they become sensitive to the same regions of the sample, and it has been feared that coupled coils might contain less distinct spatial information than uncoupled coils, yielding lower quality parallel MRI reconstructions.

Several strategies have been proposed for removing the effects of mutual inductance. First, the overlap of adjacent coil elements (or overlying elements in concentric designs[41]) may be carefully adjusted so that the shared flux between adjacent coils is zero.[4] This strategy has the disadvantage that it may restrict the geometrical layouts of the coil elements. Alternatively, capacitive or inductive connections or even networks[45] may be built between coils that are able to exactly cancel the mutual inductance between them. Additionally, shielded array designs have also been suggested.[46] Finally, specialized preamplifiers can be designed that present a large impedance to current flow at the input of each coil.[4] Because very little current can flow in response to the sample magnetization, the interactions between coil elements are limited.

Despite the strong practical incentive for effective decoupling, some studies have suggested that the mechanisms of parallel image reconstruction itself may allow for more leeway than one might at first imagine. In particular, if coupling is viewed as a linear transformation of signal and noise together, then—in principle—it should be possible to compensate for the effects of coupling by undoing that linear transformation. Of course, this linear compensation may be complicated by noise originating in preamplifiers.[47] Phantom-based experiments that introduced small amounts of coupling did result in modest SNR changes, but the small magnitude of these changes, taken together with the decoupling strategies described above, suggest that coupling is not likely to be a prohibitive barrier to array design for parallel MRI.[48]

8.3.2 Case Studies: Many-element Head Arrays for High-performance and/or Highly Parallel MRI

Numerous other practical considerations attend the design of high-quality many-element arrays—considerations such as effective cabling and cable decoupling strategies, high-performance preamplifier design, etc. These considerations are perhaps best illustrated through concrete examples, which we provide below. In particular, we examine design issues and coil performance for a number of experimental head coils that have been constructed for operation at 3 and 7 T. These designs range from 32 to 96 elements, and comparisons with lower channel count product coils serve to highlight the challenges and opportunities of many-element designs.

A 32-channel 3 T head coil was constructed on a close-fitting helmet.[49] The motivation for placing the coils as close as possible to the head was to achieve a good unloaded-to-loaded Q ratio (and thus ensure that the dominant noise source is the sample rather than the coil). Helmet shape was based on the European standard head norm EN960/1994 for protective headgear.[50] This shape will accommodate 95% of European adult male heads. Its dimensions were 222 mm anterior–posterior (AP), 181 mm left–right (LR), and 220 mm superior–inferior (SI).

Simulations have shown that, for channel counts of 16 or higher, overlapped arrays generally achieve higher SNR than gapped arrays, even with high parallel imaging acceleration rates,[51] so optimum overlap to null mutual inductance between all neighboring coils was targeted. To create a continuous overlapped array that covered the entire dome of the head, it was necessary to adopt a "soccer ball" tiling pattern incorporating pentagonal centers of symmetry,[52] as shown in Figure 8.3. Coil elements were fashioned from Pyralux flexible circuit board material (Dupont, Durham NC, USA) cut with scissors into the desired

Figure 8.3. Element geometry for the 3 T, 32-channel head coil. A soccer ball geometry was used incorporating pentagonal and hexagonal tiles. Surface coils placed at hexagonal tile positions had a larger diameter (blue, 85 mm inside diameter) than those at pentagonal tile positions (red, 60 mm inside diameter). The array is continuous over the entire crown of the head.

shapes. Gaps were cut in the copper with a small grinding tool to allow insertion of capacitors and other components into the loop. Each loop was sized and positioned to optimize the overlap with all neighboring coil elements. With the array loaded by the human head, coupling between neighboring overlapped coil elements was −12 dB or less. The coil elements positioned over hexagonal tiles were approximately 85 mm inside diameter with 5 mm track width, while those over pentagonal tiles were approximately 60 mm inside diameter. The unloaded-to-loaded Q ratio Q_{UL}/Q_L was about 11 for the larger coils and 7 for the smaller coils, which was high enough to ensure that sample noise would be the dominant noise source for these coils. Each coil element incorporated a PIN diode detuning circuit and a fuse for safety.

Cables were lifted up away from the surface coil elements to reduce interaction with other elements in the array. Thirty-two low-input-impedance preamplifiers (Siemens Healthcare, Erlangen, Germany) were arranged on stacked circuit boards behind the helmet. In order to achieve preamplifier decoupling,[4] it is necessary to transform the impedance of the preamp input to a virtual short circuit at the coil element detuning circuit. In general, this can be done through the choice of the appropriate cable length and adjustments to the input tank circuit of the preamp, though it is also possible to use lumped element phase shifters to reduce the cable length needed. Some caution is needed when adjusting the input tank circuit of the preamp, as there is an optimum setting for this circuit that allows the preamp to achieve its optimum noise figure, and deviations away from this will degrade the preamp performance. However, the noise figure varies gently for small deviations away from optimum, so this can be a useful tool, particularly for fine-tuning the position of the preamp decoupling minimum in the coil element response. For the preamps used in this coil, it was found that a cable length of approximately 700 mm was needed to achieve preamp decoupling, but such long cables are likely to interact strongly with the body coil transmit field, creating coil performance and safety problems. A series of tests were performed to determine how much the input tank circuit of the preamp could be adjusted to shorten the cable length needed without degrading the SNR significantly, and a cable length of 370 mm was chosen. Even this cable length is large enough to interact with the transmit RF field at 3 T, so once each coil element had been connected to its preamp, any remaining slack in the cable was taken up by folding it back on itself and tying it with cable ties. A coaxial cable trap was placed in front of each preamp to control induced current on the cable shields.

An identical helmet-shaped former was used for a 96-element head coil array.[53] As was the case with the 32-channel coil described above, an overlapped array was desired, so incorporation of centers of pentagonal symmetry was required to cover the whole dome of the head. In this case, the underlying geometry was not that of a soccer ball, but rather that of the carbon molecule C240 (Figure 8.4). This is a spherical molecule containing 240 carbon atoms that form a lattice in which there are 12 pentagonal rings and 110 hexagonal rings (compared to 12 and 20 pentagonal and hexagonal rings, respectively, in the full soccer ball shape). Using just one half of the C240 shape resulted in six pentagonal tiles over the dome

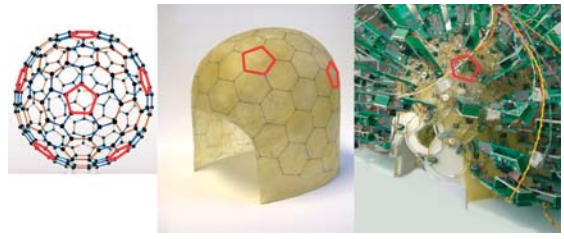

Figure 8.4. Element geometry and component placement for the 3 T, 96-channel coil. The geometry of a C240 carbon "buckyball" molecule was used as the basis for the coil arrangement, incorporating 6 pentagonal tiles and 90 hexagonal tiles covering the entire dome of the head. Wire coil elements were 50 mm in diameter, except over pentagonal tiles, where they were 42 mm in diameter.

of the head, connected by a tiling pattern of small hexagons. The tiling pattern was propagated continuously onto the lower cylindrical section of the helmet using only hexagonal tiles, resulting in a pattern that had 96 separate tiles.

Covering the same area with a larger number of coil elements necessarily requires using smaller coil elements, so coil loading becomes a primary concern. An initial 96-channel prototype was constructed using machined circuit board elements with 48 mm inside diameter and 5 mm track width and six capacitor positions for distributed capacitance.[54] With half of the elements completed, the coil was tested and the sensitivity was found to be very low compared to the 32-channel coil. Two factors were found to contribute to the poor performance—a poor Q_{UL}/Q_L for the coil elements and weak preamp decoupling.

Several design changes were implemented, each of which provided incremental gains in Q_{UL}/Q_L. The use of six capacitors proved to be unnecessary and also decreased the unloaded Q of the coil elements because of the effective series resistance of the capacitors. By switching to a design with only two capacitors (one for matching and one for tuning), the unloaded Q was increased by 29%. It was also found that the sheer amount of copper in the array (which exceeded 50% surface coverage of the helmet) lowered the unloaded Q of an element compared to when it was in free space by as much as 26%. To minimize this effect, the coil elements were constructed from 18 AWG tinned copper wire. With an effective track width of 1.15 mm, the effect on unloaded Q due to all the other conductors in the array was reduced to 2.5%. With all these modifications, the final Q_{UL}/Q_L was 4.0 for the element surrounded by the rest of the array.

In the original poorly performing prototype, the strength of the preamp decoupling effect was smaller than normal. This was characterized by using a double-decoupled probe to measure the response of a single active coil element, first with the preamp replaced by a 50 Ω load and then with the powered preamp in place. The preamp decoupling strength is characterized by the change in S_{12} across the double probe between the two conditions. For the 32-channel coil, this had been −24 dB, but for the initial 96-channel prototype it was only −18 dB. This was traced to the use of a single capacitor to meet competing constraints of matching, detuning, and preamplifier impedance transformation. In tests with eight-element prototype arrays, it was found that the preamp decoupling strength could be increased to −23 dB, and the resulting SNR increased, by using a two-stage match.

In the final design of the 96-channel coil, new preamps (Siemens Healthcare, Erlangen Germany) were used that were optimized for placement at the coil terminals, rather than some distance away at the end of a coax. The new preamp included a bi-filamentary common-mode filter and built-in bias-T for passing current through the PIN diode for active detuning.[55] It also required that the sample load be transformed to 200 Ω (rather than the usual 50 Ω) at the preamp input for optimum noise performance. This could be achieved with a single 82 pF capacitor, and there was no longer a need for a two-stage match. Preamp decoupling with this arrangement was −25 dB. The preamps were mounted radially, perpendicular to the surface of the helmet, so as to further minimize the amount of copper near the array (Figure 8.4, right). Thirty-two channels were connected to the scanner through sockets in the patient table, while the remaining 64 channels were connected to a separate set of receivers via cable bundles that were passed through the bore of the scanner.

8.4 COIL TESTING AND EVALUATION

8.4.1 General Principles and Good Practices

As described in the previous sections, the major criteria for evaluating coil array performance for parallel MRI are based on the SNR of the reconstructed images. However, measuring the SNR of an image that has been reconstructed by combining data from multiple coil elements is significantly more complicated than it is for single-channel data, and more complicated still if accelerated imaging techniques are used. Traditionally, the image SNR in MRI has been measured by choosing two regions of interest (ROI): one region inside the sample, and the other in the background noise. The mean of the region within the sample is used as the signal, and the standard deviation of the region outside of the sample is used as an estimate of the noise.

This traditional approach to measuring SNR is problematic in the context of parallel MRI for several reasons. The first reason is related to the use of magnitude data, rather than complex image pixels. The magnitude operation is nonlinear, and it introduces a bias into regions of the image that have low SNR.

Even without using parallel MRI, this noise bias can introduce measurement errors.[56] The SNR analysis of magnitude reconstructions becomes even more challenging when multichannel data are combined because the SNR for every pixel (and thus the noise bias) is generally different. Because of these complications, it is nearly always advisable to perform SNR analyses on complex-valued data, ideally complemented by a separate acquisition with no RF excitation to provide information about noise statistics.

Another difficulty encountered when measuring the SNR of an image obtained with accelerated parallel imaging occurs even when complex-valued data are used for the measurement. Because the g-factor varies spatially, a noise estimate taken in one region (e.g., outside of the sample) is not reflective of the noise in other regions. Furthermore, the noise at various pixel positions in parallel MRI is generally correlated (although, to be fair, the noise is typically not correlated between *adjacent* pixels), and the statistical analysis of an ROI does not reliably correspond to an equivalent temporal sampling. Finally, many implementations of parallel MRI perform a masking or other nonlinear operation on regions outside of the sample, which can further complicate noise measurements from those regions.

With these complications in mind, and with an eye toward rigorous coil performance evaluation rather than routine clinical use per se, we discuss two practical approaches to evaluating the SNR of parallel MRI data. The first method involves combining carefully calibrated measurements with simulations to generate voxel-by-voxel maps of predicted SNR. This approach has been used in various forms,[20,21] but is perhaps best described in a 2005 article[57] describing image reconstruction in SNR units, which is becoming a de facto standard for SNR measurement. If the noise covariance matrix $\boldsymbol{\Psi}$ and the coil sensitivities $C_l(\mathbf{r})$ of the array have been measured, then equation (8.8) (or related equations for alternative linear reconstruction approaches) can be used to calculate the noise power in each reconstructed pixel, and equation (8.11) (or its equivalents) can be used to calculate the g-factor of each pixel. The ratio of the signal to the noise power in each pixel gives the SNR in each pixel. The advantage of this approach is that it is simple to implement while avoiding the pitfalls of traditional ROI-based approaches. The disadvantage is that the SNR of the image is, in some sense, being calculated from a calibrated theoretical model and not measured directly in any particular region.

An alternative approach to SNR analysis involves the use of an imaging phantom.[12,48] A repeated set of fully sampled or undersampled acquisitions is performed and reconstructed using a parallel MRI technique of choice. The mean and standard deviation over the set of replicas for each (complex-valued) pixel in the image is measured, creating an SNR map. The average values over different regions of the SNR map are then reported. Because of the number of repetitions involved, this approach is not practical for in vivo imaging. Furthermore, in this approach, both thermal noise and intrinsic system instabilities will contribute to the measured noise. The long-term system instabilities might have various causes, including variations in the RF transmitter power or temperature changes in the components that make up the receiver circuitry. The relative contributions of system instabilities to the measured noise (compared to thermal noise) can be minimized by using pulse sequences with relatively low baseline SNR. Some balance is necessary when using this strategy because, if the SNR is too low, more samples will be required to measure each pixel's mean and standard deviation. The resulting increase in scan time may potentially increase the influence of the long-term system variations.

We note briefly that performance measures other than SNR, such as assessments of the level of artifact in reconstructed images, may be pertinent for assessment of coil designs, but they tend to be more difficult to quantify, and they can depend strongly upon the reconstruction algorithm selected. It is known, for example, that sharp intensity gradients, though in many ways useful for spatial encoding, can also lead to an increased incidence of residual aliasing artifacts since, if even small portions of high-intensity edge regions alias into comparatively low-intensity central regions, image quality in the central regions may be significantly degraded. Other reconstruction errors may occur when coil sensitivities, e.g., for multiple, small coil elements, become difficult to calibrate accurately.

8.4.2 Case Studies: Performance Evaluation of Many-element Head Arrays

The 32- and 96-channel coils described in Section 8.3.2 were compared to a standard 12-channel head coil (Siemens Medical Solutions, Erlangen, Germany). One caveat is that the

12-channel coil is significantly larger in overall dimensions (270 mm AP, 250 mm LR, 270 mm SI), and thus is not expected to perform well especially in superficial brain regions near the tight-fitting many-element array formers. SNR maps were derived from gradient echo (GRE) acquisitions (TR/TE/Flip/BW/Slice = 200/3.92/20/300/3 mm, Matrix 256×256, FoV 220×220 mm). Separate signal and noise scans were acquired, and the raw k-space data were saved. The product coil was operated in "Triple" mode where all signals from all 12 channels were recorded and reconstructed. SNR was calculated on a pixel-by-pixel basis according to the "SNR units" method.[57] Noise covariance and noise correlation coefficient matrices were calculated from the noise acquisitions. Estimates of the individual coil sensitivity profiles were generated by low-pass filtering the reconstructed images from the individual coils.

Unaccelerated data were combined using an optimum SNR combination,[4] incorporating noise covariance and coil sensitivities, and corresponding to a SENSE reconstruction with an acceleration factor of 1. SNR maps for the three coil designs are shown in Figure 8.5. For the 96-and 32-channel coils, the SNR in central regions of the brain is almost identical, and is significantly higher than for the commercial 12-channel coil. At some point, moving to larger and larger numbers of smaller elements around the head does not improve central SNR, and in fact can decrease it once coil noise becomes a significant factor with poorly loaded small elements. The main SNR advantage of having 96 elements compared to 32 is increased SNR in peripheral regions. SNR in the cortex is up to 40% higher with the 96-channel coil and, if we were interested in imaging the skin, we would benefit from a greater than twofold SNR increase there. In the comparison of these coils, we see the demonstration of an important principle: A well-constructed array does not have low SNR in the center or "poor penetration". Rather, at the center of the head it should match the performance of any lower channel count array or volume coil of equal dimensions, and offer substantial gains in SNR in the periphery. In practice, arrays can offer a small boost in central SNR compared to conventional volume-coil designs because an array can be constructed to wrap closely around the anatomy of interest, while a conventional volume resonator such as a birdcage does not perform well in close proximity to tissue, which can create uneven loading and loss of circular polarization.

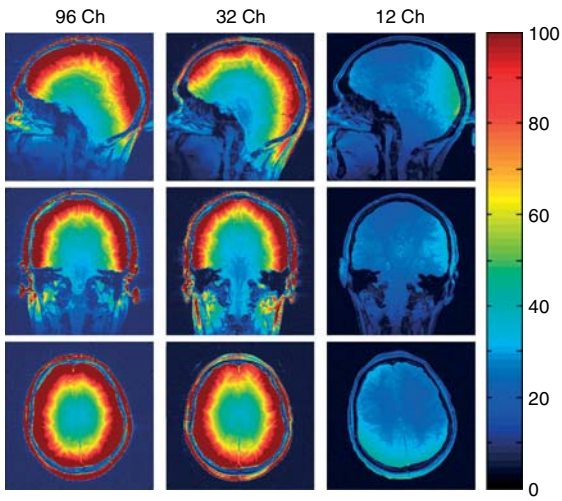

Figure 8.5. SNR maps from a 20° flip angle gradient echo acquisition. The SNR is calculated for optimum matched filter SNR reconstruction on a pixel-by-pixel basis using a standard acquisition and a noise reference scan with no RF excitation. The utility of placing coils on top of the head can be seen, despite the nulls in their individual sensitivity profiles.

The performance of the arrays in accelerated imaging was compared by using a 170 mm spherical phantom containing a fluid with $\varepsilon_r = 81$ and $\sigma = 0.97$ S m^{-1}. Raw k-space data were saved from GRE acquisitions in a transverse plane with the FoV set tight on the phantom (TR/TE/Flip/BW/Slice = 200/3.6/20/300/3 mm, matrix 128×128, FoV = 175×175 mm). SENSE g-factor maps were calculated directly from the analytic expression in equation (8.11).

Maps of $1/g$, representing the percentage of SNR retained in the SENSE reconstruction, are shown in Figure 8.6. Here, the benefit of increasing the number of elements is clear. The overall g-factor values and the peak g-factor values are significantly reduced by increasing the channel count. For example, the maximum g-factor at acceleration rate 5 with 96 channels is the same as that for acceleration rate 4 with 32 channels. For 3D acquisitions, it is often possible to accelerate also in the through plane or partition direction. The additional g-factor penalty for accelerating in the second direction is

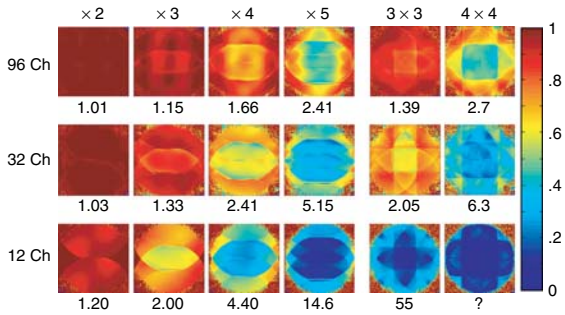

Figure 8.6. Maps of the inverse *g*-factor ($1/g$) for the 96-channel coil (top row), the 32-channel coil (middle row), and the commercial 12-channel coil (bottom row), measured in a spherical "Braino" phantom. Peak *g*-factor values are shown below each map (with the peak *g*-factor for 4×4 acceleration in the 12-element array being undefined, as the maximum total acceleration factor for 12 elements is 12). All maps are rendered with the same color scale for comparison, where low values (blue) show areas with high *g*-factor.

comparatively small, so that very high combined acceleration rates such as $3 \times 3 = 9$ or $4 \times 4 = 16$ are possible. Of course, these high acceleration rates still incur the square root of acceleration factor SNR loss associated with undersampling.

Figure 8.7 shows a direct comparison of the experimental performance of the 32-channel head array with ultimate intrinsic SNR.[26] This absolute performance mapping approach has the benefit of using a consistent absolute reference, independent of particular coil array design. Note that, with fourfold acceleration, performance is reduced as compared to the unaccelerated case, indicating that more elements are needed to approach ultimate limits in the presence of acceleration. Note also that central regions approach ultimate performance more rapidly than peripheral regions of the FoV.

8.5 COIL APPLICATION

8.5.1 General Principles

By now, coil arrays tailored for a broad spectrum of clinical and research applications of parallel imaging have been described, including body areas ranging from head to toe. The design process for a particular application or body area typically involves specifying the desired volumetric coverage, common image plane orientations, and level of acceleration, and arranging array elements accordingly to encircle the anatomy of interest or tile key body surfaces.

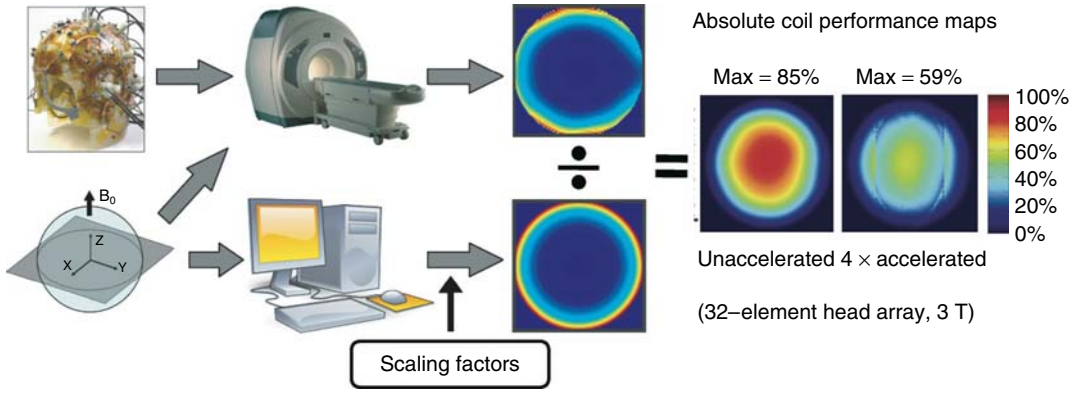

Figure 8.7. The procedure for, and results of, ultimate intrinsic performance mapping for the 32-element, 3 T head array. Ultimate intrinsic SNR is independent of coil geometry and can be used as an absolute reference against which any coil can be evaluated. Absolute coil performance maps are generated by dividing the experimentally measured SNR by the corresponding ultimate intrinsic SNR, calculated using the electrical properties of the scanned phantom and appropriately scaled by pulse-sequence-specific factors. This example shows that 32 coils are sufficient to capture a substantial fraction of the optimal performance for unaccelerated acquisitions, but that more elements would be needed to achieve comparable performance for larger accelerations. Note also that central regions of the field of view approach ultimate performance more rapidly than peripheral regions, where the ultimate intrinsic SNR is quite high.

Here we will focus on two current trends in the development of high-performance parallel imaging coil arrays: the development of "high-density" arrays of many elements, and the design of arrays for operation at high or ultrahigh magnetic field strength.

Designs similar to the 32-element head array described in Section 8.4.2 have now made their way into the clinical and commercial coil array repertoire. The 96-element array, on the other hand, remains principally a research tool, e.g., for highly accelerated imaging applications.[58] In describing the performance of both arrays in Section 8.4.2, we commented that a well-constructed many-element array is not expected to have poor penetration at depth. This point is perhaps worth amplifying, as it has traditionally been subject to certain misconceptions. Indeed, as large-scale coil arrays are constructed with increasing numbers of independent elements, and as the individual elements become smaller in size, there has been some concern that the shallower depth penetration of the individual elements might adversely affect the overall performance of the coil array. As is evidenced by the convergence of finite arrays toward the ultimate intrinsic central SNR in Figures 8.2 and 8.7, and as has also been validated in other theoretical studies,[59] this is not the case in principle (at least when coil/circuit-derived noise sources are negligible). In fact, relatively straightforward geometrical constructions, in which large elements are progressively subdivided, may be used to show that superposition of multiple elements in tightly packed arrays overcomes the limitations of individual elements. That said, when coil- or circuit-derived noise sources become significant in comparison to body-derived noise sources, the move to larger numbers of small elements can begin to degrade SNR performance. To some extent, non-body-derived noise sources may be controlled by judicious use of coil materials, careful design, and even coil cooling if necessary. The balance of noise sources is also improved at high field strength, where coils may be made smaller before they become coil-noise-dominated.

Given the broad clinical adoption of 3 T scanners, and the increasing worldwide prevalence and promise of scanners at field strengths of 7 T and beyond, significant attention has been given to the design of coil arrays for parallel MRI at high and ultrahigh field strengths. Two principal features distinguish high-field arrays from arrays designed for lower fields: (i) potentially significant perturbations of coil sensitivities at high field/frequency based on propagation effects and tissue electrical properties, and (ii) the need to balance transmit and receive considerations, given safety concerns and the increasing difficulty of achieving uniform transmit fields over large FoVs. These challenges are balanced by the appreciable benefits of parallel reception and transmission at high field strength. On the receive side, these benefits include improvements in the ultimate intrinsic SNR, reductions in the ultimate intrinsic *g*-factor, and the ability to reduce energy deposition by limiting the length of RF pulse trains. The benefits of parallel transmission will be addressed elsewhere, but it is clear that parallel transmit array designs are poised to undergo a ferment similar to that experienced for parallel reception.

8.5.2 Case Studies

A 32-channel head coil for operation at 7 T[60] was built on the same helmet-shaped former used for the 32- and 96-element arrays described in Section 8.4.2. The details of its design will not be elaborated here, but the receive array was built with the same element geometry as the 3 T, 32-channel coil and was mounted inside a detunable birdcage coil that provided transmit excitation. This 7 T array offers an interesting validation of the predictions of ultimate *g*-factor calculations, which have shown that *g*-factor should decrease with increasing field strength.[24,25] This is generally understood to be attributable to the increased field focusing that becomes possible as the wavelength of the RF in the tissue becomes shorter. Comparing *g*-factor maps obtained on a head-shaped tissue equivalent phantom using 32-channel coils built on identical helmets at 3 and 7 T (Figure 8.8), we see that the *g*-factor maps for acceleration rate 5 at 7 T are almost the same as those for acceleration rate 4 at 3 T, and similarly for rate 6 at 7 T and rate 5 at 3 T. Given that coil loading also increases with increasing frequency, enabling the use of smaller coil elements before coil noise becomes significant, there is increasing motivation and justification for exploring higher channel count arrays at ultrahigh field, if the concomitant problems of cable interactions, preamp oscillations, and coil coupling can be successfully addressed.

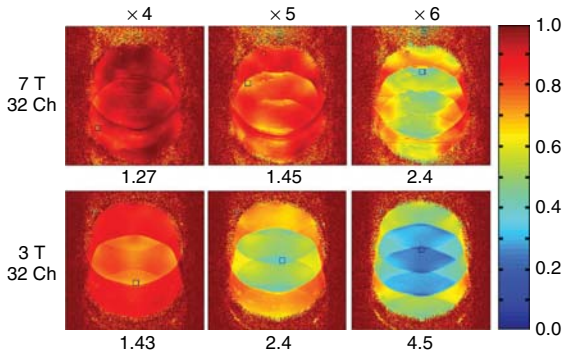

Figure 8.8. Maps of the inverse g-factor ($1/g$) for the 7 T (top row) and 3 T (bottom row) versions of the 32-channel head coil, measured in a head-shaped tissue equivalent phantom. Peak g-factor values are shown below each map. Although the two coils have identical element geometries, the g factors are significantly lower for the 7 T coil. This behavior is consistent with ultimate intrinsic SNR behavior, indicating that the increased distortion and focusing of RF fields at high magnetic field strength leads to improved orthogonality of coil sensitivities and an improved capability for spatial encoding.

8.6 TROUBLESHOOTING

With any "home-made" coil, we recommend that the first scan on each subject be performed with the body coil receiving (for 3 T and lower) or with a volume transmit coil (if available) used in transmit–receive mode. If there are any unexpected bright or dark regions in the first localizer, the scan should be stopped until the coil is checked, as this could indicate a fault in the receive array. The most common fault is a failure of the active detuning in a coil element. With rigorous design principles incorporating a fuse and a passive trap in each element, it should never be possible for the receive element to be resonant during transmit, but errors are possible, and a resonant receive element can focus RF locally and potentially injure the patient. With fuses present in the coil, the most likely outcome of active detuning failure is that the fuse will blow. You can determine which element has failed either through running a scan and saving the uncombined images from each channel, or through bench tests. When you find the fuse that has blown, you must not only replace it but also try to find out why it has failed. The most common cause of detuning failure is a broken bias wire. When current flows through the wire during active detuning, there is a Lorentz force on the wire since it is immersed in the magnetic field of the scanner, and it displaces sideways. As the sequence runs, the wires can dance back and forth with remarkable vigor, and eventually metal fatigue will cause a wire to crack and fail where it is soldered to the interface board. Therefore, it is good practice to glue or tape down these wires near where they are soldered to prevent this problem.

8.7 CONCLUSIONS

Parallel MRI techniques place unique demands upon coil array performance. The construction and the arrangement of detector coils must be chosen not only to maximize the SNR of the (unaccelerated) reconstructed data but also to provide spatial information about the magnetization within the sample. These demands have led to a tremendous expansion of the potential design choices for coil arrays. This rapid expansion has become particularly manifest in the number of available receiver channels on MR systems. There is little doubt that the widening range of parallel MRI applications, together with the progress toward ever higher magnetic field strength, will lead to array designs that combine and perhaps surpass the strategies that have been presented here. It is hoped that this brief review will provide a helpful starting point for coil designers, and that it will also serve to place into context the innovations that will undoubtedly arrive in times to come.

RELATED ARTICLES IN THE ENCYCLOPEDIA OF MAGNETIC RESONANCE

Birdcage Resonators: Highly Homogeneous Radiofrequency Coils for Magnetic Resonance

Coils for Insertion into the Human Body

Design and Use of Internal Receiver Coils for Magnetic Resonance Imaging

Multifrequency Coils for Whole Body Studies

Radiofrequency Systems and Coils for MRI and MRS

Refrigerated and Superconducting Receiver Coils in Whole Body Magnetic Resonance

Spatial Encoding Using Multiple rf Coils: SMASH Imaging and Parallel MRI

Surface Coil NMR: Detection with Inhomogeneous Radiofrequency Field Antennas

Surface and Other Local Coils for In Vivo Studies

Whole Body Machines: NMR Phased Array Coil Systems

REFERENCES

1. D. K. Sodickson and W. J. Manning, *Magn. Reson. Med.*, 1997, **38**, 591–603.
2. K. P. Pruessmann, M. Weiger, M. B. Scheidegger, and P. Boesiger, *Magn. Reson. Med.*, 1999, **42**, 952–962.
3. M. A. Griswold, P. M. Jakob, R. M. Heidemann, M. Nittka, V. Jellus, J. Wang, B. Kiefer, and A. Haase, *Magn. Reson. Med.*, 2002, **47**, 1202–1210.
4. P. B. Roemer, W. A. Edelstein, C. E. Hayes, S. P. Souza, and O. M. Mueller, *Magn. Reson. Med.*, 1990, **16**, 192–225.
5. U. Katscher, P. Bornert, C. Leussler, and J. S. van den Brink, *Magn. Reson. Med.*, 2003, **49**, 144–150.
6. Y. Zhu, *Magn. Reson. Med.*, 2004, **51**, 775–784.
7. M. A. Ohliger and D. K. Sodickson, *NMR Biomed.*, 2006, **19**, 300–315.
8. M. Bydder, D. J. Larkman, and J. V. Hajnal, *Magn. Reson. Med.*, 2002, **47**, 160–170.
9. E. N. Yeh, C. A. McKenzie, M. A. Ohliger, and D. K. Sodickson, *Magn. Reson. Med.*, 2005, **53**, 1383–1392.
10. D. K. Sodickson and C. A. McKenzie, *Med. Phys.*, 2001, **28**, 1629–1643.
11. K. P. Pruessmann, M. Weiger, P. Bornert, and P. Boesiger, *Magn. Reson. Med.*, 2001, **46**, 638–651.
12. D. K. Sodickson, M. A. Griswold, P. M. Jakob, R. R. Edelman, and W. J. Manning, *Magn. Reson. Med.*, 1999, **41**, 1009–1022.
13. M. Lustig, D. Donoho, and J. M. Pauly, *Magn. Reson. Med.*, 2007, **58**, 1182–1195.
14. D. I. Hoult and R. E. Richards, *J. Magn. Reson.*, 1976, **24**, 71–85.
15. H. Vesselle and R. E. Collin, *IEEE Trans. Biomed. Eng.*, 1995, **42**, 497–505.
16. E. M. Haake, R. W. Brown, M. R. Thompson, R. Venkatesan, *Magnetic Resonance Imaging: Physical Principles and Sequence Design*, Wiley-Liss: New York, 1999, p. 914.
17. D. I. Hoult, *Concepts Magn. Reson.*, 2000, **12**, 173–187.
18. H. Nyquist, *Phys. Rev.*, 1928, **32**, 110–113.
19. J. D. Jackson, *Classical Electrodynamics*, John Wiley & Sons, Inc.: New York, 1999.
20. M. Weiger, K. P. Pruessmann, C. Leussler, P. Roschmann, and P. Boesiger, *Magn. Reson. Med.*, 2001, **45**, 495–504.
21. J. A. de Zwart, P. J. Ledden, P. Kellman, P. van Gelderen, and J. H. Duyn, *Magn. Reson. Med.*, 2002, **47**, 1218–1227.
22. J. A. de Zwart, P. J. Ledden, P. van Gelderen, J. Bodurka, R. X. Chu, and J. H. Duyn, *Magn. Reson. Med.*, 2004, **51**, 22–26.
23. Y. Zhu, C. J. Hardy, D. K. Sodickson, R. O. Giaquinto, C. L. Dumoulin, G. Kenwood, T. Niendorf, H. Lejay, C. A. McKenzie, M. A. Ohliger, and N. M. Rofsky, *Magn. Reson. Med.*, 2004, **52**, 869–877.
24. M. A. Ohliger, A. K. Grant, and D. K. Sodickson, *Magn. Reson. Med.*, 2003, **50**, 1018–1030.
25. F. Wiesinger, P. Boesiger, and K. P. Pruessmann, *Magn. Reson. Med.*, 2004, **52**, 376–390.
26. R. Lattanzi, A. K. Grant, J. R. Polimeni, M. A. Ohliger, G. C. Wiggins, L. L. Wald, and D. K. Sodickson, *NMR Biomed.*, 2010, **23**, 142–151.
27. R. Lattanzi, D. K. Sodickson, A. K. Grant, and Y. Zhu, *Magn. Reson. Med.*, 2009, **61**, 315–334.
28. R. Lattanzi and D. K. Sodickson, In *Proceedings of the Proceedings 19th Scientific Meeting, International Society for Magnetic Resonance in Medicine*, Montreal, Canada, 2011 May, p. 3876.
29. R. F. Lee, C. R. Westgate, R. G. Weiss, D. C. Newman, and P. A. Bottomley, *Magn. Reson. Med.*, 2001, **45**, 673–683.
30. R. F. Lee, C. J. Hardy, D. K. Sodickson, and P. A. Bottomley, *Magn. Reson. Med.*, 2004, **51**, 172–183.
31. G. Adriany, P. F. Van de Moortele, F. Wiesinger, S. Moeller, J. P. Strupp, P. Andersen, C. Snyder, X. Zhang, W. Chen, K. P. Pruessmann, P. Boesiger, T. Vaughan, and K. Ugurbil, *Magn. Reson. Med.*, 2005, **53**, 434–445.
32. G. Adriany, P. F. Van de Moortele, J. Ritter, S. Moeller, E. J. Auerbach, C. Akgun, C. J. Snyder, T. Vaughan, and K. Ugurbil, *Magn. Reson. Med.*, 2008, **59**, 590–597.

33. G. Adriany, E. J. Auerbach, C. J. Snyder, A. Gozubuyuk, S. Moeller, J. Ritter, P. F. Van de Moortele, T. Vaughan, and K. Ugurbil, *Magn. Reson. Med.*, 2010, **63**, 1478–1485.

34. J. W. Carlson and T. Minemura, *Magn. Reson. Med.*, 1993, **29**, 681–688.

35. J. A. Bankson, M. A. Griswold, S. M. Wright, and D. K. Sodickson, *Magn. Reson. Mater. Phys. Biol. Med.*, 2000, **10**, 93–104.

36. M. A. Griswold, P. M. Jakob, M. Nittka, J. W. Goldfarb, and A. Haase, *Magn. Reson. Med.*, 2000, **44**, 602–609.

37. Y. Zhu, C. J. Hardy, D. K. Sodickson, R. Giaquinto, C. L. Dumoulin, G. Kenwood, T. Niendorf, H. Lejay, C. McKenzie, M. A. Ohliger, and N. M. Rofsky, *Magn. Reson. Med.*, 2004, **52**, 878–884.

38. C. J. Hardy, R. D. Darrow, M. Saranathan, R. Giaquinto, Y. Zhu, C. L. Dumoulin, and P. A. Bottomley, *Magn. Reson. Med.*, 2004, **52**, 878–884.

39. M. Weiger, K. P. Pruessmann, and P. Boesiger, *Magma*, 2002, **14**, 10–19.

40. J. V. Hajnal, D. J. Larkman, and D. J. Herlihy, In *Proceedings of the 8th Scientific Meeting of the International Society for Magnetic Resonance in Medicine*, Denver (CO), 2000, p. 1719.

41. M. A. Ohliger, R. L. Greenman, R. Giaquinto, C. A. McKenzie, G. Wiggins, and D. K. Sodickson, *Magn. Reson. Med.*, 2005, **54**, 1248–1260.

42. A. Reykowski and M. Blasche, In *Proceedings of the Proceedings of the 12th Annual Meeting of the International Society for Magnetic Resonance in Medicine*, Kyoto, Japan, 2004, p. 1587.

43. M. Buehrer, K. P. Pruessmann, P. Boesiger, and S. Kozerke, *Magn. Reson. Med.*, 2007, **57**, 1131–1139.

44. S. B. King, S. M. Varosi, and G. R. Duensing, *Magn. Reson. Med.*, 2010, **63**, 1346–1356.

45. R. F. Lee, R. O. Giaquinto, and C. J. Hardy, *Magn. Reson. Med.*, 2002, **48**, 203–213.

46. J.-X. Wang and D. B. Plewes, In *Proceedings of the 12th Annual Meeting of the International Society for Magnetic Resonance in Medicine*, Kyoto, Japan, 2004, p. 1584.

47. G. R. Duensing, H. R. Brooker, and J. R. Fitzsimmons, *J. Magn. Reson. B*, 1996, **111**, 230–235.

48. M. A. Ohliger, P. Ledden, C. A. McKenzie, and D. K. Sodickson, *Magn. Reson. Med.*, 2004, **52**, 628–639.

49. G. C. Wiggins, C. Triantafyllou, A. Potthast, A. Reykowski, M. Nittka, and L. L. Wald, *Magn. Reson. Med.*, 2006, **56**, 216–223.

50. British_Standards_Organization, Head forms for use in testing of protective helmets, Volume BS EN 960; 1995.

51. F. Wiesinger, N. De Zanche, and K. Pruessmann, In *Proceedings of the Proceedings 13th Scientific Meeting, International Society for Magnetic Resonance in Medicine*, Miami Beach, FL, 2005 May, p. 672.

52. G. C. Wiggins and L. Wald, U.S. pat. 7663367. (Feb. 16, 2010).

53. G. C. Wiggins, J. R. Polimeni, A. Potthast, M. Schmitt, V. Alagappan, and L. L. Wald, *Magn. Reson. Med.*, 2009, **62**, 754–762.

54. G. C. Wiggins, V. Alagappan, A. Potthast, M. Schmitt, C. J. Wiggins, H. Fischer, K. Jahns, J. Polimeni, and L. L. Wald, In *Proceedings of the Proceedings of the 15th Annual Meeting of the International Society for Magnetic Resonance in Medicine*, Berlin, Germany, 2007, p. 243.

55. M. Hergt, R. Oppelt, M. Vester, A. Reykowski, K. M. Huber, K. Jahns, and H. Fischer, In *Proceedings of the Proceedings of the 15th Annual Meeting of the International Society for Magnetic Resonance in Medicine*, Berlin, Germany, 2007, p. 1037.

56. C. D. Constantinides, E. Atalar, and E. R. McVeigh, *Magn. Reson. Med.*, 1997, **38**, 852–857.

57. P. Kellman and E. R. McVeigh, *Magn. Reson. Med.*, 2005, **54**, 1439–1447.

58. F. H. Lin, L. L. Wald, S. P. Ahlfors, M. S. Hamalainen, K. K. Kwong, and J. W. Belliveau, *Magn. Reson. Med.*, 2006, **56**, 787–802.

59. S. M. Wright and L. L. Wald, *NMR Biomed.*, 1997, **10**, 394–410.

60. G. C. Wiggins, C. J. Wiggins, A. Potthast, V. Alagappan, O. Kraff, A. Reykowski, and L. L. Wald, In *Proceedings of the 14th Annual Meeting of the International Society for Magnetic Resonance in Medicine*, Seattle (WA), 2006, p. 415.

Chapter 9
Transceiver Loop Arrays

Randy Duensing

Invivo Corporation, Gainesville, FL 32608, USA

9.1 INTRODUCTION

For the last 20 years, the principal focus of development in RF coils has been the receive characteristics of arrays of loop coils. This has been more than justified by the gains in signal-to-noise ratio (SNR) and the increase in resolution per unit time obtained through sensitivity encoding (SENSE)[1] and generalized auto-calibrating partially parallel acquisition (GRAPPA)[2] techniques. Although some transmit/receive local coil arrays are currently available on clinical MR systems, most coil arrays are receive-only and utilize the built-in body coil for excitation. The few transmit/receive coils available typically utilize a separate transmit coil that is designed for high uniformity (such as a birdcage) plus separate receiver loops. As far as the author is aware, the only true clinical transceiver loop array, in which the same elements are used for both transmit and receive, is the four-channel head coil array for the GE 0.7 T OpenSpeed MRI system. This coil uses large, relatively uniform elements for transmit with power flow split optimally to the four elements. The primary motivation for the use of this design is to provide a uniform excitation with high-peak RF magnetic field. Transmit/receive coil arrays have become much more common at 7 T and on other research platforms; however, these often use a variety of RF designs because of the relatively short wavelength at the Larmor frequency.

Loops have been the fundamental building block of RF coils in MRI since its origin, because the signal received is inherently a magnetic field effect. The varying magnetic field passing through the loop produces a voltage in the loop according to Faraday's law of induction. The maximum SNR from a particular point within the human body has been found to be related to the size of the loops in relation to the depth within the body.[3] The use of arrays[4] allows virtually all depths to be optimized for SNR. There is a strong duality of SNR in receive and power efficiency in excitation. For one loop or quadrature pair, the maximum SNR at a point would be produced by a coil that would also produce maximum excitation field for a given power. This reciprocity has been thoroughly discussed in the literature.[5] The difference is that receive arrays allow for the relative amplitudes and phase to be adjusted for each voxel after reception and thus allow maximum SNR everywhere. For a transmit coil, some choice has to be made because only one set of relative phases and amplitudes can be

RF Coils for MRI
Edited by J. Thomas Vaughan and John R. Griffiths

ISBN: 978-0-470-77076-4

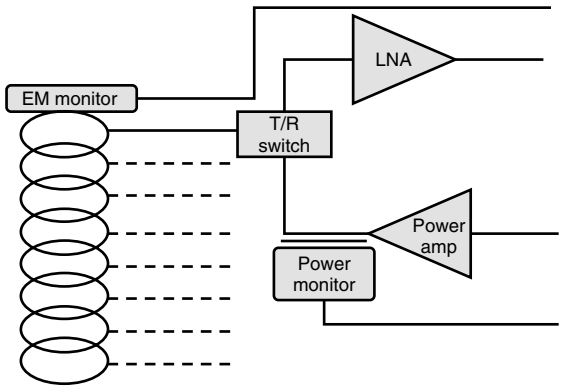

Figure 9.1. Block diagram of transceiver loop array system with detail on one channel only.

selected (except, of course, in the use of TX-SENSE or similar techniques).

A block diagram of the elements of the transceiver loop system is shown in Figure 9.1.

The lack of clinical transceiver loop arrays is actually a reflection of the difficulty associated with producing devices that have the desired performance with present technology. Numerous publications dealing with transmit/receive systems are available, with most of this work motivated by the lack of a large effective exciter. For example, few 7 T preclinical MR systems have a body coil for general excitation and thus all work must be performed with local transmit and receive coils, although not necessarily with transceiver loops. The bulk of this chapter covers the difficulties associated with designing and utilizing transceiver loop arrays and the advantages that can be obtained if these difficulties can be overcome.

9.2 MOTIVATION FOR THE USE OF TRANSCEIVER ARRAYS

A strong motivation for moving toward local transceiver arrays is that specific absorption rate (SAR) often limits the effective SNR on 3 T clinical MRI systems – either because the flip angle or the number of slices is limited to maintain safe power levels in the body. Additionally, the properties of the body often result in nonuniform excitation that also results in lower effective SNR than would be optimal. RF shimming[6] can help considerably but cannot overcome all nonuniformity, especially at higher field strengths.

One reason that transceiver loop arrays are not more ubiquitous is that the inherently varying intensity of the local magnetic field of a loop has a profoundly different result in transmit mode than in receive mode. During receive, the strong local receptivity of a loop means higher SNR, but in transmit, the high local field means a concomitantly high flip angle. Since pulse sequences are optimized for maximum SNR for a single flip angle (unless adiabatic pulses are used), the variation of flip angle inherently implies loss of SNR, whether the flip angle is higher or lower than planned.

A more recent driver for transceiver loop arrays is the advent of transmit SENSE[7] and other parallel transmit algorithms. By changing the pulse waveforms in loops with different spatial sensitivities, the length of time for a selective pulse can be shortened by a factor of 2 or more. The use of selective pulses that are matched to the desired excitation profile is varied, but includes correction of inherently nonuniform RF fields, inner volume excitation, and SAR minimization given some constraint.

9.3 CHALLENGES OF LOCAL TRANSCEIVER ARRAY COILS

While there are clear advantages to the use of transceiver loop arrays, there are significant challenges to making the most beneficial use of these advantages. These are, for the most part, practical issues of control, safety monitoring, and calibration. The question of whether loops are optimal compared to strip lines or some other form of resonator will remain open for debate because each approach has advantages for certain applications and frequency ranges. The geometry of a given design from the receive side is typically driven by obtaining the highest SNR from a given region, which in reciprocal terms is equivalent to the highest rotating B_1 field for a given power.

High local magnetic field is necessarily associated with a relatively high local electric field. In receive mode, the electric field reciprocally translates to the sensitivity to noise from that region. In transmit mode, the electric field is the driver for local power delivery. Since the electric field spatially varies, the power deposited in the tissue varies similarly. This causes extra difficulty in the calculation and monitoring of the local SAR. A high local SAR can result in heating of local tissue, and potentially in RF

burns. Any safe monitoring system must accurately estimate both local SAR and global SAR or, alternatively, local/global in vivo temperature.

There are three approaches to dealing with the nonuniformity of the electromagnetic fields around a local transmit coil. The first is exemplified by the built-in body coil. In this approach, the coil is made large and currents are distributed to produce an intrinsically uniform field. The second approach is, perhaps surprisingly, the opposite extreme. The individual elements must be small, smaller even than typically used in clinical receive arrays. The reason is that it must be possible to take a linear combination of the "unit" coils to produce the desired level of uniformity. A "unit" coil that is on the order of typical arrays, say 8–10 cm in diameter, will not, in all situations, be able to produce enough local uniformity to avoid local heating. This is one reason that there are few clinical coils using this approach. If we take a unit size of, say 4 cm diameter, then many elements would be required – over 200 elements for a cardiac coil array, for example. In principle, such a system is quite capable of high uniformity and low SAR; however, because of the small unit size the system can also be used for TX-SENSE or similar applications of spatially selective excitation. It should also be noted that using a single-pulse sequence for all channels still gives considerable degrees of freedom. The typical constraint is likely to be a certain minimum field variation over a region of interest (ROI) with minimum power and no more than a certain safe, local SAR. The third approach is the use of adiabatic pulses in which the relative field strength is much more weakly related to effective excitation; however, SAR limits the utility of this approach in many cases.

While the small element size described above has the potential to produce relatively uniform (or controlled nonuniform) excitation, in the event of failure there is the possibility of very high local electric fields, i.e., if much more power than anticipated enters a single loop. Additionally, when used for spatially selective excitation the maximum local SAR will generally increase in comparison to the uniform case. No matter what, the constraints provide for a wide range of possible total and local SAR. The logical approach to this problem is robust local power monitoring. Each unit loop could have a built-in current sensor that is monitored by the system for extreme values. Alternatively, a reflected power sensor can be used for a similar purpose. A third approach to the problem is simply a fail-safe device such as a fuse that would fail if the current reached some extraordinary level.

Complete characterization of the external fields generated by the local coil arrays can be determined by measurement of the electric and magnetic fields with resolution adequate to span the space of possible electromagnetic (EM) fields. Sensors built into each coil would provide such resolution. A figure-eight current sensor that monitors the current in a given loop can be used with premeasured field maps to scale the electric and magnetic fields associated with each loop. It should be noted that measurement of the field outside the body does not completely define the field within the body. The electrical properties of the tissues modify the EM fields compared to free space conditions.[8] The variation generally increases with frequency because the wavelength is shortened with respect to the body size. Because the tissue properties are constant, it is possible that if the in vivo fields are measured initially (i.e., through prescan field mapping), they may be able to be scaled via the sensor values, assuming that enough degrees of freedom were provided from the prescan variation. For large numbers of channels, as proposed above, it is likely that a minimal set of basis fields would be used for prescan measurement. This basis set might be used directly in the transmit process, but in any case should approximately span the space of possible excitations proposed in the scan. It is likely that a safety margin will still be employed in any clinical setting.

The preceding discussion centers around the vision of future transceiver loop systems for clinical MRI. The advantages include the ability to produce uniform excitations over defined ROIs with minimal power and SAR and the ability to execute TX-SENSE or TX-GRAPPA sequences with low wasted power levels. The requirements for these advantages include many small field sources, control of currents in such a way as to produce effective field currents that span the necessary field basis elements, and monitoring of currents to maintain safety and ensure accuracy.

9.3.1 Shared Impedance in RF Coil Transmit

One central problem with this vision is the practical difficulty of how to drive the desired current pattern given variable loading associated with different patients, coils, and coil placement. To understand the problem, consider the following. If one could drive

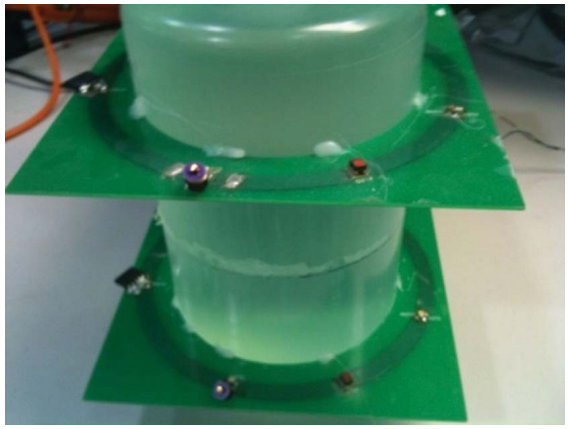

Figure 9.2. Two coaxial coils and bottle phantom.

each loop individually in a prescan procedure, then the current (and thus B_1 field) could be determined for a given voltage. Although time consuming, this procedure is clear in a conceptual sense. It would seem that after this prescan, one could then proceed with the determination of the desired fields using the individual coils as basis elements that are scaled to produce the desired net fields.

Unfortunately, this approach is a gross oversimplification of the true story. Specifically, the above approach ignores the shared impedance between elements. In general, there is both shared reactance and shared resistance between every pair of loops. Thus, driving two loops simultaneously would provide a different effective load impedance to each amplifier. This load would vary with the relative amplitude and phase of the drives, thus making the prescan data only a rough estimate of the actual behavior of the array. To make matters worse, if different pulse shapes are driven into these two loops, the dynamic impedance would vary through the pulse duration, thus changing the actual pulse shapes of the resultant magnetic fields. The degree of perturbation will be related to the total shared impedance, but in an array with a large number of loops, significant shared impedance is unavoidable.

A simple analysis can be used to demonstrate the problem associated with shared impedance. If two coupled coils are driven simultaneously with different pulse waveforms, it is interesting to look at the extremes of their behavior. Assume that at a specific point in time, the two waveforms have the same amplitude. At this moment in time, the currents are in phase. Perhaps, at a later time the waveforms are such that the amplitude of one is the negative of the other. The effective load impedance of coupled coils would vary dramatically between these two points in time.

To demonstrate how significant shared impedance may be, an example system of two coupled coils was constructed. As shown in Figure 9.2, the two circular loops of diameter 15 cm were spaced coaxially from one another by 11 cm. Each of the loops was tuned and matched to approximately 50 Ω at 63.8 MHz (the approximate Larmor frequency for protons on 1.5 T MRI systems) with the other loop open.

Measurements of S11 for the two loops are shown in Figure 9.3. When used as receive elements with decoupling preamplifiers, the impedance varies little because the impedance mismatch caused by the preamplifiers makes the shared impedance relatively small compared to the impedance from the preamplifier.[4] This masks the effect of shared impedance.

Figure 9.4 shows the reflection coefficient looking into port 2 when coil 1 is active. The plot of reflection from port 1 with coil 2 active looks essentially the same and is not reported. This shows the coupling that is masked when loop 1 is open and when preamplifier mismatch is employed. When these two loops are to be used for transmit, the shared impedance is not so easily hidden, as has been discussed in the preceding sections.

To observe the effects of shared impedance, a Butler matrix for this two-channel system was constructed. Bilateral symmetry of two coils implies that the two modes of the system are currents in phase (0°) and currents out of phase (180°). The Butler matrix is then a four-port, 0/180 splitter/combiner. A 50 Ω, discrete component version of the standard ring combiner[9] was designed and built.

Figure 9.5 shows the reflection coefficient looking into the 0° port of the hybrid when attached to the two coils. Note that the frequency at which the system is matched has moved down. This represents the so-called Helmholtz pair-like mode. Because the mutual inductance responds in-phase, the total inductance is higher and the resonant frequency is lower. Figure 9.6 shows the reflection coefficient looking into the 180° port of the hybrid when attached to the two coils. This curve represents the counter-rotating current (CRC) mode and similarly, the cancellation of the shared impedance reduces the effective inductance and increases the resonant frequency.

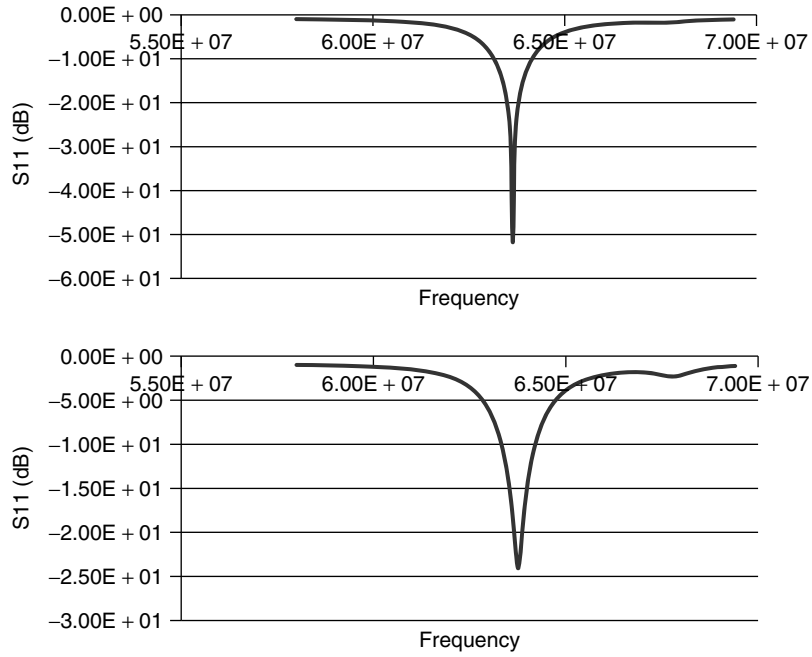

Figure 9.3. Reflection coefficients for loop 1 and loop 2, with the other loop open.

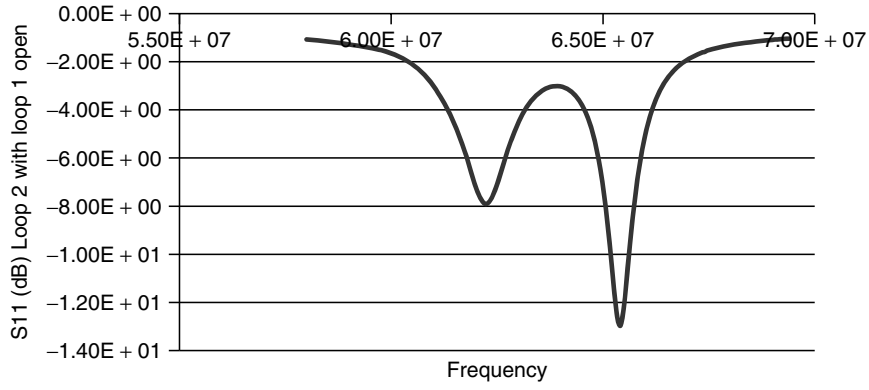

Figure 9.4. Reflection coefficient for loop 2 when loop 1 is active.

Note that these plots represent pure modes with little or no coupling to the other mode as is suggested by the single resonant frequency in each. This is the essence of the Butler matrix approach – to produce modes that are independent. Note that matching networks on each port could be added to produce 50 Ω at the frequency of interest. This would allow amplifiers to drive each mode with little interaction and little reflected power. The limitation of this approach is that in reality the system is not fixed, shared impedance varies with patient load and sometimes with the shape of flexible coils. Additionally, considerable power would be dissipated in these devices.

Perhaps, the most important point of this example is that the port impedances looking into the coils change depending on the relative amplitude and phase

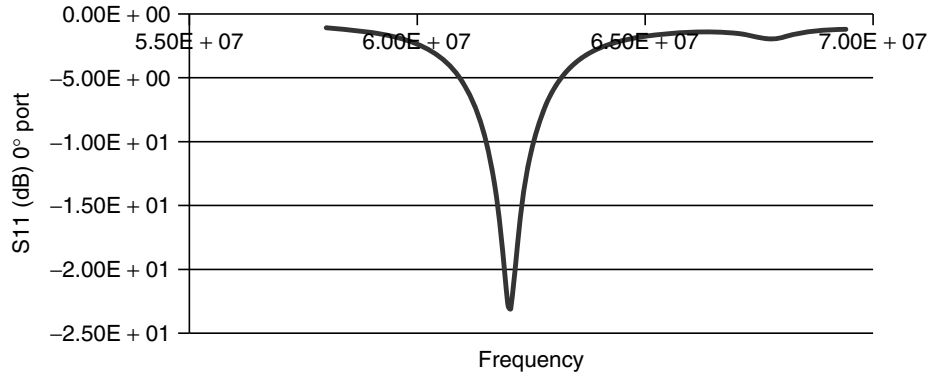

Figure 9.5. Impedance of in phase drive of the two coupled loops.

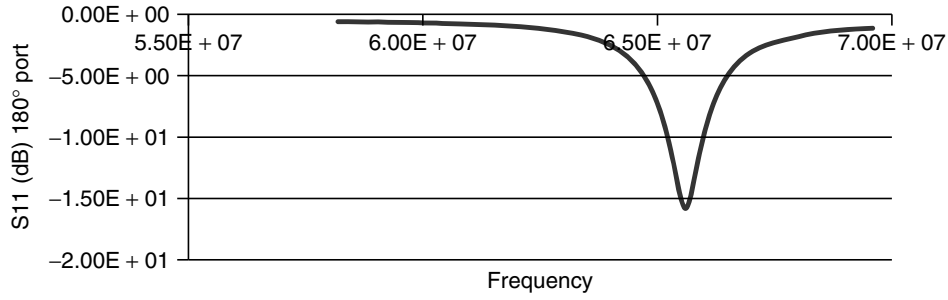

Figure 9.6. Impedance of out of phase drive of the two coupled loops.

of the drives. Unless the ports are well isolated, this will result in nonlinear amplifier behavior and thus variation of the pulse shapes from those that were intended. It has been recently shown that preamplifier mismatch does not provide noise figure behavior that is independent of shared impedance[10] and, by analogy, excitation amplifier mismatch would not be expected to provide power delivery that is independent of shared impedance.

9.3.2 Methods of Controlling Shared Impedance in Transceiver Loop Arrays

In the receive case of array elements, the shared impedance is masked using mismatched preamplifiers. Research has been carried out for the last several years to try to utilize similar philosophies to prevent varying load impedance from affecting the desired current waveform to be produced in a given loop. These approaches include Cartesian feedback,[11,12] mismatched amplifiers,[13] class D amplifiers,[14] circulators, impedance matrix measurement with pre-emphasis, and Butler matrices. Each approach is briefly explained in the following sections.

The fundamentally important step in Cartesian feedback systems is that the output signal is fed back to the input but before and after mix-up and mix-down. The effect is to increase the efficiency and linearity of the amplifier with respect to load dependence. This approach is currently being implemented in telecommunications systems and is an area of active research in MRI transceiver coil arrays.

Class D amplifiers are analogous to switching power supplies. The device is more like an on/off switch. The swing from maximum to minimum power rail voltages means that the current is not based on

the load impedance of the coil. Furthermore, the efficiency can be very high with almost all of the power being delivered to the load. The plausibility of MRI-compatible on-coil Class D amplifiers has been demonstrated.[15] Difficulties with this approach include higher order harmonics of the switching that may affect the MR spin system, and generate excess power loss if not filtered.

The circulator has the interesting property of nonreciprocal behavior, which is unusual among passive devices. By converting the energy passing through it into polarized EM signals, it is possible to make the device favor power flow in one direction. This enables an amplifier to deliver power to a load, but not receive reflected power from that load. This means that the amplifier is unaffected by an impedance mismatch. At present, the problem with circulators for the purpose at hand is that they utilize a static magnetic field and a ferromagnetic material, neither of which is compatible with the high static magnetic field of MRI systems. This implies that the circulators must remain outside of the magnetic field. Additionally, the reflected power from the coil flows to a load resistor that will have to dissipate the power associated with this effect.

The Butler matrix approach is to produce a splitter/combiner that corrects for the shared impedance of a coil matrix. This means that the ports that would be presented to the amplifiers ideally have zero shared impedance. For the two-channel case previously described, the Butler matrix device is a $0^\circ/180^\circ$ hybrid; however, the general n-dimensional case can be constructed of building blocks of this type of hybrid or a 90° hybrid. The two limitations of this approach are that the matrix may present a sizeable power loss (and therefore heating) and that the shared impedance matrix varies with patient loading, so the correction for shared impedance is only approximate unless the device is adjustable to load, or at least the impedance matrix is measured and followed by pre-emphasis correction. This adjustment would be challenging for a high channel count system but plausible.

Of course, the conceptually simplest approach is to isolate each coil element from all others, so as to make multipole elements isolated from one another. For example, a loop–butterfly combination is a simple example of a magnetic dipole and magnetic quadrupole that are inherently isolated. However, the isolation fails slightly with a nonsymmetric load (such as the human body). A further complication of this approach is that if it is taken to the extreme, then there are many coil traces that are overlapping and "unnecessary". A four-element version of this idea would have 10 loops $(4 + 3 + 2 + 1)$, whereas the same effect from a Butler matrix would have four elements.

Finally, if the impedance matrix is measured with the array in situ, then a pre-emphasis set can be calculated from the known shared impedances and the characteristics of the amplifiers. A table would be created during the production step of the MR system using measurements of the power amplifiers given a range of impedance values that would be available on the fly to correct for any set of measured values of impedance. The impedance matrix can be rapidly measured utilizing essentially a network analyzer switched between all of the ports. This is a feasible approach, if no other adequate solution is determined.

In summary, it is clear that a variety of approaches can produce near-optimal pulse shaping, given an array of real transmit elements driving power into the human body. The preferred solution is yet to be determined, but on the basis of prior experience, the author predicts that early deployments in the clinical arena are likely to utilize remote amplifiers with a Butler matrix and/or circulators and further correction in software as necessary.

9.3.3 Practicalities of Local Transceiver Systems

A purely practical problem in the design of transceiver elements is the high voltages associated with excitation. In receive elements, typically only the traps that are used to produce high impedance (and thus limiting the current for safety reasons) during transmit require high-voltage components. In transmit loops, all components are subjected to high voltages. As an example, 500 W peak power into a particular coil may be expected. Since the loop resistance in the tuned state may be on the order of 2 Ω, the current is therefore on the order of 16 A. The voltage across a reactance of 50 Ω would be 800 V, higher than the typical ratings for standard capacitors. Components are certainly available that will reliably handle the voltages expected, they just are a little larger and more expensive. Additionally, the maximum voltage expected (in failure mode) must still ensure patient safety. The housing must therefore be designed to prevent possible arcing to

the patient in the event of this high voltage. The body coil within a conventional system is well insulated from the patient, but local coils generally require more care because of housing seams and in engineering the thickness and quality of the insulating shell.

Grounding, cables, and shields are always a problem in the design of RF coil arrays. One of the major difficulties is that the shield of a coaxial cable is an antenna that is placed in near proximity to coil arrays, with each shield being physically attached to at least one coil element. This means that there is an opportunity to produce unwanted current flow on shields and to modify the desired current distribution in the coils of interest. At present, there is no magic bullet for this issue, but rather the careful design of the placement of cable shields and the use of baluns and cable traps.[16] One advantage over receive arrays is that, for the transceiver case, some cables can be removed from the excitation field of coil elements, thus relieving the need to limit cable currents to safe levels. When using a body coil for transmission, the receive cables are always passing through high-transmit field areas and must have limiting of cable current. Thus, with local transmitters, it is likely that many of the large cable traps seen on receive-only coils can be eliminated.

9.3.4 Calibration of the Magnetic Field

The development of accurate, fast methods for calibration of B_1 for excitation is an area of very active research at present. In 2010, an entire session of the International Society of Magnetic Resonance in Medicine (ISMRM) was dedicated to this problem and many approaches were presented. The crux of the matter is that parallel excitation is different from parallel reception with regard to calibration. The receive profiles in conducting samples are not the same as transmit profiles at the frequencies used for modern MRI, as has been thoroughly described in the literature. Because of the effect of the human body on the EM fields, it is currently assumed that calibration is necessary for each patient. Furthermore, because the return signal is coming from receiver coils, the relative receptivity of one coil compared to others can be determined by a simultaneous acquisition. Thus, the acquisition time for a parallel receive calibration for 100 channels is the same as for two channels. On the other hand, the time for transmit field calibration would be 50 times longer for the same two coil systems. Clearly, for many channels to be practical, substantial accelerations must be employed. Possible approaches to this challenge include the following: limiting to fewer specific transmit modes that span the likely space to be used with different pulse shapes; using compressed sensing to accelerate the acquisition of prescan data; utilizing the receive profiles as guidance for transmit profiles; and using other information to estimate transmit profiles; or, perhaps, some currently unknown approach. In any case, transmit field calibration of many channels is an open and important problem.

9.4 CONCLUSIONS

While transceiver loops are common in experimental settings, the promise of the use of dense transceiver loop arrays is high (but unrealized) for clinical MRI at 3 T and above. There are considerable challenges that must be faced, but there are also considerable potential benefits. At 3 T, SAR is often responsible for limitation of the effective SNR and this is worse at higher field strengths. In order to obtain high uniformity, but at the same time high variable fields for optimization of transmit SENSE applications, many small elements are required. This implies further difficulties in calibration, monitoring, and design complexity.

The ultimate goal is to design local transceiver loops for all parts of the body that would allow maximum benefit of SAR and controlled excitation profiles. If complete success is obtained with local transmit coils, the outcome is that the body coil can be eliminated from clinical systems. This gains significant bore space that is extremely valuable, as the superconducting material for the magnet is very expensive and the amount required is strongly dependent on magnet size.

Many opportunities for research into the challenges associated with many-channel transceiver loop array design exist today and the successful outcome of these projects has high significance for the advancement of clinical MRI in the future.

REFERENCES

1. K. P. Pruessmann, M. Weiger, M. B. Sheidegger, and P. Boesiger, *Magn. Reson. Med.*, 1999, **42**, 952.

2. M. A. Griswold, P. M. Jakob, R. M. Heidemann, M. Nittka, V. Jellus, J. Wang, B. Kiefer, and A. Haase, *Magn. Reson. Med.*, 2002, **47**, 1202.
3. W. Edelstein, T. Foster, and J. Schenck, In *Proceedings of the 4th Annual Meeting, Society of Magnetic Resonance*, London, 1985, p. 964.
4. P. B. Roemer, W. A. Edelstein, C. E. Hayes, S. P. Souza, and O. M. Mueller, *Magn. Reson. Med.*, 1990, **16**, 192.
5. D. I. Hoult, *Concepts Magn. Reson.*, 2000, **12**, 173.
6. W. Mao, M. B. Smith, and C. M. Collins, *Magn. Reson. Med.*, 2006, **56**, 918.
7. U. Katsher, P. Boernert, C. Leussler, and J. Van Den Brink, *Magn. Reson. Med.*, 2003, **49**, 144.
8. C. M. Collins, M. B. Smith, J. T. Vaughan, M. Garwood, and K. Ugurbil, In *Proceedings of ISMRM*, 2000, p. 148.
9. D. M. Pozar, *Microwave Engineering*, 2nd edn, Wiley: New York, 1998, p. 403.
10. G. R. Duensing, C. Findeklee, and A. Reykowski, In *Proceedings of ISMRM*, Montreal, 2011, p. 1883.
11. D. I. Hoult, D. Foreman, G. Kolansky, and D. Kripiakevich, *MAGMA Magn. Reson. Mater. Phys., Biol. Med.*, 2008, **21**, 15.
12. A. Kerr, J. Pauly, G. Scott, P. Stang, and M. Zanchi, In *Proceedings of ISMRM*, Montreal, 2011, p. 332.
13. K. N. Kurpad, E. B. Boskamp, and S. M. Wright, In *Proceedings of ISMRM*, Miami Beach, 2005, p. 16.
14. N. Gudino, J. A. Heilman, M. J. Riffe, C. A. Flask, and M. A. Griswold, In *Proceedings of ISMRM*, Honolulu, 2009, p. 398.
15. N. Gudino, M. J. Riffe, L. Bauer, J. A. Heilman, and M. A. Griswold, In *Proceedings of ISMRM*, Stockholm, Transmit Technology Session, #1, 2010.
16. D. M. Peterson, B. L. Beck, G. R. Duensing, and J. R. Fitzsimmons, *Concepts Magn. Reson. Part B: MR Eng.*, 2003, **19B**, 1.

Chapter 10
Characterization of Multichannel Coil Arrays on the Benchtop

Mark A. Griswold

Department of Radiology, Case Western Reserve University, Cleveland, OH 44106, USA

10.1 INTRODUCTION

In almost any modern MR scanner in use today, the factor that defines the quality of the results more than any other is the RF coil. Thus a huge amount of time, energy, and money are dedicated every year to designing optimized coils for specific applications. However, in order to accomplish this task, one must know which coil is the best among many potential solutions. While it is clear that the final determination of the quality of a coil will happen in the magnet, this is typically an expensive proposition that can waste the precious resource of time on the scanner. This is particularly difficult when testing multichannel arrays, since the complexity of the arrays can be quite large, and troubleshooting in the magnet can be prohibitively time consuming. The purpose of this chapter is to present the fundamentals of how one can almost fully characterize an RF coil array on the benchtop using a set of relatively simple tools. A key focus will be on methods to characterize and isolate coupling issues that are often the root cause of almost all problems in multichannel arrays.

RF Coils for MRI
Edited by J. Thomas Vaughan and John R. Griffiths
 ISBN: 978-0-470-77076-4

10.2 THE PLAN

At this point in the development of MRI, the construction of single channel, and even quadrature coils, is relatively well developed (see Refs 1, 2 and other articles in the Encyclopedia of Magnetic Resonance for examples). In general, one can construct a coil, connect it to a cable and a preamplifier if needed and it will usually work fine. The naïve approach then would be to take a set of single coils built in isolation and put them together in hopes of making

an array. Unfortunately, this rarely works in practice since the coils, cables, preamplifiers, decoupling networks, etc., all couple together, and destroy all of the potential gains of the multichannel array. These couplings can be incredibly complex and can lead to situations in the middle of array construction that are completely unstable, and can leave the novice builder with no apparent route back to stability other than starting over. This is a situation we want to avoid at all costs.

Our experience has also shown us that the most successful array builders are the ones who start with a clear plan of how they will approach the construction of the array, including each step of coil construction. Before anything is actually assembled, the builder will make a plan as to how each step will be characterized to ensure that it is functioning as expected. In this way, the buildup of the array always moves from one stable setup to another toward a final end goal. If problems are encountered at any step along the way, one can always more easily revert to the last stable state, and the cause of the instability can more easily be identified. Throughout this process, the goal will be to keep every coil acting as if it is in isolation. If we are successful in this process, then we will have hopefully constructed the best array possible for a given design.

While every plan should be customized based on the individual array design project, as an example, we will follow a typical plan through the rest of this chapter. Our goal will be the simple four-channel array for a 1.5 T clinical system originally presented by Roemer *et al*.[2] with a few modifications. This is a relatively straightforward array to build, and will demonstrate many of the key points of array characterization along the way. In this array, we will have four flat coils arrayed in the head–foot direction (see Figure 10.1). The cable for each coil will originate at the center of each coil in the left–right direction, and will traverse the other coils toward the feet. The preamplifiers will be located approximately 50 cm away from the coil on one common board. Each coil will have a separate active decoupling network, and this decoupling signal will be passed to the coil through dedicated signal wires. With this setup, we would typically plan at least seven stable stages of construction. At each stage, we will cover some basics of what metrics one is interested in measuring on the benchtop, and how these can be practically measured with standard RF laboratory equipment. This is meant to be a rather general plan of how to approach the construction of an array. It is clear that some of these steps can be done in completely different ways based on experience or on the particular problem at hand. As always, it is best to consult someone with experience before embarking on the construction of an array. The original *NMR phased array* paper by Roemer *et al*.[2] is still a fantastic resource for those building their first array.

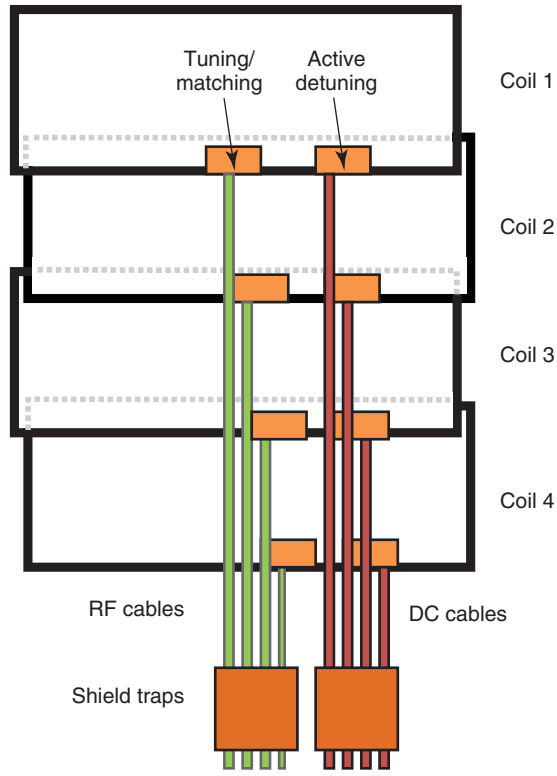

Figure 10.1. Schematic representation of the four-channel array discussed in this chapter.

10.3 NETWORK ANALYZER BASICS

The workbench tool that will be used most throughout this construction is a network analyzer. This is typically a two-port device, and can be used to measure both transmission between the ports and/or reflection from the ports. We normally characterize these effects through scattering parameters, or *S*-parameters. In

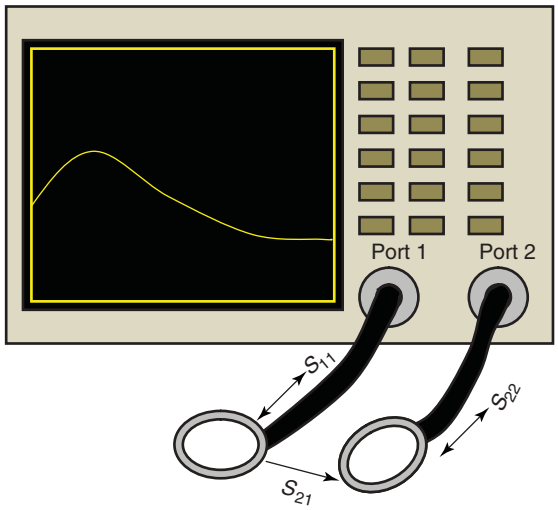

Figure 10.2. A schematic view of a network analyzer with two shielded-loop probes. The parameters S_{11} and S_{22} measure the reflection down either one of the individual ports, while S_{21} measures the transmission of RF power between ports 1 and 2. These measurements form the basis of the majority of measurements made during the construction of a multichannel array.

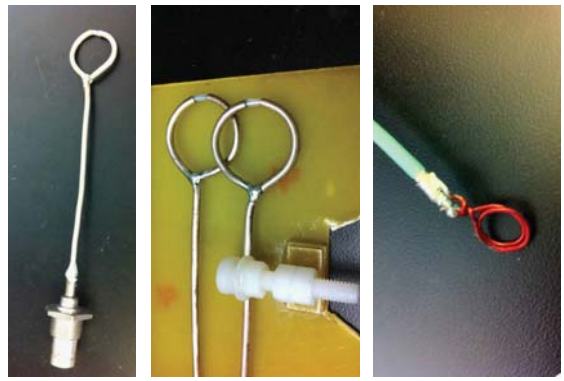

Figure 10.3. Three variants of probes used to interact with multichannel coil arrays. (a) A single shielded-loop probe made from semirigid cable. This kind of probe is useful for interacting with a single coil in reflection mode or in transmission mode when used as one unit of a pair. (b) A set of two shielded-loop probes positioned such that their coupling is minimal. In this case, a screw adjustment is provided to ensure accurate adjustment of this coupling. This kind of probe is very useful when examining single coils of the array in transmission mode. (c) A small 5 mm hand-wound inductor at the end of a coaxial cable can serve as a broadband pickup loop to adjust small elements in detuning circuits and to search for small leakage currents.

general, the S-parameters are normalized transfer coefficients and are denoted by S_{mn}, which corresponds to the power received on port m normalized by the power output on port n. As shown in Figure 10.2, the parameter S_{21} corresponds to the power received on port 2 as a function of the power output on port 1. This is a transmission mode measurement. One could also examine S_{11} to observe the reflection from a given impedance back into the same port. This is especially critical in matching a coil or amplifier to a 50 Ω system. In this case, a perfect match would correspond to zero reflected power, which would manifest itself as an S_{11} with very small magnitude (e.g., −70 dB), while a large S_{11} (approaching 1 or 0 dB) would correspond to a value far from 50 Ω. Both of these measurements are useful at various times, and it is critical for the RF coil builder to understand when to use each one as well as understanding each of their limitations.

A key tool for every coil builder to have is a set of various broadband probes that can be used to lightly couple into coils without making a direct connection to the coil. We always have at least three setups at every one of our stations. The basic unit of the first two is a shielded-loop probe. We typically make these from semirigid cable with a BNC connector on the end (Figure 10.3a). The loop size should be about 1 cm in diameter for most applications. The first setup is a pair of these connected through coaxial cables to the two ports of the network analyzer (as shown schematically in Figure 10.2). Each of these probes can be used alone to make a reflection measurement and can be used together for a transmission measurement. The second configuration is a pair of these shielded loops that are overlapped to minimize their coupling to each other (Figure 10.3b). These can be used to very efficiently measure a single coil's tuning, coupling, and quality factor (or Q-factor) for example. The final setup is a very small inductor at the end of a coaxial cable. Figure 10.3c shows an approximately 5 mm loop at the end of the relatively thin RG316 coaxial cable. This is particularly useful for characterizing small leakage currents around shield traps, detuning circuits, and preamplifiers.

10.4 INDIVIDUAL COIL TUNING AND CHARACTERIZATION

The first stage of construction for our four-channel array will be to tune each of the individual coils of the array. At this point, we want to ensure that each of the elements is tuned in isolation, so we must minimize interference from the other channels. The actual process used during this step depends heavily on the mechanical form of the coils and the housing that will be used to hold them. In the next steps, we will be finding an ideal overlap of the coils to ensure optimal geometric decoupling. A simulation (or even an experienced guess) can help provide an initial positioning of the elements. However, this is typically only an approximation. During the next stages, the coils, or some component of them, will likely be displaced from their initial position. Regardless of this, the initial tuning of each coil should be performed with the coils as close to their final position as possible, to ensure that their tuning is as accurate as possible in the final array configuration. If the array elements do move significantly, the tuning of each element should be rechecked to ensure optimal performance.

Once the initial positions are determined, each coil will need to be tuned individually. We normally position all of the elements in their approximate location, and then open all of the coils except for one by either removing a tuning capacitor or by physically opening a conductor in the loop. Our preferred method for measuring the coil tuning is to use an S_{21} (transmission) network analyzer measurement with two decoupled shielded-loop probes. Depending on the size of the array elements, one can use either a set of overlapping probes or two widely separated probes. Alternatively, one can use an S_{11} (reflection) measurement with a single probe, but we have found this method to be inaccurate in some cases because of the need to more tightly couple the probes to the coil elements. Whatever method is used, one should use some form of shield traps on the cable connected to the probes, to ensure that they do not interfere with these measurements. Ferrite beads can also be used in this situation since the probes will not be used in the magnet.

Using an S_{21} measurement, the goal is to tune the coil so that its peak S_{21} is at the frequency of interest (see Figure 10.4). We always ensure that the level of S_{21} transmission for all of these measurements is less than -40 dB to ensure that the probes themselves do not interfere with the measurements. At this point, it is also useful to measure the Q-factor of each coil, which is normally available on any modern network analyzer using the same S_{21} measurement. Knowing the isolated Q for each coil at this stage may be useful for finding subtle coupling later on in this process, especially for arrays with high numbers of elements. It will also ensure that the elements are intrinsically equal at this stage. As a note, we will almost certainly be detuning each coil circuit during the matching stage of development, but we have found that it is significantly easier for beginners to continue this process with the elements tuned at the resonant frequency until the later stages, even though it may require modifying a few capacitors twice.

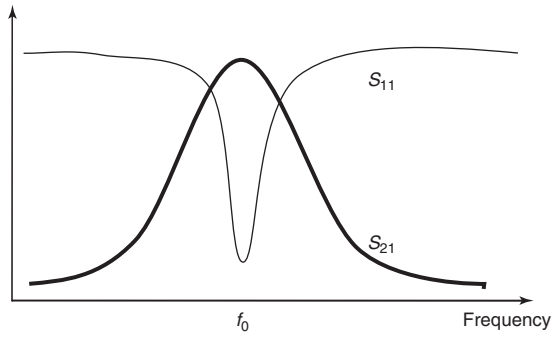

Figure 10.4. Schematic representation of a tuned coil as examined by a pickup coil in both reflection (S_{11}) and transmission (S_{21}) modes.

10.5 COIL POSITIONING FOR GEOMETRIC DECOUPLING

At this point, we should have four equal elements, each tuned to approximately 64 MHz. The next step in this process for this specific plan is to adjust the position of each of the elements to ensure that neighboring elements are maximally isolated. This is a process that should be applied pairwise. Two adjacent coils (e.g., coils 1 and 2) are closed so that they would normally be tuned at the required resonant frequency. In general, this will no longer be the case since the coils couple together. In order to cancel this coupling, we must displace the coils or some component of the coils. We normally construct coils such that they can either be positioned individually as a whole unit, or such that one conductor segment

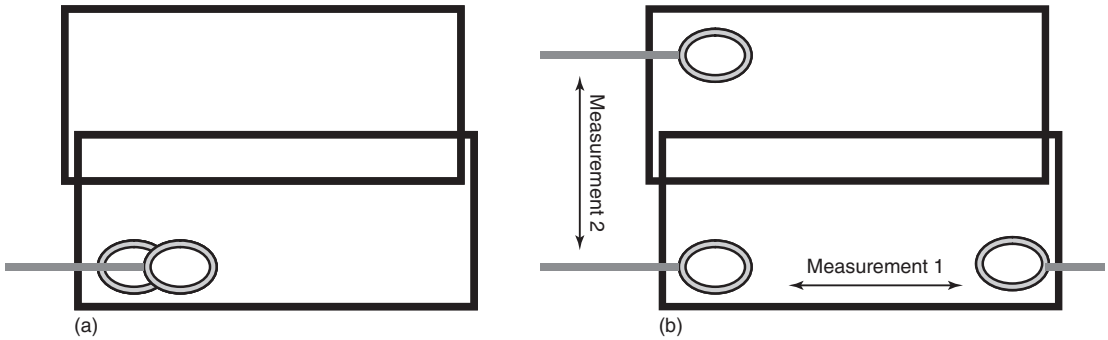

Figure 10.5. Two methods of estimating the decoupling between two adjacent coils. (a) A set of overlapped, decoupled probes can be used in transmission mode to examine one single coil of the array. (b) Alternatively, two widely separated probes can be used both to measure the splitting of a single coil (measurement 1) and to demonstrate the coupling between two different coils (measurement 2). When using two separated probes, it is essential to use ferrite beads and/or shield traps on the cables connecting to the probes. It is also useful to repeat each measurement twice with the position of each probe exchanged.

of each coil can be moved or modified to adjust the coupling between the elements. The goal of this step is to find the position of the coil or conductor such that the coupling between neighboring elements is minimal. While there is no theoretical threshold where we would say the coupling is acceptable or not, we have found that one should aim for as perfect decoupling as possible, since the later stages will only make the coupling worse, and it is best to start from a stable, uncoupled state.

There are multiple ways to monitor the coupling between coils, and we find ourselves constantly switching between the different approaches depending on the situation at hand, so having a basic understanding of all of them may be useful. The primary difficulty lies in the fact that these measurements are often asymmetrical because of the direct coupling of the probes and their cables to the array, especially through electric field coupling. Here, we will discuss two transmission mode measurements, with the primary difference between the two being the position of the probes.

The simplest way to observe the coupling is to use a set of decoupled loops (as in Figure 10.5a) positioned over one of the coils, with the total S_{21} level at about -30 to -40 dB. If the coils are coupled together, one will observe that the resonance splits into two disjointed peaks, as shown in Figure 10.6. The target is to return the situation to one where there is only one peak at the target resonance frequency, represented by the dotted line in Figure 10.6. Owing

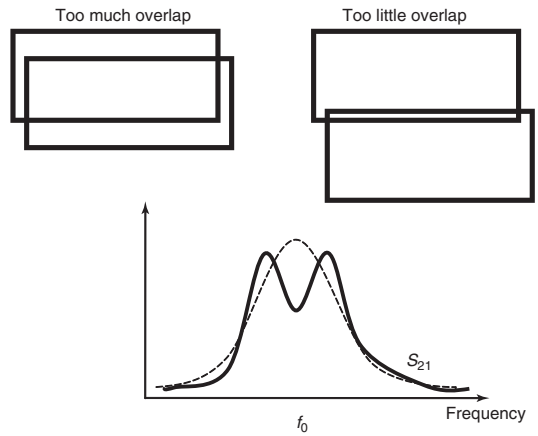

Figure 10.6. A schematic representation of peak splitting observed in a single coil when there is either too much overlap or too little overlap. It is very difficult to tell which direction one must go from a single measurement. However, worse coupling will result in a wider split, so we want to move to the situation where the peaks collapse into one peak (as shown by the dotted line).

to the potential asymmetries in the measurement, it is useful to alternate between the two coils to ensure that the situation is the same at each one. Special attention should be paid to the absolute tuning of each individual coil. When using this method, one must ensure that the frequency of the two coils stays consistent. If the modification of the position of the

coil or conductor causes a frequency shift, this must be corrected as in the previous step before continuing with the decoupling steps. It should also be noted that this method is somewhat limited if one desires a very high level of decoupling, since the situation with very low coupling can be very difficult to visualize. This is where a previous measurement of the Q-factor of the coils may be useful, since coupling can effectively decrease the apparent Q-factor.

Another way of performing this measurement is with two widely separated probes also in transmission mode (Figure 10.5b). This is particularly useful in arrays where the elements are larger. In this case, one can alternate between two measurements. In a first measurement, one puts both probes on opposite ends of a single coil. This gives a view of the tuning state of that particular coil including any splitting of the resonance. This mode is particularly useful during the early stages of decoupling where the coupling level is strong. One can then alternate between the coils to ensure that the situation is symmetrical. Again, we want to achieve the situation where we have a single resonance in both coils at our target frequency. Once the decoupling is close to optimal, one can then position the probes on opposite sides of the two coils (one coupled to each coil, but minimally coupled to each other). In this case, we want to see a minimum of power transferred between the two coils, so in this case, we are looking for a minimum of S_{21}. This measurement is very prone to asymmetries, so it is recommended that one performs this measurement twice by exchanging the position of the probes, and by testing the measurement in at least two different locations on the coils.

This process is then repeated for each pair of neighboring coils until all neighboring coils are decoupled. At each stage, one must open one coil and close another coil to ensure that only two coils are active at any one time. One cannot expect to use the array as a whole unit until much later in the process when the cables, detuning networks, and preamplifiers are attached and adjusted.

10.6 PREPARATION OF ACTIVE DETUNING NETWORKS

At this point, it is useful to address any active detuning networks on the coils. These are resonant switches that detune the coils during transmission. Thus these circuits are a critical safety component of the array, both for the patient and the MR system. These circuits are often an afterthought for novices, and can cause significant restarts and headaches if not appropriately dealt with at the right time. For this reason, we recommend adjustment of these circuits at this point in the construction process, when it is easy to monitor and adjust them while still maintaining a stable configuration when complete.

We usually perform this adjustment in two stages. Our circuits for prototype/noncommercial coils are typically designed with a fixed capacitor and a hand-wound air-core inductor. In the first stage, we open all of the coils directly on both sides of the detuning circuits and work on each detuning circuit individually, isolated from any interference from the coils. These circuits are resonant switches typically formed by an inductor in parallel with one of the capacitances of the coil, with a PIN diode to switch the circuit between on and off states. There are also usually RF chokes and DC blocking capacitors to properly route the DC currents required for switching. To adjust these components, we typically take an S_{11} measurement using a very small pickup loop lightly coupled to the inductor. In this case, one is looking for a dip in the S_{11} measurement that should correspond to the target resonant frequency (as shown in Figure 10.4). As long as the frequency is close to our target frequency, we can slightly bend the inductor to achieve the final tuning.

Once this is achieved for all of the coils, we then work individually on each coil using an S_{21} measurement and the set of overlapping decoupled probes. One at a time, we close a coil, which should make the coil resonant at our target frequency as before. If the decoupling circuit has detuned the coil, it should be retuned to the correct frequency at this stage. We then alternatively switch the PIN diode in the decoupling circuit on and off using an external DC bias. If correctly adjusted, we should observe the resonant peak turn into a resonant valley as shown in Figure 10.7. Ideally, the floor of this valley should be at our target frequency. If this is shifted to either side, an adjustment should be made to either the capacitor or inductor of the detuning circuit to bring this into the correct tune. The other measurement to make at this point is the amount of detuning provided by the detuning circuit. This is the difference between the peak height when tuned compared to the depth of the valley. The actual level required depends heavily on the application, the size of the coils, etc. However, a good rule of thumb is to adjust until this level is at least -35 dB. This is

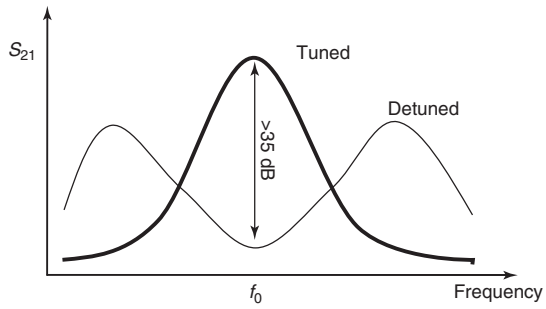

Figure 10.7. Schematic representation of the transmission curves observed in the tuned and detuned states from a single coil. A typical measurement is to estimate the difference between the peak in the tuned state and the valley depth during the detuned state. For detuning, a difference of 35 dB is a target for clinical coils. A similar effect happens when attaching a low-input impedance preamplifier, although the depth may be as small as 15 dB depending on the size of the coil, the frequency being used, and the actual characteristics of the preamplifier.

especially critical for high field clinical coils. If one circuit is not able to provide this level of decoupling, it may be necessary to include an additional detuning circuit in the loop to ensure adequate detuning. It may also be useful at this point to search for any additional resonances that may occur when these detuning networks are switched on. We typically scan the probes over the whole coil surface to ensure that there are no unforeseen resonances that develop as a function of these switching networks.

This entire process is then repeated for each of the coils in the array. At this point, we should have returned to having four equal coils, all tuned to the same frequency, and all with properly adjusted detuning networks.

10.7 CABLE PREPARATION

Another critical step that is often overlooked by novices is the preparation of the cables that connect to the coils, both RF and DC, including specific planning for routing of the cables. These cables are typically the largest source of frustration in array building if the potential problems are not adequately dealt with up front. A first stage of planning for the cables is to determine their length, since we will require a specific phase relationship between the coils and the low-input impedance preamplifiers used in arrays (see Refs 2 and 3). In general, this impedance will generate a very high reflection coefficient. Most preamplifiers in use today will have a small real impedance with some small inductive offset to maintain stability of the preamplifier, though this is highly variable between different preamplifiers at different frequencies. Whatever the input impedance of the preamplifier, its phase will play an important role in the design of the matching network for the coil. For optimum performance, one goal is that the preamplifier and matching network when coupled together should generate an open circuit at the coil terminals, in order to exclude coupled currents on the coil. Thus we must effectively transform the near-short-circuit at the input to an open circuit at the coil terminals. In general, this can be accomplished through a phase shifter. Since the cables themselves induce a phase change dependent on their length, we must effectively include the cables into the matching networks of the coils, even if that choice is as simple as choosing a half-wavelength cable (which would effectively eliminate the effect of the cable from the matching network). Because of this, and because cables are almost never exactly of the correct length, we always recommend using a matching network that allows for a phase-shifter-like adjustment.

Once the cable length is determined, one must then also consider whether common-mode currents will be an issue, and if so, how they will be dealt with. Common-mode currents are a typical source of frustration in clinical-sized coils, since they can cause significant coupling between coils mediated by cables that may not even be connected to either coil. As a rule of thumb, if the cable length is larger than 1/10 wavelength, then one should probably use a common-mode shield trap as described in Chapter 25. As described there, one typically adjusts these shield traps using an S_{21} measurement between two separated probes coupled to the outside of a coaxial cable. As with the detuning circuits, the goal is to adjust the traps until a minimum transmission occurs between the two probes.

Ideally, this step can be performed with each cable in isolation, since the shield traps should be designed in such a way that they do not directly couple to anything. This is a good point to confirm that this is in fact the case. Any leakage of the resonance from these circuits should either be shielded or taken

into account in the routing of these cables. As with the adjustment of the detuning networks, an S_{11} measurement using a small pickup loop is very useful in searching for these leakage currents.

DC cables should be dealt with in a similar fashion. Coaxial cables used to bring DC currents into the array should have the same kind of shield traps as those cables carrying RF signals. Another option for DC currents is to use a twisted pair of wires with occasional large capacitors between the ground and signal wires. In some cases, this may be adequate for rejecting common-mode currents. However, oftentimes, it is still necessary to construct shield traps around these twisted pairs to fully reject the common-mode interference. As in the coaxial case, a set of separated probes should be used to confirm that there is minimal current induced along the cables from the external field from the probes.

10.8 INPUT MATCHING AND CONFIRMATION OF CABLE PERFORMANCE

At this point, we should have four equal coils and four equal RF cables of appropriate length, each with the required shield traps in place and tuned to the correct frequency. We are now ready to connect the cables to the coils. As before, we do this on a coil-by-coil basis, with all the other coils opened. In an array, the preamplifier plays two roles: receive the signal and amplify it, and provide a high impedance at the coil terminals to exclude coupled currents. These two actions are completely different and require adjustment using different measurement techniques. We always begin with matching the coil to the preamplifier to provide maximal gain and signal-to-noise ratio (SNR) performance. For almost every amplifier used in MRI, this requires that the impedance at the preamplifier terminals be matched to 50 Ω when the coil is connected to the other end of the cable. This kind of measurement is typically done using an S_{11} measurement. In general, we always prefer to use a Smith chart for these purposes, since one always knows which element of the matching network to adjust at every stage of the matching process. (Refer to Chapter 25 for more information on this topic.)

Once a 50 Ω match is obtained at the input to the preamplifier, the cable can be connected to the preamplifier. At this point, we need to check that the phase transformation, from the low-input impedance at the preamplifier to an open circuit at the coil terminals, has been successful. The easiest way to estimate this is to use an S_{21} measurement between an overlapped, decoupled probe set. As before with the detuning networks (as shown in Figure 10.7), one should see what was previously a peak now turned into a deep valley. If the valley is not centered on our frequency of interest, then in general, we must adjust the phase shift of the matching network to correct for this shift. In most cases, if designed correctly, one can make this adjustment without significantly altering the actual match of the coil. However, it is always advisable to recheck the impedance at the preamplifiers before moving onto the next coil. The actual level of this valley will normally be less than that from the detuning circuit, but >15 dB down from the resonant peak is a typical target value.

While one could potentially move onto the next coil while leaving a finished coil in its tuned state with a connected preamplifier, we typically advise beginners to again reopen the finished coil before moving onto the next one, to truly prohibit any residual coupling from interfering with the adjustment of the neighboring coils. This again ensures that the process always moves from one stable setup to another. When all coils are finished, then we can finally have them all tuned and active at the same time (assuming everything has gone correctly up to this point!). Once this step is finished, we should have four coils connected to preamplifiers, each one of which should be nicely decoupled from all of the other coils in the array.

10.9 CONFIRMATION OF ACTIVE DECOUPLING NETWORKS

Since this is the first time that we have something that looks like a completed array, one might be tempted to run to the MRI scanner just to see how it works. Unfortunately, this can lead to utter disaster if a few final checks are not performed. The single most important step to recheck is the performance of the detuning networks before going to the magnet. The potential problem is intrinsic to any set of coupled systems tuned to the same frequency. If we think very generally about both the detuning circuits and the preamplifier front end, the mechanism is essentially the same—we very tightly couple two resonant systems that are tuned at the same frequency. One can

even relatively easily mathematically prove that the one frequency where there will be a minimal current in such a setup is at the frequency where both circuits were tuned in isolation. This is the action that we want, and this is all that we have checked up to this point. However, this situation can dramatically change as soon as a third or fourth circuit tuned to the same frequency is introduced. In almost any situation of more than two circuits, there is now the possibility of having a strong resonance at the original frequency. This is especially easy to see with four coupled circuits. Imagine the first two circuits split to $f_0 \pm 10$ MHz when coupled together. This could be as simple as one coil and its active detuning circuit. At the same time, another coil and its detuning circuit could also split to the same two frequencies, $f_0 \pm 10$ MHz. If these four circuits are then coupled together, their resonant frequencies would then split again. One of the potential resonant frequencies can clearly be directly at the original frequency. If this occurs while the coil is in the magnet, the array would be completely unprotected from the multiple kilowatt RF pulses used in a typical scanner. This will kill all of your hard work (and maybe your RF receiver front end too) in less than 1 ms! On multiple occasions, we have seen this happen in practice, where the detuning circuits become coupled together through either a coil coupling or through an unrecognized cable coupling. Thus it is highly recommended that a special effort is made to recheck the performance of each detuning circuit before moving any further. This will ensure that the coil will at least be safe when it is used in the magnet.

10.10 FINAL ARRAY CHECK WITH ALL SIMULTANEOUS ELEMENTS

At this point, the array is very close to being able to be tested in the actual scanner. However, it may be useful and more efficient to perform a few final checks on the workbench to ensure that everything is functioning properly. One very useful check is to confirm that the signal from each coil is actually being amplified by each preamplifier and that the signal level is the same for each coil. This is a relatively easy check to perform using an S_{21} measurement. We typically very lightly couple one probe to the coil while observing the output signal from the preamplifier directly connected to the network analyzer port 2. One must ensure that the input signal level does not saturate the preamplifier, so we recommend reducing the RF power from the network analyzer port 1 by approximately 30 dB using either a built-in attenuator or a separate one attached directly to the port.

Another useful process is to check for oscillations in the preamplifiers with the cables attached and with the coils in both tuned and detuned states. We have seen multiple cases where the impedance presented to the preamplifier when the coil was detuned created an unstable situation in the preamplifier, resulting in oscillations. This check can be performed relatively quickly with the small coupling loop and either an oscilloscope or a spectrum analyzer, and can save a serious headache down the road.

10.11 SUMMARY

The construction of an array for MRI can be a challenging endeavor. Approaching the construction with a clear plan for characterization of the array at each step becomes more and more critical as the array complexity increases. This chapter has shown a basic plan. However, many of these measurements should be tailored to the specific construction project at hand. These specific modifications may take years of experience to learn and apply, but the gains in image quality and performance offered by array coils should hopefully make it all worth it in the end!

RELATED ARTICLES IN THE ENCYCLOPEDIA OF MAGNETIC RESONANCE

Birdcage Resonators: Highly Homogeneous Radiofrequency Coils for Magnetic Resonance

Instrumentation for the Home Builder

Multifrequency Coils for Whole Body Studies

Conradi, Mark S.: Evolution of NMR Hardware

Radiofrequency Fields: Interactions, Biological Effects, and Safety Issues

Radiofrequency Systems and Coils for MRI and MRS

Safety Regulation in MR

Solid State NMR Probe Design

Spatial Encoding Using Multiple rf Coils: SMASH Imaging and Parallel MRI

Whole Body Magnetic Resonance Spectrometers: All-Digital Transmit/Receive Systems

REFERENCES

1. A. Haase, F. Odoj, M. von Kienlin, J. Warnking, F. Fidler, A. Weisser, M. Nittka, E. Rommel, T. Lanz, B. Kalusche, and M. Griswold, *Concepts Magn. Reson.*, 2000, **12**, 361–388.
2. P. B. Roemer, W. A. Edelstein, C. E. Hayes, S. P. Souza, and O. M. Mueller, *Magn. Reson. Med.*, 1990, **16**, 192–225.
3. A. Reykowski, S. M. Wright, and J. R. Porter, *Magn. Reson. Med.*, 1995, **33**, 848–852.

PART C
Volume Coils

Chapter 11
Birdcage Volume Coil Design

Nicola De Zanche

Alberta Health Services and University of Alberta, Edmonton, Alberta, AB T6G 1Z2, Canada

11.1 INTRODUCTION

Birdcage coils are a class of resonators invented in the early 1980s to produce circularly polarized, highly uniform, transverse radiofrequency (RF) magnetic fields within a cylindrical volume. These magnetic fields are the result of currents on longitudinal legs, or rungs, that are arranged at equally spaced angular intervals on the surface of a cylinder and joined at both ends to their immediate neighbors to form the coil's end rings (Figure 11.1a). In the nineteenth century[1], it was found by analyzing the fields of a uniformly magnetized cylinder that a current density distributed sinusoidally on the surface of a cylinder yields a uniform transverse magnetic field. This sinusoidal current density is approximated by discrete rung currents in the birdcage coil, and circular polarization is achieved by rotating the current pattern at the Larmor frequency of interest. The intensity of the nth rung current can therefore be written in phasor notation as

$$I_n = I_0 e^{i2\pi n/N} \tag{11.1}$$

where the explicit temporal dependence is omitted and N is the number of rungs, i is the imaginary unit, and I_0 is the maximum current.

The currents in the above equation occur as a result of the electromagnetic resonance properties of the ladder (or recurrent) network that consists of N equal sections, each of which contains one inductive rung, sections of the two end rings, and capacitors connected in series (Figure 11.1c). The network is planar (Figure 11.1b) and shares features with that of the magnetron,[2] such as its periodic, or cyclic, nature that allows it to support azimuthal waves. The periodicity of these waves, or modes of resonance (see Section 11.4), is an integer between 1 and N and determines the field pattern and frequency of operation. Only modes of periodicity (order) equal to 1 give rise to homogeneous fields.

The most general implementation, shown in Figure 11.1(c), contains all capacitors and is commonly referred to as the "hybrid" or band-pass birdcage topology.[3] Omitting the end-ring capacitors (i.e., replacing them with short circuits) results in the original low-pass version,[4] while omitting the leg capacitors results in the high-pass version. We note that these three topologies are not strictly those of the corresponding typical textbook filter sections but rather are types of "m-derived" filter sections[5] (respectively, band pass, low pass, and band pass). In addition to the circuit elements that

RF Coils for MRI
Edited by J. Thomas Vaughan and John R. Griffiths

ISBN: 978-0-470-77076-4

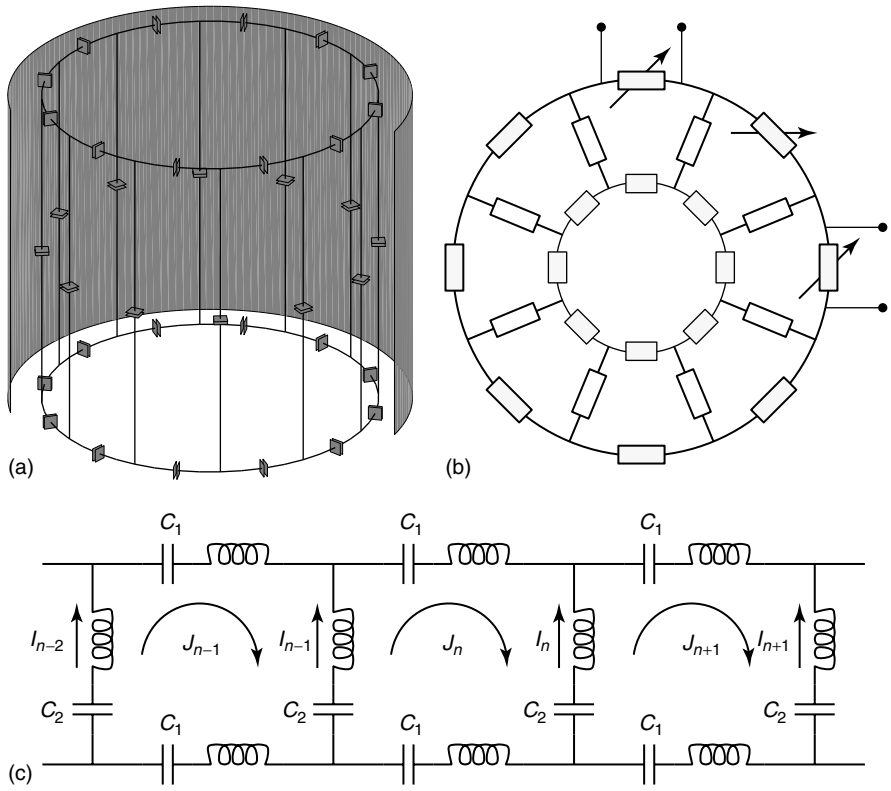

Figure 11.1. (a) Mechanical structure of the hybrid birdcage coil (cylindrical shield cut out for clarity). (b) Planar electrical topology showing typical locations of tuning elements (arrows) and coupling ports. (c) Three sections of the ladder network showing reactances and currents.

are explicitly shown, mutual inductances are present between all nonorthogonal branches of the network due to magnetic coupling through space. The effect of these numerous mutual inductances is significant and complicates analysis of the network beyond the abilities of standard filter design theory.

The birdcage resonator is placed coaxially within the bore of a magnetic resonance (MR) scanner, and thus will interact with metallic parts it contains, such as the gradient/shim coils and the cryostat's shell. The birdcage is thus often fitted with a cylindrical metallic shield (Figure 11.1a) to prevent unknown or uncontrolled interactions with the bore components of the scanner. It also provides stable RF grounding to which connections can be made while reducing radiation losses and sensitivity to external sources of noise and interference. The shield may also include a conductive cap or RF mirror at one end to improve homogeneity and sensitivity.[6]

11.2 DESIGN CONSIDERATIONS

11.2.1 Field Homogeneity

Field homogeneity in the empty birdcage coil is readily analyzed in the quasistatic limit by using the Biot–Savart law.[7] This approach allows general design guidelines to be established, although at high frequencies or in the presence of a biological load the field patterns may be sufficiently distorted to require laborious numerical simulations using the full Maxwell equations.

11.2.1.1 Coil Length

Coil length affects mostly the field homogeneity in the axial direction. Consider a coil of length l and diameter d, with a large number N of rung currents that are assumed to be filamentary and equally

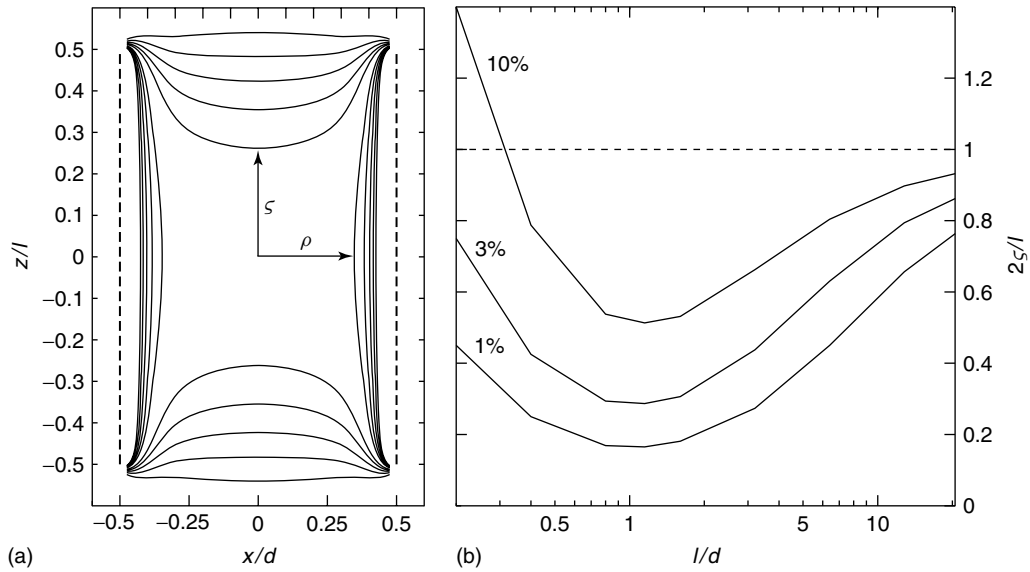

Figure 11.2. (a) Amplitude contours at 10% intervals of the circularly polarized transverse magnetic field in a longitudinal plane ($N = 8$ rungs of length l equal to 1.5 times the diameter d). (b) Axial length (2ζ) of the region of uniformity (field amplitude within 1, 3, and 10% of that at isocenter) normalized to the rung length, plotted as a function of rung length normalized to the diameter. Dashed line indicates the common asymptote at infinite rung length.

spaced around the circumference. If the effect of the end-ring currents is neglected, the magnitude of the transverse, circularly polarized field component is shown in Figure 11.2(a) for $l = 1.5d$. We observe that the largest field inhomogeneity in the axial direction occurs along the axis itself. Figure 11.2(b) shows the relative axial extent within which the field strength is maintained within 1, 3, and 10% of its value at isocenter, as a function of the ratio l/d. The 10% curve indicates that the region of uniformity is mostly shorter than the rung length except for unusually short coils ($l/d = 0.2$). For l/d close to unity, the region of 10% uniformity is approximately one-half the length of the rungs. Increases in l/d result in a slightly better than proportional increase in length of the region of homogeneity. However, increasing beyond $l/d = 2$–3 can negatively impact sensitivity (signal-to-noise ratio, SNR) when used with lossy samples that extend over the full length of the coil (see Section 11.2.3).

11.2.1.2 Number of Elements

The number of coil elements affects the field homogeneity mostly in the transverse plane. By modifying the analysis above for a coil of infinite length, with realistic values of N in the range 4–32 (typically a multiple of 4 to ensure fourfold symmetry), we observe that there is an approximately circular region (Figure 11.3) where the field magnitude remains within 1, 3, and 10% of its value at the isocenter. The relative diameter of this region is plotted as a function of N in Figure 11.4. The diameter of the 10% curve is also plotted at various rung lengths in Figure 11.4(b), where it is readily observed that inhomogeneity due to finite coil length becomes dominant when N is sufficiently large.

11.2.2 RF Shield

The presence of a cylindrical shield enclosing the birdcage resonator can be analyzed, with some approximation due to its finite length, using the method of images.[7] A shield of diameter D reduces the field amplitude by the factor $1 - \frac{d^2}{D^2}$ relative to an unshielded coil carrying the same currents. The shield also has the overall effect of reducing transverse field homogeneity compared to the unshielded coil (Figures 11.3 and 11.4). The impact is strongest for

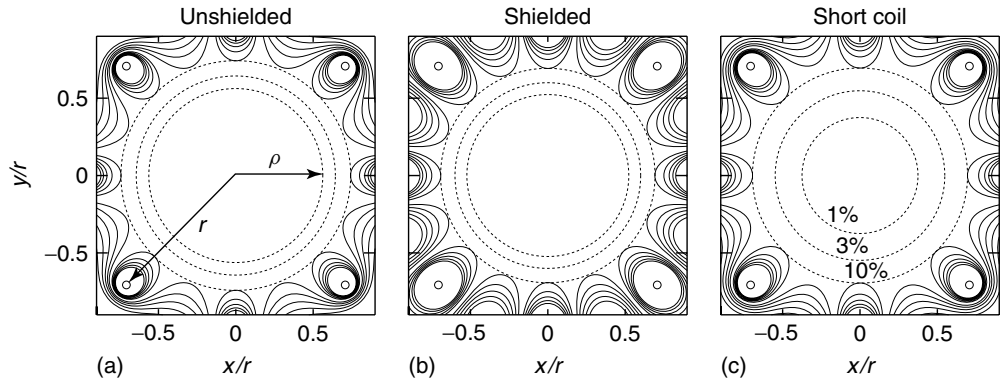

Figure 11.3. Amplitude contours at 10% intervals (solid lines) of the circularly polarized transverse magnetic field in a birdcage with $N = 8$ rungs. (a) Infinitely long unshielded birdcage. (b) Infinitely long birdcage with shield having a diameter 1.5 times that of the coil. (c) Unshielded birdcage having a length of 1.5 times the diameter (central transverse plane shown, end rings neglected). Dashed circles indicate regions in which the field magnitude is within 1, 3, and 10% of its value at isocenter.

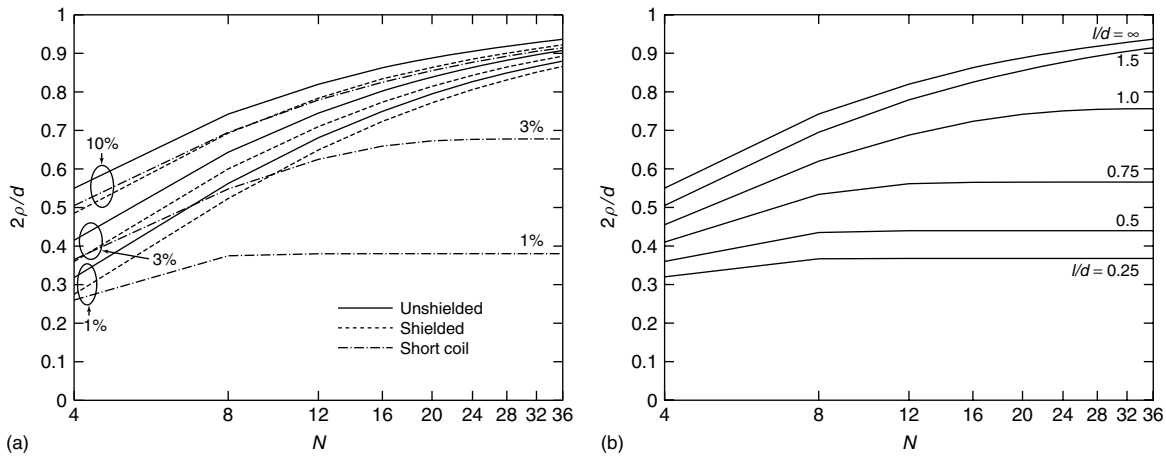

Figure 11.4. (a) Diameters (normalized to those of the coil) of the circular regions of Figure 11.3 as a function of the number of elements N, for the unshielded long coil (solid lines), shielded long coil (dotted), and unshielded short coil (dash-dot). (b) Normalized diameter of the 10% homogeneity region for coil lengths (also relative to diameter) in the range $0.25 - \infty$.

closely fitting shields, but can be compensated for by increasing the number of elements.

11.2.2.1 End Rings

The end rings must carry the currents that allow those in the rungs to form closed loops and can therefore be larger than those in the rungs (Figure 11.5). To calculate the maximum end-ring current, we can choose, without loss of generality, an instant in time in which the rung currents are given by

$$I_n = I_0 \sin\left(\frac{2\pi}{N}n - \frac{\pi}{N}\right) \tag{11.2}$$

The maximum current in the end rings occurs at a location that is at 90° from that of the rung currents, and is obtained by summation over one quadrant of

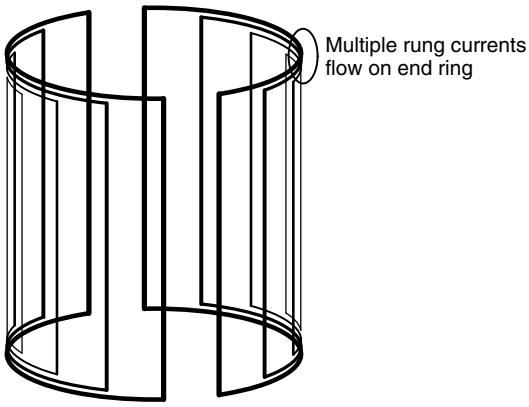

Figure 11.5. Rung currents of the birdcage coil forming closed loops through the end rings where the current intensities consequently add. Line thickness indicates qualitatively the instantaneous current magnitude.

the coil:

$$I_{\mathrm{ER}} = I_0 \sum_{n=1}^{N/4} \sin\left(\frac{2\pi}{N} n - \frac{\pi}{N}\right) = \frac{I_0}{2\sin\frac{\pi}{N}} \quad (11.3)$$

where the summation simplifies according to tables of known sums.[8] For all practical values of $N \geq 8$, the end-ring currents are greater than those in the end ring. While end-ring sections are typically short and oriented azimuthally, they can still generate transverse magnetic field components that modify the field intensity and homogeneity calculations above. For standard end-ring geometries, such as those in Figure 11.1(a), the effect is a slight improvement in axial homogeneity. In the presence of a shield, the effect of end-ring currents cannot be analyzed using the method of images.

11.2.3 Sensitivity

Sensitivity is the proportionality constant that relates field magnitude in a specific location of the resonator (and, reciprocally, its sensitivity in reception) to the currents flowing in the coil or to the square root of the power at its input terminals. These relationships are useful, respectively, to specify the maximum current and voltage handling abilities of the coil's capacitors, and to compare its SNR performance to that of other designs. The link between the two sensitivities requires knowledge of coil and sample losses and for the birdcage coil does not have a simple expression.[9]

11.2.3.1 Relative to Currents

Using the Biot–Savart law, the sensitivity at the coil's isocenter relative to the end-ring current is expressed as[9]

$$\frac{H_1}{I_{\mathrm{ER}}} = \frac{N}{\pi \mathrm{d}} \sin\frac{\pi}{N} \times \left(1 - \frac{d^2}{D^2}\right)\left(\frac{l}{\sqrt{l^2 + d^2}}\right)\left(1 + \frac{d^2}{l^2 + d^2}\right) \quad (11.4)$$

where the terms in parentheses represent the effects of the shield, finite rung length, and approximate end-ring contributions, respectively. Similar to saddle coils, the maximum sensitivity boost due to the end rings occurs for $l/d = \sqrt{2}$ in an unshielded coil, and for lower values in the presence of a shield.[10]

11.2.3.2 Relative to Input Power or SNR

Sensitivity relative to input (transmit) power is a parameter that is readily measured[9] and, unlike the sensitivity of Section 11.2.3.1, allows comparison of the SNR performance of different coil designs. A volume coil such as the birdcage produces both electric and magnetic fields over an extended volume of the sample. Electric fields (both the conservative component due to charges and the solenoidal component due to the time-varying magnetic field) generate losses in a conductive sample during transmission and, reciprocally, pick up thermal noise from the sample during reception. In in vivo MR, the sample is typically larger than the birdcage coil and the fields are confined approximately within the length of the coil. Longer coils will therefore require more input power, and yield lower SNR, than shorter coils of similar diameter.

11.2.4 Optimal Length

As was shown previously, the field homogeneity improves with increasing birdcage coil length, while SNR gets worse. Consequently, the practical choice of coil length will be a compromise between these conflicting goals. For example, a short coil is preferred for imaging axial slices near the isocenter, while a long coil should be used to cover a field of view with a large axial extent and when homogeneity is important (e.g., MR using hyperpolarized nuclei).

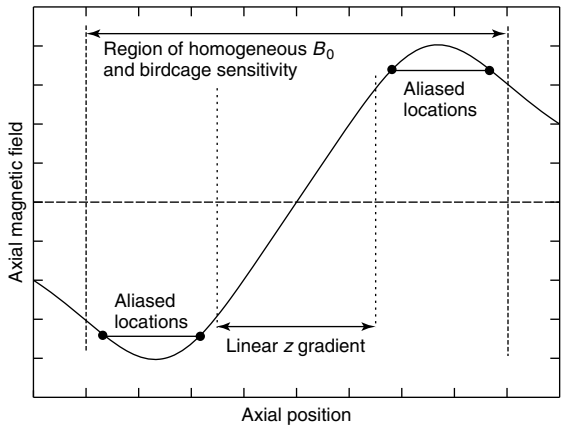

Figure 11.6. Spatial aliasing situation encountered when an excessively long volume coil is used. If the axial magnetic field due to a z gradient coil reaches a maximum and reverses within the region where B_0 is uniform, then there are multiple locations that correspond to the same field or Larmor frequency.

Bottomley *et al.*[11] have determined that a coil with $l = d$ will optimize SNR at the coil's isocenter at 25.9 MHz assuming a uniform cylindrical sample of diameter $= 0.71d$ and dominant sample losses.

Another practical constraint to birdcage coil length is determined by the spatial profiles of the static B_0 field and the z-gradient field. A spatial aliasing situation can occur (Figure 11.6) if the z-gradient field is shorter than both the birdcage and the region of uniform B_0, such as when a head gradient insert is used in a whole-body magnet. Since the gradient field must return to zero at some point along z,[12] there will be two locations that correspond to a given frequency: the one intended and one further out along z whose signal will overlap with that of the intended location if RF transmit and receive sensitivity are sufficiently large.

11.2.5 Choice of Topology

The choice of topology can depend on numerous considerations such as given below:

- Cost of capacitors: The low-pass coil has a minimum number of capacitors that is half of that of the high-pass coil (or one-third of that of the hybrid coil) and therefore can be assembled at a lower cost.
- Capacitor values: The low-pass coil uses lower capacitance values and is therefore preferred at lower operating frequencies since capacitors with large values are typically lossy; conversely, the high-pass coil uses higher capacitance values and is preferred at higher frequencies where small capacitances can be greatly affected by the presence of stray capacitances due to the sample.
- Rung length: If the rung length exceeds the $\lambda/20$ guideline, they must be capacitively split into two or more sections, resulting in either a low-pass or hybrid topology.
- Sensitivity to loading (electromagnetic balance): With a lossy dielectric load, the resonant frequency will tend to be reduced in a low-pass birdcage (due to the presence of stray capacitances through the sample in parallel with those on the coil), while in a high-pass birdcage the frequency will tend to increase because of a reduction of the rung inductances. A hybrid design with a carefully chosen C_1/C_2 ratio can therefore offer reduced frequency sensitivity to loading by canceling the two effects.
- Power deposition (specific absorption rate, SAR): Electric fields in low- and high-pass coils are fundamentally different because of the different locations and orientations of the capacitors. Total losses and the distribution of power deposition (SAR) in the patient can therefore be different depending on topology and should be modeled (see Chapter 28).
- Drive port connection: The low-pass topology is convenient for a feed connection at the central transverse plane, while the high-pass topology favors end-ring connections; the hybrid topology allows both options.

11.3 CONSTRUCTION

Constructing a typical birdcage coil requires the materials listed in Table A11.1. Details for each item are described in the following sections.

11.3.1 Mechanical

The 3D birdcage network must be rigidly supported to avoid changes in geometry which would adversely impact tuning and field homogeneity. Axial access to

the central region is typically as free of obstructions as possible. Some manufacturers have developed elaborate two-piece versions that separate into two shells to allow better patient access to regions such as the head. In such designs, the reliability and series inductance of the connections must be carefully managed.

Typical materials used to support the conductors include glass-reinforced plastic (GRP) or polymers such as acrylic (poly(methyl methacrylate), PMMA), polycarbonate, or polytetrafluoroethylene (PTFE). Some polymers can emit short-lived NMR signals from protons and other nuclei,[13] and therefore for some applications such as ultrashort-echo-time imaging the choice of former material may need to be given careful consideration. Some applications may also require the use of medical-grade hypoallergenic materials on surfaces that can come into contact with the body. Owing to the sometimes large transmit powers that are used (10 kW or more in the case of body coils) low-flammability materials (typically with at least a UL 94 rating of V-0 or equivalent) should be used in case of a malfunction that causes arcing or overheating. Materials should also have low RF losses (measured by the loss tangent of the complex permittivity) to minimize heating in transmission and maximize SNR in reception. Close contact between tissue and conductors must always be avoided to prevent coil detuning and to reduce the potential for RF burns. Therefore the rigid former is typically supplemented with a sufficiently thick layer of foam padding if it must also support the patient's weight.

The basic methods of constructing birdcage coils can be classified depending on how the rung conductors are made and supported, including thin copper strips attached to a cylindrical support or copper bars supported at regular intervals or self-supporting rods (Figure 11.7). In all cases, the space between the rungs can be opened to allow access to the sample or patient; this is particularly important for head coils in which air circulation and visual access for stimulation, entertainment, etc. are standard practical requirements.

Fabrication using thin copper strips (several tens of micrometers thick) requires either self-adhesive copper tape (e.g., that used for artwork or electromagnetic shielding) or strips etched onto flexible circuit board material (substrates such as flexible FR4 fiberglass or polyimide). The latter approach is more stable and reliable but requires additional design and fabrication effort. In both cases, the conductors or circuit boards are rigidly fastened to the outside of a cylindrical former with as much geometric accuracy as possible to avoid asymmetries that will perturb the operation of the coil. An advantage of thin copper conductors is that soldering the capacitors is straightforward.

Thick copper bars can be used for larger coils and where the resistance of thin strips becomes an issue (see Section 11.3.2.1). The bars are usually supported by high-voltage insulators attached to a rigid frame. Soldering is more challenging because of the bars' ability to transport heat, therefore mechanical fastening using screws may be preferred.

When using self-supporting rods, they must be attached to flanges that have sufficient mechanical strength to maintain the coil's shape. The rods are usually not split along their length (e.g., to create a gap for capacitors) because of the complexity of maintaining mechanical strength. If necessary, series connections can still be accommodated at the points where the rods attach to the end rings. For example, the end rings can be made of circuit board material (supported by sturdy flanges) in which both end-ring and rung capacitors can be accommodated.[14]

Figure 11.7. Typical construction methods utilizing (a) copper strips and chip capacitors, (b) copper rods for the legs and circuit board end-rings, and (c) copper bars and capacitors with ribbon leads.

11.3.2 Electrical

11.3.2.1 Conductors

The birdcage coil's conductors affect its operation through their resistance and inductance. Resistance reduces the SNR and should always be minimized by using conductors of appropriate material, shape, and cross section. At radio frequencies, the skin effect[7] distributes the current mostly on a thin layer at the conductor's surface instead of uniformly over the cross section, thus increasing the resistance. The final resistance is proportional to the square root of the frequency and depends on the shape of the outer contour of the conductor. Angular, high-curvature contours concentrate the current density and increase resistance, while rounded contours offer lower resistance and demonstrated improvements in performance especially in low-field applications.[15] Copper has a conductivity that is second only to that of silver at room temperature, but is preferred owing to its lower cost and greater mechanical reliability. At high frequencies, silver-plated copper is a common solution. Superconducting birdcage designs have also been proposed, but implementation is a significant technical challenge while the payoff is likely marginal in most situations.

A conductor's inductance describes its ability to store the magnetic energy required for electromagnetic resonance. Similar to resistance, inductance is also a function of the length and cross-sectional shape of the conductor.[16] For birdcage coil design, conductors should be designed with inductances that fall within a favorable range, avoiding excessively large or small values. The range of acceptable values depends on frequency and topology of the coil.

Inductances are too large when the capacitors required for resonance are small (typically less than 10 pF at current imaging frequencies), resulting in large voltages across all reactances. The large electric fields (see Section 11.2.3.2) will contribute to noise in reception and power deposition in the patient (SAR) during transmission. On the bench, the effect will be observed as a resonant frequency that is sensitive to the presence of dielectric loads (i.e., changes in parasitic capacitances). The solutions are to shorten the conductors, increase their cross-sectional dimensions, or smoothen the cross-sectional shape (e.g., change from flat strips to circular rods). End-ring conductors are usually as large as practical; however, for the rungs, very wide strip conductors (widths approaching one-half of the spacing between rungs) should be used with care since the rung current will be concentrated at the edges of the strip rather than at its center, with possible degradation of field uniformity. The shielding effects of the rungs themselves will also block some of the RF magnetic fields that the resonator is intended to produce and detect, thus decreasing sensitivity.[17]

Inductances are considered too small when the necessary capacitors are large enough to contribute significant losses in the resonator. Within a specific manufacturer and capacitor series, as capacitance increases the capacitors' equivalent series resistance (ESR) increases more rapidly than the reactance (i.e., the quality factor decreases), leading to an overall increase in resonator losses. In summary, inductances should be as small as possible while still avoiding the use of large, lossy capacitors.

11.3.2.2 RF Shield

Bench tests of the birdcage coil can be performed using RF shields made with inexpensive aluminum foil used for cooking. During imaging, however, the high conductivity of foils made of copper or aluminum will support significant eddy currents during switching of the gradients, resulting in image artifacts and distortion. The shield must therefore present a high impedance in the frequency range up to several tens of kilohertz while still being a good conductor at radio frequencies. Segmented or overlapped shields can be designed with this high-pass characteristic, but can introduce significant losses because of the increased path length that the RF currents must take. A common solution is to use foil made of phosphor bronze or another non-ferromagnetic metal with moderate conductivity (e.g., titanium) where the thickness is chosen to be a few skin depths[7] at the Larmor frequency of interest. Similar behavior can be obtained using a fine mesh made of stainless steel, brass, etc.

11.3.2.3 Capacitors

Discrete capacitors used in the birdcage coil's network must be chosen carefully in order to obtain the best performance from the coil. The technical documentation provided by the manufacturer should list several parameters such as ESR, voltage and current ratings, thermal coefficient, and series resonant frequency. As indicated above, the ESR of the capacitors should be as small as possible. Lossy

capacitors not only introduce noise on reception, but will also generate heat during high-power transmit pulses. Increased temperatures are a safety hazard for the patient and can lead to coil failure, as well as to observable thermal drifts of the resonant frequency if the thermal coefficient is not sufficiently low. The maximum voltage rating must also be sufficiently high to prevent breakdown during transmission. Consequently, capacitors usually have a ceramic or porcelain dielectric with a low loss tangent, high thermal stability, and high dielectric strength.

The maximum currents and voltages to which the capacitors will be subjected for a given transmit *power* is difficult to predict a priori without detailed simulations to estimate losses in the coil and sample. However, since the bandwidth and flip angle of transmit pulses are typically specified in MR sequences, it is the maximum B_1^+ required from the coil (e.g., a 0.5 ms hard 90° pulse requires $B_1^+ = 12\ \mu\text{T}$ or $H_1^+ = 9.2\ \text{A m}^{-1}$) that is specified rather than the power. The B_1^+ field is directly related to the birdcage currents according to equations (11.2–11.4), from which the voltage magnitude across each capacitor is calculated using Ohm's law for its reactance:

$$V = \frac{I}{\omega C} \tag{11.5}$$

For example, a long, unshielded head coil with 28 cm diameter and 16 elements will require end-ring and rung currents of 2.7 and 1.1 A, respectively. For a high-pass version operating at 128 MHz using 33 pF capacitors, the maximum voltage on the capacitors will be 101 V.

The tolerance in the capacitance values is very important in the birdcage coil since any asymmetry will degrade quadrature performance and field uniformity. It is not necessary, however, to go to the expense of buying capacitors with the best tolerance, which in any case is usually not better than 1%, because it is not the absolute capacitance that needs to be accurately controlled, but rather the *differences* between capacitors that are more important to maintaining symmetry. Fine-tuning of the coil frequency can be accomplished by other means, such as with variable capacitors at the coil's ports (see Section 11.3.2.7). It is possible to reduce random variations in a given set of capacitors by buying more than necessary, measuring their capacitance at a frequency near that of operation, if possible, and sorting them into groups having sufficiently close values. An impedance analyzer or capacitance meter, if available, usually gives more accurate capacitance measurements than a network analyzer. Another method is to connect several capacitors of the same nominal value in parallel, thereby reducing the standard deviation of the combined capacitance by the square root of the number of capacitors.

Capacitors made for surface mounting are usually preferred over those for through-hole mounting on printed circuit boards. The latter have wire leads that make measuring and soldering operations easier, but they introduce a series inductance that cannot be neglected, especially at frequencies above 100 MHz, and is tricky to model and account for at the design stage. A coil whose leaded capacitors are replaced by surface-mounted "chip" capacitors of the same nominal value may indeed resonate at a different frequency because of the reduced inductance. It is therefore important, if leaded capacitors are to be employed, to keep the leads as short as possible and to keep the length consistent within groups of capacitors. Some manufacturers do offer chip capacitors with ribbon leads, which have much lower inductance than traditional leads.

Series inductance is also present within the capacitor body itself and, with the capacitance, leads to series resonance at the frequency where the reactances cancel. Series resonance frequencies are also provided in capacitor data sheets and become important when high-capacitance, physically small capacitors are used at high frequencies.

11.3.2.4 Tuning and Balancing

Once a birdcage coil is assembled, coarse tuning may be required to get the order-1 modes within a few percent of the Larmor frequency of interest. It should be performed in a way that maintains electrical symmetry, i.e., the same change must be executed in the same way at all sections of the coil. Possible methods include changing or adding capacitors in parallel to those previously on the coil; adding rung or end-ring capacitors to a previously high-pass or low-pass coil, respectively; adjusting the rung length by moving one of the end rings (including "trombone" designs[18]); changing the width of rungs and/or end rings by soldering or cutting away copper strips (including cutting notches to locally increase inductance); and changing the diameter or position of the RF shield.[19]

After coarse tuning, the two order-1 mode frequencies may be split as a result of electrical

asymmetries, or imbalance, in the birdcage coil's meshes. If mechanical asymmetries can be ruled out, the origin of imbalance is usually the differences in capacitor values due to tolerance (see Section 11.3.2.3). In cases where measuring fixed capacitors and selecting a subset with matched values is impractical or insufficient, electrical symmetry can be achieved by tuning individual meshes to the same frequency by adjusting individual capacitors (e.g., using variable capacitors). Care must be taken to isolate a single mesh by disconnecting as much of the rest of the network as possible. The presence of isolated conductors can still perturb the single mesh's resonance if the frequency is high enough. This laborious method is therefore limited to lower frequencies and number of elements N. A more practical approach devised by Tropp[20] uses a first-order perturbation approach to correct imbalance using only two capacitors at appropriate locations on the birdcage network.

11.3.2.5 Matching

Matching is required to connect the coil to the MR system using coaxial cables. These connections must transfer power efficiently to and from the coil (i.e., there must be no reflections) without perturbing the electrical balance of the coil. For example, a node that normally has a fluctuating voltage should not be connected to the coaxial cable's ground conductor through a low-impedance path because the resonance frequency and current distribution will change.

Early birdcage coil designs maintained electrical balance by using inductive coupling with a coupling loop facing one of the meshes at each port.[9,21] This arrangement provides good electrical isolation between the birdcage and coaxial cable, but efficient power transmission requires a large coupling loop whose currents significantly degrade the field homogeneity.

The more common approach is to couple electrically, i.e., through coupling capacitors or through a direct galvanic connection. The most common circuits are found in Refs 9, 14, 22, and 23[9,14,22,23]. When possible, coaxial cable shields should be connected to the coil's RF shield at the virtual ground that exists at the central transverse plane.[14,23] This approach avoids the need for baluns (see Chapter 25) to block the common-mode currents that can be induced with other grounding arrangements. In the absence of a convenient method to connect the coax shield to ground, a separate ground ring is sometimes used,[24] although its electrical length can easily exceed the recommended maximum of 1/20 of a wavelength (see Sections 11.2.5 and 11.4).

11.3.2.6 Quadrature Operation

Quadrature operation requires making connections to the birdcage network at two ports that are separated by 90° (e.g., the locations shown in Figure 11.1b). Each port is coupled to one of the two linearly polarized modes, and circular polarization is achieved by driving (or receiving) with a 90° phase shift, often using a quadrature hybrid. The ports must be sufficiently isolated (by at least 20 dB) to prevent the creation of inefficient elliptical polarization. Isolation is very sensitive to asymmetries and can be optimized using an adjustable element (typically a variable capacitor) installed at a location which is at 45°, 135°, or 225° between the coupling ports (Figure 11.1b). At higher frequencies or with highly asymmetric loads, it may be beneficial to use a four-port driving arrangement.[25,26]

11.3.2.7 Fine-tuning

Fine-tuning may be needed on a day-to-day basis to adjust for frequency changes due to loading or to compensate for asymmetries that lead to splitting of the two order-1 mode resonances.[17] Such adjustments can be achieved by installing variable capacitors in parallel with the fixed capacitors of the network at two locations that correspond to those of the two ports (Figure 11.1b). The maximum difference in capacitance between that on the tuned meshes and those without tuning should be kept below 8% to avoid introducing significant field inhomogeneities.[20]

11.3.2.8 Detuning

Most birdcage coils used in clinical systems are integrated into the system bore and used to provide excitation, but are rarely used for reception, which is typically performed by arrays of surface coils to achieve higher SNR or parallel image encoding. In this application, the birdcage coil must be detuned during reception to avoid detuning the receiver coils and to prevent signal and noise coupling. Detuning is best accomplished by introducing at each rung or

end-ring section an actively controlled switch (usually based on PIN diodes) which will create an open circuit and block current flow.[27] Additional current paths must be provided for the DC control signals that operate the switches, and must be separated from the RF current paths using RF chokes.

11.4 THEORY

Lumped-element networks are accurate RF circuit models if the maximum dimension of each conductor is kept below approximately 1/20 of a wavelength, i.e., $\lambda/20$. With this restriction, the birdcage network of Figure 11.1(b) can be analyzed using either the nodal or mesh methods. The latter method is valid only for planar networks and is preferred since it leads to more compact expressions (Figure 11.1). Following the matrix treatment by Leifer,[28] the circuit equations for the N mesh currents J_n yield the eigenvalue equation $\mathbf{M}^{-1}\mathbf{E}\mathbf{J} = \lambda\mathbf{J}$ where $\lambda = (i\omega)^2$ is the eigenvalue of the mode, and ω and $\mathbf{J}$ are the corresponding angular frequency and eigenvector whose elements are the mesh currents. The leg currents are related to the mesh currents by $I_n = J_{n+1} - J_n$, $n = 0, 1, \ldots (N-1)$. The capacitances and inductances are arranged as follows in matrices that contain, respectively, the electric (see Figure 11.1c) and magnetic parameters of the network:

$$\mathbf{E} = \begin{bmatrix} -2(C_1^{-1}+C_2^{-1}) & C_2^{-1} & 0 & \ldots & 0 & C_2^{-1} \\ C_2^{-1} & -2(C_1^{-1}+C_2^{-1}) & C_2^{-1} & 0 & \ldots & 0 \\ 0 & C_2^{-1} & \ddots & C_2^{-1} & \ldots & 0 \\ \vdots & & & & & \vdots \\ 0 & 0 & \ldots & C_2^{-1} & \ddots & C_2^{-1} \\ C_2^{-1} & 0 & 0 & \ldots & C_2^{-1} & -2(C_1^{-1}+C_2^{-1}) \end{bmatrix}$$

$$\mathbf{M} = \begin{bmatrix} M_0 & M_1 & M_2 & \ldots & M_{N-1} \\ M_{N-1} & M_0 & M_1 & \ldots & M_{N-2} \\ M_{N-2} & M_{N-1} & M_0 & \ldots & M_{N-3} \\ \vdots & & \ddots & \vdots & \\ M_1 & M_2 & \ldots & M_{N-1} & M_0 \end{bmatrix} \tag{11.6}$$

The inductance matrix $\mathbf{M}$ contains the mesh self-inductance M_0 and the mutual inductances M_n between meshes that are n meshes apart. Symmetry also ensures that $M_n = M_{N-n}$. These inductance terms are calculated by summing the individual self and mutual inductances around each mesh, i.e., $M_n = 2M_{\text{leg},n} - M_{\text{leg},n-1} - M_{\text{leg},n+1} + 2(M_{\text{er},n} - M^{\text{o}}_{\text{er},n})$, where $M_{\text{leg},n}$ is the mutual inductance between rungs n meshes apart, and similarly $M_{\text{er},n}$ and $M^{\text{o}}_{\text{er},n}$ are the mutual inductances between end-ring segments in the same and opposite ends of the coil, respectively. When $n = 0$, each term represents the segment's self-inductance. Losses are assumed to be negligible.

Since both matrices are real and symmetric, the eigenvectors of $\mathbf{M}^{-1}\mathbf{E}$, which correspond to the distribution of mesh currents of the various modes of resonance, form an orthogonal basis. Orthogonality ensures that the modes can be excited independently of each other, even if they are degenerate, i.e., if they resonate at the same frequency.

If the coil is carefully constructed to achieve rotational symmetry (i.e., a rotation of $2\pi/N$ does not change the coil), the matrices will also be *circulant*, and the N eigenvectors will be the columns of the matrix whose elements are the coefficients of the discrete Fourier transform.[29] There will be $(N/2 - 1)$ degenerate pairs of eigenvectors (i.e., corresponding to the same eigenvalue and spatial frequency), plus the Nyquist mode whose elements have the same amplitude but alternate in sign ($N/2$ phase rotations for one physical rotation around the coil). The two degenerate modes having a spatial frequency of 1 are of interest in probe design because the eigenvectors

The inductance matrix $\mathbf{M}$ contains the mesh self-inductance M_0 and the mutual inductances M_n between meshes that are n meshes apart. Symmetry also ensures that $M_n = M_{N-n}$. These inductance terms are calculated by summing the individual self and mutual inductances around each mesh, i.e., $M_n = 2M_{\text{leg},n} - M_{\text{leg},n-1} - M_{\text{leg},n+1} + 2(M_{\text{er},n} - M^{\text{o}}_{\text{er},n})$, where $M_{\text{leg},n}$ is the mutual inductance between rungs n meshes apart, and similarly $M_{\text{er},n}$ and $M^{\text{o}}_{\text{er},n}$ are the mutual inductances between end-ring segments in the same and opposite ends of the coil, respectively. When $n = 0$, each term represents the segment's self-inductance. Losses are assumed to be negligible.

Since both matrices are real and symmetric, the eigenvectors of $\mathbf{M}^{-1}\mathbf{E}$, which correspond to the distribution of mesh currents of the various modes of resonance, form an orthogonal basis. Orthogonality ensures that the modes can be excited independently of each other, even if they are degenerate, i.e., if they resonate at the same frequency.

If the coil is carefully constructed to achieve rotational symmetry (i.e., a rotation of $2\pi/N$ does not change the coil), the matrices will also be *circulant*, and the N eigenvectors will be the columns of the matrix whose elements are the coefficients of the discrete Fourier transform.[29] There will be $(N/2 - 1)$ degenerate pairs of eigenvectors (i.e., corresponding to the same eigenvalue and spatial frequency), plus the Nyquist mode whose elements have the same amplitude but alternate in sign ($N/2$ phase rotations for one physical rotation around the coil). The two degenerate modes having a spatial frequency of 1 are of interest in probe design because the eigenvectors are the desired current distributions of equation (11.1). The meshes created by the end rings give rise to two additional modes that have currents only

in the end rings: the Helmholtz mode in which the end-ring currents circulate in the same sense; and, at a slightly higher frequency, the Maxwell mode in which the currents circulate in the opposite sense. If C_1 is not present (i.e., in the low-pass configuration), the natural frequency of the end-ring modes is zero and therefore they can support undesirable eddy currents induced by the switching of the gradient fields. This effect is eliminated in practice by splitting the end rings and shorting each gap with a capacitor that has a low impedance at the coil's desired operating frequency, but whose capacitance is low enough to resonate with the inductance of the end rings at a frequency well above the typical frequencies present in the gradient waveforms (tens of kilohertz). By appropriate choice of C_1, the Helmholtz mode can be tuned to the Larmor frequency and used to design a quadrature "birdholtz" coil for systems in which the patient axis is orthogonal to the B_0 field.[30]

The resonant frequency of the remaining modes are readily calculated from the properties of circulant matrices[28]:

$$\omega_k = -\sqrt{\lambda} = -\sqrt{\frac{\tilde{E}_k}{\tilde{M}_k}} = \sqrt{\frac{2}{\tilde{M}_k}\left[\frac{1}{C_1} + \frac{1}{C_2}\left(1 - \cos\frac{2\pi k}{N}\right)\right]} \tag{11.7}$$

where

$$\tilde{M}_k = \sum_{n=0}^{N-1} M_n e^{-i2\pi kn/N} \tag{11.8}$$

and

$$\tilde{E}_k = -2\left[\frac{1}{C_1} + \frac{1}{C_2}\left(1 - \cos\frac{2\pi k}{N}\right)\right] \tag{11.9}$$

can be interpreted, respectively, as the *modal* inductances and inverse capacitances. Since these functions are periodic, we can choose $k \in [-N/2 + 1, \ldots N/2]$, in which case $|k|$ is the spatial order of the respective mode. Since $\tilde{M}_k$ is typically a monotonically decreasing function of $|k|$, the frequencies

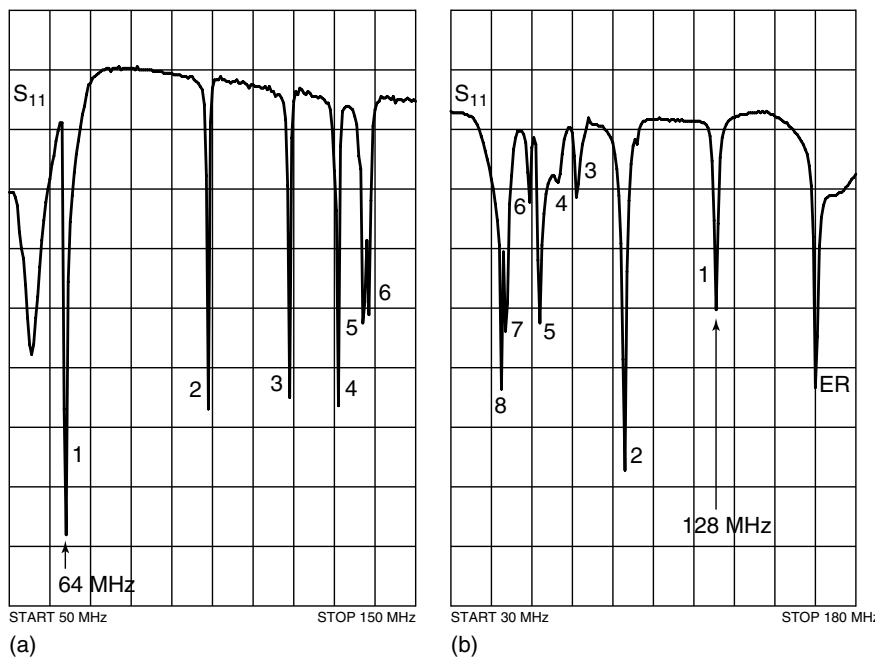

Figure 11.8. (a) Resonance spectrum from a 12-rung low-pass birdcage tuned to 64 MHz, illustrating five degenerate modes of order that increases with frequency, ending with the Nyquist mode (6) just below 140 MHz. (b) Spectrum from a 16-rung high-pass birdcage tuned to 128 MHz, illustrating seven degenerate modes of order that decreases with frequency, ending with the Nyquist mode (8). An end-ring mode (ER) is visible above the order-1 mode frequency.

of a high-pass birdcage ($1/C_2 = 0$) decrease with increasing mode order, while those of a low-pass birdcage ($1/C_1 = 0$) increase (Figure 11.8). The hybrid birdcage has intermediate frequency behavior with varying degrees of mode compression as a function of the C_1/C_2 ratio.[3] Specifically, there exists a C_1/C_2 ratio that minimizes (but does not completely eliminate) the differences in mode frequencies and allows the birdcage to be used similar to a surface coil array.[31]

11.5 CONCLUSION

The birdcage coil has become the "gold standard" volume resonator in clinical MRI systems because of its excellent field uniformity, sensitivity, and natural ability to operate in quadrature. The method of analysis presented in this chapter is accurate for unloaded coils in the lumped-element regime. However, with some empirical adjustments, body-sized coils can readily operate at frequencies up to 128 MHz and head-sized versions up to 300 MHz. In these situations, the electromagnetic field is strongly influenced by the presence of biological tissue, and accurate predictions of resonant spectrum and field distributions can be obtained only by full-wave simulation.

11.6 APPENDIX

Table A11.1. Typical bill of materials

Material	Quantity
PMMA tube (coil former)	1
PMMA tube (shield former)	1
PMMA flanges (join coil and shield)	2
Adhesive copper (rungs and end rings)	1–2 rolls
Metal foil (shield)	πdl (m^2)
High-voltage nonmagnetic variable capacitors (tuning/balance)	3 minimum
High-voltage nonmagnetic chip capacitors (coil)	Depends on N, topology (see Section 11.2.5)
High-voltage nonmagnetic chip capacitors (matching)	2 minimum
Matching inductors	Depends on circuit
Nonmagnetic coax connectors	2

RELATED ARTICLES IN THE ENCYCLOPEDIA OF MAGNETIC RESONANCE

Birdcage Resonators: Highly Homogeneous Radiofrequency Coils for Magnetic Resonance

Eddy Currents and Their Control

Field Gradients and Their Application

Probe Design and Construction

Radiofrequency Systems and Coils for MRI and MRS

Sensitivity of the NMR Experiment

Sensitivity of Whole Body MRI Experiments

Whole Body Machines: NMR Phased Array Coil Systems

REFERENCES

1. E. Mascart and J. F. Joubert, *A Treatise on Electricity and Magnetism*, Thomas de la Rue & Co: London, 1883, Vol. 1, Section 357.
2. P. Mansfield, M. McJury, and P. Glover, *Meas. Sci. Technol.*, 1990, **1**, 1052–1059.
3. J. Tropp, The Hybrid Bird Cage Resonator, In *Society for Magnetic Resonance in Medicine, 11th Annual Meeting*, Berlin, 1992, p. 4009.
4. C. E. Hayes, *et al*., *J. Magn. Reson.*, 1985, **63**, 622–628.
5. F. E. Terman, *Radio Engineer's Handbook*, McGraw-Hill: New York, 1943.
6. R. C. Samaratunga, *et al*., *Med. Phys.*, 1994, **21**, 697–705.
7. W. R. Smythe, *Static and Dynamic Electricity*, 3rd edn., McGraw-Hill: New York, 1968.
8. I. S. Gradshteyn and I. M. Ryzhik, *Table of Integrals, Series, and Products*, 6th edn., Academic Press Inc.: New York, 2000.
9. J. Mispelter, M. Lupu, and A. Briguet, *NMR Probeheads for Biophysical and Biomedical Experiments: Theoretical Principles & Practical Guidelines*, Imperial College Press: London, 2006.
10. C. P. Bidinosti, I. S. Kravchuk, and M. E. Hayden, *J. Magn. Reson.*, 2005, **177**, 31–43.

11. P. A. Bottomley, *et al*., *Magn. Reson. Med.*, 1988, **7**, 319–336.
12. J. Jin, *Electromagnetic Analysis and Design in Magnetic Resonance Imaging*, CRC Press: New York, 1999.
13. M. Marjanska, *et al*., *Magn. Reson. Med.*, 2008, **59**, 936–938.
14. J. Tropp, *Concepts Magn. Reson.*, 2002, **15**, 177–188.
15. G. Giovannetti, *et al*., *Concepts Magn. Reson. Part B: Magn. Reson. Eng.*, 2004, **20B**, 9–16.
16. F. W. Grover, *Inductance Calculations*, D. Van Nostrand Co., Inc: New York, 1946.
17. F. D. Doty, *et al*., *J. Magn. Reson.*, 1999, **138**, 144–154.
18. Y. Xu and P. Tang, *Magn. Reson. Med.*, 1997, **38**, 168–172.
19. B. J. Dardzinski, *et al*., *J. Magn. Reson.*, 1998, **131**, 32–38.
20. J. Tropp, *J. Magn. Reson.*, 1991, **95**, 235–243.
21. P. L. Kuhns, *et al*., *J. Magn. Reson.*, 1988, **78**, 69–76.
22. M. C. Leifer and S. C. Hartman, Shielded Drive for Balanced Quadrature Bird Cage Coil, U.S. Pat. 6 011 395, (2000).
23. P. B. Roemer, *et al*., *Method for Providing Multiple Coaxial Cable Connections to a Radio-Frequency Antenna without Baluns*, U.S. Pat. 4 887 039, 1989.
24. H. Merkle, *et al*., Space optimized birdcage body coil for animal MR at 500 MHz, In *Proceedings 12th Scientific Meeting, International Society for Magnetic Resonance in Medicine*, Kyoto, Japan, 2004, p. 1552.
25. F. D. Doty, *et al*., *NMR Biomed.*, 2007, **20**, 304–325.
26. T. S. Ibrahim, *et al*., *Magn. Reson. Imaging*, 2000, **18**, 733–742.
27. E. A. Barberi, *et al*., *Magn. Reson. Med.*, 2000, **43**, 284–289.
28. M. C. Leifer, *J. Magn. Reson.*, 1997, **124**, 51–60.
29. P. J. Davis, *Circulant Matrices*, 2nd edn., Chelsea Publishing: New York, 1994.
30. H. Fujita, W. O. Braum, and M. A. Morich, *Magn. Reson. Med.*, 2000, **44**, 633–640.
31. C. Leussler, J. Stimma, and P. Röschmann, The Bandpass Birdcage Resonator Modified as a Coil Array for Simultaneous MR Acquisition, In *Proceedings of the International Society for Magnetic Resonance in Medicine, 5th Annual Meeting*, Vancouver, 1997, p. 173.

Chapter 12

Double-Tuned Birdcage Coils: Construction and Tuning

Joseph Murphy-Boesch

National Institutes of Health, Bethesda, MD 20892, USA

12.1 INTRODUCTION

Methods for multiply tuning coils for MRI originated from coils designed for high-field NMR spectrometers, which by the 1970s could routinely excite and detect three different nuclei in a single sample. It was only when MRI was developed that quadrature coils were introduced and became widely used in magnetic resonance. The quadrature birdcage coil was introduced by Hayes and coworkers,[1] and it was quickly accepted as one of the most sensitive and homogeneous volume coils for proton imaging of the head and the human body. For the human head, the low-pass (LP) configuration of this coil was found to operate well for field strengths below about 1.5 T, while the high-pass (HP) configuration[2] was found to work better at higher fields. Thus, for the frequencies of low-γ nuclei and for coils smaller than that of the head coil, the LP configuration was the configuration of choice at 1.5 T. Both the LP and HP configurations of the head size birdcage coil have approximately the same sensitivity at 1.5 T. For constant impedance, the product of the field strength and the coil diameter should remain approximately constant.

Subsequent development of localization methods, such as chemical shift imaging,[3] and double resonance techniques, such as proton decoupling,[4] drove the need to obtain both images and spectra together, so that high-sensitivity spectral data could be registered with anatomy. Early methods for double-tuning NMR coils[5–7] used Foster-type networks[8] for replicating impedances at multiple frequencies. Birdcages that are double-tuned in this way create homogeneous quadrature modes at two frequencies for a total of four independent modes.[9] In addition to the birdcage, which typically consists of two end-rings connected with an even number of legs or struts, there are other coil geometries that can support birdcage modes at two frequencies. While some of these geometries may seem complicated, a goal here is to show that all birdcage modes have the same sinusoidally distributed voltages and currents and that they can be tuned in the same way. The main problem with quadrature modes is that they require a high degree of coil symmetry to maintain isolation between them.

RF Coils for MRI
Edited by J. Thomas Vaughan and John R. Griffiths

ISBN: 978-0-470-77076-4

So the main focus here is to explain how to maintain this symmetry and to restore it if it becomes degraded.

12.2 BACKGROUND

As indicated in Figure 12.1, early methods for double-tuning a birdcage coil used Foster-type networks to replace single-tuning capacitors. For the three-element network, the series capacitor is larger and is used to tune the low-frequency mode. For the high-frequency mode, this capacitor has a low impedance and has little effect. The parallel capacitor, on the other hand, is smaller and can be used to tune the high-frequency mode. The impedance of the inductor is somewhere in between them and therefore can strongly affect tuning. It is important, therefore, that the three-component networks in each capacitor gap be replicated carefully so as to maintain coil symmetry.

Another method for double-tuning birdcage coils is to tune every other leg or strut of a coil for one of the desired frequencies,[10–13] as indicated in Figure 12.2. This method relies on strong mutual coupling between meshes to ensure that circularly polarized waves can propagate at both frequencies. This type of coil was analyzed by Amari *et al*.[11] and the analysis takes into account the mutual inductance of not only neighboring meshes but also second neighboring meshes, since the repeating unit of the double-tuned birdcage is now made up of two meshes rather than one. Practical implementation of this coil was reported by Matson *et al*.[12] However, because of the difficulty of maintaining coil symmetry at the proton frequency, the alternating design was modified by placing a trap for the ^{1}H frequency in the low-frequency struts to eliminate their effect on tuning of the ^{1}H modes.

Other investigators suggested constructing entirely different conductor geometries to produce birdcage modes at two frequencies. One such geometry, suggested by Fitzsimmons and Beck,[14] was a two-birdcage configuration that placed a smaller diameter birdcage concentrically within a larger one. Once the strong inductive coupling between them was taken into account, the larger birdcage was tuned to the higher frequency while the smaller birdcage was tuned to the lower frequency. One of the strongest sources of inductive coupling between

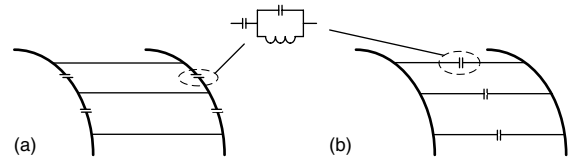

Figure 12.1. Use of a three-element network to double-tune the (a) high-pass and (b) low-pass birdcage coils. The parallel LC circuit has its resonance between the high and low frequencies of the coil.

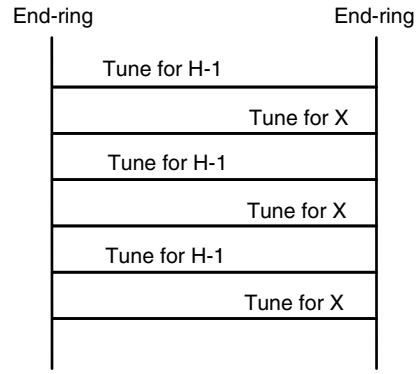

Figure 12.2. The two-ring birdcage resonator double-tuned by alternating the impedances of the struts.

the birdcage units comes from the proximity of their end-rings. Tuning of this coil is complicated by any "wobble" in the orientation of the end-rings with respect to one another, and misalignment of the end-rings can cause splitting of the linear modes at both frequencies. However, methods such as printing the end-rings on the same printed circuit board (PCB) can address this problem, as well as improve the compactness of the coil.

Another geometry that displays good circuit isolation between frequencies is the four-ring birdcage,[15] shown in Figure 12.3(a). This coil can be viewed as three birdcage structures merged together onto a single cylinder. The inner structure of this coil has a LP configuration which shares its rings with two outer structures. Identical outer structures can be either LP or HP, and in each case, the outer structures couple inductively through the inner structure to produce two new pairs of quadrature modes. One of these quadrature modes is a homogeneous mode, and it is tuned for the higher proton (^{1}H) frequency. The RF field patterns for the modes of the inner structure and the coupled outer structures are illustrated

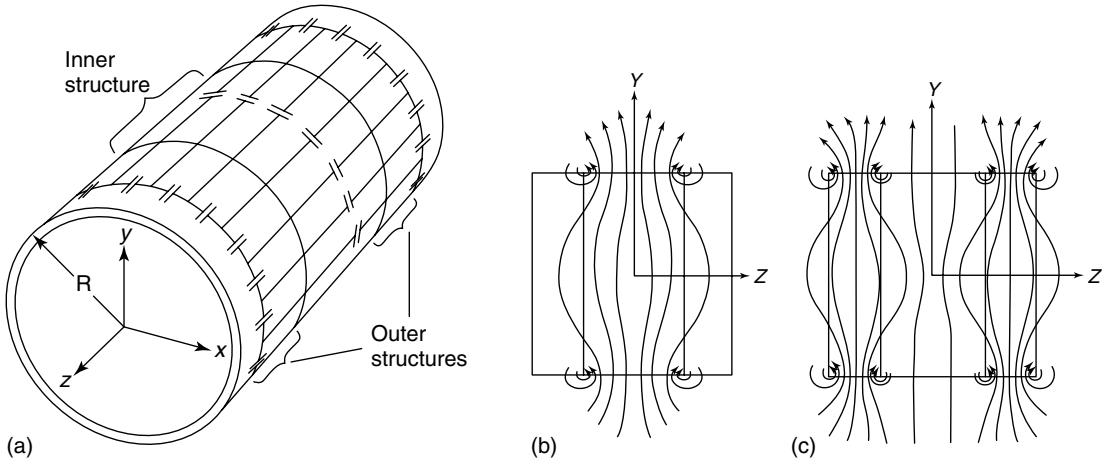

Figure 12.3. (a) The LP–HP configuration of the four-ring birdcage. (b) B_1 flux pattern for the inner (^{31}P) structure. (c) Flux pattern for the outer (^{1}H) birdcage structure in a longitudinal cut through the coil. Reprinted from *J. Magn. Reson. B*, **103**, J. Murphy-Boesch *et al*. "Two configurations of the Four-Ring Birdcage Coil", 103–114 (1994), with permission from Elsevier.

in Figure 12.3(b) and (c), respectively, in a longitudinal cut through the coil. Because the currents at different frequencies flow substantially in different conductors, circuit interactions between frequencies are relatively small. This makes the four-ring birdcage relatively straightforward to construct and tune. While the remaining sections of this chapter are focused on implementing this coil, the methods of tuning and aligning birdcage modes are quite general and applicable to all birdcage coils.

12.2.1 Birdcage Modes and Birdcage Tuning

Before assembling and tuning a birdcage coil, it is essential to have a good understanding of birdcage modes and the mode distributions associated with the two configurations. The modes of the birdcage coil are a consequence of two things: its periodic structure and the characteristic that the periodic structure wraps back on itself. This periodicity limits the modes to a finite number of discrete frequencies. These discrete modes are the frequencies of standing waves that are permitted by a single transit around the coil. In a symmetric coil, there are two standing waves for each frequency, each oriented 90° about the coil axis with respect to the other. These quadrature modes are the linear modes, and each can be represented as the superposition of two circularly polarized (CP) waves propagating in opposite directions about the coil. Quadrature linear modes and CP modes are not different modes. Rather, they are the same modes in two different representations: as two linear modes oriented quadrature, which is convenient for describing electronic connection to the coil, or as two CP modes, which is useful in understanding their function in NMR and for tuning issues related to propagation.

In the NMR application, the objective of coupling to the coil is to excite only a single circular polarization while suppressing the other. The birdcage coil is a periodic structure, comprising a series of identical resonant loops or meshes. A wave at frequency ω propagating in a single direction on a periodic structure such as the birdcage will experience successive delays of $\Delta\phi$ with each passing mesh. Indexing the meshes of a birdcage coil as $n = 0, 1, 2, 3, \ldots, N-1$, where N is the total number of meshes in the coil, the accumulated phase delay for the nth mesh, will be $\phi_n = n\Delta\phi$. Because the Nth mesh of the coil is connected back to the first, the phase delay for one transit around the coil for a mode must be a multiple of 2π. This is the Bloch condition for a periodic structure; it means that only discrete modes are allowed and that the mode must meet the (spatial) condition that $N{\cdot}\Delta\phi = k{\cdot}2\pi$, where k is the mode index of the coil ($k = 1, 2, \ldots, N/2$). The first mode ($k = 1$) is the homogeneous mode of the coil, and it accumulates 2π radians (one cycle) in one transit about the coil.

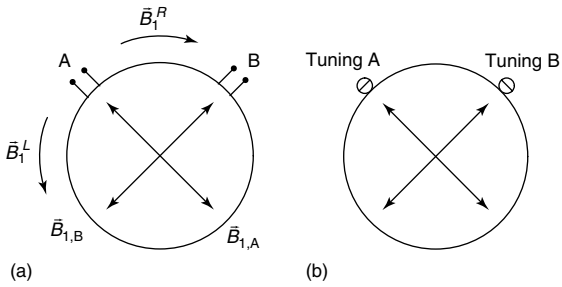

Figure 12.4. (a) External connections for coupling to the quadrature linear modes of a birdcage coil and (b) placement of variable tuning capacitors on the end-rings for tuning the HP birdcage. For the LP birdcage, the tuning capacitor locations are reversed and the capacitors are located on the legs or struts of the coil.

Currents for modes propagating in the right-hand and left-hand directions at frequency ω can be written in complex form as

$$I_n^R = I_0^R e^{j(\omega t - 2\pi nk/N)} \quad \text{and} \quad I_n^L = I_0^L e^{j(\omega t + 2\pi nk/N)} \tag{12.1}$$

and similar expressions hold for the voltages in the coil. The currents produce the CP RF fields, B_1^R and B_1^L. The CP modes can also be represented as the superposition of two linear modes, $\vec{B}_{1,A}$ and $\vec{B}_{1,B}$, according to

$$\vec{B}_1^R = \vec{B}_{1,A} - j\vec{B}_{1,B} \quad \text{and} \quad \vec{B}_1^L = \vec{B}_{1,A} + j\vec{B}_{1,B} \tag{12.2}$$

The linear modes are useful in describing the port connections to the coil, as indicated in Figure 12.4(a), and are labeled accordingly. In this complex representation of the field amplitudes, j ($j = \sqrt{-1}$) indicates a 90° phase shift of $\vec{B}_{1,B}$ with respect to $\vec{B}_{1,A}$. Each port is also oriented 90° with respect to the other, so in a symmetric coil each port drives only a single linear mode. Linear modes can likewise be expressed as sums of the CP modes according to

$$\vec{B}_{1,A} = \frac{1}{2}\left[\vec{B}_1^R + \vec{B}_1^L\right] \text{ and } \vec{B}_{1,B} = \frac{1}{2}j\left[\vec{B}_1^R - \vec{B}_1^L\right] \tag{12.3}$$

It is apparent from equation 12.2 that, if $B_{1,A}$ and $B_{1,B}$ are driven with equal amplitude and if $B_{1,B}$ is phase shifted by 90° such that $B_{1,B} = jB_{1,A}$, then the left-hand circulating field B_1^L will be suppressed. In Figure 12.4(b), the locations of variable tuning capacitors are shown for tuning each linear mode. When the linear modes are properly aligned, the port connections, as the figure indicates, one will measure a high degree of isolation between the two ports using a network analyzer.

12.2.2 Mode Distributions

How the frequencies of birdcage modes are distributed depends on the configuration of the birdcage, i.e., whether it is LP or HP. Expressions for the mode frequencies have been derived in earlier works.[16,17] In Figure 12.5(a) and (b), one can find expressions

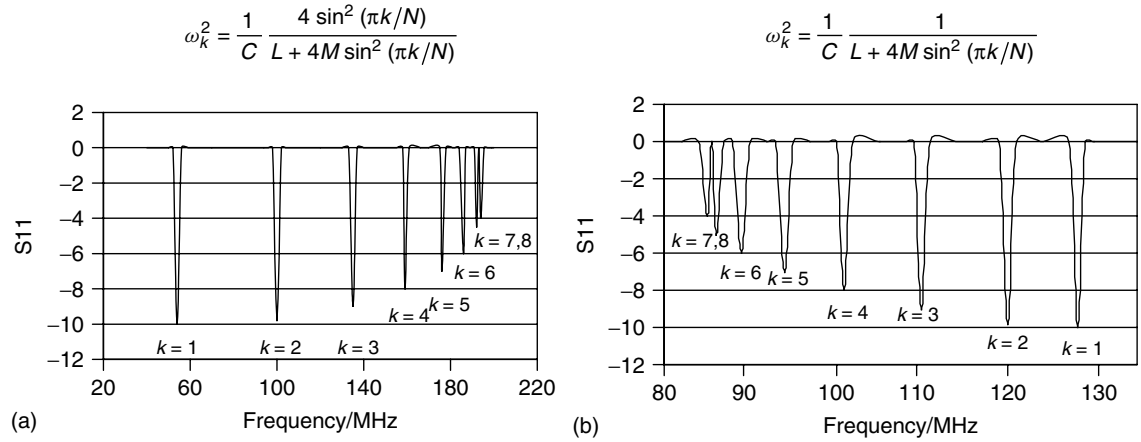

Figure 12.5. The modes of (a) the LP configuration and (b) the HP configuration for birdcage coils with $N = 16$ legs.

for the mode frequencies and representative mode distributions that one might encounter for a 3 T birdcage coil using a network analyzer. For the LP configuration, the frequencies of the modes increase with mode number, whereas for the HP configuration they decrease. For the LP–HP four-ring birdcage described here, both configurations are used, and the mode distributions can overlap. For a coil tuned for ^{1}H and ^{31}P, all modes of the HP coil are well above the ^{31}P frequency. The high-order modes of LP structure, on the other hand, extend well above the ^{1}H mode and can cause an issue with overlap. In the original implementation of the four-ring head coil, the ^{1}H mode occurred conveniently between modes 3 and 4 of the LP structure.[15] Nuclei other than ^{31}P tend to resonate at lower frequencies, so that overlap should not be a problem.

12.3 CONSTRUCTION AND INITIAL TUNING OF AN LP–HP FOUR-RING BIRDCAGE

Construction and tuning the four-ring birdcage involves assembly and tuning of the three separate birdcage structures.[15] Using a cylindrical former, the diameter of a head coil is 25.7–28 cm (10.5–11 in.), and the length is approximately the same. As a starting point, an inner birdcage structure is always configured as an LP birdcage so that it can be tuned for a lower frequency nucleus. The length of this structure should be about half the total length of the coil. A dual-tuned leg coil suitable for imaging and spectroscopy of the calf would have a diameter and length of about 15.2 cm (6 in.). Next, two identical outer birdcage structures are added at each end of the inner birdcage. These outer structures can be either LP or HP. For a head coil operating at 1.5 T or 3 T, HP outer structures have impedances more suitable for use at the ^{1}H frequency, so this discussion is limited to implementation of the LP–HP configuration of this coil. Use of more legs or struts in the coil will provide better RF field homogeneity: 8 is usually the minimum, while 16 provides excellent homogeneity out almost to the conductors.[15]

As for any birdcage, the conductors of the four-ring geometry should be fixed mechanically to maintain coil symmetry. Early research coils were machined from copper sheet and mounted on plastic cylinders.[15] While an acrylic cylinder is often used to mount birdcage coils, PVC and G-10 fiberglass materials offer superior strength. The locations of the end-rings and the connecting struts should be measured carefully on the cylinder to maintain symmetry. There should be some space at the back end of the coil to accommodate circuitry that will be used to couple to it. Knowing the precise dimensions, the coil conductors can be etched into flexible PCBs using single-clad 2 oz copper mounted on 0.010 in. FR-4 material. Alternatively, adhesive-backed copper tape can be applied over coil markings to build the conductor geometry. Location of the capacitor gaps should also be marked, and the copper tape can be gapped with a sharp tool. Both the rings and the legs should be equally spaced, and capacitor gaps can be centered on their respective segments. Maintaining the symmetry of the coil conductors will reduce the work required during coil tuning to compensate for conductor irregularities.

For tuning the four-ring birdcage, one can begin with the LP inner coil, leaving the two outer structures unpopulated with capacitors. The inner structure of the original 16-leg 1.5 T head coil used 68 pF ceramic capacitors for tuning the ^{31}P frequency at 25.7 MHz.[15] For constant coil size, capacitors can be scaled for frequency. For a different size of coil, the inductance will scale approximately with a single dimension of the coil, such as the birdcage diameter. Alternatively, there are other published data and online tools such as Birdcage Builder (Penn State University, Center for NMR Research) to solve for capacitor values. Finally, one can begin with inexpensive leaded capacitors and replace them with higher voltage types once their values have been determined. Initially, the inner birdcage should be tuned to a frequency slightly higher than will be needed. Once populated, the outer structures will tend to shift the ^{31}P mode of the inner birdcage to a slightly lower frequency. When possible, one should use the same value of capacitor in each gap, typically capacitors with 2% tolerance. If more than one value of fixed capacitor needs to be used, capacitors can be alternated on the legs. Alternatively, one can use slightly larger or smaller capacitors on legs that are fourfold symmetric, such as at the two-port connections and the locations opposite them.

For tuning, one can use two coupling loops and a network analyzer configured for an S21 or through measurement. One loop can be used to drive the coil near one end-ring and the other can be used to sense the coil field further away. For a well-tuned coil, the two linear modes will be tuned to the same

frequency, and only one mode will be observable. If there is an abnormal capacitor or some other defects in one location, the linear modes will likely split in frequency. One of the modes will generally align with this location, which aids in locating the problem. Once the coil is repaired, mode tuning should be restored. Over a wider bandwidth, one should observe the typical LP mode pattern shown in Figure 12.5(a), albeit an S21 measurement will display positive peaks rather than the negative ones.

Having performed a preliminary tuning of the inner birdcage, the two end-rings can now be populated with equal value capacitors. For the original LP–HP coil, a total of 137 pF was required in each end-ring segment to tune the outer HP structures for the ^{1}H mode.[15] If the LP structure is tuned for ^{31}P, which has a relatively high frequency for a "low-γ" nucleus, the high-order modes of this structure may appear close to the H-1 frequency. So, one may wish to temporarily short the capacitors on the inner legs in order to identify the correct ^{1}H modes that couple through them. For a 16-leg coil and ring conductor spacings of 25%–50%–25% of the total length, the H-1 mode appears between modes 3 and 4 of the LP structure. For other spacings, one may have to experiment if one runs into this problem. Increasing the length of the inner birdcage will increase the inductance of the legs and decrease the frequencies of the high-order modes, and vice versa. In principle, the high-order modes of the inner birdcage are orthogonal to the proton mode and should not couple, but in practice two-port coupling and other effects can break the coil symmetry and cause couplings. Coupling to these modes may then cause some shading in proton imaging, so it is better to separate the modes.

Within the four-ring birdcage, shown in more detail in Figure 12.6, the two outer birdcages couple strongly through the inner legs and cause the fundamental ($k = 1$) mode to split into two new modes. These new modes have co- and counter-rotating current distributions, with the co-rotating mode appearing at somewhat higher frequency. Since all high-order modes, $k = 2$ and above provide no RF field along the central axis of the coil, the co- and counter-rotating modes can be identified using the two-loop method. By placing the stimulating loop near an end-ring and the pickup loop on the coil axis, only the co- and counter-rotating modes of the $k = 1$ mode can be detected. Furthermore, since the counter-rotating mode has null in its field at the center of the coil, it can it distinguished from the co-rotating

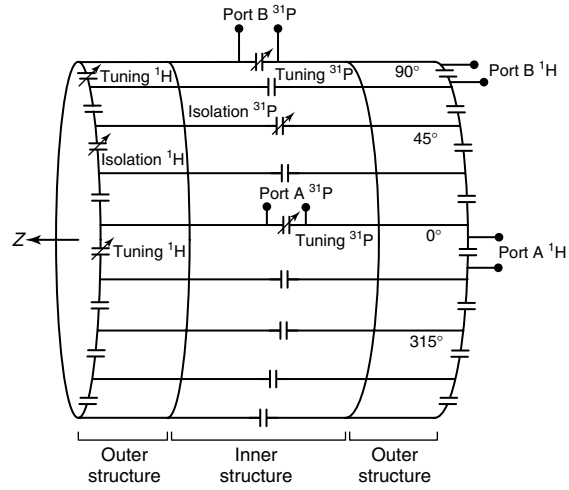

Figure 12.6. The LP–HP four-ring birdcage indicating port connections and placement of variable capacitors for tuning and for adjustment of mode isolation.

or homogeneous mode. Tuning of the outer birdcages uses many capacitors, so it is recommended that capacitors be added in a manner that maintains fourfold symmetry of the coil. For example, one can add eight capacitors at a time to the tuning locations ($0^\circ, 90^\circ, 180^\circ, 270^\circ$) and then to the isolating locations ($45^\circ, 135^\circ, 225^\circ, 315^\circ$). If too much capacitance accumulates in these positions, it can be distributed symmetrically to the remaining locations. Just as for the single-tuned birdcage, the co-rotating mode has two quadrature linear modes, and tuning and careful alignment of these modes are required to obtain true quadrature operation.

12.4 MATCHING OF THE BIRDCAGE FOR A RANGE OF HEAD SIZES

A common question is, "For which head size should the coil be tuned and matched?" For high field, the Q's of a head coil are low enough that tuning is not as critical, since both signal and noise will rise and fall together during modest tuning shifts. Matching, however, can have a stronger effect. Obviously, one should match the coil to a particular head size if there is only one head size being investigated. In general, though, one will want to match for a range of head sizes, and tuning of the coil needs to be fixed. In this case, it is preferable to match the coil to the

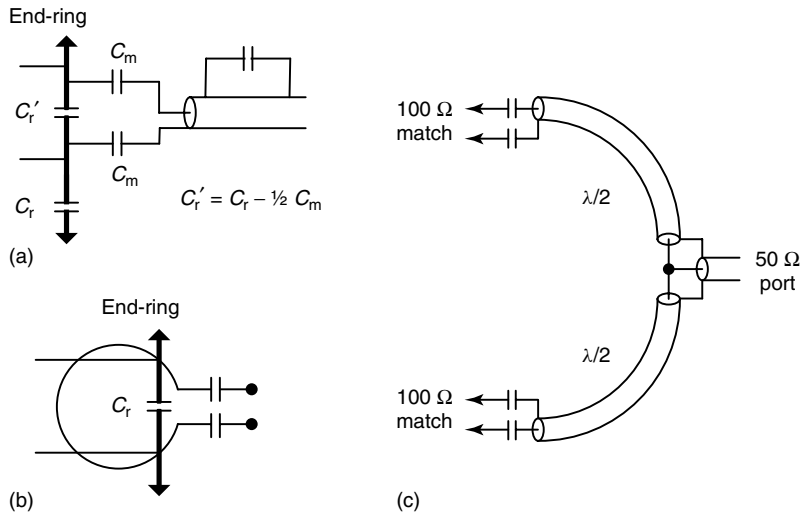

Figure 12.7. (a) Direct connection to the end-ring using balanced capacitors. (b) Inductive coupling to a single coil mesh. (c) A half-wavelength scheme for capacitive coupling to opposite sides of the birdcage.

loading of the largest size head and allow smaller head sizes to be mismatched. The reason for this is that for smaller head sizes, the Q of the coil is higher, and this compensates for the mismatch effect. In the transmit mode, the coil may reflect power, but less power is needed for a smaller head size. Similarly, in receive mode the higher Q of the coil provides more signal, compensating for the mismatch to the NMR receiver. Consequently, transmit power and signal-to-noise ratio (SNR) of the coil will be roughly flat for a wide range of head sizes.

Connection to the coil can be either a direct capacitive connection or via inductive coupling. Direct connection is often preferred because it may require less mechanical hardware and take up less space, but neither method provides a special advantage as far as SNR or transmitter power is concerned. Figure 12.7(a) shows coupling to the coil using balanced capacitors[18] and Figure 12.7(b) with a series-tuned coupling loop. Cable baluns are generally required in both cases to isolate the coil from the system cables (see Chapter 25). Additional cable baluns may be required if cables must be routed past the coil to the system connections. The capacitors and inductors used for matching should be chosen to be as small as possible to minimize effects on tuning. For capacitive coupling, the end-ring capacitor can be reduced in value by the series combination of the matching capacitors, as indicated in Figure 12.7(a). For very high frequencies, four-port coupling is recommended,[19] and a simple four-port scheme is shown in Figure 12.7(c). There are two of these networks, one for each quadrature port, so that the scheme maintains the fourfold symmetry of the coil and avoids the skewing problem associated with two-port couplers (see below).

12.4.1 Tuning and Alignment of the Linear Modes

The quadrature linear modes are sensitive to perturbations to coil symmetry caused by variation in capacitor values and misalignments of coil conductors. Tropp[16] has analyzed these variations and found that an excess or deficit of capacitance or inductance located somewhere between the port/tuning orientations will cause the linear modes to rotate away from these positions and reorient in the direction of the "disturbance" in impedance, as indicated in Figure 12.8(a). The linear mode oriented in that direction will be detuned by this reactance, and the detuning might be enough to split the frequencies of the linear modes, which can be detected with pickup loops. For linear modes that are aligned with their port connections, an S21 measurement will yield a high value of isolation between the ports, typically -20 dB or better. Port 1 of the network analyzer will drive the mode

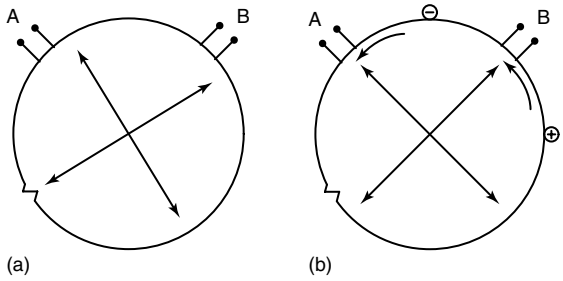

Figure 12.8. (a) A local perturbation in impedance causing the linear modes to become aligned with it and misaligned with the coil ports. (b) Alignment restored using variable capacitors at the 45° locations.

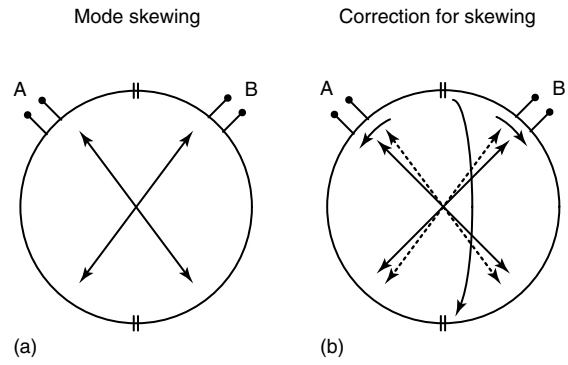

Figure 12.9. (a) Excess capacitance near the tap points causing the modes to skew. (b) The skewing corrected by moving capacitance to the other side of coil.

oriented predominantly with Port A of the coil and not the other mode, so very little signal will find its way to Port B. Misalignment of the modes will cause stronger coupling with the second mode and consequently to Port B. Correction of mode rotation and reduction of this coupling can be accomplished with additional variable capacitors placed at the 45° positions between the port connections,[15] as illustrated in Figure 12.8(b). These capacitors introduce additional positive and negative "perturbations" that counter the effect of perturbing reactances elsewhere on the coil. The 45° locations of these capacitors maximize their rotational effect, and capacitors located 90° apart rotate the linear modes in opposite directions. Because they are located midway between the tuning points, these capacitors will tune both linear modes by about the same amount, so that use of two capacitors 90° apart can compensate for one another. Increasing one capacitor has the same effect on mode rotation as decreasing the other.

12.4.2 Mode Skewing and Its Correction

The second effect of a perturbing reactance, especially if it is strong, is to cause the linear modes to rotate toward or away from one another, as illustrated in Figure 12.9(a). This can be explained by taking another look at the circularly polarized waves as they propagate around the coil. As mentioned earlier, each mesh introduces a certain amount of delay as a wave propagates past it. But if, for example, the wave encounters some additional capacitance in a mesh or a series of meshes, the wave will be slowed down. The opposite will be true in the remaining meshes. Consequently, the modes will skew away from one another in the fast meshes and toward one another in the slow meshes. This skewing was observed with inductive couplers that were used with the original 1.5 T four-ring birdcage coils.[15] Tuned couplers were used to couple to the coil, and they were also used to obtain isolation between the ports by rotating the couplers slightly above the coil. It was found that the best isolation was achieved when the couplers were rotated toward one another by about 10°. In the wave view, the waves propagating around the coil were slowed by the couplers. Because the waves spent more time on coupler side of the coil, the linear modes were skewed toward one another, causing loss of isolation when they were no longer aligned with the coupling ports.

One solution to this particular problem is to move some tuning capacitance from the coupler side of the coil to the opposite side, as illustrated in Figure 12.9(b). The CP waves experience less delay as local capacitance is reduced, the linear modes skew apart, and they then begin to align with the 90° orientations. During this process, the total capacitance is unchanged, so that coil tuning does not change appreciably. As capacitance is redistributed, the modes may become rotated, so that the isolation (45°) capacitors may need adjustment to realign the modes with their respective ports. But with each redistribution of capacitance, port-to-port isolation should improve. One can see that fixed connection to the coil is more difficult to align than with inductive couplers, but fixed capacitive coupling generally requires less space and is

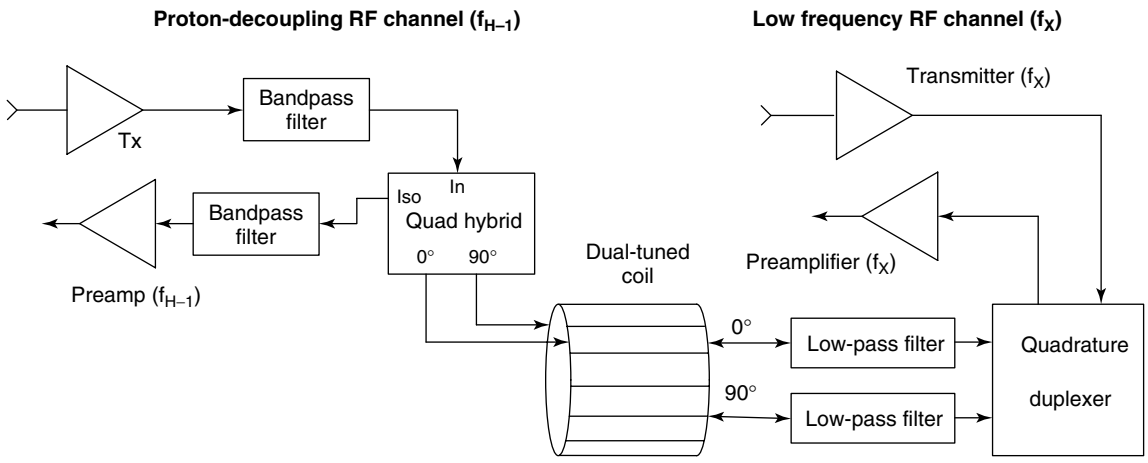

Figure 12.10. Connection of the dual-tuned birdcage to separate RF channels for acquiring images and proton-decoupled spectra from a low-frequency (X) nucleus.

now the most commonly used method of connection.

The skewing adjustment shows that it is important to maintain azimuthal symmetry to a birdcage coil, both in the coil conductors and in the distribution of capacitance. Fortunately for head coils, the Q's at high field (1.5 T and 3 T) are low enough that coil perturbations are not overwhelming. But the Q's are high enough that coupling of the coil to the human head can cause rotation of the linear modes and measurable reduction in isolation. Finally, we have seen that the external coupling networks can cause perturbations and loss of coil isolation. One means of mitigating this problem is to use four-port coupling, which restores symmetry to the coil.[19] One network for implementing four-port coupling is shown in Figure 12.7(c). For this network, two-port connections, each matched for 100 Ω, are combined at the other end of half-wavelength cables to provide a 50 Ω connection for a single quadrature port. The circuit for the other quadrature port of the coil is identical.

12.4.3 Coil Application: Proton Decoupling

If a dual-tuned volume coil has no PIN diode or other switching circuitry to disable the coil, it can be used to simultaneously transmit and receive at two frequencies. One such "double resonance" application is proton decoupling.[20] For this experiment, an excitation pulse is first delivered to the lower frequency or "X-nucleus". Then, simultaneous with signal acquisition from this nucleus, a relatively low-power decoupling waveform is transmitted to the coil at the ^{1}H frequency. A representative hardware scheme for accomplishing this is shown in Figure 12.10. In this scheme, additional RF filters are placed between the dual-tuned coil and the low-frequency receive channels to prevent the ^{1}H signal from saturating and injecting noise into the preamplifiers. Filters are also placed in the ^{1}H channel to filter noise and prevent the high-power pulse from the low-frequency electronics from damaging the ^{1}H receiver. The linearity of the preamplifiers is maintained, and out-of-band noise is filtered from the passbands of each channel.

REFERENCES

1. C. E. Hayes, W. A. Edelstein, J. F. Schenk, O. M. Mueller, and M. E. Eash, *J. Magn. Reson.*, 1985, **63**, 622.
2. J. C. Watkins and E. Fukushima, *Rev. Sci. Instrum.*, 1988, **59**, 926.
3. T. R. Brown, B. M. Kincaid, and K. Ugurbil, *Proc. Natl. Acad. Sci. U.S.A.*, 1982, **79**, 523.
4. P. R. Luyten, G. Bruntink, F. M. Sloff, J. W. A. H. Vermeulen, J. I. van der Heijden, J. den Hollander, and A. Heerschap, *NMR Biomed.*, 1989, **1**, 177.

5. M. D. Schnall, V. H. Subramanian, J. S. Leigh Jr, L. Gyulai, A. McLaughlin, and B. Chance, *J. Magn. Reson.*, 1985, **63**, 401.
6. M. D. Schnall, V. H. Subramanian, J. S. Leigh Jr, and B. Chance, *J. Magn. Reson.*, 1985, **65**, 122.
7. S. Kan, M. Fan, and J. Courtieu, *Rev. Sci. Instrum.*, 1980, **51**, 887.
8. R. M. Foster, *Bell Syst. Tech. J*., 1924, **3**, 259.
9. G. Isaac, M. D. Schnall, R. E. Lenkinski, and K. Vogele, *J. Magn. Reson.*, 1990, **89**, 41.
10. J. T. Vaughan, H. P. Heatherington, J. W. Pan, P. J. Noa, and G. M. Pohost, *Proc. Int. Soc. Magn. Reson. Med.*, 1993, **12**, 306.
11. S. Amari, A. M. Ulud, J. Bornemann, P. C. M. van Zijl, and P. B. Barker, *Magn. Reson. Med*, 1997, **37**, 243.
12. G. B. Matson, P. Vermathen, and T. C. Hill, *Magn. Reson. Med.*, 1999, **42**, 173.
13. N. I. Avdievich, A. S. Peshkovsky, and H. P. Hetherington, *Proc. Intl. Soc. Magn. Reson. Med.*, 2007, **15**, 239.
14. J. R. Fitzsimmons, B. Beck, and H. R. Brooker, *Magn. Reson. Med.*, 1993, **30**, 107.
15. J. Murphy-Boesch, R. Srinivasan, L. Carvajal, and T. R. Brown, *J. Magn. Reson. B.*, 1994, **103**, 103.
16. J. Tropp, *J. Mag. Reson.*, 1989, **82**, 51.
17. D. A. C. Kelley and J. Tropp, *Proc. SMRM*, 1988, **7**, 261.
18. J. Murphy-Boesch and A. P. Koretsky, *J. Magn. Reson.*, 1983, **54**, 526.
19. T. S. Ibrahim, R. Lee, B. A. Baertlein, A. Kangarlu, and P.-M. L. Robitaille, *Magn. Reson. Imaging*, 2000, **18**, 733.
20. J. Murphy-Boesch, R. Stoyanova, R. Srinivasan, T. Willard, D. Vigneron, S. Nelson, J. S. Taylor, and T. R. Brown, *NMR in Biomed.*, 1993, **6**, 173.

Chapter 13
TEM Body Coils

J. Thomas Vaughan

Center for Magnetic Resonance Research, University of Minnesota, Minneapolis, MN 55455, USA

13.1 INTRODUCTION

TEM body coils are a good design choice for transmit body coils at any field strength, but offer a number of advantages over other designs for 3 T and above. TEM or "transverse electromagnetic" is the most general term for "transmission line". Any circuit capable of propagating a TEM wave including coaxial lines, strip lines, microstrips, waveguides, and cavities are by definition, "TEM" coils.[1,2] A rule-of-thumb in the electronics industry is to choose distributed, TEM circuit design over lower frequency "lumped element" circuit design when the signal wavelength on the circuit exceeds 0.1λ. This is to preserve the efficiency of the circuit by minimizing radiation losses. Currents on distributed transmission line elements are also more easily controlled as will be taught in this chapter. For these reasons and more, the TEM approach to body coil design is strongly recommended.

RF Coils for MRI
Edited by J. Thomas Vaughan and John R. Griffiths

ISBN: 978-0-470-77076-4

13.2 BACKGROUND

More than most radiofrequency (RF) coils, the high-frequency body coil challenges the limits of design and performance. Body coils tuned to 128 MHz (3 T) and above are required to operate efficiently and homogeneously at unprecedented, full wavelength dimensions. The present industry approach to building body coils makes use of shielded birdcage type structures.[3] The rung currents of birdcage coils generate a homogeneous field transverse to the cylindrical coils' axes. These rung currents depend on end rings for a "return path". Refer to Figure 13.1(a). End rings can be problematic. The inductance and resonance frequency of birdcage coils are dependent on (limited by) the dimension of the end rings which in turn define the diameter of the coil. When the diameter is very large, as is the case for body coils, the axial length of the coil must be sufficiently shortened to achieve resonance at the desired operational frequency. Significantly reducing the length of the body coil, however, can limit the coil's efficiency and homogeneity over the desired field of view (FOV). End ring currents generate a B_1 field component coaxial with the B_0 field. The axial "z" component of the end ring generated field is therefore nonproductive for NMR excitation, and can result as a source of ohmic

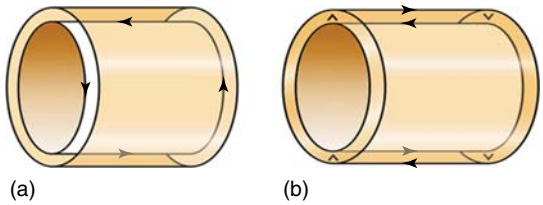

Figure 13.1. The resonance of a birdcage coil (a) is dependent on and limited by its end rings. Independent of the large, inductive, end ring circuits, the TEM resonator (b) can efficiently achieve the highest frequencies for body coils.

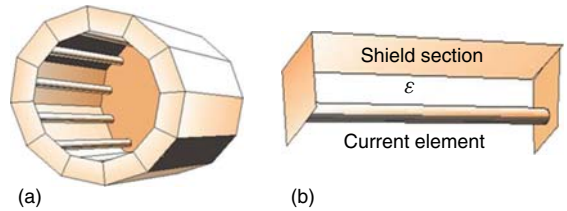

Figure 13.2. The segmented TEM volume coil (a) can be described as a toroidal array of transmission line (TEM) elements (b), formed by current elements parallel to cavity wall or shield sections. These TEM elements are the building blocks of the TEM volume coil. The impedance of these independent RF current elements can be passively or actively controlled for detuning, retuning, multiple tuning, phase shifting, amplitude modulation, transmission, and reception.

loss to induced conduction currents in the tissue load conductor. End rings can be used, however, to limit the axial extent of the coil's field, to prevent signal from beyond the gradients from folding back into the desired FOV.

To solve the efficiency, homogeneity and frequency problems associated with the end ring dependent birdcage coils, the transmission line (TEM) resonator is a good candidate.[4] The TEM design achieves the birdcage's highly homogeneous, rung current generated transverse field without the counterproductive end ring currents (Figure 13.1b). The TEM coil's return path follows the shield rather than the end rings. The inductance and self resonance of the TEM coil are therefore *independent* of the diameter of the coil. A TEM coil of a given length can be built to arbitrarily large diameters, without significantly changing the frequency of the coil. The basic TEM design derives from the first NMR coil, the coaxial cavity resonator of Pound and Purcell.[5] Schneider and Dullenkopf used the design for a high-resolution probe head.[6] Norbert Krause first developed a TEM-like design for human imaging.[7] Röschmann and Bridges advanced related structures.[8,9] The TEM design was improved for modern imaging and spectroscopy applications over the decade following by Vaughan *et al*.[1,2] In recent years, a variety of executions have extended the usefulness of the TEM design.[10–13]

It is useful to view the segmented TEM volume coil as a toroidal array of independent transmission line elements (see Figure 13.2). The resonant frequency of the larger TEM coil structure is dependent on the resonant frequency of the independent line element, modified slightly by its reactive coupling with neighboring elements in the coil. The reactance of the individual elements can be tuned in alternating patterns to effect multiple tuning for the larger coil structure.[2] The reactance between individual elements can be controlled to decouple the elements for parallel imaging applications.[14] Any number of individual elements can be driven in transmit and/or receive mode. The individual elements of the volume coil can be actively controlled to tune the coil for transmit and detune the coil for reception with local receivers such as surface coils, phased arrays, or parallel arrays. The amplitude and phase of the elements can be modulated to effect corrective RF-field shimming or volume selection.[15] Many of these advantages of the segmented TEM body coil are demonstrated in this chapter.

13.2.1 Calculated Coil Losses

The choice of the TEM body coil design compared to other potential designs is demonstrated in circuit efficiency calculations. To numerically

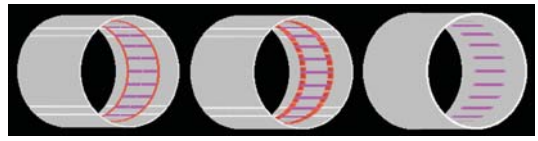

Figure 13.3. Body coil models for finite difference time domain (FDTD) calculations of frequency limits and radiation resistance for shielded and unshielded (not shown) body coils. The coil rung counts and physical dimensions are equal in all models. (a) Shielded low pass birdcage. (b) Shielded high pass birdcage. (c) TEM resonator.

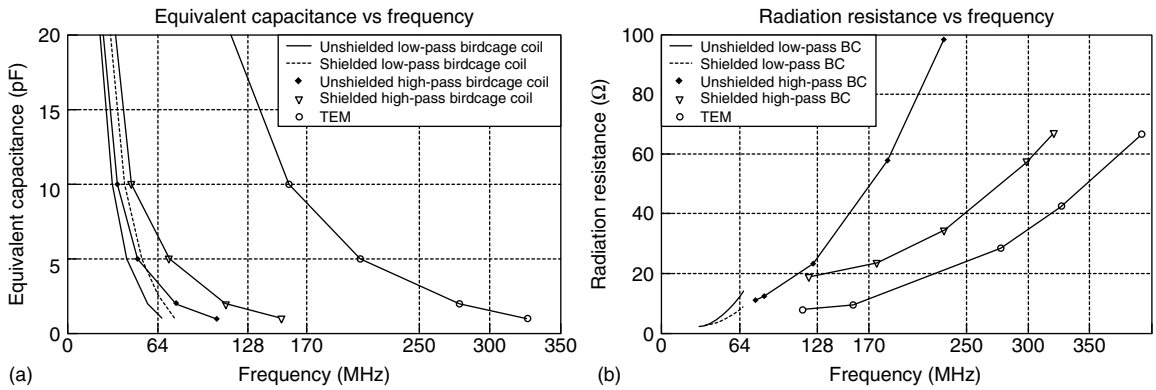

Figure 13.4. In the FDTD calculations for the Figure 13.3, coil structures, self resonance, and radiation losses are shown to limit the use of birdcage body coils to 3 T (128 MHz) and below, whereas the TEM body coil may be useful to 8 T. The plots for the low pass body coils in (b) are limited by the maximum resonant frequencies of the coils. (a) Capacitance vs frequency. (b) Radiation resistance vs frequency.

calculate the operational frequency and efficiency ranges for high-field volume coils, five unloaded coils were modeled by the finite difference time domain (XFDTD) method[16] (see Figure 13.3). Equivalent total capacitance and radiation resistance were calculated versus the transverse mode resonant frequency for high pass and low pass, shielded and unshielded birdcages, and a transmission line (TEM) resonator. All five coils had identical dimensions (58 cm i.d. $\times$ 33 cm long), and all were open on both ends. The birdcage shields and the TEM cavity were 1.0 m long and spaced 2 cm from the coil rungs. These models were in their "classical" forms; the low pass birdcage included 24 capacitors in center positions on the rungs, the high pass birdcage (HPBC) included 24 capacitors in each ring for a total of 48 in the structure, and the TEM resonator included 48 capacitors in rung positions. Capacitor positions in these models appear as gaps in the circuits of Figure 13.3. While the models faithfully reproduce the configuration of the TEM body coil tested, all three models might be improved with more highly distributed capacitances.

The capacitors shown in Figure 13.3 were assigned values to tune the resonant frequencies of the coil models, as in realized coil circuits. To determine the point at which a coil reached self resonance, the equivalent added capacitance of the structure versus the resonant frequency associated with the transverse B_1 field mode was calculated for each of the models as shown. The coil approached self resonance as the equivalent added capacitance approached zero. The results were plotted in Figure 13.4a. According to the results displayed in Figure 13.4, a 1 pF capacitance will resonate the low pass birdcage body coils at slightly higher than 64 MHz (1.5 T), with the shielded coil reaching a higher frequency than the unshielded birdcage. HPBCs reach 128 MHz (3 T) for the same 1 pF capacitance added, again the shielded version resonating higher. The TEM coil of the same dimensions and capacitance reaches 342 MHz (8 T).

To quantify the amount of energy lost to radiated fields, the radiation resistance "$R_r = 2P_r/I_m{}^2$" versus resonant frequency was calculated for each coil structure and plotted in Figure 13.4(b). P_r is the radiated power and I_m is the maximum current in the coil.[15,17] The model shielded HPBC body coil resonating at 128 MHz radiates energy to the patient load and to the magnet bore at a rate equivalent to the energy lost to a 20 Ω resistor in the coil circuit. By the same model, the TEM coil would incur approximately half this loss at 3 and 4 T Larmor frequencies. Because the TEM coil is less radiative and less inductive than the birdcage, its useful range as a full-sized human body coil approaches 350 MHz (>8 T). This prediction agrees with empirical results (Figure 13.23c).

13.3 SPECIFICATION

Specification of a TEM body coil depends on its application. TEM coils for imaging the body can be

divided into three types: surface coil, body coil, and Torso coil. Any of these may be driven in single or multichannel mode.

13.3.1 TEM Surface Array

The TEM surface array is often chosen when transmit efficiency is a top priority. Early examples of the coil (Figure 13.5) have demonstrated six times the efficiency of a whole body coil (Figure 13.6). The TEM surface array transceiver is an array of electromagnetically decoupled TEM elements independently driven by a parallel or "multichannel" transmit and receive system. This coil type is often configured as a pair with each half placed respectively anterior and posterior to the body. The number of elements used in the coil of course is dictated by the number of transmit and receive channels in the MRI system. B_1 shimming is typically employed with these multichannel arrays to maximize signal-to-noise (SNR) and uniformity, and to minimize specific absorption rate (SAR) over the ROI. In Figure 13.4 example, the TEM surface array was operated as a 16-channel transceiver to acquire the heart image (Figure 13.5c). High transmit efficiency and receive sensitivity are reasons for using closely fitted TEM surface coils for body imaging applications.[18,19] These close coils, however, severely limit VCG lead and receiver array placement near the heart, and can be heavy and restrictive to the patient, all significant compromises.

13.3.2 TEM Body Coil

The TEM body coil is selected when a large, uniform excitation field, and patient comfort are priorities (Figure 13.6a). This body coil is typically paired with local receiver arrays for high SNR image acquisition (Figure 13.6b). These factors make the TEM body coil the coil of choice for most clinical applications. The coil with inductively coupled elements can be driven with a single high power amplifier divided into four 90° phased channels at four, 90° spaced ports. In this configuration, the coil is compatible with and can be retrofitted to conventional MRI systems. Alternatively, the elements of this coil can be decoupled and driven independently with multiple RF transmit lines, and received by multiple, parallel receiver channels. Figure 13.6(a) depicts a multichannel TEM body coil for 7 T. Like commercial body coils for field strengths of 3 T and lower, this coil was built to fit into the extremely limited space between the system gradients and the magnet bore liner. This

Figure 13.5. Multichannel transceiver surface coils. (a) One of a pair of eight channel transmission line (TEM) arrays. With one coil atop and the other below the subject's torso (b), cardiac images are acquired (c).

Figure 13.6. Body coil (a) with half of receiver pair (b) used to acquire image (c) with 16 channels transmitting and 32 channels receiving.

Figure 13.7. Torso transceiver coil halves (a) with multichannel receiver pair (b). (c) The coil in place about its builder and (d) the image acquired with 16 transmit channels and 32 receiver channels.

60 cm i.d. coil is composed of 16 equally spaced, TEM transceiver elements, each being independently tuned and matched as evidenced by the 16 pairs of fiber-glass stems projecting from the coil. Electronic means of tuning and matching these elements have more recently been developed to facilitate the utility of the coil.[20–23] Sixteen-channel dedicated 1 kW power amplifier modules are also shown mounted on the end of the coil body as a demonstration of future technology.[17] Together with this 16-channel body coil a pair of 16 loop receiver arrays (32 total) was placed anterior and posterior to the subject's chest.[24] After B_1 shimming on the cardiac region, 16 body coil transmit channels were used to excite a relatively uniform ROI. Thirty two channels were used to receive the heart images (Figure 13.6c). This body coil option provides the closest approach to current clinical imaging on 3 and 1.5 T systems, where a large body coil provides uniform excitation and local arrays increase sensitivity of reception.[4,25]

13.3.3 TEM Torso Coil

The Torso coil may offer a compromise between the transmit efficiency and receive sensitivity of the TEM surface array of Figure 13.5, and the uniform excitation, local reception, and ergonomic space of the whole body coil approach shown in Figure 13.6.[18] In Figure 13.7(a), a 46 cm id, 16-channel TEM torso coil is mounted on a patient table and split for easy access.[26] This actively detuned transceiver coil can be used with loop arrays such as shown in Figure 13.7(b). The torso coil and receiver array (eight loops above, eight beneath the torso) are shown in place about the subject in Figure 13.7(c). High signal, relatively uniform B_1 shimmed cardiac images were acquired with 16 transmit channels and 32 receive channels (16 receiver channels + 16 TEM transceiver channels). While more efficient than a whole body coil, this arrangement provides more B_1 field uniformity than the surface coil transceiver, and allows room for cardiac lead placement and additional local coils, including receiver arrays and multinuclear coils. A lack of arm and shoulder space, however, is a major limitation with this choice.

13.4 COMPUTER-AIDED DESIGN

Once the coil type is specified according to its application, design begins with the numerical simulation of RF coil circuits and fields. To a large degree, a chosen coil design can be designed, characterized, and evaluated by simulations based on finite difference time domain (FDTD), finite element method (FEM), method of moments (MOM), or other commercially available EM solvers. Examples of insightful 7 T body coil design simulations follow.

13.4.1 Field Calculations for the Unloaded Body Coil

First body coil design objectives are to make certain that the FOV of the coil will efficiently and uniformly cover the desired ROI. An acceptable body coil FOV should vary less than 3 dB over a 35–45 cm diameter spherical or cylindrical volume. To determine this criterion, the EM field of a coil such as shown in Figure 13.3 should be calculated over the desired FOV in three dimensions. The 3D Maxwell B_1 field contours for a TEM body coil are shown calculated by the FDTD method in Figure 13.8.[27] The central transaxial field (Figure 13.8b) is highly homogeneous, not varying by more than 1 dB over an

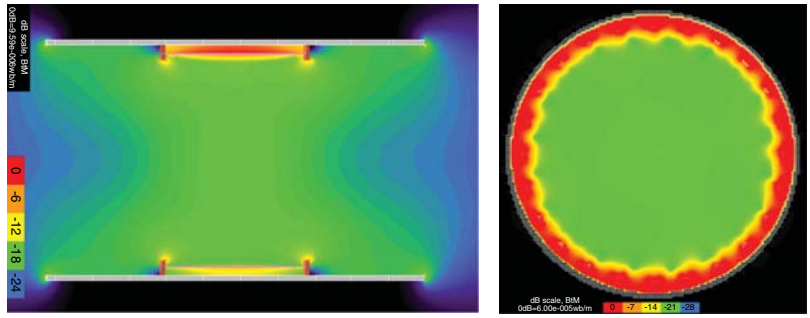

Figure 13.8. B_1 field contours (1 dB) were calculated by the FDTD method for the unloaded, quadrature driven body coil. The 33 cm coil elements (rungs) are shown in the central third of the 1 m long cavity for the coil. (a) Axial TEM B_1 field in decibels. (b) Transaxial TEM B_1 field in decibels.

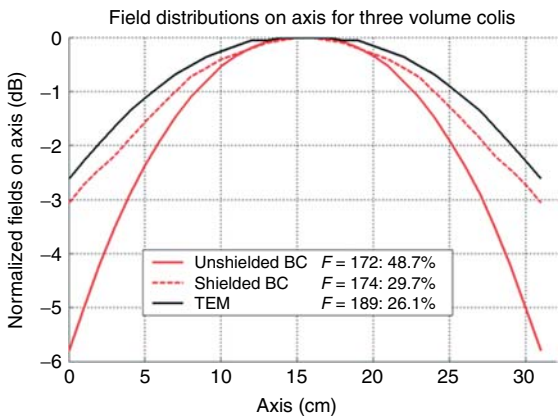

Figure 13.9. The normalized B_1 field magnitude generated along the z axes of the Figure 13.3 models is shown for the Larmor frequencies shown (approximately 4 T). Coil elements (rungs) for the birdcages and the TEM resonator are 33 cm.

80% diameter FOV. This transaxial homogeneity is typical of birdcage coils as well. To compare the axial field profile of the TEM body coil to birdcage profiles, the B_1 field contour was calculated along the z-axis of the models shown in Figure 13.3 (refer also to Figure 13.9). The relative B_1 magnitudes were normalized to respective peak B_1 fields generated by equal currents on the coil elements. Defining the axial field length of each coil as the points on the $\pm z$ axis at which the B_1 magnitude falls to 3 dB below the peak value reached in the coil center, the three equal length coils modeled are shown to have differing axial field lengths. In the Figure 13.9 example, the unshielded birdcage axial field length of 25 cm compares to the shielded birdcage field of 33 and the TEM axial field length of 38 cm. Satisfactory FOV coverage, however, cannot be determined by simulating the empty coil alone. Coil fields can change dramatically when a human body load is introduced, especially for higher frequencies.

13.4.2 The Loaded TEM Body Coil

In addition to loading the Q and shifting the frequency of the coil, introduction of a human body into the bore of the body coil results in significant changes in the B_1 and E field contours through the volume of the coil and the human anatomy. These changes are primarily due to shortwave interference patterns of the fields generated by multiple coil elements. Owing to the dielectric constant of high water content tissues, the Larmor wavelength within the human body is significantly shortened from its coil circuit and air wavelengths. At 7 T, for example, a 1 m wavelength on the coil is nominally 12 cm in the body. By this measure, the human trunk is about $3 \times 6\lambda$ in dimension. As predicted in Figure 13.4, at 300 MHz a conventional, birdcage body coil would be highly inefficient if it could be built at all. TEM coils comprised of arrays of short transmission line elements are still easily tuned to and are efficient at such high frequencies. Accordingly, the first successful 7 T body coils are of multichannel TEM design.[25,28–30] An efficient coil circuit solves only part of the high field problem. If the 300 MHz TEM coil or other

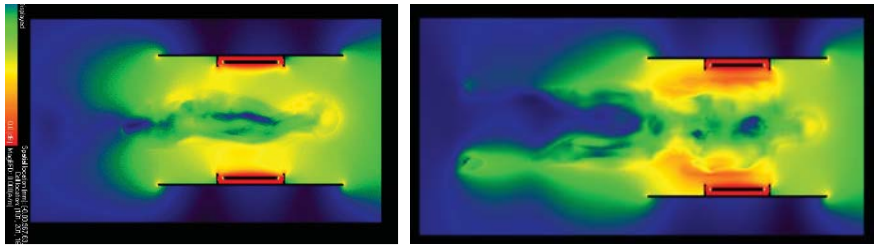

Figure 13.10. B_1 contour calculations of human body in body coil at 7 T (300 MHz). Note the strong destructive interference in the heart region (dark blue). Note also the extent of B_1 field propagating along the coil and body axis, beyond active coil elements.

multielement structure were excited with the circularly polarized RF field employed at clinical field strengths, B_1^+ contours spanning 60 dB would result (see Figure 13.10). Conventional MRI with simple circularly polarized (CP) excitation cannot generally be used for human body applications and does not work well at 3 T. Multichannel TEM designs used together with B_1 shimming offer a solution to an efficient body coil with a "manageable" field.[4,28,30]

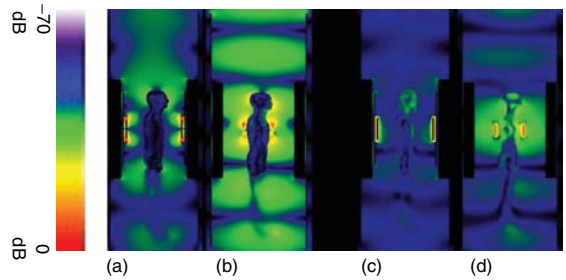

Figure 13.11. B_1 and E field calculations for TEM body and body array coils. (a, b) Calculated 300 MHz E fields propagating through the bore of a TEM body coil within a Faraday shielded magnet bore, for a TEM body coil and TEM surface array, respectively. (c, d) 300 MHz B_1 fields generated by the coil elements, "traveling" through the coil and magnet bore for the body coil (c) and local surface array pair (d).

13.4.3 Field Calculations for the Human Loaded Body Coil

Coil losses, be they from conserved or radiated fields in the coil, are mostly spent as RF losses to the tissue conductor and to the tissue dielectric in the human body.[2,31] RF field propagation and loss in a body loaded coil can be modeled as below by the FDTD method,[27] using the National Library of Medicine's Visual Human Project atlas or other models. In these models, anatomic boundaries were assigned tissue, temperature, and frequency dependent permittivity and conductivity values.[32] Then, relative RF magnetic vector potential (B_1^+) field contours were calculated for a circularly polarized, body loaded, 16 element TEM coil at 300 MHz in the Figure 13.10 example. This first model is not to demonstrate a working design, but rather to emphasize the need for a departure from conventional methods of coil design and operation. With color contours assigned 20 dB in these log scale plots, the interference patterns span 80 dB of RF field gradient. While not as severe at 3 T or lower, the B_1 field contours at these fields are still highly nonuniform.

Figure 13.11 similarly shows E and B_1 field contours propagating from the CP coil elements through the body-loaded bore. It is easy to see the "traveling waves" excited by the coil elements propagating through the bore of the 1 m long coil cavity and longer Faraday cage of the magnet bore.[25,31] While the TEM array is closer to the body and therefore couples more efficiently to the body for MR imaging, it is clear to see that neither design is immune to significant radiative losses by this mechanism.

Efficiency and B_1 uniformity are not the only criteria for successful body coil design. Refer to Figure 13.12. The coil and its application to human patients must also be safe. E and B_1 field losses to the tissues as SAR increase heating ΔT and elevated temperature, T. These quantities can and should be modeled as well when designing a body coil. While the present safety practice relies heavily on SAR models, numerical predictions of heating (ΔT) and

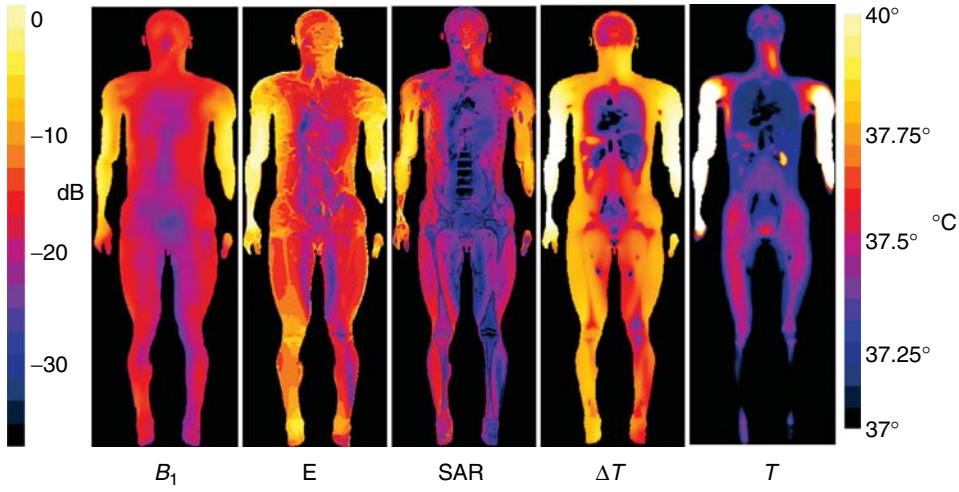

Figure 13.12. Calculated relative RF magnetic field (B_1^+), RF electric field (E), specific absorption rate (SAR), all on log scale (dB), and absolute temperature (°C) for 133 °W RF input into a 72 kg human body from a 60 cm i.d. × 1 m long TEM body coil centered on the chest at 7 T.

temperature contours (T) must be included. Temperature and not SAR, causes thermal stress, pain, and tissue damage, and is therefore the proper safety metric. Temperature is equated to SAR through six or eight additional thermodynamic and physiological parameters, depending on the bioheat equation used. SAR removed from this equation does not give the magnitude or location of true hot spots or systemic temperature rise. Thermal models must be accurate and precise to 0.2 °C. The accuracy and precision of SEMCAD X, an FDTD solver, (Zurich, CH)[33] has been corrected by our bioheat equation,[34] and validated in whole body experiments with porcine models.[35]

13.4.4 Body Coil Structure and B_1 Shimming

Multichannel TEM coil elements can be arrayed over three dimensions on the surface of a cylinder or other form to facilitate better control over the B_1 excitation field in x, y, and z. These 3D array arrangements give an additional approach that can be used alone or in combination with other approaches to maximize B_1 excitation uniformity and efficiency, and to minimize SAR (see Figure 13.13). The high pass birdcage (HPBC) coil and the 16 channel TEM coils show more traditional, "2D" designs. The 2 × 16 (two coaxial rings of 16 elements each), with both

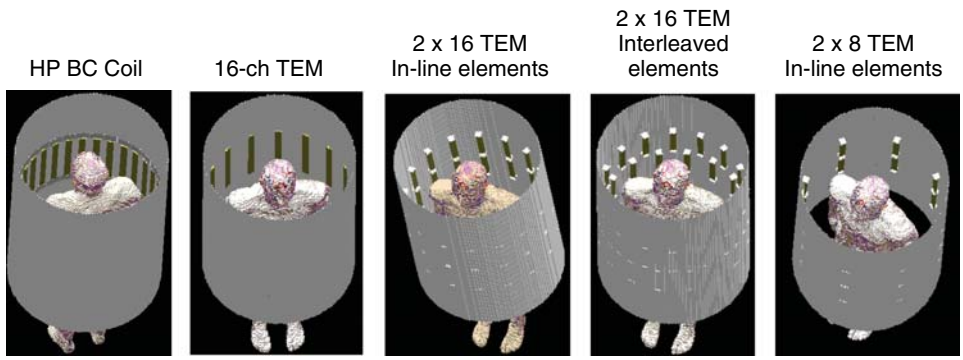

Figure 13.13. Various multichannel TEM body coil design options, referenced to the industry standard high-pass birdcage on the far left.

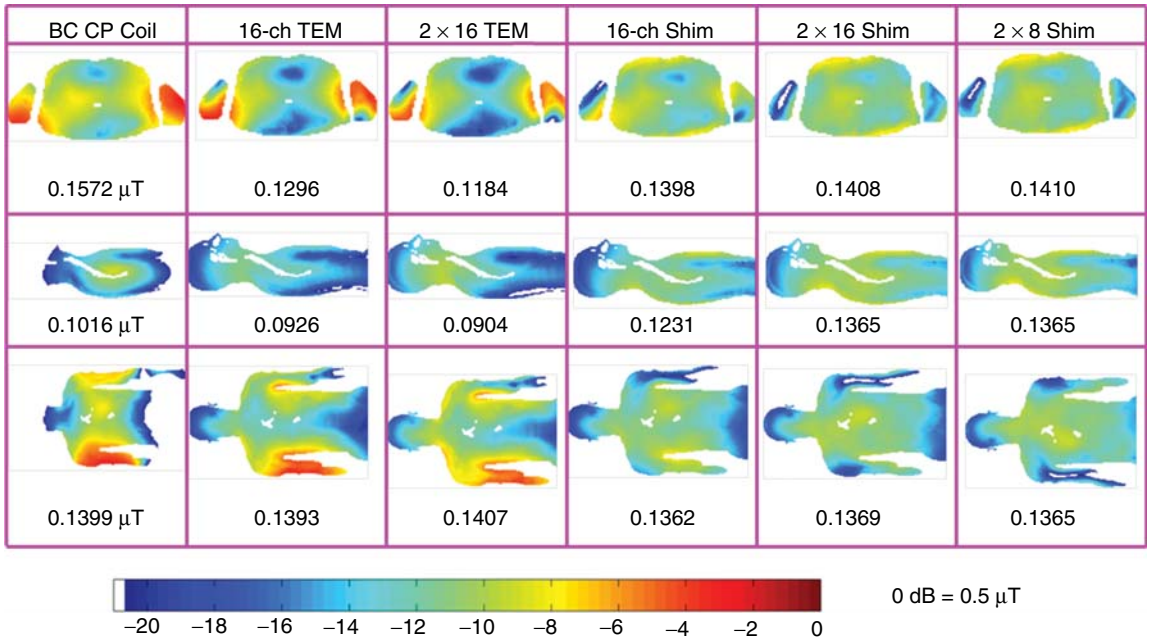

Figure 13.14. 3D body coil B_1^+ field calculations in transaxial, sagittal, and coronal, center slices. The three reference coils on the left are circularly polarized but unshimmed. The three on the right are not circularly polarized but are B_1 shimmed. Table values are B_1 field measurements averaged over the slice in units of microtesla, for a normalized SAR power input.

in-line and interleaved arrays, give three dimensions of multichannel B_1 dependent criteria optimization over an ROI. Proficient and prodigious modeling again is the only way to step through the many permutations possible to find and optimal coil configuration with this design approach. A few examples of the field simulations for these coils, with and without B_1 shimming follow in Figure 13.14.

In Figures 13.14 and 13.15, B_1 and SAR were calculated in a 72 kg male loading two, same-dimension variations of a 16 channel TEM body coil, a "2D" coil with single ring of sixteen, 35 cm long TEM elements, and a "3D" coil with two rings of eight, 17 cm elements with 1 cm spacing between the rings. All results are normalized to a global SAR. The models clearly predict significant B_1 uniformity and dampened SAR peaks achieved with B_1 shimmed, 3D coils over non B_1 shimmed 2D coils. Note the significant improvement in B_1 uniformity predicted over the body for the pair of 3D, B_1 shimmed coils on the far right, while maintaining high efficiency and low peak SAR as measured by the coil B_1 values normalized to a common SAR value.

13.5 HARDWARE DESIGN

As mentioned previously, TEM coils for imaging the body can be broadly segregated into a whole body volume coil (Figure 13.16a) or a surface array (Figure 13.16b). The trade-offs were discussed above. Considering these, one coil must be specified. The functional design and use of both coils is similar, with both coils being based on arrays of transmission line or TEM elements. For brevity and simplicity, the whole body TEM coil will continue to be used for the design example.

13.5.1 Construction Materials and Methods

Construction of a TEM body coil typically begins with a fiberglass tube with enough strength (1 cm thick) for support and of the right dimension for mounting within the bore of the magnet. This tube may serve as the i.d. or o.d. packaging of the coil. It will ideally be attached and supported to stanchions on each end of the magnet bore, allowing room so

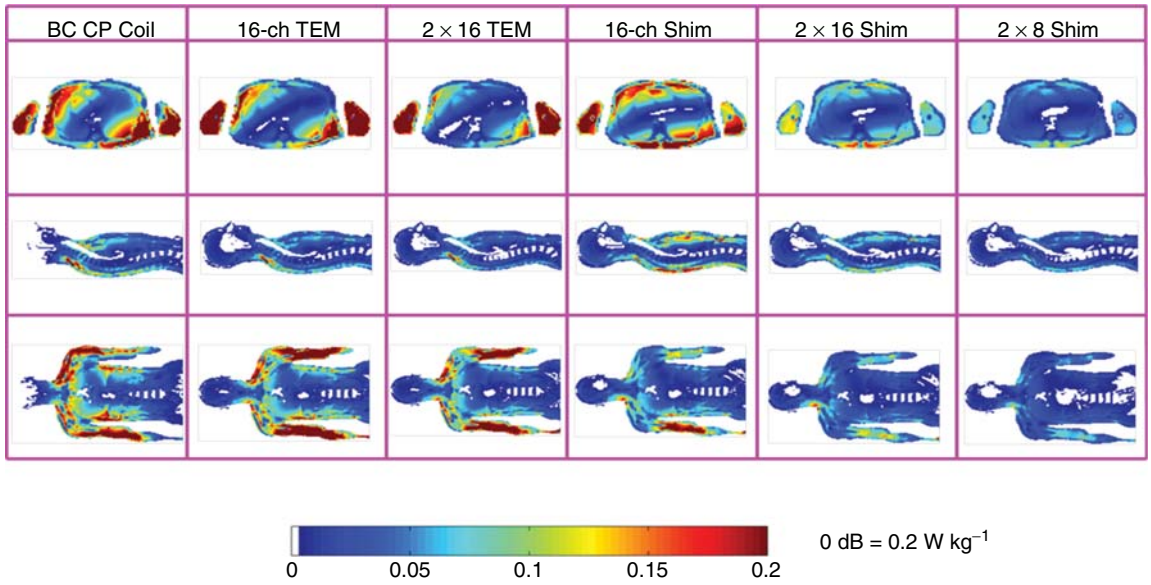

Figure 13.15. SAR calculations for the coil structures and operational conditions (CP, or B_1 shimmed) of Figure 13.13. Each column presents a center-slice transaxial, sagittal, and coronal SAR contour map for each coil. Because all models are normalized to a common SAR value, the contours show the magnitudes of localized "hot spots".

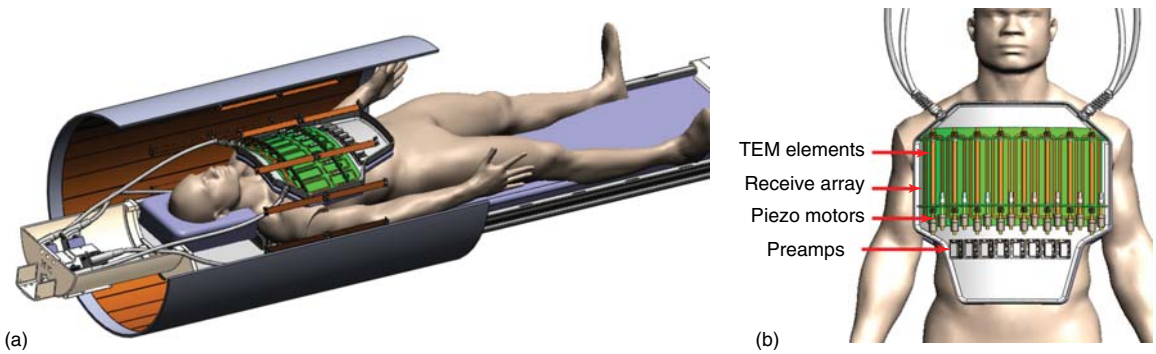

Figure 13.16. Two variations of TEM coils for body imaging are shown, (a) the TEM body coil and (b) the TEM body surface array. The TEM body coil shown is a 2 × 16, 3D configured transmit coil. A separate 2 × 16 loop receiver array is shown on the patient within. The TEM surface array includes 16 transmit channels (8 top, 8 bottom), and 32 receiver array (16 top, 16 bottom). The receiver array also includes piezo motors for remote, auto-tuning, and matching of each TEM coil element.[22]

that the coil assembly does not contact the gradient bore at any point. When this is not possible, add a thin rubber or foam pad between the body coil and the gradient bore tube on which the body coil may rest. An ideal source of the fiberglass tube is from the manufacturer of the system, in the form of the bore tube liner already installed in the MRI system. If this is the tube used, however, there will be very little space between this bore liner and the gradient tube. Manufacturers rarely leave enough room for a shielded body coil, almost never more that 2–3 cm radial space between the bore liner and the gradients. Building a shielded body coil with such a thin profile usually costs the coil in efficiency or mechanical

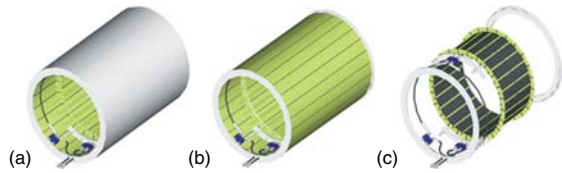

Figure 13.17. The plan for the TEM body coil is shown. (a) The freestanding, packaged body coil without the inner bore liner. In (b), the outer package/cavity support is removed to reveal the slotted TEM cavity wall. Inside and connected to the cavity wall are the current elements shown in (c). A network of two 180° hybrids and 90° quadrature hybrids with cabling is shown driving the coil at four elements 90° apart. The transmit and receive cables for the coil structure are seen projecting from the bottom of the coils.

isolation from the gradients. The coil could possibly be built on the inside of the bore liner tube, but this is often not possible because of limited space and or mounding brackets and other hardware between the bottom of the patient table and the magnet bore liner. Figure 13.17 gives an example of three layers of a TEM body coil that can be slid onto the o.d. of a standard industry bore liner tube

Shown in Figure 13.17(a), an outer package is required to support double-sided, 5 μ thick copper on a polyimide substrate, which is used for the coil cavity. A distinction is made between "cavity" and "shield" here, the cavity being integrated into circuit of the coaxial coil structure. A shield by contrast is separate from the coil circuit and is designed to separate signals between two sources, the gradients and the coil in this case. The TEM cavity wall copper is one skin depth thick for low frequency, switched gradient induced eddy current attenuation. The TEM shield is slotted in straight lines along the cylinder to allow the conductive shield to serve as a return path for the coil center conductors (rungs), but to break up circular eddy current paths induced by the gradient coils. An overlapping pattern is etched in the double clad matrix, with enough capacitance to allow strong RF conductance but to serve as a block to gradient-induced currents.[36] This double-sided, overlapping, capacitive shield can also be "tuned" to balance and cancel mutual inductance between coil elements for strong decoupling without parasitic and field perturbing capacitive bridging for multichannel coils[37] (see Figure 13.18).

The innermost layer of the TEM body coil is the circle of stripline, microstrip, or coaxial line elements.

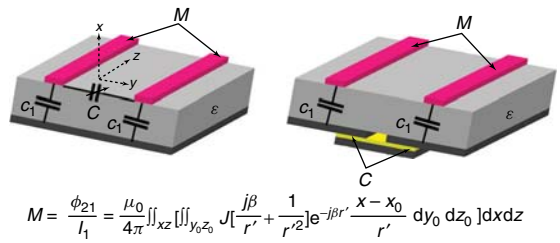

$$M = \frac{\phi_{21}}{I_1} = \frac{\mu_0}{4\pi}\iint_{xz}\left[\iint_{y_0 z_0} J\left[\frac{j\beta}{r'} + \frac{1}{r'^2}\right]e^{-j\beta r'}\frac{x - x_0}{r'}\, dy_0\, dz_0\right] dx\, dz$$

Figure 13.18. Decoupling transmission line elements. (a) A pair of TEM elements decoupled by a bridge capacitor C, creating a parasitic circuit loop that increases loss and local field perturbations in the coil. (b) Two TEM elements with mutual inductance M decoupled by cavity wall capacitance C.

These are capacitively terminated at both ends of each element, to the slotted cavity wall, typically with one element per wall segment. Over the band of MRI body coil frequencies, the most efficient coil will have at least 2.5 cm of air between coaxial elements and the cavity wall segments. The coaxial element is a shielded structure, shielding E field from the patient. A body coil with coaxial elements will measure higher Q and 1–2 dB more B_1 field per watt input, compared to a coil built with unshielded stripline or microstrip elements. However, a low loss coaxial element will add an additional 1.5 cm or so to the profile of a coil. While the most efficient coil has a radial profile of 4 cm, packaging not included, most MRI systems allow about half of this space. This is why stripline or microstrip on a Teflon dielectric core are frequently used for the thin although less efficient body coils that will fit most industry systems. Nylon makes a good structural material for the rings and other structural material in the coil. Although a bit "slippery" to machine, it does not crack like many plastics and it has virtually no NMR signal.[38]

The body coil element can range in length from 45 to 14 cm. A longer coil would generate an unnecessarily long field that will often create a signal wrap artifact from signal received from beyond the gradient coils. Elements shorter than 12 or 14 cm become inefficient. The author prefers to work with elements of 22–18 cm length for a 60 cm i.d. coil with an 80 cm × 120 cm long cavity when possible.

13.5.1.1 Body Coil Control

A TEM body coil is more than a passive resonator. Depending on the application, there are many options for mode of operation and control for this

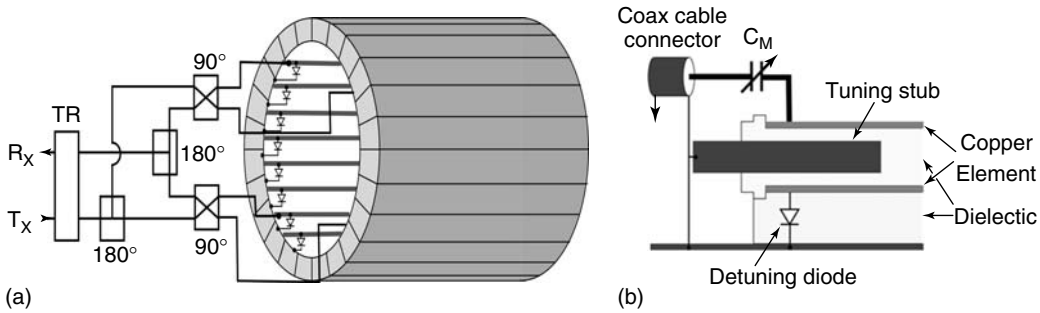

Figure 13.19. The actively detunable TEM body coil (a), with a four port quadrature drive circuit and TR switch interfacing the coil to the RF transmitter and receiver paths in the MR system. (b) Shows how a coaxial signal cable can be connected to a driven element, and how this element is tuned via the stub and detuned by the actively switched diode.

structure. For conventional, clinical (0.5–3.0 T) MRI systems with a single channel power amplifier, a TEM design with 16–32 inductively coupled elements is a very efficient body coil. In this application, this structure prefers to be driven in circular polarization at four points as shown in Figure 13.19(a). Figure 13.19(b) shows how the drive cable is attached to the end of a coaxial element with a tuning stub. These stubs are adjusted in concert to tune the frequency of a coil, or differentially to shim the RF field of the coil to optimize the coil's uniformity at a fixed position in response to image signal feedback.

As a body transmit coil, the TEM body coil must be actively detuned during the receive period when used with receiver coils. This is standard clinical protocol. Actively controlled PIN diode circuits (MA4Pk2002, M/A-COM), tune and detune the body coil for transmit and array receive functions, respectively. While the detuning diodes are shown in the shunt position, series diodes may be alternatively used to meet the requirements for many modern systems. Positive DC bias signals for the diodes are supplied with a single wire epoxied along each cavity segment from a manifold at the end of the coil. Stud mounted diodes are threaded into a copper washer,

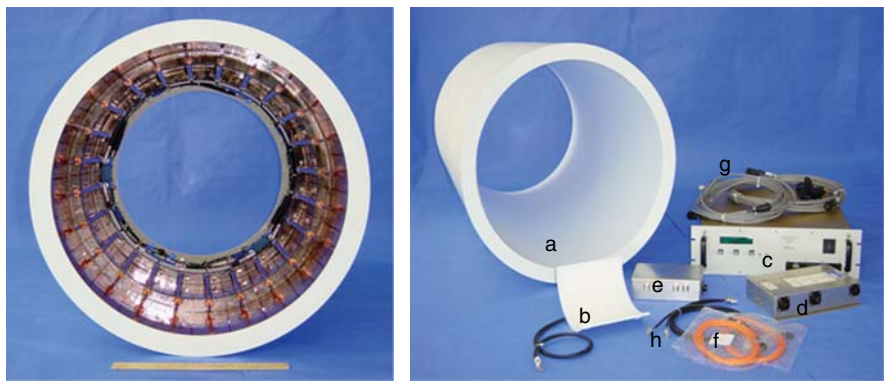

TEM body coil with elements exposed

Packaged TEM body coil with system components

Figure 13.20. The constructed TEM body coil is shown together with the complementary front-end equipment required for implementation and application of the active body coil and multi-channel receiver system. Included in the system are the homogeneous transmit coil (a), the multichannel receiver coil (b), the coil power supply and control unit (c), the optically triggered, nonmagnetic PIN diode driver unit (d), the nonmagnetic, multichannel preamplifier (e), and all of the necessary fiber optic control lines (f), power supply lines (g), and RF signal cables (h).

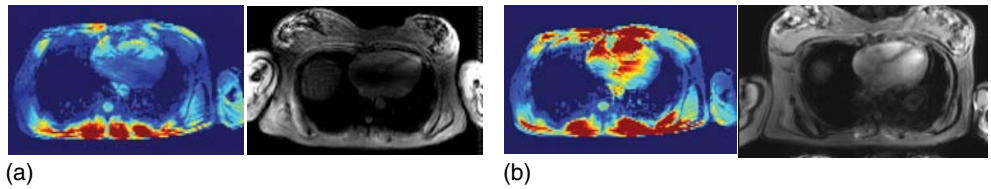

Figure 13.21. B_1 Shimming. (a) Includes an unshimmed B_1 map and image at 7 T. (b) Shows a B_1 map and image following B_1 shimming, using a TEM surface coil at 7 T.

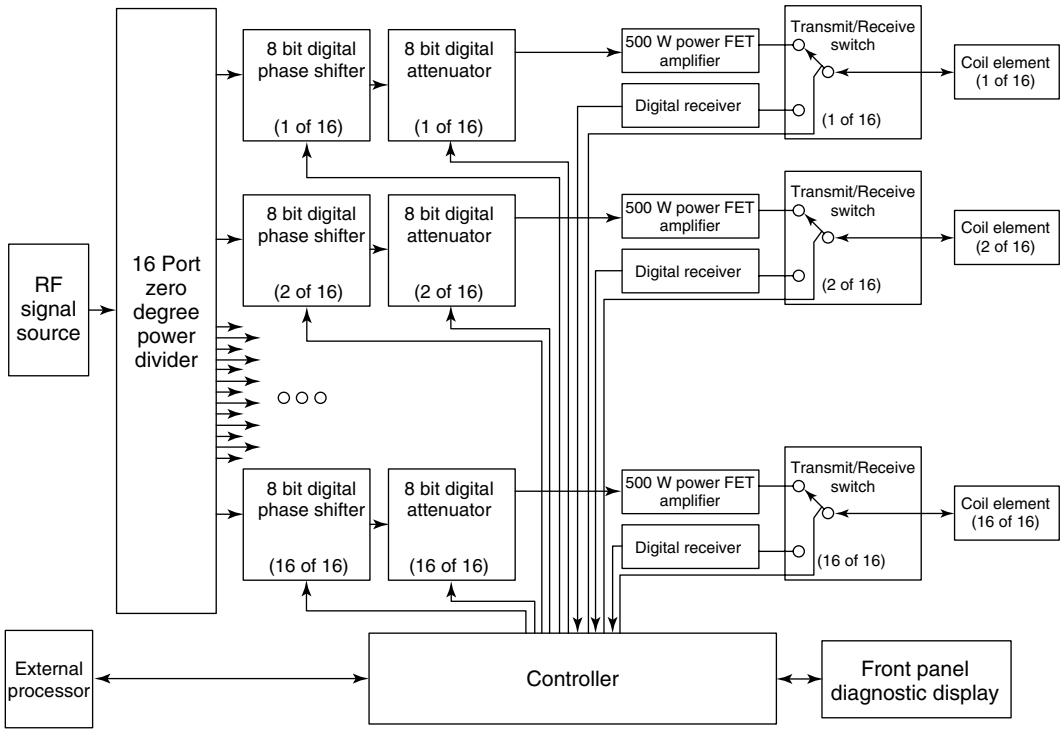

Figure 13.22. Parallel transceiver RF front end. This system capable of controlling phase, magnitude, frequency, space and timing of transmit, and/or receive signals, interfaces to a multichannel TEM coil.

or an old penny, which is in turn soldered to the cavity wall segment. This gives ample heat sink for the diodes that are operated at 100–200 mA each. Detuning every element by this approach provides for robust detuning.

13.5.1.2 Body Coil System

An actively detuned TEM body coil system together with its RF front-end interface components is shown in Figure 13.20. This complete RF front-end system employed the actively detuned TEM body coil for NMR signal excitation together with local receiver coils of the phased array and parallel array type. Not shown are the high power, nonmagnetic transmit/receive (TR) switches that completed the RF front end.[39]

In addition to improved RF circuit efficiency, dynamic control of RF currents and generated B_1 fields is a reason to choose TEM or other coil arrays over conventional monolithic resonator circuits. By controlling coil circuit currents at the individual coil element level, the B_1 transmit field can be manipulated or "shimmed" over five degrees of

freedom, namely magnitude, phase, frequency, space, and time.[36,40] Individual coil element currents are typically controlled by injecting a modulated transmit signal at each element, resulting in multiple transmit (and receive) channels driving the multielement or multichannel coil. B_1 shimming, whether interactive or algorithmic, is required to optimize the B_1 transmit field for B_1-dependent NMR parameters (uniformity, SNR, SAR, etc.) over a localized region of interest in the human head or body at high frequencies. Figure 13.21 gives an illustrative example of how adjusting relative phase angles in a simple eight channel TEM coil can be used to improve a heart image at 7 T.

Multichannel TEM body coils require a multichannel system to drive the coils. Figure 13.22 is a first example of such a system,designed and built in 2003 for the first 9.4 T human imaging experiments.[36,41,42] From left to right in the figure, this 16 channel, parallel transceiver system was designed to convert a single power amp into 16 transmit channels by mean of a 1×16 power splitter. New research systems are now offered with eight or more programmable frequency synthesizers directly feeding channel dedicated RF power amps, 2 kW each. Frequency can be adjusted at this stage. Next in line for each channel are the programmable phase shifters and programmable attenuators for programmable phase and gain control. Moving along each channel to the right of Figure 13.22, we reach the TR switch, capable of controlling space and time. With the TR switch and active detuning in the coil, different coil elements can be switched in and out to control spatial field patterns about the body. All of the elements from the frequency synthesizer to a pulse programmer, phase and gain controller, and TR switch can be used to modulate an RF signal in time. Such a flexible and versatile RF front end facilitating so many degrees of freedom for RF field manipulation at the coil is bringing new approaches to MR imaging. Combined with the parallel receive chain makes for an even more powerful MRI system–coil interface.

13.6 BENCH TESTING AND EVALUATION

Examples of bench tests for actual TEM body coils follow. A 56 cm i.d. TEM body coil was tuned and evaluated at 128 MHz (3 T), 170 MHz (4 T), and at 347 MHz (8 T+) on the electronics test bench. A network analyzer was used to measure the S11 reflection and S12 transmission characteristics for each coil. The S11 spectra shown (Figure 13.23) demonstrate that each body coil was easily tuned and well matched at the respective operational frequencies indicated. The characteristic transverse field mode for number N runged TEM coils is the second lowest in a spectral field of $N/2 + 1$ resonant modes for the coil.[2] Relative coil circuit efficiency was determined by measuring Q ratios and B_1 gains with a field probe. Tuned and matched to 128 MHz, the unloaded to 75 kg subject loaded coil Q ratio was $Q_u/Q_l = 740/50$, and at 170 MHz the ratio was 720/40. The Q measurements for a single coil at 344 MHz were $Q_u/Q_l = 520/30$. The high Q values for the unloaded TEM body coil can be observed as the narrow line widths of the S_{11} spectra below. The lines are too narrow in fact to show the full −50 dB impedance match conditions reached by the resolution allowed by the full spectral bandwidth of the S_{11} plots. The relative B_1 gain of each coil was determined by the S_{12} measurement obtained by driving the body coil with a calibrated transmit power input and receiving the B_1 field generated with a calibrated field probe placed in the center of the body coil, and aligned with the field for maximum signal. It is significant to note that the B_1 gain was preserved for the TEM body coil, from 128 MHz (3 T) to at least 342 MHz (8 T). Also notable is the fact that B_1 field contributions from resonances adjacent to the transverse field mode are negligible. According to these network measurements, the full-sized TEM body coil is efficient and well behaved up to 8 T.

13.6.1 Test and Evaluation

Before a coil or array is put into service, it is rigorously tested, evaluated, and characterized both on the bench and in the magnet. Coil resonance, Q, and isolation, in both the loaded and unloaded condition as well as dynamic detuning are verified on the bench. In the magnet, coil coupling, image homogeneity, transmit efficiency, and SNR are characterized. Unfortunately, for high-field coils these conventional metrics are often insufficient to completely characterize and describe the transmit degrees of freedom, spatially varying characteristics of the coils, and the potential synergy of RF coil fields and imaging methodology.

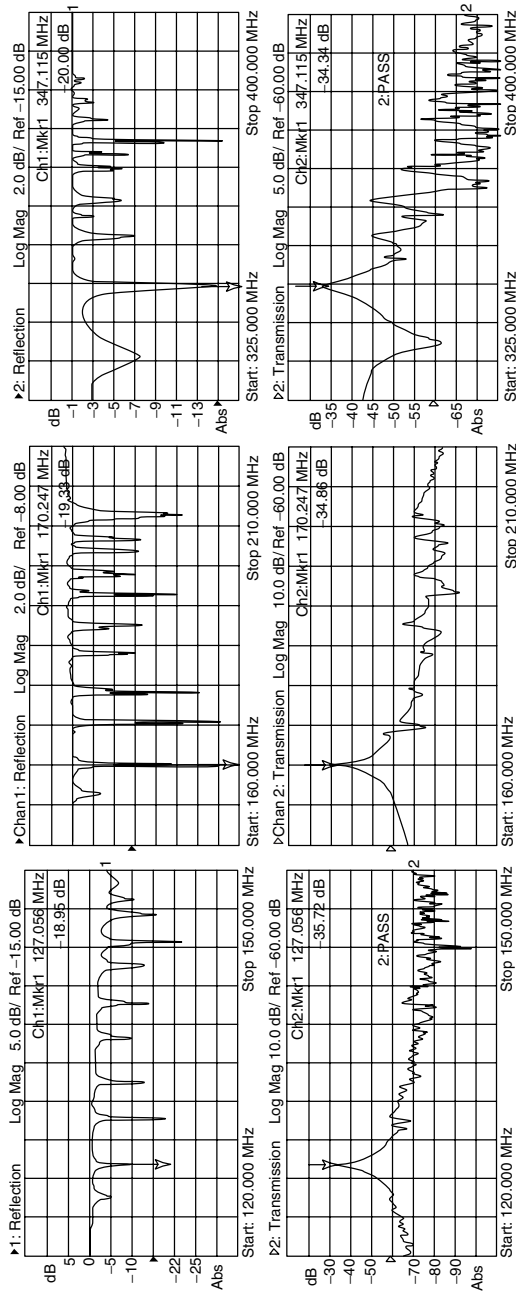

Figure 13.23. RF spectra are shown for the TEM body coil at 128 MHz, S11 (top), S12 (bottom) (a); 170 MHz, S11 (top), S12 (bottom) (b); and 348 MHz, S11 (top), S12 (bottom) (c). On the bench, the TEM body coil is easily tuned and matched upward to 350 MHz (8 T).

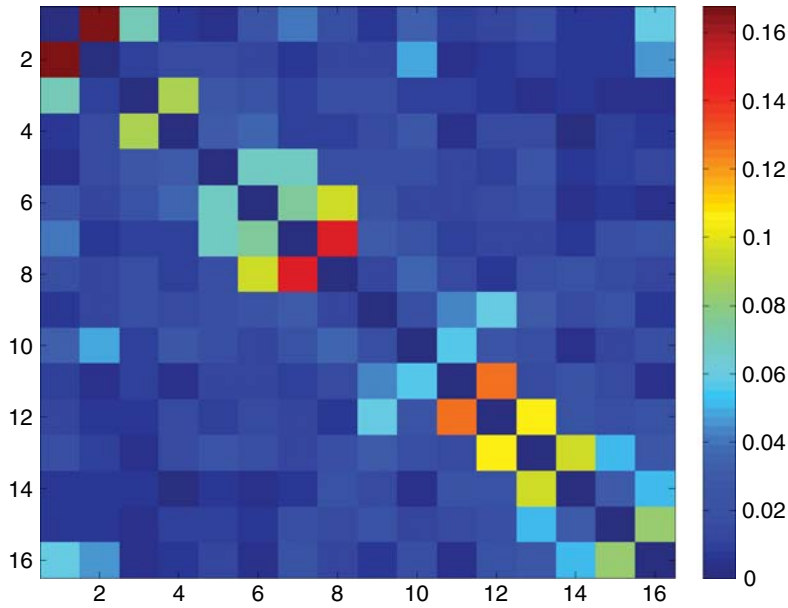

Figure 13.24. The noise covariance matrix. The loaded coil is computed from the collected noise data. B_1^+ shimming calibration data is then acquired.

More characterization is needed. The noise covariance matrix,[43] Figure 13.24, of the loaded array is computed from the collected noise data. B_1^+ shimming calibration data is then acquired.[44] Individual receiver data is used to calculate receiver-sensitivity maps and geometry-factor maps,[43] The magnitude of the B_1^+ is mapped with two fully relaxed gradient echo images collected with excitations nominally set to 60° and 120° (double angle method).[45] Additionally, the 60° excitation gradient echo image is carefully post-processed so that the result is in SNR units.[46] Using the B_1 map, the SNR image, and acquisition parameters, the SNR image is converted into intrinsic SNR units, which describes receiver performance independent of transmit performance (Figure 13.14d).[47] By combining the above data, single-channel transmit field maps can be synthesized to predict the transmit efficiency for any B_1^+ shim. The transmit efficiency versus transmit homogeneity can then be calculated for a region and reported for the constraints of 90%, 80%, and 70% transmit homogeneity. EM modeling is used to predict the SAR, change in temperature, and absolute temperature, (Figure 13.12). Imaging five volunteers for each coil would be sufficient to report a coil's characteristics statistically. However, optimizing a coil prototype is an iterative process often requiring additional volunteers per coil. This coil characterization provides the information needed to predict parallel acceleration performance, transmit efficiency, transmit homogeneity, and the SNR for an arbitrary imaging sequence.

13.7 SAFETY

13.7.1 Testing and Evaluation

Before a body coil is used in human studies, it should be verified "safe" on live, anesthetized, human adult sized pigs. In this experiment, an anesthetized pig is placed within an RF body coil. Fluroptic temperature probes are inserted into model directed hot regions of the pig. An RF pulse protocol is applied to the pig-loaded coil, and temperature vs time is recorded and correlated. In the body coil safety power calibration experiment, RF power is gradually increased until the Food and Drug Administration (FDA) temperature guideline (2°C above core for body) is identified. With temperature correlated to SAR, the RF

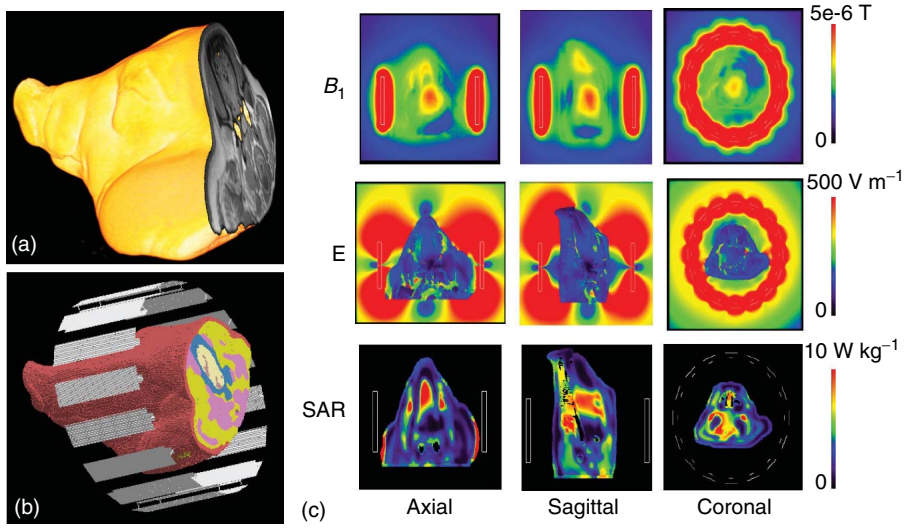

Figure 13.25. In the model above, (a) shows a pig's head rendered from MR images. (b) A FDTD model of the pig head with segmented anatomy in a TEM coil. (c) The center slice B_1 fields, E fields, and SAR in 3D.

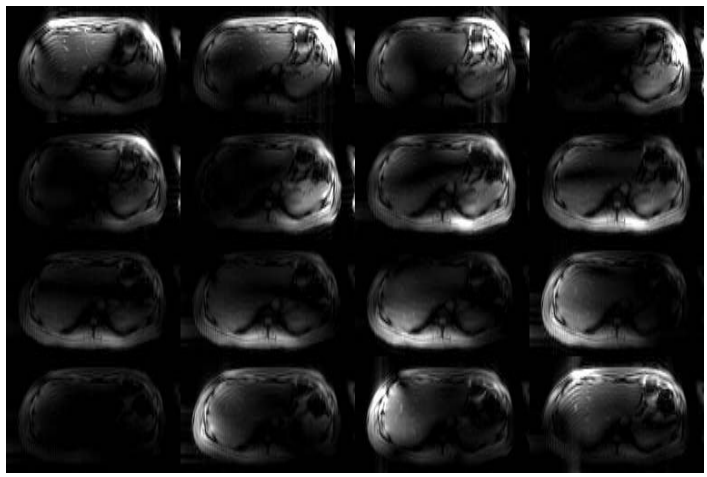

Figure 13.26. This Fast Low Angle SHot (FLASH) data set was acquired with the 16 channel, whole body TEM Coil shown in Figure 13.6. Each image was acquired with a single, different coil element: 16 unique images for 16 unique elements. A data set like this is acquired to assure all coil elements are operational.

power output of each transmit channel can be monitored for temperature safety compliance. The farm pig is recommended by the World Health Organization for hyperthermic studies because of relative similarities between human's and pig's mass, skin, and physiology. RF heating (the actual safety issue) can be calculated and measured in porcine models of adult human weight to identify the RF power level limit that can be safely transmitted from a particular body coil (see Figure 13.25). The FDA has specified guidelines for RF energy dosimetry to the human body in two ways: (i) average and local SARs as discussed above or (ii) RF-power deposition must not create a core temperature increase in excess of 1 °C or localized heating to greater than 38 °C in the head, 39 °C in the torso or 40 °C in the

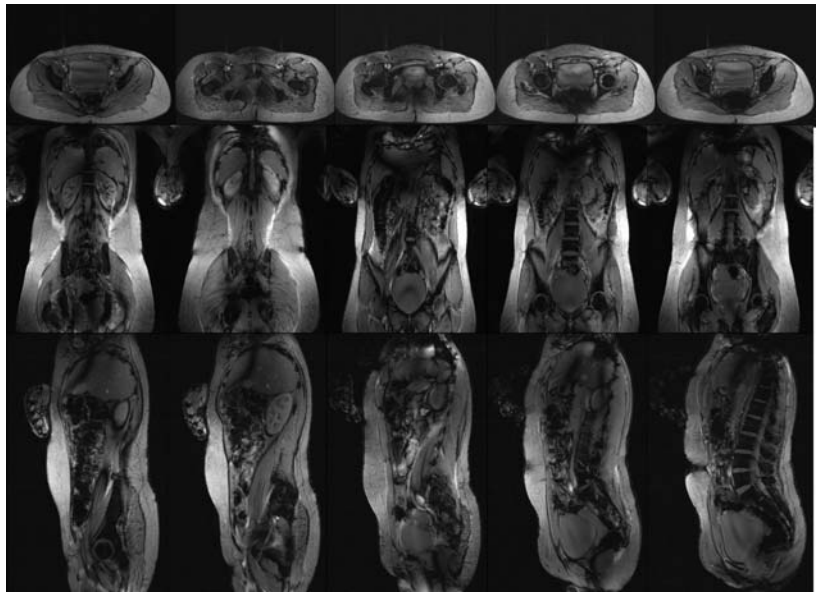

Figure 13.27. A full 3D data set is shown here with five transaxial, five coronal, and five sagittal images from the length of the torso. These were also acquired with the Figure 13.6, 16 channel TEM body coil in transmit and receive mode with B_1 shimming and by the following protocol: GRE, Res $= 1 \times 1 \times 5$, repetition time (TR)/echo time (TE) $= 60/5$, Nom flip $= 120$, acq $= 14$ s, FOV $= 300 \times 440$, Nex $= 2$, SAR $< 2\,\mathrm{W\,kg^{-1}}$. The images are quite uniform with the main artifacts being from susceptibility gradients around the bowel and lungs.

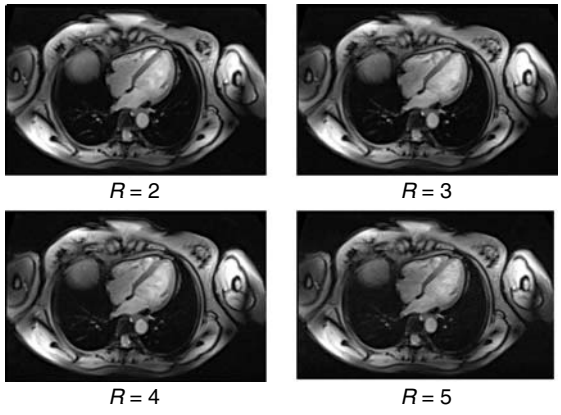

Figure 13.28. The heart is perhaps the toughest organ to image and this one is from the most challenging field strength tried, 7 T. These cine frames at increasing R values are gradient echo images acquired with the 16 channel TEM body coil of Figure 13.6, with B_1 shimming, and the 32 channel receiver also shown in Figure 13.6.

extremities. Equating the power loss density or SAR to temperature through the bioheat equation, predictive temperature contours can be calculated for 3D body models as well.[48] It is realized that many coil builders reading this chapter will not have access to or regulatory approval for animal studies. Phantom testing should be performed instead to characterize the electro dynamic and thermal safety qualities of a coil.

13.7.2 Safety Assurance Implementation

To assure human safety with body coil use, system power monitors must be set using either (i) FDA SAR guideline limits for head and body or (ii) measured SAR values correlated to FDA temperature guideline limits, whichever is the lower value. In this manner, the more conservative practice will be applied. RF power can be monitored per channel in multichannel transceiver coils. To monitor forward and reverse power for an 8 element coil will ideally require a 16 channel power meter although fewer meters could be switched between channels. Any such safety system should be hardwired into a fail-safe feedback loop within the MRI system. A priori information can be determined from SAR and temperature modeling

and measurement, and used to establish and set RF power limits, per coil, load, and power setting for a given experiment. Additionally, when any preset limit is exceeded on single or multiple elements, a redundant failsafe will blank RF power input and will disconnect the power supply to all power amplifiers.

13.8 BODY COIL APPLICATIONS

This chapter ends with Figures 13.26–13.28 demonstrating the safe and successful application of the first and to date only whole body, multichannel body coil at 7 T. These results should give confidence to the reader that these coils operate safely and successfully, even at the most extreme 7 T limits. Most design approaches and considerations presented for body coils in this chapter are equally defective for head coils and may pave the way for human head imaging at the highest fields contemplated. For example in wavelength dimension, a 7 T body coil scales to a head coil at 15 T.

ACKNOWLEDGMENTS

NIH-R01 EB000895, NIH-R01 EB006835, NIH-R01 EB007327, NIH-P41 RR08079

RELATED ARTICLES IN THE ENCYCLOPEDIA OF MAGNETIC RESONANCE

Birdcage Resonators: Highly Homogeneous Radiofrequency Coils for Magnetic Resonance

Coils for Insertion into the Human Body

Multifrequency Coils for Whole Body Studies

Radiofrequency Fields: Interactions, Biological Effects, and Safety Issues

Radiofrequency Systems and Coils for MRI and MRS

Refrigerated and Superconducting Receiver Coils in Whole Body Magnetic Resonance

Spatial Encoding Using Multiple rf Coils: SMASH Imaging and Parallel MRI

Surface and Other Local Coils for In Vivo Studies

Surface Coil NMR: Detection with Inhomogeneous Radiofrequency Field Antennas

Whole Body Machines: NMR Phased Array Coil Systems

REFERENCES

1. J. T. Vaughan, H. P. Hetherington, J. Harrison, J. Otu, J. L. W. Pan, P. Noa, J. A. den Hollander, and G. M. Pohost, *Phys. Med.*, 1993, **IX**, 7.
2. J. Vaughan, H. Hetherington, J. Otu, J. Pan, and G. Pohost, *Magn. Reson. Med.*, 1994, **32**, 206.
3. C. E. Hayes, W. A. Edelstein, J. F. Schenck, O. M. Mueller, and M. Eash, *J. Magn. Reson.*, 1985, **63**, 622.
4. J. T. Vaughan, G. Adriany, C. Snyder, J. Tian, T. Thiel, L. Bolinger, H. Liu, L. DelaBarre, and K. Ugurbil, *Magn. Reson. Med.*, 2004, **52**, 851.
5. E. Purcell, H. Torrey, and R. Pound, *Phys. Rev.*, 1946, **69**, 37.
6. H. Schneider and P. Dullenkopf, *Rev. Sci. Instrum.*, 1977, **48**, 68.
7. N. Krause, 'Siemens Aktiengesellschaft, Munich, Assignee. High Frequency Field System for Nuclear Magnetic Resonance apparatus, USA', 1985.
8. P. Röschmann, 'Philips, Assignee. High-Frequency Coil System for a Magnetic Resonance Imaging Appartus, USA', 1988.
9. J. Bridges, 'Cavity Resonator with Improved Magnetic Field Uniformity for High Frequency Operation and Reduced Dielectric Heating in NMR Imaging Devices, USA', 1988.
10. B. Baertlein, O. Ozbay, T. Ibrahim, R. Lee, Y. Yu, A. Kangarlu, and P. Robitaille, *IEEE Trans. Biomed. Eng.*, 2000, **47**, 535.
11. X. L. Zhang, K. Ugurbil, and W. Chen, *Magn. Reson. Med.*, 2001, **46**, 443.
12. B. Beck, D. Plant, S. Grant, P. Thelwall, X. Silver, T. Mareci, H. Benveniste, M. Smith, C. Collins, and S. Crozier, *MAGMA*, 2002, **47**, 579.
13. G. Bogdanov and R. Ludwig, *Magn. Reson. Med.*, 2002, **47**, 579.
14. J. J. T. Vaughan, UAB Research Foundation, assignee. Radio frequency volume coils for imaging and spectroscopy. U.S. Pat. 5,886,596 (March 23, 1999).

15. K. Ugurbil, G. Adriany, P. Andersen, W. Chen, M. Garwood, R. Gruetter, P. G. Henry, S. G. Kim, H. Lieu, I. Tkac, T. Vaughan, P. F. Van de Moortele, E. Yacoub, and X. H. Zhu, *Magn. Reson. Imaging*, 2003, **21**, 1263.
16. K. S. Kunz and R. J. Luebbers, *The Finite Difference Time Domain Method for Electromagnetics*, CRC Press: Boca Raton, 1993, p. 448.
17. J. T. Vaughan and D. Myer, 'RF Coil Element Mounted Power Amplifiers', Montreal, 2011.
18. C. J. Snyder, L. DelaBarre, G. J. Metzger, P. F. van de Moortele, C. Akgun, K. Ugurbil, and J. T. Vaughan, *Magn. Reson. Med.*, 2009, **61**, 517.
19. G. J. Metzger, C. Snyder, C. Akgun, T. Vaughan, K. Ugurbil, and P. F. Van de Moortele, *Magn. Reson. Med.*, 2008, **59**, 396.
20. C. Snyder, C. Rogers, L. DelaBarre, M. Robson, and J. T. Vaughan, In *Proceedings of the 19th Annual Meeting of ISMRM. Montreal*, Quebec, 2011. (Accepted as an e-poster).
21. S.-M. Sohn, A. Gopinath, and J. T. Vaughan, 'Electrically Auto-Tuned RF Coil Design', Montreal, Quebec, 2011.
22. C. Snyder, L. DelaBarre, J. Tian, C. Akgun, and J. T. Vaughan, 'Using Piezoelectric Actuators for Remote Tuning of Transmit Coils', Stockholm, 2010, p. 1523.
23. C. J. Snyder and J. T. Vaughan, 'Remotely Adjustable Reactive and Resistive Electrical Element and Method', Appl. 61/158345 2009.
24. C. Snyder, L. DelaBarre, G. Metzger, K. Ugurbil, and J. T. Vaughan, In *Proceedings of the 19th Annual Meeting of the ISMRM* , Montreal, 2011, (Accepted as Oral Presentation).
25. J. T. Vaughan, C. J. Snyder, L. J. DelaBarre, P. J. Bolan, J. Tian, L. Bolinger, G. Adriany, P. Andersen, J. Strupp, and K. Ugurbil, *Magn. Reson. Med.*, 2009, **61**, 244.
26. C. Snyder, L. DelaBarre, J. Tian, C. Akgun, G. Metzger, S. Moeller, K. Ugurbil, and J. Vaughan, *Using Separated Volume Transmit and Local Receiver Arrays for Body Imaging at 7 T*, ISMRM: Honolulu, April 2009, p. 4761.
27. REMCOM. 'XFDTD EM Field Modeling Software', State College.
28. T. Vaughan, L. DelaBarre, C. Snyder, S. Mangia, J. Tian, M. Waks, S. Shillak, L. Petropoulos, G. Adriany, P. Andersen, J. Strupp, and K. Ugurbil, 'Whole Body Imaging at 7 T with a 16 Channel Body Coil and B1 Shimming', Toronto, April 2008, p. 152.
29. J. T. Vaughan, C. J. Snyder, L. J. DelaBarre, and K. Ugurbil, 'RF Coil Designs for 7 T Cardiac Imaging', Stockholm, 2010.
30. J. T. Vaughan, C. Snyder, L. Delabarre, J. Tian, G. Adriany, P. Andersen, J. Strupp, and K. Ugurbil, 'Clinical Imaging at 7 T with a 16 Channel Whole Body Coil and 32 Receive Channels', Honolulu, April 2009, p. 391.
31. J. T. Vaughan, in *Ultra High Field Magnetic Resonance Imaging*, eds P. Robitaille and L. Berliner, Springer: New York, 2006, Vol. 26, pp. 127.
32. F. Duck, *Physical Properties of Tissue*, Academic Press: London, 1990.
33. X. SEMCAD, 'Reference Manual for the SEMCAD X Simulation Platform for Electromagnetic compatibility, Antenna Design, and Dosimetry', 2006, Version 11.0.
34. D. Shrivastava and J. T. Vaughan, *J. Biomech. Eng.*, 2009, **131**, 074506.
35. D. Shrivastava and J. T. Vaughan, 'Development of an Anatomically Accurate Porcine Head Model to Study Radiofrequency Heating due to MRI', Stockholm, 2010.
36. J. Vaughan, Massachusetts General Hospital, assignee. RF coil for imaging system. U.S. Pat. 6,633,161, 2003.
37. J. T. Vaughan and J. Tian, 'Regents of the University of Minnesota, Assignee. Coil Element Decoupling for MRI'. (April 22, 2010).
38. M. Marjanska, M. Waks, C. J. Snyder, and J. T. Vaughan, *Magn. Reson. Med.*, 2008, **59**, 936.
39. J. T. Vaughan, G. Adriany, M. Garwood, E. Yacoub, T. Duong, L. DelaBarre, P. Andersen, and K. Ugurbil, *Magn. Reson. Med.*, 2002, **47**, 990.
40. T. Vaughan, L. DelaBarre, C. Snyder, J. Tian, C. Akgun, D. Shrivastava, W. Liu, C. Olson, G. Adriany, J. Strupp, P. Andersen, A. Gopinath, P. F. van de Moortele, M. Garwood, and K. Ugurbil, *Magn. Reson. Med.*, 2006, **56**, 1274.
41. J. Vaughan, G. Adriany, K. Ugurbil, P. Andersen, and J. Strupp, 'University of Minnesota, assignee. Parallel Transceiver for Nuclear Magnetic Resonance System. USA', 2005.
42. J. T. Vaughan, L. DelaBarre, C. Snyder, J. Tian, P. Andersen, J. Strupp, G. Adriany, P. F. van de Moortele, and K. Ugurbil, *9.4 T Human Imaging: Preliminary Results*, ISMRM: Seattle, 2006, p. 529. (ISMRM).

43. K. P. Pruessmann, M. Weiger, M. B. Scheidegger, and P. Boesiger, *Magn. Reson. Med.*, 1999, **42**, 952.

44. P. F. Van de Moortele, C. Akgun, G. Adriany, S. Moeller, J. Ritter, C. M. Collins, M. B. Smith, J. T. Vaughan, and K. Ugurbil, *Magn. Reson. Med.*, 2005, **54**, 1503.

45. E. Insko and L. Bolinger, *J. Magn. Reson., Ser. A*, 1993, **102**, 82.

46. P. Kellman and E. R. McVeigh, *Magn. Reson. Med.*, 2005, **54**, 1439.

47. G. Adriany, P.-F. Van de Mortele, F. Wiesinger, S. Moeller, J. Strupp, P. Andersen, C. Snyder, X. Zhang, W. Chen, K. Pruessmann, P. Boesiger, J. Vaughan, and K. Ugurbil, *Magn. Reson. Med.*, 2005, **53**, 434–445.

48. C. M. Collins, W. Z. Liu, J. H. Wang, R. Gruetter, J. T. Vaughan, K. Ugurbil, and M. B. Smith, *J. Magn. Reson. Imaging*, 2004, **19**, 650–656.

Chapter 14
TEM Arrays, Design and Implementation

Carl Snyder

Department of Radiology, Center for Magnetic Resonance Research, University of Minnesota, Minneapolis, MN 55455, USA

14.1 INTRODUCTION

Transverse electromagnetic (TEM) resonators and arrays are aptly named, as they are any coil or resonators that excite a TEM mode. There are many different implementations of the TEM coil and array, with common examples being named microstrip or stripline arrays,[1] TEM arrays,[2] transmission line arrays,[3] planar strip arrays,[4] and lumped-element planar strip arrays.[5] TEM arrays can also include such structures as coplanar strips, two-wires, or coaxial resonators.[6] These arrays are important because they have been used extensively for head,[3] cardiac,[7] prostate,[8,9] endometrial,[10] and liver[11] imaging at ultra-high fields.

Since the microstrip array is one of the easiest and most common TEM arrays to design and implement, microstrip arrays are discussed exclusively. In this chapter, we discuss the theoretical and practical/experimental aspects of designing a singular microstrip coil and how to incorporate an optimized microstrip coil into a multichannel microstrip array.

RF Coils for MRI
Edited by J. Thomas Vaughan and John R. Griffiths

ISBN: 978-0-470-77076-4

14.2 THEORETICAL CONSIDERATIONS

14.2.1 General Configuration

Figure 14.1(a) shows the TEM microstrip resonator. It consists of a center conductor with width (w_c), separated from the ground plate with width (w_g) by a dielectric of height (h). The dielectric between the center and ground conductors has a relative permittivity (or "dielectric constant") ε_r. The overall resonator length is (l). Both the center conductor and the ground plate have a certain thickness (t); however, it is assumed to be negligible ($t/h < 0.005$).

Figure 14.1(b) shows the electric and magnetic fields (E- and H-fields, respectively) when the microstrip resonator is propagating in the TEM mode. The sketch of the field lines shows that the majority of the E-field is localized inside the dielectric, whereas the H-field propagates beyond, outside of the strip. If the relative permittivity of the dielectric is greater than 1, then the microstrip will, strictly speaking, propagate a quasi-TEM mode. The quasi-TEM mode or hybrid TM–TE mode propagation occurs because the phase velocity above the center conductor, in free space, will be the speed of light c, whereas the phase velocity below the

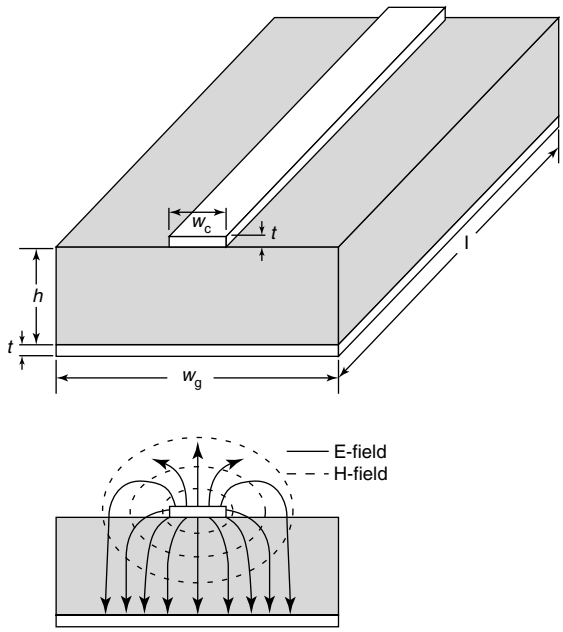

Figure 14.1. The basic microstrip structure. (a) w_c is the conductor strip width; w_g is the ground conductor width; t is the conductor thickness; h is the dielectric height; and l is the length of the resonator. (b) shows the electric (E-field) and magnetic field (H-field). Note that how most of the electric field is contained within the dielectric, while magnetic field extends both above and into the dielectric.

center conductor, in the dielectric, will be $c/\sqrt{\varepsilon_r}$. This discontinuity in the phase velocity between free space and the dielectric can create longitudinal E- and H-fields, ($E_z \neq 0$; $H_z \neq 0$). These longitudinal fields are small relative to the transverse fields and the overall phase velocity of the microstrip is $c/\sqrt{\varepsilon_e}$, where ε_e can be approximated as

$$\varepsilon_e = \frac{\varepsilon_r + 1}{2} + \frac{\varepsilon_r - 1}{2}\left(\frac{1}{\sqrt{1 + 12\left(\frac{h}{w_c}\right)}}\right) \qquad (14.1)$$

14.2.2 Characteristic Impedance

Microstrip resonators can only propagate a TEM or quasi-TEM mode when the characteristic impedance, Z_0, is between 20 and 120 Ω. Impedances lower than this propagate higher order modes and impedances higher than this in MRI coils will most probably violate the microstrip assumption that the transverse dimensions are much less than half the wavelength in the dielectric. The characteristic impedance of a microstrip is

$$Z_0 = \frac{60}{\sqrt{\varepsilon_e}} \ln\left(8\frac{h}{w_c} + \frac{w_c}{4h}\right) \qquad \text{when } w_c/h < 1 \qquad (14.2)$$

or

$$Z_0 = \frac{120\pi}{\sqrt{\varepsilon_e}\left[\frac{w_c}{h} + 1.393 + \frac{2}{3}\ln\left(\frac{w_c}{h} + 1.444\right)\right]} \qquad \text{when } w_c/h > 1 \qquad (14.3)$$

14.2.3 Resonance Condition

In order to reach resonance, a microstrip needs to be either $\lambda/4$ or $\lambda/2$ in length and can be either open- or short circuited. Practically, $\lambda/2$ open-circuit resonators provide the greatest B_1 field and sensitivity at the center of the coil and are, therefore, predominantly used for all MR imaging and spectroscopy. $\lambda/4$ and short-circuited resonators are only employed when an asymmetric field is wanted or necessary.

While Lee[4] has previously shown the use of true $\lambda/2$ microstrip resonators, their long lengths (~2.35 m at 1.5 T or 0.5 m at 7 T with an $\varepsilon_r = 1$) are impractical to implement. While the use of dielectrics with high relative permittivities has been proposed in order to reduce the length of the microstrip resonator, it is more practical to use shunt capacitors to reduce the electrical length.

14.2.4 Tuning and Matching Conditions for the Capacitively Shunted Microstrip Resonator

The input impedance of the capacitively shunted microstrip shown in Figure 14.2 is

$$Z_{IN} = \frac{Z_{C_1} Z_0 (Z_{C_2} + j Z_0 \tan(\beta l))}{Z_0 (Z_{C_1} + Z_{C_2}) + j (Z_{C_1} Z_{C_2} + Z_0^2) \tan(\beta l)} \qquad (14.4)$$

where $Z_{C_1} = 1/j\omega C_1$, $Z_{C_2} = 1/j\omega C_2$, and β is the phase constant.

$$\beta = \frac{\omega_0 \sqrt{\varepsilon_e}}{c} \qquad (14.5)$$

where c is the speed of light and $\omega_0 = 2\pi f$ is the angular Larmor frequency.

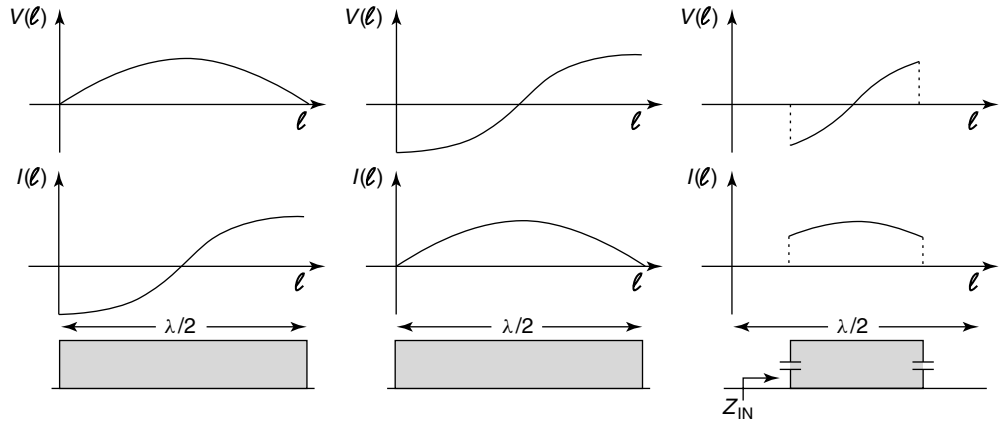

Figure 14.2. The voltage and current distributions along the length of a microstrip resonator for (a) a short-circuited microstrip, (b) an open-circuited microstrip, and (c) a capacitively shunted microstrip. Owing to the current distribution along the short-circuited microstrip (a) the magnetic field generated from this resonator will be asymmetric, while the open-circuited (b) and capacitively shunted (c) microstrip will generate a symmetric field along the length of the resonator.

In the case of the microstrip resonator, both discrete capacitors should be equivalent ($Z_{C_1} = Z_{C_2}$ and $C_T = C_1 = C_2$). Different capacitive values will lead to an asymmetric magnetic field, along the length of the resonator with the region of the greatest magnetic field strength being shifted toward the capacitor with the lower impedance.

By applying the resonant condition of a parallel resonant circuit to equation (14.4), the value for the two shunt tuning capacitors, C_T, for a microstrip of a given length and phase velocity is

$$C_T = \frac{\cos(\beta l) + 1}{\omega_0 Z_0 \sin(\beta l)} \tag{14.6}$$

14.2.5 Quality Factor of Microstrip Resonators

The unloaded quality factor, Q_u, of the transmission line resonators is

$$Q_u = \frac{\pi}{2\alpha l} \tag{14.7}$$

where α is the attenuation constant due to losses in dielectric, α_d, and the conductor, α_c

$$\alpha = \alpha_d + \alpha_c = \frac{k_0 \varepsilon_r (\varepsilon_e - 1) \tan\delta}{2\sqrt{\varepsilon_e}(\varepsilon_r - 1)} + \frac{R_s}{Z_0 w_c} \tag{14.8}$$

where k_0 is the radial wave number, $\tan\delta$ is the loss tangent of the dielectric, and R_s is the surface resistivity of the conductor.

The loaded quality factor, Q_L, of the transmission line resonators is

$$Q_L = R_L \frac{\pi}{2\alpha l} \tag{14.9}$$

where R_L is the resistive loss of the load.

14.3 PRACTICAL CONSIDERATIONS

Mircostrip resonator optimization, similar to that of any other array, is highly dependent on the application and the field strength in which the array will be used. However, with that being said, there are several known parameters that affect the performance of the microstrip resonator regardless of application or field strength. The three most frequently adjusted parameters for microstrip optimization are the dielectric height (h), dielectric permittivity or constant (ε_r), and the conductor width (w_c). The length (l) of the array is also considered in optimization studies and while it does influence the performance of the array, in practice, the length of the array is often determined by the dielectric used and the field of view necessary for the application. The length of the array should not be longer than necessary, especially at ultra-high field strengths, as the extra inductance adds to radiative losses and reduces the self-resonance frequency of the resonator. A fourth parameter that is very rarely considered but can have significant consequences to the microstrip design is the ground plate.

14.3.1 Dielectric Height

Figure 14.1(b) shows the field lines for a microstrip resonator and explains how the dielectric height affects the behavior of the coil. If the dielectric height between the center conductor and the group plate is very narrow, the field will be concentrated and confined near the coil, creating a strong B_1 field very close to the coil, but it drops off rapidly. Conversely, a microstrip resonator with a wide dielectric height will not confine the B_1 field as much and will allow for greater penetration of the B_1 field into the sample, but have less sensitivity near the coil.

14.3.2 Relative Permittivity

Dielectrics with low relative permittivity should be preferred over dielectrics with high relative permittivity; optimizations of single element microstrip resonators at low field strengths have shown that air ($\varepsilon_r = 1$) yields the highest SNR.[12] Dielectrics with high permittivities should only be used when it is necessary to reduce the circuit length. They can also be used to reduce the coupling between TEM elements in an array. Regardless of the permittivity of the dielectric, it is crucial that the dielectric does not have a high loss tangent (δ).

14.3.3 Center Conductor Width

Optimizing the center conductor width is similar to optimizing the dielectric height, in that there are compromises involved in choosing a narrow strip over a thick strip. A thin, narrow conductor strip generates a very strong B_1 field near the conductor, but the field falls off rapidly and consequentially does not couple to the sample very well. Wider strips generate a weaker B_1 near the coil but couple better to the sample.

Recently, interesting work has been performed on changing the strip's impedance by changing its physical geometry in order to improve both the penetration and homogeneity of the profile.[13]

14.3.4 Ground Plate

The ground plate, which is usually a forgotten parameter, is essential to an efficient microstrip array. If designed incorrectly, the ground plate can decrease the transmit efficiency, perturb and reduce the B_1 fields, generate eddy currents, and increase mutual inductance between resonators. To avoid this, the ground plate needs to be sufficiently wide ($w_g \ll w_c$ and $w_c \ll h$) such that it does not perturb the field lines. If the ground plate width is too narrow, the resonator will perform more like a parallel plate resonator or a two-wire loop. In addition, if the ground plate is too narrow or discontinuous, there will be RF "leakage" behind the resonator, which can lead to reduced efficiency and possible image artifacts. Conversely, an RF ground plate that is too wide may increase eddy currents during the imaging experiment; a double-sided slotted shield is the best way to compensate for this.[14] The ground plate should be thicker than 2 skin depths at the frequency of interest to reduce resistive losses in the resonator, but not thicker than 5 skin depths as it increases the risk of eddy currents.

The individual microstrip resonator is the building block of a microstrip array, and once the individual coil is optimized for the specific application, it can be replicated into an array. Just as the individual coils have parameters that need to be optimized, the array also has parameters that need to be optimized. The channel count number and decoupling strategies between coils are considered below.

14.3.5 Coil Number

A recent 7 T study has shown that doubling the coil number (from 8 channels to 16 channels) improves the transmit efficiency by 22%, improves the SNR by 22%, improves the parallel imaging performance, and decreases the local and global SAR in the prostate.[15] It was also shown that increasing the channel count significantly increased the coupling between channels and aggressive methods were needed to decouple the elements; however, despite this, it is always beneficial to increase the channel count, if the channels can be decoupled efficiently.

14.3.6 Decoupling Strategies

Owing to its complexity, an analytical closed form solution for the mutual inductance and capacitance between two microstrip resonators, based on physical

dimensions, is beyond the scope of this chapter. The full analytical solution for the mutual inductance and capacitance between coupled microstrips is described by Gupta *et al*.[16]

As with any array, decoupling TEM coils within an array is important for B_1 shimming, increased SNR, possibly decreased SAR, and improved image homogeneity. Owing to the smaller width of the TEM element (when compared to loop elements), these coils can be packed tightly together, which also increases coupling. In addition, because of the topography of the coils, means of decoupling remain limited, with capacitive decoupling being predominant. Fortunately, although there are several proven methods of capacitive decoupling that can provide excellent decoupling for a given load, for moderately coupled TEM elements (~12 dB of isolation or greater), a single decoupling capacitor bridging the neighboring elements is sufficient. As with loop arrays, the reactive impedance of the decoupling capacitors,[17] C_d, is equal to

$$C_d = \frac{1}{\omega^2 M}$$

where M is the mutual inductance between the coils.

However, when the isolation between two neighboring elements is less than 12 dB, more aggressive decoupling strategies are usually required. In this case, a second decoupling capacitor bridging the two neighboring ground plates is required. Here, the two capacitors are tuned in concert to provide the greatest decoupling possible.[15]

Using a distributed capacitor along the ground plate has recently been suggested as a novel method for decoupling TEM elements.[18] This method is elegant because it simultaneously creates a continuous RF shield along the ground plate while decoupling two neighboring elements; however, it can be problematic to construct. Small changes to the physical geometry of the distributed capacitor can create significant changes in the impedance between the two neighboring elements. Therefore, it is important to have a good understanding of the loading conditions a priori before installing this decoupling method.

Decoupling capacitors are lossy, and can create parasitic current loops and field perturbing loops, potentially destroying the desired field profile of the coil; therefore, the least amount of decoupling possible to achieve greater than 18 dB of isolation between nearest neighbor channels should be used. Finally, during transmit, due to the B_1^+ shim, significant current and voltage drops across the decoupling capacitors are possible, the magnitude and distribution of which can vary with B_1^+ shimming. Depending on the phase set, following B_1^+ shimming, it is possible that the voltage drop across the decoupling capacitor can be nearly twice the output voltage of the amplifiers, with the current through the capacitor being proportional to reactive impedance of the capacitor. This needs to be considered when determining the appropriate power rating of the decoupling capacitors.

14.4 CONCLUSION

Here, we have discussed the TEM array, more specifically the microstrip array. Both the theory and practical implementations of a singular element and how to replicate the singular element into a multichannel array were discussed.

ACKNOWLEDGMENTS

NIH-R01 EB000895, NIH-R01 EB006835, NIH-R01 EB007327, NIH-P41 RR08079

RELATED ARTICLES IN THE ENCYCLOPEDIA OF MAGNETIC RESONANCE

Conradi, Mark S.: Evolution of NMR Hardware

Dadok, Josef: High-Field NMR Instrumentation

Decoupling Methods

High-Field Whole Body Systems

Probe Design and Construction

Radiofrequency Systems and Coils for MRI and MRS

Surface and Other Local Coils for In Vivo Studies

Surface Coil NMR: Detection with Inhomogeneous Radiofrequency Field Antennas

Whole Body Machines: NMR Phased Array Coil Systems

REFERENCES

1. C. Snyder, L. DelaBarre, P.-F. Van de Moortele, A. Styczynski Snyder, C. Akgun, J. Tian, G. Metzger, K. Ugurbil, and J. Vaughan, In *Proceedings of the 16th Annual Meeting of ISMRM*, Berlin, 2007, **164**.
2. J. T. Vaughan, C. J. Snyder, L. J. DelaBarre, P. J. Bolan, J. Tian, L. Bolinger, G. Adriany, P. Andersen, J. Strupp, and K. Ugurbil, *Magn. Reson. Med.*, 2009, **61**, 244–248.
3. G. Adriany, P. F. Van de Moortele, F. Wiesinger, S. Moeller, J. P. Strupp, P. Andersen, C. Snyder, X. Zhang, W. Chen, K. P. Pruessmann, P. Boesiger, T. Vaughan, and K. Ugurbil, *Magn. Reson. Med.*, 2005, **53**, 434–445.
4. R. F. Lee, C. R. Westgate, R. G. Weiss, D. C. Newman, and P. A. Bottomley, *Magn. Reson. Med.*, 2001, **45**, 673–683.
5. R. F. Lee, C. J. Hardy, D. K. Sodickson, and P. A. Bottomley, *Magn. Reson. Med.*, 2004, **51**, 172–183.
6. D. M. Pozar, *Microwave Engineering*, 2nd edn, John Wiley & Sons, Inc: New York, 1998.
7. C. J. Snyder, L. DelaBarre, G. J. Metzger, P. F. van de Moortele, C. Akgun, K. Ugurbil, and J. T. Vaughan, *Magn. Reson. Med.*, 2009, **61**, 517–524.
8. G. Metzger, P.-F. Van de Moortele, C. Akgun, C. Snyder, S. Moeller, J. Strupp, P. Andersen, D. Shrivastava, J. Vaughan, and G. Adriany, *Magn. Reson. Med.*, 2010, **64**, 1625–1639.
9. G. J. Metzger, C. Snyder, C. Akgun, T. Vaughan, K. Ugurbil, and P. F. Van de Moortele, *Magn. Reson. Med.*, 2008, **59**, 396–409.
10. A. L. Styczynski Snyder, C. Snyder, P.-F. Van de Moortele, L. DelaBarre, I. S. Haddidin, A. Truskinovky, J. T. Vaughan, K. Ugurbil, M. Garwood, and S. Michaeli, In *Proceedings of the 16th Annual Meeting of ISMRM*, Berlin, 2007, 573.
11. A. L. Styczynski-Snyder, C. J. Snyder, L. DelaBarre, P.-F. Van de Moortele, J. T. Vaughan, K. Ugurbil, M. Garwood, and P. J. Bolan, In *Proceedings of the 16th Annual Meeting of ISMRM*, Berlin, 2007, 729.
12. A. Kumar and P. A. Bottomley, *Magn Reson Med*, 2006, **56**, 157–166.
13. C. Akgun, L. DelaBarre, H. Yoo, S. Sohn, C. Snyder, G. Adriany, P.-F. Van deMoortele, A. Gopinath, K. Ugurbil, and J. T. Vaughan, In *Proceedings of the 20th Annual Meeting of ISMRM*, Montreal, 2011.
14. J. T. Vaughan, G. Adriany, C. J. Snyder, J. Tian, T. Thiel, L. Bolinger, H. Liu, L. DelaBarre, and K. Ugurbil, *Magn. Reson. Med.*, 2004, **52**, 851–859.
15. C. J. Snyder, L. Delabarre, S. Moeller, J. Tian, C. Akgun, P. F. Van de Moortele, P. J. Bolan, K. Ugurbil, J. T. Vaughan, and G. J. Metzger, *Magn. Reson. Med.*, http://onlinelibrary.wiley.com/doi/10.1002/mrm.23070/abstract.
16. K. C. Gupta, R. Garg, I. J. Bahl, and P. Bhartia, *Microstrip Lines and Slotlines*, Artech House: Boston, 1996, Vol. xvi, p. 535.
17. J. Wang, In *Proceedings of the 4th Annual Meeting of ISMRM*, New York, 1996, 1434.
18. J. T. Vaughan, C. J. Snyder, L. DelaBarre, J. Tian, G. Adriany, P. Anderson, J. Strupp, and K. Ugurbil, In *Proceedings of the 17th Annual Meeting of ISMRM*, Honolulu, 2009, 391.

Chapter 15

TEM Transceiver Head Array Coils for Ultra High Magnetic Fields

Gregor Adriany

Department of Radiology, Center for Magnetic Resonance Research, University of Minnesota, Minneapolis, MN 55455, USA

15.1 INTRODUCTION

At ultra high fields (since the associated ^{1}H frequencies are in the ultra high frequency (UHF) range, which is defined to be between 300 MHz and 3 GHz), there is a considerable interest in multielement transmit array systems that are capable of supporting a high number of independent channels for RF transmission. This interest comes from the fact that high and ultra high field MR is performed in a frequency regime, where the wavelength is on the order of, or smaller than, the dimensions of the human anatomy under investigation. This leads to prominent wave behavior, nonuniform B_1 field patterns, and a significant difference between transmit and receive B_1 fields.[1–5]

While the principle of improved B_1 homogeneity at very high fields by means of individual resonance element adjustments in volume coils has been demonstrated by Vaughan for the head and body,[6,7] extension of these principles toward transmit array coils with decoupled individual resonance elements has not been pursued until fairly recently. With the current strong interest in ultra high field MR systems, the MR engineering community has a renewed interest in addressing these questions through development of coils and RF front ends with true multichannel transmit capability.[8–16] Recently, it has also been demonstrated that because of the more complex sensitivity profiles of each coil element and the increased signal-to-noise ratio (SNR), high magnetic fields significantly improve the maximal achievable parallel imaging performance.[17–19] This, along with the introduction of MR transmit systems that allow for control of the RF waveform on multiple channels, opens up exciting new research directions.[20–23] Such complex systems can be used to support more refined RF shimming methods to mitigate sample-induced RF nonuniformities for particular subjects and regions of interest (ROI).[24–28] It is expected that body applications upward of 3 T and head applications above 7 T, in particular, will benefit from the capability for control of the transmit B_1 fields on multiple channels.

Since transmit arrays can, of course, still be combined with additional receive-only arrays, it is expected that such combinations will maximize possibilities both to influence the transmit $B_1{}^+$ and to acquire with optimal SNR and parallel imaging signal

RF Coils for MRI
Edited by J. Thomas Vaughan and John R. Griffiths

ISBN: 978-0-470-77076-4

reception B_1^-. These complex RF systems hold much promise in providing the MR research field with novel solutions to many of the problems encountered with B_1 homogeneity, specific absorption rate (SAR), and fast image acquisitions at high magnetic fields.[29–35]

There are a number of RF-coil-design-related challenges that need to be addressed when building transmit coil arrays at ultra high fields. The coil dimensions are no longer small compared to the wavelength; thus, coil current phase effects have to be considered. At high fields, sample losses clearly dominate but radiation losses cannot be neglected and should be reduced.[2,36] Various coil decoupling methodologies have been proposed[37–41] and have shown to yield excellent transmit coil separation. Other challenges relate to the need of fast B_1 mapping techniques for multiple RF coils; it has been shown that relative transmit B_1 phases can be obtained in a very short time in a transmit array,[42] allowing for fast, efficient, local B_1 phase shimming; and fast magnitude B_1 mapping methods have also been introduced.

One promising design approach that addresses many of the mentioned issues simultaneously is the use of stripline transmission lines as building blocks for transceiver arrays.[14,15,43–47] Most importantly, such arrays make use of the fact that at very high frequencies, radiation losses and coil coupling are best addressed by coil designs that incorporate a ground plane or an RF shield into the resonance structure. Ultra high field surface coils can similarly be built with an RF ground plane in close proximity[48,49] or a ground plane as an integral part of the resonant structure in the form of transmission line elements.[43,44,47,50–52] Furthermore, the broadband decoupling characteristic of transmission line elements[39,43] built with dielectric materials with a low-loss tangent δ such as polytetrafluorethylene (PTFE, "Teflon") reduces the difficulties of decoupling near neighbor elements. Indeed, the short wavelength at high fields aids the use of arrays of short transmission lines, which in turn permits coil arrays with a very higher number of transmit elements for increased possibilities to affect the B_1^+ in all three spatial dimensions.[27,53]

15.2 PRACTICAL CONSIDERATIONS

TEM-type coils rely on efficient inductive coupling between the individual elements of the coil. In order to gain the ability to decouple the individual resonant elements in a TEM-type volume coil—which is desired for a TEM transmit array—two significant design modifications can be pursued. First, the strong coupling has to be reduced by increasing the distance between resonant elements and counteracting remaining mutual coupling through capacitive decoupling—for circumscribing coils, this effectively leads to a reduction in the number of elements. Examples of this approach are decoupled TEM body coils at 3 T and 7 T.[54,55] A second approach is to introduce a minimal dielectric loss material such as Teflon between conductor and RF shield. This results in a shortened wavelength and an increase in the ability to contain magnetic and electrical fields between shield and conductor. This supports a decrease in the distance between conductor and shield without the significant B_1 transmit performance loss usually associated with closely shielded structures. The reduced shield distance, in turn, will allow for tighter spacing between elements. Particularly for head arrays, this allows a more desirable distribution of the overall RF power and gives reduced local SAR (see Chapters 30 and 31). In the following sections, various related considerations are discussed when pursuing the path of decoupled head TEMs.

15.2.1 Length of the TEM Striplines

A number of practical considerations have to be taken into account in the construction of coils for a stripline TEM transceiver array. The major design considerations are the overall coil geometry (circular/elliptical/flexible), the number of coil elements, and the design parameters for the individual coil elements. Assuming a quasi-TEM mode of propagation, the wavelength in the stripline is given by $\lambda = \lambda_0/\sqrt{\varepsilon_{\text{eff}}}$, where λ_0 is the free space wavelength and ε_{eff} is the effective relative dielectric constant.[56] With a typical PTFE dielectric constant of 2.1 and $\lambda/2$ resonator, this would indicate a maximal resonator length to achieve, for example, an ~300 MHz resonance (7 T) in the order of 34 cm. However, in practice, the associated B_1 field profile of a pure $\lambda/2$ resonator with the maximal B_1 in the center of the resonator and fall-off to null current toward either ends is not desirable. Realistic stripline lengths for head coils are between 8 and 20 cm. In order to achieve resonance in such shortened striplines, capacitors on either ends between the stripline conductor and the

shield are required. Typical values of these capacitors for 7 T coils are between 3.3 pF (18 cm) and 10 pF (8 cm). Further details regarding placement and calculation of the exact capacitor values are described by Snyder (see Chapter 14) and in the literature.

15.2.2 Choice of Material

The choice of material utilized between conductor and shield in a stripline-type resonant element, is foremost driven by the desire to achieve high mechanical stability with minimal dielectric loss tangent δ and permittivity. Teflon is a good choice for head coils with eight and more circumscribing elements. For head coils with up to eight elements, however, alternative materials or combination of materials—including no dielectric material (air)—can be considered because of the reduced next neighbor coupling. Brunner,[57] for example, utilized a sandwich construction of PTFE sheets and polymethacrylimide closed-cell foam.

To reduce gradient-induced eddy currents, it is important to reduce the thickness of the copper shielding material to about the skin depth for the given operating frequency. In practice, this leads to an RF shielding copper thickness of around 4–5 μm for operating frequencies of ~300 MHz. A good choice of material currently on the market is a product that uses a flexible polyimide film laminate as the carrier for a 5 μm copper film (Sheldahl, Northfield, MN, Novaclad®). Industrial strength adhesive tape (3 M™, St Paul, MN, adhesive transfer tape 467 MP) can be used to securely bind such materials to the Teflon dielectric.

15.2.3 Distance Between Elements

For dielectric materials such as PTFE ($\varepsilon_r \approx 2.1$) and material thicknesses between conductor and ground plane of 12–15 mm, a minimum distance between adjacent elements in the order of ≥5 cm is acceptable and good capacitive decoupling (~−12 to 15 dB) can then be achieved. This allows the building of head arrays with up to 16 circumferentially arranged elements (Figure 15.1). The value of the decoupling capacitor required between the elements for such a coil is in the order of 1.5–2.5 pF. For eight-channel head coils, this distance will naturally increase and, in practice, eight-element stripline-type head arrays can be built with minimal decoupling capacitor values of 1.2–1.5 pF or even without decoupling capacitors. Examples of this approach are eight-channel centrally fed head arrays presented by Brunner and Orzada.[57,58]

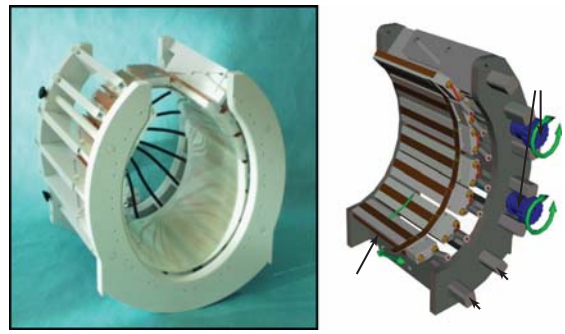

Figure 15.1. An example of a 16-channel stripline head array.[61] The coil allows for task presentation due to shortened transceiver stripline elements in the front.

15.2.4 Decoupling Option

While either inductive decoupling[41] or capacitive decoupling[59] schemes are in principle possible, for stripline-type arrays, the most straightforwardly implementable decoupling option is clearly capacitive decoupling between neighboring coil elements (Figure 15.2). Particularly for eight or a lower number of transmit element arrays (higher RF power per channel compared to 16- and 32-channel coils), it is important to use a variable decoupling capacitor with a high-voltage rating, ~2.5 kV or better. A good choice for head applications is nonmagnetic high-voltage PTFE trimmers, which are available in a small package size and range from 1 to 10 pF.

15.2.5 Choice of Coaxial Cable, Connectors, and Capacitors

For head arrays, coaxial cables such as RG 223, RG 316, and RG 400 are excellent choices in terms of cable insertion loss and flexibility. From a practical point of view, the potential appeal of RG 400 vs other choices is that the coaxial cable dielectric is PTFE

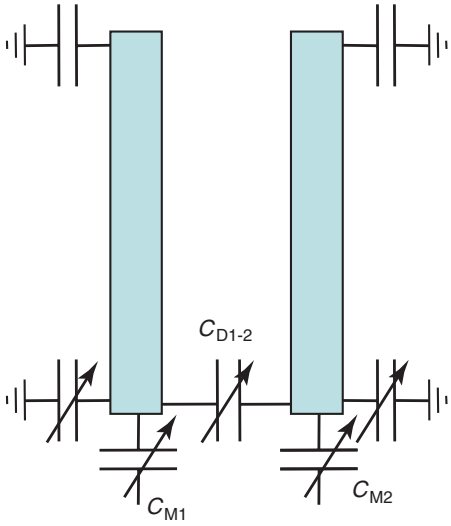

Figure 15.2. Basic capacitive decoupling circuitry between neighboring coil elements. The capacitor C_{D12} is connected directly at the feedpoint between neighboring conductor strips. RF shields are kept separate for the individual elements and connected, as indicated in Figure 15.3, through the common coaxial cable grounds in λ/4 distance.

based and heat resistant, which simplifies soldering of the inner conductor or shield to the capacitors and circuit boards.

For transceiver head coils, both BNC and QMA connectors are suitable in terms of size, convenience of use, and RF power handling capacity. QMA is a newer type connector family specifically designed to allow for a quick-connect. Use of QMA jack bulkhead connectors, for example, allows for denser connectorization as compared to BNC bulkhead—an example is shown in Figure 15.3.

Multilayer high Q ceramic chip capacitors with a high peak voltage rating of at least 2.5 kV are a good choice for all fixed value capacitors—examples are Johanson Technology E series, American Technical Ceramic (ATC) 100 C series capacitors, and Voltronic 25 series. Since most manufacturers offer these types of capacitors also with an MR-incompatible magnetic barrier termination (Nickel), it is important to explicitly specify a nonmagnetic termination code. A good choice for variable capacitors is nonmagnetic PTFE trimmers with a peak voltage rating of at least 2.5 kV and a 1–10 pF capacitance range—examples are Voltronic NMNT 10-6. Since the package sizes increase with voltage ratings, it is impractical for head

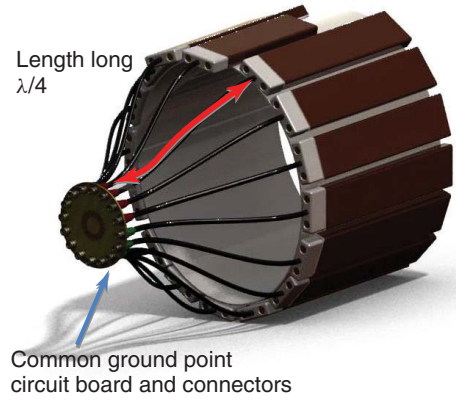

Figure 15.3. Illustration of a common RF ground point implementation for a 16-channel head array.

applications to utilize capacitors beyond a 6 kV withstanding voltage.

15.2.6 Cable Traps

In practice, for stripline elements with individual ground conductors, finding a common ground point for the individual array elements can be very difficult without cable traps. For a head array, there is however a simple, yet very effective way to avoid individual cable traps by creating a common ground point at an ∼λ/4 distance coaxial cable length from the feed circuitry (see Figure 15.3). For a RG 400 coaxial cable at 300 MHz, this length is ∼17 cm. To avoid gradient-induced eddy current problems, it is however important to realize this as an RF ground point and not a DC ground point. This can, for example, be accomplished by soldering ceramic chip capacitors of values in the range of 330–620 pF between neighboring cables and RF connectors—such high values are effectively short at UHF-operating frequencies. In practice, this can be most reliably accomplished with a dedicated circuit board for the merging point. This board is designed for secure mounting of the coaxial connectors (i.e., QMA bulkhead jacks as shown in Figure 15.3) with patches to allow soldering of chip capacitors between neighboring connectors.

Another important practical way to improve cable resonances and the resulting lower coil Q-factors is to introduce a secondary outside RF shield to the stripline transceiver coil structure. This was first

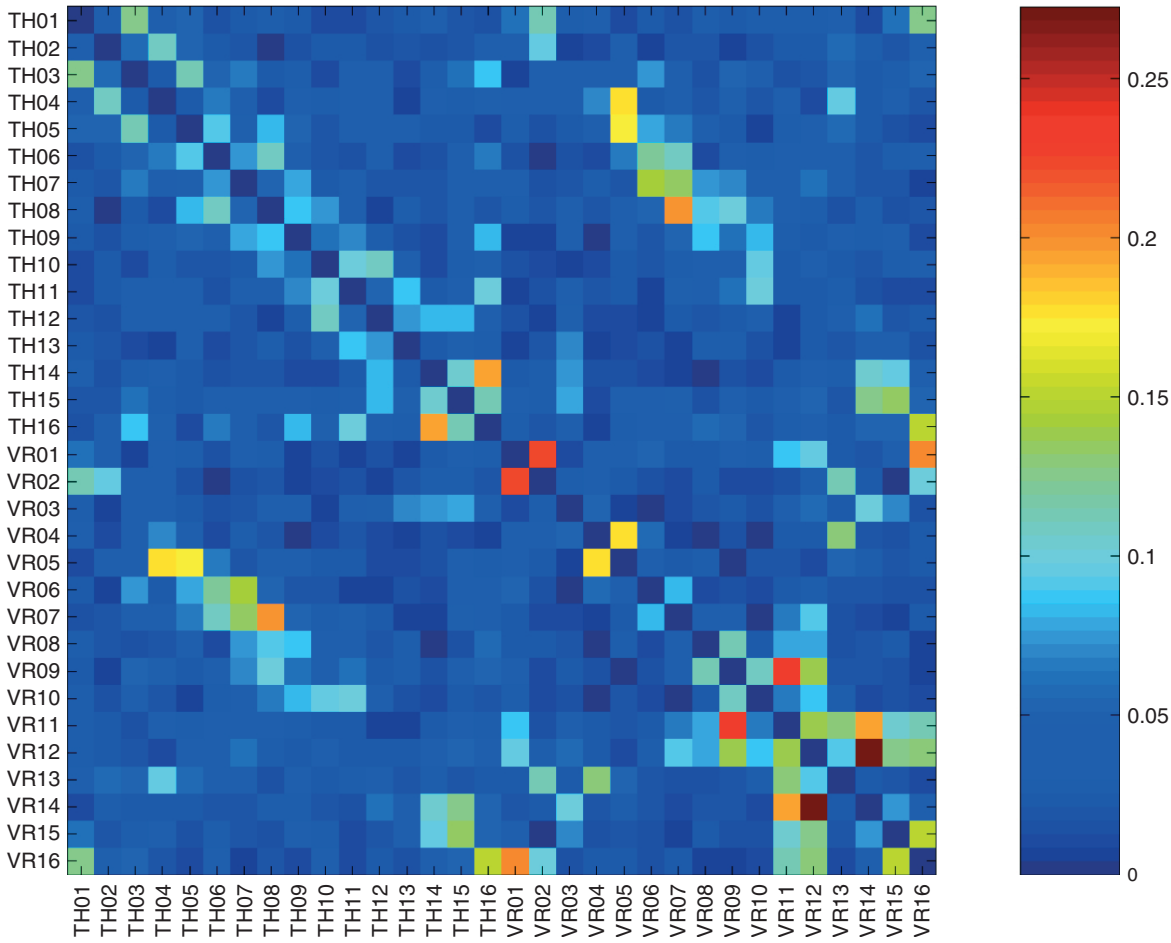

Figure 15.4. The achievable correlation matrix for a 32-channel stripline array with capacitive decoupling between neighboring coils.

proposed by Brunner *et al*.[57] and was recently described in detail by Zhang *et al*.[60] However, care has to be taken that such an outer RF shield does not generate unwanted gradient eddy currents.

15.3 CONCLUSION

Through use of dielectric materials such as Teflon, capacitive decoupling between neighboring elements, trap circuitry, and RF shielding, it is relatively straightforward to build stripline transceiver head arrays with a high channel count of 16 or 32 (Figures 15.4 and 15.5). Compared to loop-based transceiver arrays, striplines typically allow for tighter spacing and a potentially higher total number of array elements. On the other hand, owing to the higher Q-factor of striplines compared to loops, stripline arrays typically require more extensive subject-dependent tune and match adjustment with consequences for the total setup time. For improved B_1^+ control and reduced SAR in all spatial dimensions, it will continue to be important to realize stripline arrays not only circumscribing but also with multiple splits along the longitudinal direction.

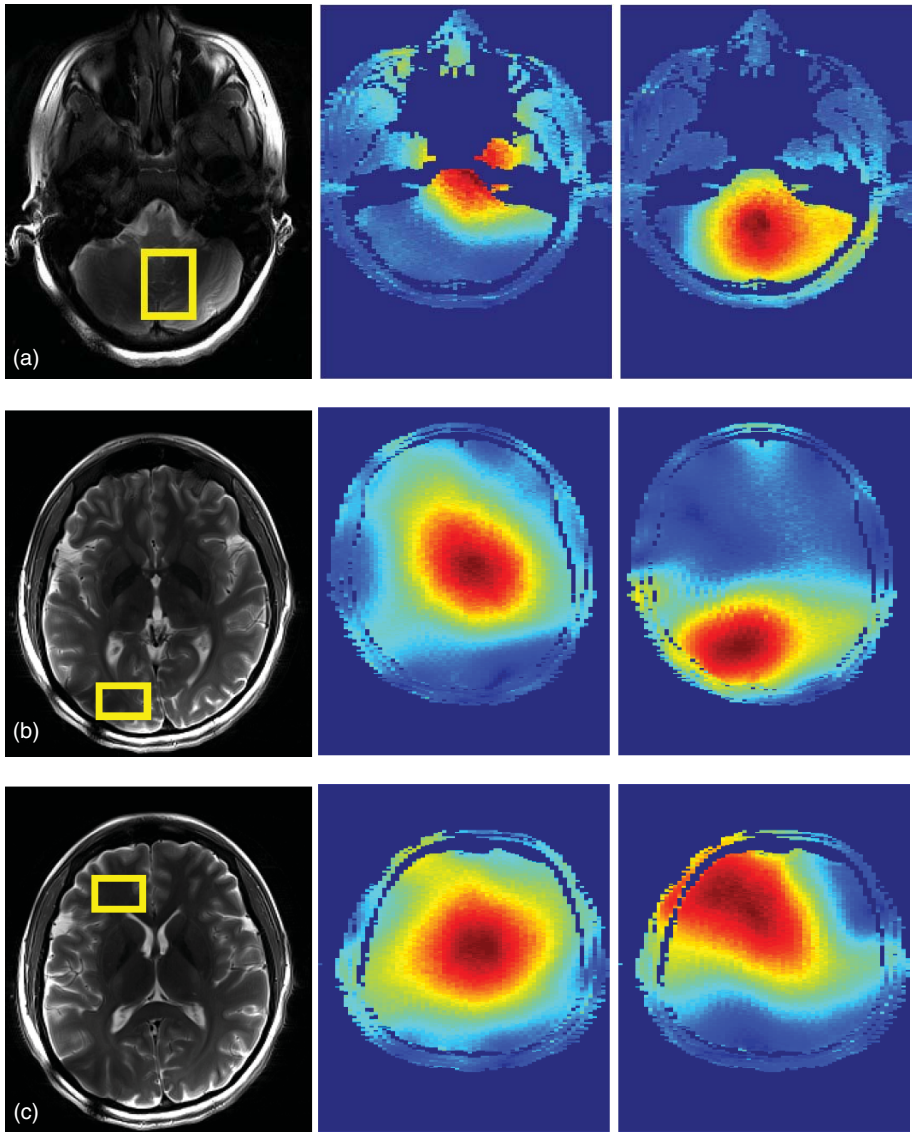

Figure 15.5. RF shimming ability utilizing a 16-channel stripline array. (a) Cerebellum, ~3 × RF efficiency gain after shimming. (b) Occipital cortex, ~2 × RF efficiency gain post shim. (c) Frontal white matter ~2 × RF efficiency gain post shim[62].

ACKNOWLEDGMENTS

NIH-R01 EB000895, NIH-R01 EB006835, NIH-R01 EB007327, NIH-P41 RR08079

RELATED ARTICLES IN THE ENCYCLOPEDIA OF MAGNETIC RESONANCE

High-Field Whole Body Systems

Inorganic Solids

Probe Design and Construction

Purcell, Edward M.: Research in Nuclear Magnetism

Radiofrequency Fields: Interactions, Biological Effects, and Safety Issues

Radiofrequency Systems and Coils for MRI and MRS

Sensitivity of the NMR Experiment

REFERENCES

1. G. H. Glover, C. E. Hayes, N. J. Pelc, W. A. Edelstein, O. M. Mueller, H. R. Hart, C. J. Hardy, M. O'Donnel, and W. D. Barber, *J. Magn. Reson.*, 1985, **64**, 255.
2. J. R. Keltner, J. W. Carlson, M. S. Roos, S. T. Wong, T. L. Wong, and T. F. Budinger, *Magn. Reson. Med.*, 1991, **22**, 467–480.
3. D. I. Hoult, *Concepts Magn. Reson.*, 2000, **12**, 173–187.
4. T. S. Ibrahim, A. M. Abduljalil, B. A. Baertlein, R. Lee, and P. M. Robitaill, *Phys. Med. Biol.*, 2001, **46**, 2545–2555.
5. C. M. Collins, Q. X. Yang, J. H. Wang, X. Zhang, H. Liu, S. Michaeli, X. H. Zhu, G. Adriany, J. T. Vaughan, P. Anderson, H. Merkle, K. Ugurbil, M. B. Smith, and W. Chen, *Magn. Reson. Med.*, 2002, **47**, 1026–1028.
6. J. T. Vaughan, H. P. Hetherington, J. G. Harrison, J. O. Otu, J. W. Pan, and G. M. Pohost, *Magn. Reson. Med.*, 1994, **32**, 206–218.
7. J. T. Vaughan, G. Adriany, C. J. Snyder, J. Tian, T. Thiel, L. Bolinger, H. Liu, L. DelaBarre, and K. Ugurbil, *Magn. Reson. Med.*, 2004, **52**, 851–859.
8. G. R. Duensing, D. M. Petersen, B. L. Wolverton, and J. Fitzsimmons, In *Proceedings of the 6th Annual Meeting of ISMRM*, 1998, p. 441.
9. D. C. Alsop, T. J. Connick, and G. Mizsei, *Magn. Reson. Med.*, 1998, **40**, 49–54.
10. E. B. Boskamp and R. F. Lee, In *Proceedings of the 10th ISMRM*, Honolulu, Hawaii, USA, 2002, p. 903.
11. J. T. Vaughan, U.S. Pat. 6,633,161 (2003).
12. J. T. Vaughan, G. Adriany, K. Ugurbil, P. Andersen, and J. Strupp, U.S. Pat. 6,969,992 (2003).
13. D. I. Hoult, G. Kolansky, D. Kripiakevich, and S. B. King, *J. Magn. Reson.*, 2004, **171**, 64–70.
14. G. Adriany, P. F. Van de Moortele, F. Wiesinger, S. Moeller, J. P. Strupp, P. Andersen, C. Snyder, X. L. Zhang, W. Chen, K. P. Pruessmann, P. Boesiger, T. Vaughan, and K. Ugurbil, *Magn. Reson. Med.*, 2005, **53**, 434–445.
15. T. Vaughan, L. DelaBarre, C. Snyder, J. Tian, C. Akgun, D. Shrivastava, W. Liu, C. Olson, G. Adriany, J. Strupp, P. Andersen, A. Gopinath, P. F. van de Moortele, M. Garwood, and K. Ugurbil, *Magn. Reson. Med.*, 2006, **56**, 1274–1282.
16. R. G. Pinkerton, J. P. Near, E. A. Barberi, R. S. Menon, and R. Bartha, *Magn. Reson. Med.*, 2007, **57**, 455–458.
17. F. Wiesinger, K. P. Pruessmann, and P. Boesinger, In *Proceedings of the International Society for Magnetic Resonance in Medicine*, Honolulu, Hawaii, USA, 2002, p. 191.
18. P. J. Ledden and J. H. Duyn, In *Proceedings of the International Society for Magnetic Resonance in Medicine*, Honolulu, Hawaii, USA, 2002, p. 324.
19. F. Wiesinger, P. F. Van De Moortele, G. Adriany, N. De Zanche, K. Ugurbil, and K. P. Pruessmann, *Magn. Reson. Med.*, 2004, **52**, 953–964.
20. U. Katscher, P. Bornert, C. Leussler, and J. S. van den Brink, *Magn. Reson. Med.*, 2003, **49**, 144–150.
21. Y. Zhu, *Magn. Reson. Med.*, 2004, **51**, 775–784.
22. P. Ullmann, S. Junge, M. Wick, F. Seifert, W. Ruhm, and J. Hennig, *Magn. Reson. Med.*, 2005, **54**, 994–1001.
23. K. Setsompop, L. L. Wald, V. Alagappan, B. Gagoski, F. Hebrank, U. Fontius, F. Schmitt, and E. Adalsteinsson, *Magn. Reson. Med.*, 2006, **56**, 1163–1171.
24. B. K. Li, F. Liu, and S. Crozier, *Magn. Reson. Med.*, 2005, **53**, 1251–1257.
25. S. Clare, M. Alecci, and P. Jezzard, *Magn. Reson. Imaging*, 2001, **19**, 1349–1352.
26. P. F. Van de Moortele, C. Akgun, G. Adriany, S. Moeller, J. Ritter, C. M. Collins, M. B. Smith, J. T. Vaughan, and K. Ugurbil, *Magn. Reson. Med.*, 2005, **54**, 1503–1518.
27. W. Mao, M. B. Smith, and C. M. Collins, *Magn. Reson. Med.*, 2006, **56**, 918–922.
28. G. Metzger, P. F. Van de Moortele, C. Snyder, H. G. Vaughan, and K. Ugurbil, In *Proceedings of the International Society for Magnetic Resonance in Medicine*, 2007, p. 799.

29. D. K. Sodickson and W. J. Manning, *Magn. Reson. Med.*, 1997, **38**, 591–603.
30. K. P. Pruessmann, M. Weiger, M. B. Scheidegger, and P. Boesiger, *Magn. Reson. Med.*, 1999, **42**, 952–962.
31. M. Weiger, K. P. Pruessmann, C. Leussler, P. Roschmann, and P. Boesiger, *Magn. Reson. Med.*, 2001, **45**, 495–504.
32. J. A. de Zwart, P. J. Ledden, P. Kellman, P. van Gelderen, and J. H. Duyn, *Magn. Reson. Med.*, 2002, **47**, 1218–1227.
33. M. P. McDougall, S. M. Wright, and D. G. Brown, In *Proceedings of the 11th ISMRM*, Toronto, Canada, 2003, p. 472.
34. M. A. Ohliger, P. Ledden, C. A. McKenzie, and D. K. Sodickson, *Magn. Reson. Med.*, 2004, **52**, 628–639.
35. D. K. Sodickson, C. J. Hardy, Y. D. Zhu, R. O. Giaquinto, P. Gross, G. Kenwood, T. Niendorf, H. Lejay, C. A. McKenzie, M. A. Ohliger, A. K. Grant, and N. M. Rofsky, *Acad. Radiol.*, 2005, **12**, 626–635.
36. J. T. Vaughan, M. Garwood, C. M. Collins, W. Liu, L. DelaBarre, G. Adriany, P. Andersen, H. Merkle, R. Goebel, M. B. Smith, and K. Ugurbil, *Magn. Reson. Med.*, 2001, **46**, 24–30.
37. J. Wang, In *Proceedings of the International Society for Magnetic Resonance in Medicine*, New York, 1996, p. 1434.
38. J. Jevtic, In *Proceedings of the International Society for Magnetic Resonance in Medicine*, 2001, Vol. 1, 17.
39. A. Kumar and P. A. Bottomley, In *Proceedings of the International Society for Magnetic Resonance in Medicine*, Honolulu, Hawaii, USA, 2002, p. 322.
40. X. Z. Zhang and A. Webb, *J. Magn. Reson.*, 2004, **170**, 149–155.
41. B. Wu, X. Zhang, P. Qu, and G. X. Shen, *J. Magn. Reson.*, 2006, **182**, 126–132.
42. P. Van de Moortele, C. Snyder, L. DelaBarre, C. Akgun, X. Wu, J. Vaughan, and K. Ugurbil, In *International Symposium on Biomedical Magnetic Resonance Imaging and Spectroscopy at Very High Fields 2006*, Wuerzburg, Germany, 2006, p. 15.
43. R. F. Lee, C. R. Westgate, R. G. Weiss, D. C. Newman, and P. A. Bottomley, *Magn. Reson. Med.*, 2001, **45**, 673–683.
44. X. Zhang, K. Ugurbil, and W. Chen, *Magn. Reson. Med.*, 2001, **46**, 443–450.
45. R. F. Lee, C. J. Hardy, D. K. Sodickson, and P. A. Bottomley, *Magn. Reson. Med.*, 2004, **51**, 172–183.
46. G. Adriany, A. Gözübüyük, J. Ritter, C. Snyder, P. F. Van de Moortele, S. Moeller, J. T. Vaughan, and K. Ugurbil, In *Proceedings of the 14th International Society for Magnetic Resonance in Medicine*, 2006, Vol. 1, 126
47. A. Kumar and P. A. Bottomley, *Magn. Reson. Med.*, 2006, **56**, 157–166.
48. K. C. Ong, H. Wen, A. S. Chesnick, S. Duewell, F. A. Jaffer, and R. S. Balaban, *J. Magn. Reson. Imaging*, 1995, **5**, 773–777.
49. G. Adriany, E. Yacoub, I. Tkac, P. Andersen, H. Merkle, J. T. Vaughan, and K. Ugurbil, In *8th ISMRM*, 2000, Vol.1, 563.
50. J. T. Vaughan, J. M. Vaughn, H. P. Hetherington, J. G. Harrison, P. J. Noa, and G. M. Pohost, In *Proceedings of the Society for Magnetic Resonance in Medicine*, New York, 1993, p. 1332.
51. X. Zhang, K. Ugurbil, and W. Chen, *J. Magn. Reson.*, 2003, **161**, 242–251.
52. G. Adriany, P. F. Van de Moortele, P. Andersen, J. Strupp, J. Ritter, C. Snyder, S. Moeller, J. T. Vaughan, and K. Ugurbil, *Proceedings of the 12th ISMRM*, 2004, p. 1604.
53. G. Adriany, A. Gözübüyük, E. J. Auerbach, P. F. Van de Moortele, P. Andersen, S. Moeller, J. T. Vaughan, and K. Ugurbil, In *Proceedings of the 15th International Society for Magnetic Resonance in Medicine*, 2007, p. 168.
54. P. Vernickel, P. Roschmann, C. Findeklee, K. M. Ludeke, C. Leussler, J. Overweg, U. Katscher, I. Grasslin, and K. Schunemann, *Magn. Reson. Med.*, 2007, **58**, 381–389.
55. J. T. Vaughan, C. J. Snyder, L. J. DelaBarre, P. J. Bolan, J. Tian, L. Bolinger, G. Adriany, P. Andersen, J. Strupp, and K. Ugurbil, *Magn. Reson. Med.*, 2009, **61**, 244–248.
56. X. Zhang, K. Ugurbil, R. Sainati, and W. Chen, *IEEE Trans. Bio-med. Eng.*, 2005, **52**, 495–504.
57. D. O. Brunner, N. D. Zanche, J. Frohlich, D. Baumann, and K. Pruessmann, O. Kraff, L. Schaefer, I. Brote, A. Bahr, T. Bolz, S. Maderwald, M. E. Ladd, and A. K. Bitz, In *Proceedings of the 15th International Society for Magnetic Resonance in Medicine*, 2007, p. 448.

58. S. Orzada, O. Kraff, L. Schaefer, I. Brote, A. Bahr, T. Bolz, S. Maderwald, M. E. Ladd, and A. K. Bitz, *Proceedings of the 17th ISMRM* , Honolulu, HI, 2009, Abstract, p. 3010.

59. J. Wang, In *Proceedings of the International Society for Magnetic Resonance in Medicine*, 1996, Vol.3, 1434.

60. X. L. Zhang, B. Wu, C. S. Wang, D. A. C. Kelley, D. Xu, D. B. Vigneron, and S. J. Nelson, *IEEE Trans. Med. Imaging*, 2010, **29**, 179–184.

61. G. Adriany, P. F. Van de Moortele, J. Ritter, S. Moeller, E. J. Auerbach, C. Akgun, C. J. Snyder, T. Vaughan, and K. Ugurbil, *Magn. Reson. Med.*, 2008, **59**, 590–597.

62. U. E. Emir, E. J. Auerbach, P. F. Van De Moortele, M. Marjanska, K. Ugurbil, M. Terpstra, I. Tkac, and G. Oz, *NMR Biomed.*, 2012, **25**(1), 152–160.

Chapter 16

Transverse Electromagnetic (TEM) Coils for Extremities

Nikolai I. Avdievich

Department of Neurosurgery, Yale University, New Haven, CT 06520, USA

16.1 INTRODUCTION

Conventional high-field RF coils for the human limbs and heads are typically formed from rigid cylinders. The use of this design requires that either the coil slides over the subject or, alternately, the subject slides into the coil. For patients with impaired or limited mobility, this can make positioning difficult. Additionally, when receive-only arrays are used within the transmission coil, the ability to both place and visualize the location of the array is limited. These limitations can be overcome using a split "two-piece" coil. Split unshielded birdcage coils have been described for field strengths up to 3 T.[1] Because of the presence of end ring RF currents, split birdcage coils require a continuous electrical connection between two halves of the coil.[1] Additionally, most high-field (>3 T) head-sized volume RF coils use a shield surrounding the entire coil to decrease radiation losses.[2] For shielded birdcage RF coils, both the coil and the shield must be separated and reliably reconnected electrically during each use, which complicates both the fabrication and utilization. However, transverse electromagnetic (TEM) RF volume coils,[3–8] because of use of through-space inductive coupling between resonant elements, can circumvent this limitation, since the two halves of the coil do not require electrical continuity (see Chapter 6). Also the TEM design has been demonstrated to have certain advantages over the birdcage design at higher fields (>3 T) (see Chapter 26).[5,9–11] The TEM design has been successfully applied for head and body volume coils up to 7 T.[3–5,8,12] The TEM coil inductance depends on the ratio of the RF shield diameter to the inside diameter of the coil[3] rather than on the absolute value of the coil diameter such as in the birdcage coils. The latter does not take into account the dependence of the birdcage inductance on the distance to a shield, which is substantially weaker than its dependence on the coil radius. Thus, it is much easier to scale the TEM coil size up while keeping the inductance low. This design decreases radiation losses and improves current distributions (no end ring current). Quantitative comparisons of the TEM and birdcage designs at frequencies greater than 120 MHz have demonstrated the advantages of the TEM over the most commonly used design of the birdcage coil (straight cylindrical shield, flat rungs).[5,9–11] For

RF Coils for MRI
Edited by J. Thomas Vaughan and John R. Griffiths

ISBN: 978-0-470-77076-4

example, Vaughan *et al*.[5] reported that a quadrature TEM head coil was almost 20% more efficient than a similar-sized birdcage coil at 4 T.

The concept of a split TEM volume coil has been first suggested in the works of Vaughan *et al*.[13–15] Technical details of the design and construction have been discussed in the work of Avdievich *et al*.[16] This chapter describes the detailed design, construction, and performance analysis of split 4 T TEM volume coils for the human knee and head. It also provides a comparison of the performance of the split TEM coils with their corresponding one-piece counterparts.

16.2 BACKGROUND

16.2.1 Effect of Splitting the Coil and Rationale for the Adjustment Procedure

To better understand the effect of splitting the coil, we can view the N-element TEM volume coil as a multimode structure supporting N modes resonating at different frequencies constrained by the boundary condition that the total phase shift is $2\pi n$ ($0 \leq n \leq N/2$) per complete revolution about the coil in the radial direction.[3] Thus, the lowest frequency corresponds to zero periods (currents in all elements are in phase), the second lowest corresponds to one period, third lowest to two periods, and so on. The lowest and the highest modes are two singlets ($n = 0$ and $n = N/2$) with the rest of the modes being a set of degenerate doublets.[3] The lowest frequency doublet ($n = 1$) provides two degenerate modes with the most homogeneous RF magnetic field (B_1) distribution, which can be driven in quadrature (see Chapter 3) to produce a circularly polarized field. Figure 16.1(a) shows distributions of RF currents (I_{RF}) for these two modes in the legs of a nonsplit 16-element volume coil. As experimentally demonstrated previously, splitting the shield reduces the inductive coupling between the elements adjacent to the splits, thereby spoiling the isolation between these two linear modes by mixing them with higher modes.[16] The modes of the resonator can also be considered as a set of standing waves produced by the interference of two waves propagating from element to element from the driving point in opposite radial directions, similar to a transmission line. Viewing the set of TEM elements as a transmission line can help to analyze the change in the I_{RF} distribution leading to mode mixing. Reducing the coupling between

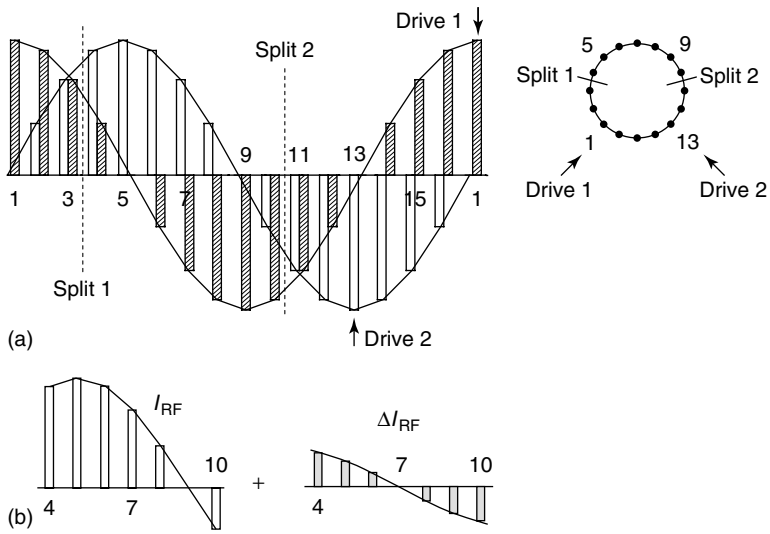

Figure 16.1. (a) Theoretical distribution of the RF current in the resonance elements of a 16-element TEM quadrature volume coil for the two most homogeneous degenerated modes. Picture of the coil with all the elements numbered are shown schematically in the right side of the figure. It also presents positions of the two splits and two driving points. (b) Distribution of the RF current (I_{RF}) and the changes of the RF current (ΔI_{RF}) in the top seven elements (elements 4–9) of the TEM coil generated by splitting the coil.

the elements adjacent to the splits results in reflection of the propagating waves at the discontinuities created by the splits. Reflection from both splits produces changes in the RF current (ΔI_{RF}) in each TEM element with the distribution of the ΔI_{RF} having a half-wavelength profile over each part of the split coil. The decrease of the coupling between the elements adjacent to the splits is equivalent to a decrease of the impedance viewed from the perspective of the propagating wave. Therefore, this results in an increase of the I_{RF} in the elements adjacent to the splits. It is similar to a transmission line loaded at its terminus by an impedance $Z < Z_0$, where Z_0 is characteristic impedance of the transmission line. In the limiting case of $Z = 0$, the voltage measured at the end of transmission line equals zero and the current is maximized. Figure 16.1(b) demonstrates distribution of ΔI_{RF} due to splitting, which cuts the coil in two unequal parts with seven elements in the top portion and nine elements in the bottom portion. As an example, ΔI_{RF} is shown for the top portion of the coil. The distribution of the ΔI_{RF} produced by reflection near the splits will have a half-wavelength shape in both portions of the split coil, with the maximal increase of I_{RF} in the elements adjacent to the splits and no change in the elements located in the middle between the two splits (top and bottom elements, 7 and 15).

Commonly, to simplify the tuning of a multimode coil, those elements that affect only one of the modes without changing the others are used. Therefore, changing impedance of elements 1 and 9 (5 and 13) shifts the frequency only for the mode that has maximum current in these elements (Figure 16.1a). The resonance frequency of the other mode is not affected since it carries no current in these elements. To restore the isolation between the linear modes of the quadrature TEM, the elements 3, 7, 11, and 15 can be utilized. These elements strongly affect the isolation between the modes of the closed TEM because of their location at 45° relative to the driven elements.[17] For the split TEM, only elements 7 (top) and 15 (bottom) should be used since they are located at the null of standing wave for ΔI_{RF} (Figure 16.1b) and do not perturb the ΔI_{RF} distribution. Intuitively, one might try to compensate for the decrease in coupling between two elements adjacent to the split by increasing current in these elements. However, this neglects the interaction with other elements of the TEM and does not resolve the problem.

16.3 COIL CONSTRUCTION

16.3.1 Coil Design and Materials

A 16-element TEM open-end quadrature volume coil for knee imaging (Figure 16.2a and b) and a closed-end (Figure 16.2c and d) quadrature volume coil for brain imaging were built[16] using coaxial

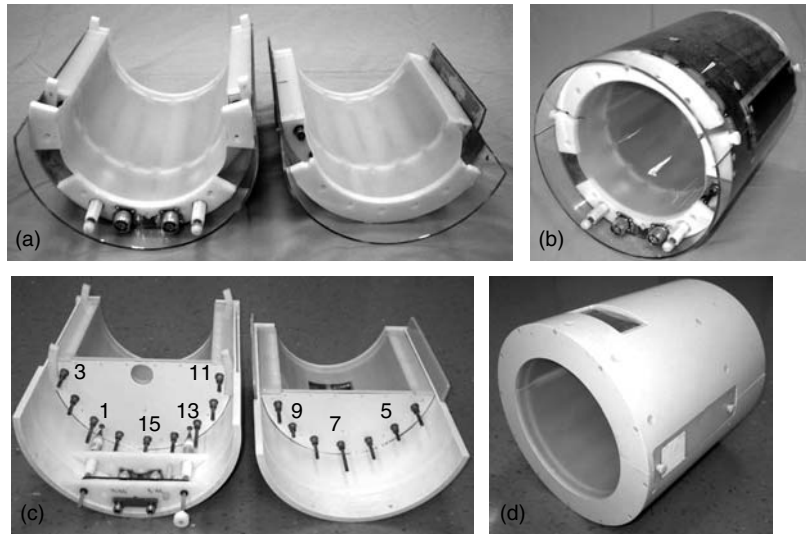

Figure 16.2. Assembled and disassembled pictures of (a and b) knee and (c and d) head split TEM volume coils.

resonant elements with Teflon inserts as described by Vaughan *et al*.[3] Copper tubes with 12.5 mm outer diameter (OD) (wall thickness 0.6 mm) and 6.4 mm OD were utilized to construct the outer shell and central conductor of the TEM elements, respectively. The open-end split TEM coil for the knee was 20 cm in length with an RF shield diameter of 24.8 cm and an element ID (inner diameter, measured at the element centers) of 21 cm. The coil had an ID clearance of 18.8 cm, which could be further reduced. The head coil had one end closed and shielded for improved homogeneity of the RF field.[3] The head coil was 21 cm in length with an RF shield diameter of 33.2 cm, an element ID of 27.5 cm, and an ID clearance of 25.3 cm. The outer shell of the open-end split coil was constructed using a 25.4 cm OD acrylic cylinder with a 3.2 mm wall thickness. The split head coil was built from a 35.6 cm OD polyvinyl chloride (PVC) pipe with 1.2 cm walls. The shield for both coils was constructed from a 50 μm polyamide film with a 5 μm copper layer laminated on top of it (Gould Electronics, Eastlake, OH). This thickness of the copper is approximately equal to the skin depth at 170 MHz (^{1}H frequency at 4 T). This allowed us to preserve a high unloaded Q-factor for the TEM resonator while suppressing gradient eddy currents.[3,4,10,11] To provide a view for patients, the top portion of the head coils had a window opening (11×5.5 cm) covered by a copper mesh, which was electrically connected to the shield at the edges (Figure 16.2d). Comparison of the TEM coils with and without window cut revealed no change in the coil performance. The coils were split into two parts (nine elements in the lower portion and seven in the top portion) with no electrical connection between them. Both TEM coils were driven in quadrature using capacitive matching and a two-port drive (Figure 16.1) with the driven elements located at the bottom of the coils[3,15] and separated by 90°. Quadrature driving was provided using high-power 90° hybrids (MAC Technology, Klamath Falls, OR). Adjustable matching of the coils within the magnet was provided by high-voltage variable capacitors (Jennings Technology, San Jose, CA) connected to the driven elements (see Chapter 25). To restore the coupling between the TEM elements located near the splits, electrically insulated additional pieces of copper foil were placed at both sides of the TEM coils overlapping the split (Figure 16.2). These side shields were constructed from the same type of foil as the major shield and positioned symmetrically near the splits at about 3 mm from the major shield (distance determined by plastic insulation). They measured 5 cm in width and 22 cm in length.

The performance of the split coils was compared to their one-piece counterparts. The one-piece, open-end TEM coil[18] used for knee imaging was larger so as to provide easy access of the leg and had a shield diameter of 33 cm and element ID of 27.5 cm. Performance of this coil was compared to the split TEM knee coil. The nonsplit closed-end head coil had exactly the same size and geometry as the spilt head coil. A spherical 2.0 L (16 cm diameter, 50 mM NaCl) phantom was used for the head coil and a cylindrical 2.0 L (12 cm diameter, 50 mM NaCl) phantom for the knee coil.

16.3.2 Bench Testing and Tuning Procedures

16.3.2.1 Bench Testing

Although there was no provision for variable tuning within the magnet, the variation in resonance frequency from head to head (<200 kHz) was much smaller than the resonance line width of the loaded coil (~3 MHz).[16] Thus subject-dependent changes in resonance frequency did not significantly alter performance. The subject-dependent change in resonance frequency for the split TEM knee coil was also substantially smaller than the coil's resonance line width (~2.5 MHz). The shift in resonance frequency was less than 0.4 MHz when the coil was positioned over the calf, knee, and thigh of the same individual. In spite of a fairly small gap (1–2 mm) between the shields of the top and the bottom coil's portions, coupling between the two elements adjacent to the split was reduced by about 40% in comparison to the coupling between other adjacent elements. The coupling was evaluated by measuring the frequency split between two resonance lines produced by a pair of elements with all other elements removed from the volume coil.[19] The coupling was restored to 75% of the value measured for two elements located at the bottom (or top) by using the side shields (Figure 16.2).

The unloaded Q-factors of both TEM coils were unaffected by the splits. The Q-factors were measured from frequency dependence of the S_{11} reflection coefficient of the matched coils, using the doubled ratio of the resonance frequency to the resonance width at the −3 dB level. The ratio of unloaded to phantom loaded Q-factors, Q_U/Q_L,

were 700/60 and 740/70 for head and knee coils, respectively. Splitting of the shield also did not significantly affect the separation between the TEM modes, which measured 8–10 MHz for the split knee coil and 10–12 MHz for the split head coil.

Each coil was initially adjusted to obtain sufficient isolation (better than −12 dB) between the modes. This was achieved by changing impedance of top and bottom elements and then tuning the coil using a procedure developed in our laboratory.[20] After tuning, the isolation S_{12} between linear modes of each quadrature coil was better than −20 dB on the phantoms and a human head or a knee.

16.3.2.2 Tuning Procedure

Figure 16.3 shows a picture of the apparatus and a block diagram of the tuning method for TEM volume coils.[20] In this method, rotation of a small magnetic or a dielectric probe in close proximity to the TEM elements produces a shift of the resonance frequency proportional to the square of the amplitude of the RF current flowing in the corresponding element. Probes were mounted on the end of G10 plastic rod and rotated using a small DC motor as shown in Figure 16.3. The angular position of the probe was determined using a small infrared (IR) source/receiver and a disk mounted on the G10 rod (Figure 16.3). The transistor–transistor logic (TTL) signal, generated by IR triggering system was used to start the network analyzer. By measuring changes of the S_{11} reflection coefficient caused by the modulation of the resonance frequency, the distribution of the current in all of the TEM elements can be visualized simultaneously on a network analyzer, as shown in Figure 16.4. To observe the S_{11} modulation, which reflects the current distribution in the TEM elements (Figure 16.4b), the network analyzer was externally triggered in the linear amplitude mode with the frequency sweep turned off. This method allows for easy and quick bench measurements of the current distribution in the resonant elements for each linear mode of the volume coil. By adjusting the sinusoidal symmetry of the current distribution,[21] the optimal homogeneity of the B_1 field can be obtained. The currents in resonant coaxial elements are adjusted by varying their impedance, which is achieved by changing the extent of the overlap between the central rod and its shell (a change in capacitance).

Splitting the shield, and the consequent reduction of the coupling between the elements adjacent to the splits, substantially decreased isolation between two linear modes of the TEM coil, thereby compromising the quadrature performance of the coil. The reduction in mutual inductive coupling between adjacent elements from the introduction of a very small split in the shield suggests that the TEM structure supports some residual RF currents flowing in the shield in radial direction near the ends of the coil perpendicular to the coil axis. This is similar to end ring currents in birdcage coils. Introduction of a small split (much smaller than a wavelength) in a shield of a resonator parallel to RF currents should not substantially modify the RF field distribution or cause mode coupling. However, introducing a split perpendicular to current flow will have a substantial effect.[22]

Figure 16.5(a) shows the distribution of current in the split knee TEM coil elements measured for one of the linear modes with the coil driven at element 13 after the coil was adjusted using the tuning method described above. For convenience, the plot observed on

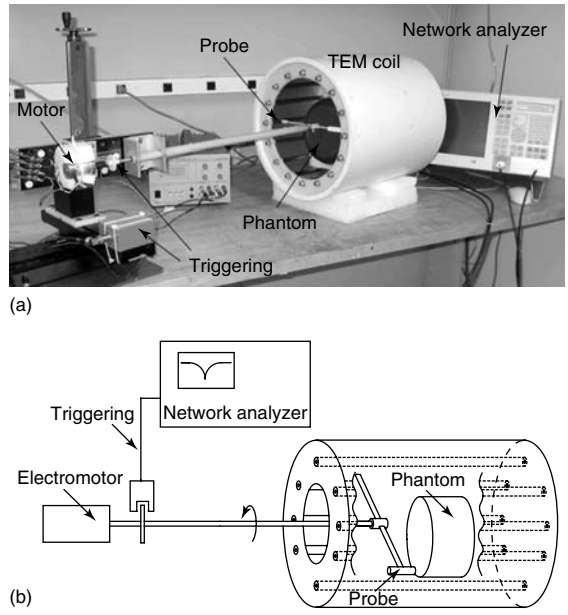

Figure 16.3. (a) Picture and (b) block diagram of the TEM coil tuning method. A ferrite probe was rotated in close proximity to the TEM elements to produce a shift of the resonance frequency and modulate S_{11}. To visualize the modulation of S_{11}, which reflects the current distribution in the TEM elements, the network analyzer was used in the linear amplitude mode with the frequency sweep turned off. The network analyzer was externally triggered from the rotation of the probe.

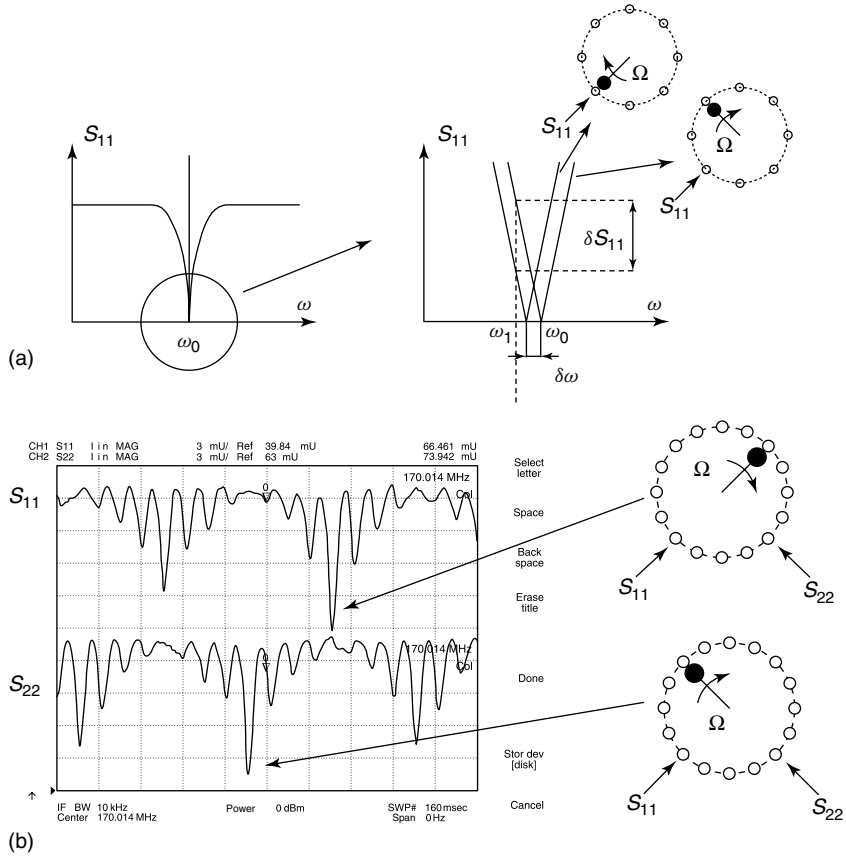

Figure 16.4. (a) Frequency dependence of the S_{11} reflection coefficient. The bottom linear part of the dependence is magnified on the right side of the figure. Two curves, measured at one of the driving ports (S_{11}) correspond to probe positions near TEM elements with maximum (bottom element) and zero (top element) RF current. The network analyzer is used in the CW mode at a fixed frequency equal to ω_1. (b) Distribution of the current in both linear channels of the TEM volume coil as observed on the network analyzer. The tuning method allows visualization of the two distributions of current for both linear modes simultaneously. Each peak in the current distribution corresponds to the probe passing near TEM elements. The right side of the figure correlates two elements with corresponding peaks in the current distribution.

the network analyzer (Figure 16.4) has been flipped vertically and normalized. The measurement was performed after the coil was adjusted to restore the isolation between the two modes. Since the method detects the square of the amplitude of current and is not sensitive to the phase,[20] both halves of the sinusoidal distribution have the same sign. As seen from the figure, the current distribution is not symmetric. Specifically, the current is increased in the elements adjacent to the splits (elements 4, 11, and 12) compared to elements distant from the splits (elements 6, 14, and 15) as was discussed above. Figure 16.5(b) shows the symmetric current distribution measured for one of the linear modes of the one-piece TEM volume coil. To restore the symmetry of the current distribution of the split TEM coil, the current in the elements adjacent to the splits as well as their immediate neighbors (elements 2, 5 and 9, 12) can be somewhat decreased by decreasing the capacitance of the TEM elements (by pulling the central conductors out). In practice, it was not possible to completely restore the symmetry without degrading the isolation between two linear modes. The isolation between the modes was adjusted primarily by decreasing the current in elements 7 (top) and 15 (bottom). Adjusting these two elements was the most effective way to

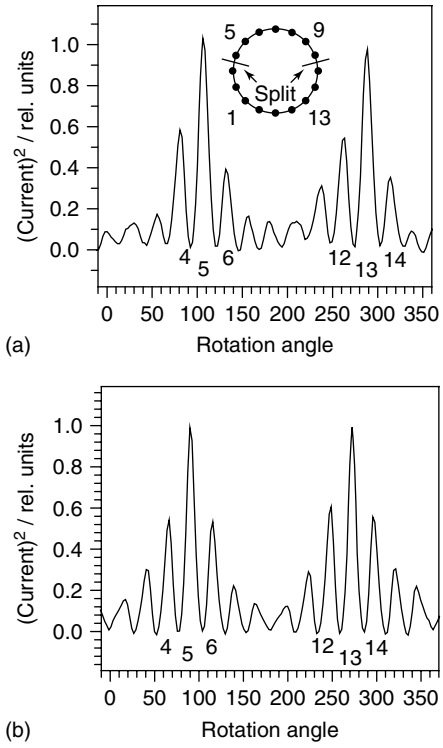

Figure 16.5. (a) The distribution of RF currents in elements of the quadrature TEM split knee volume coil measured for one of the linear modes after the coil has been tuned and adjusted. (b) The distribution of current in elements of continuous nonsplit TEM coil measured similarly as in (a).

restore the mode isolation as compared to tuning the other elements. The analogous distribution was also measured for the other linear mode of the TEM coil with the current increased in elements adjacent to the splits. The distribution of current flowing in TEM elements was also measured for the split head coil and produced a very similar pattern to that shown in Figure 16.5(a).

16.4 COIL TESTING AND EVALUATION

16.4.1 Imaging Procedure

All images were obtained on a 4 T Varian Inova system (Varian Associates, Inc., Palo Alto, CA). Knee images were obtained using T_1-weighted fast spin-echo sequence with TR (repetition time) = 1.2 s, TE (echo time) = 26.4 ms, echo train length = 16, 18 slices, slice thickness = 3 mm, gap = 3 mm, and in-plane resolution = 0.625 mm (matrix size 512 × 256, field of view (FOV) = 320 × 160 mm for sagittal and coronal images; matrix size 256 × 256, FOV 160 × 160 for axial images). The data were acquired with a single average.

To test the head coil performance, gradient echo images of the phantom and a human head were collected using 128 × 128 and 256 × 256 resolution, respectively, 1.5 mm slice thickness, 20 × 20 cm FOV, TE = 50 ms, TR = 400 ms, and flip angle = 30°. To provide anatomical contrast, a T_1-weighted inversion recovery gradient echo sequence was used with TR = 2500 ms, TIR (inversion recovery time) = 900 ms, a 90° excitation pulse, and a slice thickness of 1.5 mm with 128 × 128 resolution over an FOV of 19.2 × 19.2 cm. Echo planar images (EPI) brain images were acquired using a T_2*-weighted gradient echo EPI pulse sequence (TR/TE = 5000/25 ms, FOV = 256 × 256 cm, matrix 64 × 64 pixels, slice thickness = 4 mm, flip angle = 90°) without interleaving. All brain images were acquired with a single average.

The efficiency of the coils was assessed by determination of the B_1 field required to produce a 90° rotation using a slice-selective excitation pulse in a transverse slice in the center of the RF coil longitudinally in the head, knee, and tissue mimicking phantoms. To eliminate the effects of shaping the RF pulse, the B_1 value in kilohertz (or μT) per 1 kW of power was calculated based on the equivalent maximum amplitude square pulse duration. The homogeneity of the coils was measured by acquiring B_1 maps of the transmit field using the procedure described by Pan *et al.*[23] using 64 × 64 resolution and 3 mm thickness.

16.4.2 Testing Results

After bench adjustment, the half-volume coils were evaluated in the scanner. The residual asymmetry of the current distribution did not substantially affect the quality of the images or the overall coil performance. Figure 16.6 demonstrates transverse, sagittal, and coronal T_1-weighted spin-echo images of a human knee obtained using the split TEM knee coil. The split TEM knee coil was about 15–20% more efficient than the larger one-piece open-end TEM

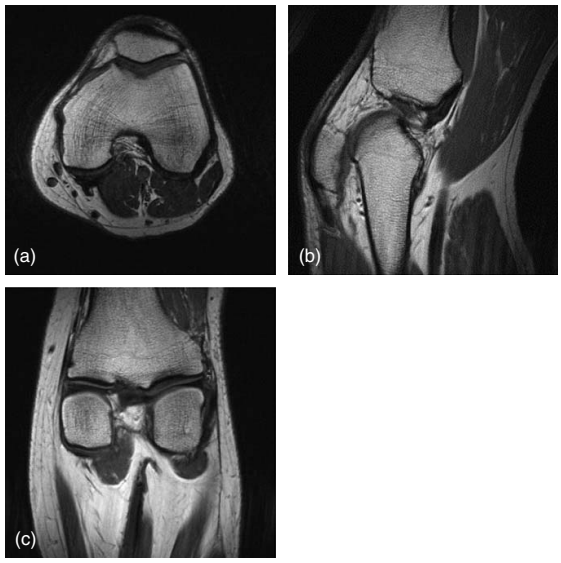

Figure 16.6. (a) Transverse, (b) sagittal, and (c) coronal human knee spin-echo images obtained using split TEM volume knee coil.

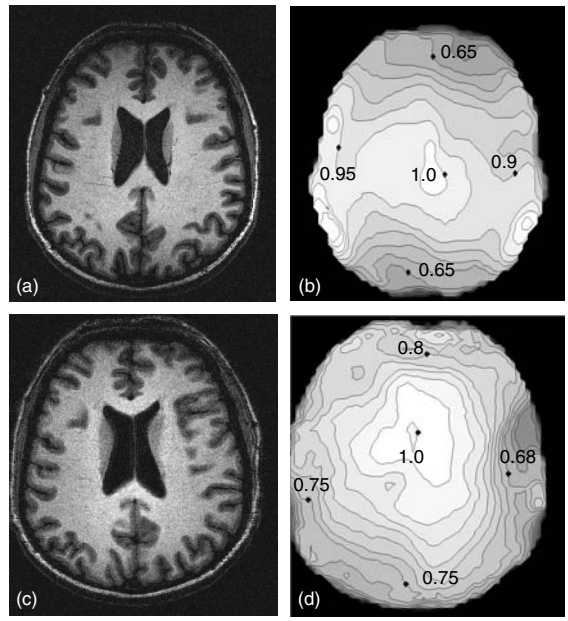

Figure 16.7. Gradient echo human brain images and B_1 maps of the corresponding slices obtained using the split TEM volume head coil (a and b) and continuous nonsplit TEM coil (c and d) of the same size.

coil, which was evaluated by measuring the power required to produce a 90° pulse of a certain length. A similar result was obtained for 2.0 L cylindrical leg-mimicking phantom. This increase in transmission efficiency of the split TEM can be attributed to a decrease in coil volume (due to a change in the coil diameter) as well as to minimizing the extension of the B_1 field from the wider coil's openings. The small decrease in signal at the very top of the coil is most likely due to the residual asymmetry of the current distribution. The split TEM knee coil generated a circularly polarized RF magnetic field B_1 of 1.43 kHz (or 33.6 μT) in amplitude in the central transverse slice of an average size human knee using 1 kW RF. Since the size of a human knee can vary, this measurement was also performed for 2.0 L cylindrical phantom (12 cm diameter, 50 mM NaCl). B_1 of 2.0 kHz (or 47 μT) per 1 kW was obtained.

Figure 16.7 shows head images and B_1 field maps obtained with the split TEM head coil and the one-piece TEM coil of the same size. All the images and the B_1 maps demonstrate a very characteristic pattern of increased magnitude in the center of the brain as compared to the periphery due to destructive interference.[4,24–26] The magnitude of the B_1 field measured at the top and the bottom of the split coil is ~10–15% lower in comparison to the analogous positions for the one-piece coil. Conversely, the B_1 field produced at the left and right sides of the split coil was ~20–25% greater than the B_1 field from the same locations for the one-piece coil. These in vivo measurements are in good agreement with the differences in current distribution between the two coils obtained by our bench measurements. The symmetric current distribution of the one-piece coil (Figure 16.5b) produced a symmetric B_1 map pattern (Figure 16.7d). In contrast, the higher current near the splits (Figure 16.5a) in the split coil enhances the B_1 field at the left and the right sides of the volume coil (Figure 16.7b). The alteration in B_1 distribution, however, did not substantially degrade the quality of the images shown in Figure 16.7(a) and (c).

The split TEM head coil generated a circularly polarized RF magnetic field B_1 of 1.1 kHz (or 25.8 μT) in amplitude in the central transverse slice of a human head using 1 kW RF. This is similar to or better than previously reported for a nonsplit quadrature TEM head volume coil of similar size (diameter at the element centers 27 cm, length 21 cm) that provided the equivalent of a 255 μs, 90° square pulse in the central transverse slice of the head using 1 kW RF

power.[4] This corresponds to a B_1 field amplitude of 0.98 kHz (or 23 μT). The effectiveness of the quadrature TEM head coil in producing circularly polarized RF magnetic field using a B_1 mapping method[23] was also evaluated. The ratio of the B_1^+ and B_1^- components of the circularly polarized magnetic field rotating clockwise and counter clockwise, respectively, averaged over the entire human head, measured better than 10 dB. This indicates that the average loss of the amplitude of the transmit B_1^+ field due to the contribution of the B_1^- component was less than 5%. Finally, the average B_1 field (measured over the entire slice) as well as power required to produce a 90° pulse in the transaxial slice at the center of the coil were approximately the same for both split and nonsplit TEM head coils within the error of the experiment (±1 dB). In comparison, a commercially available 3 T split head-sized birdcage coil (USA

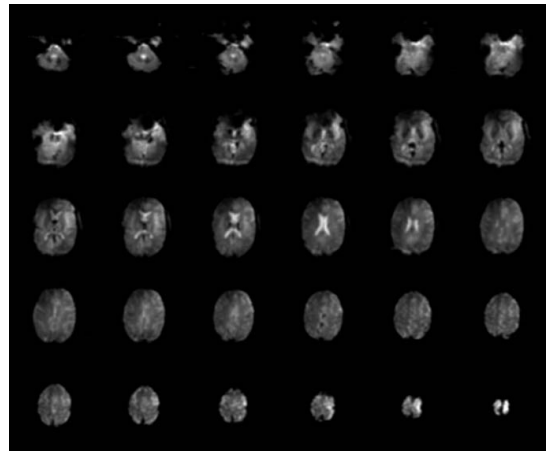

Figure 16.8. EPI images of a human brain obtained using the TEM split head coil.

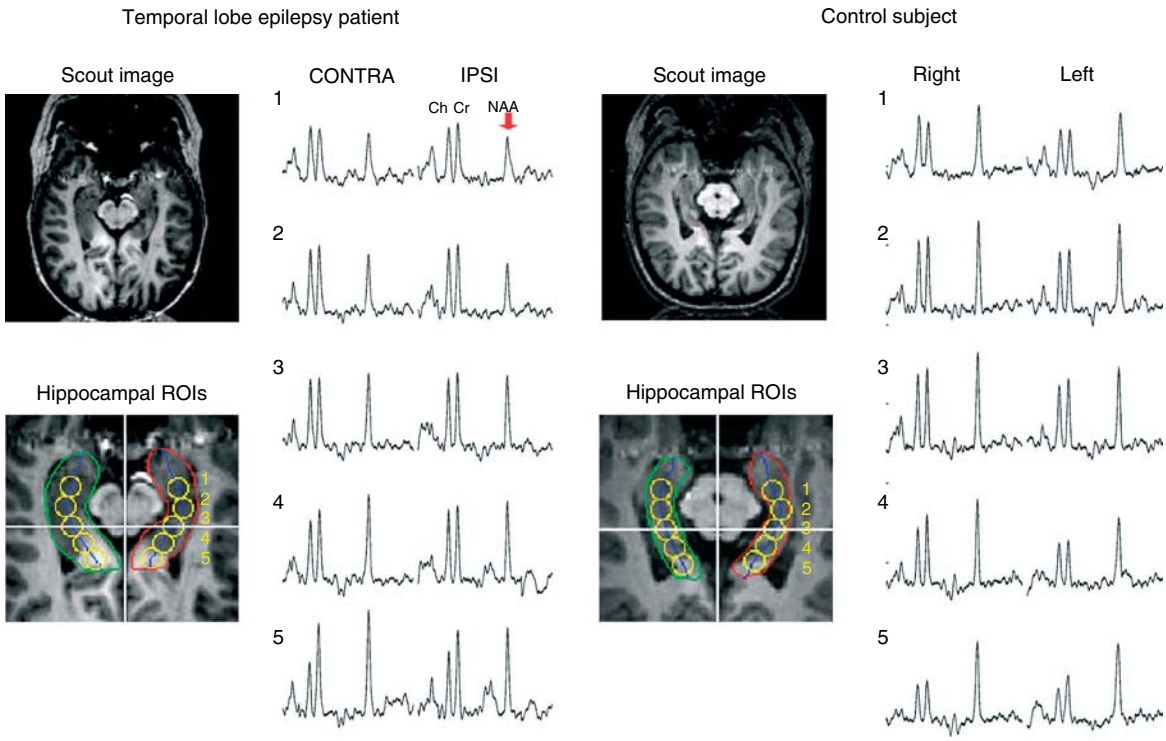

Figure 16.9. Data from a patient with temporal lobe epilepsy (a) and a control subject (b). The patient data includes a scout image, an expanded region of the scout image identifying the location of selected spectra (yellow circles) from the ipsilateral and contralateral hippocampi. Displayed to the right of the images are spectral data from the selected locations. The equivalent data is shown for the control subject. The resonances of interest, NAA, creatine (Cr), and choline (CH) are labeled.

Instruments, Aurora, OH) generated a B_1 field of 0.82 kHz (19.3 μT) per 1 kW of power using the standard Siemens head phantom.

Figure 16.8 presents EPI data obtained using a split head coil. No evidence of substantial eddy current artifacts was observed in the images.

16.5 APPLICATIONS

One of the primary advantages of high-field imaging in vivo is the increased signal-to-noise ratio (SNR) and spectral resolution afforded for spectroscopic imaging. However, to accrue the theoretical advantages of high-field spectroscopic imaging, coil sensitivity and homogeneity must be preserved. Displayed in Figure 16.9 are spectroscopic imaging data acquired with the split-head TEM coil from a patient with temporal lobe epilepsy and a control subject. All data were acquired at 4 T using a Varian Inova console and a quadrature head coil. The hippocampal data was collected using a modified LASER sequence (10 mm thickness, 80 × 100 mm in-plane FOV selection) in combination with two dimensions of phase encoding (24 × 24, FOV = 192 × 192 mm, 19.2 min) angulating the plane along the temporal pole.[27] To provide reproducible selection criteria across patients and controls, the hippocampal voxels were reconstructed using a voxel shifting method.[28,29] In the control data, the ratio of *N*-acetyl aspartate (NAA)/Cr is >1.2 for all pixels from both hippocampi. In contrast the patient with temporal lobe epilepsy shows substantially reduced NAA/Cr values (>0.8) from the anterior portions (loci 1 and 2) of both hippocampi. Further, NAA/Cr at a given location (e.g., locus 1) is lower in the ipsilateral as opposed to the contralateral hippocampus. The observation of reduced NAA/Cr as a marker for the presence and severity of neuronal injury can be used to localize and lateralize seizures in epilepsy patients.[30–34]

RELATED ARTICLES IN THE ENCYCLOPEDIA OF MAGNETIC RESONANCE

Birdcage Resonators: Highly Homogeneous Radiofrequency Coils for Magnetic Resonance

Probe Design and Construction

Whole Body Machines: NMR Phased Array Coil Systems

REFERENCES

1. D. M. Peterson, C. E. Carruthers, B. L. Wolverton, K. Meister, M. Werner, G. R. Duensing, and J. R. Fitzsimmons, *Magn. Reson. Med.*, 1999, **42**, 215.
2. M. D. Harpen, *Magn. Reson. Med.*, 1993, **29**, 713.
3. J. T. Vaughan, H. P. Hetherington, J. O. Otu, J. W. Pan, and G. M. Pohost, *Magn. Reson. Med.*, 1994, **32**, 206.
4. J. T. Vaughan, M. Garwood, C. M. Collins, W. Liu, L. DelaBarre, G. Adriany, G. P. Andersen, H. Merkle, R. Goebel, M. B. Smith, and K. Ugurbil, *Magn. Reson. Med.*, 2001, **46**, 24.
5. J. T. Vaughan, G. Adriany, M. Garwood, T. Yacoub, T. Duong, L. DelaBarre, P. Andersen, and K. Ugurbil, *Magn. Reson. Med.*, 2002, **47**, 990.
6. J. F. Bridges, U.S. Pat. 4 751 464 (1988).
7. G. Bogdanov and R. Ludwig, *Magn. Reson. Med.*, 2002, **47**, 579.
8. N. I. Avdievich and H. P. Hetherington, *Magn. Reson. Med.*, 2004, **52**, 1459.
9. G. Adriany, J. T. Vaughan, P. Andersen, H. Merkle, M. Garwood, and K. Ugurbil, In *Proceedings of the 3rd Annual Meeting of ISMRM*, Nice, France, 1995, p. 971.
10. J. T. Vaughan, In *Proceedings of the 6th Annual Meeting of ISMRM*, Sydney (NSW), 1998, p. 646.
11. J. Tian, and J. T. Vaughan, In *Proceedings of the 11th Annual Meeting of ISMRM*, Toronto, Canada, 2003, p. 2354.
12. J. T. Vaughan, G. Adriany, C. J. Snyder, J. Tian, T. Thiel, L. Bolinger, H. Liu, L. DelaBarre, and K. Ugurbil, *Magn. Reson. Imaging*, 2004, **52**, 851.
13. J. T. Vaughan, G. Adriany, and K. Ugurbil, U.S. Pat. 6 788 056 B2 (2004).
14. J. T. Vaughan, M. Garwood, and K. Ugurbil, *'Transactions 2001 Antenna and Propagation Society International Symposium'*, 2001, Vol. 1, 378.
15. J. T. Vaughan, G. Adriany, M. Waks, M. Watson, T. Thompson, H. Liu, G. Berghoff, K. Sundquist, and K. Ugurbil, In *Proceedings of the 11th Annual Meeting of the ISMRM*, Toronto, Canada, 2003, 718.
16. N. I. Avdievich, K. Bradshaw, J. H. Lee, A. M. Kuznetsov, and H. P. Hetherington, *J. Magn. Reson.*, 2007, **187**, 234.
17. J. Tropp, *J. Magn. Reson.*, 1991, **95**, 235.

18. J. H. Hwang, J. W. Pan, S. Heydari, H. P. Hetherington, and D. T. Stein, *J. Appl. Physiol.*, 2001, **90**(4), 1267.

19. J. Tropp, *J. Magn. Reson.*, 1997, **126**, 9.

20. N. I. Avdievich, V. N. Krymov, and H. P. Hetherington, *Magn. Reson. Med.*, 2003, **50**, 13.

21. C. E. Hayes, W. A. Edelstein, J. F. Schenck, O. M. Mueller, and M. Eash, *J. Magn. Reson.*, 1985, **63**, 622.

22. C. P. J. Poole, *Electron Spin Resonance: A Comprehensive Treatise on Experimental Techniques*, Wiley: New York, 1983.

23. J. W. Pan, D. B. Twieg, and H. P. Hetherington, *Magn. Reson. Med.*, 1998, **40**, 363.

24. G. H. Glover, C. E. Hayes, N. J. Pelc, W. A. Edelstein, O. M. Mueller, H. R. Hart, C. J. Hardy, M. O'Donnell, and W. D. Barber, *J. Magn. Reson.*, 1985, **64**, 255.

25. C. M. Collins, W. Liu, W. Schreiber, Q. X. Yang, and M. B. Smith, *J. Magn. Reson. Imaging*, 2005, **21**, 192.

26. P. F. Van de Moortele, C. Akgun, G. Adriany, S. Moeller, J. Ritter, C. M. Collins, M. B. Smith, J. T. Vaughan, and K. Ugurbil, *Magn. Reson. Med.*, 2005, **54**, 1503.

27. A. A. Cohen-Gadol, J. W. Pan, J. H. Kim, D. D. Spencer, and H. H. Hetherington, *J. Neurosurg.*, 2004, **101**, 613.

28. H. P. Hetherington, R. I. Kuzniecky, K. Vives, O. Devinsky, S. Pacia, D. Luciano, B. Vasquez, S. Haut, D. D. Spencer, and J. W. Pan, *Neurology*, 2007, **69**, 2256.

29. D. B. Twieg, D. J. Meyerhoff, B. Hubesch, K. Roth, D. Sappey-Marinier, M. D. Boska, J. R. Gober, S. Schaefer, and M. W. Weiner, *Magn. Reson. Med.*, 1989, **12**, 291.

30. H. Hetherington, R. Kuzniecky, J. Pan, G. Mason, R. Morawetz, C. Harris, E. Faught, T. Vaughan, and G. Pohost, *Ann. Neurol.*, 1995, **38**, 396.

31. R. Kuzniecky, H. Hetherington, J. Pan, J. Hugg, C. Palmer, F. Gilliam, E. Faught, and R. Morawetz, *Neurology*, 1997, **48**, 1018.

32. R. Kuzniecky, J. Hugg, H. Hetherington, E. Butterworth, E. Bilir, E. Faught, and F. Gilliam, *Neurology*, 1998, **51**, 66.

33. R. Kuzniecky, J. Hugg, H. Hetherington, R. Martin, E. Faught, R. Morawetz, and F. Gilliam, *Neurology*, 1999, **53**, 694.

34. W. J. Chu, R. I. Kuzniecky, J. W. Hugg, B. Abou-Khalil, F. Gilliam, E. Faught, and H. P. Hetherington, *Magn. Reson. Med.*, 2000, **43**, 359.

Chapter 17

Antennas as Surface Array Elements for Body Imaging at Ultra-high Field Strengths

A. J. E. Raaijmakers and C. A. T. van den Berg

Department of Radiotherapy, University Medical Center Utrecht, Utrecht 3508GA, The Netherlands

17.1 INTRODUCTION

With the advent of ultrahigh field imaging (>7 T), RF coils have to be designed for ultrahigh frequencies. Although head imaging is performed routinely at ultrahigh field strengths, the higher frequency is posing severe challenges for body imaging on these platforms. This is caused by the following: first, the wavelength decreases with increasing frequency. At 7 T, the wavelength in tissue is shorter than the transverse body dimensions, which results in interference patterns as shown by Vaughan *et al*.[1] Secondly, the higher frequency causes a reduced penetration depth. On the transmit side, the B_1^+ levels that can be achieved become lower. On the receive side, the obtained signal-to-noise ratio (SNR) gain from moving to higher field strengths is reduced by the decreased sensitivity of the coils. Thirdly, the higher frequency causes higher specific absorption rate (SAR) levels that have to be compensated by long repetition time (TR) values to avoid tissue heating.

These problems are partially addressed by using a multitransmit surface coil array. Surface elements (rather than a volume coil) are used because of their higher B_1^+ efficiency: more B_1^+ for the same amount of power. Multitransmit means that the phases and amplitudes of all elements can be adjusted. In this way, the interference pattern of B_1^+ within the patient can be controlled to ensure constructive interference at the region of interest.[2]

For an optimal performance of the coil array, the design of the individual elements is critical. They need to generate as large as possible B_1^+ at the region of interest, while depositing as little as possible SAR. Additionally, low coupling is advantageous. This chapter shows that, for deeply located targets, the classical method of designing a coil is no longer applicable. Instead, the coils have to be regarded and designed as antennas. The recently presented "single-side adapted dipole antenna" is an example of such a design.[3]

In the early days of MR imaging, the B_1 field was generated by a solenoid coil as depicted in Figure 17.1. In the years and decades that followed, widespread shapes and geometries were introduced to generate the B_1 field. These included loop coils, Helmholtz pairs, birdcage coils, transverse

RF Coils for MRI
Edited by J. Thomas Vaughan and John R. Griffiths
 ISBN: 978-0-470-77076-4

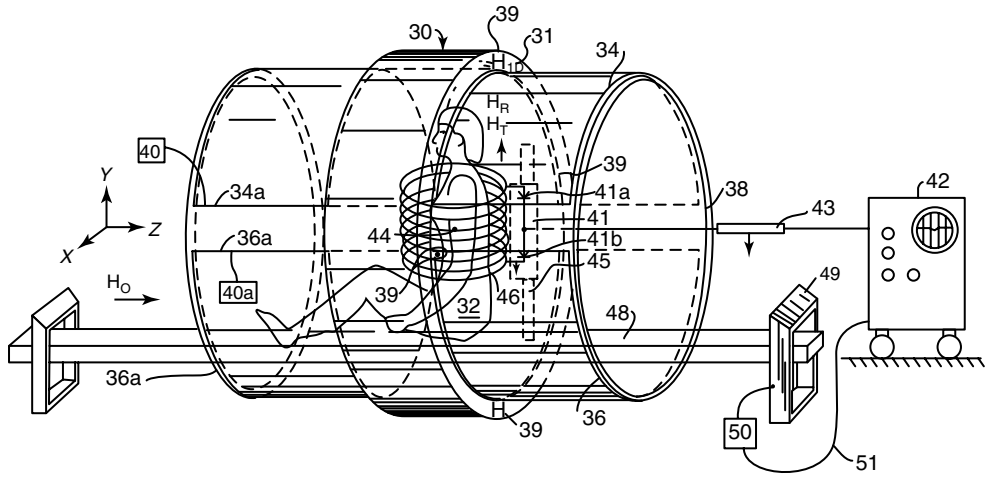

Figure 17.1. Drawing from an early MRI patent (1981) by Damadian.[4] The RF coil is a solenoid.

electric-magnetic (TEM) resonators, and microstrip elements. Many of these are used with several elements simultaneously in a RF coil array. With every advance in B_0 field strength, new designs have been presented. They are all, however, still referred to as *coils*.

The name "coil" for the B_1 field applicators is because of the working principle of RF coils in classic MR imaging: It is based on the principle that currents will generate a B_1 field. This is the principle for elements that are clearly coils such as solenoids, Helmholtz pairs, and loop coils. But this is also the principle for structures that do not have the coil-like geometry such as birdcages, TEM resonators, and microstrip elements. Generating B_1 field by currents has effectively become the definition of a coil. And owing to the principle of reciprocity, elements that are meant to receive signals are also called coils. Note that all coils are designed as resonant structures to maximize their efficiency and/or sensitivity.

However, at high frequencies, coils start to behave as antennas. Close to the coil, a region exists where the B_1 field is very high. These are the reactive fields that are associated with the traditional desired resonance operation of the coil. But at larger depths inside the tissue, the reactive fields will have decayed and the so-called radiative fields become more dominant. Here, the RF field distribution has turned into an electromagnetic wave that propagates away from the coil. At high field strengths, generating such an electromagnetic wave is therefore a more suitable way of achieving the required B_1 in more deeply located body regions.

This requires designing the coils on the entirely different principles of antenna engineering. It even raises the question whether coils should still be called coils. B_1 antennas would be more appropriate. However, because the term "RF coils" is and has been the name for the RF applicators of an MR system over many years, we shall continue to use the word "coil" as well. An antenna could, in this perspective, be regarded as a "special coil".

17.2 THEORY

In the early days, B_1 coils were—just like the B_0 coils—designed by the law of Biot–Savart:

$$\boldsymbol{B}(r) = \frac{\mu_0}{4\pi} \int \frac{I\,\mathrm{dl} \times r}{|r|^3} \tag{17.1}$$

where

$\boldsymbol{B}(r)$ = magnetic field strength at position r
μ_0 = permeability of free space
dl = differential coil segment
I = current in coil segment.

However, the law of Biot–Savart can be derived from the fourth law of Maxwell, where the term $\partial E/\partial t$ is considered negligible,

$$\nabla \times \boldsymbol{B} = \mu_0\, J + \mu_0 \varepsilon_0 \frac{\partial \boldsymbol{E}}{\partial t} \tag{17.2}$$

where
J = current density
ε_0 = permittivity of free space
$\boldsymbol{E}$ = electric field strength.

It is therefore only valid at DC and low frequencies, because at high frequencies considerable E-fields will be induced everywhere due to Faraday's law

$$\nabla \times \boldsymbol{E} = \frac{\partial \boldsymbol{B}}{\partial t} \tag{17.3}$$

and the term $d\boldsymbol{E}/dt$ can no longer be neglected. Worse, at high frequencies (high B_0 field strengths), the E-fields that are cogenerated along with the B-fields will generate an electromagnetic wave that will be emitted from the coil. In fact, at high frequencies, coils start to behave as antennas.

17.2.1 Electromagnetic Waves

In electromagnetic waves, the E-field and the B-field show a periodic behavior in both time and space. Also, the E- and B-fields are orthogonal to each other and to the propagating direction. Figure 17.2 shows a schematic representation of E- and B-fields in a propagating wave.

A propagating wave is characterized by its frequency. Depending on the medium that it traverses, the wavelength follows from the frequency, equation (17.4). Thus, at higher frequencies, wavelengths are smaller. Also note that the relative dielectric permittivity in air is 1, but the relative dielectric permittivity in human tissues has a wide range of values, resulting in an "effective" permittivity of 36–60.[5] As a consequence, the wavelength at 7 T in the body is 13–17 cm.

$$\lambda = \frac{c}{f} = \frac{1}{f\sqrt{\mu\varepsilon}} =^{a} \frac{\lambda_0}{\sqrt{\varepsilon_r}} \quad k = \frac{2\pi}{\lambda} \tag{17.4}$$

where
λ = wavelength
c = speed of light in medium
f = frequency
μ = permeability of medium
ε = permittivity of medium
λ_0 = wavelength in free space
ε_r = relative permittivity of medium
k = wave number
[a]: If $\mu_r = 1$
μ_r = relative permeability of medium.

In a propagating wave, two quantities are of particular importance. Note that they are calculated from the magnetizing field $\boldsymbol{H}$ which is linearly related to $\boldsymbol{B}$ by

$$\boldsymbol{B} = \mu\boldsymbol{H} = \mu_0\mu_r\boldsymbol{H} \tag{17.5}$$

where $\boldsymbol{H}$ is the magnetizing field strength.

17.2.1.1 Poynting Vector

The power flux of a wave is expressed by the Poynting vector $\boldsymbol{S}$, equation (17.6). It is the energy that is carried by the wave per unit time and area and it is therefore expressed in watts per meter square. It is a vector quantity, calculated by the vector product of the electromagnetic wave components $\boldsymbol{E}$ and $\boldsymbol{H}$. Its direction specifies the direction of energy flow.

$$\boldsymbol{S} = \boldsymbol{E} \times \boldsymbol{H} \tag{17.6}$$

17.2.1.2 Wave Impedance

The wave impedance η is a parameter that characterizes an electromagnetic wave. It is the ratio of the electromagnetic wave components $\boldsymbol{E}$ over $\boldsymbol{H}$, equation (17.7). A wave traveling freely in a medium has a wave impedance that is equal to the equilibrium wave impedance of the material η_{medium} [equation (17.8)]. This equilibrium value is a property of the material. Close to sources (antennas) and interfaces, the wave impedance will deviate from this equilibrium value. For waves propagating inside "wave guides", the wave impedance can have a wide range of values. Wave guides are a study on their own in RF and microwave engineering.[6,7] Traveling wave imaging, as introduced by Brunner and van den Berg, is

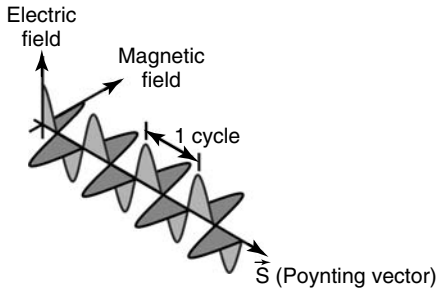

Figure 17.2. E-field and B-field orientation in a propagating wave.

based on this phenomenon, where the RF shield of the MR scanner acts as the wave guide.[8,9]

$$\eta = \frac{\boldsymbol{E}}{\boldsymbol{H}} \tag{17.7}$$

where η is the wave impedance

$$\eta_{\text{medium}} = \sqrt{\frac{\mu}{\varepsilon}} \tag{17.8}$$

where η_{medium} is the equilibrium wave impedance of the medium.

If propagating waves hit a boundary between two media, part of the wave will be reflected and part of the wave will be refracted, according to Snell's law. For a wave impinging orthogonally to the boundary this law reads as follows:

$$R = \frac{\eta_1 - \eta_2}{\eta_1 + \eta_2} \tag{17.9}$$

where

R = reflection coefficient

η_1, η_2 = equilibrium wave impedances of the media.

If the material properties are similar, the reflection is less.

17.2.2 MR Imaging: RF Coils or RF Antennas?

An antenna is designed to emit an electromagnetic wave. A coil, in contrast to an antenna, is designed to generate B-fields. For DC currents, the resulting B-field can be calculated by the law of Biot–Savart [equation (17.1)]. For AC currents, the law is, in principle, not valid, but for low frequencies and regions close to the coil, the law of Biot–Savart can still closely predict the behavior of the coil. At further distance and/or higher frequencies, the law fails. This is because the oscillating B-fields will generate oscillating E-fields due to Faraday's law. These E-fields, together with the already present B-fields, will generate an electromagnetic wave, propagating away from the coil.

17.2.3 Near Field and Far Field

On the basis of this behavior, two regions can be distinguished:

Close to the coil, the B-field generated by the currents in the coil is much larger than the E-fields that are generated concomitantly. Or more precisely, the E/B ratio is much smaller than the local equilibrium wave impedance, because the B-fields are high and the E-fields are low. Therefore, only a small fraction of the B-field is associated to the propagating wave. The major part of the B-field is associated to the so-called reactive field that is generated by the currents. These fields cause an alternating power flow direction by which the energy is trapped near the coil and will not be emitted to the surroundings. Since a coil is a resonant system, these fields are the resonant fields of the coil, and they will increase with increasing quality factor (Q-factor). In antenna theory, this region is called the *near field*.

With increasing distance from the coil, the B-fields and the E-fields decrease. But the reactive part of the electromagnetic field will decrease more rapidly than the radiative part. As a consequence, the region far away from the coil is characterized by pure propagating wave behavior. Here, the E- and B-fields have a fixed relation to each other (equilibrium wave impedance) and the power flow (Poynting vector) is always directed outward, away from the coil. This region is called the *far field* or *radiation zone* in antenna theory.

The regions described above display the extreme characteristics of an electromagnetic field around a coil or antenna. In between these regions, the field pattern will gradually change from one to the other. This is called the *transition zone*.

17.2.4 Estimating the Extent of the Near Field and the Far Field

For MR imaging coil design, it is important to know whether the target imaging region is located in the near field (design a coil) or in the far field (design an antenna). Vice versa, it is important to know the extents of the near field and the transition zone. Several rules of thumb are known for estimating the extent of the near field and the start of the far field.[10] For instructional purposes, we highlight one method.

Equation (17.10) describes the fields of a (small) magnetic dipole. A magnetic dipole is an infinitesimally small loop coil, e.g., the magnetization of a voxel in MR imaging. The magnetic field of such a dipole is the equivalent to the B_1 field of a loop coil. It depends on a $1/r^3$ term, a $1/r^2$ term, and a $1/r$

term. Close to the dipole, the $1/r^3$ term will dominate. This region is called the *near field*. In the next region, the transition zone $1/r^2$ will dominate. (Note that Biot–Savart also predicts a quadratic drop-off with distance.) In the furthest region, the term $1/r$ dominates. This is the far field. Note that with a $1/r$ drop-off of field strength, the Poynting vector will decrease with $1/r^2$, which is consistent with the fact that the same amount of energy has to spread out over an ever-increasing spherical shell area. These regions are indicated by Figure 17.3, where the dipole field is plotted next to $1/r$, $1/r^2$, and $1/r^3$. The logarithmic plot clearly shows how the behavior goes from $1/r^3$ to $1/r^2$ into $1/r$. By equating the terms $1/r^3$ and $1/r$ in relation to each other [equation (17.11)], one can calculate the "crossover point" at $r = \lambda/2\pi$. This is the center of the transition zone where the field decays by $1/r^2$. Note that the presence of the e^{-jkr} term in all expressions in equation (17.10) is responsible for the periodicity of the wave. Also, if the medium is conductive, this term will result in an additional exponential decay of the fields.

$$E_\varphi = -j\frac{\omega\mu_0 m\, k^2}{4\pi}\left(\frac{j}{k\,r}+\frac{1}{(k\,r)^2}\right)\sin(\theta)\mathrm{e}^{-jkr} \tag{17.10a}$$

$$H_\theta = j\frac{\omega\mu_0 m\, k^2}{4\pi\eta_{\text{medium}}}\left(\frac{j}{k\,r}+\frac{1}{(k\,r)^2}+\frac{-j}{(k\,r)^3}\right)\sin(\theta)\mathrm{e}^{-jkr} \tag{17.10b}$$

$$H_r = 2j\frac{\omega\mu_0 m\, k^2}{4\pi\eta_{\text{medium}}}\left(\frac{1}{(k\,r)^2}+\frac{-j}{(k\,r)^3}\right)\cos(\theta)\mathrm{e}^{-jkr} \tag{17.10c}$$

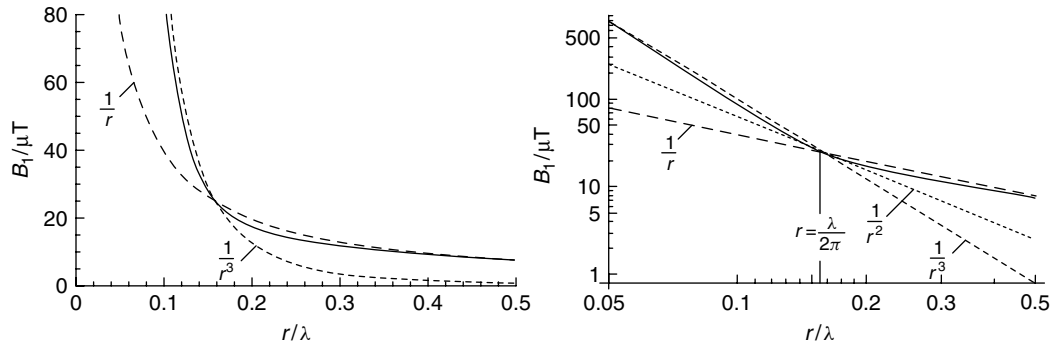

Figure 17.3. Magnetic field strength of a magnetic dipole as a function of distance r over wavelength λ.

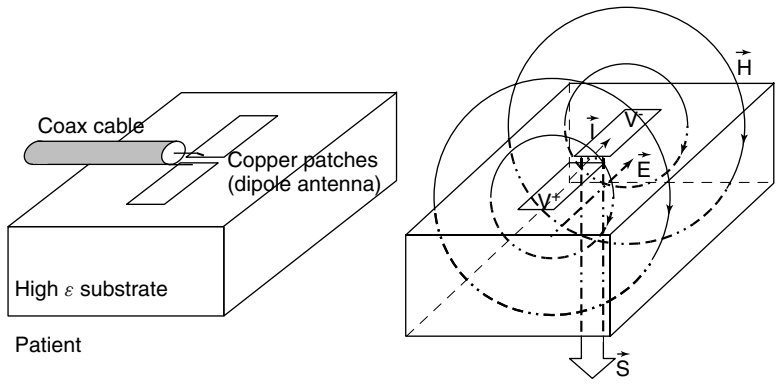

Figure 17.4. The single-side adapted dipole antenna (radiative antenna). (a) Schematic drawing. (b) Currents and voltages, H- and E-fields, and the resulting Poynting vector **S**.

where m is the dipole magnetic moment

$$\frac{1}{k\,r} = \frac{1}{(k\,r)^3} \Rightarrow r = \frac{1}{k} = \frac{\lambda}{2\pi} \approx 0.16\lambda \qquad (17.11)$$

Although these models are a simplification of a RF coil in MR imaging, they do show the principle mechanism by which near field and far field can be discriminated—the rate of the decrease in amplitude of the fields. It is also important to realize that the near-field and far-field boundaries are relative to the wavelength. This means that at larger frequencies, the near field and far field will respectively end and begin at distances closer to the coil or antenna.

17.2.5 Coils Vs Antennas: Design Principles

A coil needs large currents to generate a large B_1 field. It is therefore designed as a resonant structure with a high quality factor (Q-factor). The unloaded vs loaded Q-factor ratio is used to verify that there are no significant coil losses. This design ensures large reactive fields in the near-field region.

An antenna needs currents and voltages on its structures to generate the required B- and E-fields that constitute an electromagnetic wave. The resulting B- and E-fields should create a Poynting vector that is oriented toward the target region. In addition, the E- over B-field ratio (wave impedance) should be as close as possible to the equilibrium wave impedance. As a consequence, antennas will have a low Q. This has the extra advantage of low interelement coupling.

17.3 THE SINGLE-SIDE ADAPTED DIPOLE ANTENNA

At 7 T, the wavelength in tissue is approximately 17 cm. A typical deep-body target such as the prostate (10 cm depth) is therefore, considering Section 17.2, likely located in the far field. The RF coil should then definitely be regarded as an antenna: it should aim at generating far field efficiently with as little as possible near field.

The requirements for antennas when imaging deep-body parts are the same as those for the field of locoregional hyperthermia.[11] In this field, cancerous regions in the body are heated up a few degrees Celsius to make them more sensitive to radiotherapy and/or chemotherapy. The heating is achieved by an array of RF antennas that aims at delivering high levels of energy to the target, while preventing excessive heating in other parts of the body. The similarity is obvious and therefore, antenna designs in hyperthermia are also likely to be applicable to MR imaging.

One example of such an antenna from the field of hyperthermia is the single-side adapted dipole antenna.[3] It consists of a dipole antenna mounted upon a dielectric substrate with a high permittivity (Figure 17.4). The substrate is placed adjacent to the skin of the patient. The total length of the dipole should equal one half of the wavelength in the substrate material. In this way, maximum current will be generated in the center and voltage maxima will appear at the endings of the dipole. As a consequence, the primary B-field is rotating around the longitudinal axis of the element while the E-field is oriented along the longitudinal axis (Figure 17.4). The high permittivity of the substrate will augment the E-field within the substrate, resulting in a larger Poynting vector into the substrate and toward the patient. Another way of looking at it is that the dipole antenna dimensions are matched to the wavelength in the substrate and not to the wavelength in air. Radiation into air is therefore inhibited because the antenna is simply too small.

The high permittivity of the substrate shortens the wavelength, which enables the construction of a dipole antenna within reasonable dimensions. The shorter wavelength has another advantage. A dipole antenna is an electric (and not a magnetic) antenna. In its near field, electric field components dominate and these should be kept out of the patient because they generate undesired energy deposition (SAR). Therefore, the thickness of the substrate should be sufficient to avoid the antenna near field from entering the tissue. Iterative simulations have shown that this thickness should approximately be at least one quarter of a wavelength.

To avoid losses, the conductivity of the substrate should be negligible. The permittivity of the substrate should be high and preferably should match the (effective) permittivity of the body tissue on which it will be placed. This will ensure minimal reflections of the generated wave at the interface of substrate and tissue [equation (17.9)]. Additionally, the material susceptibility should be similar to that of the body tissue, to avoid B_0 distortions in the target region. Distilled water is a material that fulfills these requirements and can easily be obtained. However,

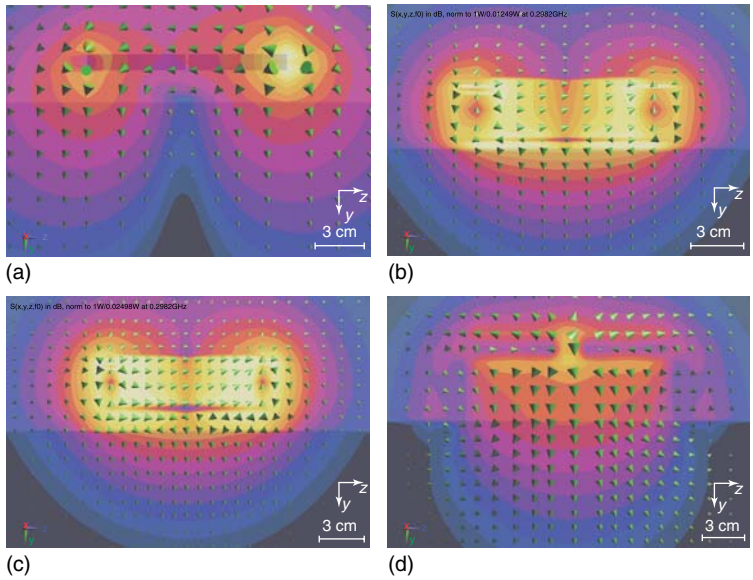

Figure 17.5. Poynting vector distributions inside the elements and in the upper part of the phantom, normalized for 1 W delivered power. (a) Loop coil, (b) microstrip 5 mm spacer, (c) microstrip 15 mm spacer, and (d) radiative antenna.

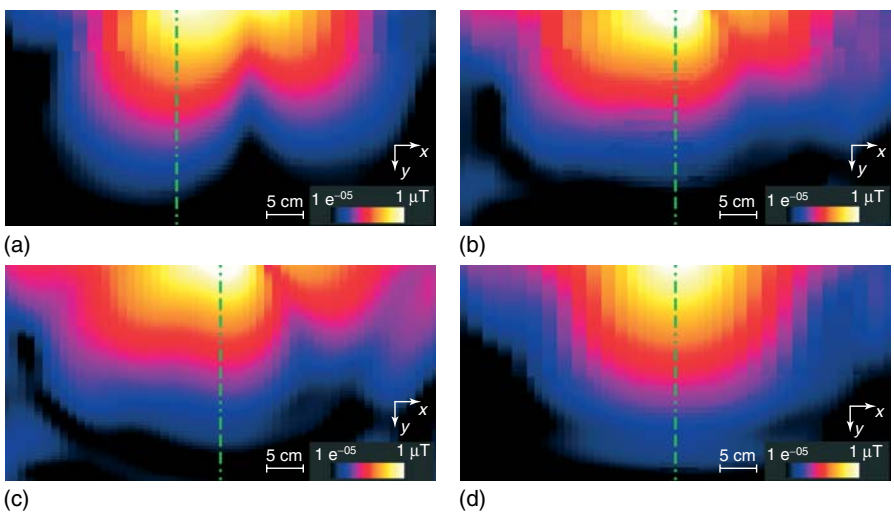

Figure 17.6. B_1^+ distributions in the transversal z-plane, in logarithmic scale, normalized for 1 W delivered power. (a) Loop coil, (b) microstrip 5 mm spacer, (c) microstrip 15 mm spacer, and (d) radiative antenna. Dashed lines indicate profiles as presented in Figure 17.7.

a solid material would be more convenient. Suitable solid materials can be found in the wide range of ceramics that are used in high-power RF electronics. Also, these ceramics have a much lower conductivity than distilled water.

The single-side adapted dipole antenna is an example of a radiative antenna. It has been designed to emit a propagating wave into the tissue. Although less specific, the shorter term "radiative antenna" is used instead throughout this chapter.

Table 17.1. Quantitative results

	B_1^+ (μT)		SAR_{max} (W/kg)	$SAR_{max}/(B_1^+)^2$ (W/kg/μT²)	
	@10 cm	@15 cm		@10 cm	@15 cm
Loop coil	2.26	0.809	663	130	1014
Stripline 5 mm	1.96	0.620	4037	1055	10518
Stripline 15 mm	1.89	0.647	2149	603	5135
Radiative	2.67	0.980	1381	194	1438

·B_1^+ and maximum SAR values (1 g averaged SAR) at 10 and 15 cm depth in the phantom, normalized to 1 W delivered power. Additionally, the maximum SAR relative to B_1^+ is presented at both depths.

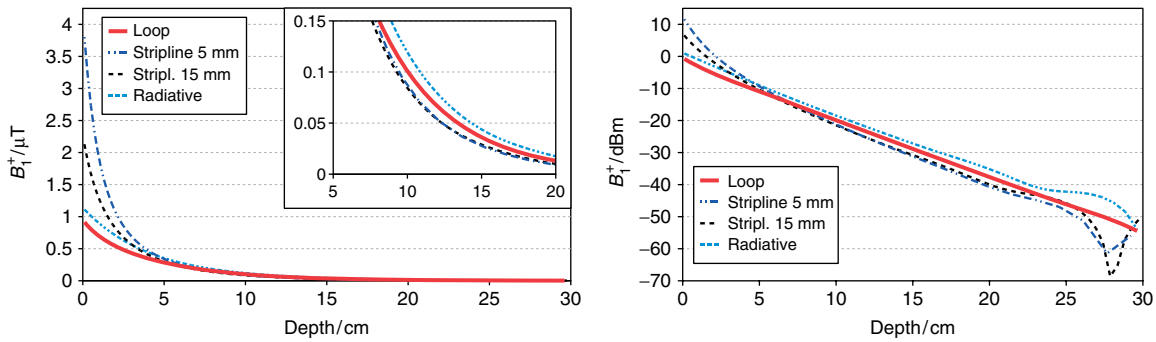

Figure 17.7. In-depth B_1^+ profiles for all investigated elements, normalized for 1 W delivered power. All profiles are drawn as indicated in Figure 17.6. (a) Linear profiles, with magnification in inlet. (b) Logarithmic profiles.

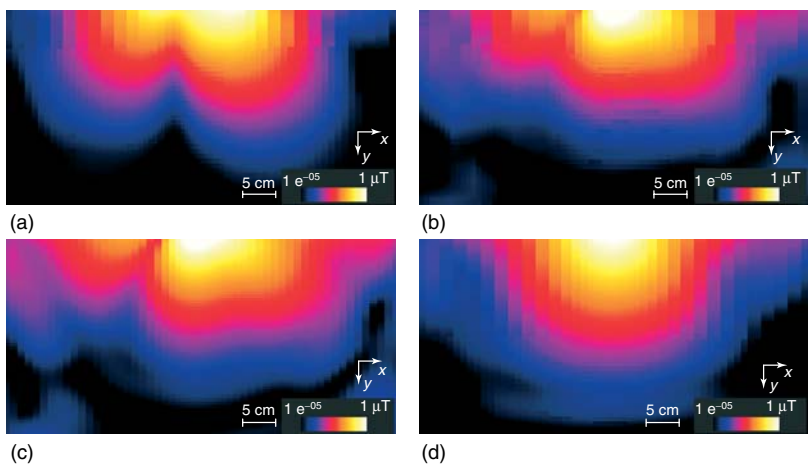

Figure 17.8. B_1^- distributions in the transversal z-plane, in logarithmic scale, normalized for 1 W delivered power. (a) Loop coil, (b) microstrip 5 mm spacer, (c) microstrip 15 mm spacer, and (d) radiative antenna.

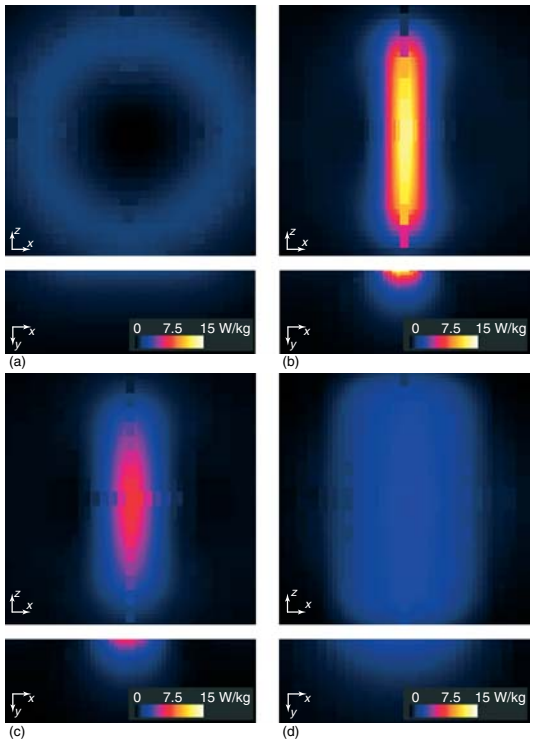

Figure 17.9. SAR distributions in the transversal z-plane with the maximum SAR and in the coronal x-plane directly below the element, linear color scale, normalized for 1 W of delivered power. (a) loop coil, (b) microstrip 5 mm spacer, (c) microstrip 15 mm spacer, and (d) radiative antenna.

17.4 SINGLE-ELEMENT ANALYSIS

In a recent publication, we have demonstrated the beneficial properties of a radiative antenna in comparison to more conventional coil array elements.[3] These conventional coil array elements include a loop coil (10 cm diameter) and 2 microstrip designs (10 cm length) with a 5 or a 15 mm spacer to the patient. All elements were tested by simulating their performance on a large cubic phantom with permittivity and conductivity of 36 and 0.45 S m^{-1}, respectively. The simulations were performed using the FDTD package SEMCAD X (Speag, Zurich, Switzerland).

Figure 17.5 shows the resulting Poynting vector distribution. The microstrip elements show a Poynting vector that is directed along the longitudinal axis within the element and the spacer. Only inside the phantom is the Poynting vector oriented outward. The radiative antenna, however, shows a Poynting vector orientation that is directed downward into the phantom through the entire substrate. In this way, a propagating wave is generated within the substrate. When the wave impinges on the phantom surface, the wave is already in the far-field mode. The loop coil, remarkably, also shows a Poynting vector oriented downward into the phantom. However, the Poynting vector distribution is inhomogeneous, with the largest energy flux under the loop conductor and zero energy flux on the central axis.

As a consequence of these differences in Poynting vector distribution, a difference in B_1^+ distribution is expected.

Figure 17.6 shows the B_1^+ distributions for all investigated elements. While the B_1^+ distributions of the microstrip elements and the loop coil are irregular and asymmetric, the B_1^+ distribution of the radiative elements is much more homogeneous and almost symmetric. To evaluate the B_1^+ penetration of all elements, profiles have been drawn along the dashed lines in Figure 17.6. These profiles are indicated in Figure 17.7. These profiles show clearly that the resonant microstrip elements achieve higher B_1^+ at the surface, close to the element, while the radiative elements and the loop coil have lower B_1^+ gain at the surface but reach a higher B_1^+ level in the deeper parts.

These results relate to the transmit efficiency. However, they also translate directly into the receive capabilities of these elements: the intrinsic SNR of a receive or transceive element is proportional to the B_1^- per unit power that the element can (or could) deliver when operating in transmit mode.[12] These distributions are shown in Figure 17.8. They show that the B_1^- distribution of any single element is the mirror image of the B_1^+ distribution of the same element. The results in Figure 17.7 therefore also show the relative SNR profiles for all investigated elements. Additionally, since the B_1^+ distributions of the radiative elements are symmetric, the B_1^- and B_1^+ distribution are the same for the radiative elements. This results in having maximum sensitivity where the B_1^+ excitation is the largest. Quantitative results are presented in Table 17.1.

Another important transmit element characteristic is the energy deposition in the tissue that may result in considerable temperature rise (see Chapter 33 by Shrivastava). In our publication,[3] we addressed this issue by simulating the SAR distributions of the individual elements: loop coil, microstrip elements, and the radiative antenna. Figure 17.9 shows

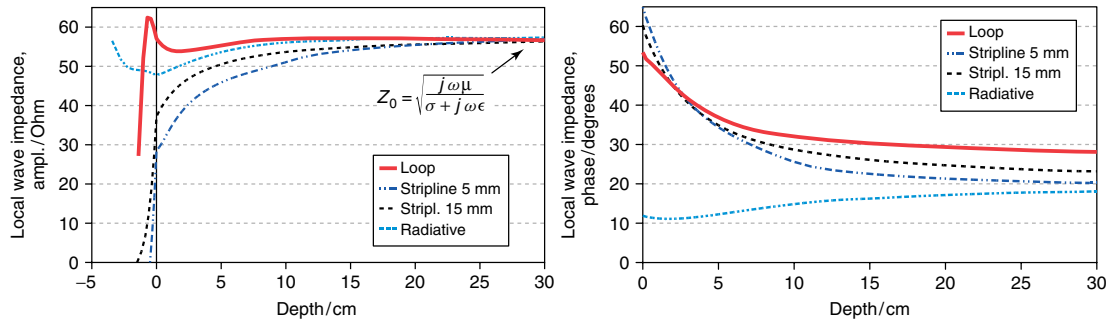

Figure 17.10. Local wave impedance profiles of electromagnetic field distribution for all investigated elements in depth. The formula for equilibrium wave impedance in a dielectric medium is indicated in the graph. All graphs converge to this value.

Figure 17.11. Array of radiative antennas around pelvis for volunteer measurement.

the SAR distributions in the coronal ($x-z$) plane at the surface just below the element and the transverse ($x-y$) plane across the location of maximum SAR. All distributions are normalized to 1 W power delivery. The loop coil shows a clear loop-shaped SAR pattern that also shows the lowest maximum SAR level. The radiative antenna has a higher SAR level but not as high as that of the microstrip elements. To make an honest comparison, the SAR level should be normalized to the $B_1{}^+$ level that can be obtained by an element at the depth of interest. These values are indicated in Table 17.1. The loop coil has a larger area to distribute its energy and therefore shows a lower maximum SAR value than the radiative antenna. If the surface area of the radiative antenna is increased to square dimensions (which we tested by simulation), the SAR distribution of the radiative antenna also shows lower SAR values. However, the elements then become too large to be used conveniently in an array around a human pelvis.

To further characterize the electromagnetic field distribution of the radiative antenna in comparison to the other elements, the local wave impedance as a function of depth was extracted from the simulation results (Figure 17.10). The diagram shows that the electromagnetic field distribution of all elements approaches a propagating wave at sufficient distance from the element. This is indicated by the fact that the local wave impedance approaches the equilibrium wave impedance of the medium that is 55.7 Ω. The diagram also shows that the loop coil and the radiative antenna approach this value sooner, i.e., their near field is smaller.

Note that the microstrip elements start off with a low local wave impedance (E/H ratio). So at the surface of a phantom/patient, they will generate large B_1 values and relatively low E-fields. This may lead to the erroneous conclusion that these elements are more beneficial, because they will generate low E-fields and consequentially lower SAR. However, Figure 17.9 shows that the microstrip elements have a higher SAR at the surface than the loop coil and the radiative antenna.

This is explained by the following: owing to their low E/H ratio, microstrip elements have relatively low sample losses. This causes them to have a high quality factor: large currents for the same amount of power. These large currents generate large B-fields in the near field of the antenna. (This is the working principle of a classical coil in MR imaging.) However, these B-fields are so large that although the E/H ratio is beneficial, the corresponding E-fields are still

Figure 17.12. Imaging results of array of eight radiative antennas on a volunteer. (a) Spoiled gradient echo (T_{1W}) transverse image of prostate and pelvis: TE/TR = 3.6 ms/40 ms; resolution = $0.5 \times 0.5 \times 3$ mm^3; and NSA = 4. (b) Turbo spin echo (TSE) (T_{2W}) transverse image of prostate and pelvis: TE/TR = 85 ms/3000 ms; resolution = $0.5 \times 0.5 \times 3$ mm^3; TSE-factor = 18; and NSA = 2. (c) Sagittal image with same sequence parameters.

higher than for the other elements, resulting in higher SAR values.

All these results show that the radiative antenna is a very suitable element for body imaging at high magnetic field strengths. However, the loop coil turns out to be quite suitable as well, although its field patterns are more irregular. It therefore must be an efficient antenna too. This is contradictory to what is known about the radiation pattern of a loop coil in free space: it radiates predominantly in the plane of the loop orthogonal to the loop coil axis and not along its axis. However, in the presence of a conductive medium such as a patient, things apparently change. The loading of the loop coil by the conductive tissue causes the impedance of the loop coil to increase. Consequently, the voltage gradient and the E-fields along the loop increase. This may cause the E/H ratio around the loop coil to approach the equilibrium wave impedance of the conductive medium. If then the loop coil dimensions fit the wavelength in the tissue, it becomes an effective antenna and generates a wave inside the tissue. Additionally, the loop coil dimensions are too small to emit a wave into the other half-space filled with air. This may explain the beneficial properties of the 10 cm diameter loop coil.

17.5 VOLUNTEER IMAGING RESULTS

In our publication, we also demonstrated volunteer imaging results.[3] A transceive surface array was constructed from eight radiative elements as depicted in Figure 17.11. The elements were aligned in a belt-shaped manner around the pelvis. S_{12} measurements were performed to measure the coupling, which was less than −15 dB between any two elements.

In this way, prostate images were acquired as depicted in Figure 17.12. The resulting images clearly show the urethra, the central gland, and the peripheral zone of the prostate.

The maximum $B_1{}^+$ level within the prostate was 10 μT with 8×200 W net power arrival at the elements. This value was measured with a single voxel STEAM sequence by gradually increasing the transmit amplitude.

17.6 FINAL REMARKS

With the advent of ultrahigh field body imaging (>7 T), the target imaging region appears to have shifted from the near field and the transition zone into the far field. For this reason, it becomes more appropriate to think of RF coils in MRI as antennas. By using design principles for antennas, a new kind of element has been developed: the single-side adapted dipole antenna. We have shown that it is more beneficial than high-Q resonant elements. Volunteer images have been obtained with an array of eight of these antennas.

The next generation MR platforms will have even higher field strengths. Scanners already exist for 9.4 and 11.7 T. At those field strengths, coil design by antenna principles will become more important, because far-field conditions will by then also apply for head imaging. Also, the presented single-side adapted dipole antenna will become more suitable because the dimensions of the antenna will become smaller. This will allow the construction of a denser array with more elements. The smaller dimensions may also facilitate the use of these elements for head imaging.

REFERENCES

1. J. T. Vaughan, C. J. Snyder, L. J. DelaBarre, P. J. Bolan, J. Tian, L. Bolinger, G. Adriany, P. Andersen, J. Strupp, and K. Ugurbil, *Magn. Reson. Med.*, 2009, **61**, 244.
2. G. J. Metzger, C. Snyder, C. Akgun, T. Vaughan, K. Ugurbil, and P. F. Van de Moortele, *Magn. Reson. Med.*, 2008, **59**, 396.
3. A. J. E. Raaijmakers, O. Ipek, D. W. J. Klomp, C. Possanzini, P. R. Harvey, J. J. W. Lagendijk, and C. A. T. van den Berg, *Magn. Reson. Med.*, 2011, **66**, 1488.
4. R. V. Damadian, *Apparatus and method for nuclear magnetic resonance scanning and mapping*, U.S. Pat. 4411270 (1981).
5. B. van den Bergen, C. A. T. van den Berg, D. W. Klomp, and J. J. W. Lagendijk, *J. Magn. Reson. Imaging*, 2009, **30**, 194.
6. N. Marcuvitz, *Waveguide handbook* (IEEE Electromagnetic wave series), 1986.
7. S. F. Mahmoud, *Electromagnetic Waveguides: theory and application* (IEEE Electromagnetic wave series), 1991.
8. D. O. Brunner, N. De Zanche, H. Fröhlich, J. Paska, and K. P. Pruessmann, *Nature*, 2009, **457**, 994.
9. C. A. T. van den Berg, L. W. Bartels, and J. J. W. Lagendijk, *Using the natural resonant modes of the RF cavity for whole body excitation at 7 T*, ISMRM Workshop on advances in High field MR, 2007.
10. C. Capps, *Near field or far field?* EDN magazine http://www.edn.com/contents/images/150828.pdf'.
11. H. Kroeze, J. B. van de Kamer, A. A. C. De Leeuw, and J. J. W. Lagendijk *Phys. Med. Biol.*, 2001, **46**, 1919.
12. S. M. Wright and L. L. Wald, *NMR Biomed.*, 1997, **10**, 394.

PART D
Special Purpose Coils

Chapter 18
Catheter Coils

Ergin Atalar

Electrical & Electronics Engineering Department, Bilkent University, Ankara, TR-06800, Turkey

18.1 INTRODUCTION

Magnetic resonance imaging (MRI) is a very powerful tool for diagnostic imaging; however, it is very seldom used for guiding interventional procedures. On the other hand, in many procedures the quality of the guiding image modality is less than perfect, and therefore MRI can be considered as an alternative.

Among these interventional procedures, the percutaneous cardiovascular procedures have a special place. Today, most of these procedures are conducted under the guidance of X-ray fluoroscopy. Using this guidance method, the catheters include guidewires that are visible, but this projection-based imaging modality provides very little information on the tissue or organ of interest. MRI appears to be a natural alternative to X-ray based imaging for this purpose because of its high tissue contrast. In addition, MRI has no ionizing radiation. High X-ray exposure to the patient, especially to children, can be harmful. This is also a significant problem for the physician who is conducting the procedure on a daily basis. MRI solves this problem as well. Therefore, MRI has a great potential to replace X-ray in guiding some of the percutaneous cardiovascular procedures.

While the advantages of MRI over X-ray fluoroscopy are apparent, it is also very obvious why currently MRI cannot replace X-rays. The patient access is poor in MRI scanners, although development of short and wide-bore magnets has alleviated this problem. MRI-compatible equipment such as patient monitoring systems has limited availability. Most catheters and guidewires are not compatible with MRI. While these or similar problems are real, they are not fundamental limitations. The most important limitation of MRI compared with X-ray fluoroscopy is its poor visualization of the interventional devices. In MRI, most interventional devices appear dark, and therefore it is possible to visualize them only if a thin slice imaging method is used. The interventional devices get lost in the body when thick slice imaging is used.

This very fundamental problem of the poor visualization of catheters gave rise to the research field of catheter tracking under MRI. This effort resulted in the development of the catheter coils, i.e., the catheters that can be tracked using the MRI signals that are received by small coils embedded inside the catheters.

The development of catheter coils did not have a single motivation. The other motivation is to obtain high-resolution images of the blood vessels. As is well known in the field of MRI, the shape, size,

RF Coils for MRI
Edited by J. Thomas Vaughan and John R. Griffiths

ISBN: 978-0-470-77076-4

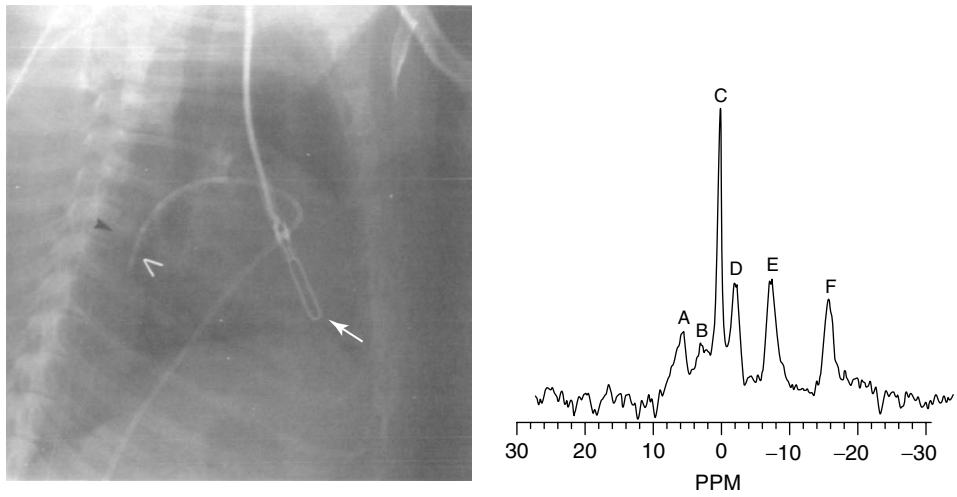

Figure 18.1. An X-ray image of the first catheter coil and a ^{31}P spectrum obtained using this coil. In the 1983 article by Kantor *et al*.,[1] the details of the novel procedure are explained.

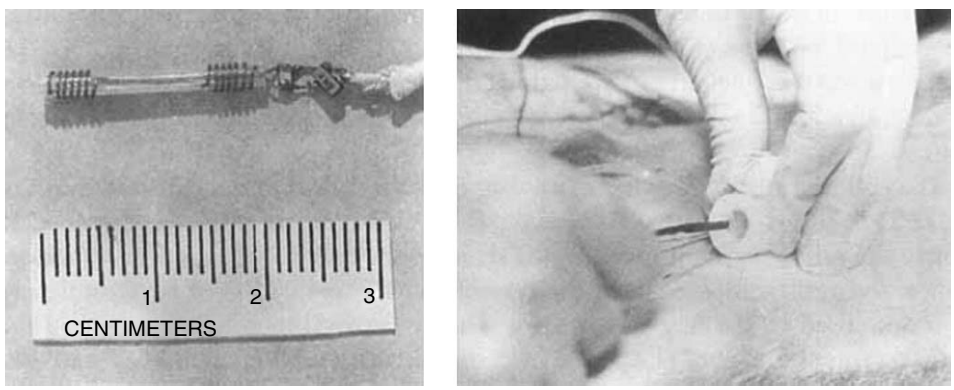

Figure 18.2. First demonstration of the opposed solenoid design for a catheter coil by Dr Hurst *et al*.[2] The overall probe diameter was reported as 3.2 mm or 10 Fr.

and position of the receiver radiofrequency (RF) coils have critical importance for the signal-to-noise ratio (SNR) of the acquired images. With rather straightforward manipulation of the pulse sequences, the increase in the SNR can be used for higher image resolution. As the RF coils get closer to the point of interest, the SNR is expected to be improved and therefore higher image resolution can be obtained. With this motivation, researchers have investigated the placement of small receiver coils, so-called catheter coils, inside the blood vessels.

The interest in development of catheter coils developed immediately after commercial MRI scanners became available. In 1984, Dr Howard Kantor, while working at the NIH, tested the first catheter coil concept for increasing the SNR in ^{31}P NMR spectra.[1] As is well known, the ^{31}P signal is very weak compared to the signal of proton and therefore obtaining a clinically useful result is often difficult. On the other hand, one of the key components in the SNR in a magnetic resonance experiment is the position and the design of the receiver coil. SNR can be increased significantly by reducing the size of the coil and placing it close to the region of interest. In Dr Kantor's case, the region of interest was the heart. He and

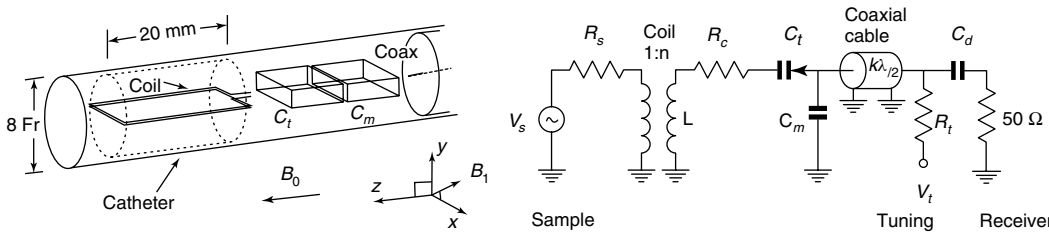

Figure 18.3. Detailed description of a catheter coil embedded inside an 8 Fr catheter. (Reproduced from Ref. 4. © Elsevier Inc., 1993.)

his colleagues placed a small loop (7.5 × 24 mm, two turns) inside the heart. They tuned the coil using a single capacitor and obtained ^{31}P spectra of the myocardium, as shown in Figure 18.1. This pioneering approach triggered interest in catheter coils and resulted in many more publications on the subject.

Three research groups led by Dr Gregory C. Hurst of Case Western Reserve University,[2] Dr Alastair J. Martin of the University of Toronto,[3] and Dr Krishna Kandarpa of Brigham and Women's Hospital[4] demonstrated the use of catheter coils for high-resolution imaging of blood vessels almost simultaneously. While the designs of Dr Hurst and Dr Martin were based on opposed solenoid coils (Figure 18.2), the design of Dr Kandarpa was a small rectangular loop (elongated loop) placed in an 8 Fr (1 Fr is 1/3 mm) catheter (Figure 18.3). Using this design, Dr Kandarpa showed high-resolution images of excised human arteries. These designs are discussed later.

In the mean time, the first catheter tracking was initiated by Dr Jerome L. Ackerman of Massachusetts General Hospital (MGH) with his pioneering work published as a 1986 *Society of Magnetic Resonance in Medicine Annual Meeting* abstract.[5] In this work, Dr Ackerman explains the use of a small RF coil for tracking the position of interventional devices (Figure 18.4). Later, this work was extended by Dr Charles L. Dumoulin in a 1993 article in an elegant way.[6] In this method, Dr Dumoulin applies non-slice-selective RF pulses followed by three orthogonal readout gradients to obtain the projection of the catheter in three orthogonal axes. From this information, it becomes rather trivial to find the location of the tip of the catheter. This method was later used by many researchers.

In the next section, the designs of catheter coils are discussed.

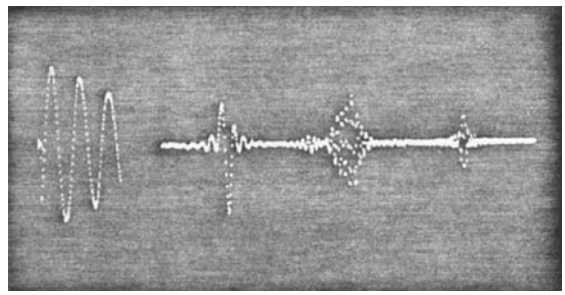

Figure 18.4. First demonstration of catheter tracking. In the experiment, a doped water sample was placed in a 7 mm diameter solenoid coil. The first signal is the free-induction decay. The later echoes were acquired in the presence of *x*, *y*, and *z* gradients. The frequency of each echo determines the position of the catheter in the corresponding direction.

18.2 CATHETER COIL DESIGNS

Researchers have developed many catheter coil designs. In the evaluation of the performance of these designs, in addition to their ability to help track the position of the catheter and/or acquire high-resolution images of the blood vessels, their mechanical properties are of critical importance. We start this section with a discussion on the mechanical properties of catheters.

One of the most important mechanical properties of catheters and guidewires is their dimension. The dimension of a catheter is usually measured in Fr (abbreviation of French), which determines its maximum diameter (a 3 Fr catheter's diameter is 1 mm). While a 15 Fr catheter can be considered very large, a 3 Fr catheter is small. Size selection depends on the specific application.

Most catheters have one or more lumens for different functions. Some lumens are used for holding guidewires and others for injecting therapeutic or

contrast agents. These lumens can also be used for delivering other vascular devices to remote body parts. Obviously, the dimensions of these lumens are also critical. For example, a standard guidewire diameter (usually measured in inches; 0.035, 0.025, and 0.014 in. are typical guidewire dimensions but other dimensions are also used) needs to be used for the lumens that hold guidewires.

Stiffness is a critically important mechanical property of catheters, and it varies greatly with the application of the device. A typical guidewire has a stiff shaft for improved torque (ability to turn the distal end of the guidewire by rotating its proximal end) and pushability (ability to transfer the longitudinal force from the proximal end to the distal end); however, the distal end of the guidewire should be very soft for entering into delicate vessels without damaging them. Guiding catheters have similar stiffness properties. These properties of guiding catheters and guidewires enable the interventionists to navigate inside the body. Other types of catheters, such as balloon catheters, are navigated inside the blood vessels with the help of guidewires and guiding catheters, and therefore their torque or pushability are not critical, but they should be as soft as possible.

The above-mentioned mechanical properties determine the kinds of RF coils that can be embedded inside a catheter. Obviously, a large and rigid RF coil is not desirable inside a flexible and thin catheter, since it may alter the mechanical properties of the catheter. In the next subsections, various designs that can be placed inside catheters are discussed. We will start with the design of the elongated loop.

18.2.1 Elongated Loop Design

As mentioned above, flexibility is of critical importance in catheter coil design. However, when a coil flexes, its inductance may change, and therefore the tuning of the coil and its performance may degrade. In order to resolve this issue, a conductor loop is formed using two parallel wires by shorting them out at the distal end and using the proximal end as the terminal of the loop coil. Since the inductance of this design does not change significantly when the wires flex, it is ideal for a catheter coil design.

The early demonstration of this design by Atalar *et al.*[7] is shown in Figure 18.5. In this design, the two capacitors, which were used for tuning and matching of the coil, respectively, were placed right at the terminal of the coil. While the coil itself was 4 Fr in size (diameter: 1.33 mm), the maximum diameter of the design (around the region where the capacitors are placed) was 9 Fr (diameter: 3 mm). Decoupling is achieved by placing a shunt PIN diode on the coaxial cable. The position of the diode is adjusted to minimize induced currents on the leads when the PIN diode is on. The design is further miniaturized in Ref. 8 to 5 Fr by using microfabrication techniques. Both in vivo and ex vivo tests were conducted to demonstrate the performance of the design.

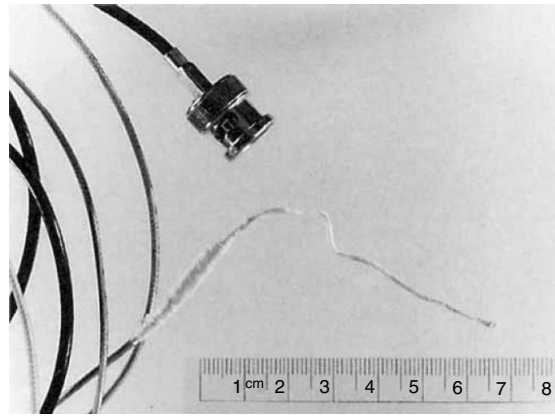

Figure 18.5. Picture of an elongated loop design. (Reproduced from Ref. 7. © John Wiley & Sons Ltd, 1996.)

In order to understand the sensitivity of a coil, one can use the reciprocity principle and assume an imaginary unit current applied at the terminal of the coil and use the transverse component of the magnetic field created by this current as the sensitivity of the object. When the magnetic field is normalized by the square root of the real part of the impedance measured at the terminal of the coil, the sensitivity of the coil can be obtained.

The sensitivity of elongated loop designs as RF receiver coils depends on many parameters. This design provides the best quality images when the axis of the catheter is along the main magnetic field. In this case, the sensitivity of the catheter drops with the square of the distance to the catheter; it is relatively uniform along its length and also in the circumferential direction. When the orientation of the catheter is not along the main magnetic direction, circumferential sensitivity variations are observed. In addition, when the length of the coil increases, sensitivity variation along its length can be observed. In the designs reported in the literature, approximately

10 cm long catheter coils are used in 1.5 T MRI scanners. The separation between wires plays a critical role in the coil's performance. An RF coil designer who designs surface coils knows that the diameter of a coil should be approximately the same as the depth of the point of interest in the body. One may form an analogy between the wire separation of an elongated coil by the surface coil's diameter, but in this case since the wire separation is always smaller than the point of interest (typically wire separation is 0.5 mm whereas the point of interest is typically farther away than 5 mm), the SNR of the acquired images with elongated loop designs increases with increase in the wire separation. In addition to these parameters, the dielectric material that covers the coil has a significant role in the performance of the design. As might be expected, the performance of the design improves with thick insulation. The insulation material, especially around the tuning and matching capacitors, should have low losses. Teflon is a preferred material for this purpose. The wire diameter also is critical in the design. The losses in the coil are mainly due to the resistance of the wire (eddy current losses are typically negligible in this design), and therefore thick wires are preferred. Because of its MR compatibility and superelasticity properties, one may consider nitinol as a conductor material but its rather poor conductivity makes it a nonideal choice. Since the skin depth at the Larmor frequency is only a few micrometers, one may consider using silver- or gold-plated nitinol for this purpose. On the basis of the mechanical design constraints, the designer needs to optimize the wire length, diameter, separation, and insulation thickness. As mentioned above, proper choice of the wire and insulation materials is also important.

When manufacturing an elongated loop coil, fixed-value capacitors are typically used for tuning and matching, mainly because of their small size. The desired capacitance values can be obtained by placing multiple capacitors in parallel. One alternative method is to adjust the length of the coil for a given tuning capacitance value. As in the surface coil tuning process, distributing the capacitance around the elongated loop is a preferred method. This method not only reduces the load dependence of the resonance frequency but also improves SNR, although only slightly because in the elongated loop design the main loss source is the conductivity of the wires. Since the quality factor of an elongated loop design is rather low (around 10), tuning and matching is relatively easy compared to that in surface coils.

When calculating the sensitivity of the coil, unbalanced currents should be considered. Unbalanced currents are the currents on the outer surface of the coaxial cable. If a current is applied to a transmission line with two parallel wires, it is expected that the currents on the wires are equal in magnitude but opposite in direction. In this condition, the current is considered to be "balanced", and all the electrons flowing from one wire return from the other one. If a coaxial cable is used, when equal and opposite currents flow on the inner conductor and the shield, the magnetic field generated by this balanced current is totally trapped in the dielectric material of the coaxial cable and no magnetic field can be observed outside the shield. On the other hand, if the currents on the inner conductor and the shield are unbalanced, the excess current flows on the outer surface of the shield. The magnetic field generated by the current in the wire is not totally trapped inside the dielectric of the coaxial cable but leaks into the medium around the coaxial cable. When a coaxial cable is connected to an electrically asymmetric elongated loop coil, unbalanced currents are observed that reduce the SNR of the acquired images and cause asymmetrical sensitivity in the circumferential direction. In order to eliminate these unbalanced currents, electrical symmetry needs to be maintained, and also, when possible, balun circuits should be used. Since balun circuits are typically very bulky, a bazooka balun using double-shielded coaxial cables can be used. As can be understood from the above discussion, dealing with unbalanced currents is often difficult. If it is ignored, they cause significant image artifacts and SNR degradation.

Tuning and matching of the elongated loop design is a significant problem. If one wants to achieve the maximum SNR, the tuning and matching capacitors should be placed at the end of the loop before connecting the elongated loop to the coaxial cable. To reduce the unbalanced currents, a symmetrical tuning/matching circuit is preferred. Since the presence of this circuit reduces the flexibility and increases the diameter of the design, alternative approaches are discussed in the literature. Placing a single tuning capacitor without a matching capacitor inside the catheter is an alternative if the designer accepts an associated SNR loss. Some designers place no capacitors in the catheter and tune the design remotely by placing the related circuit elements in a box outside the catheter. This results in

a significant performance loss, but the flexibility of the design is not compromised. In cases where the inductance of the loop changes when the catheter flexes inside the body, adjustment of tuning may be necessary. Electronic tuning using a varactor diode has been proposed to solve this issue.[4] Although this is an attractive alternative to fixed capacitors, the varactor diodes generate additional noise and degrade the performance of the design. The resulting compromise must be considered during the design. In short, in tuning an elongated loop, the designer should consider all the mechanical and electrical constraints.

One other important aspect of the elongated loop design is decoupling the design from the transmitter coil (this is typically a birdcage coil). As mentioned earlier, PIN diode-based decoupling circuits are used in the elongated loop designs; however, this alone is not enough to obtain the desired decoupling. Induced currents on the coaxial cable of the design should be handled with care. As mentioned when describing the sensitivity of the coil, these unwanted induced currents may be decreased using balun circuits. If there is strong coupling between the transmit coil and the elongated loop design, it may cause significant amplification of the RF electric field around the coil, leading to excessive heating and possibly a burn. Testing of the design in adverse conditions is necessary to ensure patient safety.

In the literature, elongated loop design can be seen in many forms. One of the most interesting designs is the expandable coil.[9] As was previously mentioned, as the separation between two parallel wires increases, the SNR of the acquired images increases. On the other hand, the size of the catheter limits the maximum wire separation in the elongated loop design. This problem is addressed by designing an expandable loop (Figure 18.6). In this design, one of the main drawbacks is that the shape of the coil after expansion may not be reproducible and therefore the inductance of the coil may vary, causing incorrect tuning of the coil. In the publication by Quick *et al*.,[9] this issue is addressed by using a loop made of a superelastic material or mounting it on a balloon catheter.

One other elongated loop design that can be seen in the literature is the cardiac electrophysiology (EP) signal measurement catheter.[10] Two wires that are used for EP signal measurements are also used as the wires of the elongated loop. In this work, Susil *et al*.[10] showed that with the same catheter it is possible to measure the EP signal and also continuously track the position of the catheter under MRI.

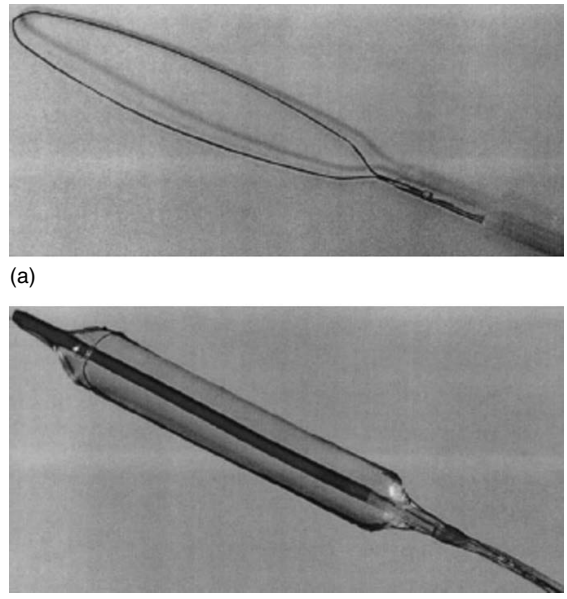

Figure 18.6. Expandable loop design. (a) Self expanding loop and (b) balloon-mounted loop designs. (Reproduced from Ref. 9. © John Wiley & Sons Ltd, 1999.)

An elongated loop can be twisted[11] in order to enable accurate tracking of the position of the catheter. By twisting the loop, periodic signal voids are obtained along the length of the catheter. This pattern is easy to recognize and therefore easy for tracking.

In short, the elongated loop catheter coils have been very well studied, and parameters that affect their performance are very well known.

18.2.2 Loopless Design

Miniaturization of catheter coils is a challenge. As discussed in the elongated loop design, reducing the catheter size reduces the SNR performance of the design, since the separation between the wires decreases. In order to solve this problem, the loopless design has been proposed. In this design, the current is applied to an antenna that does not have a closed loop. One may think that the loop is closed by conduction through the body. Since there is no loop in the design, the common name of "coil" cannot be

used for this type of RF receivers, but instead the word "antenna" is used.

The loopless antenna design was first described by Ocali and Atalar[12] as a coaxial cable with an extended inner conductor. Since no other elements are involved in this design, the diameter of the antenna is solely determined by that of the coaxial cable. Although very thin coaxial cables exist, mechanical constraints limit the minimum diameter of the design. In, Ref. 13, a 0.014 in. diameter loopless design was reported in the form of a guidewire.

In Ref. 12, the SNR performance of the loopless design was optimized by adjusting the whip length (extending the inner conductor beyond the end of coaxial cable). When a bare wire is used, the optimum whip length becomes approximately equal to a quarter wavelength where the wavelength is measured in the body at the Larmor frequency. This value is approximately 10 cm for 1.5 T and 5 cm for 3 T scanners. As described by Susil *et al*.,[14] the optimum whip length can be decreased by coiling the whip and increased by insulating it with a dielectric material. Note that the dielectric constant of the body (and water) is typically much higher than that of any dielectric material one may use. Even a very thin layer of insulation has a very strong effect on the optimum whip length.

As in the elongated loop design, the loopless design provides no significant sensitivity variation in the circumferential direction. The loopless design's sensitivity drops approximately in proportion to the distance to the antenna. Note that, in the elongated loop design, the sensitivity drops approximately with the square of the distance. Therefore, while the elongated loop design outperforms the loopless design when imaging regions are very close to the catheter, its performance degrades rather quickly, and further away from the catheter the loopless design outperforms the loop design. The sensitivities of typical designs are approximately equal when the point of interest is at a distance of 7 times the wire separation of the loop design.

The sensitivity of the loopless design along its length shows a significant variation. At the junction point (where the whip of the antenna starts and the coaxial cable ends), the sensitivity is maximal, whereas at the tip of the whip the sensitivity is nearly zero. The sensitivity also drops toward the proximal end of the loopless antenna. When the shaft (coaxial cable) is insulated, the sensitivity is extended. This property of the loopless antenna has been explained by Susil *et al*.[14]

One of the main problems with the loopless antenna design is that its sensitivity is very low at its distal end. To alleviate this problem, Qian *et al*.[15] showed that tapered insulation for the whip could be used. Placing a short solenoid with a single connection to the end of the whip without a return path has also been proposed by Serfaty *et al*.[16] for using this design as a guiding catheter.

An important property of the loopless antenna is that its optimum impedance is close to that of a typical coaxial cable, and therefore with remote tuning and matching no significant loss of performance is observed. In fact, in many instances it can be directly connected to the preamplifier. As in the elongated loop design, a PIN diode can be used for decoupling purposes. The decoupling circuit helps in reducing the current induced on the loopless antenna during transmission of RF pulses to the body coil. A PIN diode placed as a shunt between the inner conductor and the shield of the coaxial cable a quarter wavelength away from the junction point will perform the desired decoupling if we assume that the scanner supplies a DC current to turn the diode on during RF transmission by the body coil. The DC current turns the PIN diode on, or reduces its RF impedance, and the quarter-wavelength cable transforms this impedance to a high value at the junction point. Note that, in order to obtain an effective decoupling, this high impedance should be in the order of 1 kΩ. Although other designs for decoupling are possible, this design is effective and also puts the decoupling circuitry outside the catheter, and so it is preferred in most designs. Some designers place a series capacitor after the PIN diode in order to block any DC current flow to the antenna as a safety feature, since leakage of the DC current to the body may be hazardous. As described in this paragraph, the tuning, matching, and decoupling circuits are relatively straightforward in the loopless antenna.

One other important issue related to the loopless antenna is prevention of induced shield currents. In the design, the shield currents are used as a part of the antenna and should not be blocked during reception; however, the shield currents that are induced during RF transmission on the antenna should be prevented. This is partly achieved by the decoupling circuit, which was mentioned in the previous paragraph. Additional measures for preventing these currents are necessary in order to eliminate excessive heating of

the body. The balun circuits that are used for the elongated loop designs can also be used for this design. A very common approach is to integrate a balun circuit to the external decoupling circuit. This prevents any excessive current flowing from outside to the body during RF transmission. In addition to this, a second RF shield can be used in the form of a bazooka balun. Since a second shield would increase the diameter of the design and possibly affect the flexibility, it is usually not desired. When proper care is taken, shield currents can be eliminated with these three methods.

18.2.3 Solenoid Coils

Using a solenoid as a catheter coil is a common alternative to the elongated loop and loopless designs.[5,6] A very short solenoid is often used for determining the position of the catheter inside the body. In this design, 10 or more turns of thin copper wire are used in the form of a solenoid on the tip of a small catheter. Typically, no tuning capacitance is used next to the solenoid, but instead the signal is carried outside the catheter using a twisted pair or coaxial cable. In these designs, no decoupling circuits are used since these coils are used mostly for obtaining positional information and therefore the uniformity of the signal around them is not a serious concern. Multiple solenoids can be used simultaneously to obtain visualization of other parts of the catheter.

18.2.4 Opposed Solenoids

The opposed solenoid is the third basic type of catheter coil. By placing two solenoids facing each other, a relatively uniform field is obtained outside the catheter.[3,17,18] This idea was termed also an "inside-out coil" to emphasize this property. An early use of this design was for the investigation of oil wells.[19]

A most interesting property of this design is that, when it is aligned with the main magnetic field, it provides a fairly uniform sensitivity in the region between the solenoids. This improved uniformity comes at the cost of SNR performance degradation. In the publication by Hurst *et al*.[2] (Figure 18.7), a field-effect transistor was placed inside the catheter after a tuning capacitance. Placing a preamplifier as close as possible to the catheter not only decreases the cable losses but also, more importantly, decreases the sensitivity of the design to inductance changes.

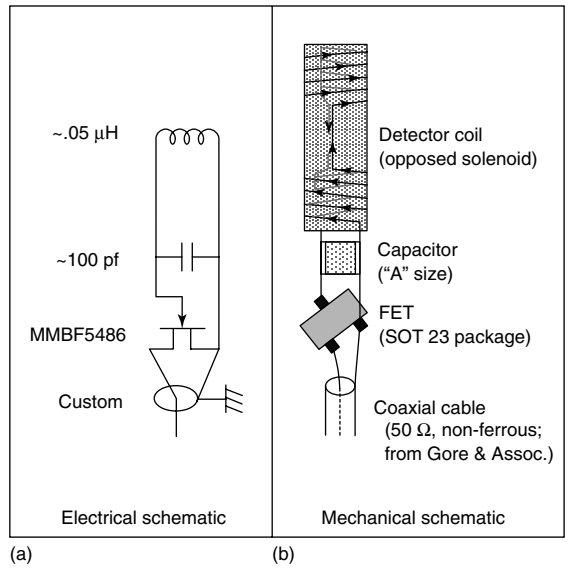

Figure 18.7. Opposed solenoid design. (a) Electrical schematics and (b) mechanical schematics. (Reproduced from Ref. 2. © John Wiley & Sons Ltd, 1992.)

All other properties of this design are very similar to those of the elongated loop design.

18.2.5 Inductively Coupled RF Coil

The inductively coupled RF (ICRF) coil[20] differs from the all other designs since it requires no cable connection to the MR scanner's hardware. Use of inductively coupled coils in MRI was initially demonstrated in the form of implanted coils[21] for animal experiments.

In this design, a coil is tuned but not connected to any wire; instead it is embedded inside a catheter. When the catheter is imaged using conventional surface coils, an amplified signal around the coil can be observed. This property of the ICRF coils can be explained using the reciprocity principle. Assume that an imaginary current is applied to the terminal of the receiving surface coil. The current on the surface coil induces a magnetic field inside the body, including the region where ICRF coil resides. Since the ICRF coil is tuned to this frequency, the external magnetic field induces a high current in the coil. This

induced high current, in turn, results in a high but local reactive magnetic field. In an MRI image, this local reactive magnetic field appears as strong signal amplification. Figure 18.8 summarizes the inductive coupling phenomenon.

This idea was later extended for possible visualization of stents.[22] Since stents are usually made out of metals, with a slight change in their structure and by adding a tuning capacitor they may become visible under MRI.

One issue related to ICRF coils is that active decoupling circuits cannot be used with this design since there is no wired connection to the scanner hardware. Although in some cases coupling during transmission may be used as an advantage, it may also be a safety problem, and also a high flip angle around the catheter may cause image artifacts. This problem can be solved using passive decoupling, e.g., by using back-to-back Shottky diodes or low turn-on voltage fast switching diodes.

With this technique, the tissue around the ICRF coil appears bright compared to the rest of an image acquired using a surface coil. When the MRI signal is acquired using multiple surface coils, it is possible to extract the ICRF-related signal from the rest of the signal. This is best described as using reverse polarized reception. In MRI, the echo signal comes circularly polarized. If a receiver is tuned to be sensitive to reverse circular polarization, no signal is expected to be received except when there is an ICRF coil inside the body. The ICRF coil picks up the forward circularly polarized signal and creates a linearly polarized reactive field. It is known that a linearly polarized field can be thought of as the sum of two opposing circularly polarized fields (forward and reverse). Since the receiver coil is tuned to the reverse field, it does not detect any signal directly originating from the body but it detects the signal originating from the ICRF coil. When multiple receiver coils are used, signals acquired from these coils can be combined such that only the reverse sensitivity remains and therefore only the signal from ICRF coil remains on the images. A detailed description of this complex phenomenon can be found in Ref. 23, but, in short, if one acquires the ICRF coil images using multiple coils, the background information can be separated from the ICRF images by an image processing technique. This is especially important if one wants to track the position of a catheter inside the body accurately.

18.3 APPLICATIONS

Currently, catheter coils are mostly used as parts of investigational devices. There are, however, many applications that may utilize catheter coils.

18.3.1 Imaging

One of the basic problems of catheter coils is improving the image quality and resolution by increasing the SNR. Comparing the above designs is not possible without knowing the exact conditions in which each design will be used. For example, if space is very limited, the loopless design should be considered. One should also always examine whether the same or similar image quality could be obtained as when using surface coils.

With the aim of quantifying the SNR performance of internal coils with respect to the best surface coil, the ultimate theoretical value that one can obtain using a surface coil has been calculated in a study by Ocali and Atalar.[24] It is known that the MRI signal is related to the transverse component of the magnetic field generated by a coil when a unit current is applied at the terminal of the coil, and the noise is related to the electric field generated by the same coil under the same conditions. To find the maximum SNR value, the magnetic field needs to be maximized and the electric field needs to be minimized. In their calculation, an optimization problem was solved by assuming that there is an infinite freedom of designing surface coils. In solving this problem, instead of trying the find the optimum coil geometry, only the electromagnetic field inside the body was considered. In the Ocali and Atalar article,[24] the ultimate value of the intrinsic SNR was solved numerically and various existing coil designs were tested under different conditions. The study showed that the current technology is not far from the maximum attainable SNR. In the article by Kopanoglu *et al*.,[25] this study was extended to obtain an analytical formula for the ultimate intrinsic SNR. As can be seen from these formulations, the maximum attainable SNR reaches infinity at the surface of the body and decreases in proportion to the 2.5th power of the distance from the surface. To

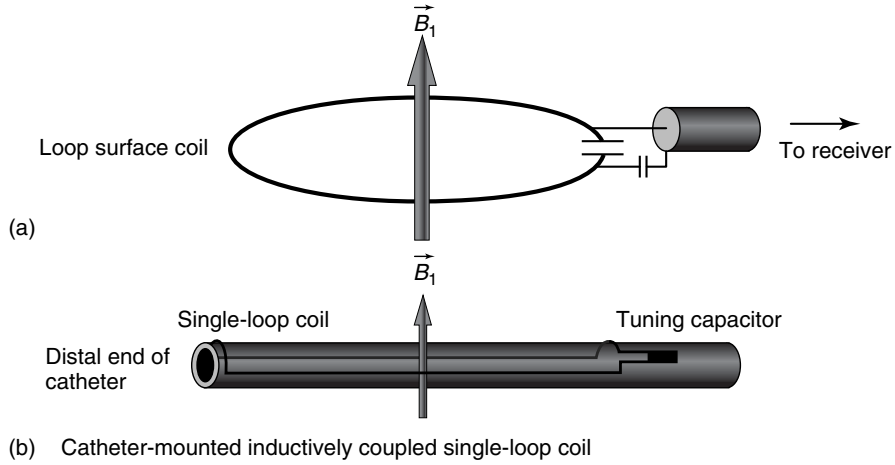

Figure 18.8. Inductively coupled coil design. Coupling between (a) surface coil and (b) catheter-mounted inductively coupled coil is described. (Reproduced from Ref. 22. © John Wiley & Sons Ltd, 2002.)

achieve an SNR value higher than this value, an internal coil (or catheter coil) is necessary. Similar to this ultimate intrinsic SNR calculation, a calculation for the internal coils can be conducted[26] by assuming that there is a cylindrical volume at the center of the body in which one can place the internal coil. In Figure 18.9, a comparison of the maximum attainable SNR using only surface coils with the SNR produced by a combination of internal and surface coils is shown. On the same graph, the performance of a loopless design is also shown, to demonstrate its relative performance compared to the maximum attainable SNR. As can be seen from the graph, the loopless antenna outperforms even the best surface coil when the point of interest is close to the center. However, it seems that the loopless antenna is far from the best internal antenna. The other designs have to be investigated, but placing an antenna in a 0.75 mm diameter hole (as in the example shown in Figure 18.9) is a challenge.

One of the main problems with internal MR coils is that their sensitivities are not uniform and the images obtained using these coils cannot be used for diagnostic purposes unless the signal intensity variations are corrected. In some publications, signal intensity correction techniques are used to show high-quality images; however, currently all automated signal intensity correction methods also degrade the underlying images and therefore are not preferred.

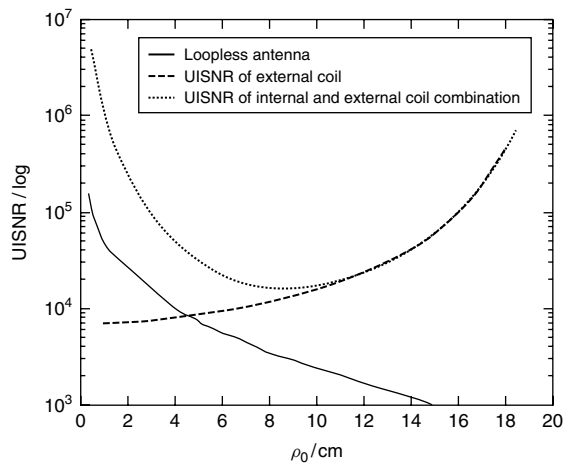

Figure 18.9. Comparison of SNR obtained using an optimum surface coil, an optimum combination of internal and surface coil, and a loopless antenna. In the calculation of this curve, a 20 cm radius cylindrical object is assumed. It is also assumed that this object has a cylindrical space in the middle with a radius of 0.375 mm. A loopless antenna is assumed to be placed inside this central space.

18.3.2 Tracking

One of the most important reasons to embed a catheter coil in a catheter is to visualize the catheter's position during MRI. Real-time

tip-tracking techniques have been implemented on commercial scanners for finding the position of small solenoidal catheter coils. The general method that was proposed by Ackerman *et al*.[5] is still valid, although some novel improvements have been developed.[27]

Embedding coils inside the catheter for the purpose of finding the position of a catheter is termed *active catheter tracking*. It should be noted that "passive catheter tracking" is an alternative to active catheter tracking. In the passive tracking technique, a marker that may cause an image artifact is positioned on the catheter. Although this technique is relatively simple to implement, finding the position of the artifact is not trivial during a complex vascular procedure. If the artifact is large, it obscures the underlying image and therefore is not preferred, but if it is too small, it becomes hard to visualize and causes loss of the catheter in the body. Active catheter tracking solves this issue at the cost of increased complexity and RF safety problems, which will be discussed later.

In addition to the solenoid, the loopless antenna design has also been used for active tracking. This method enables complete visualization of the catheter shaft[8] with a high frame rate. Later, this method was extended to include visualization of the catheter within its background while updating the catheter images at a high frame rate, with background information acquired at a lower rate.[28] Guttman *et al*.[29] used active catheter tracking within a 3D visualization tool.

Active catheter tracking techniques have been proposed for different catheter designs. Guiding catheters and guidewires became MR-visible with the help of the loopless design, and this pair was used to guide a balloon angioplasty procedure.[30] Again, this design was used inside a vascular needle to guide septal puncture[31,32] and also for creating a shunt between the portal vein and vena cava.[33] An injection catheter has been manufactured using a similar design[34] and used to inject therapeutic agents into the heart.[35] Since this chapter is more geared toward the technical aspects of catheter coils, these specific applications are not discussed in detail.

18.4 SAFETY ISSUES

The use of catheter coils inside the human body raises safety issues.[36] In testing the effectiveness of the design, it is always necessary to check whether there are any safety problems. When verifying the safety of a catheter coil design, it is important to understand the issues related to RF heating.

It is very well documented that, when a bare wire with a resonant length is placed inside the body during an MRI examination, a significant temperature rise at the tip of the wire can be observed.[37] Even when these long metallic objects are insulated, some significant heating may be observed. As discussed earlier, induced currents on the catheter coils can be prevented by using active and passive decoupling circuits as well as by balun circuits.[36] In order to decrease the possibility of excessive heating, alternative methods have been proposed including optical transmission lines.[38] Extensive tests in worst case conditions should be conducted on phantoms before using these designs on humans. In a typical phantom safety test procedure, the highest allowed specific absorption rate (SAR) is applied to the phantom while the catheter coil is inside the phantom and the temperature rise in the immediate vicinity of the catheter coil should then be measured. Note that the SAR applied to the phantom should be measured rather than trusting the manufacturer-supplied values since the latter are often higher than what is actually applied to the phantom. It should also be noted that the position of the catheter coil inside the body may vary and therefore it is advisable to conduct these tests in all the extreme positions that the catheter coil may take up in the body. When the temperature rise is less than $2\,^{\circ}\mathrm{C}$ over an extended period (20 min), one may assume that catheter coil is safe to use.

Gradient-induced currents on catheter coils may cause peripheral nerve stimulation. Although it has not been documented yet, it is feared that these currents may be at a sufficient level to arrest the heart. By using a thin layer of insulation, gradient-induced currents on catheter coils can be prevented and therefore this effect is not an important concern.

While embedding a coil inside the catheter, the mechanical safety of the design needs to be investigated. Especially when embedding electronic circuit elements such as capacitors and diodes inside a catheter, the mechanical properties of the catheter may be compromised. Mechanical tests well known to catheter engineers should be applied to these designs. These tests include fatigue, integrity, torque, and pushability.

When these problems are carefully investigated, catheter coils can safely be used in diagnostic and interventional procedures.

18.5 CONCLUSION

In this chapter, a summary of the current catheter coil designs was given. Some technical details are omitted in order to make the text readable. A reader interested in the design or use of catheter coils should also read original articles on this subject, some of which can be found in the bibliography of this chapter. In addition to the basic catheter coil types that were discussed above, the reader may find other designs. The content of this chapter should be able to help the reader in understanding the other catheter coil types that are not mentioned here.

RELATED ARTICLES IN THE ENCYCLOPEDIA OF MAGNETIC RESONANCE

Bioeffects and Safety of Radiofrequency Electromagnetic Fields

Coils for Insertion into the Human Body

Design and Use of Internal Receiver Coils for Magnetic Resonance Imaging

Jolesz, Ferenc A.: The Development of Interventional MRI

REFERENCES

1. H. L. Kantor, R. W. Briggs, and R. S. Balaban, *Circ. Res.*, 1984, **55**, 261–266.
2. G. C. Hurst, J. Hua, J. L. Duerk, and A. M. Cohen, *Magn. Reson. Med.*, 1992, **24**, 343–357.
3. A. J. Martin, D. B. Plewes, and R. M. Henkelman, *J. Magn. Reson. Imaging*, 1992, **2**, 421–429.
4. K. Kandarpa, P. Jakab, S. Patz, F. J. Schoen, and F. A. Jolesz, *J. Vasc. Interv. Radiol.*, 1993, **4**, 419–427.
5. J. Ackerman, M. Offutt, R. Buxton, and T. Brady, *Rapid 3D Tracking of Small RF Coils*, Montreal, Quebec, 1986, pp. 1131–1132.
6. C. L. Dumoulin, S. P. Souza, and R. D. Darrow, *Magn. Reson. Med.*, 1993, **29**, 411–415.
7. E. Atalar, P. A. Bottomley, O. Ocali, L. C. Correia, M. D. Kelemen, J. A. Lima, and E. A. Zerhouni, *Magn. Reson. Med.*, 1996, **36**, 596–605.
8. E. Atalar, D. L. Kraitchman, B. Carkhuff, J. Lesho, O. Ocali, M. Solaiyappan, M. A. Guttman, and H. K. Jr Charles, *Magn. Reson. Med.*, 1998, **40**, 865–872.
9. H. H. Quick, M. E. Ladd, G. G. Zimmermann-Paul, P. Erhart, E. Hofmann, G. K. von Schulthess, and J. F. Debatin, *Magn. Reson. Med.*, 1999, **41**, 751–758.
10. R. C. Susil, C. J. Yeung, H. R. Halperin, A. C. Lardo, and E. Atalar, *Magn. Reson. Med.*, 2002, **47**, 594–600.
11. M. Burl, G. A. Coutts, D. J. Herlihy, R. Hill-Cottingham, J. F. Eastham, J. V. Hajnal, and I. R. Young, *Magn. Reson. Med.*, 1999, **41**, 636–638.
12. O. Ocali and E. Atalar, *Magn. Reson. Med.*, 1997, **37**, 112–118.
13. B. Qiu, P. Karmarkar, C. Brushett, F. Gao, R. Kon, S. Kar, E. Atalar, and X. Yang, *Magn. Reson. Med.*, 2005, **53**, 986–990.
14. R. C. Susil, C. J. Yeung, and E. Atalar, *Magn. Reson. Med.*, 2003, **50**, 383–390.
15. D. Qian, A. M. El-Sharkawy, E. Atalar, and P. A. Bottomley, *Magn. Reson. Med.*, 2010, **63**, 797–802.
16. J. M. Serfaty, X. Yang, P. Aksit, H. H. Quick, M. Solaiyappan, and E. Atalar, *J. Magn. Reson. Imaging*, 2000, **12**, 590–594.
17. A. J. Martin, A. I. Gotlieb, and R. M. Henkelman, *J. Magn. Reson. Imaging*, 1995, **5**, 93–100.
18. A. J. Martin and R. M. Henkelman, *Magn. Reson. Med.*, 1994, **32**, 224–229.
19. J. A. Jackson, L. J. Burnett, and J. F. Harmon, *J. Magn. Reson. (1969)*, 1980, **41**, 411–421.
20. H. H. Quick, M. O. Zenge, H. Kuehl, G. Kaiser, S. Aker, S. Massing, S. Bosk, and M. E. Ladd, *Magn. Reson. Med.*, 2005, **53**, 446–455.
21. M. D. Schnall, C. Barlow, V. H. Subramanian, and J. S. Leigh, *J. Magn. Reson.*, 1986, **68**, 161–167.
22. H. H. Quick, H. Kuehl, G. Kaiser, S. Bosk, J. F. Debatin, and M. E. Ladd, *Magn. Reson. Med.*, 2002, **48**, 781–790.
23. H. Celik and E. Atalar, *Magn. Reson. Med.*, 2011, DOI: 10.1002/mrm.23030.
24. O. Ocali and E. Atalar, *Magn. Reson. Med.*, 1998, **39**, 462–473.

25. E. Kopanoglu, V. B. Erturk, and E. Atalar, *Magn. Reson. Med.*, 2011, **66**(3), 846–858.

26. H. Celik, Y. Eryaman, A. Altintas, I. A. Abdel-Hafez, and E. Atalar, *Magn. Reson. Med.*, 2004, **52**, 640–649.

27. C. L. Dumoulin, R. P. Mallozzi, R. D. Darrow, and E. J. Schmidt, *Magn. Reson. Med.*, 2010, **63**, 1398–1403.

28. P. Aksit, J. A. Derbyshire, J. M. Serfaty, and E. Atalar, *Magn. Reson. Med.*, 2002, **47**, 53–60.

29. M. A. Guttman, R. J. Lederman, J. M. Sorger, and E. R. McVeigh, *J. Cardiovasc. Magn. Reson.*, 2002, **4**, 431–442.

30. J. M. Serfaty, X. Yang, T. K. Foo, A. Kumar, A. Derbyshire, and E. Atalar, *Magn. Reson. Med.*, 2003, **49**, 258–263.

31. A. Arepally, P. V. Karmarkar, C. Weiss, E. R. Rodriguez, R. J. Lederman, and E. Atalar, *J. Magn. Reson. Imaging*, 2005, **21**, 463–467.

32. A. N. Raval, P. V. Karmarkar, M. A. Guttman, C. Ozturk, R. Desilva, R. J. Aviles, V. J. Wright, W. H. Schenke, E. Atalar, E. R. McVeigh, and R. J. Lederman, *Catheter. Cardiovasc. Interv.*, 2006, **67**, 637–643.

33. A. Arepally, P. V. Karmarkar, D. Qian, B. Barnett, and E. Atalar, *J. Vasc. Interv. Radiol.*, 2006, **17**, 1165–1173.

34. P. V. Karmarkar, D. L. Kraitchman, I. Izbudak, L. V. Hofmann, L. C. Amado, D. Fritzges, R. Young, M. Pittenger, J. W. Bulte, and E. Atalar, *Magn. Reson. Med.*, 2004, **51**, 1163–1172.

35. D. L. Kraitchman, A. W. Heldman, E. Atalar, L. C. Amado, B. J. Martin, M. F. Pittenger, J. M. Hare, and J. W. Bulte, *Circulation*, 2003, **107**, 2290–2293.

36. M. E. Ladd and H. H. Quick, *Magn. Reson. Med.*, 2000, **43**, 615–619.

37. C. J. Yeung, R. C. Susil, and E. Atalar, *Magn. Reson. Med.*, 2002, **47**, 187–193.

38. S. Fandrey, S. Weiss, and J. Muller, *IEEE Trans. Med. Imaging*, 2008, **27**, 1723–1727.

Chapter 19
Microcoils

Andrew G. Webb

Department of Radiology, Leiden University Medical Center, Leiden 2333, The Netherlands

19.1 INTRODUCTION

This chapter describes the design, construction, and testing of radiofrequency (RF) coils with dimensions significantly less than 1 mm (microcoils) for both nuclear magnetic resonance (NMR) spectroscopy and imaging. NMR spectroscopy is one of the most widely used and versatile analytical techniques for both liquid and solid samples. Many samples, however, cannot be analyzed using NMR owing to the inherent low sensitivity of the technique. In particular, when the mass of a particular sample is limited, the data acquisition times required to obtain useful spectra become unrealistically long. Technological efforts to improve the sensitivity of NMR have included increases in the strength of static magnetic fields, the development of cryogenically cooled detectors, and the use of hyperpolarization techniques. This chapter concentrates on an approach that uses very small, highly sensitive RF detectors. In this approach, mass-limited samples are dissolved in very small volumes (typically nanoliters to microliters) of solvent to match the volume of the RF coil. Although simple in concept, there are many challenges, including the optimization of static (B_0) magnetic field homogeneity and efficient loading of small sample volumes into the detector. In addition to their high sensitivity, small coils have several other advantages. In the case of electrically conductive samples, there is a reduction of the loading effects of the sample compared to larger coils. Small coils produce very high B_1 fields (in the megahertz range) and so they can excite very large bandwidths, which is particularly useful for solid samples. Small coils permit the design of probeheads containing more than one coil, enabling high sample throughput. Finally, magnetic resonance imaging (MRI) studies can be performed on samples as small as single cells, allowing fundamental biological studies to be carried out.

19.2 BACKGROUND

The signal to noise (S/N) of an NMR experiment is defined to be the peak signal divided by the root mean square (rms) noise[1]:

$$S/N = \frac{k_0 \frac{B_1}{i} V_s N \gamma \frac{h^2}{4\pi^2} I(I+1) \frac{\omega_o^2}{kT3\sqrt{2}}}{V_{\text{noise}}} \quad (19.1)$$

where V_s is the sample volume, k_0 is a constant that accounts for spatial inhomogeneities in the B_1

RF Coils for MRI
Edited by J. Thomas Vaughan and John R. Griffiths

ISBN: 978-0-470-77076-4

field, k is Boltzmann's constant, I is the spin angular momentum quantum number, γ is the gyromagnetic ratio, N is the spin density (number of spins per unit volume), h is Plank's constant, T is the absolute temperature measured in Kelvin, ω_0 is the Larmor frequency, V_{noise} is the total noise received from the coil and sample, and the factor of $\sqrt{2}$ is introduced since the noise measured is rms. The sensitivity of an RF coil is defined as the B_1 field that is produced by unit current, B_1/i.

The most simple and efficient RF coil, which also produces a relatively homogeneous B_1 field, to design at dimensions less than 1 mm is a solenoidal coil. For a coil of radius a, length l, and with n turns, the sensitivity is given by

$$\frac{B_1}{i} = \frac{\mu n}{2a\sqrt{1 + [l/2a]^2}} \tag{19.2}$$

Using this simple model, and assuming that the length-to-diameter ratio is kept constant, the coil sensitivity increases as the inverse of the coil diameter. Therefore, the S/N per unit volume of sample also increases as the inverse of the coil diameter. Exact calculations of the S/N in solenoidal coils at high frequencies and small diameters must also take into account proximity and skin depth effects.[2] Results have shown that, for coils of diameter greater than 100 μm, the S/N per unit volume of sample is inversely proportional to the coil diameter. For coils of diameter below 100 μm, the dependence is inversely related to the square root of the coil diameter.[2]

19.3 COIL CONSTRUCTION

19.3.1 Manually Wound Solenoidal Coils

The components required for the construction of wire-wrapped solenoids are (i) thin, high-purity copper wire; (ii) a capillary as the coil former and sample holder; (iii) nonmagnetic fixed and variable capacitors for impedance matching; (iv) a perfluorinated liquid for magnetic susceptibility matching[3]; and (v) a container that surrounds the microcoil and holds the perfluorocarbon. The diameter of copper wire is ~1/7th the outer diameter of the coil, and so typically ranges from 25 to 150 μm. Below 25 μm the wire becomes easily breakable. Since the windings of the solenoid are very close together, it is most convenient to have a thin plastic insulation layer, e.g., 6-μm-thick polyurethane, around the wire. The most commonly used vendor for such wire is California Fine Wire, Grover Beach, CA. The former for wrapping solenoids is usually a fused silica capillary coated with polyamide, since it has high tensile strength, can support high pressures, and is available from many vendors in a large variety of inner and outer diameters; Polymicro, Phoenix, AZ is one of the world's largest suppliers. Capillaries are used without removing the polyimide coating, since this significantly reduces their strength. The capillary is first wiped to remove contaminants, rinsed under a high-pressure water jet, washed with deionized water, sprayed with compressed air to remove dust, and allowed to dry. It is then centered in a pin vise and the pin vise holder is tilted upward at an angle of approximately 20°. A standard microscope with magnification between 5 and 10 is used in combination with a simple fiber-optic light source. A 5-cm length of wire, weighted at both ends (binder clips provide a low-tech solution), is draped over the capillary for two turns. The wire is glued to the capillary using nonpermanent cyanoacrylate adhesive and allowed to dry. One weight is then removed, and the pin vise is rotated to wrap the coil. For a closely wrapped solenoid, no gap is left between each of the turns. For a spaced solenoid, two wires are used, with the sacrificial "spacer" wire being half the diameter of the wire that will remain. Typically about eight extra turns are wound, compared to the final required number. The final turn is glued with permanent adhesive and the whole assembly is allowed to dry. In the final step, the remaining weight is removed, the extra turns are unwound, and this end is then glued with permanent adhesive. Two examples of hand-wound solenoids are shown in Figure 19.1(a).

In order to impedance-match the coil, very small nonmagnetic fixed (100B2R2PN, American Technical Ceramics, Huntington Station, NY) and variable (Johansen 5641, Boonton, NJ) capacitors are used in a standard balanced pi-network configuration. The smallest solder tip available is recommended. A plastic bottle is now fitted around the assembly (having been cut in half previously) and glued back together to form a container for the perfluorocarbon. Normally the matching network is placed on the outside of the bottle, so that the variable capacitors can be accessed. Finally, the coaxial cable is connected to the matching network. For most coils, a miniature semirigid coaxial assembly (e.g., UT85SS, Rosenberger Micro-coax, Collegeville, PA) is used since this is also easy to ground to the outside shield

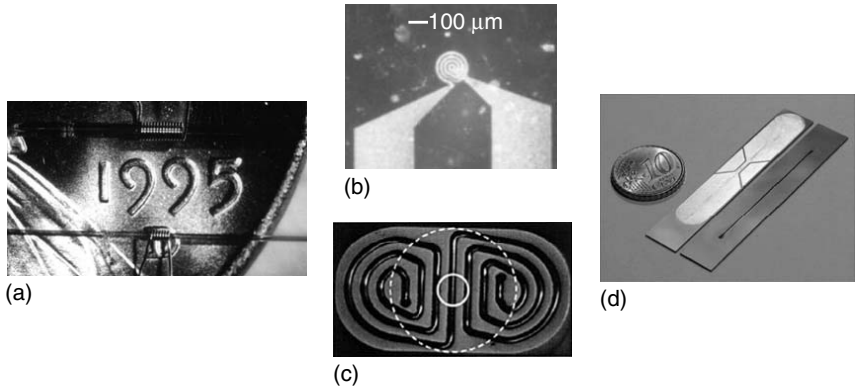

Figure 19.1. Examples of different types of RF microcoils. (a) Hand-wound solenoids with diameters 350 μm (upper) and 150 μm (lower); (b) a commercial surface microcoil produced by Bruker for microimaging; (c) a butterfly microcoil[4] for integration with an optical microscopy slide; (d) two halves of a microfluidic NMR chip based on a stripline design.[5]

of the probe body, although larger coaxial cables can also be used. The container is now filled with the fluorocarbon. A variety of perfluorocarbons can be used for impedance matching, but an inexpensive option that can be ordered in high volumes is FC-43 (3 M, Minneapolis, MN). It should be noted that the resonance frequency of the RF coil will decrease quite significantly (up to several tens of megahertz) when the perfluorocarbon is added.

19.3.2 Microfabricated Planar Coils

The other form of microcoil that can be produced in most laboratories without the need for sophisticated fabrication equipment is of planar geometry. The advantages of a planar over a solenoidal geometry include the ability to integrate the MR coil into a standard microscope slide, enabling direct comparisons between NMR and optical microscopy,[6] as well as easy integration of a sample chamber with the coil[7]; the major disadvantage is the inhomogeneous B_1 field produced. The first step in the production of submillimeter planar coils is to generate a photolithographic mask. This can then be used to etch a copper-clad laminate (usually either Teflon or polyamide). If required, via holes can be drilled into the laminate for the connection of the two ends of the coil. Two examples are shown in Figure 19.1(b) and (c). It should be noted that the thickness of the copper should be several times the skin depth at the frequency of use to minimize the coil loss. Simple etching techniques can also be used for a third type of RF coil design, planar coils based upon striplines,[5] as shown in Figure 19.1(d). The basic elements are one or more conductive surfaces separated by a dielectric. The general idea of the stripline is that the electric field is contained largely within the dielectric material, thus avoiding heating of the sample.

There are several other types of microcoils that require much more sophisticated manufacturing techniques, and so these are only briefly mentioned here. Three-dimensional solenoids can be produced, for example, by laser etching or microcontact printing. Microslot probes,[8] in which a small slot is introduced into a conductor and a strong B_1 field is produced in the slot by "current crowding", can be produced using planar ion-beam etching.

19.3.3 Multiple Resonant Circuits

Simple proton-only microcoils are used for almost all microimaging experiments. However, for high-resolution NMR studies, it is essential to be able to run multidimensional heteronuclear experiments, and so the microcoil should be tuned to multiple frequencies. Figure 19.2 shows one such design[9] in which the solenoid is tuned to four different nuclei. The L1–C1 trap presents a very low impedance at low frequency and high impedance at high frequency. The L2–C6–C7 tank circuit appears as a high impedance path at the proton frequency, but as a very low impedance path

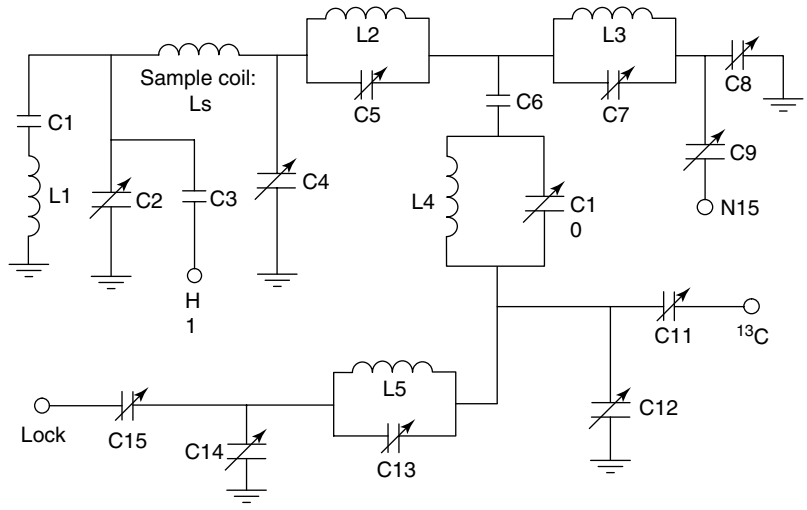

Figure 19.2. Circuit diagram for a triple-tuned (plus lock) solenoidal coil. (Reproduced from Ref. 9. © Elsevier, 2003.)

at the ^{15}N frequency. The proton channel has the shortest electrical path to the sample coil in order to minimize signal loss. LC trap circuits at both ^{15}N and ^{13}C frequencies are used between the ^{15}N and ^{13}C channels, and the lock channel is attached to the ^{13}C channel with a trap circuit at the ^{13}C frequency.

19.4 COIL TESTING AND EVALUATION

19.4.1 Electrical Characterization

Electrical characterization of the coils is normally performed using a network analyzer and conventional methods of measuring Q-values. Since the conductor thickness used to construct such coils is very small, microcoils are characterized by very low Q-values compared to much larger coils. Webb and Grant[10] have reported Q-values of 30–35 for coils with an outer diameter of 355 μm: for coils up to 1 mm Q-values are rarely above 100 for operating frequencies in the 400–750-MHz range. One feature of such coils is the very large tuning range, typically hundreds of megahertz for a 1–30 pF variable tuning capacitor, for example. For coils of these dimensions, losses are coil-rather than sample-dominated, meaning that the coil Q is not reduced by the introduction of a lossy sample, and that no shift in frequency is produced by samples with widely varying dielectric and conductive properties. For multiple-tuned circuits, such as the one shown in Figure 19.2, standard S_{11} and S_{21} measurements are made for each of the channels, with S_{11} values of greater than −20 dB and S_{21} values of greater than −15 dB between each channel being the goal.[9]

19.4.2 Spectral Resolution and Signal to Noise

Most commercial NMR probes have well-defined specifications for S/N and spectral resolution. There is no extensive literature for custom-built microcoils, but the results of Olson *et al.*[10] provide a good starting point. A solution of 5% chloroform in fully deuterated acetone is used to measure the spectral resolution. Linewidths at the 50% height (full-width half-maximum (FWHM)), 0.55% and 0.11% are then measured. For a coil with a diameter ∼1 mm, length ∼2 mm, and observe volume 1.5 μl, at 600 MHz Olson *et al.* report respective values of <1 Hz, <10 Hz, and <20 Hz, as shown in Figure 19.3. Values at lower field strengths should be correspondingly smaller. Alternatively, one can measure the baseline resolution of the anomeric protons in a sucrose/D_2O solution: resolution of ∼90% is equivalent to the values reported for the chloroform lineshape. For high-resolution NMR, obtaining

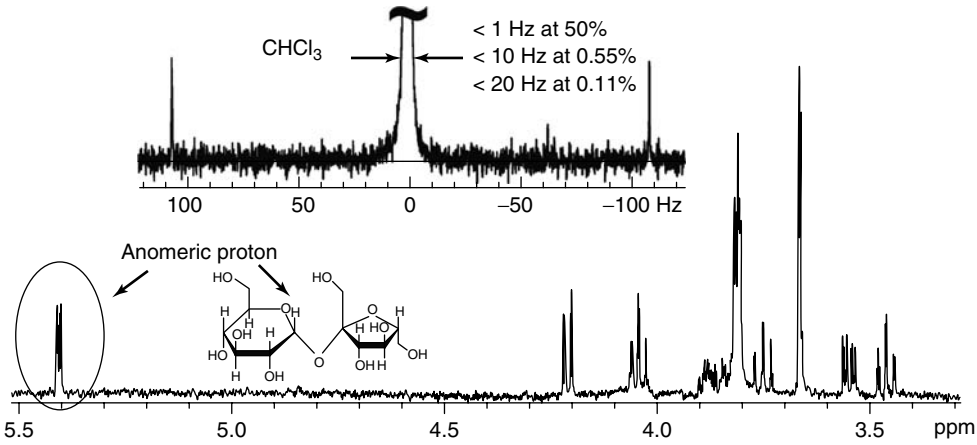

Figure 19.3. Typical NMR line shape of 5% $CHCl_3$ in acetone-d^6 at 600 MHz, single scan, no line broadening. (Inset) Illustration of mass sensitivity for 1 nmol of sucrose in D_2O (3 μl of 0.33 mM (340 ng total mass); 256 scans in 10 min, 500 MHz, 0.7-Hz line broadening; $S/N > 10$ for the anomeric proton at 5.4 ppm). (Reproduced from Ref. 10. © American Chemical Society, 2004.)

subhertz resolution is critical; for applications such as microimaging and solid-state NMR the criteria can be relaxed considerably. Also, as reported by Webb and Grant, increasing the filling factor of the coil also increases the spectral linewidth.[11]

In terms of S/N measurements, Olson *et al.* have reported values for microcoils using a 10 mM sucrose/D_2O solution. Their numbers are reported at 600 MHz for a single scan. Line broadening of 0.7 Hz is applied to the time-domain signal, and the rms noise value calculated over a bandwidth of 200 Hz in a spectral region well away from any resonances. The signal intensity of the anomeric peaks of sucrose is used. The S/N per mM (concentration sensitivity) sucrose was measured as 3.2, and the S/N per mmol (mass sensitivity) was calculated to be 2130, using the relationship $S_c = S_m * V_{obs}$, where S_c is the concentration sensitivity, S_m is the mass sensitivity, and V_{obs} is the observe volume of the coil. Appropriate scaling factors can be incorporated for experiments performed at different field strengths (as shown for 500 MHz in Figure 19.3), and/or using microcoils with different dimensions.

19.5 APPLICATIONS

There have been a number of extensive reviews[12,13] of the applications of MR microcoils in both spectroscopy and imaging, and so the following represents a distillation of the most common current applications. Additional areas include multiple-coil probeheads[14] (taking advantage of the small size of individual microcoils), solid-state applications[15] (benefiting from the very high B_1 fields), and ultrahigh-frequency NMR (enabled by the very high self-resonant frequency of microcoils).[16]

19.5.1 High-Resolution NMR

Most of the practical applications of small-coil NMR use sample volumes in the low microliter range. This allows the acquisition of spectra within a few minutes, for 1D scans, or a few hours, for 2D or heteronuclear scans, using analyte concentrations in the low millimolar range. One example of a protein study,[17] shown in Figure 19.4, used a commercial microcoil probe from protasis/MRM. The volume of the TXI HCN z-gradient microcoil NMR probe is 5 μl with an active volume of 1.5 μl. Experiments were performed using proteins from the Thermotoga maritima proteome, in particular, the conserved hypothetical protein, TM0979. The very short ^{13}C pulsewidths achievable using a microcoil are particularly important in a number of pulse sequences; in this particular study, it was possible to record a single HCCH-TOCSY spectrum across the full aliphatic and aromatic side-chain carbon range.

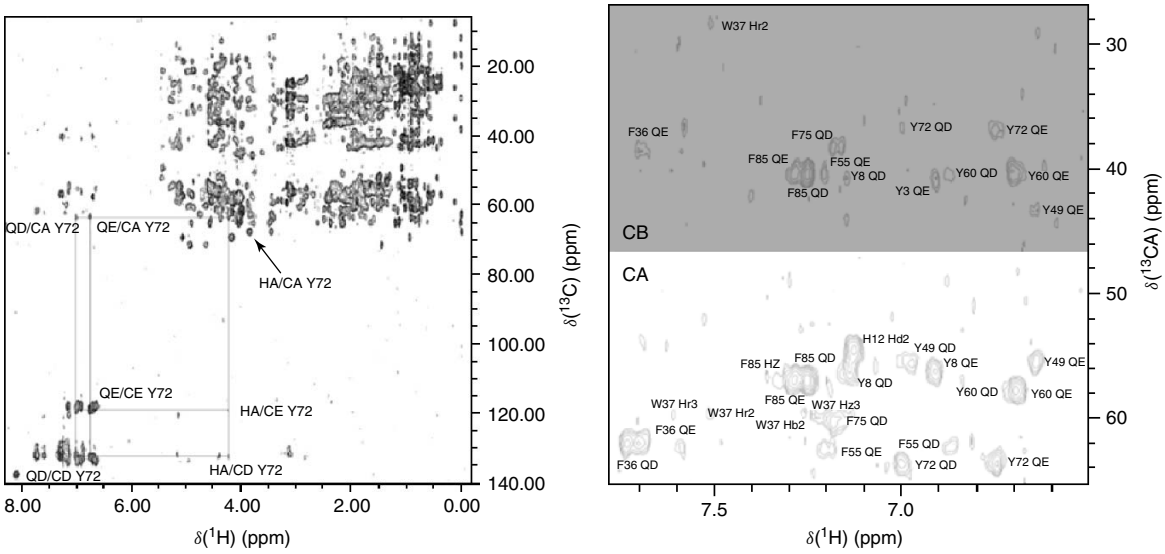

Figure 19.4. (a) 2D [^{1}H,^{13}C] aliphatic-aromatic HCCH-TOCSY FLOPSY-16 spectrum of ^{13}C/^{15}N TM0979 obtained with a microcoil. (b) Enlargement of the C_α/C_β carbon chemical shift-proton aromatic chemical shift region. The C_β cross-peak area is highlighted with a gray box. (Reproduced from Ref. 17. © American Chemical Society, 2004.)

This experiment allows complete side-chain assignment of all amino acids in a protein within a single spectrum, shown in Figure 19.4. The correlation between the aliphatic and aromatic carbons is normally very difficult owing to the large carbon chemical shift range (aliphatic carbons, 0–75 ppm; aromatic carbons, 115–140 ppm), which corresponds to a bandwidth of roughly 20 kHz at 14.1 T. Neither standard 5-mm NMR probes nor cryoprobes are rated for the high-power levels required to produce Hartman–Hahn mixing over this broad chemical shift range.

19.5.2 NMR-Coupled Microseparations

The small detection volumes associated with NMR microcoils make it a natural choice for coupling with chemical microseparation techniques such as capillary liquid chromatography (cLC),[18] capillary electrophoresis,[19] and capillary isotachophoresis.[20] In general, microseparation techniques enable faster analysis, higher concentration elution peaks, and less chromatographic dilution than their larger scale counterparts. As mentioned earlier, the use of small coils is ideally suited to small total sample amounts, present as relatively high concentrations in small volumes. The majority of hyphenated NMR-detected studies carried out thus far have used cLC as the separation technique. The mode of hyphenation consists of a long transfer capillary from the cLC separation column (which is usually magnetic), up through the magnet bore to the NMR probe, as shown in Figure 19.5. Typical transfer capillary inner diameters are narrow, between 50 and 100 μm, to minimize peak dispersion and broadening after the separation; flow rates are usually ~5 μl min^{-1}. In order to increase the filling factor of the probes, and therefore the S/N of the NMR experiment, a "bubble cell" or flow cell is often used. Using this type of setup, Grynbaum *et al.*[21] were able to separate tocopherol homologues using a highly shape-selective stationary phase; Figure 19.5 shows the spectra extracted from the 2D chromatograph.

19.5.3 MR Microimaging

MR microscopy has traditionally been somewhat loosely defined as corresponding to an image with one or more spatial dimensions having a resolution less than 100 μm, although in practice the resolution is usually far superior to this. Aguayo[22]

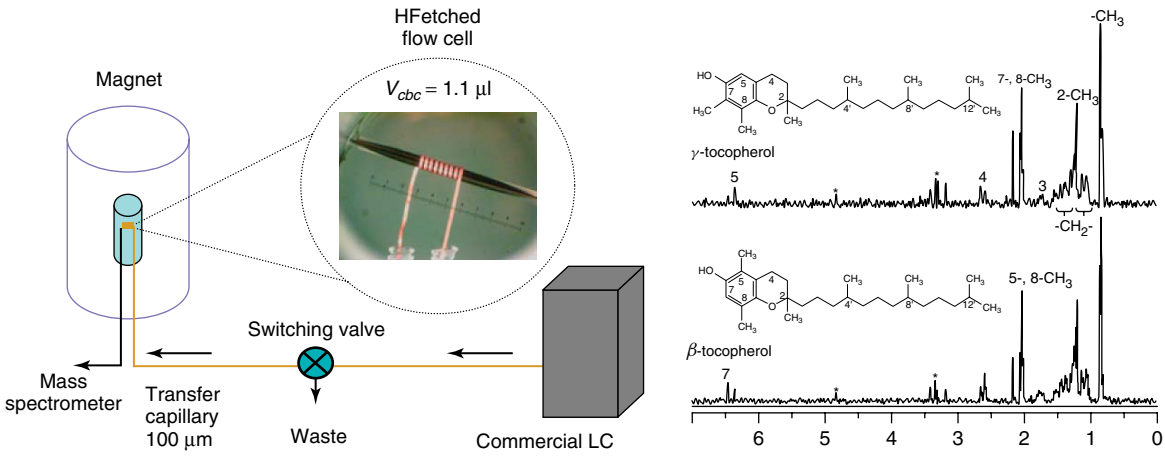

Figure 19.5. (a) Schematic of the physical setup used to hyphenate chemical microseparations to microcoil NMR detection and, optionally, mass spectrometry. (b) Extracted NMR spectra of the tocopherol isomers at the corresponding signal maxima. (Reproduced from Ref. 21. © Elsevier, 2007.)

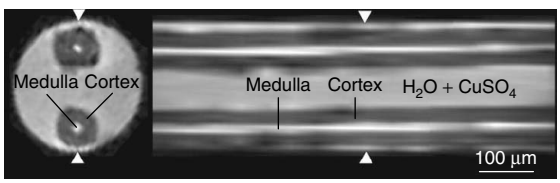

Figure 19.6. NMR images of two hairs from the same European taken from a 3D data set acquired with protocol 1. (a) Axial plane and (b) longitudinal section. The arrows indicate the slice position in the other image. The hairs are contained in a capillary that is otherwise filled with doped water. The two regions, cortex and medulla, are clearly resolved and show different signal amplitude. (Reproduced from Ref. 24. © John Wiley & Sons, Ltd, 2008.)

and Jacobs[23] established the utility of MR microscopy in biological systems in earlier work. The fundamental limit to spatial resolution in MR microscopy is the molecular diffusion coefficient. Although strong gradients can be used to minimize the FWHM of this blurring function, there are practical limits to the maximum gradient strength that can be achieved. Using microcoils, a number of researchers have reported very high spatial resolutions. For example, Weiger *et al.*[24] have reported isotropic spatial resolution of $3 \times 3 \times 3$ µm^3 on samples of human hair using a surface microcoil shown in Figure 19.1(b). Representative images are shown in Figure 19.6.

19.6 TROUBLESHOOTING

There is relatively little troubleshooting associated with the circuitry and RF coil itself. The most problematic parts are often the fluidic junctions that link the fused silica capillary (or bubble cell) on which the RF coil is formed and the sample delivery device. Since the capillary is very small in diameter, it is usually necessary to have particulate filters in-line for on-flow applications. A decrease in the level of the perfluorocarbon surrounding the coil, due perhaps to evaporation from high-power decoupling applications, is immediately recognized by a severe degradation in the spectral linewidth. An alternative cause for linewidth degradation, though not so severe, is the wire having come loose from the former. Given that the RF coil is encased within the fluorocarbon-containing holder, repair of such probes is quite difficult, and it is usually simpler to remake the coil and attach it to the grounded probe body and semirigid coaxial cable. The situation is particularly challenging for multiple-coil probes, which has prompted the development of a modular inductively coupled design for easy replacement of individual coils.[25]

REFERENCES

1. D. I. Hoult and R. E. Richards, *J. Magn. Reson.*, 1976, **24**, 71.

2. T. L. Peck, R. L. Magin, and P. C. Lauterbur, *J. Magn. Reson. B*, 1995, **108**, 114.
3. D. L. Olson, T. L. Peck, A. G. Webb, R. L. Magin, and J. V. Sweedler, *Science*, 1995, **270**, 1967.
4. R. A. Wind, P. D. Majors, K. R. Minard, E. J. Ackerman, D. S. Daly, G. R. Holtom, B. D. Thrall, and T. J. Weber, *Appl. Magn. Reson.*, 2002, **22**, 145.
5. P. J. van Bentum, J. W. Janssen, A. P. Kentgens, J. Bart, and J. G. Gardeniers, *J. Magn. Reson.*, 2007, **189**, 104.
6. P. M. Glover, R. W. Bowtell, G. D. Brown, and P. Mansfield, *Magn. Reson. Med.*, 1994, **31**, 423.
7. B. Gimi, S. Eroglu, L. Leoni, T. A. Desai, R. L. Magin, and B. B. Roman, *Concepts Magn. Reson. B.*, 2003, **18**, 1.
8. Y. Maguire, I. L. Chuang, S. G. Zhang, and N. Gershenfeld, *PNAS*, 2007, **104**, 9198.
9. Y. Li, T. M. Logan, A. S. Edison, and A. Webb, *J. Magn. Reson.*, 2003, **164**, 128.
10. D. L. Olson, J. A. Norcross, M. O'Neil-Johnson, P. F. Molitor, D. J. Detlefsen, A. G. Wilson, and T. L. Peck, *Anal. Chem.*, 2004, **76**, 2966.
11. A. G. Webb and S. C. Grant, *J. Magn. Reson. B*, 1996, **113**, 83.
12. L. Ciobanu, A. G. Webb, and C. H. Pennington, *Prog. NMR Spectrosc.*, 2003, **42**, 69.
13. A. P. Kentgens, J. Bart, P. J. van Bentum, A. Brinkmann, E. R. van Eck, J. G. Gardeniers, J. W. Janssen, P. Knijn, S. Vasa, and M. H. Verkuijlen, *J. Chem. Phys.*, 2008, **128**, 052202.
14. M. A. Macnaughtan, T. Hou, J. Xu, and D. Raftery, *Anal. Chem.*, 2003, **75**, 5116.
15. K. Yamauchi, J. W. G. Janssen, and A. P. M. Kentgens, *J. Magn. Reson.*, 2004, **167**, 87.
16. M. B. Kozlov, J. Haase, C. Baumann, and A. G. Webb, *Solid State Nucl. Magn. Reson.*, 2005, **28**, 64.
17. W. Peti, J. Norcross, G. Eldridge, and M. O'Neil-Johnson, *J. Am. Chem. Soc.*, 2004, **126**, 5873.
18. K. Albert, *On-line LC-NMR and Related Technologies*, John Wiley & Sons: Chichester, NY, 2002.
19. N. Wu, T. L. Peck, A. G. Webb, R. L. Magin, and J. V. Sweedler, *J. Am. Chem. Soc.*, 1994, **116**, 7929.
20. R. A. Kautz, M. E. Lacey, A. M. Wolters, F. Foret, A. G. Webb, B. L. Karger, and J. V. Sweedler, *J. Am. Chem. Soc.*, 2001, **123**, 3159.
21. M. D. Grynbaum, C. Meyer, K. Putzbach, J. Rehbein, and K. Albert, *J. Chrom. A*, 2007, **1156**, 80.
22. J. B. Aguayo, S. J. Blackband, J. Schoeniger, M. A. Mattingly, and M. Hintermann, *Nature*, 1986, **322**, 190.
23. R. E. Jacobs and S. E. Fraser, *J. Neuro. Meth.*, 1994, **54**, 189.
24. M. Weiger, D. Schmidig, S. Denoth, C. Massin, F. Vincent, M. Schenkel, and M. Fey, *Concepts Magn. Reson. B.*, 2008, **33B**, 84.
25. T. Wang, L. Ciobanu, X. Zhang, and A. G. Webb, *Concepts Magn. Reson. B*, 2008, **33**, 236.

Chapter 20

Cryogenic and Superconducting Coils for MRI

Sven Junge

Bruker Biospin MRI GmbH, Ettlingen 76275, Germany

20.1 INTRODUCTION

One of the most important goals for radiofrequency (RF) coil design is the improvement of the sensitivity and the optimization of the RF coils with respect to coil geometry and further design principles. MR imaging and spectroscopy (MRI/MRS) on small animals demand high spatial or temporal resolution, which in turn requires a high signal-to-noise ratio (SNR). In contrast to human applications, the spatial resolution required for small animals is up to a factor of 10 smaller that leads in a decrease of the sensitivity by a factor of the order of 1000. On the one hand, the SNR could be increased by increasing the signal, e.g., by increasing the static magnetic field (commercial animal scanners up to 17 T are available) or by hyperpolarization of certain nuclei. But such systems are not only expensive, they also require a change of the imaging parameters with respect to susceptibility artifacts caused by the increased tissue inhomogeneities and altered relaxation times. In addition, inhomogeneity of the RF fields will cause further difficulties. On the other hand, the SNR can be increased by decreasing the noise of the sample or of the different components of the receive chain of the MR system. The optimization of room temperature (RT) coils is in most cases limited by theoretical and practical constraints. Some optimization can be achieved by changing the geometry to decrease dielectric losses in the sample and the introduction of high-quality components to reduce the intrinsic coil losses. Such changes will typically lead in an increase of only several percent in the sensitivity of the optimized coils. The sample noise also decreases with decreased coil size. Changing the coil geometry from one-coil to multiple-coil elements surrounding a volume of interest leads to the development of so-called array coils, which are commonly used for human and animal MR applications (see Chapters 7 and 10). For small animals, the observed tissue volumes are of a size that renders the sample noise contributions comparable or smaller than the thermal noise contribution and noise contribution caused by resistive losses of the RF coils and the components of the receive chain. The SNR can thus be increased by decreasing the noise of the sample, and for high-field

RF Coils for MRI
Edited by J. Thomas Vaughan and John R. Griffiths

ISBN: 978-0-470-77076-4

animal scanners the dominant noise source is the conductive sample. Noise contributions from the sample are the thermal noise due to the thermal motion of the charge carriers, and the so-called dielectric losses due to the electrical field of the RF field. Decreasing the sample temperature of live animals is not usually possible, but reduction of the thermal noise and resistive losses of the RF receive chain will produce a significant increase of the SNR.

In the past, several studies on in vivo applications at multiple field strengths have demonstrated improved SNR with superconducting and cooled normal metal RF coils. The first publications, between 1980 and 1995, used high-temperature superconducting (HTS) material or cooled copper coils.[1–7] Some publications have discussed these methods for human imaging at low fields,[8–13] for MR microscopy,[2,14–17] and for animal imaging.[18–25]

Most of these publications reported mainly the MR methods and SNR comparisons, but a few have discussed the technical aspects of cryogenic and superconducting RF coils.[2,9,18,21,25–28,38,39] This chapter deals with the basic design considerations for cryogenically cooled RF-coils for animal imaging with respect to physical, mechanical and thermal limitations and their associated challenges.

20.2 PHYSICAL LIMITATIONS AND RF-DESIGN CONSTRAINTS

For design of cryogenically cooled RF coils, the most important questions are the optimum coil size and the achievable SNR gain when cooling the coil from RT to low temperature (LT). A very general formulation of SNR is expressed[27] by

$$SNR \approx F^{\frac{1}{2}} \frac{\omega\left(\frac{B_1}{1}\right)}{\sqrt{4\ K_b\ R_{eq}\ T_{eq}}} V_0\ M_T \sqrt{\frac{t_0}{t_R}} \sqrt{t_{scan}} \quad (20.1)$$

We neglect all terms that are not strongly related to the RF-coil sensitivity; this includes the noise factor F (which accounts for the additional noise power from the MR system), transversal magnetization M_T, the total scan time t_{scan}, the repetition time t_R, and the sampling window duration t_0. In addition, the elementary encoded volume V_0 and the coil current I are set to unity and to unit current, respectively; this formula is simplified and the SNR is expressed in terms of B_1 and noise introduction:

$$SNR \approx \frac{\omega B_1}{\sqrt{4K_b\ R_{eq}\ T_{eq}}} \quad (20.2)$$

A gain in SNR can be achieved either by increasing the effective RF field B_1 per unit current in the sample volume or by reducing the noise sources (loss mechanism) represented by the term $R_{eq}T_{eq}$. Several different noise sources interact with the RF coil and are represented by four major terms:

$$R_{eq} = (R_M + R_E) + R_c + R_\Omega = R_s + R_c + R_\Omega \quad (20.3)$$

R_M is the magnetic loss by magnetic field induced currents in the sample, R_E is the electric loss by stray capacitive coupling between the sample and the RF coil, R_c is the resistive loss of the RF coil, and R_Ω is the radiative loss. The magnetic loss R_M and electric loss R_E are combined into the so-called samples loss R_s.

Simplifying these four loss mechanism to the two dominant parts of losses for RF detection that are temperature dependent, the SNR can then be expressed as

$$SNR \approx \frac{\omega B_1}{\sqrt{R_s T_E + R_c T_c}} \quad (20.4)$$

In the following, we do not take into account any dependencies of the B_1-efficiency with respect to the coil geometry and sample conductivity that are not dependent on the temperature of the RF coil. We take a closer look at the denominator of equation (20.4), the losses (noise), and their dependency upon temperature and frequency. At first, we distinguish two domains. On the one hand, we have the case when the sample losses dominate $R_s T_s \gg R_c T_c$ and for this case the SNR is independent from the resistive coil losses R_c and their temperature T_c. On the other hand, when the coil losses dominate $R_s T_s \ll R_c T_c$ then the SNR can be improved, e.g., using better conductive coil conductors or lowering the coil temperature. For the design of superconducting (cryogenically cooled) coils, it is recommended to operate in the domain dominated by coil losses. The question is how the boundary between these two domains represented by the equality $R_s T_s = R_c T_c$ is dependent on coil-size and frequency.

For a rough estimation regarding the coil size that will be usable for cryogenically cooled coils, we examine the sample resistance R_s and coil resistance R_c for a single-loop copper coil under the boundary condition of a semi-infinite sample, ignoring the

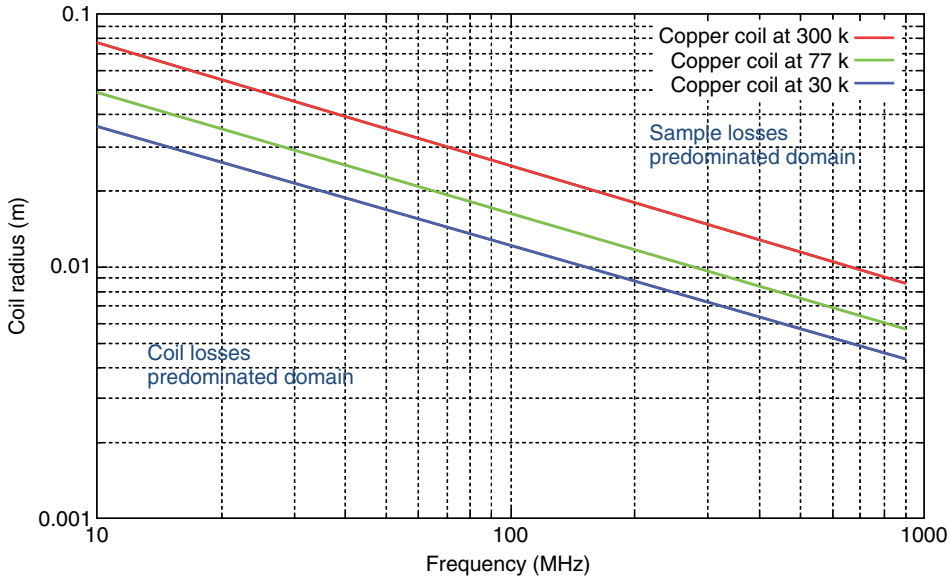

Figure 20.1. Sample and coil losses predominated domains in frequency and size coordinates. The tissue conductivity σ was chosen to an average value of 0.66 S m^{-1},[27] the electrical resistivity ϱ_c to be 5.81 × 10^7 S m^{-1} for RT, a temperature coefficient of 0.004 was used for 77 K, 30 K[30] and the factor $\xi \frac{\alpha}{r}$ was chosen to be 45.

gradient of scalar potential and considering only the vector potential A. For this case, the resistances will be given[27] as

$$R_s \approx \frac{2}{3\pi}\mu_0{}^2\sigma\omega^2 n^2 a^3 \arctan\left(\frac{\pi a}{8d}\right) \qquad (20.5)$$

$$R_c = \sqrt{\tfrac{1}{2}\rho_c\mu_0\omega}\cdot n^2\xi\frac{a}{r} \qquad (20.6)$$

where r and a are the radii of the wire and the average radius of the coil, respectively, σ and ϱ_c are the tissue conductivity and the electrical resistivity of the coil wire and the so-called proximity factor ξ. For, single-loop copper coils ($n = 1$), the boundaries of the noise domains for different radii and frequencies are calculated and are given in Figure 20.1. The crossover between the two domains for room temperature copper coils in a frequency range from 100 to 800 MHz is given by coil radii between 2.5 and 0.9 cm. Below these radii, the coil losses dominate! The crossover for cooled copper at 77 K (LN_2) will halve the respective coil radii and this will have an influence on B_1-field distribution and reduction of the penetration depth[29]! Even lower temperatures, e.g., 30 K or the usage of HTS material can still improve the sensitivity but the coil radius has to be reduced to 1.2–0.45 cm with respect to frequencies from 100 to 800 MHz.

When designing a cryogenically cooled RF coil, it is important to know the SNR gain at the desired frequency for the chosen coil radius. The SNR gain when cooling a coil from room temperature (RT) to low temperature (LT) can be evaluated from the ratio of the two noise contributions as follows[21]

$$SNR_{gain} = \frac{SNR_{LT}}{SNR_{RT}} = \frac{\sqrt{R_s T_s + R_{c,RT} T_{c,RT}}}{\sqrt{R_s T_s + R_{c,LT} T_{c,LT}}} \qquad (20.7)$$

For practical purposes, it is best to quantify the SNR gain in terms of parameters that can be measured, e.g., by the so-called quality factor Q. For the coil alone, $Q = \omega L/R$, where L is the RF coil inductance, and for the other expressions, an equivalent Q

Table 20.1. Measured quality factors for unloaded and loaded conditions (equivalent to a mouse head) of a transmission line resonator based on CFA-2 base material

Loading	Frequency [MHz]	Q-factor (RT)	Q-factor (77 k)
Unloaded	401.6	320	1100
Loaded	401.2	280	740

Figure 20.2(a): inner radius 7 mm.

is defined by using the appropriate resistance term in equation (20.7). The term ωL then cancels out, and leads to expression (20.8). The equation for the SNR will then be changed to

$$SNR_{\text{gain}} = \frac{SNR_{\text{LT}}}{SNR_{\text{RT}}} = \sqrt{\frac{T_{\text{RT}} \cdot Q_{\text{UL,RT}}^{-1} + T_{\text{RT}} \cdot Q_{\text{sample,RT}}^{-1}}{T_{\text{LT}} Q_{\text{UL,LT}}^{-1} + T_{\text{RT}} \cdot Q_{\text{sample,LT}}^{-1}}}$$

$$Q_{\text{sample}}^{-1} = Q_{\text{L}}^{-1} - Q_{\text{UL}}^{-1} \qquad (20.8)$$

where the inverse of the quality factor of the sample (Q_{sample}) is calculated by the difference of the inverse of the quality factors of the loaded (Q_{L}) and unloaded (Q_{UL}) coil. We can still evaluate the real SNR gain by measuring the Q-factor at different temperatures for a given coil radius.

Measured Q factors for a double-sided transmission line resonator (TLR) (Figure 20.2) with an inner radius of 7 mm are given in Table 20.1. The coil was cooled by liquid nitrogen (LN_2) and loaded with a phantom that represented the same RF losses as a mouse head. With the measured values listed in Table 20.1, a gain of a factor of 2.2 in SNR was found, confirming that the system was operating in the coil-noise-dominated regime. A very rough estimation of the benefit of cooling RT-coils is possible for the limiting case $T_{LT} \rightarrow 0$ and for the SNR-gain estimation the values at room temperature are sufficient. For this case, equation (20.8) will change to

$$SNR_{\text{gain}} = \frac{SNR_{\text{LT}}}{SNR_{\text{RT}}} = \sqrt{\frac{1}{1 - \frac{Q_{\text{L,RT}}}{Q_{\text{UL,RT}}}}} \qquad (20.9)$$

With the measured values of Table 20.1, the result is an SNR gain of a factor 2.8 as an upper theoretical limit.

Finally, we can conclude that for the design of cryogenic coils, the maximum radius has to be chosen carefully with respect to the operating frequency and loading conditions. Because of these design constraints, the use of cryogenically cooled coils at *high field* is more appropriate for *small* animal applications than for large animals and human applications. In the next paragraph we take a closer look at the technical aspects with respect to the RF development and manufacturing of cryogenically cooled and superconducting coils.

20.3 TECHNICAL ASPECTS OF CRYOGENIC AND SUPERCONDUCTING COILS

As seen from the previous paragraph the coil size has to be sufficiently small for applications at higher frequencies. Conventional surface coils that use discrete elements to build the R-L-C-resonance circuit are not always optimal. Despite possibly limited temperature operating specifications of commercially available capacitors, the use of ceramic chip capacitors may require too much space, setting a miniaturization limit, and generating higher local losses inside the sample with respect to the high local electrical RF field in the vicinity of the capacitors. In addition, the soldering introduces several technological difficulties for cryogenic operation of resonance circuits built by discrete elements. An alternative is

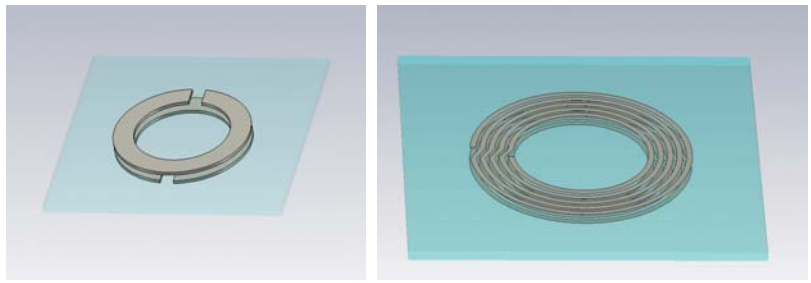

Figure 20.2. (a) Transmission line resonator: two planar split rings deposited on each side of a dielectric substrate. The gaps in the rings are diametrically opposed. (b) Multi-transmission line resonator: two planar multiturn split rings deposited on each side of a dielectric substrate. The gaps in the rings are diametrically opposed.

the usage of so-called monolithic designs and the use of distributed capacitors.[18] Among other coil designs commonly used for self-resonant high-Q structures are so-called transmission line resonators (TLR: Figure 20.2a) and multiturn transmission line resonators (MTLR: Figure 20.2b)[2,31] made either of copper or HTS material. The basic principle of a TLR is a pair of planar, electric conductive rings facing each other, and separated by a dielectric substrate. Each ring has a gap and the gaps are diametrically opposed to each other. The MTLR is based on the same principle, but uses more than one turn with several concentric rings on different radii connected in series. Because of the increased inductance value of the MTLR, the frequency range is more limited compared to the TLR and will be best used for lower frequencies. The electric conductors can be made either from copper or HTS material. The conductivity σ or resistivity $\rho = 1/\sigma$ of copper material ($\sigma = 58 \cdot 10^6$ S m^{-1} at 20° C) exhibits a nearly linear dependency with respect to temperature down to approximately 30 K.[30] Cold copper can provide a coil noise reduction of about 20 at 77 K and more at lower temperature.[18] But compared to HTS material cooled below their critical temperature, the resistivity of copper is up to 3 orders of magnitude higher. Very high Q-values can be achieved with the introduction of HTS material for RF coils, in a range from 1000 to 500 000 dependent on the coil size, temperature, frequency, and the static magnetic field. Many HTS materials are commercially available with critical temperatures up to 90–140 K. Among others, YBaCuO (Yttrium-barium-copper-oxide) with a critical temperature of 90 K has been used for MRI coils.[9–13,18,26,32,37]

Unfortunately, there are some difficulties concerning the use of HTS materials, and a detailed knowledge of their superconducting properties at radiofrequencies and their magnetic field dependency is required.[32] First, the conductivity of an HTS material is strongly nonlinear with temperature. During the transition from the normal to the superconducting state, it undergoes a phase transition. The material thereby changes its condition. Above the so-called critical temperature the material is normal or semiconducting, below this temperature the electrical DC-resistance disappears and it becomes superconducting. The second point is that conductivity of HTS materials is strongly dependent on the outside magnetic field and is primarily characterized by the so-called London penetration depth. This penetration depth depends on many parameters,[32] including the temperature and static magnetic field. The current density that superconducting material can handle is also severely limited. The material makes a transition from the superconducting state back to the normal state when the so-called critical current is exceeded. This major problem has to be directly addressed when HTS coils operate as transmit/receive coils. Too high current densities increase the surface resistance, and the nonlinear power dependency could result in nonlinear derivations of the flip angle during pulse excitation. Last but not least, there are the question of costs and manufacturing. In general, the production of HTS material and especially double-sided deposition of HTS on a substrate can be handled by only a very limited numbers of commercial suppliers (e.g., Theva, Munich, Germany) or some research laboratories.[18,25,27] Compared to copper coils, HTS coils are much more expansive and need longer production times.

In view of the above problems, engineers only use HTS coils instead of cold copper coils for demanding applications and high-performance expectations. But in any case, all self-resonant structures need careful design before the production process. Today, generally 3D electromagnetic (EM) simulations permit fast and accurate analysis of the behavior of high-frequency RF antennas, e.g., by CST Microwave Studio (CTS, Darmstadt, Germany). Cryogenically

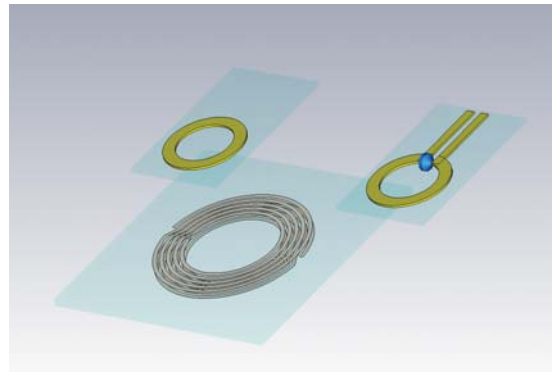

Figure 20.3. Principle design for matching and tuning of a multi-transmission line resonator (MTLR) with tuning loop (left) and inductive coupling loop (right). The coupling between the tune loop, inductive coupling loop, and the MTLR is performed by shifting the tune or coupling loop beside the coil away or close to the MTLR.

cooled coils present a narrow frequency response because of their low internal losses and need precise adjustment to the desired resonance frequency. Most analytical solutions will not take into account the whole environment, but with modern 3D EM simulations, the engineer is able to handle this topic and the coil characteristic can be calculated precisely before manufacturing (see Chapter 27). A careful evaluation with numerical methods is strongly recommended to prevent too many fabrication and pretuning iteration cycles including multiple cool downs and opening of the cryostat when the RF coil is inside the cryogenic probe. The results of 3D EM simulations are very helpful for calculating and predicting very precise Q-values, frequency responses, current densities, and RF-field distributions of RF coils.[33] In this context, another major question has to be evaluated and decided in the design process—the tuning and matching scheme (Figure 20.3).[18] The RF feeding and matching is usually done by an inductive coupling with a standard pickup-loop coil. The technique avoids solder connections that are difficult with HTS-materials. The mutual coupling between the parallel resonant pickup loop and the RF coil is adjusted geometrically to match the RF coil to the generally used standard 50 Ω impedance of the RF system.[18] The narrow bandwidth of HTS-coils could be a drawback that becomes more important at low field and for fast imaging methods where the receiver-bandwidth may limit the performance of the MRI-scan and results in imaging artifacts. The inductive coupling can be used in the so-called overcoupled mode to widen the bandwidth of the RF coil[34] in cases when the bandwidth is too small and limits the performance of the MR scanner.

Tuning of cryogenically cooled coils without discrete elements can be achieved in two different ways.[18] In the first approach, additional dielectric material of a high permittivity and low-loss tangent can be placed above or below the RF coil. Depending on its position, it will achieve tuning by decreasing the resonance frequency. This method has the advantage of preserving the internal low resistance and losses of the coil. Alternatively, the resonance frequency can be adjusted by positioning a small short-circuited copper coil beside the cryogenically cooled RF coil.[18] The mutual coupling of both coils increases the resonance frequency leading to a decrease of the equivalent inductance of the RF coil. But with that method, in contrast to the use of additional dielectric material, it is necessary to keep an eye on the additional losses that will be introduced if the mutual coupling becomes too strong. This may in some cases limit the usable tuning range.

We also have to consider mechanical design constraints on the design of cryogenically cooled probes, which are outlined in Section 20.4.

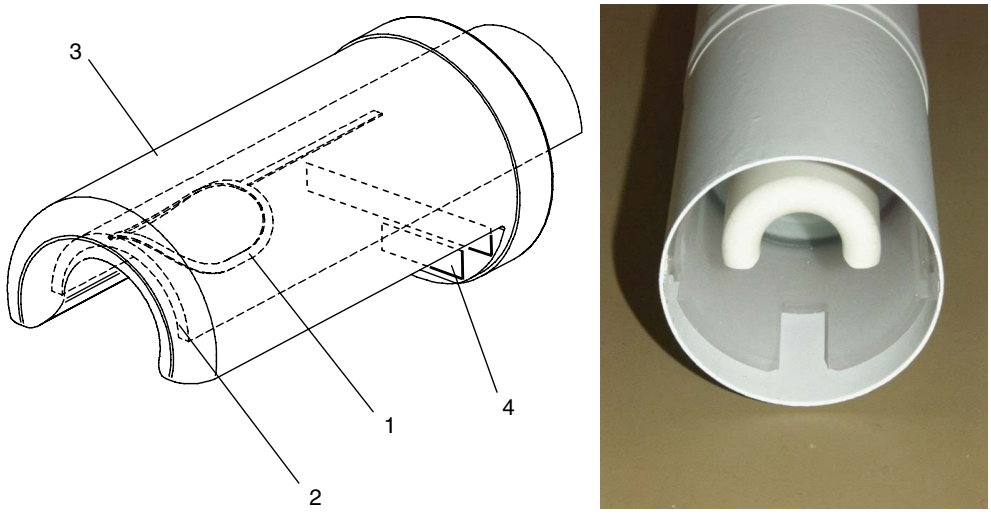

Figure 20.4. Principle design of a cryo-coil Dewar and cryostat: (1) RF coil; (2) cold finger; (3) ceramic Dewar; and (4) heater.

20.4 MECHANICAL, THERMAL DESIGN CONSTRAINTS AND PERFORMANCE

There are several different possibilities for cooling superconducting coils. The easiest way is direct immersion of the RF coil in a bath of cryogenic liquid such as liquid nitrogen (LN_2) placed inside a container for thermal isolation. The measurements can only be performed after all the coolant has been consumed because of the mechanical vibrations caused by the boiling of the coolant.[28] Such an arrangement is not very user-friendly, but it is cheap (the LN_2 container may be made either from polystyrene composite or just PVC) and in some cases can be useful for evaluation purposes.

A more convenient, but much more involved and expensive cooling method is the use of closed cycle cryocoolers and the introduction of a cold-head either in the direct vicinity of the RF-coil or located at a certain distance from the probe head in combination with a so-called cold finger. We take a closer look at an exemplary cryogenic system later. In Figure 20.4, the principle design of a cryogenic probe head is shown.[20,35]. The RF coil (1) is mounted on a cold finger (2) surrounded by a housing (3)—Dewar. The challenge is to place the RF coil as close as possible to the object under investigation in order to obtain an optimum RF performance and to thermally isolate the RF-coil operating at a cryogenic temperature range of 20–30 K from the test object that will have an temperature equal to or slightly higher than room temperature (animal). The most efficient way for isolation is the use of insulating vacuum. This means that the volume between the RF coil mounted on the cold finger and the housing will be evacuated, with a residual vacuum of about of 10^{-6} mbar. Such a Dewar housing reduces the two dominant heat transmission processes (heat conduction and heat convection). For additional reduction of the radiation in conventionally used Dewars, the walls are mirrored by a coating material. But this technique cannot be used with RF coils, as unacceptable RF losses may be incurred. Despite the thermally insulated vacuum, the wall will be cooled in an undesired manner by heat radiation and this may have undesirable consequences, especially for live animals. This problem is solved either by processes guiding a liquid of a suitable temperature through a gap between the cold RF coil and the housing that is in contact with the test object, or by a warm airflow between the cold housing and the test sample. In both cases, the distance between the RF coil and the test object is disproportionally large for applications on small animals and may greatly limit the SNR that can be achieved. A more convenient way is the use of the separating wall as a heating device that will produce a suitable temperature for the test object.[35] The heating device for the separating wall can be conveniently placed at the back end of the Dewar (No. 4 in Figure 20.4) and is thus sufficiently far away from the RF coil. To prevent poor RF performance of the cold RF coil, the separating wall and the cold finger are best manufactured from a material that has poor electrical conductivity, ideally less than 10^{-8} S m^{-1}, and a thermal conductivity more than 80 W K^{-1} m^{-1}. A number of ceramic materials that fulfill these requirements are commercially available, e.g., aluminum nitride (AlN), beryllium oxide (BeO), or aluminum oxide (Al_2O_3).

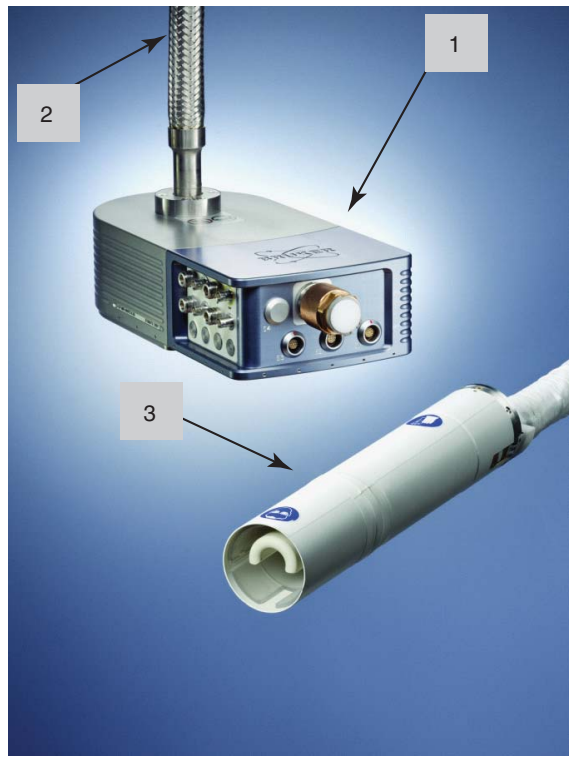

Figure 20.5. MRI CryoProbe™ (Bruker BioSpin MRI GmbH, Ettlingen, Germany) with three main parts: cryogenic preamplifier (1), interconnection (2), and RF coil head (3).

A probe head for animal applications at high fields is shown in Figures 20.4 and 20.5[19,20,35,36]; this configuration includes all the cryogenic parts in one system and potentially offers an optimum performance. This probe design along with the Dewar described above has a coil-to-sample distance of as little as 1 mm! The probe consists of three main parts: the RF coil head, the flexible cryogenic interconnection, and the cryogenic preamplifier module that contains the preamplifier and the interfacing electronics.[36] It is important that the preamplifier and the RF connection between the RF coil and the preamplifier are cold too. Usually, these two components of a room temperature RF system are also at room temperature, which does not matter because the noise introduced by the sample and RF coil is already the limiting factor of the noise of the entire RF system. But for cryogenically cooled coils, it is essential to reduce the noise introduced by all components, from the RF coil to the preamplifier and the preamplifier itself. The preamplifier in this setup is placed outside of the magnet and operated at a temperature of 77 K. The cryogenically cooled RF probe is placed inside the gradient system (Figure 20.6), and can be easily removed to be stored, still in the cold state, outside the magnet bore (Figure 20.6) when the MR system is being operated without the cryogenically cooled probe. Next, we take a closer look at the whole cryogenic cooling system.

The effort for operation of a cryogenically cooled RF probe is not insignificant. Using very low temperatures requires special attention to stable temperature control, high-thermal isolation, and cooling uniformity; and last but not least, additional safety measures for the operator and the animal have to be implemented in the whole system. The principle components of the cryogenic cooling system for operation of a cryogenically cooled coil for routine imaging are shown in Figure 20.7.[20,21,36] This cooling system takes care of the cooling as well as the temperature and cryogenic control of the RF probe. The three main parts are the CryoCooling Unit, the helium compressor, and a transferline. The CryoCooling Unit is connected via a vacuum-isolated transferline to the probe head that bridges the separation from the CryoCooling Unit, cools that device remotely and also keeps vibrations away from the probe head. The CryoCooling Unit shown here consists of a two-stage Gifford–McMahon cold head. The first cooling stage provides the cooling of the preamplifier, while the second stage provides a second significantly lower temperature level and is used for cooling the cryogenically cooled RF coil. The system is based on

(a) (b)

Figure 20.6. Installation of cryogenically cooled coil at a 9.4 T BioSpec-system (Bruker BioSpin MRI GmbH, Ettlingen Germany). The MRI CryoProbe™ is installed at the magnet service end and the RF coil head can be easily removed to be stored still in the cold state outside the magnet bore when the MR system is being operated without the cryogenically cooled probe (a). The CryoCooling Unit for cooling and control of the cryogenic operation of the MRI Cryo-Probe can be installed right beside the magnet because of the low stray field of the Ultra Shield and Refrigerated (USR)-magnet system (b).

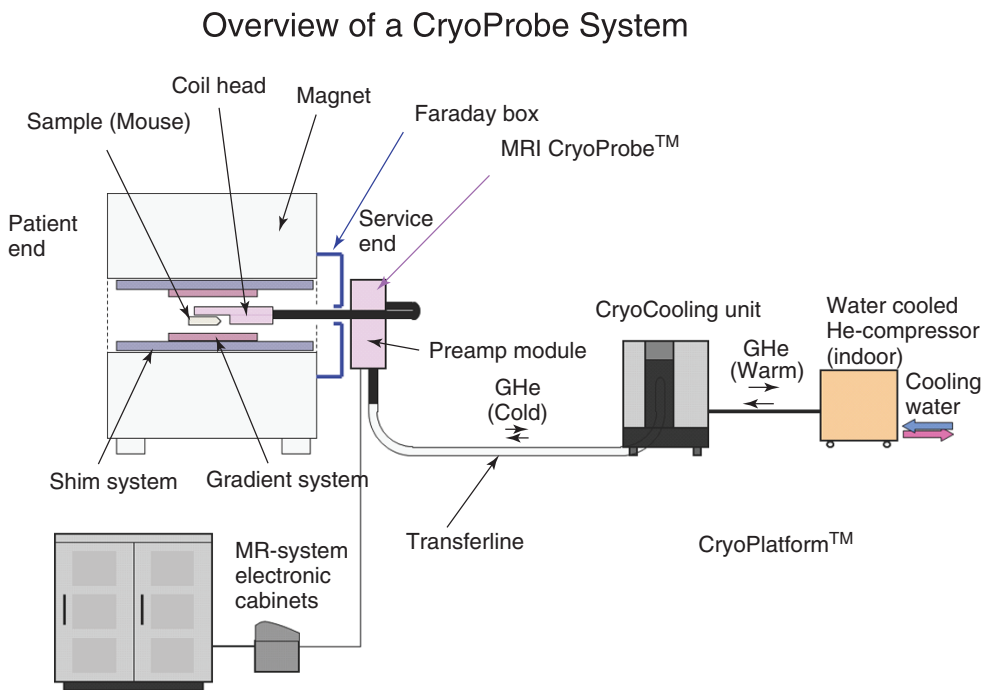

Figure 20.7. Overview for support and operation of a cryogenically cooled RF probe inside an MRI system. The MRI CryoProbe™ is cooled via a Transferline from the CryoPlatform. The CryoPlatform™ including the computer-controlled CryoCooling Unit and the He-compressor drives a cryo-cooler that operates on the basis of expansion of He-gas for cooling of the cryogenic probe. The He-compressor has substantial heat dissipation and is water cooled.

the principle of expanding compressed helium, and the cooler is driven by the helium compressor. The helium compressor has substantial heat dissipation and is either water or air cooled. In operation, the closed cycle cooling needs no helium refill. The system is completely computer controlled for temperature and pressure, and many safety measures are incorporated for long-term operation without user interaction including an entirely automatic cool down, cold operation, and warm-up of the cryogenic system.

A major key point of the performance of a cryogenically cooled RF probe is the SNR gain, so SNR distribution must be evaluated carefully. The increase of the SNR and image quality should be verified either with phantoms or by the target applications, and an example is shown in Figures 20.8 and 20.9. These images show a comparison of the image quality between a cryogenically cooled transmit/receive (Tx/Rx) copper coil versus a quadrature, receive-only surface coil of comparable size. Figure 20.8 compares the SNR distribution acquired along a line through a mouse brain with a rapid acquisition with relaxation enhancement RARE (Rapid Acquisition with Relaxation Enhancement)[40] sequence with a very long repetition time. The signal distribution differs for both coils. We observe a center brightening of the signal that is related to the fact that we are using a Tx/Rx surface coil as the cryogenically cooled RF coil. The signal intensity for the cryogenically cooled RF coil is the product of the inhomogeneous transmit profile and a receive profile that is typical for small surface coils. For excitation of the room temperature quadrature receive-only coil, a homogenous transmit volume coil was used. For the experiment, the transmit gain of the Tx/Rx cryogenically cooled RF coil was adjusted such that the maximum signal intensity is in the center of the mouse brain, and in this setting an SNR gain of a factor of 3 in the center of the mouse brain was observed. Another comparison is shown in Figure 20.9. For this experiment, a FLASH (Fast Low Angle SHot)[41] sequence was used and the signal was integrated over the whole mouse

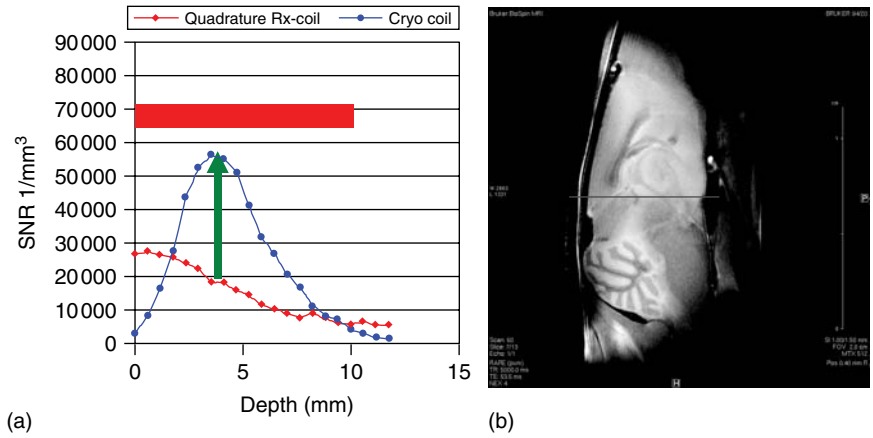

Figure 20.8. SNR comparison (a) at 9.4 T for a transmit/receive linear cryogenically cooled coil and a RT quadrature, receive-only coil—mouse brain (postmortem). (b) RARE, eight echoes and non-triggered (repetition time (TR) = 5000 ms, echo time (TE) = 53 ms, and resolution = (40 × 40 × 1000) μm^3).

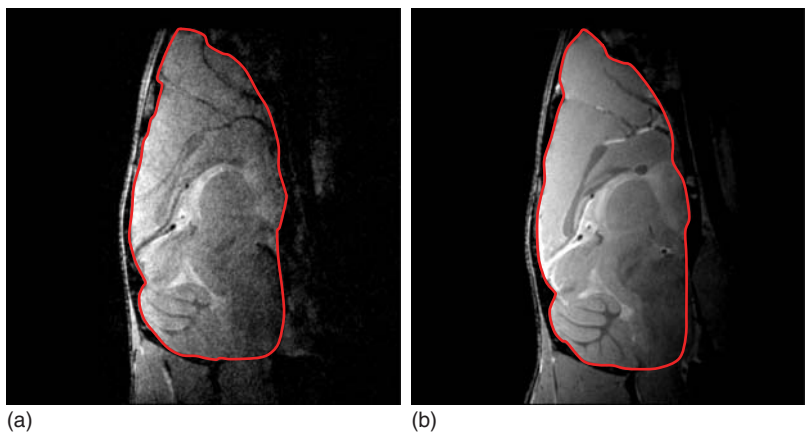

Figure 20.9. Comparison of the image quality for a RT quadrature, receive-only coil (a) and a transmit/receive quadrature MRI CryoProbe (b). In the bordered region, the overall SNR gain for the MRI CryoProbe™ is a factor of 2.8 (Mouse in vivo : FLASH, TR = 400 ms, TE = 3.8 ms, resolution = (78 × 78 × 500) μm^3, and total experiment time (TET) = 3 min 24 s).

brain for the comparison; the result is a factor of 2.8 improvement in SNR. The high image quality for real in vivo applications is shown in Figure 20.10. With an in-plane resolution of about 29–47 μm and with this high SNR and resolution, it is possible to observe the molecular cell layers (e.g., Purkinje cell layers) in the mouse brain.[21]

The high sensitivity of a cryogenically cooled RF coil allows the acquisition of highly resolved in vivo images with 30–50 μm in-plane resolution within an appropriate acquisition time. This increased SNR of the cryogenically cooled RF coil could in principle be used for anatomical studies to increase further the in-plane resolution. Alternatively, it would allow a reduction of the total acquisition time for the same resolution by a factor of 4 or more; leading either to a considerable increase of screening throughput or to an increased temporal resolution of time-course

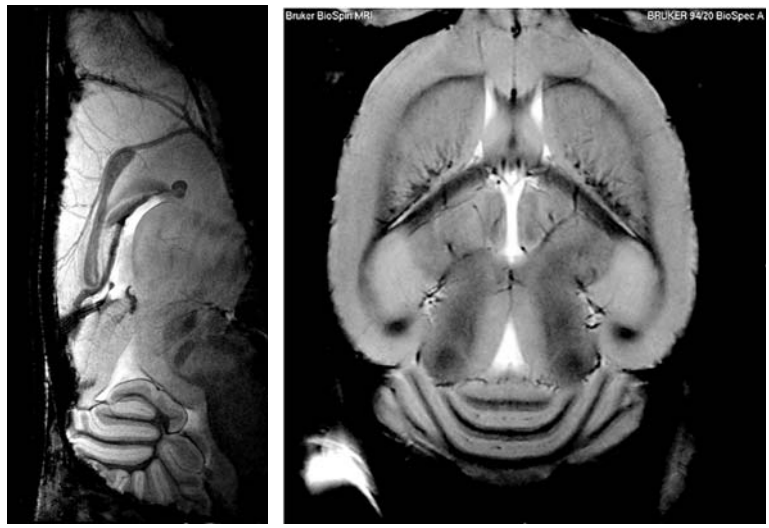

Figure 20.10. High-resolution image of a mouse brain at 9.4 T acquired with a linear (a) and quadrature (b) MRI CryoProbe™. (a) Mouse brain (in vivo): FLASH T_2^* weighted, TR = 350 ms, TE = 22 ms, field of view (FOV) = 15 × 15 mm, matrix = 512 × 512, resolution = (29 × 29 × 500) μm^3, and TET = 6 min. (b) Mouse brain (in vivo): RARE, eight echoes—non-triggered, TR = 4200 ms, TE = 37.5 ms, number of averages (NA) = 2, FOV = 18 mm × 18.8 mm, matrix = 384 × 384, resolution = (47 × 49 × 400) μm^3, and TET = 6 min 42 s.

studies, e.g., for functional magnetic resonance imaging (fMRI). The use of cryogenically cooled coils may emerge as a cost-efficient solution for increasing the sensitivity of MRI/MRS studies.

REFERENCES

1. R. D. Black, T. A. Early, and G. A. Johnson, *J. Magn. Reson., Ser. A*, 1995, **113**, 74–80.
2. R. D. Black, T. A. Early, P. B. Roemer, O. M. Mueller, A. Mogro-Campero, L. G. Turner and G. A. Johnson, *Science*, 1993, **259**, 793–795.
3. A. S. Hall, B. Barnard, P. Mcarthur, D. J. Gilderdale, I. R. Young, and G. M. Bydder, *Magn. Reson. Med.*, 1988, **7**, 230–235.
4. A. S. Hall, N. Alford, T. W. Button, D. J. Gilderdale, K. A. Gehring, and I. R. Young, *Med. Reson. Med.*, 1991, **20**, 340–343.
5. M. Jerosch-Herold and R. K. Kirschman, *J. Magn. Reson.*, 1989, **85**, 141–146.
6. P. Styles, N. F. Soffe, C. A. Scott, D. A. Cragg, F. Row, D. J. White, and P. C. I. White, *J. Magn. Reson.*, 1984, **60**, 397–404.
7. P. Styles, N. F. Soffe, and C. A. Scott, *J. Magn. Reson.*, 1989, **84**, 376–378.
8. E. Gao, K. C. Chan, M. S. Chow, K. K. Wong, B. Yan, J. Fang, E. X. Wu, D. Kacher, G. Young, F. A. Jolesz, Q. Y. Ma, and E. S. Yang, Superconducting MR Helmholtz coil pair for human imaging with improved üpenetration, In *Proceedings 9th Annual Meeting ISMRM*, UK, 2001, p. 1113.
9. J. C. Ginefri, L. Darrasee, and P. Crozat, *Magn. Reson. Med.*, 2001, **45**, 376–382.
10. J. C. Ginefri, L. Darrasse, and P. Crozat, human skin microscopy using a superconducting receiver coil, In *Proceedings 7th Annual Meeting ISMRM*, USA, 1999, p. 2129–2132.
11. J. C. Ginefri, L. Darrasse, P. Crozat, and S. Serfaty, *J. Phys. IV*, 1998, **8**, 245–248.
12. L. Darrasse, L. Chiron, J.-C. Ginefri, M. Poirier-Quinot, T. Trollier, A. Ravex, J. Tanchon, J.-M. Poncet, J.-P. Arnaud, A. Gauthier, L. Guillemet, P. Crozat, A.-L. Coutrot, E. Dufour-Gergam, J.-P. Gilles, J.-P. Grandchamp, M. Woytasik, E. Martincic, J.-M. Quemper, *ITBM-RBM*, 2004, **25**(5), 254–259.
13. Q. Y. Ma, K. C. Chan, D. F. Kacher, E. Gao, M. S. Chow, K. K. Wong, H. Xu, E. S. Yang, G. S. Young,

J. R. Miller, and F. A. Jolesz, *Acad. Radiol.*, 2003, **9**, 978–987.

14. J. R. Miller, S. E. Hurlston, Q. Y. Ma, D. W. Face, D. J. Kountz, J. R. MacFall, L. W. Hedlund, and G. A. Johnson, *Magn. Reson. Med.*, 1999, **41**, 72–79.
15. S. E. Hurlston, W. W. Brey, S. A. Suddarth, G. A. Johnson, and E. G. Fitzsimons, *Magn. Reson. Med.*, 41, **1999**, 1032–1038.
16. F. Odoj, E. Rommel, M. Kienlin, and A. Haase, *Rev. Sci. Instrum.*, 1998, **69**, 2708–2712.
17. A. C. Wright, H. K. Song, and F. W. Wehrli, *Magn. Reson. Med.*, 2000, **43**, 163–169.
18. J. C. Ginefri, M. P. Quinot, O. Girard, and L. Darrasse, *YMETH*, 2007, **43**, 54–67.
19. R. Haueisen, D. Marek, M. Sacher, K. Ugurbil, and S. Junge, Cryogenic probe setup for routine MR imaging on small animals at 9.4 T, In *Proceedings 22nd Annual Meeting ESMRMB*, Switzerland 2005, p. 80 (22nd Ann Meeting ESMRMB, Basle).
20. R. Haueisen, D. Marek, M. Sacher, K. Ugurbil, and S. Junge, Flexible Cryoprobe-setup for mice brain imaging and spectroscopy at 9.4 T, In *Proceedings 23rd Annual Meeting ESMRMB*, Switzerland 2006, p. 110 (23nd Ann Meeting ESMRMB, Basle).
21. N. Radzwill, R. Haueisen, D. Marek, M. Sacher, and S. Junge, In *Proceedings of the 15th Annual Meeting ISMRM*, Berlin, 2007, p. 3267.
22. D. Ratering, C. Baltes, J. Nordmeyer-Massner, D. Marek, and M. Rudin, *Magn. Reson. Med.*, 2008, **69**, 1440–1447.
23. S. Wecker, E. Kiistennann, B. Radenmacher, and M. Hoehn, *Proceedings 10th Annual Meeting ISMRM*, Honolulu, USA, 2002, p. 870–878.
24. J. Wosik, K. Nesteruk, L.-M. Xie, M. Strikovski, F. Miller, J. H. Wang Jr., M. Bilgen, and P. A. Narayana, *Physica C*, 2000, **341–348**, 2561–2564.
25. J. Wosik, K. Nesteruk, L.-M. Xie, L. Xue, J. A. Bankson, and J. D. Hazle, A novel planar design of 200 Mhz superconducting array, In *Proceedings 11th Annual Meeting*, Canada, 2001, p. 2373.
26. K. H. Lee, M. C. Cheng, K. C. Chan, K. K. Wong, S. S. Yeung, K. C. Lee, Q. Y. Ma, and E. S. Yang, *IEEE Trans. Biomed. Eng.*, 2004, **51**, 2024–2029.
27. L. Darrasse and J. C. Ginefri, *Biochimie*, 2003, **85**, 915–937.
28. M. Vester, F. Steinmeyer, B. Roas, G. Thummes, and K. Klundt, High temperature superconducting surface coil with liquid nitrogen or pulse tube refrigeration, In *Proceedings 5th Annual Meeting ISMRM*, Vancouver, Canada, 1997, p. 1528.
29. J. Mispelter, M. Lupu, and A. Briguet, *NMR Probeheads for Biophysical and Biomedical Experiments: Theoretical Principles and Practical Guidelines*, Imperial College Press, 2006, ISBN:1-86094-637-2.
30. Electrical Conductivity and Resistivity, http://www.ndt-ed.org/EducationResources/CommunityCollege/Materials/Physical_Chemical/Electrical.htm NDT Education Resource Center, Brian Larson, Editor, 2001–2011.
31. S. Megherbi, J. C. Ginefri, L. Darrasse, and G. Raynaud, *Microsyst. Technol.*, 2005, **12**, 38–43.
32. J. C. Ginetri, L. Darrasse, and P. Crozat, *IEEE Trans. Appl. Superconductivity*, 1999, **9**, 4695–4701.
33. S. Junge and F. Seifert, Simulated electromagnetic characteristics of RF-coils at 3 T consistent with measurements, *Proceedings 19nd Annual Meeting ESMRMB*, France 2002, p. 424–432 (19nd Ann Meeting ESMRMB, Cannes).
34. A. Raad and L. Darrasse, *Magn. Reson. Imaging*, 1992, **10**, 55–65.
35. R. Haueisen, D. Marek, and S. Sacher, NMR probe head with heated housing, U.S. Pat. 7,358,735B2 (2008).
36. M. Sacher, D. Marek, T. Leutenegger, D. G. Baumann, and R. Haueisen, U.S. Pat. 7,501,822 (Mar 2009.)
37. M. S. Chow, S. M. Yeung, K. H. Lee, Q. Y. MA, and E. S. Yang, A two-channel HTS thin-film phased array coil for low field MRI, In *Proceedings 11th Annual Meeting ISMRM*, Canada, 2001, p. 2372.
38. M. J. Hennessy, I. L. Pykett, T. W. Skloss, X. Yuan, D. J. Kountz, and D. Lauterbache, A RF high temperature superconducting two coil array, In *Proceedings 7th Annual Meeting ISMRM*, USA, 1999, p. 2076.
39. W. Kwok, Z. You, and J. Zhong, Improved high resolution imaging with 4-element liquid nitrogen phased array coil and VD-AUTO-SMASH at 1.5 T, In *Proceedings 11th Annual Meeting ISMRM*, Canada, 2001, p. 430.
40. J. Hennig, A. Nauerth, and H. Friedburg, *Magn. Reson. Med.*, 1986, **3**, 823–833.
41. A. Haase, J. Frahm, D. Matthaei, W. Hänicke, K. D. Merboldt, *J. Magn. Reson.,* 1986, **67**, 258–266.
42. H. Liebel, W.I. Jung, and M. Westphal, Ultra-Shielded and Refrigerated (USR) Superconducting Magnets, SpinReport 154/155, G. Wolff, Bruker BioSpin GmbH, 2004, ISSN 1612-4898, p. 64–66.

Chapter 21

Litz Coils for High Resolution and Animal Probes, Especially for Double Resonance

F. David Doty and George Entzminger Jr

Doty Scientific Inc., Columbia, SC 29229, USA

21.1 INTRODUCTION

The RF coil is of critical importance for obtaining maximum signal to noise (S/N) in magnetic resonance imaging (MRI), and many papers have been published on this subject. However, over the past two decades, the majority of articles on MRI RF coils have focused on large coils, where sample losses strongly dominate, or on microcoils, where sample and capacitor losses are negligible. Few have addressed the midrange coils, seen in the majority of small-animal applications, where all the sources of loss (coil, capacitor, sample, shield, and transmission lines (TRLs)) are important. The human MRI market is more than an order of magnitude larger than the small-animal (or preclinical) MRI market; so it is not surprising that advanced and generally sufficient software tools have been available commercially from several vendors for nearly a decade for applications where coil losses are not too important, while fully satisfactory options for midrange coils have become available only more recently.

Another difference between many clinical magnetic resonance (MR) volume coils and those for small-animal research is that the former are often intended for a rather narrow range of loadings, while the latter are often desired to operate as optimally as possible from the nearly unloaded condition (in which coil and capacitor losses dominate) to the case of being stuffed to the limit. This, along with the higher operational frequencies, makes tunability more of a challenge. Often the tuning/matching circuitry must be separated from the coil by a distance greater than 20% of the free-space wavelength, and this makes optimization complex.

The focus of this chapter is on midrange coils—coils where the product (fd) of the frequency f and the coil diameter d is generally in the range of 2–30 MHz-m. This would include, for example, mouse brain and body coils from 125 to 800 MHz, and rat body coils up to 400 MHz. Coils in this range (except near the upper end) are often perceived by research managers to be relatively simple to optimize and build. Hence, many MR research programs have

RF Coils for MRI
Edited by J. Thomas Vaughan and John R. Griffiths
 ISBN: 978-0-470-77076-4

electronics and machine shop facilities devoted to building such coils.

We begin by presenting a brief overview of MR S/N analysis, followed by brief discussions of some coils commonly used in small-animal MR and large-volume nuclear magnetic resonance (NMR)—both linear and quadrature coils. Some of the details of practical design are then presented so that the reader will better understand what is involved in making coils of this type.

21.2 S/N IN COMPLEX COIL CIRCUITS

The S/N following a single 90° pulse when all the resistive losses (coil, capacitors, and sample) are at the same temperature T_n, may be expressed in a number of ways. The following equation has been found to be useful in coil design[1,2]:

$$S/N = \left[\frac{\hbar^2\sqrt{2\pi\mu_0}}{12k_B^{3/2}}\right]\left[\frac{n_S\gamma I_x(I_x+1)\sqrt{T_2^*}}{T_S\sqrt{T_n+T_P}}\right] \times(\eta_E\eta_F Q_L V_S)^{1/2}\omega^{3/2} \quad (21.1)$$

where $\hbar$ is Plank's constant divided by 2π, μ_0 is the permeability of free space, k_B is Boltzmann's constant, n_s is the number of spins at resonance per unit volume, γ is the magnetogyric ratio, I_x is the spin quantum number, T_2^* is the effective spin–spin relaxation time, T_S is the sample temperature, T_n is the probe noise temperature, T_P is the effective preamp noise temperature, η_E is the RF efficiency (the fraction of power dissipated in the sample coil), η_F is the magnetic filling factor of the sample coil, Q_L is the matched, loaded, circuit quality factor, V_S is the sample volume, and ω is the Larmor precession frequency, γB_0.

The primary problem with equation (21.1) is that it has not been easy to calculate magnetic filling factor with good accuracy except for very simple cases until rather recently. Filling factor has sometimes been defined as the magnetic energy in the transverse component of the magnetic field throughout the sample divided by the total magnetic energy U throughout all space (recall $U = I^2L/2$ for a simple coil). However, in order for the concept to apply properly to circular polarization (CP), it is better to define η_F in terms of the *transverse rotating* field component B_1:

$$\eta_F = \frac{\int_S B_1^2 dV_S}{\mu_0 U} \quad (21.2)$$

Note that this is the ratio of the energy in the positive rotating circularly polarized transverse field within the sample to the total magnetic energy, and thus B_1 is a constant field, and not an oscillating field.

If we assume that T_P is quite small compared to T_n (a reasonable assumption with state-of-the-art tuned preamps, except perhaps for cryoprobes) and losses are confined to a single resistor R_0 of temperature T_n in series with a lossless sample coil and capacitor, then for given MR test conditions (sample, B_0, T_2^*, T_S, and method) the following equation can be derived, either from equation (21.1) or from the principle of reciprocity[2–6]:

$$S/N \propto \frac{B_1 V_S}{i\sqrt{R_0 T_n}} \quad (21.3)$$

where i is the sample-coil current and B_1 is the mean RF CP field generated within the sample by the current i. Since the Johnson noise voltage is proportional to $(R_0 T_n \delta f)^{1/2}$, from equation (21.3) it is clear that the signal voltage is proportional to $B_1 V_S/i$. This expression for signal voltage is valid irrespective of the noise,[5] but it is seldom convenient. Equation (21.3) is easily cast into the following form,[2,7] which is more useful in practical probe design and evaluation, where power is dissipated in numerous losses of uniform temperature T_n in a complex circuit:

$$S/N \propto \frac{B_1 V_S}{\sqrt{P_T T_n}} \quad (21.4)$$

In the above, P_T is the total transmitter power (power applied at the disconnected preamp port, so that TRL losses are properly included) required to generate B_1. Both, equations (21.3) and (21.4), usually without the T_n in the denominator, are commonly referred to as statements of the principle of reciprocity, though more precise definitions have been developed. (Note that for linear polarization, B_1 is half of the peak RF field strength. Also, the B_1 field strength is often indicated by the reciprocal of the pw90, the time required to rotate the magnetization 90°.)

The above expressions fail when the various losses are at significantly different temperatures. Clearly, one cannot ignore the T_n factors in cryoprobes, which are now in widespread usage for liquid NMR and are beginning to appear for solid NMR and microimaging. Equation (21.4) is easily extended to handle complex circuits where various losses are at significantly

different temperatures as follows[7,8]:

$$S/N \propto \frac{B_1 V_S}{\sqrt{\sum P_n T_n}} \tag{21.5}$$

where P_n is the transmit power dissipated in the nth resistance of temperature T_n when generating B_1, and the summation is over all resistances (sample, coils, capacitors, shields, and TRLs) in the circuit. An easy way to show this is to transform each loss into an equivalent resistor R_n in series with the sample coil.[8] In large coils at high fields, the summation in the denominator is dominated by the power dissipated in the sample, which is near 310 K for in vivo applications. Since sample loss is proportional to the integral of σE^2 over the full sample, where σ is the sample conductivity and E is the electric field, optimization of coils for these cases is primarily directed at minimization of the integral of E/B_1.

In most midrange coils, losses in the sample coil, capacitors,[9] and TRLs are also significant, and the complete circuit must be optimized. Equation (21.5) may be cast into the following form,[8] which is often more easily related to the results from linear circuit simulation software in the analysis of complex circuits:

$$S/N \propto \frac{v_c V_S}{\sqrt{L_C V_C \sum P_n T_n}} \tag{21.6}$$

where L_C is the sample-coil inductance, V_C is the coil volume, and v_c is the *voltage* generated across the sample coil when pulse power P_T is applied at the impedance-matched port. The L_C in the denominator may be initially surprising. However, the derivation of the above is straightforward for any specific sample-coil type, and it has been experimentally validated in numerous experiments.[7] Equation (21.6) shows that the relative S/N (for a given sample coil, T_2^*, etc.) in a complex circuit (containing various capacitors, matching coils, and TRLs between the matching elements, sample coil, transmit/receive (T/R) switch, and preamp) is indicated simply by the voltage induced at the sample coil by a given power applied at the disconnected preamp input port. It is important to emphasize that equation (21.6) is not useful for "coil optimization", and that is not its purpose. Rather, it is useful for optimization of the rest of the circuit needed for tuning, matching, and connecting the coil to the preamp; and for that purpose we find this equation indispensable, whether or not the T_ns are all equal.

Thus, the midrange RF "coil" optimization problem usually consists of two major parts: (i) minimization of the integral of E/B_1 for the sample coil (where the numerator is integrated over the full sample, and the denominator is integrated only over the homogeneous field region), and (ii) maximization of the efficiency of delivering RF power to the coil when viewed from a transmit perspective—even if the coil is for receive only. Perturbation methods permit accurate workbench measurement of the magnetic filling factor,[4] and Q_L may be easily measured. However, the first task can only be fully addressed using full-wave software with effective algorithms for handling conductor surface losses. The second task is best addressed using common linear circuit simulators, such as ARRL Radio Designer, SPICE, Ansoft Designer, or GENESYS. While the simplified analytical approaches usually presented in the professional literature are useful in providing insights, we find the numerical tools to be superior in practice—a point that we will emphasize. Equation (21.6) usually works for cryoprobes only if one is careful to view the coil and matching network from the perspective of the preamp during receive, which is often quite different from the circuit during transmit.

It is important to keep in mind several assumptions in the above analyses: (i) the preamp's noise temperature is low compared to that of the coil circuit; (ii) T_2^* is not adversely affected by coil magnetism (an issue that is generally of no consequence in the design of coils larger than 80 mm but often becomes of critical importance for coils smaller than 12 mm); and (iii) the frequency-domain filter bandwidth is equal to $1/(\pi T_2^*)$. This noise bandwidth may be established by exponential multiplication of the signal acquisition prior to the Fourier transform (FT) or by signal processing (such as line broadening) after the FT.

21.3 FULL-WAVE 3D EM SOFTWARE

One of the last challenges to be adequately addressed in full-wave 3D electromagnetic simulation tools was that of resistive losses in foil conductors in regions of very high field gradients. Simple analytical expressions based on empirically modified skin-depth models give amazingly accurate coil losses for specific types of coils, including solenoids and surface coils, over a wide range of conditions[10]; but the accuracy of similar expressions for volume coils is limited.[11] We selected Microwave Studio (MWS)

of Computer Simulation Technology (CST) in 2002 because at that point it consistently gave better agreement with experiments than other 3D software we evaluated for midrange coil problems.[7,12] Since then, others have shown that Ansoft HFSS and other tools also give accurate results for small-coil problems.[13] The CST software is based on a discretized solution of the integral formulation of Maxwell's equations; hence, the method is referred to as *finite integration technique* (*FIT*).[14] To solve these equations, a calculation domain is defined enclosing the application problem. An important part of obtaining accurate solutions with reasonable mesh sizes lies in the detailed handling of mesh elements containing several different materials, especially when one material is a lossy metal and another material is a dielectric. The software vendors have put considerable effort into optimizing the calculation of the mean effective fields and losses within these troublesome cells that generally cover most of the surfaces of conductors in complex structures or may even be divided by several thin sheets of conductors.

The discretized mesh equations can be solved either in the time domain by a transient finite difference time-domain (FDTD) approach or in the frequency domain using second-order harmonic relations. An advantage of the transient method is that it provides a broad-spectrum solution. We observe that the CST time-domain solver generally gets the RF copper losses right within ~10% (the typical limit of our experimental accuracy) for thick conductors and wires. Similar accuracy is seen for foil conductors when the current densities are not too different on opposite sides of the foil. However, where current densities are radically different on opposite sides of the foils, as happens frequently in volume coils for example, it has often underestimated copper losses significantly.

In all our simulations, the tuned coil is excited with a broadband 50-Ω pulse source of Gaussian distribution, 14.14-V peak, centered very near resonance, which delivers 0.5 W to the coil when matched to 50 Ω. Also, the simulation space (which includes the coil, sample, and shield) has copper boundaries. The mode frequencies are usually calculated within 2% of the experimental values (even for double-resonance coils), and the calculated B_1 magnitude usually agrees within 5% with the MR experiment. While the B_1 magnitude has sometimes been off by 15%, the E/B_1 integral is probably generally accurate within a few percent.

21.4 LINEAR-POLARIZATION VOLUME COILS

Solenoids permit the highest S/N when sample losses are not dominant and B_0 homogeneity is not critical,[15] and they also can achieve very high $\boldsymbol{B}_1$ homogeneity. However, saddle coils are used for most NMR spectroscopy for two compelling reasons: they permit much higher spectral resolution, and they are compatible with automatic sample exchange.[16,17] Another advantage of the saddle coil is that two of them can be oriented orthogonally with excellent performance of each in double-resonance experiments.

The S/N disadvantage of the solenoid compared to the optimized saddle coil begins to fade as soon as sample losses become significant. The Alderman–Grant coil,[18] as shown in Figure 21.1, demonstrated that capacitive segmentation is a very effective method of dramatically reducing sample losses because the voltage builds up only over half of the inductance of a similar one-turn saddle coil before it gets reversed by a segmenting capacitor. Also, the quadrupolar symmetry of the conservative $\boldsymbol{E}$ field reduces its average value throughout the sample. Numerical optimization by Kost showed

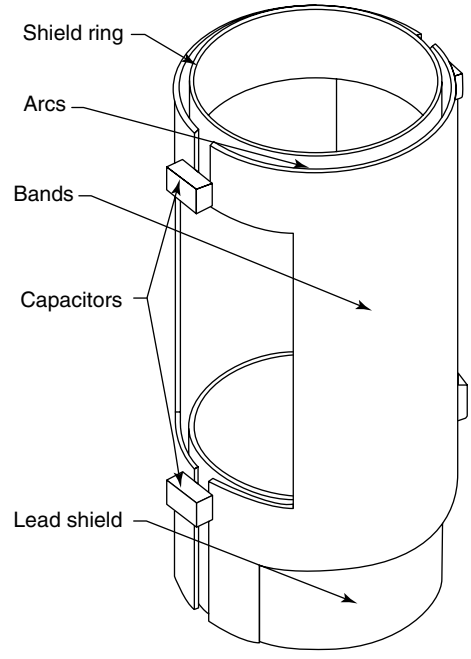

Figure 21.1. The Alderman–Grant saddle coil.

that the optimum subtended angle of the window was about 90° for best B_1 homogeneity.[19]

Both multiturn saddle coils and solenoids continue to be the coils of choice for many applications, especially in NMR spectroscopy.[20] The microsolenoid, which has been well understood only very recently,[21] is usually preferred for sample sizes below 2 mm; and the multiturn saddle coil is usually the volume coil of choice for *fd* in the range of 2–6 MHz-m for double resonance—and sometimes as high as 10 MHz-m. The Alderman–Grant coil has often been used for the 5–15 MHz-m range—usually with a mean subtended angle of ~120° for improved orthogonal flux transparency when an orthogonal coil is needed for double resonance.

The primary limitations of the Alderman–Grant coil are limited B_1 homogeneity and transverse flux transparency. These limitations may be addressed by using parallel conductors with insulated crossovers in a way that forces a more optimal surface current distribution.[11,22] At the same time, both Q_L and η_F may be improved, and the capacitive segmentation may be extended for improved tuning with larger samples at higher frequencies. Coils with parallel conductors with insulated crossovers have been denoted as Litz coils.

The primary surface pattern, as shown in Figure 21.2 laid out flat, is the basic version of what has been denoted the center-fed one-turn (CF1T) Litz coil.[11,22,23] This is the simplest, significant improvement on the Kost optimization[19] of the slotted resonator[24] or single-turn saddle coil,[25] which has similar inductance. There are two parallel paths on each side of this coil with an insulated crossover (not fully shown) such that each path, by symmetry, has the same inductance. Hence, each path carries the same current, irrespective of the azimuthal locations, axial locations, or frequency. The azimuthal locations are chosen for a balanced optimization of B_1 homogeneity, η_F, and Q. With typical foil widths, the optimum mean azimuthal subtended angles of the inner and outer loops are 91° and 156°. Compared to the Kost coil, the diameter of the homogeneous sample volume (6% rms inhomogeneity) is increased from 65 to 78% of the coil's diameter, the Q is increased by ~15%, and the coil has excellent transparency to transverse RF flux. For a prescribed inhomogeneity, the filling factor is increased by over 40%, primarily because of the large increase in the permissible sample volume. Since it is not capacitively segmented, its performance is usually suboptimal for single-resonance, fixed-frequency applications above ~5 MHz-m. However, it is often the best choice for *fd* in the range of 3–11 MHz-m when a wide tuning range is desired, such as ^{31}P to ^{13}C for mouse and rat applications at 4.7–14 T. Of course, there is significant capacitance between the two parallel paths at the crossovers, and this introduces a parasitic high-frequency mode. If this coil is used for the low-γ channel in double resonance, its high-frequency parasitic mode can be near the ^1H frequency, which could lead to tuning difficulties. Also, as the coil has rather low inductance (for example, ~26 nH for a short 30-mm coil inside a large shield) lead losses can be fairly substantial if not properly addressed when multinuclear tuning is desired. As mentioned earlier, detailed RF circuit modeling is useful. A balanced TRL, such as a twisted pair, from the coil to the matching network generally gives better results than other options.

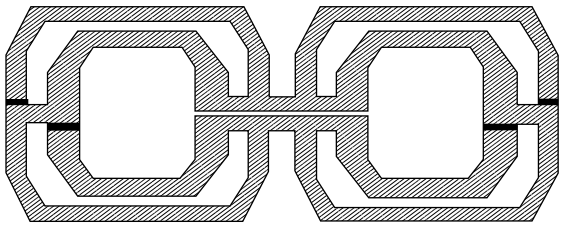

Figure 21.2. Primary foil pattern (side 1) for the basic CF1T Litz coil. Crossovers on the back side of the laminate are partially shown with solid lines. Tuning capacitors are added across the central gap.

The 24-mm linear coil shown in Figure 21.2 achieves 20 μs ^1H pw90 for a hard 50-W pulse for a mouse head imaging at 4.7 T—which is better than that obtained with birdcages. In-plane resolution, as shown in Figure 21.3, of 175 μm is readily obtained for a T_2-weighted, spin-echo, multislice experiment, no contrast agent, 128 × 128, 0.4-mm slice (12 nl voxel), $T_R = 3$ s, $T_E = 20$ ms, NEX = 1.

It is possible to further improve B_1 homogeneity and extend the useful range by capacitive segmentation and use of more parallel current paths among which the currents are optimally divided. Figure 21.4 illustrates the foil patterns, laid out flat, for what has been designated the symmetric quarter turn (SQT) Litz coil (the current paths execute a quarter turn around the $\boldsymbol{B}_1$ axis before their inductance is capacitively negated). The homogeneous B_1 region extends

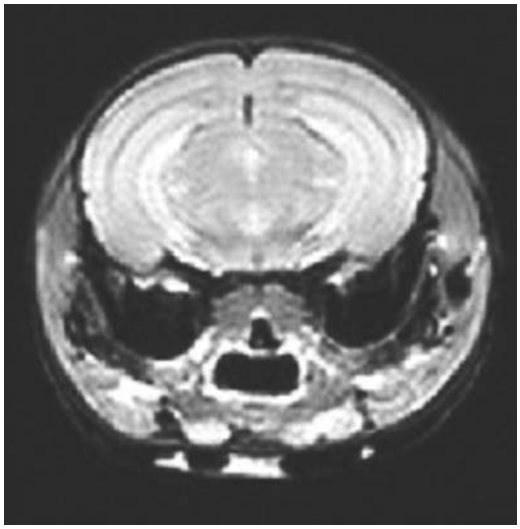

Figure 21.3. Live mouse brain at 4.7 T using a linear Litz coil. Biomedical MR Laboratory, Washington University, St. Louis, MO.

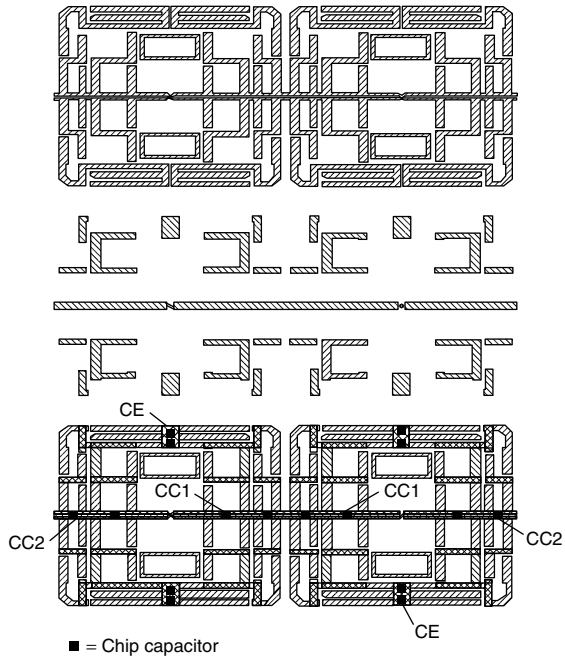

Figure 21.4. Foil patterns, side-1, side-2, and superimposed, for the SQT Litz coil. End-segmenting capacitors (CE) and central segmenting capacitors (CC1 and CC2) are placed as shown.

radially to 84% of the coil diameter and axially to the inside of the arcs on which the end-segmenting capacitors (CE) are mounted. (Note that the isolated closed loops at the ends of the central flux windows improve B_1 homogeneity by reducing the peak fields otherwise seen in these areas. Otherwise, the coil is quite similar to the one previously described in detail.[11]) Both B_1 homogeneity and S/N of this linear coil are generally better than that of the 16-rung CP birdcage for closely shielded cases with long samples (extending well beyond the coil) with *fd* below 20 MHz-m.[26] For example, a 16-cm SQT coil at 125 MHz proved superior to CP birdcages and transverse-electromagnetic (TEM) resonators of similar dimensions.[26] The unloaded-to-loaded Q ratio in the reference CP coils exceeded three (indicating excellent optimization), but still the linear coil achieved higher S/N. Another useful attribute of this coil is that it may be tuned over a relatively wide range (compared to the birdcage) with little degradation in B_1 homogeneity or S/N, as it does not rely on capacitive phase shifts to achieve the desired current distribution. This coil (or one very similar[11]) has been used in numerous applications from 18 mm at 600 MHz to 160 mm at 125 MHz. In some cases, they have been tunable from ^{19}F to ^{1}H.

The primary disadvantage of the SQT coil is the extra axial space required at the ends (needed to achieve the reduced current concentrations there), as this prevents it from being effective for head coils—whether for mouse or man. A drawback for small coils is that the segmenting chip capacitors needed at the center of the coil may lead to shimming artifacts for coils below 20-mm diameter. Yet another limitation is that since much of the surface is covered by the copper foil pattern, it is not as easy to see the sample through the coil—a desirable feature in working with small animals. This last limitation is not important in closely shielded RF coil modules, as the shield is opaque, but the more convenient approach for small animals in horizontal-bore magnets is a platform with a removable RF shield and fuller access to the coil and animal. Hence, the birdcage, or a derivative, as discussed in the next section, is often selected even where the SQT might provide higher S/N—such as for mouse liver up to 400 MHz and rat liver up to 200 MHz.

The SQT coil is often used for the ^{1}H channel in double-resonance, where its *fd* is in the range of 5–20 MHz-m. An orthogonal CF1T Litz coil is then often used for the low-frequency channel. Couplings

between the orthogonal coils generally limit this approach to 25 MHz-m for the ^{1}H coil.

21.5 CIRCULAR POLARIZATION (CP) VOLUME COILS

The birdcage is arguably an ideal volume coil for generating uniform CP, which generally allows a 40% increase in S/N compared to linear polarization from the same coil, as well as a factor of 2 reduction in specific absorption rate (SAR).[27–30] Because the birdcage and its common variants (low pass, balanced low pass (BLP), balanced high pass (BHP), high pass) have been discussed and analyzed in numerous papers over the past two decades,[4,30–33] it will not be reviewed here. Rather, we mention only a few points that are particularly important to small-animal applications and then look a little more closely at a variant that is advantageous for many small-animal applications—the Litzcage™.

Since tuning capacitors scale inversely with the square of the frequency but inverse linearly with the size, smaller capacitances are generally needed in birdcages for small-animal applications than in common human applications. Consequently, the effects of stray capacitances are often relatively greater in small-animal coils, and the problem is exacerbated by the fact that loaded Qs are much higher. Accommodating wide ranges of loads presents challenges for small CP coils at high fields.

Tropp has shown, both theoretically and experimentally,[32,34] that symmetry in the birdcage is *not* critical for the case of the human head at 3 T and higher, where the *fd* product is 30 MHz-m or greater, as in such cases dielectric resonance effects within the sample have dominant effects on the field profiles. However, this is not the case for most small-animal applications, where *fd* is usually less than 20 MHz-m and sometimes under 5 MHz-m (mouse body at 200 MHz). For such cases, tuning symmetry is quite important.

Even with perfect symmetry, at least 12 rungs are required for adequate B_1 homogeneity in a closely shielded small birdcage when a relatively large region of uniformity (ROI) is needed. Such coils typically have an easy tuning range of less than 1% with good homogeneity and channel separation, while sample tuning shifts can be as large as 8% for the small, heavily loaded birdcage.[4] However, the 8-section birdcage is about twice as robust (tunable and correctable) as the 12-section birdcage, partly because it is possible to attach two adjustment variables to nodes at 45° with respect to the feed planes, which simplifies the symmetrization problem when tuning to different loads.[34] Corrections in the 12-rung birdcage, on the other hand, tend to mix more with all tune and match adjustments, which complicates the process. While the 45° nodes are available in the 16-section birdcage, it has twice as many distinct capacitors and thus about half the tuning range in small coils.

Crozier observed that capacitor losses are usually quite significant in small birdcages, and for this reason the small 8-section coil (such as for rat liver below 400 MHz) usually has higher Q and S/N than the 12- or 16-section small coil,[35] an observation confirmed by many others.[36] He also showed that a significant increase in the usable *fd* limit and Q of the 8-section high-pass birdcage could be obtained by using two bands in parallel in each section rather than a single wide rung.[35] With a single wide rung per section, most of the current flows near the edges, so removing the copper from the rung centers has little affect on copper losses, while it reduces electric field couplings to the sample and thus improves the Q. Still the homogeneity is that of the 8-rung coil, and it is degraded by the fact that the current in a birdcage always crowds to the worst side of the rungs. For example, when the rotating B_1 is aligned with X, the current crowds to the edges of the rungs closer to the XZ plane. When the phase is aligned with Y, the current crowds to the edges closer to the YZ plane. In an 8-section birdcage, this leads to a substantial reduction in homogeneity compared to the calculations based on imposed uniform current distributions.

Varian (now Agilent) has demonstrated that small birdcages with even more than 16 rungs can be produced by integrating the capacitors into the double-clad low-loss laminate.[37] These Millipede™ coils have demonstrated exceptional B_1 homogeneity in small coils with mineral-oil samples.[37] They have also demonstrated impressive images in a multiple-mouse application with high dosage of contrast agent at 7 T,[38] but details of the RF performance of the current products are not readily available. An advantage of this approach is that it reduces the susceptibility artifacts from chip capacitors, which are often quite significant in very small coils.

Another avenue pursued by Varian is ultrathickening of the conductors in the conventional birdcage by

bending and extending the conductor foil edges in the radial direction.[36] They report an 8-rung, 550-MHz, 7-mm example in which the radial thickness of the conductors is 30% of the coil inner radius r_1 and the shield radius r_2 is $3r_1$. Here, compared to a reference thin-foil 12-rung case with the same r_1 and r_2, a 50% improvement in Q with a 20% loss in filling factor was obtained for a constant sample volume, giving a 15% gain in S/N. However, the B_1 homogeneity of the 8-rung thick coil was naturally quite inferior to that of the 12-rung thin coil. Similar approaches have been discussed and evaluated by other researchers,[22] but usually there is not enough space available between the coil and an outer coil or the shield for such an approach to be practical.

The TEM coil is a favorite of many researchers in high-field human applications,[32,39] and the strip-line variant has been used in some small-animal applications.[40] Analysis using multiconductor TRL theory achieved remarkable agreement between experiments and theory in predicting unloaded mode frequencies for a number of linearly driven cases, including 7.5 cm at 200 MHz and 13.4 cm at 300 MHz.[41] Apparently, it is difficult to achieve satisfactory quadrature operation in such coils for small-animal applications with slotted RF shields. This is at least partly because the inhomogeneous modes are closer than in the birdcage and its derivatives.[32] Our experience suggests this difficulty in achieving clean quadrature tuning—at least for $fd > 12$ MHz-m—also frequently extends to the BLP birdcage, which is topologically similar to the TEM and strip-line coils. We have found the matching methods presented shortly for the BHP birdcage to be more robust and predictable with this topology.

The homogeneity of the Crozier coil may be improved by inserting an insulated crossover at the center of each pair of rungs, as shown in Figure 21.5,

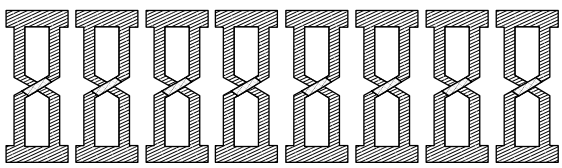

Figure 21.5. An approximation of one surface of the high-pass Litzcage foil pattern. Insulated crossovers are shown with solid lines. A more accurate portrayal of the crossovers can be seen later in Figure 21.9.

in what has been denoted the Litzcage.[42,43] The central crossover (by symmetry) forces the current to be equal in each of the two parallel paths in that section, which gives a significant improvement in B_1 homogeneity over the alternative 8-section CP coils (either a single wide rung or the Crozier version), in which the current concentrates on the side closer to the rotating B_1 axis. With the crossovers between the parallel paths, the currents are always equally divided between the two parallel paths and B_1 homogeneity is improved for cases well below dielectric resonance conditions—i.e., for fd less than ~20 MHz-m. Figure 21.6 compares the calculated B_1 map for the Crozier coil and Litzcage for a 25-mm coil at 300 MHz.

From an RF circuit perspective, the homogeneous mode is almost indistinguishable from that of Crozier's parallel-rung 8-section birdcage,[35] which is, of course, quite similar to the conventional birdcage. However, the 30% reduction in stray capacitance in the Litzcage (relative to the 8-rung birdcage) allows it to tune ~15% higher. The simulations show that the Litzcage has homogeneity and S/N at least as good as that of the ideal 12-rung birdcage while retaining the tuning ease and robustness of the 8-rung birdcage. The 8-section Litzcage has been used at fd up to 41 MHz-m (20.5 cm, 200 MHz), but the 16-section BHP birdcage is generally a better choice beyond 25 MHz-m, especially in larger coils, where the extra modes caused by the crossovers can create difficulties. Also, with the central crossovers, accurate 3D full-wave simulations are much more computationally intensive.

As discussed earlier, S/N is proportional to $B_1/P_i^{1/2}$. (Measuring B_1 at a known power is also one of the best methods of evaluating the accuracy of MRI RF coil simulation software.) NMR measurements on a 21-mm diameter, 20-mm length, 750-MHz Litzcage yielded a 90° pulse length of 22 μs for a square 50-W pulse on a pure water sample in an 18-mm diameter NMR tube with a Q_L of 100.[44] We suspect higher than expected RF eddy current losses in the external RF shield contributed to a relatively low Q in this case. The external, gradient-transparent, RF shielding is seldom recognized as a significant source of signal loss, but in fact that can be the case for small-animal coils with closely spaced external shields. We have found that the standard method (overlapping slotted shields on double-clad Duroid laminate) can sometimes add very high losses. Lower shield losses can often be

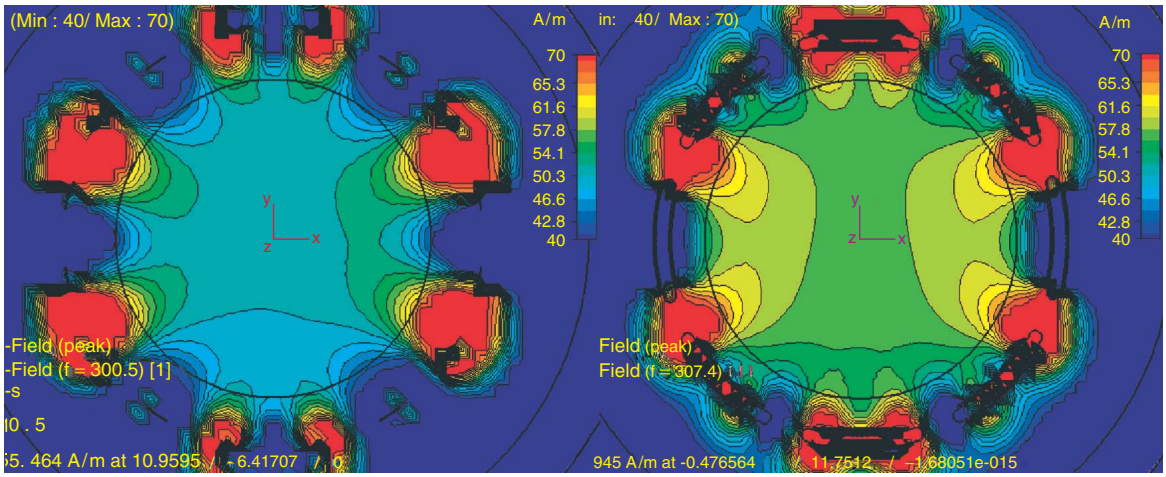

Figure 21.6. B_1 field in the central xy-plane for the Crozier coil (left) compared to the Litzcage (right) for low fd ($f = 300$ MHz, $d = 25$ mm). The mean field strength is ~10% higher for the Litzcage and inhomogeneities near the rungs are less. Contour increments are approximately 2.5% of the central value.

obtained using single-layer gapped foil with discrete chip capacitors across the gaps in the regions where the azimuthal RF-current densities are high. For a more detailed study on shield slotting requirements, see Ref. 45.

21.6 RF CIRCUIT MODELS FOR SMALL, TUNABLE CP COILS

Several factors conspire to make it difficult to achieve high B_1 homogeneity in small-animal coils. It is sometimes difficult to achieve the necessary precision in the capacitor mounting, or in the uniformity of the shield spacing around the coil. The capacitor accuracy required to place the resonance within the tuning range (the range that keeps the loaded peak-to-peak relative rung-current errors below 15%) is very tight for two-point quadrature drive in small, high-frequency birdcages. For an 8-rung BHP birdcage, mean-capacitor-value accuracy must be within 1.5%.[4] A short 18-mm coil of this type (for mouse-brain studies) at 750 MHz requires tuning capacitors of ~3.9 pF—including stray capacitances, which varies from 0.2–0.5 pF depending on the sample. Hence, the stray variability exceeds the required tolerance by more than a factor of 2, which makes this coil with 2-point-drive problematic. Moreover, the maximum useful tuning range for a small 8-section BHP birdcage with standard 2-point-drive is ~1.3%—well under typical sample-induced tuning shifts. Four-point-drive networks can achieve up to 5% tuning range with good symmetry and efficiency; but they have more parasitic modes, so it is quite useful to have a good circuit model to be better able to handle them.

Figure 21.7 illustrates a simple circuit model that usually gives the accuracy needed for the small, 8-rung, BHP birdcage or Litzcage. To represent the nearest-rung couplings (L_C), each rung includes two ideal transformers, one on either side of the central plane—e.g., rung 2 includes transformers [2,12,3,13] and [13,23,14,24]. A TRL at each end of each rung completes its self-inductance and furnishes most of the stray capacitance per rung (e.g., [11,12] and [14,15] in rung 2). Most of the losses appear as corrected attenuation coefficients in the TRLs representing the rungs. Appropriate values for the characteristics of the TRLs and the rung couplings L_C may be determined adequately by conventional methods.

One channel of an effective quad-balance network is shown in Figure 21.8. The two series transmission lines force the needed symmetry, greatly improving tuning range with good symmetry and making it easier to achieve adequate channel isolation. The unlabeled capacitors are simply eddy-current-blocking capacitors (RF shorts). L_M is used to move the common mode well away from the differential mode. L_T

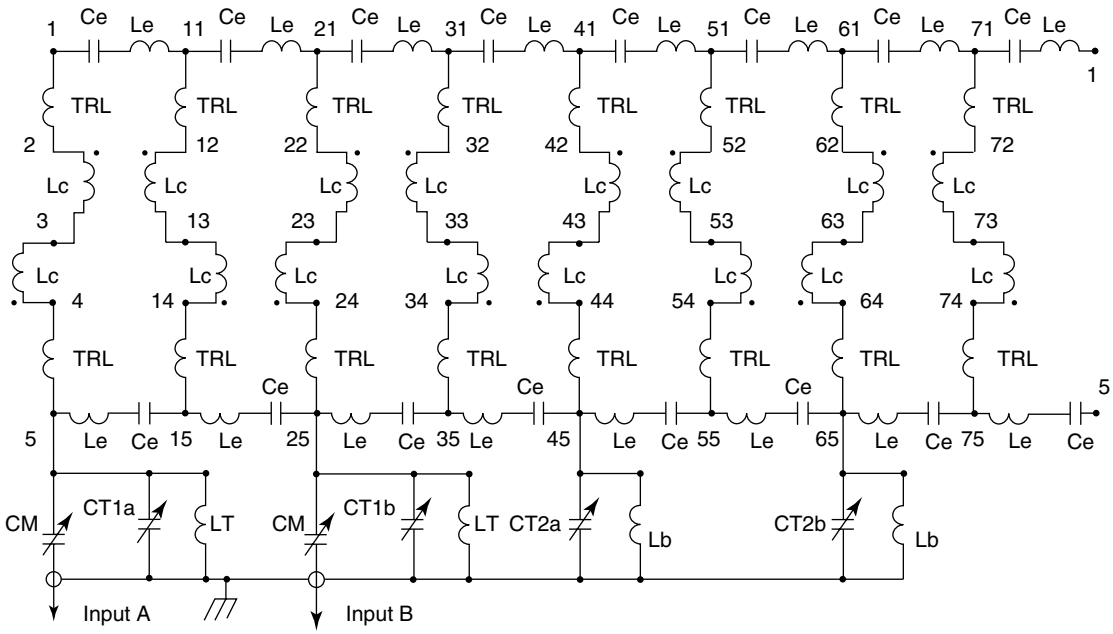

Figure 21.7. A useful RF circuit model for the 8-section small-animal BHP birdcage. Elements between nodes 1 and 5 correspond to rung 1, between nodes 11 and 15, rung 2, etc. Nodes 1 and 5 on the right are connected to the same on the left.

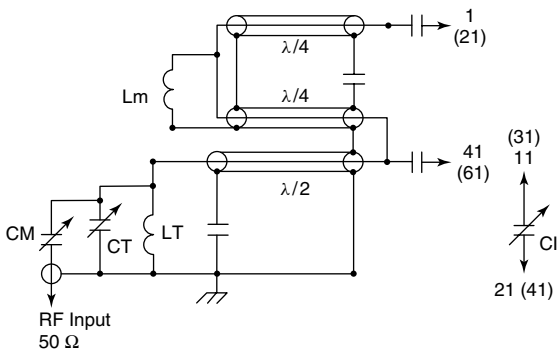

Figure 21.8. One channel of a 4-point-drive network with node numbers appropriate for connection to Figure 21.7.

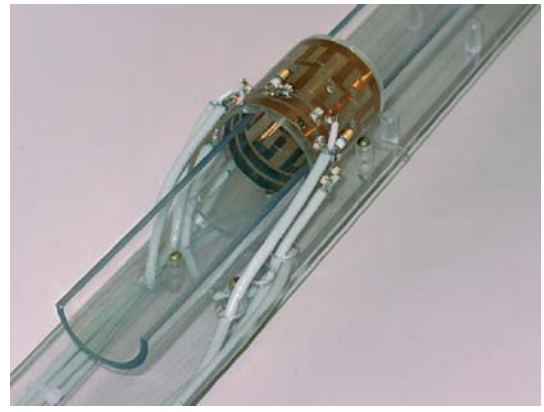

Figure 21.9. A Doty Litzcage for rat head MR in a horizontal bore.

tunes out half of the sum of the tuning variable C_T and the mean match variable C_M, thereby doubling the useful tuning range. The λ/2 feed line allows the placement of the variable capacitors well away from the coil for maximum openness and access around the coil. With low-loss coaxial lines, the total signal loss added by the balancing network is typically a few percent. An example for the horizontal bore is shown in Figure 21.9. Complex life support and physiological monitoring systems (such as those made by SAII, Stony Brook, http://www.i4sa.com/) may be set up, possibly along with surgical procedures,[43] on the live animal. The coil assembly (platform) slides inside an external RF shield.

21.7 NMR/MRI EXPERIMENTAL RESULTS

The array of NMR spectra of variable pulse widths in Figure 21.10 from one of our first linear Litz coils (a predecessor of that shown in Figure 21.4), with sample diameter 88% of the coil diameter, demonstrates the high B_1 homogeneity of the Litz coil.[22] The single-pulse, proton Bloch decay NMR spectra are arrayed sequentially as the RF pulse width is increased in 9 μs increments from 9 μs to over 500 μs with 5 s recycle delays between spectra. The spectra were acquired at 7.06 T on a saline sample 36 mm in diameter, 25 mm in length, inside a 41-mm diameter Litz coil with $h_1 = 27$ mm and a 50-mm external RF shield diameter. Note that the amplitude of the 4.5π (810°) pulse is over 60% of the amplitude of the $\pi/2$ pulse, which essentially corroborates the calculated B_1 field variation.

A 25-mm diameter, 300-MHz Litzcage similar to that pictured in Figure 21.9 permitted 50-μm isotropic resolution (0.125 nl voxel) on four fixed mouse embryos simultaneously, one of which is shown in Figure 21.11.[46] It is important to appreciate that only a slightly lower performance would have been achieved with the linear Litz coil in this case. The voxel volume reduction of two orders of magnitude compared to Figure 21.3 was primarily from (i) the use of a high level of contrast agent; (ii) the increased image acquisition time (here, 14.6 h for the complete 3-D data set, rather than a few minutes); (iii) the use of a 3D gradient echo sequence; and (iv) the higher field.

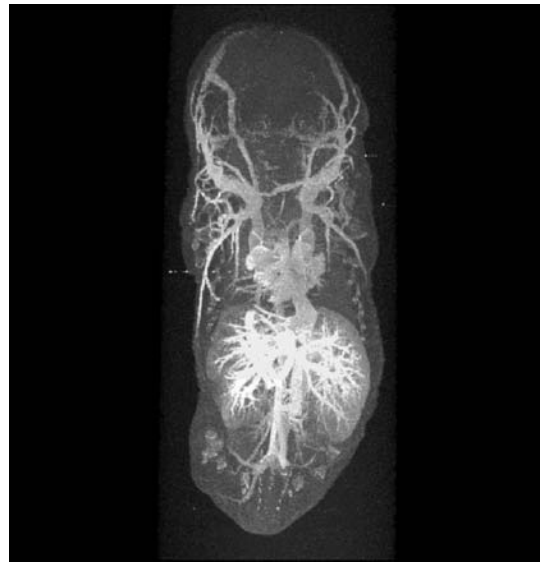

Figure 21.11. Mouse embryo with 50-μm isotropic resolution obtained with a 25-mm Litzcage at 300 MHz using contrast agent GSA-Gd-DTPA[46].

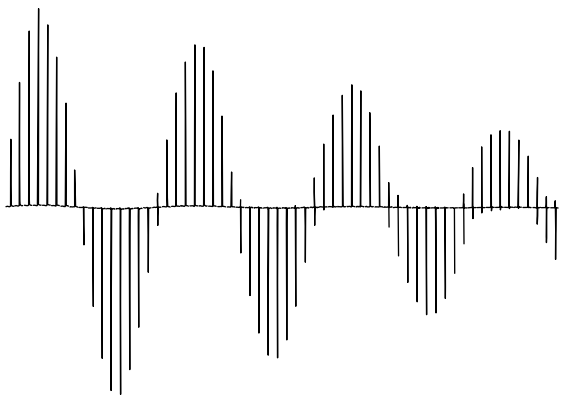

Figure 21.10. Proton nutation NMR experiment on mid volume of 36 mm × 25 mm cylindrical phantom in an SQT coil of 41-mm diameter.[22] 810° and 90° pulses is 60%.

The 300-MHz, 25.4-mm coils were tested both on the bench and in the 7-T magnet, as summarized in Table 21.1. A 30 mM saline sample (diameter 19 mm × length 22 mm), as in the simulations, was used.

Table 21.1. Test data for 300-MHz low-pass (LP) Litzcage (LC) and 12-rung LP birdcage (BC)

	Caps	Tuning range, MHz		Q_L (−3 dB)		Isolation (dB)		B_1 homo	pw90
Coil	pF	Unloaded	Loaded	Unloaded	Loaded	Unloaded	Loaded	810/90(%)	μs@19 W
LC-right	10.3	292–306	291–305	83	64	22	25	86	60
LC-left	10.3	296–306	295–305	80	62.5	22	25	80	69
BC-right	6.2	296–303	295–302	90	66	18	20	87	64
BC-left	6.2	295–302	294–301	84	60	18	20	78	52

As seen from Table 21.1, the tuning range on the Litzcage was 10–14 MHz. The frequency shift from the short phantom was only 1 MHz, but about three times that shift could be expected from a large mouse. Both coils showed good B_1 homogeneity, as seen by the ratio of the signal amplitudes of the 810° pulse to that of the 90° pulse, with the Litzcage showing less difference between the two channels than the 12-rung birdcage. Half-height linewidth on the cylindrical sample was 17 Hz for the LC and 42 Hz for the BC. The best isolation between the two channels of the 12-rung LP birdcage for the loaded case was only about 14 dB, so the 4-point drive network was added. This improved the isolation to 20 dB and also reduced the frequency shift from sample loading effect.

Over the past 14 years, these and similar Litz coils[22] have been used in a number of systems at fields from 1.5 to 25 T and at diameters from 300 to 6 mm. In most cases where comparative data were available, the performance of the Litz coil (in S/N, tuning range, and RF homogeneity) surpassed that of a reference conventional birdcage—though, of course, the Litz coils were generally made only for cases where they were expected to be advantageous. The coils were etched according to numerical optimizations without experimental fine-tuning for B_1 homogeneity. Related Litz coils have also been used in numerous high-resolution NMR probes for liquid samples, where spectral resolution better than 0.005 ppm has been achieved.

21.8 CONCLUSION

The geometries used for the Litz coils described in this chapter result in significant improvements in B_1 homogeneity, S/N, and RF field transparency for the intended sample sizes and types. Linear Litz coils are the preferred option in cases where double resonance, tuning simplicity, and good field homogeneity are the main desired operational characteristics. The linear Litz coils offer field homogeneity nearly as good as a birdcage without the tuning complexity for many samples.

For some sample types, especially in small-animal, single-resonance MRI studies, the Litzcage coil gives S/N enhancement because of CP and slight improvement in field homogeneity compared to the linear coils. The Litzcage also offers significant improvement in tuning range and simplicity compared to the birdcage in many cases.

RELATED ARTICLES IN THE ENCYCLOPEDIA OF MAGNETIC RESONANCE

Birdcage Resonators: Highly Homogeneous Radiofrequency Coils for Magnetic Resonance

Cryogenic NMR probes: Applications

ESR Probes as Field Detectors in MRI

Instrumentation for the Home Builder

Multifrequency Coils for Whole Body Studies

NMR Microscopy: Resolution

Probe Design and Construction

Probes for High Resolution

Radiofrequency Systems and Coils for MRI and MRS

Refrigerated and Superconducting Receiver Coils in Whole Body Magnetic Resonance

Sensitivity of the NMR Experiment

Solid State NMR Probe Design

Surface and Other Local Coils for In Vivo Studies

Whole Body Machines: NMR Phased Array Coil Systems

REFERENCES

1. A. Abragam, *Principles of Nuclear Magnetism*, International Series of Monographs on Physics 32, Oxford University Press: London, 1961.
2. F. D. Doty, *Probe Design and Construction*, The Encyclopedia of Nuclear Magnetic Resonance, (eds D. M. Grant and R. K. Harris), John Wiley & Sons, Published Online: 15 Mar, 2007. DOI: 10.1002/9780470034590.emrstm0414.
3. D. I. Hoult and R. E. Richards, *J. Magn. Reson.*, 1976, **24**, 71–85, Published Online: 15 SEP, 2007.
4. F. D. Doty, G. Entzminger, C. Hauck, and J. P. Staab, *J. Magn. Reson.*, 1999, **138**, 144–154.

5. D. I. Hoult, *Sensitivity of the NMR Experiment*, The Encyclopedia of Nuclear Magnetic Resonance, eds. D.M. Grant and R.K. Harris, John Wiley & Sons, 1996, Vol. 7, pp 4256–4266.
6. J. S. Tropp, In *Presented at the 12th ISMRM. Poster 1646,* Kyoto, 2004.
7. F. D. Doty, G. Entzminger, J. Kulkarni, K. Pamarthy, and J. P. Staab, *NMR Biomed.*, 2007, **20**, 304–325.
8. F. D. Doty and S. Shevgoor, In *Poster presented at Rocky Mountain Conference*, Denver, 2005. http://www.dotynmr.com/PDF/OptiMAS_ENC05.pdf.
9. F. D. Doty, *Solid State NMR Probe Design*, The Encyclopedia of Nuclear Magnetic Resonance, (eds D. M. Grant and R. K. Harris), John Wiley & Sons, Published Online: 15 Mar, 2007. DOI: 10.1002/9780470034590.emrstm0515.
10. A. Kumar, W. A. Edelstein, and P. A. Bottomley, *Magn. Reson. Med.*, 2009, **61**, 1201–1209.
11. F. D. Doty, G. Entzminger, and C. D. Hauck Jr, *J. Magn. Reson.*, 1999, **140**, 17–31.
12. F. D. Doty, J. Kulkarni, C. Turner, G. Entzminger, and A. Bielecki, *J. Magn. Reson.*, 2006, **182**, 239–253.
13. W. W. Brey, A. S. Edison, R. E. Nast, J. R. Rocca, S. Saha, and R. S. Withers, *J. Magn. Reson.*, 2006, **179**, 290–293. http://www.bme.ufl.edu/documents/edison_research_article2_research.pdf.
14. T. Weiland, *Int. J. Numer. Model.*, 1996, **9**, 295–319. Also see: www.cst.de
15. D. I. Hoult, *Prog. NMR Spectrosc.*, 1978, **12**, 41–77.
16. D. M. Ginsberg and M. J. Melchner, *Rev. Sci. Instrum.*, 1970, **41**, 122–123.
17. A. P. Zens, NMR Probe Coil System, U.S. Pat. 4,398,149, 1983.
18. D. W. Alderman and D. M. Grant, *J. Magn. Reson.*, 1979, **36**, 447–451.
19. G. J. Kost, S. E. Anderson, G. B. Matson, and C. B. Conboy, *J. Magn. Reson.*, 1989, **82**, 238–252.
20. L. F. Fuks, F. S. C. Huang, C. M. Carter, W. A. Edelstein, and P. B. Roemer, *J. Magn. Reson.*, 1992, **100**, 229–242.
21. Y. Li, A. G. Webb, S. Saha, W. W. Brey, C. Zachariah, and A. S. Edison, *Magn. Reson. Chem.*, 2006, **44**, 255–262. http://www.bme.ufl.edu/documents/edison_research_article1_research.pdf
22. F. D. Doty, Low-Inductance Transverse Litz Foil Coils, U.S. Pat. 6,060,882, 2000.
23. F. D. Doty and G. Entzminger Jr, Center-fed Paralleled Saddle Coils for Multinuclear Double-Resonance NMR or MRI, U.S. Pat. 6,175,237, 2001.
24. H. J. Schneider and P. Dullenkopf, *Rev. Sci. Instrum.*, 1977, **48**, 68–73.
25. F. D. Doty, Parallel Single Turn Resonator for NMR, U.S. Pat. 4,641,098, 1987.
26. F. D. Doty, W. Bass, Q. Yang, G. Entzminger, J. H. Wang, G. N. Doty, L. L. Holte, and M. B. Smith, *Presented at 10th ISMRM*, Honolulu, 2002. http://www.dotynmr.com/PDF/KNE_SML.pdf.
27. C. E. Hayes, W. A. Edelstein, J. F. Schenck, O. M. Mueller, and M. Eash, *J. Magn. Reson.*, 1985, **63**, 622–628.
28. W. Edelstein, *RF Systems and coils for MRI & MRS*, The Encyclopedia of Nuclear Magnetic Resonance, eds. D.M. Grant and R.K. Harris, John Wiley & Sons, 1996, Vol. 6, pp 3950–3954.
29. C. E. Hayes, *Birdcage and other high homogeneity RF coils for whole body magnetic resonance*, The Encyclopedia of Nuclear Magnetic Resonance, eds. D.M. Grant and R.K. Harris, John Wiley & Sons, 1996, Vol. 2, pp 968–974.
30. J. Tropp, *J. Magn. Reson.*, 1989, **82**, 51–62.
31. J. Tropp, *J. Magn. Reson.*, 1997, **126**, 9–17.
32. J. Tropp, *Concepts Magn. Reson.*, 2002, **15**, 177–188.
33. M. C. Leifer, *J. Magn. Reson.*, 1997, **124**, 51–60.
34. J. Tropp, *J. Magn. Reson.*, 1991, **95**, 235–243.
35. (a) S. Crozier, K. Luescher, L. K. Forbes, and D. M. Doddrell, *J. Magn. Reson. Ser. B.*, 1995, **109**, 1–11; (b) S. Crozier and D. M. Doddrell, *RF Resonator for NMR*, U. S. Pat. 5,642,048, 1997.
36. T. de Swiet, W. H. Wong, M. Romo, J. Finnigan, and S. Burns, NMR Resonators Optimized for High Q Factor, U.S. Pat. 6,667,674, 2003.
37. W. H. Wong and S. Sukumar, In *Presented at 8th ISMRM. Poster 1399*, Denver, 2000.
38. J. Dazai, N. A. Bock, B. J. Nieman, L. M. Davidson, R. M. Henkelman, and X. J. Chen, *Magn. Reson. Med.*, 2004, **52**, 709–715.
39. C. M. Collins, W. Liu, J. Wang, R. Gruetter, J. T. Vaughan, K. Ugurbil, and M. B. Smith, *J. Magn. Reson. Imaging*, 2004, **19**, 650–656.
40. G. Bogdanov, G. Kueppers, J. A. King, and C. F. Ferris, In *Presented at the 9th ISMRM. Poster 1093*, Glasgow, 2001.

41. G. Bogdanov and R. Ludwig, *Magn. Reosn. Med.*, 2002, **47**, 579–503.

42. F. D. Doty, G. Entzminger, Z. Rafique, L. Holte, and T. Welsh, In *Presented at the ENC. Asilomar*, 2002, http://www.dotynmr.com/PDF/RFLC_.pdf.

43. F. D. Doty, N. Laws, L. Holte, J. P. Staab, J. Zempel, and J. R. Garbow, In *Presented at the 11th ISMRM*, Toronto, 2003.

44. F. D. Doty, G. Entzminger, J. P. Staab, J. D. Gravel, and H. D. Plant, *Presented at the 44th ENC*, Savannah, April, 2003.

45. M. Alecci and P. Jazzard, *Magn. Reson. Med.*, 2002, **48**, 404–407.

46. Y. Z. Wadghiri, A. Schneider, E. N. Gray, O. Aristizabal, D. H. Turnbull, and D. E. Gutstein, *Presentation # 18, at the 14th ISMRM*, Seattle, 2006.

Chapter 22
Millipede Coils

Ernest W. H. Wong

Agilent Technologies, Santa Clara, CA 95051, USA

22.1 INTRODUCTION

As animal models have profoundly transformed biomedical research in the last decade, small animal MRI has become an essential tool in preclinical studies. A small animal MRI system includes a high-field superconducting magnet with magnetic field strength as high as 16 T. The magnet bore size, however, is only 200–400 mm, which is much smaller than that of a human whole-body MRI magnet. A picture of a typical small animal MRI magnet is shown in Figure 22.1.

Inside a small animal MRI magnet bore, a high-duty-cycle gradient coil is required for high-resolution imaging. A typical small animal MRI gradient coil has a gradient strength of 100 G cm^{-1} and an inner diameter between 60 and 260 mm. The smaller the gradient coil inner diameter, the higher is the gradient strength.

A radio frequency (RF) resonator is positioned inside the gradient. It transmits RF power to an animal sitting inside the resonator and detects NMR signals from the animal. A typical mouse resonator requires an inner diameter of 30–40 mm. Therefore, the spacing between the inner and the outer diameter of an RF resonator can be as small as 10 mm. Limited space is a major challenge in small animal RF resonator design.

Also, a small animal has a much smaller physical size than a human. The voxel dimension in a typical small animal imaging experiment is only 0.15 mm^3. To detect NMR signals from such a small voxel, the RF resonator must be extremely sensitive. Circular polarization detection,[1] which increases the sensitivity by 40%, is necessary. Finally, a small animal may occupy up to 90% of the space inside an RF resonator for higher filling factor. As the result, a resonator with a uniform RF profile over the entire sample space is highly desirable.

Limited space, high sensitivity, and a large volume with RF homogeneity are the three major challenges in small animal RF resonator design. Small-sized birdcage resonators were initially constructed to meet these challenges.[2] However, they are difficult to build.[3] A small variation in chip capacitor values or their positioning can cause a large distortion in the circuit symmetry and poor RF homogeneity will result. Even when a perfect small-sized 16-leg birdcage resonator is built, the region of intrinsic RF homogeneity is only 75% of the sample space.

RF Coils for MRI
Edited by J. Thomas Vaughan and John R. Griffiths

ISBN: 978-0-470-77076-4

Figure 22.1. A typical 210 mm bore superconducting magnet for small animal MRI.

To improve small birdcage resonator design, chip capacitors must be eliminated and more legs should be added to the birdcage resonators. In this chapter, we introduce a new type of birdcage resonator design, which has hundreds of legs in a resonator and is optimized for small animal imaging applications. Since a 100-leg birdcage resonator does not look like a birdcage anymore, we decided to call it by a different name: the *millipede coil*.[4]

The basic circuit properties of a millipede coil are discussed in the next section. It is followed by a description of spiral millipede coils used in multifrequency probes. Then, a special type of low magnetic susceptibility (low-μ) millipede coil is introduced. These coils are particularly useful in the construction of microimaging probes and high-resolution spectroscopy probes.

22.2 MILLIPEDE COILS

It is assumed that the readers are familiar with the basic design principles of conventional RF coils and birdcage resonators. Readers who wish to get more information in these topics may find Refs 5–7 useful. In this section, we will emphasize the differences between a millipede coil and a regular birdcage resonator. Although the basic circuit principles of a millipede coil are similar to those of a birdcage resonator, their physical appearances are very different. Figure 22.2 shows a picture of a 16-leg birdcage resonator (a) and a millipede coil (b). The birdcage resonator has 16 legs (elements), while the millipede coil has 200 legs. The birdcage resonator has 32 chip capacitors soldered on the top and the bottom rings, whereas there are no chip capacitors attached to the millipede coil.

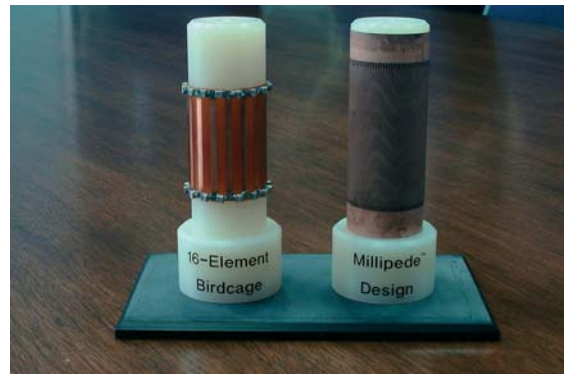

(a) (b)

Figure 22.2. A 16-leg birdcage resonator (a) and a 200-leg millipede coil (b).

In addition to the appearance, there are some major design differences between a 16-leg birdcage resonator and a 200-leg millipede coil.

22.2.1 Inductance

The resonance frequency of a resonator depends on its inductance and capacitance. The effective inductance of a birdcage resonator is the sum of the self-inductance of the elements and the mutual inductance between the elements.[8] In birdcage resonators, the gaps between the elements are large and only the mutual inductances from the nearest neighbors have to be considered. Also, the values of the mutual inductance are small compared to those of the self-inductance. The effective inductance is dominated by the self-inductances.

In millipede coils, on the other hand, the elements are very close to each other. As a result, the values of the mutual inductances are large and the mutual inductances from far away elements are not negligible. Thus mutual inductance becomes a

significant portion of the effective inductance. This means that both the overall physical dimension of the coil and the detailed arrangement of the elements are equally important in millipede coil design. This design approach is opposite to that of the transverse electromagnetic (TEM) resonator where the mutual inductances between elements are minimized.[9]

Readers who are familiar with the birdcage resonator design will be aware that a birdcage resonator with N elements will have $N/2$ pairwise degenerate modes. Similarly, a millipede coil with 200 elements will have 100 pairwise degenerate modes. That means a large number of resonance modes in a resonator. Fortunately, if we use the low-pass design,[5] only the most homogeneous mode, the $m = 1$ mode, has to be considered and it has the lowest resonance frequency. The higher order modes are spaced out to higher frequencies because of the large mutual inductances in a millipede coil.

22.2.2 Capacitance

The capacitors of a millipede coil are built into its structure. No additional chip capacitors are required. In Figure 22.3, the so-called interdigital capacitor design is shown. The capacitors are made out of hundreds of fine metal strips extending from the top and the bottom rings. They are interdigitally arranged and form a capacitance in between. The value of the capacitance depends on the gap between the adjacent strips and the length of their overlap. It also depends on the dielectric constant of the substrate on which the metal strips are formed. The desired resonance frequency can be achieved by adjusting the capacitance during the design cycle.

The interdigital capacitor is one type of highly distributed capacitor. Its electric fields are spread out all over the coil. As the result, the risk of electrical arcing is reduced. Furthermore, the widths and the gaps of the conductive strips are so small in comparison with the coil radius that the stray electric fields do not extend to the sample space. This results in a smaller frequency shift when a sample is loaded and a lower dielectric loss from the sample.

Another interesting point about the design shown in Figure 22.3 is that the conductive strips of the interdigital capacitor are the inductive elements of the coil as well. These space-efficient elements allow us to populate hundreds of them on a small cylindrical surface.

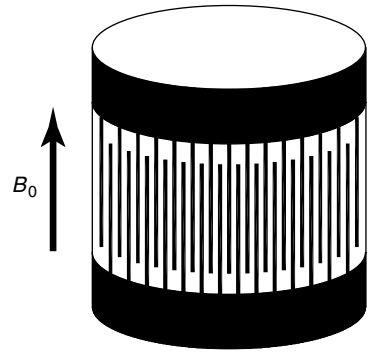

Figure 22.3. A millipede coil with interdigital capacitance design. The capacitors are built into its structure. The millipede coil axis is aligned with the direction of static magnetic field B_0.

22.2.3 Resistance and Quality Factor Q

The cross-sectional area of a single conductive strip is small, so its resistance is relatively large. Fortunately, in the millipede coil design there are hundreds of these elements arranged in parallel. The effective resistance is then reduced by an order of magnitude. It should be noticed that the reduction of the effective resistance depends on the current profile. The current profile of a millipede coil is a single sinusoidal function for the $m = 1$ mode, which is the same as that of a birdcage resonator.

Another possible source of coil resistance is the dielectric loss from the substrate. Low-loss dielectric substrates, such as Duroid 5880 (Rogers Corporation, Chandler, AZ, USA), are used to minimize this type of loss. A millipede coil usually has a quality factor (Q) in the order of 100's, which is high enough for most small animal applications.

22.2.4 Power Handling

A small animal imaging system is usually equipped with a kilowatt RF amplifier. Although a millipede coil is so efficient that it does not require a kilowatt of power to operate, preventing the RF coil from being burned out accidentally by the kilowatt amplifier is an important engineering task. Millipede coils are designed with hundreds of current paths in parallel so that the ohmic heating is spread out over the entire coil. This design maximizes the surface areas for heat radiation.

Also the capacitive elements are arranged in series with respect to the voltage drop. Even though the gaps between the conductive strips are small, the voltage drops across them are small too. This reduces the risk of arcing.

22.2.5 B_0 Homogeneity

The B_0 homogeneity is also referred to as the *magnetic field homogeneity*. Millipede coils have no chip capacitors in their construction. This removes a major source of magnetic susceptibility artifact. It is also worth pointing out that millipede coils have a high degree of cylindrical symmetry. This coil geometry is very favorable for high magnetic field homogeneity, as pointed out by Howard Hill.[7]

22.2.6 B_1 Homogeneity

B_1 homogeneity is also referred to as the *RF homogeneity*. With hundreds of legs, millipede coils exhibit an extraordinarily high RF homogeneity.[10] In Figure 22.4, an image of a mineral oil phantom obtained with a millipede coil is shown on the right and an image of a similar phantom obtained with a birdcage resonator is shown on the left for comparison. It is obvious that the RF shading on the edges of the image obtained with the birdcage resonator does not appear on the image obtained with the millipede coil. Even with a larger diameter phantom, the RF profile is uniform over the entire sample space in a millipede coil.

22.2.7 Filling Factor

Because of the excellent shading-free RF profile in millipede coils, samples can be placed very close to the inner diameter of the coils. This will increase the filling factor. As we know, the sensitivity is directly proportional to the filling factor.[11] Maximizing the filling factor will have a positive impact on the sensitivity.

Also, readers may notice that the millipede coil shown in Figure 22.3 looks like an assembly of two Faraday shields pointing to each other. When the coil is the Faraday shield itself, we do not need an additional electric field shield between the coil and the sample.

22.2.8 Sensitivity

In addition to their Q and filling factor, millipede coils can also be driven in circular polarization, or the so-called quadrature detection, to maximize the sensitivity. Similar to birdcage coils, millipede coils have two degenerate modes, which can be used for

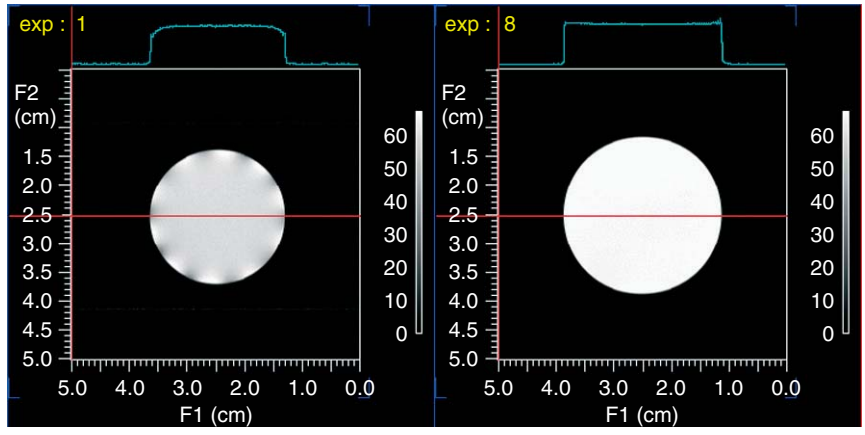

(a) (b)

Figure 22.4. Axial spin-echo images of mineral oil phantoms obtained with a millipede coil (b) and a birdcage resonator (a). The lines in the middle of the images indicate the cross-section positions, and the top of the images show the cross-section intensity profiles.

quadrature detection. The benefits of quadrature detection are to increase the sensitivity by a factor of $\sqrt{2}$ and to reduce the excitation power by a factor of 2.[1]

Increasing the number of elements in millipede coils can improve the coil efficiency, the B_1/I ratio, as illustrated by Joel Mispelter *et al*.[12] However, the B_1/I ratio is not a strong function of the number of elements. Also, increasing the number of elements will decrease the cross section of each element, so its benefit in sensitivity is not completely certain.

22.2.9 Tuning and Matching

Similar to birdcage resonators, millipede coils have narrow frequency tuning ranges. However, unlike birdcage resonators, millipede coils cannot be tuned by changing a single chip capacitor. To tune a millipede coil, a movable metal ring is placed over the coil such that the capacitance or the inductance of all elements can be changed simultaneously.[13] This tuning method also preserves the cylindrical symmetry of the coil.

Conventional matching methods used in birdcage resonators can be applied to millipede coils. Both capacitive coupling and inductive coupling are effective.

22.2.10 Manufacturability

Millipede coils are constructed with low-loss, flexible circuit board materials. The circuit pattern can be produced by standard etching methods. This manufacturing method removes the variations associated with chip capacitors. As the result, millipede coils can be easily reproduced. We have successfully built several batches of 20 identical millipede coils for multi-mouse coil array applications.[14] Within each of these coil arrays, millipede coils must be identical to a very tight specification. It would be a nightmare if we chose to use chip capacitors to construct these coil arrays.

22.2.11 Limitations

Millipede coils are subjected to dielectric resonance effects and the so-called field focusing effect at high magnetic fields with electrically conductive samples.[15] Fortunately, a typical mouse millipede coil has a diameter of only 30–40 mm. The dielectric resonance effect and the field focusing effect are not significant for proton signals up to 9.4 T (400 MHz).

Millipede coils are not suitable for double tuning. There are just too many elements and resonance modes in these coils. Nevertheless, it is possible to build multifrequency probes using millipede coils to take the advantage of their wonderful properties. In the next section, we shall discuss the methods of building multifrequency probes with several millipede coils.

22.3 SPIRAL MILLIPEDE COILS FOR MULTIFREQUENCY PROBES

Multituned birdcage resonators are often used in multifrequency imaging probes because of their excellent RF homogeneity. Many multituned birdcage resonator designs have been reported in the literature.[16,17] Double-tuned birdcage resonators use twice the number of lumped-element components to double-tune each leg such that two $m = 1$ modes result at the sample space simultaneously. Unfortunately, this approach is not practical for millipede coils, which have hundreds of legs.

There is, however, another approach for double tuning: the concentric coils approach. Two independent RF coils, one with a larger diameter than the other, are positioned concentrically to produce uniform RF field at the sample space simultaneously. This approach works well when the interactions between the two concentric coils are small. In the case of linearly polarized coils, the interaction can be minimized by carefully positioning two concentric coils orthogonally. However, millipede coils are circularly polarized coils, and both radial orthogonal directions are occupied by their two degenerate modes. It is therefore not possible to sufficiently reduce the interaction between two concentric millipede coils by carefully positioning them. A new way to arrange the concentric millipede coils orthogonally is needed, as described below.

22.3.1 The Spiral Millipede Coil

First, we have to introduce a new type of millipede coil: the "spiral millipede" coil. Spiral millipede coils

have helical legs shown in Figure 22.5. The conductive legs starting from the top conductive ring spiral down on a cylindrical surface toward the bottom conductive ring. The conductive legs starting from the bottom conductive ring spiral up on the same cylindrical surface toward the top conductive ring. Both sets of spiral conductive legs form an interdigital capacitor between the top and the bottom rings. The angle by which the conductive legs rotate between two rings will be hereinafter referred to as the "twist angle". The twist angle for a millipede coil of the straight kind, as shown in Figure 22.3, is zero. The twist angle of the spiral millipede coil shown in Figure 22.5 is 2π. The twist angle of a millipede coil of a spiral kind may be either positive or negative, depending on the direction of the spiraling of the legs.

Spiral millipede coils have similar electrical properties as those of the straight millipede coils. The only difference is the directions of the RF fields that they produce. Since the RF currents in spiral millipede coils flow along the conductive legs, which are spiraling along the coil, the RF fields generated by the RF currents are also spiraling along the coil. In other words, the RF fields of a spiral millipede coil have their directions rotate around the central axis along the coil. This RF profile is substantially different from that of a millipede coil of the straight kind, whose RF fields remain in one direction along the coil.

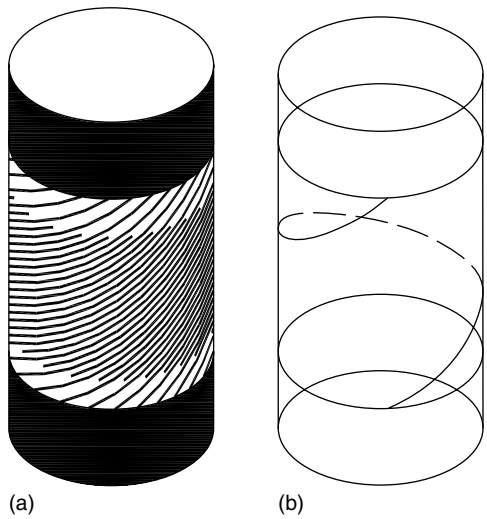

Figure 22.5. A spiral millipede coil with hundreds of elements, twisted by an angle of 2π, is shown in (a). A single element showing the angle of 2π twists is illustrated in (b) for clarity.

22.3.2 Inductive Transparency between a Straight and a Spiral Millipede Coil

These spiral millipede coils provide excellent options. When a spiral millipede coil, such as that shown in Figure 22.5, is placed concentrically over a straight millipede coil, their inductive interaction disappears; i.e., their mutual inductance is zero or they are "inductively transparent". The only restriction is that the RF window lengths of the two coils, i.e., the distances between the top and the bottom rings, have to be identical and have to be aligned. This phenomenon can be explained in the following way.

The reason for two coils to interact with each other is that the magnetic field generated from the first coil will induce a nonzero emf in the second coil. If the total induced emf is reduced to zero, the two coils will be inductively transparent. A spiral millipede coil generates rotating RF fields along the coil. A concentric straight millipede coil with the same RF window length will capture the entire rotated RF fields. Since the twist angle of the spiral millipede coil is 2π, the sum of the entire rotated RF fields will be zero and no net emf will be induced in the straight millipede coil. The result is that a straight and a 2π spiral millipede coil are inductively transparent.

To extend the concept, if the twist angle of a spiral millipede coil is 4π, the sum of its entire rotated RF fields captured by a straight millipede coil is also zero. So, properly placed straight and 4π spiral millipede coils are also inductively transparent. In fact, any spiral millipede coil with a twist angle equal to an integral multiple of 2π will be inductively transparent to a straight millipede coil. This includes negative integers, in which case the spiral millipede coil is rotating in the opposite direction.

One immediately realizes that a 2π spiral millipede coil is orthogonal not only to the straight millipede coil but to a -2π spiral millipede coil as well. In fact, any two spiral coils with twist angles differing by an integral multiple of 2π are orthogonal to each other. This phenomenon introduces a new orthogonal dimension so that theoretically the number of concentric orthogonal coils that can be put together will no longer be 2 but infinite.[18]

22.3.3 Multifrequency Probes

To build a multifrequency millipede probe, one can place a 2π spiral millipede coil concentrically over a straight millipede coil and place a -2π spiral millipede coil outside the assembly, as shown in Figure 22.6. The $m = 1$ mode of each coil can be tuned to the same frequency for a coil array or to different frequencies for a multifrequency probe.

In this design, the circular polarization detection capability of each coil is preserved. Since all coils are independent of each other, they can be designed separately. When they are placed together, their original frequencies are maintained. This property makes this design approach very attractive. To build a multifrequency probe, we only have to design several singly tuned coils and place them together.

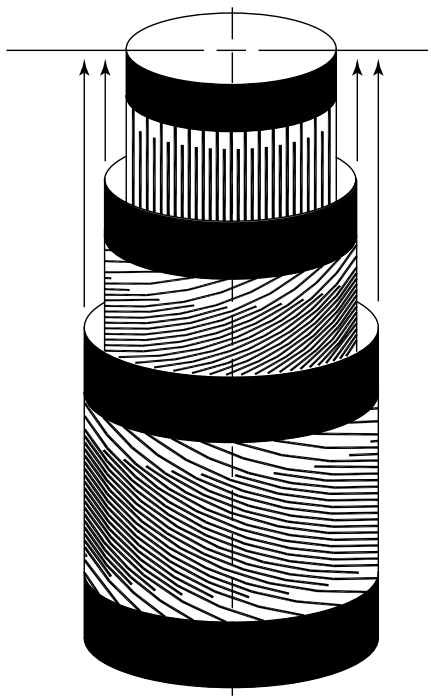

Figure 22.6. A triple-tuned millipede coil assembly is shown. It contains an inner straight millipede coil and two outer spiral millipede coils with twisted angles of 2π and -2π. These three millipede coils are inductively transparent to each other. The design also preserves the quadrature detection capability of each coil.

The limitation of this design is that only the innermost coil has the optimum filling factor. The outside coils have lower filling factor and Q. So it is not recommended to have more than three layers of coils in practice. Although the coils are inductively transparent, they can have capacitive interactions. To reduce the capacitive interactions, the coils should be separated by an adequate spacing. This further reduces the filling factor of the outer coils. So the most sensitive channel has to be the innermost coil.

Although this spiral coil concept was developed in millipede coils,[19] it can be applied to different volume coil structures such as saddle coils and birdcage resonators.

22.4 LOW-MAGNETIC-SUSCEPTIBILITY MILLIPEDE COILS

Microimaging of tiny objects requires even smaller coils to maximize the filling factor. Small coils are so close to samples that the effect of coil magnetic susceptibility is always a major concern. As pointed out by Howard Hill,[7] there are two important methods to minimize coil magnetic susceptibility artifacts: (i) the geometry and symmetry and (ii) a careful choice of materials. Millipede coils have high cylindrical symmetry. So all we have to do is to design a millipede coil with low-μ materials for microimaging.

In Figure 22.7, a low-μ millipede coil assembly is shown. This low-μ millipede coil is made out of two parts: the top half and the bottom half. Both halves have many conductive strips extending out from a conductive ring and they are machined from low-μ

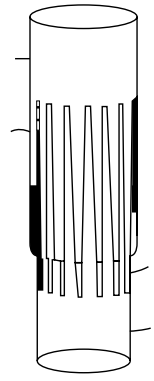

Figure 22.7. A low-μ millipede coil design.

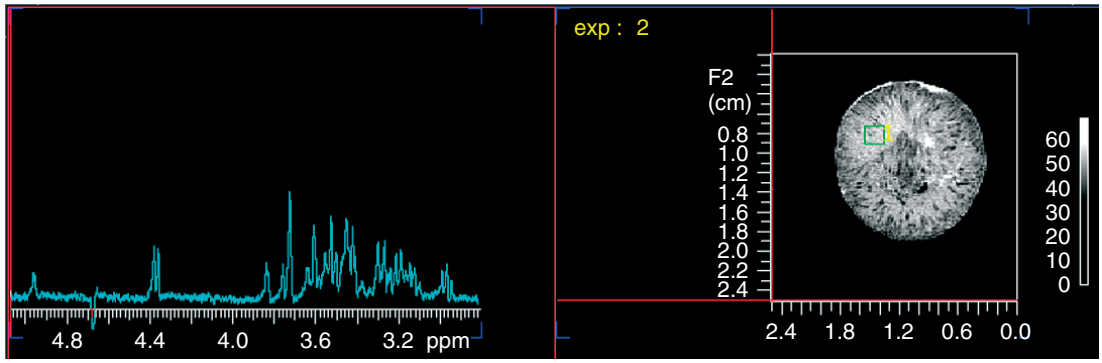

(a) (b)

Figure 22.8. The image in (b) is a cross section taken from a grape. A 1 mm^3 region of interest was specified for the localized spectroscopy experiment. The water-suppressed high-resolution spectrum is shown in (a). The bandwidth of the (Gaussian) water suppression pulse was set to 40 Hz so that the anomeric proton signals can be resolved. Only the linear gradient was used for shimming.

materials. The top half has a larger diameter and it is inserted into the bottom half, with an insulated tube in between. The conductive strips from both halves form the capacitance of the coil and the resonance frequency depends on the amount of the overlap of the conductive strips. The circuit principles of these low-μ millipede coils are identical to those of the regular millipede coils, so the advantages of the RF homogeneity and sensitivity follow.

22.4.1 Low-μ Millipede Coils for Microimaging Probes

A small-diameter microimaging probe with a low-μ millipede coil was evaluated.[20] Excellent magnetic field (B_0) and RF field (B_1) homogeneity were achieved. In Figure 22.8, the result of a demanding localized spectroscopy experiment using the low-μ millipede coil is shown.

22.4.2 Low-μ Millipede Coils for High-resolution Liquid Probes

The use of a low-μ millipede coil in a high-resolution liquid probe was first reported at ENC 2003.[21] A 500 MHz, 5 mm triple-resonance ($^1H/^{13}C/^{15}N$) pulse field gradient (PFG), high-resolution probe, such as the one shown in Figure 22.9, was demonstrated. In

Figure 22.9. A triple-resonance ($^1H/^{13}C/^{15}N$) PFG high-resolution liquid probe with a low-μ millipede coil.

this triple-resonance probe, a straight low-μ millipede coil tuned to the ^1H frequency was located in the middle, and a spiral saddle coil with a 2π twist angle

was placed outside the millipede coil. The spiral saddle coil was multiply tuned to the ^{13}C and ^{15}N frequencies. A PFG was also added to the probe to make it a fully loaded high-resolution spectroscopy probe. Multidimensional spectroscopy experiments were performed with this triple-resonance probe and excellent results were achieved.

22.5 ADDITIONAL INFORMATION

In this chapter, we have described the millipede coil design with interdigital capacitors in detail. There are other millipede coil designs as well.[4] Each of them has its own advantages and disadvantages. But all of them show excellent RF homogeneity as a result of their large numbers of legs.

Although millipede coils can be actively decoupled,[22] using such a coil as a transmit-only coil does not offer much advantage over a birdcage resonator. For a transmit-only coil, only the RF homogeneity at the very center is important. Also, the sensitivity performance is solely dependent on the receive-only coil.

Low-μ millipede coils have shown promise in microimaging and high-resolution probe applications. A low-temperature version of these low-μ millipede coils has been proposed.[23] Even a superconducting millipede coil, which is made out of a high-temperature superconductor, has been studied.[24]

RELATED ARTICLES IN THE ENCYCLOPEDIA OF MAGNETIC RESONANCE

Birdcage Resonators: Highly Homogeneous Radiofrequency Coils for Magnetic Resonance

Multifrequency Coils for Whole Body Studies

Probe Design and Construction

Probes for High Resolution

Surface and Other Local Coils for In Vivo Studies

REFERENCES

1. D. I. Hoult, C. N. Chen, and V. J. Sank, *Magn. Reson. Med.*, 1984, **1**, 339.
2. C. E. Hayes, U.S. Pat. 4 694 255 (1987).
3. S. Crozier, K. Luescher, L. K. Forbes, and D. M. Doddrell, *J. Magn. Reson.*, 1995, **B109**, 1.
4. W. H. Wong, U.S. Pat. 6 285 189 (2001).
5. C. E. Hayes, Birdcage resonators: highly homogeneous radiofrequency coils for magnetic resonance, in *Encyclopedia of Nuclear Magnetic Resonance*, eds D. M. Grant and R. K. Harris, John Wiley & Sons, Published Online: 15 Mar, 2007. DOI: 10.1002/9780470034590.emrstm0033.
6. F. D. Doty, Probe design and construction, in in *Encyclopedia of Nuclear Magnetic Resonance*, eds D. M. Grant and R. K. Harris, John Wiley & Sons, Published Online: 15 Mar, 2007. DOI: 10.1002/9780470034590.emrstm0414.
7. H. D. W. Hill, Probes for high resolution, in *Encyclopedia of Nuclear Magnetic Resonance*, eds D. M. Grant and R. K. Harris, John Wiley & Sons, Published Online: 15 Mar, 2007. DOI: 10.1002/9780470034590.emrstm0415.
8. M. C. Leifer, *J. Magn. Reson.*, 1997, **124**, 51–60.
9. J. T. Vaughan, U.S. Pat. 5 557 247 (1996).
10. W. H. Wong and S. Sukumar, In 8th ISMRM, Denver (CO), 2000.
11. A. Abragam, *Principles of Nuclear Magnetism*, Oxford University Press: New York, 1961, p. 74.
12. J. Mispelter, M. Lupu, and A. Briquet, *NMR Probeheads for Biophysical and Biomedical Experiments*, Imperial College Press: London, 2006, p. 373.
13. S. C. Hartman and W. H. Wong, U.S. Pat. 6 236 206 (2001).
14. N. A. Bock, B. J. Nieman, J. B. Bishop, and R. M. Henkelman, *Magn. Reson. Med.*, 2005, **54**, 1311.
15. D. I. Hoult, *J. Magn. Reson. Imaging*, 2000, **12**, 46.
16. A. R. Rath, *J. Magn. Reson.*, 1990, **86**, 488.
17. J. Murphy-Boesch, Multifrequency coils for whole body studies, in *Encyclopedia of Nuclear Magnetic Resonance*, eds D. M. Grant and R. K. Harris, John Wiley & Sons, Published Online: 15 Mar, 2007. DOI: 10.1002/9780470034590.emrstm0329.
18. W. H. Wong, S. Unno, and W. Anderson, U.S. Pat. 6 420 871 (2002).
19. W. H. Wong and S. Sukumar, In 10th ISMRM, Honolulu (HI), 2002.
20. W. H. Wong, J. Finnigan, and S. Sukumar, In 41st Exp. NMR Conf., Pacific Grove, CA, 2000.

21. W. H. Wong, W. Anderson, J. Finnigan, J. Moore, and N. Murali, In 44th Exp. NMR Conf., Savannah, GA, 2003.

22. W. H. Wong and A. R. Rath, U.S. Pat. 6 552 544 (2003).

23. W. A. Anderson, W. H. Wong, and J. Finnigan, U.S. Pat. 6 876 200 (2005).

24. W. H. Wong and M. A. Romo, U.S. Pat. 6 377 047 (2002).

PART E
Coil Interface Circuits

Chapter 23
Receiver Design for MR

David I. Houlte

Institute for Biodiagnostics, National Research Council Canada, Winnipeg, Manitoba, MB R3B 1Y6, Canada

23.1 INTRODUCTION

The precession of the bulk nuclear magnetic moment immediately following a radiofrequency (RF) pulse is most easily detected by the transient RF voltage it induces in a surrounding receiving coil. The factors governing the strength of that signal and of its accompanying random noise are the subject of many reviews in the Encyclopedia of Magnetic Resonance, and papers elsewhere. However, far less is published on how faithfully to record the signal and its accompanying noise, in a computer or other electronic device, with negligible distortion, minimal loss of signal-to-noise (SNR), and no spurious interference. This is not a trivial task, and the difficulties spring from three primary sources: (i) The massive disparity in the RF pulse and signal amplitudes leading to amplifier overload, recovery, and safety problems; (ii) The high frequency of the NMR signal (up to 1 GHz); and (iii) The signal's large potential dynamic range (up to 10^6)—from less than the noise (typically a fraction of a microvolt) to a fraction of a volt depending on the experiment in question. A visualization of some of these problems is shown in Figure 23.1.

Digital recording is, of course, the function of an analog-to-digital converter (ADC), but at the time of writing (2011), no ADC can cope with the above specifications, as high sampling frequencies are generally accompanied by poor resolution. Increasing the data sampling frequency, via Nyquist's sampling theorem,[1] admits a greater bandwidth Δf and this, in turn, passes more noise and therefore diminishes signal dynamic range and the required ADC resolution. However, this positive factor is usually no match for the rapid loss of ADC SNR and resolution (actual number of bits, or more likely *effective* number of bits, taking all sources of error into account) that accompany increased sampling frequency in the RF range. Thus, if the noise has a flat frequency spectrum, there is a broad optimum in the data sampling rate, which, from a cursory survey of the 20 011 ADC literature,[2] appears currently to be in the region of 200 MHz with a 16 bit converter. The solution to the problem of recording higher frequencies is to reduce electronically the NMR signal's frequencies, in the past even to the point of creating audio frequencies by subtraction of the transmitter

RF Coils for MRI
Edited by J. Thomas Vaughan and John R. Griffiths

ISBN: 978-0-470-77076-4

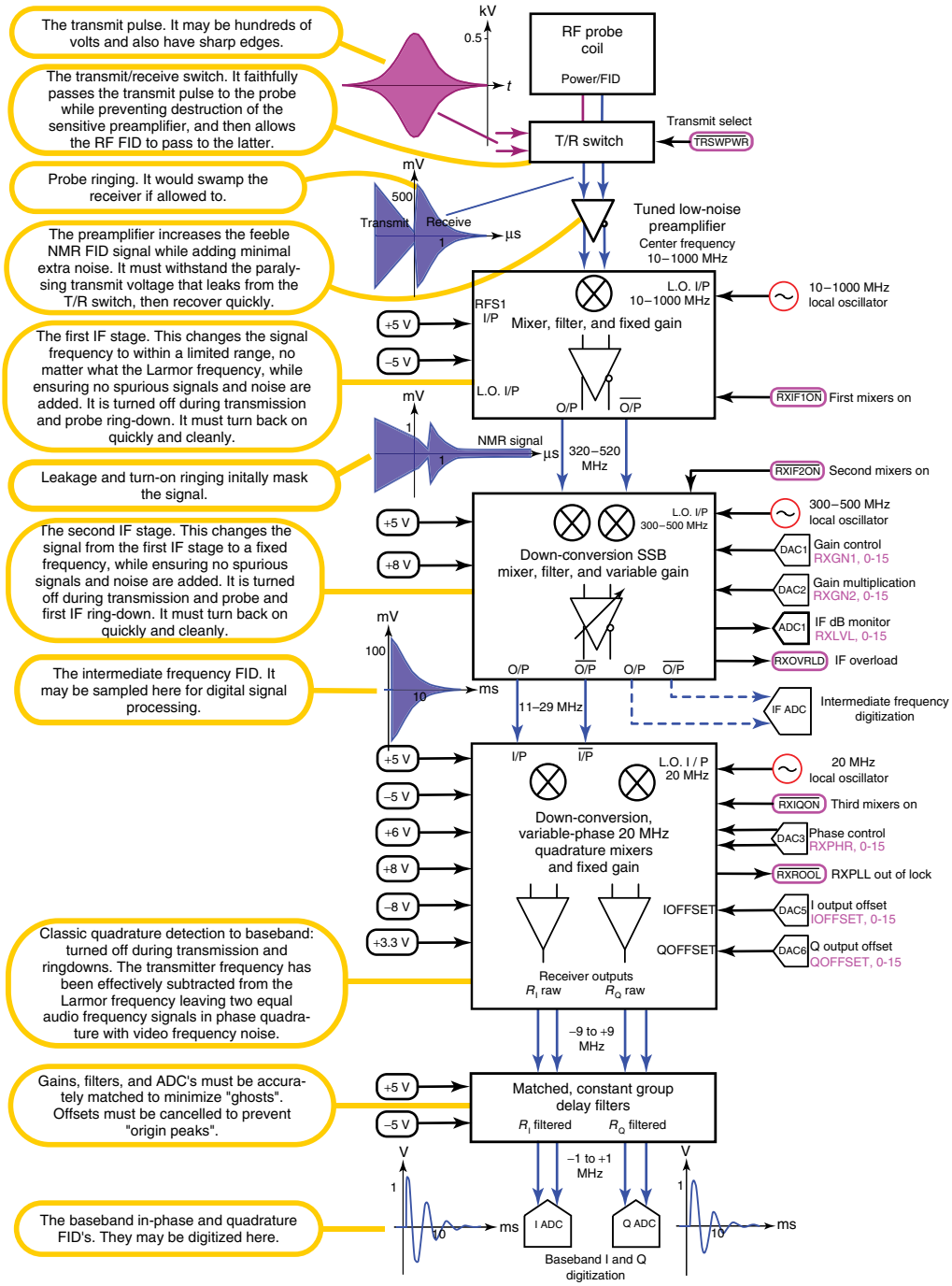

Figure 23.1. A commented flow diagram of a modern, multinuclear NMR heterodyne receiver. A digitized signal may be extracted at an intermediate frequency, thereby dispensing with the final quadrature detection.

frequency—so-called baseband detection. Thus the primary purpose of this chapter is to describe in some detail the factors affecting the design of the analog electronic device—the NMR receiver—that performs this task while retaining the high fidelity mentioned above. We shall also briefly consider some of the factors associated with digital signal processing.

For convenience, we shall split the receiver analysis into blocks in a manner that is traditional, and one design among the many possibilities is shown in Figure 23.1. However, it should immediately be realized that electronic components are no respecter of such partitioning and that similar defects, compromises and analytical techniques may be applicable throughout. Further, in the final analysis, the receiver must be viewed as an entity, for the design of one part is never entirely independent of the others. With these points in mind, we begin by looking in detail at the first active device the signal and noise encounter having left the receiving coil—the preamplifier. We then turn more briefly to other sections of the receiver, as many of their issues will already have been discussed.

23.2 PREAMPLIFICATION

Key Specifications

Noise figure; optimum source impedance; gain; recovery time; stability; bandwidth; input impedance; group delay; magnetic field immunity and compatibility; distortion; power.

23.2.1 Noise Figure

Any electronic manipulation (amplification, frequency-changing, etc.) adds unavoidable noise (random voltages) to the signals emanating from the probe receiving coil. Noise should not be confused with electromagnetic interference (EMI), which can also easily be added to the signal but which originates from outside the NMR system and is usually manmade. Like any other electrical signal, noise can be spectrally analyzed. Consequently, it is sometimes assigned a frequency dependence ($1/f$, etc.) or a color (pink, blue, etc. in analogy to the visible spectrum) on the basis of the slope of its spectrum.[3,4] However, in the vast majority of RF applications, noise is "white" over the frequency range of interest; in other words, its power spectrum is flat and, unless otherwise stated, whiteness is assumed here and in the literature. When such noise is from a passive object (e.g., an NMR probe) it is commonly known as *Johnson noise*.[5,6] Johnson noise usually originates from the interaction of carrier electrons with the randomly vibrating atoms in a conductor (electron–phonon interaction), but also, in a biological MR or MRI experiment, from the Brownian motion of the electrolytes in the sample. As random motion is a measure of temperature, it is not surprising that there is a linkage between noise, temperature, and the electronic element—resistance—that generates heat when current flows. Indeed, Johnson noise is sometimes known as *thermal noise*. This linkage is formally expressed in the fluctuation-dissipation theorem[7] and the ensuing Nyquist formula[6]

$$N_S = \sqrt{4\kappa T_S R_S \Delta f} \equiv \beta\sqrt{R_S} \qquad (23.1)$$

where N_S is root mean square noise voltage, κ is the Boltzmann constant, T_S is the source temperature in kelvin, R_S is its resistance in ohms, and Δf is the bandwidth in hertz of the measuring device. The constant β is introduced for brevity in later use. Thus in a bandwidth of 1 kHz, a 50 Ω resistance at "room temperature" (290 K is the usual definition in electronics theory—the species *ingeniarius electronicus* originated in northern climes prior to the advent of central heating) generates roughly 28 nV of noise, and this is the noise we should expect over a 1 kHz bandwidth about the Larmor frequency ω_0 from any NMR probe that has been matched to 50 Ω. This is a remarkably small voltage, and it is a testament to the quality of modern transistors that such a voltage can be amplified with the addition of very little extra noise.

The majority of preamplifiers used in NMR (though not necessarily in MRI with receive-only coils—see Section 23.2.9) are designed for compatibility with standard 50 Ω coaxial cable: it is then tacitly assumed that the signal source has an impedance Z_s of 50 Ω resistive—for example, a probe tuned and matched to 50 Ω—and we shall ultimately assume likewise. (The other standard, used mostly in communications, is 75 Ω.) However, it should not be assumed that a "50 Ω preamplifier" has input and output impedances of 50 Ω—quite the contrary is often true, and indeed there are advantages to having an input impedance radically different from 50 Ω, as will be shown below. To understand this assertion, an examination of the role of the preamplifier in signal reception must

begin with a reputable electrical model of its first transistor. Various models are available, but that of Figure 23.2(a) is simple yet reasonably accurate at radio frequencies.[8] Its main defect is that it ignores C_{bc}, the base-collector or gate-drain capacitance. (The model can also be used with field effect transistors.)

In the figure, a signal source of impedance $Z_S = R_s + jX_s (j = \sqrt{-1})$ is connected to the base of a bipolar transistor operating in common-emitter mode. The signal itself is a voltage V_S, while the Johnson noise N_S associated with the real part R_S of the source impedance is given by equation (23.1) above. The reactive part of the impedance is X_s. Of key

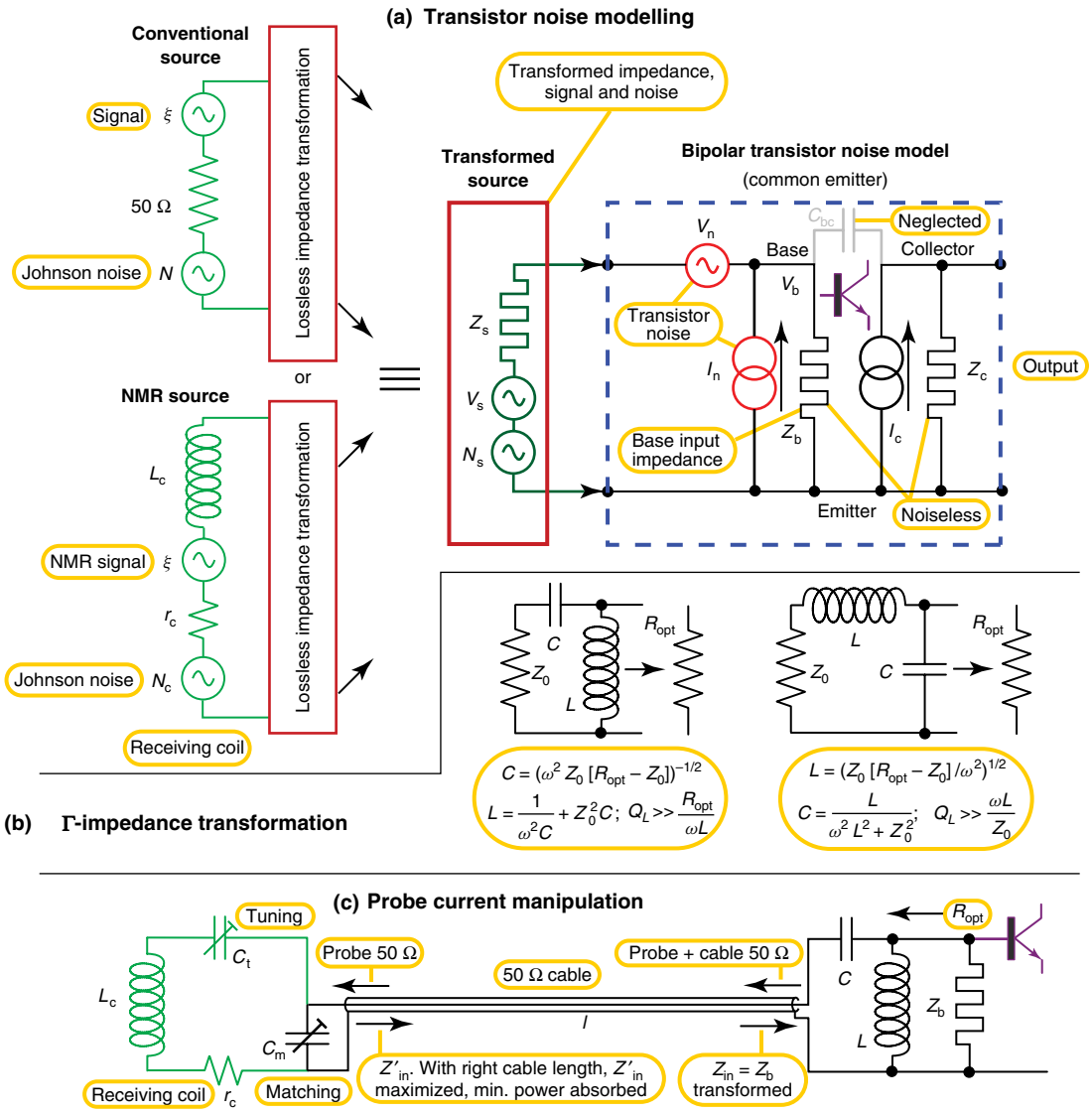

Figure 23.2. Modeling transistor noise, noise matching, and current blocking. In (a), a common equivalent transistor noise circuit is shown, and it is used in the text to prove that the source impedance must be transformed to a value V_n/I_n to optimize the noise performance. In (b), common lumped element Γ-transformation networks are shown while in (c), a model for minimization of probe current during signal reception is given.

importance in the model is the relationship of R_S not only with noise N_S but also with the signal voltage V_S. It is assumed, as shown, that the source actually includes a lossless impedance transformation of some sort, and in such a transformation, by the principle of conservation of energy, V_S^2/R_S must be a constant. For example, with a conventional 50 Ω source of EMF ξ, $V_S^2/R_S = \xi^2/50$; with an NMR receiving coil with induced free induction decay (FID) voltage ξ and effective coil resistance r_c, $V_S^2/R_S = \xi^2/r_c$. Thus, for calculative purposes, we let

$$V_S = \xi_0\sqrt{R_S} \tag{23.2}$$

where ξ_0 is a normalized EMF. Note that the source SNR V_S/N_S remains constant under such a lossless impedance transformation, again by virtue of the principle of conservation of energy. In the following calculations, resistance R_S will be the primary variable; the reactive portion X_S of the source impedance varies in a manner that is dependent on the details of the transformation, but at any particular frequency it can always be forced to a particular value, notably zero, by the addition of capacitance or inductance. (Note that capacitors and inductors generate noise only to the extent that they have resistance.)

The transistor model itself (Figure 23.2a) has a base input impedance Z_b, which for the purposes of modeling is considered noiseless. The noise in bandwidth Δf is represented instead by a noise voltage source V_n and a constant current noise source I_n, and in practice, these sources may be lightly correlated. Then, across base impedance Z_b is a voltage V_b due to the signal V_s, its associated noise N_s, and the transistor noise. The output of the transistor is represented by a constant current source $I_c = g_m V_b$ in parallel with a noiseless collector impedance Z_c, and the amplified signal is passed on from this point to the collector load, a second stage of preamplification (*q.v.*), and thence the receiver chain. Here, g_m is the transconductance. We shall not consider I_c further at the moment, relying instead on the proportionate base voltage V_b as a measure of signal and noise. Essentially, all quantities are being referenced to the device input, which is a common ploy throughout electronics.

Having set the scene, our goal now is to maximize the SNR of the collector current (base voltage) by optimization of source resistance R_s. We begin by considering the signal ξ_b that is passed to the transistor base. By potential division, it is

$$\xi_b = V_S\frac{Z_b}{Z_b + Z_S} = \xi_0\sqrt{R_S}\frac{Z_b}{Z_b + R_S + jX_S} \tag{23.3}$$

Likewise, the source noise N_s suffers the same change. Now, consider the noise at the transistor base. This is more difficult to calculate. Consider first the voltage N_{b1} created by the transistor constant current noise source applied to Z_S and Z_b in parallel. It is

$$N_{b1} = I_n\frac{Z_b(R_S + jX_S)}{Z_b + R_S + jX_S} \tag{23.4}$$

Now, consider the voltage N_{b2} created by the transistor voltage noise V_n. It is

$$N_{b2} = V_n\frac{Z_b}{Z_b + R_S + jX_S} \tag{23.5}$$

If N_{b1} and N_{b2} were totally correlated, they would add linearly; if they were uncorrelated, they would add quadratically. Thus for partial correlation, we may write for their combined voltages

$$N_{b12}^2 = |N_{b1}|^2 + |N_{b2}|^2 + 2\gamma\,|N_{b1}|\,|N_{b2}| \tag{23.6}$$

where γ is a correlation factor, ranging from 0 (no correlation) to 1 (full correlation), which is dependent both on the noise correlation and any phase difference. Finally, the source noise is uncorrelated with the transistor noise and therefore adds quadratically to the noise in equation (23.6) under all circumstances. Summing, the mean square noise at the base is

$$N_b^2 = \left(\frac{Z_b Z_b^*}{|Z_b + R_S + iX_S|^2}\right)(\beta^2 R_S + I_n^2\left(R_S^2 + X_S^2\right) + V_n^2 + 2\gamma V_n I_n\sqrt{R_S^2 + X_S^2}\,\Big) \tag{23.7}$$

Hence, from equation (23.3), the square of the SNR Ψ at the transistor base is given by

$$\Psi^2 = \left(\frac{S_b}{N_b}\right)^2 = \frac{\xi_0^2 R_S}{\beta^2 R_S + I_n^2(R_S^2 + X_S^2) + V_n^2 + 2\gamma V_n I_n\sqrt{R_S^2 + X_S^2}} \tag{23.8}$$

Importantly, note that the base input impedance of the transistor has dropped out of the equation. When there is no correlation ($\gamma = 0$), Ψ^2 is easily maximized by differentiation with respect to R_S and X_S, and we obtain the well-known result for so-called optimal noise

matching: $R_S = R_{opt} = V_n/I_n$ and $X_S = 0$. Equation (23.8) for the SNR then reduces to

$$\Psi_{opt}^2 = \left(\frac{S_b}{N_b}\right)^2 = \frac{\xi_0^2 R_{opt}}{\beta^2 R_{opt} + 2(1+\gamma)V_n^2} \tag{23.9a}$$

or equivalently and succinctly

$$\Psi_{opt}^2 = \left(\frac{S_b}{N_b}\right)^2 = \frac{V_{opt}^2}{N_{opt}^2 + N_A^2} \tag{23.9b}$$

where V_{opt} and N_{opt} are the signal and noise, respectively, from the optimized source, and N_A is the effective noise from the transistor. For a perfect transistor, $V_n = N_A = 0$, and so $\Psi_{opt} = \Psi_{max} = \xi_0/\beta = V_{opt}/N_{opt}$. It may be shown that correlation has little effect on the optimal values but, as shown in the equation, it reduces the SNR. It is strongly emphasized that the optimal source resistance R_S has little or no connection with the input impedance Z_b; it is generally considerably less.

For unit bandwidth at a specified frequency with a source temperature $T_S = T_0 = 290$ K (in practice, room temperature), the ratio

$$F'_A = \frac{\Psi_{max}^2}{\Psi_{opt}^2} = 1 + \frac{2(1+\gamma)V_n^2}{4\kappa T_0 R_{opt}} \equiv 1 + \frac{N_A^2}{N_{opt}^2} \tag{23.10}$$

is known as the *spot noise factor*. Its value in decibels $F = (10\log_{10} F')$ is known as the *spot noise figure*. A good low-noise RF transistor has a noise figure less than 1 dB *once the source impedance has been transformed to optimal resistance* R_{opt}; in other words, it then degrades the available SNR by less than 12%. Occasionally, the noise figure is expressed as an effective device noise temperature

$$T_A = \frac{2(1+\gamma)V_n^2}{4\kappa R_{opt}} \tag{23.11}$$

The square of the noise factor is then $1 + T_A/T_0$, and the total noise is as if from a source of resistance R_{opt} at temperature $T_A + T_0$. A device having a noise figure of 1 dB has an effective noise temperature of 75 K. (Note that noise factor can also be defined as the square root of F'. However, in recent years, this usage has become less common. It is also common to see SNR defined as a power ratio—the square of Ψ. However, we remain here with the conventional NMR definition.)

23.2.2 Device Selection and Source Transformation

It was assumed in the above analysis that a lossless impedance transformation changed the source resistance R_S to the optimal value R_{opt}. A lossless transformation is, of course, a fiction, but it is emphasized that one must strive for a superb transformation if an excellent noise figure is to be obtained. For low-noise bipolar transistors, R_{opt} is generally in the range 50–300 Ω, while for metal-oxide-semiconductor field-effect transistor (MOSFETs) of various types, R_{opt} is considerably larger, being typically in the range 400 Ω to several kilohms. As a rough rule, the higher the frequency, the smaller the value of R_{opt}. If the source resistance is 50 Ω, then by selecting a bipolar transistor (or two in parallel) for which $R_{opt} = 50$ Ω, no transformation is needed and a broadband preamplifier may be constructed. However, the author's experience is that broadband designs rarely give excellent noise figures, perhaps because the noise contribution from the second stage of amplification (see below) can rarely be optimized.

The selection of a suitable transistor depends on a number of factors. Below roughly 20 MHz, R_{opt} for a MOSFET is so large that to obtain an excellent impedance transformation from 50 Ω, the inductor that must be part of the transformation network may have to be excessively large physically so to have an adequate quality factor. Its large reactance will also limit the bandwidth rather severely. On the other hand, at such low frequencies, many bipolar transistors are beginning to exhibit *flicker noise* ($1/f$ noise, pink noise[4]) that degrades the noise figure. Flicker noise is a low-frequency phenomenon probably associated with carrier generation and recombination[9] during direct current flow. Turning to the high end of the NMR frequency spectrum, MOSFETs may also be proscribed if the preamplifier is to sit in a high magnetic field. The definition of "high" depends on the construction technique of the MOSFET and the semiconductor employed. As a general rule, silicon MOSFETs are safe in most common NMR fields, but devices with high electron mobility (HEMFETs, GaAs, GaN, etc.) may exhibit considerable variation of gain, noise figure, and optimal source impedance with orientation in the field. Little is published on this issue,[10] and it is therefore important to check performance in the field before settling on a particular transistor. At Larmor frequencies of hundreds of

megahertz and in fields of, say, 7 T, the author has found that SHF (super high frequency, 3–30 GHz) SiGe bipolar transistors (e.g., BFP 740) have excellent noise figures (~ 0.5 dB) with negligible field dependence. However, bipolar transistors have slightly inferior distortion ($q.v.$) characteristics in comparison with MOSFETs.

Given that the NMR signal usually covers a very limited frequency range, if, as is usual, $R_{opt} > Z_0 = 50\ \Omega$, a simple (reverse) Γ-section network (see Figures 23.2b and 23.3a) usually suffices to effect the desired (narrow-band) impedance transformation. Great care, however, must be taken to ensure that the inductors and capacitors have the highest possible Q-factors. This generally precludes ferrite-based inductors and, of course, if the preamplifier is to sit in a magnetic field, their use is, in any case, forbidden. If a low-loss RF printed circuit board is not used, it is advisable to mount components, including the transistor base, "in the air", either on small Teflon standoffs or by using component leads. This minimizes losses in the board dielectric. Even when using a low-loss board, it may be advisable to remove the ground plane below the components to reduce parasitic capacitance.

23.2.3 Noise Figure Measurement

There are commercial instruments available for measuring noise figure, but if the rest of the NMR receiver and computer are available, they can be used to advantage, with a minimum of programming, as a high-quality rms RF voltmeter. When the optimal source resistance is unknown (e.g., the manufacturer only specifies the transistor at, say, 2 GHz but the noise performance looks wonderful), it is helpful to invoke equation (23.7) and solder various resistors R_S across the transistor base-emitter junction (AC-coupled, of course). We assume here that the transistor is part of a functioning amplifier designed for the purposes of testing. If we may assume that $R_S << Z_b$ and $\gamma = 0$, then equation (23.7) reduces to

$$N_b^2 \simeq \left(V_n^2 + \beta^2 R_S + V_n^2 \frac{R_S^2}{R_{opt}^2} \right) \qquad (23.12)$$

and, by fitting the curve of mean square noise versus source resistance R_s, R_{opt} can be approximately found. (It is assumed that the reader is familiar with RF construction techniques and that the parasitic inductance and capacitance of R_S are always minimized.)

In a similar vein, one of the simplest and most accurate ways to measure the noise figure is by varying the temperature T_S of the source. However, of necessity, this implies that the source must be some distance from the transistor and therefore that well-shielded coaxial cable must be used. This in turn restricts the source resistance to the characteristic impedance Z_0 of the cable, 50 Ω, and an impedance transformation to R_{opt} must therefore take place within the preamplifier. Let room temperature be T_H in kelvin, giving recorded noise N_H and let the second temperature be T_L kelvin, giving recorded noise N_L. (Liquid nitrogen is commonly used, in which case $T_L = 77$ K). Then, from equation (23.10) it may be shown that

$$F_A = 10 \log_{10} \left(1 - \frac{T_L}{T_H} \right) - 10 \log_{10} \left(1 - \frac{N_L^2}{N_H^2} \right) \qquad (23.13)$$

When using liquid nitrogen, the spot noise figure is less than 1 dB when N_H/N_L is greater than 3.83 dB. In making the measurement, ensure with the aid of a network analyzer that both resistances, as measured at the remote ends of their respective cables and *at their operating temperatures*, are accurately Z_0 and that there is no chance of interference entering the resistors, cables, or preamplifier. If the noise figure is poor, the fault can lie in the preamplifier or anywhere in the receiver chain. If the gain of the preamplifier is normal and it originally had a good noise figure, it is unlikely that the noise figure has degraded and the cause should initially be sought elsewhere.

23.2.4 The Input Impedance and the Probe

The input impedance Z_{in} of a well-designed preamplifier is the first transistor's base (gate) impedance Z_b modified by feedback through the base–collector (gate–drain) capacitance and the reverse action of the input transformation network, as shown in Figure 23.2(c). If Z_b were equal to R_{opt}, then at the spot frequency of interest—the Larmor frequency—Z_{in} would equal Z_0, normally 50 Ω. However, we have seen that Z_b is usually considerably larger than R_{opt}. (Note, though, that it is possible in advanced designs to set the input

impedance with the aid of feedback.[11]) It has been known for 40 years that the input impedance is a parameter of considerable importance in NMR, yet all too often it is ignored. With correct utilization, it can, with no loss of SNR, speed up ringdown of low-frequency probes,[11] reduce radiation damping,[12,13] and block current in coupled probes.[14] As an example of its use, consider its effect on radiation damping using the circuit of Figure 23.2(c). We have introduced in the figure an important extra variable: the length l of cable between the probe and the preamplifier. At the Larmor frequency, when the probe is matched to 50 Ω, the 50 Ω cable maintains that source impedance at the preamplifier input; however, in the reverse direction, because the preamplifier input impedance Z_{in} is *not* 50 Ω, that impedance is transformed to a new value Z'_{in} at the probe.

Let the effective parallel input resistance of the transistor be $R_{\text{b}}(R_{\text{b}} = 1/R_l[1/Z_{\text{b}}])$. Then with the action of the Γ-impedance transformation network of Figure 23.2(b), the input impedance of the preamplifier may be shown to be

$$Z_{\text{in}} = Z_0\left(\frac{R_{\text{opt}} + j\alpha R_{\text{b}}}{R_{\text{b}} + j\alpha R_{\text{opt}}}\right); \quad \alpha = \sqrt{\frac{Z_0}{R_{\text{opt}} - Z_0}} \tag{23.14}$$

The cable of length l transforms this impedance to the new value

$$Z'_{\text{in}} = Z_0\frac{-Z_0 + \mathrm{e}^{4j\pi l/\lambda}(Z_0 + Z_{\text{in}}) + Z_{\text{in}}}{Z_0 + \mathrm{e}^{4j\pi l/\lambda}(Z_0 + Z_{\text{in}}) - Z_{\text{in}}} \tag{23.15}$$

where λ is wavelength in the line. Finally, at the Larmor frequency, this impedance is in series with the source—the 50 Ω of the tuned and matched probe. Of particular interest are the extrema of Z'_{in}. These are real, are separated by $\delta l = \lambda/4$, and may be shown to be $R_{\text{opt}}Z_0/R_{\text{b}}$ and $R_{\text{b}}Z_0/R_{\text{opt}}$. Remembering the source impedance Z_0, the resulting powers absorbed from the NMR system are

$$W_{\min} = \frac{V_{\text{S}}^2}{Z_0\left(1 + \frac{R_{\text{opt}}}{R_{\text{b}}}\right)}; \quad W_{\max} = \frac{V_{\text{S}}^2}{Z_0\left(1 + \frac{R_{\text{b}}}{R_{\text{opt}}}\right)} \tag{23.16}$$

and the ratio of the two powers is simply $R_{\text{b}}/R_{\text{opt}}$.

The absorbed power (and hence the amount of "radiation" damping—a misnomer, see Ref. 13) is clearly under the control of the circuit designer: one chooses a transistor with a large ratio of effective parallel input resistance R_{b} to optimal source resistance R_{opt} and then manipulates the cable length to minimize the absorption. This phenomenon was observed by scientists from the Perkin-Elmer Corporation in Beaconsfield, UK, in the early 1970s; however, it is not widely understood or employed. Note that the input impedance Z_{in} of the preamplifier depends not only upon the transistor but also on the design of the transformation network and it is not necessary, as is sometimes claimed, for that impedance to be very low for power reduction to be effective. All that is important is that the (complex) impedance be very different from the cable characteristic impedance Z_0 (scattering parameter $|s_{11}| \Rightarrow 1$); correct choice of line length then performs the appropriate transformation for minimal damping. It is emphasized that, in radiation damping, it is power that is important and the ratio of resistances R_{opt} and R_{b} is the determining factor.

When minimizing *total* probe current in imaging, as opposed to minimizing *in-phase* current for reduction of radiation damping, the details of the probe and its matching affect the equation and each situation must be assessed on its merits. However, the important variable is still the cable length l. In this case, it is adjusted so that Z'_{in} is a (lossy) inductance that resonates in parallel with matching capacitor C_{m} to create a relatively high impedance.[14]

23.2.5 Stability and Neutralization

In passing, it is worth noting that over a small bandwidth centered on the Larmor frequency, the measured noise from a rigorously shielded probe, tuned and matched to 50 Ω, should be the same as that from a 50 Ω source at the same temperature. (Remember that the effective source temperature in biological experiments may be 37 °C.) If it is not, and interference can be ruled out (disconnect the transmitter, a potential source of noise), it is possible that the preamplifier is oscillating—perhaps at a frequency beyond the range of the measuring equipment. One of the simplest checks for oscillation is to monitor the direct current drawn by the preamplifier. If it changes when a 50 Ω load is disconnected, when the probe is connected or when the length of line to the probe is altered, oscillation is almost certainly taking place.

Considering first oscillation in the vicinity of the Larmor frequency when a probe is attached, it must

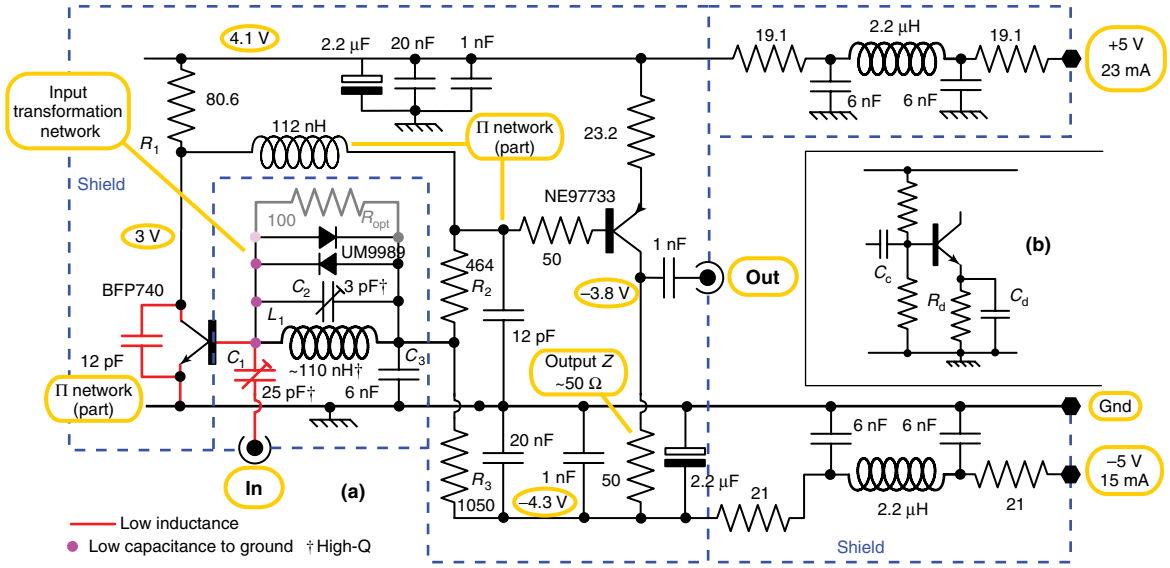

Figure 23.3. A preamplifier for use at a center frequency of 125 MHz is shown in (a). It employs an SHF bipolar transistor which, regardless of orientation, functions normally in a field of 7 T with a noise figure ~0.6 dB. Its gain is 30 dB with a bandwidth ~50 MHz and it employs direct coupling with feedback to speed recovery from overload and aid stability. The classic method of DC stabilization shown in (b) results in long recovery times from overload and is not recommended.

be remembered that the latter only presents a resistive impedance of 50 Ω at one frequency—the Larmor frequency. Away from resonance, the impedance can be almost anything, and it therefore follows that the preamplifier design must be *unconditionally stable*—it must not oscillate under any source and/or load conditions. Single-stage stability may be assessed on the bench with a high degree of confidence with the aid of a network analyzer and Rollett's stability criterion.[15,16]

$$K = \frac{1 - s_{11}s_{11}^* - s_{22}s_{22}^* + |s_{11}s_{22} - s_{12}s_{21}|^2}{2|s_{21}s_{12}|} \tag{23.17}$$

If $K > 1$ over a large range of frequencies about that of interest, the amplifier is unconditionally stable. Here s_{11} etc., are the standard scattering parameters[17] measured by a network analyzer. Instability is usually caused by the base–collector (gate–drain) capacitance C_{bc} providing a feedback path from collector to base for the collector voltage V_c. A time-honored method of cancelling the feedback over a limited bandwidth is to generate the voltage $-V_c$ (e.g., with a tuned inverting transformer as a collector/drain load) and feed this voltage back to the base via a second capacitance $C_N = C_{bc}$, a technique known as *neutralization*.[18] Capacitor C_N is correctly adjusted when a change in the collector load (caused by a judiciously applied finger?) produces no change in the transistor (preamplifier) input impedance.

Oscillation may occur at frequencies much greater than the Larmor frequency, and there are two main causes of such SHF oscillation: through air leakage and excessive gain. The high Q-factor inductor in the input impedance transformation network can act as a good antenna at SHF, receiving signal from other portions of the preamplifier, and therefore, it should always be shielded, together with the rest of the transformation network (see Figure 23.3a). The author's preferred shielding strategy is to bisect the transistor with the shield wall, thereby isolating the collector (drain) from the base (gate). If rigorous shielding fails to quell SHF oscillation, the only other solution is to reduce the stage gain, as it is probably the base–collector capacitance that is the feedback path and any neutralization has long since failed to be effective at such high frequencies. Note that many commercial shielding walls and boxes are tin-plated steel, and if the preamplifier is to be in or near the magnet, the use of phosphor-bronze or tin-plated copper is preferable. However, the shielding should not be so thick that eddy currents during

gradient switching create appreciable torque and vibration. The same applies to the box in which the preamplifier is mounted. Beware too of magnetic connectors and coaxial lines with copper-plated steel central conductors.

23.2.6 The Second Stage and Dynamic Range

The job of the preamplifier is to raise the signal and source noise to a sufficiently high level that extra noise N_R injected by later stages of the receiver is negligible. On the other hand, excessive gain is undesirable as it restricts the dynamic range. To understand this statement, *reductio ad absurdum*. If the gain is so large that the receiver is almost overloaded by the amplified noise, there is clearly no "headroom" for a signal that is larger than the noise. Thus, it is good design practice to limit the preamplifier gain to the minimum necessary for good noise performance—additional (variable) amplification may be added later in the reception chain as needed. Note that dynamic range is an important concept in receiver design and should be considered at each point in the design (see Figure 23.1). To assess the minimum preamplifier gain α, we require a measure of the noise figure F_R of the rest of the receiver (noise factor F'_R), and a typical value is 10 dB. From equation (23.10), the noise factor of the combined preamplifier and the receiver can be shown to be

$$F'_{\text{total}} = 1 + \frac{N_A^2}{N_{\text{opt}}^2} + \frac{N_R^2}{\alpha^2 N_{\text{opt}}^2} = F'_A + \frac{F'_R - 1}{\alpha^2} \tag{23.18}$$

an example of the Friis equation[16]. Then, if only a 1% degradation in SNR is allowed (0.05 dB), the gain α ranges essentially linearly from 28.9 dB for $F_A =$ 0 dB to $\alpha = 25.9$ dB for $F_A = 3$ dB. It follows that a common preamplifier gain specification is 30 dB.

For reasons of stability alluded to earlier, it is inadvisable to attempt to produce such gain with a single transistor, and thus, preamplifiers usually have two stages. It is immediately obvious that the second stage must have in its own right a good noise figure. This in turn implies that the output impedance of the first stage (transformed if necessary) must be close to R_{opt} and that its minimum gain must be dictated by equation (23.18). It is left to the reader to show that, if the noise figure of the second transistor is 1.5 dB, a minimum first-stage gain is 15.5 dB ($\times$6). If the first-stage output impedance cannot be R_{opt} or the second-stage noise figure is greater, then greater first-stage gain will be needed.

Other factors that enter into the design equation at this juncture are the output impedance and the bandwidth of the preamplifier. A limit to the latter (broadband preamplifier users, take note) can be set by *imaging* in the heterodyning process that is discussed below: noise at a certain frequency f_a well removed from the Larmor frequency is treated as if it were at the Larmor frequency f_0 and thus adds to the legitimate noise. In this regard, it must be remembered that at frequency f_a, the impedance presented to the first transistor by the probe, line and transformation network could be very high. The noise then would mostly be due to the noise current I_n flowing through the base impedance and could be considerably larger (e.g., $\times$5) than the optimal at the Larmor frequency. If this *image noise* is to contribute less than 1% of the total, then the preamplifier response at frequency f_a must be considerably attenuated—by 31 dB for the example of $\times$5.

When designing the second stage of amplification, we may therefore wish to include a filter and Figure 23.3(a) includes one possible design among many. A π-section filter links the stages, providing direct current coupling to the second transistor, as well as SHF grounding of the first transistor's collector—this improves SHF stability. Another possibility is to combine a neutralization transformer with a tuned circuit as mentioned previously. It is also possible to place a filter on the preamplifier output, but the performance is then dependent on the input impedance of the rest of the receiver. In some applications, notably Cartesian feedback,[19,20] it is important to minimize the *group delay* $d\phi/d\omega$ through the preamplifier (ϕ is phase). The former is, of course, dependent on the filter characteristics, and a compromise must be effected between group delay, filter rolloff, and bandwidth. The greater the intermediate frequency(ies) ($q.v.$) of the receiver, the greater the frequency difference $f_a - f_0$ can be, the greater the allowable bandwidth, and the smaller the group delay.

Finally, note that, while it is conventional to design a preamplifier so that its output impedance is close to 50 Ω, a trade-off may be involved. The purpose of a 50 Ω value is to eliminate standing waves on the cable connecting the preamplifier to the rest of the receiver. However, if the input impedance of the latter is also 50 Ω, there already can be no standing

waves so the effort is wasted. Further, the load on the preamplifier's output transistor is then 25 Ω, thereby reducing gain and, perhaps more importantly, dynamic range (see Section 23.5.1). In the design of Figure 23.3(a), the DC-coupled, emitter-biased PNP low-noise transistor has a 50 Ω resistor as its collector load. The latter is then AC-coupled to deliver the output. If desired, and with a suitable adjustment of negative line voltage, the resistor may be replaced with a large inductance or even a tuned circuit with a low quality factor so as to increase the output impedance.

23.2.7 Biasing and Recovery Time

During an RF pulse, the preamplifier is usually grossly overloaded with a voltage that is dependent on the protection mechanism—the transmit/receive (T/R) switch (*q.v.*). However, it is rare for a T/R switch in and of itself to provide sufficient protection, and in Figure 23.3(a), it may be seen that there are crossed high-frequency signal diodes (typically Schottky diodes[16]) in parallel with the input transformation network's inductor L_1. Working in concert with the reactance of network capacitor C_1 as a potential divider, these limit the voltage on the transistor's base to the order of 1 V, the exact figure depending on the choice of diode and the parasitic lead inductance. However, the diodes in their nonconducting state have a capacitance $C_d \sim 1$ pF, which modifies the effective inductance of L_1. Thus, L_1 is made slightly less than the calculated value, and the small variable capacitor C_2 in conjunction with the diode capacitances allows for adjustment to the correct effective value. With this crossed diode strategy, the transistor is now protected from destruction, but one must be aware that gross overload and rectification in both the first and second transistors can still occur. It is also possible for the overload to temporarily change the capacitance C_d of the diodes for many milliseconds after the overload has ceased, probably as a result of charge storage in spurious energy levels associated with impurities in the semiconductor.[21] This in turn can modulate the phase of the signal. In a spectacular manifestation of the phenomenon, the author once built a preamplifier that oscillated for 10 ms after each pulse. Placing a small light in the preamplifier stopped the oscillation, presumably by ejecting electrons for the spurious energy levels.

Rectification can have profound consequences upon the biasing of the transistors long after the pulse has ceased if precautions are not taken. The worst type of bipolar transistor biasing is classical emitter decoupling, shown in Figure 23.3(b). The value of the decoupling capacitor C_d is determined not by the biasing resistor R_d but rather by the emitter resistance R_e of the transistor ($\omega_0 R_e C_d \gg 1$), which typically is much less than R_d. During overload, capacitor C_d charges with time constant $\sim 2R_eC_d$ but after the pulse it only discharges with time constant R_dC_d, which is much longer. The transistor is biased off, and is therefore out of action, for a time $\sim 5R_dC_d$, and as it slowly begins to conduct again, the amplitude of the signal recovers before the phase. The possibility of rectification must be taken seriously throughout the receiver, and it is important to check the discharge time constant of every capacitor in the signal path. This is particularly the case with coupling capacitors such as C_c in Figure 23.3(b), which should not be made too large. Even the power supplies may need to be examined in this regard, as they may have "drooped" during a pulse due to the extra current being drawn during overload. In the design shown in Figure 23.3(a), the coupling between the transistors is direct, and stabilized by negative feedback. The recovery time is a fraction of the time constant C_3 times the resistance composed of R_1, R_2, and R_3. With FETs the problem is less serious, particularly if a low-impedance line provides the bias on the gate via the transformation network inductor.

23.2.8 Power Lines

Power lines are a neglected part of RF design, but they do pose some challenges. Most commercial preamplifiers (even supposedly MR-compatible devices) utilize ferrite *chokes* and capacitors in a π-filter configuration to suppress interference. Chokes are large lossy inductances that absorb RF energy on a power line and help reject line-borne interference. However, these components lose their efficacy if the preamplifier is in a magnetic field of greater than roughly 10 mT. If such an amplifier is in a shielded room or Faraday cage, as is generally the case with MRI, this is of little import. However, if the amplifier is near an NMR magnet in a laboratory, the loss of filtering can be serious. It can also be difficult to detect, as away from the magnet on the bench the rejection of interference appears to be according to

specification. In Figure 23.3(a), it may be seen that the power line filters each comprise an inductor, a resistor, and capacitors. The use of multiple capacitors is an example of a facet of all components that must be kept keenly in mind when working at radio frequencies: there are no pure components; all are a combination of resistance, capacitance, and inductance in various measures and only the ratios vary with the type of component. Thus the 2.2 μF capacitor on the positive rail serves to stabilize the power at low frequencies but presents as a lossy inductance at higher frequencies. At those frequencies, this is shorted out by the 20 nF capacitor and at even higher frequencies by the 1 nF capacitor. Any resonance will have a low Q-factor, thanks to the electrolytic capacitor's lossy nature, but to make sure, there are also 19.1 Ω resistances in the line. These resistances provide extra filtering, but introduce a time constant that could affect recovery from overload. Without them, however, there is a risk of a low-frequency resonance of moderate Q-factor that could also prolong recovery. In essence, a compromise has been effected with respect to recovery time.

Two further aspects of so-called power line decoupling merit attention. First, inefficient decoupling in an amplifier can cause oscillation as RF power is fed back from a stage with high signal levels to one with lower levels. If ferrite chokes are used, oscillation can then occur when the device is in a magnetic field and promptly cease when it is withdrawn for examination! Second, decoupling stringency can be considerably relaxed if an amplifier is *differential*. In a differential amplifier, both the signal and its inverse are amplified and, in consequence, there is considerable cancellation of RF voltages on power lines. Preamplifiers are no exception to this rule and the author has occasionally used balanced designs with two input transistors, partly because they alleviate probe balance problems but also because they increase dynamic range by 3 dB.

23.2.9 Receive-only Coils

With receive-only coils in MRI, it is advantageous to place the preamplifiers directly on the coil housing (see Figure 23.4d). Then, the receiving coil is tuned and matched to R_{opt} for the chosen transistor, rather than to 50 Ω. The signal exit point is across one of the tuning capacitors. A balanced π-section network may be employed, but not merely for impedance transformation; rather, it serves with PIN and crossed diodes as a switch to protect the preamplifier from the pulses. (The latter may also be balanced, essentially comprising two preamplifiers in parallel.) The network's components are invariably chosen so that they resonate with the associated coil's tuning capacitor when the PIN and/or crossed diodes are conducting, thereby presenting a high blocking impedance to the flow of induced current during transmission.

23.3 TRANSMIT/RECEIVE SWITCH

Key Specifications

Noise figure; insertion loss, reception; insertion loss, transmission; isolation; power; distortion.

23.3.1 The Crossed Diode T/R Switch

The quintessential NMR T/R switch is the classic λ/4 design of Lowe and Tarr[22] shown in Figure 23.4(a). Originally, this switch used crossed diodes—diodes in antiparallel, as shown—that conduct sufficiently at voltages greater than 1 V to be considered a short circuit, but that have a high impedance at much lower voltages. During transmission (see Chapter 24), the diodes therefore conduct and the impedance transformation properties of the quarter-wave line ensure that there is a high impedance in parallel with the transmitter and probe that degrades (but only slightly) the power passed from one to the other. In reception, on the other hand, with its much lower voltages, there is a direct path from the probe to the preamplifier with isolation of the transmitter. The switch, however, has defects: it cannot pass faithfully low powers from the transmitter to the probe (e.g., the zero-crossings of sinc pulses), and the diodes (either a single pair or multiple pairs for higher power handling) have capacitance of the order of 1 pF per diode when not conducting. Thus, it is common for low-power pulses to exhibit appreciable *crossover distortion*, while during high-frequency reception the isolation of the transmitter from the receiver may be poor. This results in noise being passed from the transmitter to the preamplifier and the former should therefore be gated off during signal reception. To combat the latter problem while exacerbating the former, two sets of crossed diodes separated by a λ/4 line may be inserted in the transmitter output, and/or the diodes may be part of

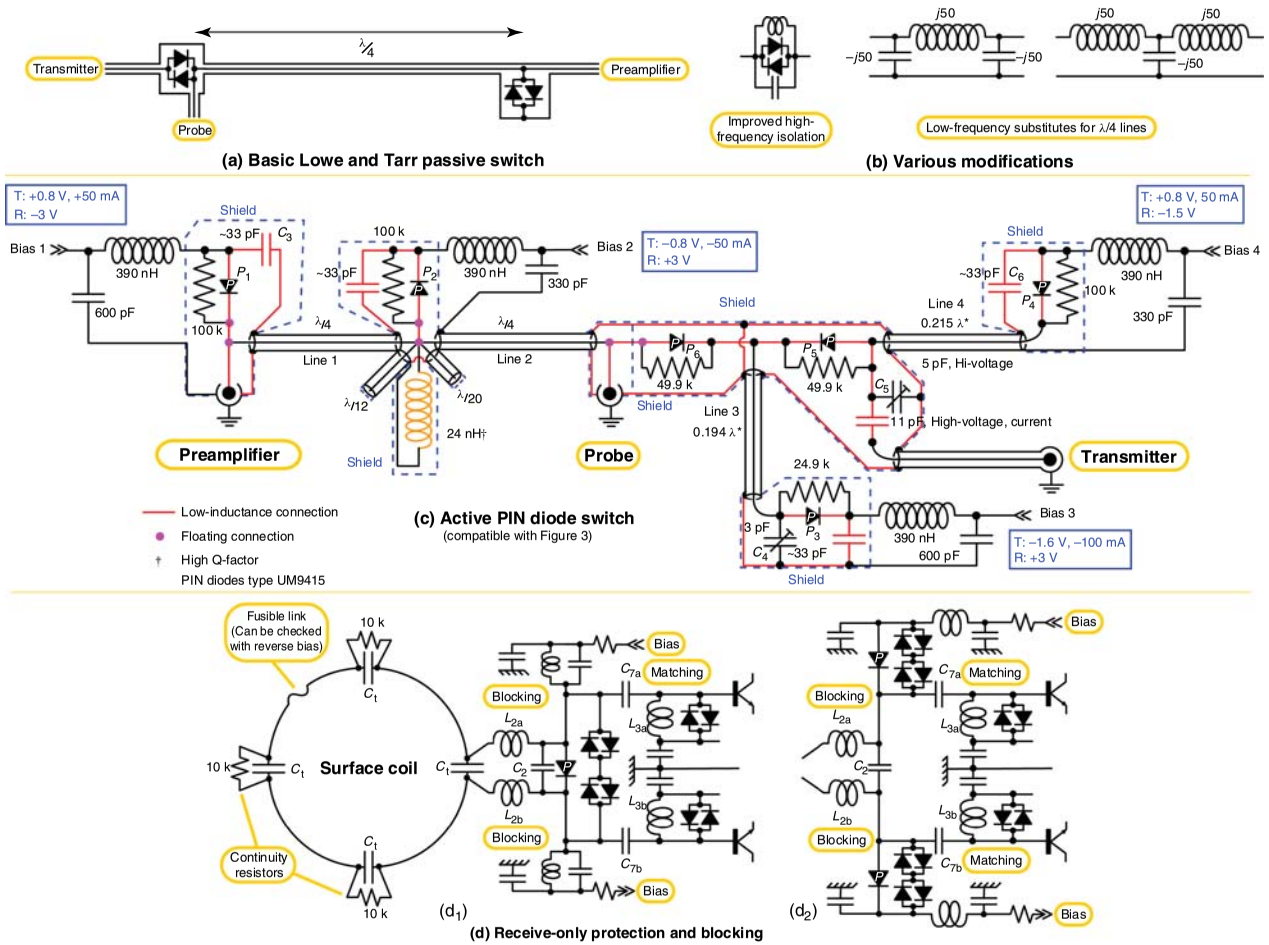

Figure 23.4. Transmit/receive switching. In (a), the classic λ/4 design of Lowe and Tarr is shown. It may be modified or enhanced by the substitutions shown in (b) or their conjugates. Most switches, such as the advanced PIN diode circuit of (c), are in some manner derived from this model. This switch, designed for use at 300 MHz, can handle 300 W with a transmitter isolation during reception of 70 dB. Compatible with the preamplifier of Figure 23.3(a), it degrades the noise figure by ~0.2 dB. The line lengths shown are the design values and may need adjustment, depending on layout. Variable capacitor C_6 can have a low working voltage but C_5 must be able to withstand a minimum of 200 V. In (d), two ways of protecting a balanced preamplifier attached to a receive-only coil are shown.

a tank circuit tuned to reject small signals at the Larmor frequency, as shown in Figure 23.4(b). However, a more modern solution is to use PIN diodes.[23]

23.3.2 The PIN Diode T/R Switch

PIN diodes have a relatively large layer of intrinsic semiconductor sandwiched between P- and N-doped end layers, and nonmagnetic versions specifically for MRI are available.[23] If direct current is passed through the diode, the large charge stored in the intrinsic layer provides a reservoir that allows the diode to conduct for a limited time (e.g., $\tau_r = 2\ \mu s$) during the application of reverse voltage; τ_r is known as the *reverse recovery time*. Thus at frequencies much higher than $1/\tau_r$, alternating current may pass, and the higher the frequency, the greater the allowed current. Equally though, when one wishes to turn the diode off by reverse-biasing it, the charge must be removed and this takes a time $\sim\tau_r$. It follows that the diode and its biasing current must be chosen appropriately for the operating conditions.[23] If a condition of "charge starvation" is reached with excessive RF current, the effective series resistance of the diode may increase dramatically with resulting signal distortion (amplitude and phase) and eventual diode failure. In some MRI uses, this could compromise patient safety. On the other hand, excessive charge storage results in long switching times. A typical small-signal "on" RF resistance for a PIN diode is less than $1\,\Omega$ for direct currents of 100 mA, while its "off" impedance is typically capacitive at a few picofarads. Sometimes, a negative bias voltage is needed to attain this capacitance value, in which case attention must be paid to the reverse breakdown voltage of the device.

The fact that direct current is needed to turn on a PIN diode automatically implies that a blocking circuit is needed to isolate the DC supply from the RF power and vice versa. The direct current must enter the circuit at a point that has a low RF impedance to ground for optimal protection. This, of necessity, sets a limit on the switching time between transmit and receive, because a blocking circuit cannot pass the high frequencies that are associated with rapid switching. Another operational wrinkle is the fear that associated with the flow of direct current through the diode there might be flicker noise that would degrade the noise performance during signal reception. Thus, the conventional wisdom is that all PIN diodes should be off during signal reception, while to avoid reverse voltage breakdown all diodes should be on during transmission. However, at sufficiently high frequencies, flicker noise is negligible.

Figure 23.4(c) shows a 300 W T/R switch for use at 300 MHz that embodies the principles above and has excellent performance, partly due to the use of low-loss, semirigid coaxial lines that are all nominally $\lambda/4$ in length. Diodes P_1–P_6 are all conducting during transmission and are off during reception, their bias being provided through three π-section filters. These filters are driven from amplifiers (not shown) with an optimal output resistance that minimizes ringing during switching and thereby reduces switching times to under 1 μs. During transmission, in conjunction with the crossed diodes in the preamplifier, diode P_1 protects the latter, for via capacitor C_3 there is a low impedance to ground in parallel with the preamplifier input. Approximately a quarter wavelength away, this configuration is repeated. At the probe terminal, the low impedance of P_2 and its associated biasing circuitry has been transformed by line 2 to the maximum possible so as to not influence unduly the transmitted power. Note that this requires optimization of the line length. Lines 3 and 4 behave similarly, and present further high parallel impedances, with optimization being available via capacitor C_5. RF power then passes relatively unscathed from the transmitter terminal through diodes P_5 and P_6 to the probe terminal. The insertion loss during transmission is approximately 0.5 dB.

In signal reception, the aim is to severely attenuate leakage from the transmitter. The first line of defense is line 4 and PIN diode P_4. As the latter is off and effectively a small capacitor, a high impedance terminates the line and the latter therefore presents almost a short circuit across the transmitter terminal. Equally, line 3 also presents a low shunt impedance (adjustable with capacitor C_4), which in conjunction with the high series impedance of diodes P_5 and P_6 creates a π-section attenuator that attenuates leakage by 70 dB. In contrast, there is an unhindered connection from the probe terminal to the preamplifier, the capacitance of diode P_1 creating a minor perturbation to the $50\,\Omega$ impedance that can be accommodated in the settings of the preamplifier noise matching network. The insertion loss during signal reception is roughly 0.2 dB and the noise figure of the preamplifier is degraded by the same amount by the addition of the switch. To save space, it is common practice at lower frequencies to roll lines into a helical or other compressed form.

However, if the switch is used inside an imaging magnet, one should be aware that the ensuing solenoids can couple strongly to the switched field gradients. As this can cause undesirable torque and vibration, the ground connections at one end of each line should be multiple capacitors in parallel with a resistance that damps the ensuing low-frequency tuned circuit. PIN diode switches can be made as "stand-alone" devices (mimicking crossed diodes) by incorporating detection circuitry that automatically turns on the diode currents when an RF pulse is present. However, the switches do not then pass low transmitter powers and again exhibit crossover distortion.

Two remaining facets of Figure 23.4(c) merit attention. First, at high frequencies, the inductance (a few nanohenries) of the PIN diode package can give a reactance that is considerably larger than the diode's "on" resistance; this degrades the performance. Thus in the figure, the diode inductances are tuned out with series capacitors that resonate the ensemble at the Larmor frequency. Now, it is quite common for a high-power RF pulse to contain odd-order harmonics, and as the diode inductances are not cancelled at these frequencies, considerable harmonic power may reach the preamplifier, with destructive consequences. Thus, a second facet of the figure is the presence of two *stubs*—open-circuit lines—with lengths $\lambda/12$ and $\lambda/20$ that short out third and fifth harmonics. At the fundamental Larmor frequency, the stubs act as capacitances and so their partial shorting effect is annulled with the aid of a very high quality resonating inductance.

23.3.3 Low Frequency Switches

At lower frequencies, $\lambda/4$ lines can become inconveniently long and lumped components are preferred. A basic design principle is that a $\lambda/4$ line in a switch may be replaced with either π-section or T-section filters whose components' reactances are $50\,\Omega$ at the frequency of interest. However, if the line is carrying direct current, as in Figure 23.4(c), then the arm(s) must be inductive if there is a straight replacement. If, in a design, lines meet, connected components may be coalesced. An additional weapon in the armory is the transformer, and its use as an isolator of direct current can sometimes reduce the component count. An unusual example is shown in Ref. 24.

23.3.4 Switches on Receive-only Coils

Lumped components are also preferred when a preamplifier is mounted directly on an MRI receiver coil. Here, the role of the switch is to block current in the coil during transmission as well as to protect the preamplifier. Owing to the importance of maintaining electrical balance with MRI coils, it is preferable that the switch and preamplifier also be balanced. The circuits of Figure 23.4(d) fulfill this requirement. During transmission, the PIN diode(s) is (are) on and the two equal inductors L_{2a} and L_{2b}, now in series, resonate with one of the coil tuning capacitors C_t to form a high-impedance blocking circuit. The balanced preamplifier meanwhile is protected by the low impedance of the PIN diode(s) and the crossed diodes on the bases of the transistors. (The extra pairs of crossed diodes provide backup.) Noise-matching is accomplished by appropriate choices of capacitors C_2 and C_{7a} and C_{7b}, and of inductors L_{2a} and L_{2b}. Note that both high- and low-impedance biasing schemes are shown. While the circuit of Figure 23.4(d_2) has more components, it may better protect the transistors from common mode voltages. Finally, it must be remembered that all components reside in the powerful alternating B_1 field of the transmitter. Thus, considerable voltages can be induced in printed circuit paths and inductors. Shielding is important, but a useful trick is to use toroidal inductors, which are relatively immune to exterior coupling.

23.4 FREQUENCY CHANGING (HETERODYNING)

Key Specifications

Noise figure; conversion gain; bandwidth; impedances; carrier isolation; signal isolation; power; distortion; phase noise.

23.4.1 Basic Principles

It was stated in the introduction that reduction of the NMR signals' frequencies by subtraction of a reference frequency was required. This is accomplished in an electronic component commonly referred to as a *double-balanced mixer*[16] or a *demodulator*. It creates new signals (*sidebands*) whose frequencies are the

sum and difference of those of the input and reference signals—the latter is usually called the *carrier* or the *local oscillator* (LO). We therefore begin by briefly examining how such a device works. We forgo a detailed circuit analysis, as many of the principles discussed in reference to the preamplifier apply.

Older mixers typically used ferrite transformers and diode bridges to perform the mixing function (*ring modulators*) and had to be kept well away from magnetic fields; it is now common, however, to use an integrated circuit employing a design known as a *Gilbert cell*.[25] For both devices, though, the principle of operation is the same: the polarity of the LO signal determines whether the RF signal or its inverse is passed through the device. Essentially, the LO is converted into a square wave of amplitude A and phase ψ that multiples the signal $\xi_0 \cos(\omega_0 t + \phi)$ as shown in Figure 23.5 ($\omega_0 = 2\pi f_0$, etc.). Now, a square wave of frequency ω_c may be Fourier-analyzed as

$$V_{\mathrm{LO}} = \sum_{n=1,3,5\ldots}^{\infty} \frac{4A}{\pi n}(-1)^{\frac{n-1}{2}} \cos[n(\omega_c t + \psi)] \tag{23.19}$$

where n is an integer, and upon multiplication of the signal we obtain

$$V_{\mathrm{IF}} = \sum_{n=1,3,5\ldots}^{\infty} \frac{2\xi_0 A}{\pi n}(-1)^{\frac{n-1}{2}} \{\cos[(n\omega_c - \omega_0)t + (n\psi - \phi)] + \cos[(n\omega_c + \omega_0)t + (n\psi + \phi)]\} \tag{23.20}$$

This function contains all frequencies $n\omega_c \pm \omega_0$ and the sidebands decrease in size with increasing order n. It is usual to use a mixer in its first harmonic mode ($n = 1$), though the author once built a spectrometer using the third harmonic. Because the mixing process retains phase information, it is sometimes known as *phase-sensitive detection*. Note that there will always be small amounts of even harmonics ($n = 2, 4, \ldots$) in the carrier because of circuit imperfections and that the output will contain the results of these imperfections, as well as small amounts of the original LO square wave and the signal. Normally, a manufacturer will specify (in decibels) the rejection of these various unwanted signals. Only one of the frequencies $n\omega_c \pm \omega_0$ is usually passed on down the receiver

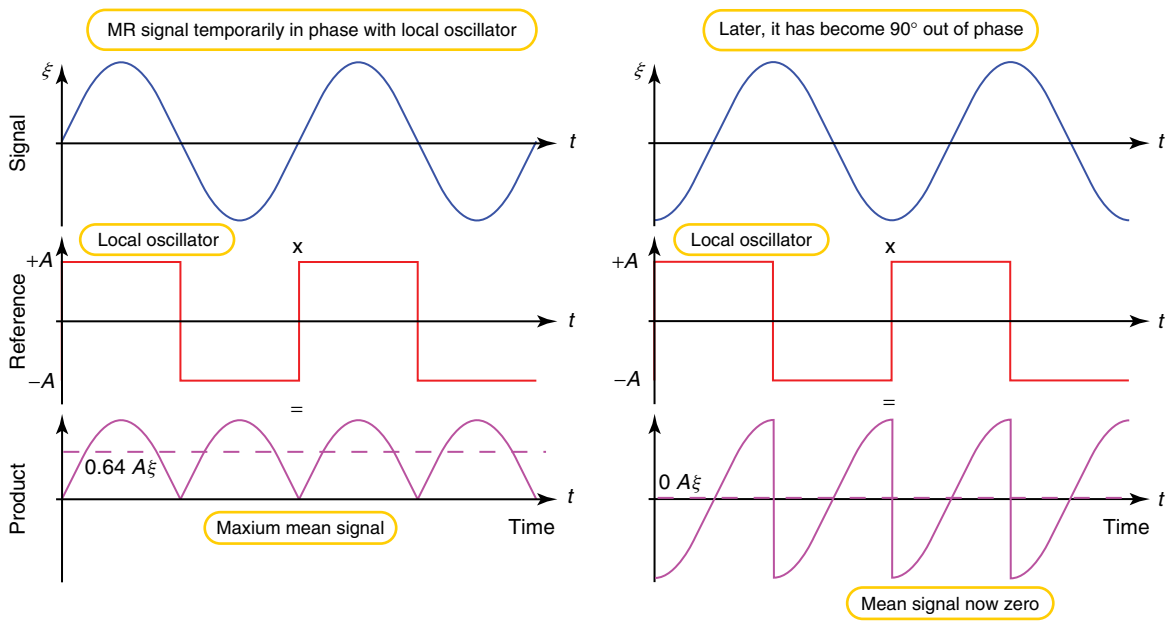

Figure 23.5. The principle of frequency changing or phase-sensitive detection. An NMR signal at almost the same frequency as that of a square wave LO is shown. In (a), at a particular point in time, the two signals are temporarily in phase and their product has a substantial average value. However, sometime later in (b), the two signals have attained a 90° phase difference, thanks to their frequency difference, and the mean product is now zero. The filtered product—essentially the mean—therefore slowly oscillates at the difference frequency.

chain, and that frequency is often known as an *intermediate frequency* (*IF*) for reasons to be shortly discussed. Other frequencies are normally severely attenuated by filtering (see Figure 23.1) before they reach the ADC so as not to appear in the final recording—they lie well outside the *passband* of the receiver and are in one of its *rejection bands*. The passband is the bandwidth needed for the application at hand. For NMR, it is rare for a passband of greater than 250 kHz to be needed, this figure usually being determined in spectroscopy by chemical shift range and in MRI by read-gradient strength. However, for undesirable signals to be sufficiently attenuated, e.g., −80 dB, the response of the filters may well be such that the rejection bands only begin ± 2.5 MHz away from the signal frequency. The quantity $2A/\pi n$ (with usually $n = 1$) is known as the *conversion gain* of the mixer. With an active (integrated circuit) mixer, such as Analog Devices' AD8243, the conversion gain is normally greater than 1; with a passive device such as a diode or FET *ring modulator* (another term for a double-balanced modulator) it is less than 1, for example −8 dB. Note that the noise figure of mixers is sufficiently bad, typically being in the range 8–15 dB, that manufacturers often do not quote the value. Both Gilbert cell mixers and diode mixers can be broadband, but FET devices, while typically exhibiting less distortion (see Section 23.5.1), are normally tuned as they possess relatively large capacitances.

23.4.2 The Intermediate Frequency

It is normal for a frequency change to occur immediately following preamplification. The main reason for this arrangement is that, if variable gain is needed for any reason, it is generally cheaper and easier to introduce it at a lower, relatively constant frequency. However, it is important to be aware that some commercial integrated circuits that are advertised as having "variable gain" are actually combinations of fixed-gain amplifiers with variable attenuation between them. Such a design strategy is preferably avoided, as it limits dynamic range. For example, suppose we have a signal that is so large that it needs IF amplification by only a factor of 20 dB to just make the noise large enough to be sampled while producing the maximum signal any amplifiers or ADCs can handle. If there is amplification by 30 dB followed by attenuation of 20 dB and final amplification of 10 dB (a total of 20 dB), the first amplifier in the chain will be overloaded, leading to distortion (see Section 23.5.1).

The lowest possible intermediate frequencies in the mixing process are obtained when the reference frequency f_c is just to one side or even in the midst of the NMR spectrum—so-called baseband detection. A direct frequency conversion to baseband, however, is generally inadvisable. LO frequency f_c is then within the passband of the preamplifier and the receiver, and it is almost impossible to prevent leakage of the LO signal into the preamplifier, where it is then amplified. The result is a DC offset on the output of the mixer which can be interpreted by the spectrometer's computer as an NMR signal with an exceedingly long transverse relaxation time—a so-called origin peak. Leakage into the preamplifier or probe can be down power lines, on the exterior of cables, through air, etc., and the amount is subject to uncontrollable vagaries such as the movement of people, temperature, cable routing, or humidity. Thus, it is normal for the signal to be converted initially to an IF f_i such that neither the carrier frequency *nor its harmonics* lie anywhere near the passband (of width Δf) of the receiver. This criterion immediately suggests that, for guaranteed immunity to carrier detection at any frequency (a typical desired rejection is −80 dB), the reference frequency f_c should ideally always be at a *higher* frequency than any Larmor frequency f_L, and that the passband should be the minimum needed. In other words,

$$f_c \gg f_i + \Delta f/2; \quad f_i = (f_c - f_0) \quad (23.21)$$

The exact meaning of "very much greater than" is determined by the combined rolloff of the various receiver filters that follow the mixing process, and it is common for some of those filters to occur directly after a mixer so as to maximize once again the dynamic range of subsequent stages. This is because the presence of spurious signals lowers the amount of signal that can be passed before an amplifier overloads. The combination of mixer, passband filter, and amplification is known as an *IF stage*.

Unfortunately, as a general rule, the higher a carrier frequency, the more expensive it is to generate. Thus, if it is feasible, a lower LO frequency is sometimes used, in which case

$$|nf_c - f_i| \gg \Delta f/2; \quad f_i = (f_0 - f_c) \quad (23.22)$$

Nor must we forget that the signal itself, albeit greatly attenuated, can pass through the mixer. Thus, we must

add the requirement that

$$|f_0 - f_i| \gg \Delta f/2 \tag{23.23}$$

Generalizing, attention should be given to *all* frequencies present in the NMR equipment to ensure that all lie well outside the passband. The author still recalls discovering many years ago that the pulse programmer in a certain manufacturer's instrument was generating a harmonic that lay in the midst of the phosphorus spectrum. The magnet's field strength had to be altered to circumvent the problem. Such spurious signals generated by an instrument itself are sometimes referred to as *spurs* or *birdies*. For a receiver designed for multinuclear use, the above frequency criteria can rapidly become quite complex, and a computer is often used to assess designs because the rejection characteristics of mixers and filters are not difficult to program. A consequence, however, of this type of analysis is that in some circumstances it may be better first to *increase* the NMR frequencies and then lower them in a second mixing and IF stage. The jargon describing this process is that we *upconvert* and then *downconvert*: we use a *multiple IF receiver*.

23.4.3 Single Sideband Generation

It has been seen in equation (23.20) that the act of mixing produces sum and difference frequencies, or sidebands, and it is common practice to remove the undesired sidebands by filtering. However, while this practice can function well at low Larmor frequencies, at higher frequencies it may well pose difficulties. For example, suppose an IF of 10 MHz has been chosen as a suitably low frequency for analog-to-digital conversion and that the Larmor frequency is 64 MHz. A mixing process with a carrier frequency of 54 MHz would fully accept signals at 64 and 44 MHz and so the preamplifier must reject noise at 44 MHz as well as at other frequencies. For a rejection of 20 dB (which degrades the noise figure by 0.05 dB, but see the Section 23.2.6), a passband filter with a Q-factor of roughly 27 or greater is needed which, while a little high, is feasible. However, if the Larmor frequency were 750 MHz, rejection of 730 MHz by 20 dB would require a filter with a Q-factor of roughly 330, which is unacceptably high from the points of view of both stability and practicality.

There are two solutions to this problem: single sideband (SSB) generation and the use of a second IF stage. We consider the former first. SSB operation relies on the simple trigonometric formula

$$\cos[(\omega_0 \pm \omega_c)t] = \cos\omega_0 t \cos\omega_c t \pm \sin\omega_0 t \sin\omega_c t \tag{23.24}$$

Thus, to remove one sideband (sometimes called *image rejection*), we need a second mixing wherein both the carrier and the signal have phase shifts of 90° relative to the first mixing while maintaining the same amplitudes. (A device that generates two equal signals having a 90° phase difference is known as a *quadrature splitter*.) The two results are then added or subtracted depending on which sideband is to be suppressed. However, making 90° phase shifts accurately at radio frequencies with analog components whose values may drift with time and change with frequency is no easy matter. To assess the potential size of an undesired sideband, we analyze the formula

$$\begin{aligned} P = {} & \cos\omega_0 t \cos\omega_c t \\ & \pm(1+\beta)\sin(\omega_0 t + \gamma)\sin(\omega_c t + \delta) \end{aligned} \tag{23.25}$$

where β, γ, and δ represent small errors in amplitude and phases. It may then be shown that the ratio R of the amplitude of the undesired signal at frequency $\omega_0 + \omega_c$ relative to the amplitude of the desired signal at frequency $\omega_0 - \omega_c$ is approximately

$$R = \sqrt{\beta^2 + (\gamma + \delta)^2} \tag{23.26}$$

A rejection factor of greater than 20 dB ($R < 0.1$) is always obtained by ensuring that the signal amplitude and the sum of the phase errors reside within the circle of radius R: for example, if amplitudes are matched to better than 7% with phases errors no greater than 2°. This specification can be met fairly easily at fixed frequencies ω_0 and ω_c and, with great care, rejections ~40 dB can be obtained. However, the specification is far more difficult to attain over a large bandwidth, though there are *polyphase network* designs[26] that accomplish this over at least an octave (a doubling of frequency).

23.4.4 An Additional IF Stage

The problem of image rejection is particularly acute in a multinuclear spectrometer. We have already mentioned the need for SSB techniques at 750 MHz (^{1}H)

with an IF of 10 MHz. However, if we also wish to observe at say 303 MHz (^{31}P), a second SSB circuit will be needed because one quadrature splitter cannot produce a good 90° phase shift over such a large frequency range. Thus, we might decide first to convert our signals to 115 MHz, before the conversion to 10 MHz with a 105 MHz carrier. We could then reject the image frequency of 95 MHz with a suitable filter. However, we now have generated a new problem—how do we observe a nucleus in the vicinity of 115 MHz, for example ^{2}H at 115.107 MHz, while fulfilling all the strictures above about spurious signals and signal breakthrough in mixers? Clearly, we have to change the IF, and this can be done either by switching to new circuitry or by employing the octave bandwidth quadrature splitter mentioned above with a variable-frequency LO, typically a *frequency synthesizer* (a device that produces frequencies that are phase-coherent with a reference frequency). Manufacturers have their own method of dealing with such problems, but no matter the method employed, one must keep a very close eye on the frequency changes and filtering to ensure that spurious signals are adequately rejected, negligible extra noise is added, and the full NMR spectrum of the selected nuclear species is accommodated.

23.4.5 Quadrature Detection to Baseband

Prior to the advent of digital signal processing, in which an IF is sampled by an ADC, it was common practice to perform a final frequency subtraction in which the transmitter frequency was effectively subtracted from the Larmor frequency. If the transmitter frequency is in the midst of the spectrum, this can result not only in the origin peak described earlier but also in a loss of information because it is now impossible to differentiate between a signal +1 kHz off resonance and another −1 kHz off resonance. This problem is a variant of image rejection, and to retain the SNR and spectral frequency sign data, one must perform two separate mixings in which the carriers are accurately 90° apart in phase and the gains and filters of the two resulting baseband signal channels are accurately matched—*quadrature detection* of the signal is employed.[27,28] The two signals are then separately digitized and the two digital streams treated as the components of a list of complex numbers. As discussed above, it is very difficult to achieve an image rejection of greater than roughly 40 dB using analog electronics and so spectra obtained with this technique by Fourier transformation of the complex digitized signal routinely had *ghosts*: a small signal at frequency $-\delta f$ off resonance was generated by a large signal at frequency $+\delta f$. In addition, the origin peak mentioned earlier was present. (A complex Fourier transform can be considered to perform the equivalent of the addition or subtraction in equation (23.24) that completes SSB mixing, in addition to applying a set of frequency changes followed by integration.)

Initially, the problem was solved by setting the transmitter frequency to one side of the NMR spectrum so that the ghosts and origin peak were not in the bandwidth of interest. However, it was quickly recognized that transmitter power could be saved by placing the transmitter in the midst of the spectrum and so a simple, cyclically ordered phase sequence (CYCLOPS) was employed[29] wherein, on successive data acquisitions, the phase of the transmitter was advanced by ∼90°. The computer then, with total accuracy, applied successive −90° phase shifts before summing the data streams. The consequence of this manipulation was that the rejection of ghosts was as R^2 rather than R (equation (23.26)), and it was possible to obtain a rejection factor approaching 80 dB.

While sampling of the IF virtually eliminates ghosts and origin peaks and with this the need for CYCLOPS, there are still instances where baseband detection is useful, principally when Cartesian feedback is used.[19,20] With this technique, the transmitter's low-power sections are used *during reception* to feed the received signal back to the probe, the filters in the two baseband amplifiers being designed to confer stability to the feedback. The principal advantage of Cartesian feedback in signal reception is that it blocks current flow far more efficiently than the preamplifier (Section 23.2.4), thereby virtually eliminating "radiation" damping[30,31] and coupling between multiple imaging coils.[20] While the details are outside the scope of this chapter, it is worth noting that advances in digital electronics have made possible the generation of highly accurate, quadrature phase carrier signals. To generate 10 MHz square waves in quadrature phase, a 40 MHz signal is divided by 4 in a *Johnson counter*.[32] Meanwhile, laser-trimmed resistors have given unprecedented accuracy to surface-mounted components and matching of gains and DC offsets

to one part in a thousand is quite feasible. The result is a rejection of ghosts and origin peaks to better than −50 dB. As the dynamic range in most images is far less than this, it is rare that other rejective measures must be taken, but if they are needed, the application of a frequency offset or CYCLOPS is still viable. At the time of writing, the full digitization of Cartesian feedback is being researched.

23.4.6 Phase Locking

No matter how the NMR signal is finally passed to the computer, there is a key requirement that repetition of an experiment produce the same result; in particular, the phase of the FID or echo must remain constant, and this should hold even if there is a change in the repetition rate of the experiment. (We discount here changes due to magnetic resonance effects such as partial echo formation.) To accomplish this, the LOs used in the receiver must have exactly the same frequencies as those used in the transmitter: there can be no drift or wandering between the two that causes the phase difference between them to vary (see Section 23.4.7). A common method of attaining this goal is to lock all frequencies to a high-stability, temperature-controlled reference source, often a master 10 MHz oscillator in a frequency synthesizer. Thus, if an instrument uses more than one IF, two synthesizers might be locked together, and the synthesizer manufacturer will usually provide an option whereby the instrument's own internal 10 MHz master oscillator can be replaced by an external master source.

23.4.7 Phase Noise

Throughout this section, it has been assumed that the LO has a perfectly defined frequency. However, just as the NMR signal has associated noise, so does the LO signal and, in the conversion of that (usually) sinusoidal signal to a square wave, the presence of noise influences slightly the times at which transitions from $+A$ to $-A$ and vice versa take place and may even cause "jitter" in the transitions if there is insufficient hysteresis in the conversion process. In other words, the period of the square wave suffers from small random variations. In addition, the manner in which a frequency synthesizer or other generator creates the LO signal (e.g., via a phase-locked loop) may cause the phase of that signal to have small random variations—there is *phase noise*[33]—and the effect on the zero-crossings is similar. We may *effectively* write for the generator output

$$V_{\mathrm{LO}} = A\exp\{j[\omega_{\mathrm{c}}t + \chi(t)]\} \tag{23.27}$$

where $\chi(t)$ is a small random phase function of time t. If we look at the start of the on-resonance, *correctly phased* FID, either by quadrature detection to baseband or by computer manipulation of a digitized IF, essentially $\omega_0 = \omega_{\mathrm{c}}$ and we may see the effect of the noise on the signal:

$$\begin{aligned} V_{\mathrm{on-resonance}} &= \left[V_{\mathrm{LO}}\mathrm{e}^{-t/T_2}\cos\omega_0 t\right]^{\mathrm{filtered}}_{\omega_0=\omega_{\mathrm{c}}} \\ &= \frac{\xi_0 A}{2}\mathrm{e}^{-t/T_2}\mathrm{e}^{j\chi(t)} \\ &\simeq \frac{\xi_0 A}{2}\mathrm{e}^{-t/T_2}[1 + j\chi(t)] \end{aligned} \tag{23.28}$$

The noise is overwhelmingly in the imaginary part of the detected signal as shown in Figure 23.6(a), and importantly, *it is proportional to the signal size* $\xi_0\mathrm{e}^{-t/T_2}$. This is the essential distinguishing feature of phase noise and, whenever "peculiar" noise is observed, phase noise should be suspected and the signal amplitude altered to see if the noise changes.

Phase noise is one of the most neglected and least understood factors in NMR signal reception and one of the most difficult to detect and specify accurately. In consequence, manufacturers of synthesizers and signal generators (particularly digital devices) are able to hide or obscure its significance with ease. *Caveat emptor*! The detection difficulty arises because the phase noise function $\chi(t)$ is usually not white but has a $1/f$ or even a $1/f^2$ noise spectrum. Upon Fourier transformation, it is then manifest as noise localized about a large spectral peak (e.g., a water peak in ^{1}H high-resolution spectroscopy), as shown in Figure 23.6(b). The noise is difficult to quantify because of the large dynamic range. A specification such as "90 dB below the carrier at 1 kHz offset" sounds excellent until it is realized that it says nothing about the noise's frequency spectrum and the bandwidth over which the measurement was made. The noise might only be 50 dB below the carrier at 100 Hz offset in a bandwidth of 1 Hz. The only measurement method known to the author that can be reasonably successful is to take two unlocked identical generators of interest running at the same frequency

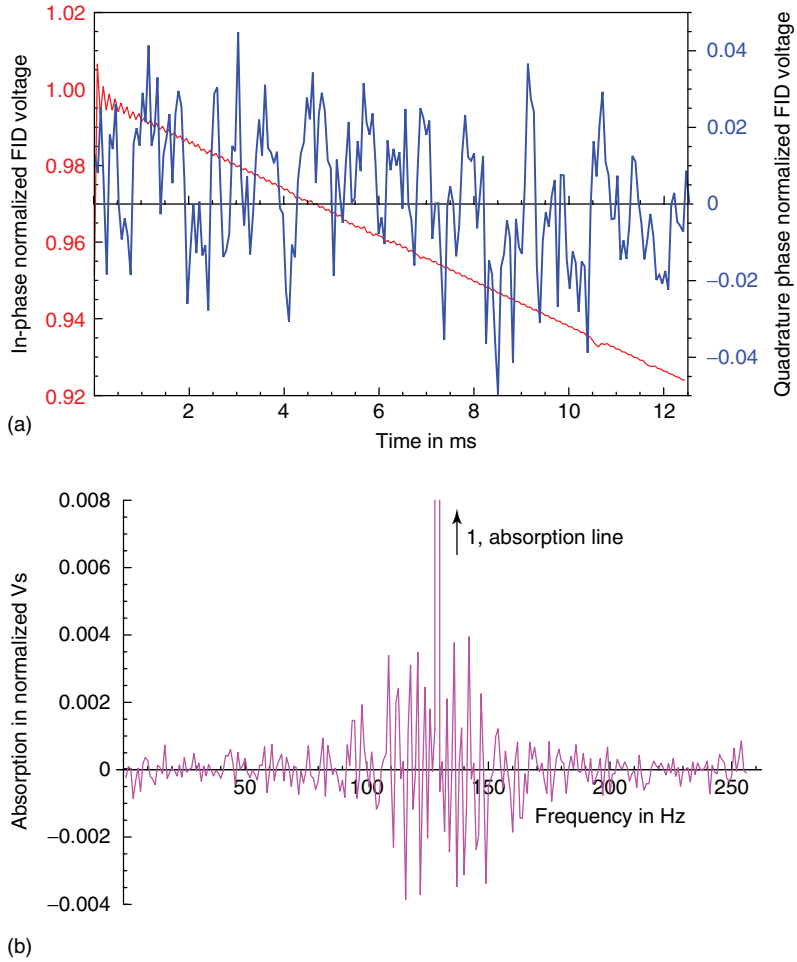

Figure 23.6. Phase noise. The traces in (a) show, *with different offsets*, the in-phase and quadrature components of the start of an on-resonance free induction decay affected by bad phase noise in a LO. The phase noise is overwhelmingly manifest in the quadrature signal and has a Lorentzian spectrum of bandwidth 20 Hz and an amplitude of 1°. Thus well off-resonance, the phase noise varies as $1/f$. (b) Shows the magnified absorption spectrum (unity height) and the $1/f$ noise is clearly evident.

(they will of course slowly drift in frequency relative to one another) and in a mixer use one as the LO and the other as the signal source. The resulting baseband signal is then captured for a second or so when the two generators have drifted into quadrature phase and the signal is, on average, zero. Spectral analysis then reveals the nature and size of the noise, as compared to the noise in the absence of a signal; readers can doubtless think of more sophisticated computational methods to counteract the drift and to average several measurements. Of course, if the two generators lock together, thanks to coupling between them, the measurement may not be representative within the bandwidth over which the generators are able to "pull in" to a locked condition.

Finally, it is important to recognize that noise on the main magnetic field B_0 is also manifest as phase noise, albeit in the signal. The final effects are similar to those already described. Because phase is the temporal integral of frequency f, if the noise on the field varies as f^n, the phase noise varies as f^{n-1}. Field noise can be caused by gradient,

shim, and field-offset power supplies as well as by steel-framed building vibration and random motion of nearby magnetic objects, for example, passing vehicles outside.

23.5 GENERAL TOPICS

23.5.1 Distortion

We now examine remaining design aspects that are common to all parts of the receiver, beginning with distortion.[34] No electronic device is entirely linear in its response and this is particularly true of amplifiers and mixers. Thus, the device's output may be expressed as a polynomial expansion of voltage V_{in}, usually with dominant odd orders. Consider the application of an alternating voltage V_{in} to the polynomial expansion

$$V_{\text{out}} = \sum_{n=0}^{\infty} C_n V_{\text{in}}^n; \quad V_{\text{in}} = A\cos(\omega t + \phi) \qquad (23.29)$$

where n is an integer and the C_n are constants. Note that C_1 is the small-signal gain of the device. Harmonics of the signal, with frequencies $m\omega$ (m is an integer), are generated and we may Fourier analyze V_{out} to obtain their amplitudes:

$$V_{\text{out}} = \sum_{m=0}^{\infty} E_m[C_n, A]\cos(m[\omega t + \phi]) \qquad (23.30)$$

where coefficients E_m are combinations of all the constants C_n and a polynomial in signal size A. For example, $E_3 = A^3C_3/4 + 5A^5C_5/16 + 21A^7C_7/64 + \ldots$. Note the absence of even-order terms. Coefficient E_0 represents *rectification* of the signal—the production of a direct voltage—and $E_0 = C_0 + A^2C_2/2 + 3A^4C_4/8 + 5A^6C_6/16 + \ldots$. Note the absence of odd orders.

Such notation is unwieldy, so the coefficients C_n of the polynomial expansion are typically *not* quoted by manufacturers; rather the *results* E_m of applying signals to the device are quantified in a manner that is practical but involved, and initially rather impenetrable. First, a common method of quantifying the point at which significant overload of a device (and therefore distortion) begins to occur is to report the input voltage A_{IP1} at which the first-order ($m = 1$) output (effectively the gain) is reduced by 1 dB from that expected; i.e., $E_1 = 0.89C_1A$. Voltage A_{IP1} is known as the *input 1 dB compression point*. However, in data sheets it is often expressed not as a voltage but as a power *P1dB* relative to a given value, typically 1 mW. Thus, assuming a 50 Ω system, a 1 dB compression point of 13 dBm (the "m" means "relative to 1 mW") would translate to an rms voltage of $A_{\text{IP1}} = 1$ V. With a variable gain device, it sometimes makes more sense to specify the *output* power (*OP1dB*) at which the compression occurs but, regrettably, this distinction is not always made abundantly clear.

Moving on to specifying distortion, the simplifying assumption is usually made that only the first term in any expression for E_{m} is significant, and if the goal is to have negligible harmonic generation, the assumption is generally valid. Further, as the coefficients C_n tend to decrease rapidly with increasing order, only second- and third-order distortions are usually specified. Thus, we may write the approximations

$$E_1 \simeq C_1A; \quad E_2 \simeq C_2A^2/2; \quad E_3 \simeq C_3A^3/4 \qquad (23.31)$$

The approximations for E_1 and E_3 are plotted on a log–log scale in Figure 23.7. The resulting straight lines are valid where solid and extrapolations where dashed, and they intercept at the *third-order intercept point*. A similar point exists for second-order distortion, but the latter is generally of less concern as it is typically smaller than the third order.

Intercept points tend once again to be defined in terms of specific (but hypothetical) input voltages or power, but it is emphasized that such voltages may well lie beyond the threshold for device damage. Thus

$$A_{\text{IP2}} = \frac{2C_1}{C_2}; \quad A_{\text{IP3}} = \sqrt{\frac{4C_1}{C_3}}; \quad \cdots \qquad (23.32)$$

When the intercept points are expressed in power terms relative to 0 dBm (1 mW), the notation IP2_{dBm}, IP3_{dBm}, etc., is often used, and a rule of thumb for many amplifiers is that IP3 is roughly 10 dB above the 1 dB compression point.

Now, it is the *relative* size of the distortion in a device's *output* that is usually of interest and from the above equations we have that

$$\frac{E_2}{E_1} = \frac{A}{A_{\text{IP2}}} = \frac{E_1}{C_1A_{\text{IP2}}} \equiv \frac{E_1}{E_{\text{IP2}}};$$
$$\frac{E_3}{E_1} = \frac{A^2}{A_{\text{IP3}}^2} = \frac{E_1^2}{C_1^2A_{\text{IP3}}^2} \equiv \frac{E_1^2}{E_{\text{IP3}}^2}; \quad \cdots \qquad (23.33)$$

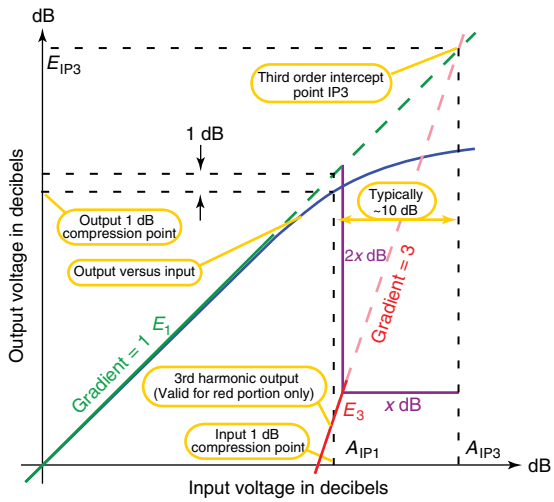

Figure 23.7. Common representations of amplifier distortion using a log–log plot of output versus input. When the output is 1 dB less than that expected from the small-signal gain, the signal is said to be compressed by 1 dB. The third harmonic of the signal (heavy red line) varies as the cube of the input voltage, so on a log–log plot it has a gradient of 3. It therefore intercepts, albeit in extrapolation, the linear gain line. If the input is x dB less than this point, the third-order signal is then $2x$ dB less than the linear signal—but only in the region of validity. Note that if the third-order distortion is measured by a two-tone test, the red line is shifted up by 4.8 dB.

where E_{IPm} is the mth *output intercept point* (see Figure 23.7). Thus, in general,

$$\log E_m = \log E_1 - (m-1)(\log A_{\mathrm{IPm}} - \log A) \tag{23.34}$$

In words, to find the amount of mth-order distortion in the output when working in decibel, we find how many decibels the input is below the intercept point and then subtract $(m-1)$ times this value from the output (in decibels). This statement is clarified in Figure 23.7 for the case of the third harmonic (the magenta lines). Hopefully, study of the figure will produce enlightenment!

If the harmonics are outside the passband of the receiver, it might be thought that they are irrelevant. However, this is not so, as is demonstrated by a so-called two-tone test. If, in equation (23.29) we let

$$V_{\mathrm{in}} = A\cos([\omega+\delta\omega]t+\phi)+A\cos([\omega-\delta\omega]t+\phi) \tag{23.35}$$

representing a strong doublet, then in the passband, additional third-order terms are created of the form

$$E_3 = \frac{3C_3A^3}{4}\{\cos([\omega+3\delta\omega]t+\phi) + \cos([\omega-3\delta\omega]t+\phi)\} \tag{23.36}$$

giving, with the original tones, a spectral quartet. Note that the amplitudes of these sidebands are three times greater than the third harmonic of equation (23.31). Thus, the *two-tone third order intercept point* is IP3/$\sqrt{3}$: it is -4.8 dB down ($10\log_{10}1/3$) on the third-order harmonic intercept point. Note too that the sidebands' phase is ϕ, not 3ϕ; thus they cannot be removed with a transmitter phase-cycling sequence.[29]

23.5.2 Transient Effects

During transmission, the preamplifier is grossly overloaded even with the best T/R switch, and it is therefore advisable to shut down the receiver during the pulse, for example by switching off the LOs to the mixers. Indeed, the receiver must be shut down for considerably longer for the probe rings. A good strategy is to open the T/R switch (but not the receiver) once the ringing from the probe is less than 100 mV, because if the preamplifier has been optimally connected (Section 23.2.4), its input impedance may absorb energy and speed ringdown.[11,24] It might be thought that the correct time to open the receiver for business is when the probe ringing has subsided into the Johnson noise (for an isolated probe this can be as long as $40Q/\omega_0$). However, it is impossible to turn on the receiver without introducing a transient switching voltage, a spike lasting a few nanoseconds. Such spikes induce ringing in the various filters in the receiver, and the narrower the filter bandwidths and the more rapid those bandwidths' roll-offs, the longer the ringing will last. (The transient filter behavior is evaluated from the Fourier transform of the filter transfer function, i.e., from its complex spectrum.) Thus, a general staggered switching strategy is to turn each stage in the receiver on when the transients from the previous stages have decayed to the size of the insipient switching transient. Depending on the frequency, the application, and the receiver design, such a process may last anywhere from 0.1 to 100 μs. This interval is commonly known as the *receiver dead time*.

Imaging applications normally employ echoes, so the dead time is rarely an issue. However, in the

collection of FIDs, one wishes to minimize the dead time so as not to lose the start of the signal. Once this has been done, however, one must not forget the transient responses of the various filters to the abrupt start of the *signal itself*. This topic was thoroughly analyzed in the days when computer memory was expensive and digital-to-analog converters were slow.[35] However, even when sampling at a low IF rather than at baseband, it is worth bearing this factor in mind.

23.5.3 Filters

Filters have been mentioned throughout the chapter but no details have been given. This is because the topic is vast and cannot be isolated from the design of the receiver as a whole. The reader is therefore referred to the huge literature available, as well as to the World Wide Web (see Section 23.7). We give two practical references, Refs 36, 37. The ideal bandpass filter has no group delay ($d\phi/df = 0$), does not ring, and has infinitely fast frequency rolloff outside its passband. Within the passband, its response is flat. It also does not exist. The minimum passband for *all* filters combined is the MR spectral bandwidth, which can be as large as 250 kHz, as has been remarked earlier. Over this frequency range, there should be little variation in the frequency response and a *ripple* (response oscillating slightly with frequency) of a fraction of a decibel is a common standard. In general, the amount of ripple can be traded against bandwidth and filter complexity. To good accuracy, a linear variation of phase ϕ with frequency (constant group delay) is also desirable, particularly when the center frequency is low (e.g., at baseband); at radio frequencies over the small NMR spectral bandwidth, this is virtually guaranteed as the filter bandwidth will generally be much larger than the spectral bandwidth. However, this goal also applies to the sum of *all* filtering in the receiver, so the requirement of linearity is somewhat more stringent than might at first be imagined. Nonlinearity of phase response with frequency can lead to spectral baseline artifacts and difficult spectral phase adjustment. Outside the passband, the rapidity with which the response must fall is determined by the proximity of possible spurs and the need to restrict imaging of noise in the heterodyning (mixing) process. It too can be traded against bandwidth. The author's preference is for *four-pole filters*[36,37] of various types, augmented where necessary by notch filters for removal of specific frequencies. (The transfer function of a four-pole filter is described by a mathematical formula whose denominator is a fourth-order polynomial in $s = j\omega$, $j = \sqrt{-1}$. A notch filter's simplest conception is a tuned parallel LC circuit in the signal path that rejects a specific frequency.) However, *elliptic filters*[37] may be preferable when minimal group delay is wanted. An unusual balanced filter is shown in Figure 23.8. This filter is for use in a 20 MHz IF strip and it rejects all harmonics above the second to better than 40 dB. The same design can be used up to 500 MHz with appropriate dimensional scaling, thanks to the excellent electrical characteristics of a toroidal winding.

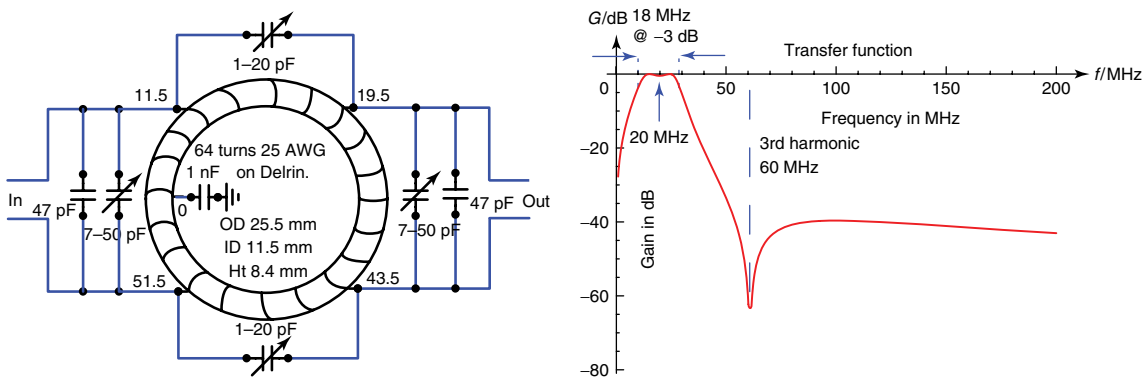

Figure 23.8. An unusual balanced bandpass filter with notch rejection of the third harmonic. While component values and dimensions are shown for a 20 MHz center frequency, thanks to the small self-capacitance of a toroidal winding and its relatively small stray magnetic field, the design is viable with scaling to over 500 MHz.

23.6 DIGITAL SIGNAL PROCESSING

23.6.1 Signal Sampling

The limitations of ADCs have been briefly discussed in the introduction. Once the NMR signal has been digitized, the full power of digital signal processing can be unleashed and, once again, this is a vast topic (a Web search generated nearly three million results) that mostly cannot be addressed here. A respected reference is Ref. 38. However, a few basic points are germane, and the first is the choice of the sampling frequency. It is well known that to retain information and avoid ambiguity, a signal at frequency f must be sampled at a rate greater than $2f$[1]. What is less well known is that sampling at a lower rate is sometimes permissible and that it can change the frequency of the data. Figure 23.9 shows an extreme case where a 101 MHz signal is sampled at 100 MHz. The resulting data clearly oscillates at 1 MHz. Thus, if an IF NMR signal covered the range 101.2–101.3 MHz (a 100 kHz spectral bandwidth), it would be unambiguously sampled and the resulting signals would cover a range 1.2–1.3 MHz, albeit with an excessive number of points. To reduce the number of points so as to improve computational efficiency, we might wish to *undersample* at a lower rate, say 5 MHz, and the resulting points are shown in green in Figure 23.9. There is still a clearly defined 1 MHz digitized signal, and there would be no ambiguity for frequencies between 100 and 102.5 MHz. However, frequencies outside this range would be aliased; for example, a signal at 89 MHz would also present as having a frequency of 1 MHz.

It follows that, if a signal is to be successfully undersampled with no loss of SNR, the *noise* must have a bandwidth less than half the sampling rate. Thus, to maintain the SNR with a 5 MHz sampling rate, the quality factor of a simple tuned circuit filter centred on 101.25 MHz would have to be at least 40, which is a little high for good temperature stability and phase linearity. The mistake is sometimes made of choosing an ADC with excellent resolution (e.g., 16 bits) *at the sampling rate*. However, it must be remembered that the signal being captured has a far higher frequency, and it is imperative that the ADC be able to give its full resolution while capturing a voltage in a time interval in the picosecond range. In addition, limiting the noise bandwidth reduces the noise in the time domain so that the resolution demands are further increased. The arguments presented in the introduction thus come into play once again; clearly, determining optimal specifications/sampling rates is a complicated business, and the "natural" bandwidth of the instrument may be a substantive factor.

23.6.2 Decimation

Once an optimum has been found, Fourier transforming the several million data points comprising an FID or echo and then discarding all but the small spectral

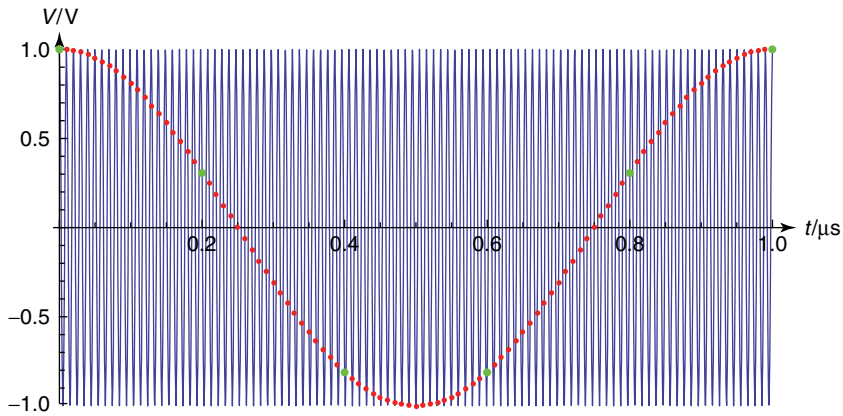

Figure 23.9. A demonstration of undersampling. The signal, of frequency 101 MHz, is sampled every 10 ns (red points). The resulting data clearly oscillate at 1 MHz. The green points show the result of sampling every 200 ns. Oscillation of the data at 1 MHz is still clearly visible.

bandwidth of interest is an inefficient computational process. An alternative approach, and the one generally used, is therefore to *decimate* the data in a specialized integrated circuit. The verb has its origins in the selection for execution of 1 in 10 mutinous Roman soldiers by the drawing of lots; in the digital case, the sampling rate is reduced by ignoring all but every mth sample. Now we have seen that a reduction of the sampling rate requires a reduction of bandwidth to maintain the SNR, and decimation is no exception to the rule. Thus, it is preceded by digital filtering, usually a *finite impulse response* (*FIR*) *filter,*[38] whose description is beyond the scope of this chapter.

Following decimation, the digitized signal can be efficiently Fourier-analyzed to obtain spectral data and, because the frequencies in our example all have the same sign (effectively, the reference frequency sits to one side of the spectrum), there are no concerns of corruption by ghosts and origin peaks. Of vital importance, however, is that the sampling rate ν_1 and the clock rate ν_2 of the digital signal processing integrated circuit be locked to the master oscillator referred to in Section 23.4.6, and that the repetition rate of experiments be connected to the final sampling rate. Thus, one might have a final sampling rate of 1 MHz after decimation, in which case the time resolution of the pulse programmer could only be 1 μs. Clearly, this restriction can be lifted if the digital signal processing mimics baseband analog quadrature detection. Happily, this can be done without introducing the imperfections of ghosts and direct voltage offsets.

23.7 RESOURCES

23.7.1 Information

In conclusion, it is emphasized that the present chapter is merely an introduction to a subdiscipline of a huge and complex subject—RF electronics engineering—that is constantly changing and evolving as integrated circuit design rapidly advances. To keep their documentation timely and relevant, electronics manufacturers have embraced the World Wide Web, as it confers agility, allows customers to search both by desired function and part number, and saves huge printing costs for data that are destined soon to be obsolescent. *Data sheets* with specifications form the heart of electronic documentation—each product has one—and while they can often be overwhelming to the uninitiated, manufacturers invariably have numerous *application sheets* full of tips and explanations. Electronics engineers worldwide have also been zealous in providing independent technical explanations of terms and functions with varying degrees of success (e.g., Ref. 16) but with remarkably few errors. For example, "Googling" the terms "filter poles" in 2011 resulted in over 8 million hits while restricting the search to books resulted in 97 000 hits. Note that many books on electronics have limited Web previews that facilitate browsing. With these resources, interested readers can rapidly fill any voids in their knowledge.

23.7.2 Components

Procurement of small quantities of electronic devices is best handled through online companies that specialize in diverse stocks and overnight delivery. Examples of such companies are Digi-Key, Newark, Mouser, RS Components, Farnell, etc. A few of the many manufacturers of RF products the author has used are given below:*

1. Agilent: Network analyzers, powers supplies, oscilloscopes, etc.
2. Amphenol: RF connectors and cables
3. Analog Devices: Large range of integrated circuits and semi-conductors
4. American Technical Ceramics: High quality-factor capacitors
5. Coilcraft: Inductors and capacitors
6. Emerson: RF connectors and cables
7. Freescale: RF power transistors and FETs
8. Honeywell: RF switches
9. Infineon: RF transistors
10. Intersil: RF transistors
11. Johanson: High-quality-factor fixed and variable capacitors
12. Maxim: Semiconductor switches
13. Microsemi: Switching diodes and PIN diodes for MRI
14. Mini-Circuits: A complete range of small RF amplifiers, mixers, etc.
15. MMD Components: Voltage-controlled crystal oscillators
16. Tektronix: RF oscilloscopes and other instrumentation
17. Programmed Test Sources: Frequency synthesizers

*Disclaimer: The mention of a company's name or product in this chapter in no way constitutes endorsement by the National Research Council of Canada, its institutes, or employees.

RELATED ARTICLES IN THE ENCYCLOPEDIA OF MAGNETIC RESONANCE

Abdominal MRA

Bacteriorhodopsin and Rhodopsin

Dipolar Field and Radiation Damping: Collective Effects in Liquid-State NMR

Magnetic Resonance with Conducting and High-Dielectric Samples

Sensitivity of the NMR Experiment

Sensitivity of Whole Body MRI Experiments

REFERENCES

1. H. Nyquist, *Trans. AIEE*, 1928, **47**, 617; Reprinted in *Proc. IEEE*, 2002, **90**, 280.
2. An example may be found at http://www.analog.com/en/analog-to-digital-converters/ad-converters/products/index.html. May. 2011.
3. Definition of noise colour, http://en.wikipedia.org/wiki/Colors_of_noise. May. 2011.
4. Federal Standard 1037C, U.S. Department of Commerce, National Telecommunications and Information Administration, Aug. 7, 1996. http://www.its.bldrdoc.gov/fs-1037/ fs-1037c.htm. May. 2011.
5. J. B. Johnson, *Phys. Rev.*, 1928, **32**, 97.
6. H. Nyquist, *Phys. Rev.*, 1928, **32**, 110.
7. C. W. Helstrom, *Probability and Stochastic Processes for Engineers*, MacMillan: New York, 1984.
8. C. D. Motchenbacher and J. A. Connelly, *Low Noise Electronic System Design*, Wiley: New York, 1973.
9. J. B. Johnson, *Phys. Rev.*, 1925, **26**, 71.
10. D. I. Hoult and G. Kolansky, In A magnetic-field-tolerant-noise SiGe pre-amplifier and T/R switch, *Proceedings of the International Society of Magnetic Resonance in Medicine*, 2010, Stockholm and references therein.
11. D. I. Hoult, *Rev. Sci. Instrum.*, 1979, **50**, 193.
12. D. I. Hoult, *Concepts Magn. Reson.*, 1997, **9**, 277.
13. D. I. Hoult and N. S. Ginsberg, *J. Magn. Reson.*, 2001, **148**, 182.
14. P. B. Roemer, W. A. Edelstein, C. E. Hayes, S. Souza, and O. M. Mueller, *Magn. Reson. Med.*, 1990, **16**, 192.
15. J. M. Rollett, *IRE Trans. Circuit Theory*, 1962, **9**, 29.
16. An excellent resource for all ultra-high frequency topics, http://www.microwaves101.com. May. 2011.
17. E. W. Matthews, *IRE Trans. Microwave Theory Tech.*, 1955, **3**, 21. See also Ref. 16.
18. C. Bowick, *RF Circuit Design*, 2nd edn., Newnes: Oxford, 2008.
19. D. I. Hoult, G. Kolansky, and D. Kripiakevich, *J. Magn. Reson.*, 2004, **171**, 57.
20. D. I. Hoult, G. Kolansky, D. Kripiakevich, and S. B. King, *J. Magn. Reson.*, 2004, **171**, 64.
21. J. Lindmayer and C. Y. Wrigley, *Fundamentals of Semiconductor Devices*, van Nostrand: Princeton, NJ, 1965.
22. I. J. Lowe and C. E. Tarr, *J. Sci. Instrum. (J. Phys. E)*, 1968, **1**, 320.
23. Microsemi-Watertown, *The Pin Diode Circuit Designer's Handbook*, Microsemi Corp.-Watertown: Watertown (MA), 1998. http://www.qsl.net/n9zia/pdf/pin_diode_handbook.pdf. May. 2011.
24. D. I. Hoult, *J. Magn. Reson.*, 1984, **57**, 394.
25. B. Gilbert, *IEEE J. Solid-State Circuits*, 1968, **3**, 365.
26. M. G. Gingell, *Electron. Commun.*, 1973, **48**, 21.
27. A. G. Redfield and R. K. Gupta, in *Advances in Magnetic Resonance*, ed J. S. Waugh, Academic Press: New York, 1971.
28. J. D. Ellett, M. G. Gibby, U. Haeberlin, L. M. Huber, M. Mehring, A. Pines and J. S. Waugh in *Advances in Magnetic Resonance*, ed J. S. Waugh, Academic Press: New York, 1971.
29. D. I. Hoult and R. E. Richards, *Proc. R. Soc. Lond. A*, 1975, **344**, 311.
30. P. Broekaert and J. Jeener, *J. Magn. Reson.*, 1995, **A113**, 60.
31. A. Louis-Joseph, D. Abergel, and J. Lallemand, *J. Biomol. NMR*, 1995, **5**, 212.

32. A good example of a Johnson counter, http://www.vias.org/feee/shiftreg_07_02.html. May. 2011.

33. E. Rubiola, *Phase Noise and Frequency Stability in Oscillators*, CambridgeUP: Cambridge, 2010.

34. I. Poole, *Newnes Guide to Radio and Communications Technology*, Newnes: Oxford, 2003.

35. D. I. Hoult, C.-N. Chen, H. S. Eden, and M. Eden, *J. Magn. Reson.*, 1983, **51**, 110.

36. A. B. Williams and F. J. Taylor, *Electronic Filter Design Handbook*, McGraw-Hill: New York, 1996.

37. I. Hickman, *Newnes Practical RF Handbook*, Newnes: Oxford, 1993.

38. J. G. Proakis and D. G. Manolakis, *Digital Signal Processing*, 4th edn., Prentice Hall: Upper Saddle River (NJ), 2007.

Chapter 24

Radiofrequency Power Amplifiers for NMR and MRI

Daniel P. Myer

Communication Power Corporation (CPC), Hauppauge, NY 11788, USA

24.1 INTRODUCTION

Radio frequency power amplifiers (RFPAs) are a vital subsystem of any NMR spectrometer (NMRS) or MRI scanner (MRIS). Familiarity with its fundamental function, capabilities, and limitations will prove beneficial to technologists of the various disciplines involved with the design, development, and use of these machines. The objective is to provide an overview of amplifier technology, terminology, specifications, as well as testing and evaluation along with future trends in RFPA architectures.

A comprehensive definition of RF pulse parameters is initially provided, as the sole purpose of the RFPA is the amplification of the RF pulse sequence. Amplifier specifications are delineated and explained in detail with reference to their impact on the RF pulse sequences. Following the nomenclature, methods of testing and analysis are covered, so one can verify performance. A section on application is provided to discuss current and future amplifier architectures, and finally a quick overview of troubleshooting is also included to relate ways in which amplifier performance anomalies can manifest in terms of degradation of system performance.

RF Coils for MRI
Edited by J. Thomas Vaughan and John R. Griffiths

ISBN: 978-0-470-77076-4

24.2 BACKGROUND

A system- and high-level block diagram of an RFPA is shown in Figure 24.1. The architecture of any NMR/MRI RFPA will generally resemble this block diagram. The function of each block is as follows:

1. The pre-driver and driver are low-power amplifier stages that raise the power level of the small, low-level input signal up from the milliwatt range to a level high enough to drive the high-power PA sections. Many PAs may be required to achieve higher power output levels, so divider/combiner networks are deployed to algebraically sum multiple amplifier output power levels together.
2. The directional coupler separates out precise, proportional samples of forward and reflected

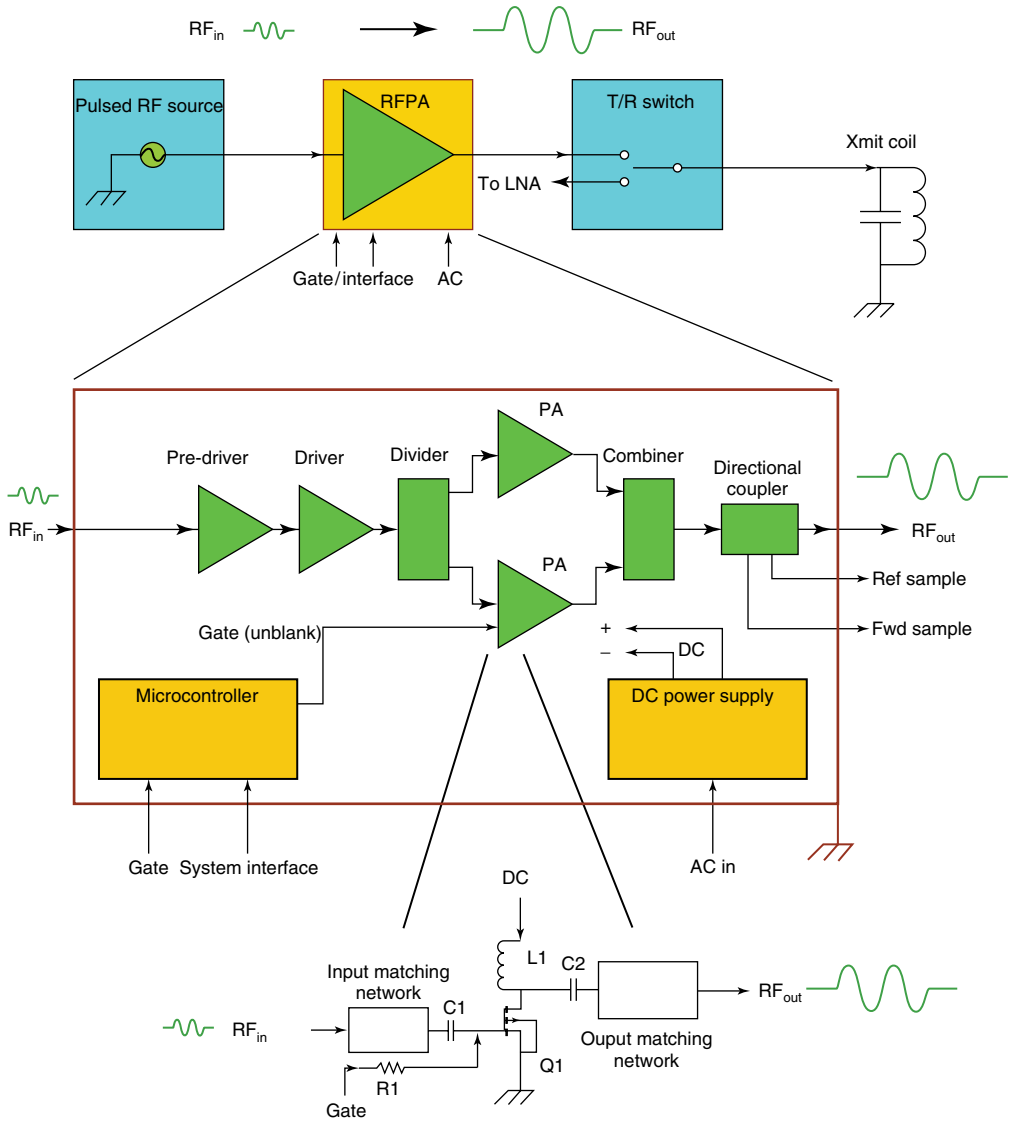

Figure 24.1. RFPA architecture.

signal power for internal/external power monitoring and fault detection.

3. The DC power supply converts AC line voltages into DC voltages that are suitable to operate the pre-driver, driver, PAs, and the microcontroller.
4. The microcontroller is essentially a microcomputer which continuously runs a fixed program loop that monitors several vital operating parameters throughout the RFPA chassis: DC voltages, currents, pulse width, duty factor, RF output power, load voltage standing wave ratio (VSWR), and temperature. In the event any of these parameters get excessive to a point where damage to the RFPA is imminent, the microcontroller will put the system into a fault mode, shut off appropriate circuits, and send out a system status via the system interface.
5. The circuit-level schematic at the bottom of Figure 24.1 shows a basic amplifier stage which consists of input/output matching networks,

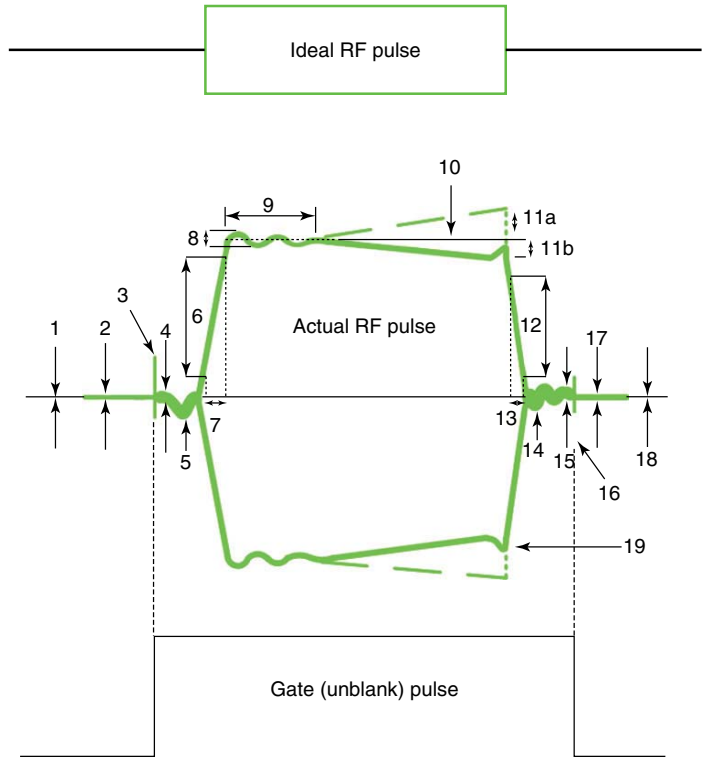

Figure 24.2. RF intrapulse parameters.

an active device (Q1), coupling/decoupling components (C1, C2/L1, respectively), DC supply, and gating voltages. This level of circuit breakdown illustrates what is found architecturally in a pre-driver, driver, or RFPA amplifier stages. Essentially, only two things are done to the RF power that enters an RFPA: transfer and amplification. Any RF circuit in an RFPA does either of these functions. In Figure 24.1, the input/output matching networks are responsible for matching the system 50 Ω impedance with the low impedances of the RF transistors for maximum power transfer. The coupling/decoupling components (C1, C2, and L1) transfer the RF and DC energy in the appropriate directions. The transistor Q1 amplifies the RF signal.

As stated, the basic function of RFPA is simple: amplify or increase the power of an RF pulse signal applied to its input. If the RFPA were ideal, that is *all* it would do: the output would be an *exact* replica of the input waveform, and only the amplitude would be greater by some fixed multiple. But conventional RFPAs are not ideal and they will invariably distort the signal it is meant only to amplify. Just how much it can distort the signal and what is allowable is to be covered.

Since the sole purpose of the NMR/MRI RFPA is to amplify an RF pulse, it is important to fully understand the parameters that define the ideal RF pulse and also define what RF pulse actually emerges from an RFPA. With that knowledge, it is easier to understand how amplifier performance anomalies degrade the characteristics of an ideal pulse.

Referring to the ideal pulse in the top portion of Figure 24.2, an RF pulse train has several defining parameters; since it is ideal, we assume all of them to be perfect. Propagating from the baseline on the left, we have a 0 V reference line, continuing to the rising edge of the pulse, which goes from 0 V to a fixed amplitude in zero time. The pulse continues *exactly* at the fixed amplitude until the end of the pulse width duration and, again in zero time, the amplitude drops to exactly 0 V.

Table 24.1. Pulse parameter definitions

Reference numbers from Figures 24.2 and 24.4	Parameter name	Description	Dimension
1, 18	Ideal, 0 V reference line	Mathematical construct, point of reference for all pulse voltages	Volts
2, 17	Blanked noise voltage	Noise voltage out of RFPA when blanked	Volts
3	Bias enable transient voltage	Voltage spike exiting RFPA when RFPA is initially unblanked pre-RF pulse	Volts
4, 15	Unblanked noise voltage	Noise voltage out of RFPA when unblanked	Volts
5	Pulse preshoot	Amplifier output 0 V reference deviation prior to pulse rise	%
6	Pulse rising edge	10–90% voltage transition range	Volts
7	Pulse rise transition duration	Time required for amplifier to transition from 10% to 90% of peak output voltage	Micro-/nanoseconds
8	Rising pulse overshoot	Portion of RF pulse that exceeds 100% amplitude during post rising transition duration	%
9	Pulse overshoot ringing/decay time	Time for damped sinusoidal envelope peak to decay	Micro-/nanoseconds
10	100% pulse RF amplitude reference	Point on RF pulse that is chosen to be 100%, usually after overshoot and ringing are done	% or volts
11a, b	Pulse tilt positive/negative	Amount that peak RF voltage slopes throughout pulse width duration	%
12	Pulse falling edge	90–10% voltage transition range	Volts
13	Pulse falling transition duration	Time required for amplifier to transition from 90 to 10% of peak output voltage	Micro-/nanoseconds
14	Post pulse backswing	Amplifier output 0 V reference deviation after pulse fall time	%
16	Bias disable transient	Voltage spike exiting RFPA when RFPA is blanked post-RF pulse	Volts
19	Falling pulse overshoot	Portion of RF pulse that exceeds final tilt amplitude pre-falling transition duration	%
20	AM–AM distortion	Interpulse amplitude ratio distortion, also known as gain linearity	Decibels
21	AM–PM distortion	Interpulse relative phase distortion, also known as phase linearity	Degrees
22	Amplitude stability	Long-term gain stability over time	Decibels per hour
23	Phase stability	Long-term phase stability over time	Degrees per hour
24	Phase-error, over-pulse	Phase shift across the duration of a pulse width	Degrees

Let us observe the RF pulse after it has exited a nonideal RFPA. The "actual RF pulse" in Figure 24.2 shows an amplifier's output in the time domain, and for illustrative and explanatory purposes, most forms of time-domain pulse distortion that a typical NMR/MRI RFPA can induce are included. It is interesting to note that, while it takes about four parameters to define an ideal RF pulse, that is, amplitude, frequency, pulse width, and duty factor, it now takes over 20 parameters to characterize a pulse that has been through a nonideal amplifier. Table 24.1 defines the pulse parameters qualitatively. Note that there are two main classes of time-domain pulse distortion: intrapulse distortion; that is, distortion of the pulse per se, or relative to the ideal form of the input (see Figure 24.2); and interpulse distortion, which is distortion of a pulse relative to other pulses in the sequence (see Figure 24.4).

24.3 RFPA SPECIFICATIONS, DEFINITION, AND QUANTIFICATION

Any RFPA can be fully specified by quantifying its RF performance in three domains. A "domain" is simply the x-axis of a basic $x-y$ plot. In the case of RFPAs, x will be a "stimulus" that will be varied (i.e., frequency, power etc.) while certain "response" parameters (i.e., gain, phase etc.) are monitored. The domains necessary to be analyzed to fully characterize an RFPA's RF performance are the time, frequency, and power. The specifications will be conveyed for NMRS, MRIS and, where materially different, for electron paramagnetic resonance (EPR) instruments. Nuclear quadrupole resonance (NQR) demands are generally satisfied by amplifier specifications that work for MRI requirements; only the operating frequency is usually very low (100 kHz–5 MHz).

24.3.1 RFPA Specifications, Time Domain

With the RF pulse parameters defined, specifying the RFPA in the time domain is a natural transition. Note that all specifications in the time domain are in dimensions or ratios of voltages and *not* power (even though *power* amplification is the central focus). The rationale for specifying in the voltage dimension is more than likely a legacy issue; i.e., "that is the way it was always done". One can safely argue that this is the case, as power meters that could visually display a time-domain RF pulse waveform in terms of power dimensions (i.e., watts or dBm) did not become commercially available until the early 1990s, which was years after NMR/MRI time-domain specifications had long been defined and measured by oscilloscopes, which only measure voltage.

24.3.1.1 Generic Time-Domain Specifications

Before getting into specific time-domain requirements, an RFPA for NMR/MRI must meet certain operating pulse requirements. It should be pointed out that an amplifier optimized for pulse operation is vastly different than one that is designed for continuous wave (CW) applications although the RF circuitry is similar. The primary difference between the two amplifiers is the power supply and heat management technologies. A CW amplifier requires a large DC supply to satisfy the demand for high average power. With high average power comes the need to effectively remove heat, so the heat sinks and fans are substantially larger for a CW RFPA. A pulse RFPA is optimized to provide very high RF power pulses with precise fidelity, but for only short periods. The duration of time that a pulse RFPA can put out maximum power is defined as its maximum pulse width. For NMRS, maximum pulse widths are on the order of 300–500 ms; for MRIS, maximum pulse widths are on the order of 20–300 ms. The average power requirements (duty factor) for both NMRS and MRIS are on the order of 10–15% maximum.

24.3.1.2 Bias Enable, Disable Transient

Transistors in RFPAs are typically fed a DC operating voltage through some type of inductive circuit (see Figure 24.1, L1). The purpose of the inductive circuit is to pass DC power to the transistor easily while preventing the amplified RF signal from working its way back into the DC supply. A problem occurs when the bias current is pulsed, i.e., the rapidly changing current generates voltage spikes roughly governed by the familiar equation $V_L = L_1\ (\mathrm{d}i/\mathrm{d}t)$, where V_L is voltage across L_1, L_1 is decoupling inductance, $\mathrm{d}i$ is change in bias current, and $\mathrm{d}t$ is bias current rise/fall time. This voltage spike can make its way to the output of the RFPA even if no input RF signal is applied. The duration of this transient is generally very short and currently has not been shown to inhibit or corrupt images or data; therefore, while it is shown for completeness, it is not formally specified.

24.3.1.3 Pulse Preshoot, Postpulse Backswing

This distortion occurs directly after an RFPA has been unblanked (or the RF pulse is terminated) and appears in the time domain as a half or more cycles of a low-frequency signal superimposed on the unblanked noise voltage. It originates in the RFPA output device and is from the bias and operating current energy of the transistors "fly wheeling" (energy being alternatively stored and discharged) between inductive and capacitive decoupling and coupling circuits, respectively (see Figure 24.1; L1 and C2). Since it is a very low frequency signal, it will be filtered out by the transmit coil. It is generally not specified because of its ultimate removal by this coil.

24.3.1.4 Rise, Fall Time

Now formally renamed by the IEEE as "transition duration", "rise time" is the amount of time an amplifier takes to transition its output at a given power level from 10% to 90% of the voltage waveform. Conversely, "fall time" is the amount of time an amplifier takes to transition its output at a given power level from 90% to 10% of the voltage waveform. *Specification (for both rise and fall time): NMRS: <100 ns, MRIS: 250 ns–10 μs (application dependent), EPR: <25 ns.*

24.3.1.5 Overshoot, Rising/Falling Edge

This distortion usually occurs from inductively stored energy within the RFPA's circuitry. An RFPA (especially the ones used in NMR) has to transition from zero to full power in about 100 ns, and this requires large amounts of current to be switched through inductors very rapidly. This rapid current change causes a voltage spike on the rising and falling edges of the pulse, which gets superimposed on the RF pulse. *Specification (for both rising and falling edge overshoot): NMRS: <5%, MRIS: <13%.*

24.3.1.6 Pulse Overshoot Ringing/Decay Time

As with the pulse preshoot, energy is being flywheeled between inductive and capacitive circuits in the RFPA; this generates a lower frequency, damped sinusoidal wave that is imposed on the initial portion of the RF pulse following the RF rise time and modulates its amplitude. This specification is for the time it takes for the amplitude modulation to drop to less than 5% of the peak RF pulse amplitude. *Specification: NMRS: <500 ns, MRIS: <5 μs.*

24.3.1.7 Pulse Tilt (Formerly Pulse Droop or Amplitude Decay)

When an RFPA is pulsed, it is rapidly switched from "off" to "on" states. When the RF transistors in the amplifier are off, they are at certain temperature; when they are turned on, the temperature of the transistor rises. This increase in temperature can lower (or for certain transistors, raise) the gain of the device over time. If the gain lowers with an increase in temperature, a negative tilt (amplitude of RF pulse lowers with increasing time from left to right) occurs. The converse is true for a transistor whose gain increases with increasing temperature; the tilt is now positive, with the amplitude increasing with time. It should be noted while on the topic of pulse tilt that there exists *no formal definition* of tilt characterization; i.e., there is no IEEE or any other standard that specifies exactly what two points on a given pulse waveform at which to marker the tilt reference points. This has and will continue to be subject to individual interpretation, as a pulse waveform with either a continuously rising or falling amplitude has no formally defined "100%" point. In light of this, quantified specifications for tilt do exist and are included, though it is up to the amplifier manufacturer and end user to concur on where to marker the pulse waveform so they can mutually agree on an acceptable level of pulse tilt. *Specification: NMRS: <5% over a 10 ms rectangular pulse, MRIS: <8% over a 20 ms rectangular pulse.*

24.3.1.8 Amplitude/Phase Stability, Long Term

Most of the RF pulse distortion covered to this point addresses a performance deviation local and specific to an individual pulse. Long-term amplitude and phase stability is concerned with the amplitude and phase characteristics over thousands or millions of pulses during the course of a given pulse sequence. Ideally, it is desired to amplify every pulse exactly the same way without any change in amplitude or phase over a period of time, which can be minutes or several hours. However, changes in environment, primarily ambient temperature, can alter the relative amplitude and phase of an amplifier, as the RF power transistor's gain and insertion phase are influenced by temperature. *Specification: NMRS, MRIS: <0.2 dB over 24 h period, phase stability: NMRS, MRIS: 3° over a 24 h period with the ambient temperature being held constant.*

24.3.1.9 Phase Error Over-Pulse

This type of phase distortion occurs across the duration of a rectangular RF pulse. In cases where the pulse tilt is substantial, the change in output power across the pulse incurs some AM–PM (amplitude modulation to phase modulation) distortion. This means the phase shift from the input to the output of the amplifier changes slightly across the time duration of the pulse width.

Specification: NMRS/MRIS: <5° across a 10 ms pulse width

24.3.1.10 Unblanking, Blanking Propagation Delay Time

(Note: there are two types of unblanking/blanking delay times. The first is relative to the RFPA and is defined below; the second pertains to the RF pulse sequence and how the unblank TTL gating signal is timed relative to the RF pulse and is simply the delay time between the median TTL gating transition duration and the immediately following RF pulse transition duration.)

To reduce the amount of electrical noise an amplifier emits during the NMR/MRI signal acquisition period, the output stages of an RFPA are shut off by removing the bias voltages to the transistors. The objective is to quickly turn the RFPA on, send through some RF pulses, and then quickly turn it off. The signal applied to the RFPA is called a *gating* or *unblank* signal. It is typically a TTL signal and is synchronous with the RF pulse sequence. It is desirable to have the RFPA ready for action as soon as the gating signal is applied. The measure of an amplifier's ability to rapidly turn on and be ready for operation is called the *unblanking delay* and is measured from the median (50% voltage point) of the gating TTL signal to the median (50% voltage point) of the following RF pulse. (*Note*: the test TTL gating signal and the rectangular input RF pulse should have exact, synchronized rise times, assuming the amplifier is TTL active high; TTL high = amplifier unblanked.)

Specification: NMRS: 1 μs, MRIS: 2 μs, EPR: 50 ns

24.3.2 RFPA Specifications, Frequency Domain

This class of specifications covers the RFPA's performance at different frequencies. Ideally, the perfect RFPA would perform *exactly* the same at one key nuclear frequency as it would at another. The specifications listed below define and quantify certain amplifier parameters such that reasonable uniform performance is achieved at each nucleus.

24.3.2.1 Generic Frequency Domain Specifications

The bandwidth of an RFPA is simply the range of frequencies within which the amplifier is expected to comply with certain specifications such as output power, linearity, pulse tilt, etc. An RFPA can be operated outside the specified bandwidth; its performance, however, can and will be compromised.

24.3.2.2 Power Gain

Amplifier power gain is simply a measure of how much a particular RFPA will amplify the power of a signal applied to its input. The equation for power gain is: $G(\text{dB}) = 10 \log \frac{P_{\text{out}}}{P_{\text{in}}}$. The way to determine how much power gain an RFPA needs for a particular requirement is fairly straightforward: simply take the maximum output power required (P_{out}) and the maximum input signal power available and substitute the values into the gain equation. Typically, the available input power from most signal sources is on the order of 1 mW or 0 dBm. So, for example, if a kilowatt of output power was required, an amplifier with +60 dB of gain is needed.

Specification (NMRS, MRIS): $G(\text{dB}) = 10 \log \frac{P_{\text{out}}}{0.001}$ *where* P_{out} *is the required maximum peak power (in watts)*

24.3.2.3 Gain Flatness

The wider the bandwidth a particular amplifier can cover, the harder it is to maintain a constant power gain across the bandwidth. It is more important to have better gain flatness centered on the key nucleus frequency (±500 kHz) than to try to sustain it over frequencies between nuclei where the amplifier will not be operated. There is then the need to specify two types of gain flatness: broadband (or multinuclear) gain flatness and nucleus-centered gain flatness (where the bandwidth is ±500 kHz centered about the key nucleus frequency).

Specification (NMRS, MRIS): Broadband gain flatness: Power gain (in dB) ±3 dB, Nucleus-centered gain flatness (±500 kHz): Power gain (in dB) ±0.2 dB

24.3.2.4 Harmonic Content

An ideal linear amplifier, if one were to graph the output power versus input power, would give a perfect straight line (see Figure 24.3) where the slope of the line would be the power gain amplification factor. This is simply a number that the input power is

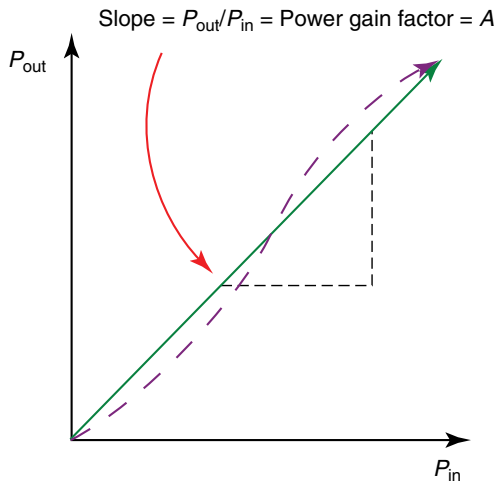

Figure 24.3. RFPA transfer functions.

multiplied by to give the output power. Another characteristic of a linear transfer function is that the output frequency spectrum of the RFPA's output power is simply a larger amplitude replica of the input RF frequency spectrum.

Practical RFPAs are not perfectly linear (the nonlinearity arising from the quasilinear transfer characteristics of the RF power transistors) and the power gain amplification factor is not a linear multiple but actually a complex transfer function with nonlinear terms. Because of the nonlinear terms, there will be output frequency spectra not only at in the input frequency spectrum but also at integral multiples (2, 3, 4, . . ., n) of the input frequency. This is known formally as *harmonic distortion* or *harmonic content*. The bulk of the harmonic energy will be filtered out by the transmit coil, so low-pass filtering of the RFPA's output is usually not required.

Specification (NMRS, MRIS): even-order harmonics: −20 dBc, odd-order harmonics: −12 dBc

24.3.2.5 Spurious RF Output Emissions (Oscillation)

There are many forms of amplifier stability. Amplitude stability, for example, is a measure of the amplifier's ability to maintain a constant output level over long pulse sequence durations. A generic definition of amplifier stability is its ability to maintain an output that is in some way controlled by the input. Spurious RF outputs are erratic frequency components that an RFPA puts out that can be either within its operational bandwidth or outside. The spurious output is sometimes caused by inadequate filtering of the output DC feed lines that couple RF signal power from the output of the RFPA to the input. They can be initially generated when an RF input is applied, yet can remain when the RF input is shut off. They are generally non-harmonic-related and can be close to or far away from the frequency of the carrier. Wherever they are located, however, they are referenced in amplitude to the carrier frequency.

Specification (NMRS, MRIS): < −50 dBc

Another type of amplifier stability is "Load-Pull" stability. This is a measure of the RF amplifiers ability to maintain stable (or a spurious-free spectral) operation while the output (or input) is subjected to various load impedances. Historically, amplifiers have been unrealistically specified as "unconditionally stable" for any magnitude/phase of source/load impedance.

The problem with an "unconditionally stable" requirement is that there is an infinite amount of source and load impedance combinations to apply to an amplifiers terminals. In practicality, this simply cannot be verified.

In reality, the only true "unconditionally stable" two port network is a passive (Gain <1) network.

There is no such thing as an "unconditionally stable" amplifier in the real world.

A more realistic way to specify and be able to verify amplifier stability is to define a load space on the Smith Chart and pick load Reflection Coefficients with discrete magnitude and phase values on which to test for spurious response. For example, a specification for amplifier stability may read: Conditionally stable for up to 3:1 load VSWRs, rotational about the Smith Chart at 45 degrees increments with less than −50 dbc of spurious frequency components.

24.3.2.6 Input VSWR (Input Return Loss)

Input voltage standing wave ratio or input VSWR is measure of how close the input impedance of the amplifier is to an ideal 50 Ω resistor. The closer it is, the better it is matched to the RF signal source (assuming it has a 50 Ω output), and the better this match, the more the power transfer from the pulse

signal source to the RF amplifier. A 1:1 VSWR is a perfect match (i.e., all the power from the RF signal source will enter the RF amplifier). The higher the first number goes, the worse the impedance match is and, consequently, the less will be the power that enters the RFPA's input.

Return loss is simply another way to express input match, in this case as a logarithmic ratio of forward and reflected power. $\text{Returnloss(dB)} = -10 \log P_r / P_f$

Specification (NMRS, MRIS): Input VSWR: <2.0:1, input return loss: < −9.5 dB

24.3.2.7 Output Noise (Blanked)

The NMR signal, be it from a patient or a sample, is very faint. One way to improve the signal-to-noise ratio (SNR) is reduce all unnecessary electrical noise from the environment where the NMR signal is present. An RFPA generates quite a bit of noise while it is on, as it has a large amount of gain. The best way to reduce electrical noise out of an RFPA would be to simply shut it off. The problem with that is it takes far too long to turn the entire amplifier system on and off for it to be effectively used in an NMR/MRI system. The next best thing is to shut off only the final stages of power amplification. This is accomplished by shutting off the bias to the output transistors, as they can be switched on/off in under a microsecond. There will still be some noise output even with the output stage blanked off, to be sure, but the noise output now is tolerable.

Specification (NMRS, MRIS): 20 dB over thermal noise.

24.3.2.8 Noise Figure

An RFPA's job is to transmit sometimes very large amounts of RF power into a sample or patient. The magnitude of this RF energy is very large in comparison to the NMR signal. It may not seem essential for an RFPA to have a low-noise output while it is transmitting since the very thing it is tasked to do is to generate RF power and lots of it. Why then would noise figure be important? The reason is that there are applications where the RFPA is transmitting at one frequency while the RF receivers are listening at another, and the lower the noise figure of the RFPA, the less it will interfere with this second frequency.

Specification (NMRS, MRIS): <10 dB.

24.3.3 RFPA Specifications, Power Domain

This is the last of the three domains. In this area of specifications, the stimulus to be varied is power; that is, the input power to the RFPA is swept across a certain dynamic range (range of power levels, usually 30–40 dB). For example, if an RFPA is driven to full power at 0 dBm input, this unit would be tested with an input RF power level of −40 to 0 dBm. While the power is being varied, certain response parameters are being recorded such as gain and phase linearity.

24.3.3.1 RF Power Output

An RF power amplifier's output power capability is by far the first and foremost parameter that comes to mind when discussing an RFPA. How much power to use for a particular application in an NMRS or MRIS depends on several factors: coil (probe) limitations, specific absorption rate (SAR) values, the part of the anatomy to be scanned (i.e., head, extremities, or whole body), etc. It is beyond the scope of this discussion to quantitatively convey how to specify a maximum power output level for all applications. What can be discussed, however, is a rough estimate of what has been typically used to date. NMR RFPAs usually deposit their outputs into to some chemical sample, which is generally not large in volume. Most NMR applications run at less than 500–2000 W of peak power up to 400 MHz; from 400 MHz to 1 GHz, 100–500 W is adequate, and from 1 to 2 GHz, 30 to 100 W amplifiers have been deployed.

MRIS RF power requirements can vary widely, as discussed. For extremities (arms, legs) in the 1–3 T realm, 500–2000 W is common; for head imaging, 4–8 kW; and for whole body, amplifiers with up to 35 kW have been used. For higher fields (4, 7, 8, 9.4, 10.5, and eventually 11.7 T), requests for power levels of up to 10–32 kW are common. Multichannel 3 T systems are running at 4 kW per channel, and multichannel 7 T RFPAs are designed for 1 kW per channel.

NQR applications have operated in the 2–4 kW range, and the far less common EPR experiments have be executed with anywhere from 400 to 2000 W.

Although NMR and MRIS RFPAs are primarily used for pulsed applications, there are certain applications where they can be required to run in CW

mode. In this event, the required CW power is usually no more than 10% of the amplifier's maximum peak RF output power.

24.3.3.2 Gain Linearity

Pulse sequences can contain RF waveforms that have precisely proportioned amplitude ratios. An ideal linear amplifier has the unique characteristic that its output power is proportional to the input power. Figure 24.3 shows this graphically, which is a plot of output power vs. input power. The linear trace is called a *transfer function*; it describes the transfer relationship of the input to output power of an amplifier. The slope of the line is the power gain factor "*A*", which (in an ideally linear amplifier; a solid, straight plot) is some fixed constant number *regardless* of what power level the output is. In actuality, the transfer function will not have a slope with a constant power gain factor, but one that will change over the dynamic range of the amplifier (dashed, curved plot). What this translates into is that an amplifier will amplify signals at low power with one level of gain, at medium power with another level of gain, and at high power with yet another level. This translates to a nonlinear gain transfer function. Figure 24.4 shows how different amplitude pulses get different power gain factors (A_1 and A_2). The gain linearity specification quantifies how far from the ideal linear operation can an actual amplifier deviate. In cases where the deviation from ideal is severe, the carefully proportioned amplitude ratios in a given pulse sequence can change dramatically.

The gain linearity specification must come with a definition of dynamic range requirement, as it must be understood and clarified, a priori, where the amplifier will be expected to be operated in terms of output power level. Usually, the dynamic range is taken from the maximum specified output power level to some amount of dB down from this level. The amount of dynamic range defined as a minimum should be 20 dB, typically 40 dB, and in extreme performance applications 60 dB.

Specification (NMRS, MRIS): Gain linearity over 40 dB dynamic range: ±1 dB of gain variation.

24.3.3.3 Phase Linearity

It takes a finite amount of time for a signal to make its way through an RFPA from its input connector

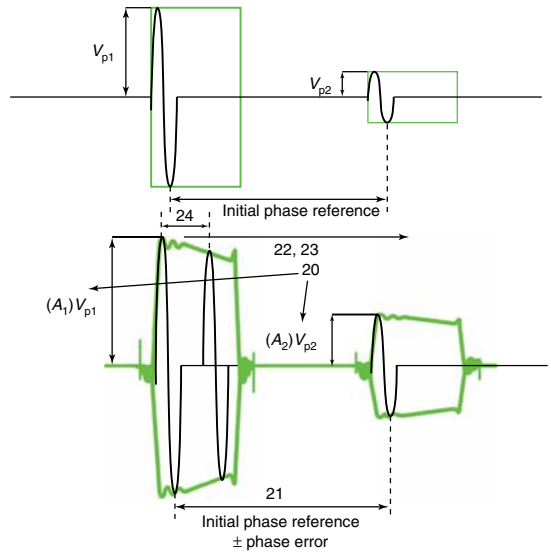

Figure 24.4. Interpulse amplitude/phase relationships.

to its output, and, although it makes it through very fast (on the order of nanoseconds), there is a definite time expended. This delay time is called *propagation delay*, and integral to this measurement is the parameter insertion phase. This is a measure of relative phase shift from the input to the output of the RFPA. As with gain linearity, it would be preferable to have this relative phase shift remain constant across the defined dynamic range of the RFPA. If the phase shift were constant, then relative phase relationships between low-power and high-power pulse signals would be preserved throughout the amplification process. If the relative phase shift changes over the dynamic range, then the phase relationships will be altered. This deviation is defined as *phase linearity* and, as with gain linearity, it comes paired with a defined dynamic range. The root cause of phase nonlinearity is a parasitic junction capacitance present in all types of RF power transistors. This capacitance varies as a function of output power; so, as the output power changes, so does this capacitance, and along with it the relative phase shift through the RFPA.

Specification (NMRS): Phase linearity over 40 dB dynamic range: ±5° of insertion phase variation. Phase linearity (MRIS): ±7.5° of insertion phase variation.

24.3.4 Safety Specifications and System Compatibility Considerations (IEC-60 601 and CE Mark)

Up to this point, the primary focus has been on the amplifier performance relative to its ability to accurately reproduce an RF pulse sequence with an acceptable degree of fidelity. There are two other broad areas of amplifier specifications that are worth covering in general so that the end user or system engineer can be informed of their implications.

Safety is of primary importance with *any* electrical device (see Chapter 32), and RFPAs are certainly no exception. SAR is concerned with how much average RF power is deposited into a patient; one should be *very* clear on what the limitations are and take appropriate protection and have limiting devices in place to automatically shut the RF amplifier off in the event that SAR guidelines are exceeded. It is strongly recommended to have operationally redundant protection measures (i.e., independent, simultaneously operating average RF power monitoring devices) to limit RF power (see Chapter 33).

In addition to patient safety, safety concerns of the individuals who work with the RF power amplifier hardware are equally important.

The safety protocol for both SAR and medical equipment is covered under the IEC-60 601 safety standard. From the equipment perspective, an RFPA compliant to IEC-60 601 will have undergone several months of independent safety tests performed on the unit. Organizations such as Underwriters Laboratories (UL) conduct thorough safety tests, including (but certainly not limited to) verification that the outer chassis is adequately grounded, wire insulation is appropriate for the voltage on a given conductor, circuit breakers and fuses are properly rated for deployment, and various and single-point circuit failures will not present a hazard to the user. Perhaps most important, for a unit that is marked as a "UL recognized component", throughout the duration of that RFPA's manufacturing life cycle the manufacturer will be subject to random audits to confirm that the product is made in conformance to the original UL-approved design in terms of materials and components and also that the appropriate UL-mandated production safety verification tests are conducted with test equipment that is calibrated and within its specified calibration cycle.

System electromagnetic compatibility (EMC) is covered by the IEC-60 601 and the CE mark. The CE mark is what the manufacturer applies to an RFPA after the unit has undergone and passed a battery of safety and EMC tests. EMC tests are concerned with two major attributes of the RFPA: emissions and susceptibility. RFPAs generate a large amount of RF energy; the emissions aspect of EMC/CE testing measures the RFPA's ability to limit and contain its own radiated (RF energy emitted out of the RFPA chassis into its environment) and conducted (RF energy exiting the RFPA on the interface and AC power cables connected to the unit) energy. This is a rough measure of how much an RFPA's operation may affect adjacent equipment.

The susceptibility portion of EMC/CE testing attempts to measure an RFPA's vulnerability to radiated (RF energy it receives from other equipment through the air) and conducted (RF energy it receives internally conducted through AC power lines and interface cables) energy.

In summary, the CE mark/EMC testing is a measure (however, by no means *a guarantee*) of how well an RFPA might perform in a given system environment. A unit that has a CE mark should be less likely to interfere with other equipment; and conversely, its operation should be less impaired by other co-located noise-generating electrical device, environmental disturbances (such as electrostatic discharge, ESD), lightning, and AC power line surges and dips.

24.3.5 RFPA Amplifier Classes

RFPAs are designed to run in certain "classes" of operation. A class of operation loosely defines how the transistors in an RFPA amplify an RF pulse signal. Transistors operating in Class A amplify the full 360° of the RF sinusoidal signal. Class A amplifiers are the most linear, most rugged (ability to tolerate bad loads), least efficient (<20%), and most expensive class of amplifiers. Transistors operating in Class AB amplify slightly more than 180° of the RF sinusoidal signal. Class AB offers a tradeoff between acceptable linearity, ruggedness, efficiency (approximately 50%), and cost effectiveness. Class D/E amplifiers that operate in switch mode (the transistors are switched on/off at the input RF frequency) are highly efficient (approximately 70%), yet extremely nonlinear and require complex linearity error correction networks to make them usable for MRI.

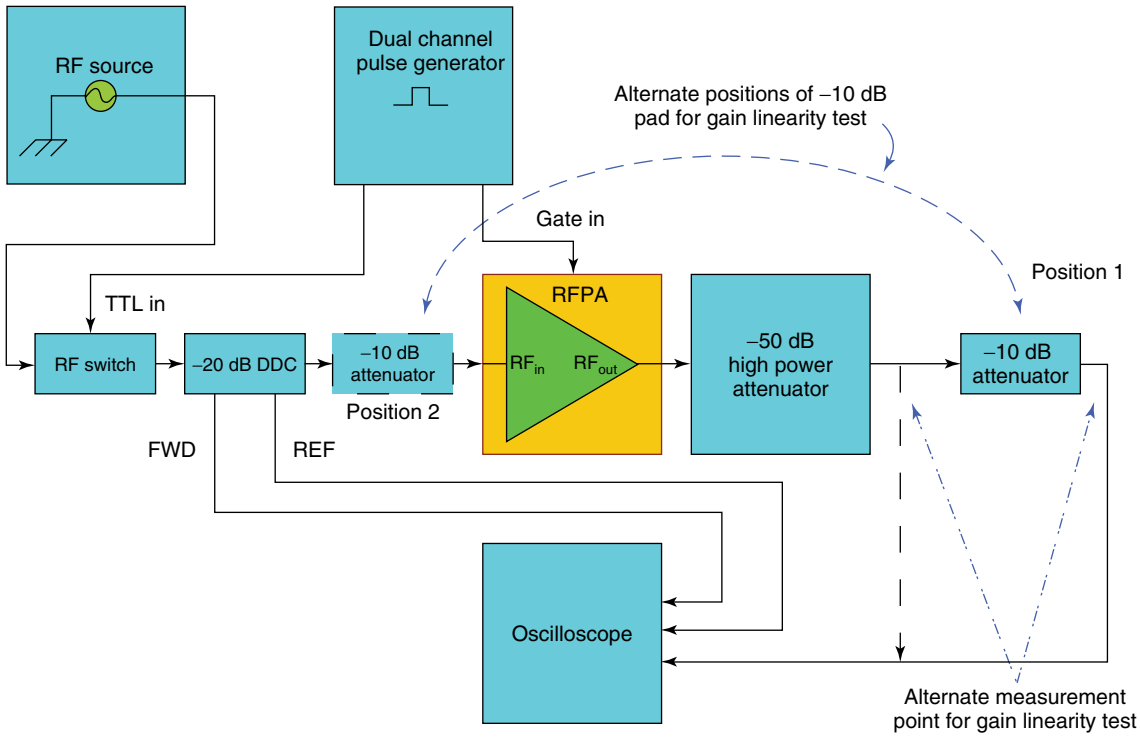

Figure 24.5. RFPA test configuration.

24.3.6 RFPA Testing and Evaluation

The goal of this section is to provide the technologist with quick, cost-effective, and, most importantly, easy way to test and evaluate an RFPA's performance. It is not intended to cover comprehensive test procedures; it will describe brief, discrete tests that use test equipment found in most NMR/MRI facilities and, if properly executed, can reasonably verify if an RFPA is functional within a certain specification.

Figure 24.5 shows only one required test equipment configuration and very few of the pieces of equipment needed for measurement. The other necessary test equipment is as follows (remember to be certain to use only equipment that is within its recommended calibration cycle):

- An RF signal source capable of covering the entire frequency range of the RFPA, and with at least 10 dBm (10 mW) output capability of stable, clean (spurious and harmonic-free) sinusoidal signal.
- A dual-channel pulse generator, with TTL output levels and the ability to synchronize its two pulse outputs yet independently vary the pulse width and duty factor of each channel.
- A four-channel digital storage oscilloscope, with a frequency capability well in excess (at least three times) the maximum frequency of the RFPA's upper limit.
- A high-speed RF switch with switching speed on the order of 5 ns, and one that will switch the CW RF output from the RF source, producing a waveform that approaches an ideal RF pulse as closely as possible; i.e., fast rise/fall times, zero overshoot, ringing, and pulse tilt.
- A dual directional coupler (DDC) with a coupling value of −20 dB, directivity of better than −20 dB, and insertion loss less than −0.75 dB across the operating bandwidth of the RFPA. Be certain to obtain exact coupling values vs. key nucleus frequencies.

Table 24.2. Amplifier test data

Measurement	Dimension	F(low)	F(mid)	F(high)
1) Forward coupling (measured)	dB			
2) Reflected coupling (measured)	dB			
3) −50 dB attenuation (measured)	dB			
4) −10 dB attenuation (measured)	dB			
5) Test power output	dBm			
6) $V_{\text{p-p}}$ at −10 dB attenuator output	Volts			
7) Rising transition duration	ns			
8) Falling transition duration	ns			
9) Pulse overshoot	%			
10) Pulse tilt	%			
11) Input forward power	dBm			
12) Input reflected power	dBm			
13) Input return loss = (11–12)	dB			
14) Gain = (5–11)	dB			
15) Power (−10 dB pad at position 1)	dBm			
16) Power (−10 dB pad at position 2)	dBm			
17) Gain compression/expansion (15–16)	dB			

- Two attenuators, one, a −50 dB high power attenuator that can handle *both* the peak and average RF power output of the RFPA under test; and the second, a lower power −10 dB power attenuator that can handle the RFPA's peak and the average RF power output of the RFPA *after* −50 dB of output signal attenuation. Be certain that both attenuators operate over the bandwidth of the RFPA under evaluation. Obtain the exact attenuation values at key nucleus frequencies either from the manufacturer or using the oscilloscope method described.
- All required RF test cables, connectors, and adapters capable of handling the peak and average RF power levels from the RFPA's output.

24.3.7 Useful Equations and Conversions

For simplicity, the tests have been designed such that only one measurement device, the digital oscilloscope (also known as a *scope*), is required. A scope only measures voltages, so conversion from volts to watts is required for tests where the power level must be known. Equations to do this conversion are presented along with ways to convert and work with power in dBm (power referenced to 1 mW) as this will make calculations significantly easier.

A simple sine wave is shown in Figure 24.4; the scope measures it in the time domain as a peak-to-peak voltage that is denoted as 2 (V_{p1}). To convert this measured voltage to power, we first must convert the peak-to-peak voltage to an rms value: $v_{\text{rms}} = (v_{\text{p1}})\,(0.707)$. For all the tests, the input impedance of all devices must be 50 Ω (including the scope input port). With that in mind, the power measured of the sinusoidal waveform of Figure 24.4 $P_{\text{measured}} = (v_{\text{rms}})^2/50$. Finally, as you will see shortly, if this number is converted to dBm with the equation $\text{Power(indBm)} = 10\log(P_{\text{measured}}/0.001)$, many calculations will be simplified.

With all this in mind, proceed as follows:

1. Set the RF source to the lowest operating frequency (flow) of the RFPA.
2. Set the pulse generator to have a pulse width of 1 ms and 10% duty factor on the channel feeding the TTL control on the RF switch; set the channel feeding the gate input to the RFPA to unblank 10 μs before the RF pulse is turned on and to blank 10 μs after the RF pulse is turned off.
3. Using the oscilloscope (the amplifier under test is disconnected at this point and is turned off as steps 3 through 6 are for calibrating the coupler and power attenuators), apply +10 dBm to the input of the DDC and measure the voltage at the forward (FWD) port. Convert this to dBm and subtract from 10 dBm; this is the exact coupling

value (truncate coupling value beyond the tenth of a decibel). Repeat for the reflected (REF) port. Enter this value in the appropriate row/column in Table 24.2.

4. Using the oscilloscope, apply +10 dBm to the input of the −50 dB pad and measure the voltage at the output port. Convert this to dBm and subtract from 10; this is the exact attenuation value. Repeat for the reflected −10 dB pad. Enter these values in the appropriate rows/columns in Table 24.2.
5. To solve for the peak to peak voltage to be measured on the oscilloscope (that is measuring voltage on the output of the 50 and 10 db attenuator) which would correspond to a full power reading, covert the full power in watts to dbm, subtract the high power attenuators attenuation value in db from this value. Then convert the remaining number from dbm to watts, then from watts to peak to peak voltage.
   For example, given a 1 kW amplifier:

$$P_{\text{out}}(\text{max}) = 1\ \text{kW} = 60\ \text{dbm}$$
$$60\ \text{dbm} - 60\ \text{db(from 50 and 10 db attenuators)} = 0\ \text{dbm} = 0.633\ \text{volts peak to peak}$$

6. Connect the equipment as shown in Figure 24.5, and increase the drive output of the RF source until the full output power of the amplifier is reached (i.e., the voltage from the calculation in step 5 is seen on the oscilloscope).
7. Use the scope to fully measure and characterize the pulse performance in terms of rise time, overshoot, tilt, and fall time. Enter these values in the appropriate rows/columns in Table 24.2.
8. Measure the peak-to-peak voltage at the DDC FWD and REF ports. Convert these values to dBm and enter them in the appropriate rows/columns in Table 24.2. Remember that the voltages measured by the oscilloscope are scaled-down voltages whose magnitude was reduced by the DDC and output attenuator. To get the actual voltages at the terminals of the RFPA, remember to covert the voltage read by the oscilloscope to power (in dBm), and then add the respective attenuation or DDC coupling values to this power to get the actual power at the input/output ports of the RFPA.
9. Move −10 dB pad to input of the RFPA, measure the voltage at the output of the −50 dB attenuator, convert to dBm, and subtract from power level measured previously out of −10 dB pad. Enter this value in the appropriate row/column in Table 24.2.
10. Once all the values are entered, you can now know what the rise/fall times, overshoot, ringing, and tilt values are, and can calculate output power, gain, single-point gain, linearity (either compressive or expansive), and input return loss.
11. Repeat the process over the low, mid-, and high frequencies of the RFPA's bandwidth or simply at key nuclei frequencies.

Upon completing the tests and the associated calculations, the data can be compared with the RFPA's published specifications. Bear in mind that the test technique presented will yield fairly good results but may differ from the manufacturer's data due to difference in test technique and measurement uncertainty.

24.4 RFPA SYSTEM INTEGRATION

With the performance of the RFPA verified, it is time to integrate the RFPA into the system. A few topics are worth mentioning when installing an RFPA:

1. **Rack-mounting:** Most RFPAs come in a standard 19 in. rack-mountable package. A rack without front/rear doors is preferable (but not mandatory) from an air flow perspective. Mount the RFPA on the lowest spot available for a low center of gravity and a stable rack. If you are to make one and *only one* connection properly, be certain to adequately ground the RFPA chassis to the rack ground (using 6 gauge green/yellow band wire) and ground the rack to the NMR/MRI system ground. The amplifier rack should also be seismically bolted to the equipment room floor.
2. **Location:** The amplifier should be as close to the coil as possible to minimize cable losses (especially at high fields such as 7 T). Most RFPAs can work in fringe fields of up to 50 G, so a balance would be as close to the coil as possible without materially exceeding this level of fringe field.
3. **RF connectors:** A few quick words on connectors. First, there is no magic number for maximum peak/average power handling capability; several factors weigh in: operating frequency range, load mismatch, ambient temperature, altitude, and manufacturer. What is listed here is fairly conservative. It is beneficial to be familiar with the following connectors: *BNC:* good

for RF input (0 dBm power levels) cables and gating signals. The following connector power ratings apply up to 2 GHz: *SMA:* Can be used up to 1 kW peak, 100 W average power, *Type N:* 10 kW peak, 500 W average power. *Type SC:* 50 kW peak, 2 kW average power. *Type 7/16th*: 13 kW peak, 3 kW average.

4. **RF Coaxial Cables:** There are literally dozens of RF coaxial cable types. The primary parameters to bear in mind when selecting an RF cable are insertion loss (in dB per foot), peak/average power handling capability, flexibility (if you intend to move it frequently), and cost. And speaking of cost, especially at high fields (4, 7, 9.4 T, etc.), the RF cable is *not* an item to cut corners on. An RFPA for 9.4 T may cost \$50 000–\$100 000. A coax cable run with poor loss characteristics of −3 dB can cost you \$25 000–\$50 000 in RF power! A few recommendations are Times Microwave LMR-400, Andrew heliax, and HF Electronics Ecoflex.

24.4.1 Protection

Coil research can be a trial-and-error process in which the RFPA can be subjected to extreme load VSWRs that can be detrimental. Poor load VSWRs can send large amounts of reflected power back at the output of the RFPA and may damage its transistors. Electronic protection (i.e., VSWR fault circuitry) can shut the amplifier down in the event excessive reflected power is detected, but VSWR fault circuits engage on the order of microseconds and some RFPA damage can occur in this time duration. The most effective RFPA protection involves the installation of circulators in line with the output. Any reflected RF power will be instantaneously diverted to a high-power RF isolation load. The main drawbacks with circulators are they are narrowband, lossy, and available only at frequencies down to about 120 MHz.

24.5 RFPA SYSTEM APPLICATIONS: CURRENT AND FUTURE

The NMR/MRIS RFPA architecture has changed little in the past 20–25 years. Tube amplifiers currently represent a fairly cost-effective modality for narrowband proton amplifiers at 1.5 and 3 T. These are slowly being supplanted by solid-state equivalents. At field strengths of 3 T and higher, obtaining a uniform B_1 field presents a substantial challenge. To alleviate this issue, multichannel RF amplifiers (typically anywhere from 8 to 16 amplifier channels) have been deployed for B_1 shimming. The amplifier requirements and specifications do not vary much; only, now the individual amplifier channels need to be matched for insertion gain and phase. Matrixed amplifiers (amplifiers that can switch between multichannel mode and combined amplifier mode) are now being used where there is a desire to use the RFPA in a conventional single output or switch to a multichannel output mode. The primary challenges in multichannel (B_1 shimming) RFPAs are the gain/phase matching of up to 16 independent channels, especially if the amplifiers are broadband. Another issue is the coupling between transmitter elements, which can lead to high levels of reflected power into the RFPA's output and "virtual VSWR" fault triggering (i.e., reflected power that is not from an adverse load but from element- to-element coupled power).

There is an ongoing move to develop amplifiers that can be located either in the bore (high-field compatible) or mounted just outside the bore. High-efficiency amplifiers may find uses as they run nearly twice as efficiently as conventional Class

Table 24.3. Troubleshooting matrix

Amplifier performance anomaly	Symptom
Excessive gain nonlinearity	Slice profile distortion
Excessive phase nonlinearity	Slice profile distortion
Excessive pulse tilt	Slice profile distortion
Excessive pulse overshoot	Slice profile distortion
Excessive rising/falling transition duration	Slice profile distortion
Excessive blanked noise output	Low signal-to-noise ratio, noisy image
Gain instability	Image ghosting/shading
Phase instability	Image ghosting
Spurious oscillation	Image artifacts/streaking
Low power output	Inability to achieve desired flip angles, increased spatial distortion

AB amplifiers, which may make them a suitable candidate for "in-field" RFPAs.

24.6 TROUBLESHOOTING MATRIX

Table 24.3 provides a brief matrix that lists several types of amplifier performance anomalies and links them with possible manifestations of system performance degradation. Note that these are only possible causes that can be RFPA-related; there may be other subsystem problems that can also cause similar issues.

RELATED ARTICLES IN THE ENCYCLOPEDIA OF MAGNETIC RESONANCE

Radiofrequency Pulses: Response of Nuclear Spins

FURTHER READING

F. Chan, J. Pauly, and A. Macovski, *Magn. Reson. Med.*, 1992, **23**, 224.

Chapter 25
Impedance Matching and Baluns

David M. Peterson

McKnight Brain Institute, University of Florida, Gainesville, FL 32610, USA

25.1 INTRODUCTION

This chapter demonstrates the basic techniques for coil matching and balancing because the radio-frequency (RF) coil is the first stage that is used in the receiver chain: it determines the signal-to-noise ratio (SNR) that can be achieved with that particular coil setup. The optimization of the RF magnetic resonance imaging (MRI) coil needs to consider high-frequency effects, balancing, sample radiation, tissue loading, and multiple coil interactions.[1] This chapter covers balancing and matching. It also covers the use of cable traps[2–5] which aid in the overall stability of the circuit and the coil matching by rejecting the common mode current. Matching schemes can range from a single-ended unbalanced match to partially balanced[1,6] and then completely balanced circuits[7,8] that can be applied in general to all coils and arrays of coils. Inductive matching is acknowledged, and an accurate description by Chen and Hoult can be found on page 136 of their book.[1] Although inductive coupling is an effective way to ensure that a balanced match does occur in the RF coil, it poses other issues. One negative aspect of using inductive coupling to match is near-field perturbation, introduced by the coupled coil, which may introduce small changes to the net field of the RF coil that are visible in the reconstructed image. However, a second issue arises from the safety features required for a receive-only coil: where PIN (positive-intrinsic-negative) diode-controlled traps are used for decoupling during transmission on the receive-only coil, they would require extra wires and chokes to use the inductive coupling method, which is especially important when imaging human subjects. Cable traps are discussed in depth to provide the user with a basic understanding of how to implement them for better-performing coils. This knowledge gained from this chapter, coupled with other articles in the Encyclopedia of Magnetic Resonance, will provide the user with a complete view of RF MRI coil design and applications.

25.2 BACKGROUND

Most traditional matching techniques for RF circuits can be found in various references from electrical engineering, the American Radio Relay League (ARRL),[9] or even MRI-specific references.[1] MRI

RF Coils for MRI
Edited by J. Thomas Vaughan and John R. Griffiths

ISBN: 978-0-470-77076-4

coil engineering is identical to standard RF antenna engineering,[10,11] in regard to matching, because both transform the antenna or coil impedance to the source impedance of 50 Ω. However, a key difference is that the cable should not be part of the MR coil, so the match in all cases should be at the input to the coil. There are cases for remote matching; however, they are not covered in this chapter.[12] The rationale for matching to 50 Ω is to achieve the highest possible SNR and it is understood that the low-noise preamplifier performs optimally when the source impedance is 50 Ω because the preamplifier is "noise matched" at this impedance. However, this assumption also holds true even for the preamplifier used on phased array coils where the input impedance is low, typically <5 Ω. Although there is an impedance mismatch and the coil is no longer power matched to the receiver, this mismatch is used to inductively decouple the coil from its surroundings (i.e., other coils in the array).[13] The impedance mismatch does not reduce the SNR even though it reduces the power delivered to the preamplifier. This is because at high frequencies, it is known that the coils couple through the lossy sample. Thus attaching a coil matched to 50 Ω to a low impedance preamplifier greatly reduces the current flow in the coil during reception, which increases the isolation between loops of an array without sacrificing SNR. However, a problem associated with impedance matching is where the coil couples to the grounded shield of the coaxial cable. This problem is compounded when multiple cables and coils are in close proximity to each other, and a prime example of this is phased array coils. In conventional antenna design, the common method is to wrap the cable or cables around a ferrite core.[9] This creates a large inductive reactance that effectively blocks the unbalanced current from flowing on the shield of the coaxial cable, reducing the losses associated with the shield currents, including radiation losses. Obviously, a ferrite is not appropriate in the MR environment, where strong magnets are used; therefore, in MR applications a narrowband equivalent of the ferrite can be made from lump elements. The simplest way to make a cable trap is to wrap the coaxial cable into an inductor and attach a capacitor across the ends of inductor formed by the shield. By making a resonant structure, the same effects as using a ferrite can be achieved.[8]

Prior to balancing and matching, it should be noted that an MRI coil for a high-field system can be approximated as a lossy inductor as long as the system is not too large. The losses, which can be modeled as resistances, come from many sources: coil components, conductors, capacitively or inductively coupled sample resistance and radiation resistance. Therefore, some basic steps should be taken to ensure that the coil is ready for balancing and matching. In general, the coil should fit into a $\lambda/2\pi$ diameter sphere to be considered electrically small and thereby represented using lump elements. It is important to note that the electrical size may vary from its physical size, making it difficult to accurately describe the structure, but distributing capacitors around the loop force the current to behave like an electrically small antenna. The distributed capacitance should be located away from tissues or shielded to prevent unnecessary losses associated with the electric fields that the capacitors generate.[1] Once the basic coil geometry is constructed, accounting for the previously discussed losses, a match circuit and cable traps can be employed.

25.3 GENERAL MATCHING CIRCUITS

There are many configurations that an MRI coil can take such as the surface coil discussed by Ackerman[14] (see Chapter 1); the quadrature surface coil as discussed by Hyde[15]; double tuned surface coils by Schnall[16] (see Chapter 4); phased arrays as discussed by Roemer[13] (see Chapter 7) and transceiver loop arrays by Duensing[17] (see Chapter 9). Moving away from surface coils, then there are volume configurations such as the double tuned birdcage presented by Murphy-Boesch[18] (see Chapter 12) and transverse electromagnetic mode (TEM) coils presented by Vaughan[19]. All these configurations of MRI coils have one thing in common; they all require matching and balancing to the transmitter or receiver, as appropriate.

In order to concentrate solely on the matching schemes, all matching is applied to an electrically small single loop with a single break for a coil that is assumed to be a fixed tune and match. This loop is shown in Figure 25.1. The input impedance at a particular frequency can be measured at the gap using a network analyzer and a $\lambda/2$ cable. Alternatively, the network analyzer can be calibrated to "zero" or the equivalent length of a $\lambda/2$ cable, allowing the coil builder to use the exact length of cable needed for a particular coil project without regard

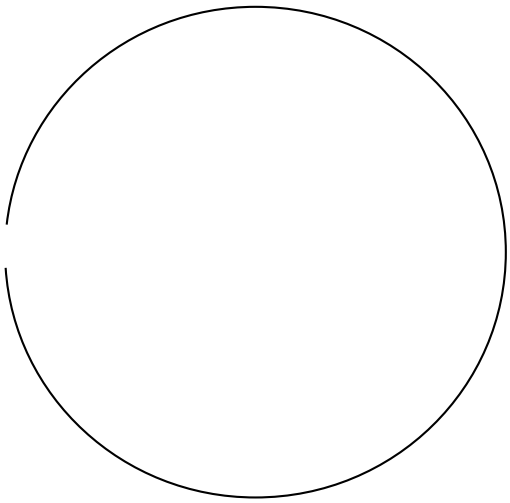

Figure 25.1. An electrically small loop.

to making precisely a $\lambda/2$ cable. Once the input impedance measurement to the coil is obtained, which is a resistance and an inductance, then a variety of matching schemes can be used to match the coil to the load and source. The loop should be placed on the object it is going to image (or suitable phantom) for matching.

25.3.1 The Simple Unbalanced Match

The first matching scheme is for only a single frequency, because reactive components are used in their simplest configuration with just a series component and a shunt component, shown in Figure 25.2. By examining the voltages at the gap of the loop shown in Figure 25.1, the voltage will decrease continuously from V_a to V_b around the loop, where $V_a = V(1 + jx_m/50)$ and, of course, $V_b = 0$. By having a varying voltage around the loop, the loop will couple capacitively to anything at ground or virtual ground. The primary coupling from this loop comes from the top half where the voltage is stronger. Because of this, cable shields may have an unbalanced current caused by the coupling from the loop and any large dielectric, such as the human body, will have a current induced from this effect. Another additional current path may be through the sample, which may cause an electric dipole to form and could result in substantial radiation.

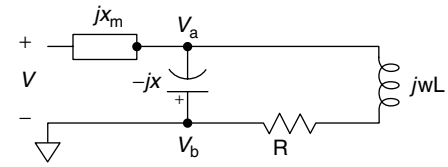

Figure 25.2. Example of a simple unbalanced match.

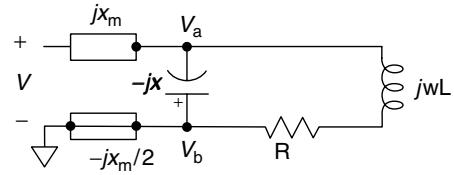

Figure 25.3. Example of a simple partially balanced match.

25.3.2 The Simple Partially Balanced Match

The next matching scheme reduces the coupling shown by the circuit in Figure 25.2 by adding an additional matching element, as shown in Figure 25.3. Now an asymmetric voltage is present, which results in the voltages $V_a = V(1 - jx_m/100)$ and $V_b = V(jx_m/100)$. The potential difference in this circuit is the same; however, now some of the voltage is antisymmetric at the centerline of the coil. There still remains a voltage V, which is unbalanced. While this matching scheme makes improvements, the performance of those improvements is heavily related to the coil design; however, several points can be made. First, no net coupling to a cable that lies along the coil center axis will result from the antisymmetrical voltage. The voltage coupled to a lossy dielectric will only have half of the power versus the previously described circuit and the antisymmetric currents that are induced in the dielectric tend to be an electric quadrupole instead of an electric dipole, thus greatly reducing the radiation from this effect.

25.3.3 The Discrete Balun to Balance a Circuit

When the topology is changed from the previously described matching circuits to a discrete balun, this can be used for matching, as well as balancing the voltage on the coil, as is shown in Figure 25.4.

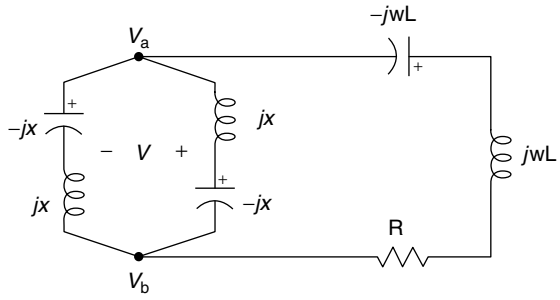

Figure 25.4. Example of a balun to balance a circuit.

Now the voltages become $V_a = V(1/2 - jx_m/100)$ and $V_b = V(1/2 + jx_m/100)$, where the voltage is now symmetric and half as much in amplitude as the previous circuit. This again produces half as much radiation from the electric dipole and half the power loss in the sample compared with the previous case. However, in this case, coupling to a centrally located cable can occur; therefore, this circuit can then change to a completely balanced circuit.

25.3.4 The Truly Balanced Match

In this case, shown in Figure 25.5, y is chosen to equal 50 (the system match), therefore, $V_a = -jV(1 + jx/100)$ and $V_b = jV(1 + jx/100)$, where these formulas describe a perfectly balanced voltage between V_a and V_b, resulting in a much lower potential for cable and sample coupling. These are a few examples of circuit types that can be used to match an MRI coil.[8]

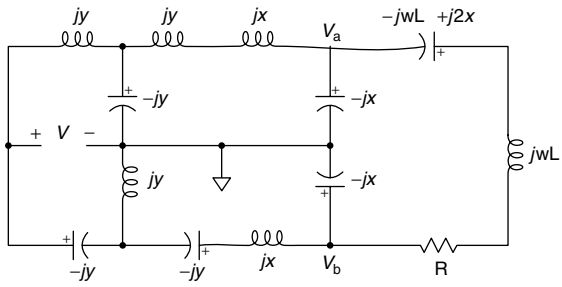

Figure 25.5. Example of a truly balanced match.

25.4 THE SMITH CHART

One of the more useful tools on the network analyzer is the Smith chart. The Smith chart was developed in the 1930s by Philip Smith and associates and has become a staple tool in RF and is shown in Figure 25.6. Its original intention was as a computational tool using a graphical-based method to simplify the complex mathematical operations involving variables of the type $x + jy$, which can typically be used to describe the overall match of an RF coil. The Smith chart is a very valuable tool because it allows immediate visualization of whether a particular matching scheme is capable of achieving the desired match. In addition, the modern network analyzer conveniently displays the real and imaginary impedance of a measurement device, which aids in the design of the matching circuit. The network analyzer measures the reflection coefficient Γ, which is equal to $Z_2 - Z_1/Z_2 + Z_1$. Ignoring the preamplifier impedance mismatch, and assuming a 50 Ω system, maximum power transfer occurs when $Z_1 = Z_2$. The network analyzer Smith chart is normalized to 50 Ω; therefore, 50 Ω is at the origin and the measurements are displayed with reference to the origin and do not need to be converted, unlike when doing Smith charts manually and is pictured in Figure 25.7. There are many good sources of reference to learn how to use the Smith chart and there are many computer applets that can be found with a quick Internet search that will allow fast calculation of matching circuits. These resources can be used to understand the measurements on the Smith chart and use the resources at hand to calculate a matching circuit and implement it.[11,20,21] An excellent book for further understanding of the Smith chart is "RF circuit design", details of which are in the Section "Further Reading".

The reflection that is attained should be less than −15 dB; however, beyond −20 dB there is no practical sense in trying to achieve the "ultimate" match, as it really has no effect on the final SNR, especially when the coil is hooked up to a low-impedance preamplifier. Even in the 50 Ω system, at −15 dB of reflection, approximately 97% of the power is transferred; at −20 dB, 99% of the power is transferred: the 1–3% loss is negligible when compared to the noise figure of the overall system.

Once the coil has been properly matched to the load, it may be noticed that there are cable interactions, which are observed as fluctuations of the

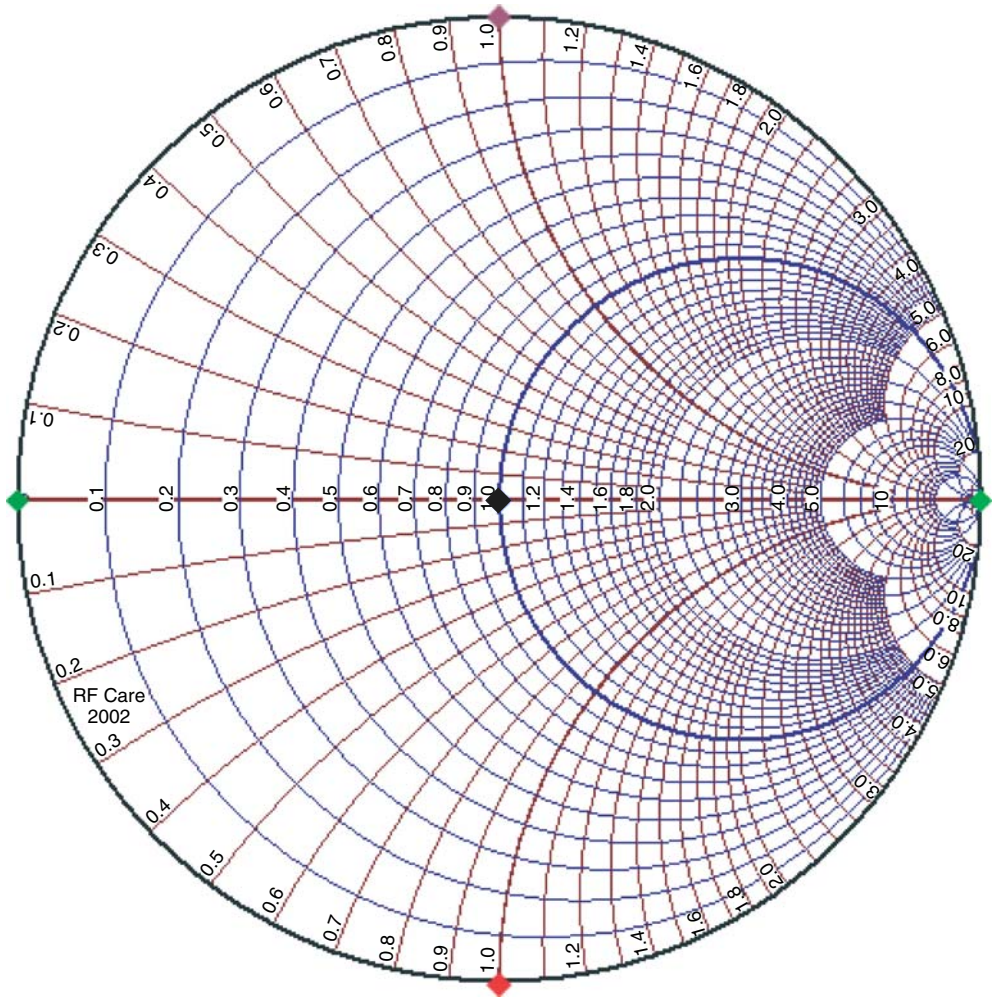

Figure 25.6. Smith chart.

reflection on the network analyzer. If this is the case, then cable traps should be employed to reduce the cable shield currents and stabilize the coil/cable system.[2–5]

25.5 CABLE TRAPS

Common mode signals can be present on the shield of an RF coil cable. As the cable length approaches free-space wavelength or greater, common mode signals can no longer be ignored, because of the significant impact that they have on patient safety and coil performance. Other factors may include coil-to-shield interactions, coupling to other resonant circuits in the system, or coupling to an external case, such as a body coil. However, if the cable shield is truly grounded, then signal on the shield could not exist. The common mode signal is identified as an unwanted signal that occurs on the common or ground, where ground is considered to have zero potential. If this is true, then any average input signal on the common is unwanted. In the case of this work, the shield of the coaxial cable is ground,[22] and we are concerned with suppressing unwanted or common mode signals on the cable shield.

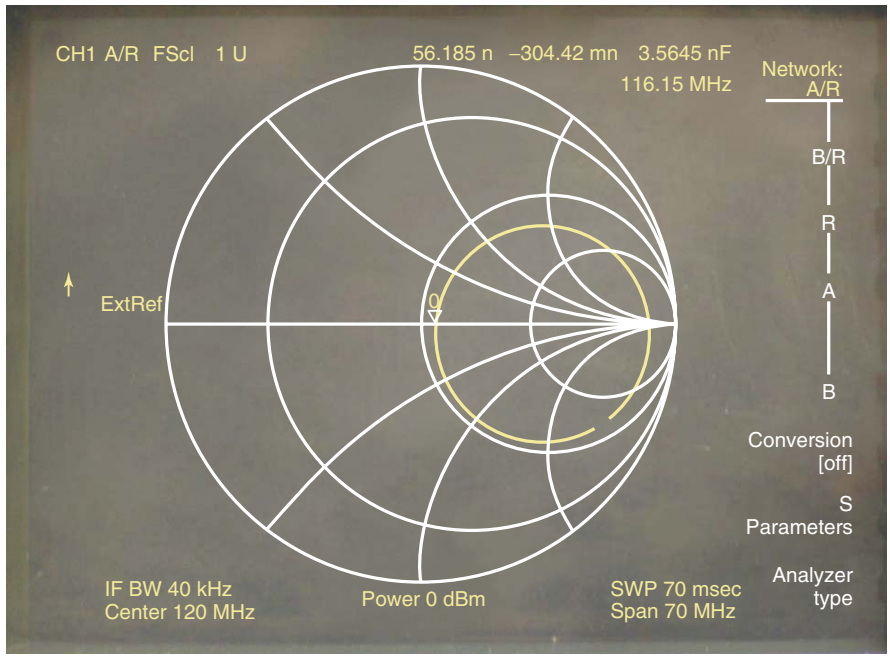

Figure 25.7. Smith chart on a network analyzer.

25.5.1 Theory of Common Modes

As frequency increases, the common mode signals on the cable shield take on characteristics of antennas. The shorter wavelengths of these higher frequencies force the coaxial shield to act as an antenna of arbitrary length and generate antenna current patterns[21] as shown in Figure 25.8, where the maxima occur at distances from the receiver coil corresponding to an odd number of quarter-wave lengths (i.e., 1/4λ and 3/4λ).[10] These issues raise concern for patient safety, since the patient can become part of a conductive loop, which dramatically increases the risk for an RF burn. The secondary detrimental effect is the loss in SNR from excess noise that is introduced into the MR system. The combination of efficient dipole behavior and increased common mode signals directly correlates to measurable currents on the shield of a coaxial cable.

There are two common configurations in which surface coils are used in MRI examinations. The first is the transceiver case, in which the surface coil acts as a transmitter and receiver. The second, but more common case is the receive-only one, in which the coil only acts as the receiver. However, common mode signals for either the surface coil

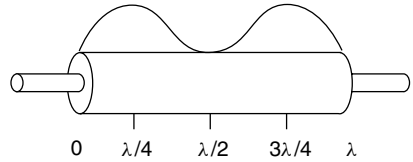

Figure 25.8. Electromagnetic wave traveling down the shield of a transmission line.

case or volume coils can be reduced through the use of balanced matching circuits[1,6,8] and cable shield traps.[2–5]

25.5.2 Application of Cable Traps to Suppress the Common Mode

There are three basic cable traps that can be easily constructed. The first can be constructed by simply forming an inductor with the coaxial cable and then placing a capacitor across the windings of the shield as shown in Figure 25.9. The second case is identical to the first, except a cable that contains multiple coaxial cables is wound into an inductor and the common shield is resonated to prevent current flow

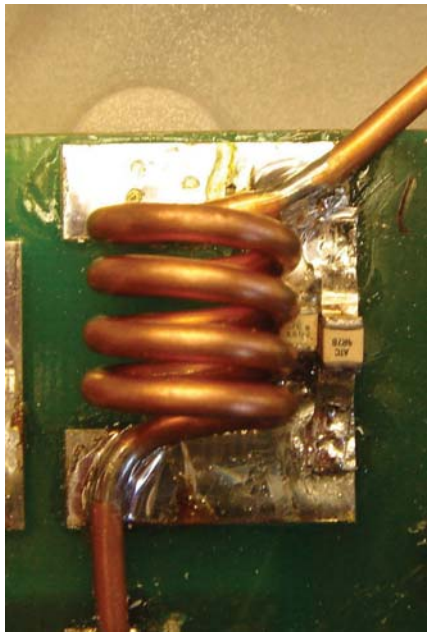

Figure 25.9. Single coaxial-cable-wound trap.

on the outer shield, as shown in Figure 25.10. The final trap is an innovative solution in which a separate resonating structure is coupled to a cable as shown in Figures 25.11 and 25.12.[23]

The common mode current can also be measured on the shield of a cable using current probes and a network analyzer (a typical setup is shown in Figure 25.13), thereby verifying the amount of suppression that the cable trap is providing. A cable trap should provide no less than 20 dB of suppression in order to be effective. The effects of a good cable trap are immediately noticed on a cable/coil system and is shown in Figure 25.14. Any perturbation to the reflection measurement on the network analyzer will be greatly reduced or eliminated.

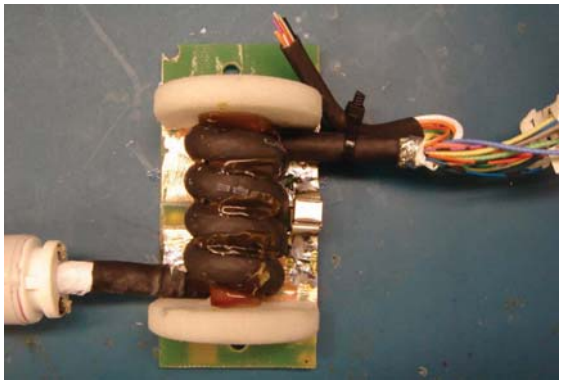

Figure 25.10. System cable trap, multiple conductors, and single shield.

Figure 25.11. Floating shield cable trap.

Figure 25.12. Floating shield cable trap installed on a system cable.

25.6 TROUBLESHOOTING AND CONCLUSIONS

Troubleshooting the matching circuit is typically a very simple process as there is little that can go wrong. Check all connections and solder joints; if they are good, recheck your initial impedance measurement without the match and verify the calculations. Check the component values on an impedance analyzer if they are suspect. As for cable traps, the suppression can be directly measured: if the required suppression is not achieved the cable trap can be moved to a point where "high" shield currents are

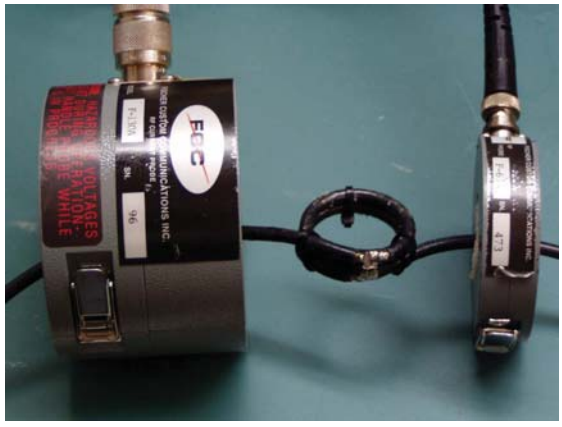

Figure 25.13. Cable trap measurement.

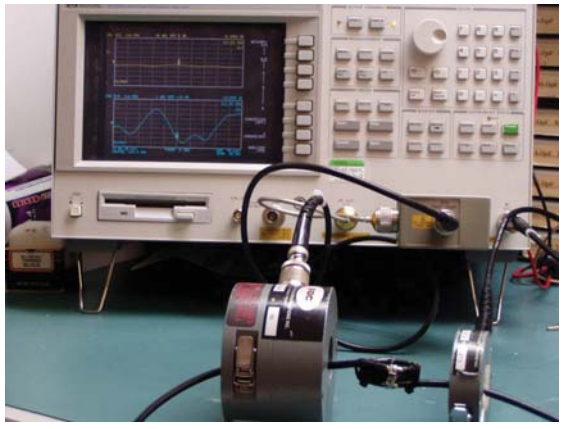

Figure 25.14. Cable trap measurement showing results on the network analyzer.

measured without a trap to achieve the suppression required for the application.

REFERENCES

1. C. N. Chen and D. I. Hoult, *Biomedical Magnetic Resonance Technology*, IOP Publishing Ltd: New York, 1989.
2. H. Barfuss, H. Fischer, D. Hentschel, R. Ladebeck, A. Oppelt, R. Wittig, W. Duerr, and R. Oppelt, *NMR Biomed.*, 1990, **3**, 31.
3. B. L. Beck, D. M. Peterson, G. R. Duensing, and J. R. Fitzsimmons, In *Eighth Scientific Meeting and Exhibition*, International Society for Magnetic Resonance in Medicine: Denver, CO, 2000.
4. D. Peterson, B. Beck, and G. Duensing, In *ISMRM Tenth Scientific Meeting and Exhibition*, Honolulu, HI, 2002.
5. D. M. Peterson, B. L. Beck, G. R. Duensing, and J. R. Fitzsimmons, *Magn. Reson. Eng.*, 2003, **19B**, 1.
6. J. Murphy-Boesch and A. P. Koretsky, *J. Magn. Reson.*, 1983, **54**, 526.
7. G. Duensing and S. Varosi, In *ISMRM Fifth Scientific Meeting and Exhibition*, Vancouver, 1997.
8. D. M. Peterson, G. R. Duensing, and J. R. Fitzsimmons, MRI Basics and Coil Design Principles, RF Design, 1997(January), New York: NY, p. 56.
9. *The ARRL Handbook for the Radio Amateur*, ed. C. Hutchinson, 62nd edn., American Radio Relay League: Newington, CT, 1985.
10. F. E. Terman, *Radioengineer's Handbook*, McGraw Hill: New York, 1943.
11. P. Vizmuller, *RF Design Guide*, Artech House: Boston, MA, 1995.
12. F. Doty, G. Entzminger, J. Kulkarni, K. Pamarthy, and J. P. Staab, *NMR Biomed.*, 2007, **20**, 304.
13. P. B. Roemer, W. A. Edelstein, C. E. Hayes, S. P. Souza, and O. M. Mueller, *Magn. Reson. Med.*, 1990, **16**, 192.
14. J. Ackerman, T. Grove, G. Wong, D. Gadian, and G. Radda, *Nature*, 1980, **283**, 167.
15. J. S. Hyde, A. Jesmanowicz, T. M. Grist, W. Froncisz, and J. B. Kneeland, *Magn. Reson. Med.*, 1987, **4**, 179.
16. M.D. Schnall, V. Harihara Subramanian, J. S. Leigh Jr, and B. Chance, *J. Magn. Reson.*, 1985, **65**, 122.
17. G.R. Duensing,, D.M. Peterson, B.L. Beck, and J.R. Fitzsimmons, in *Eighth Scientific Meeting and Exhibition*, International Society for Magnetic Resonance in Medicine: Denver, CO, 2000.
18. J. Murphy-Boesch, R. Srinivasan, L. Carvajal, and T.R. Brown, *J. Magn. Reson. B*, 1994, **103**, 103.
19. J.T. Vaughan, H.P. Hetherington, J.O. Otu, J.W. Pan, and J.M. Pohost, *Magn. Reson. Med.*, 1994, **32**, 206.
20. D. M. Pozar, *Microwave Engineering*, 2nd edn., John Wiley & Sons Inc.: New York, 1997, 716.
21. F. Ulaby, *Fundementals of Applied Electromagnetics*, Prentice Hall: New Jersey, 1999, 433.

22. R. Morrison, *Grounding and Shielding Techniques in Instrumentation*. 3rd edn., Wiley-Interscience: New York, 1986, 172.

23. D. Seeber and J. Menon, *Magn. Reson. Eng.*, 2004, **19B**, 26.

FURTHER READING

C. Bowick, J. Blyler, and C. Ajluni, *RF Circuit Design* 2nd edn., Elsevier Inc.: Boston, 2008, p. 86.

PART F
Coil Modeling and Evaluation

Chapter 26

Radiofrequency MRI Coil Analysis: A Standard Procedure

Rostislav A. Lemdiasov[1] **and Reinhold Ludwig**[2]

[1]*Insight Neuroimaging Systems, 11 Canterbury St., Worcester, MA 01610, USA*
[2]*ECE Department, Worcester Polytechnic Institute, 100 Institute Road, Worcester, MA 01609, USA*

26.1 INTRODUCTION

When designing radio frequency (RF) coils for magnetic resonance imaging,[1–3] there is often a need to compare competing coil/coil array architectures in terms of their field uniformity, field of view, and signal-to-noise ratio (SNR). Numerical simulations can accomplish this comparison effectively prior to manufacturing, and thereby save significant resources as well as time-to-market constraints. Assessing the most suitable design among many competing candidates for the intended applications, allows us efficiently proceed with prototyping and field testing.

Full-wave numerical methods including the finite difference time domain (FDTD), finite element method (FEM), and method of moments (MoM) have been widely used to simulate MRI coils and predict their performance.[4] These computational methods alone, however, are not sufficient to characterize an RF coil. In general, they have to be combined with proper post-processing steps to render a valid assessment of the coil.

For many design engineers, one of the major figures of merits in coil performance is a high SNR. Roemer *et al*.[5] describe how one can maximize the SNR for a coil array. Signals received by individual channels of the receive coil array need to be combined with certain weights to achieve the highest SNR at a certain point in space within a particular spatial domain. The weights are calculated based on the magnetic B_1 field patterns of particular channels and also on the resistance matrix of the system. The authors propose that the computation of the resistance matrix is carried out by integrating the electric fields over the load.

Wright and Wald[6] concentrated on a problem of calculating the SNR for coil arrays. Unlike Roemer,[5] their approach is more computationally tractable. However, the problem of calculating the resistance

RF Coils for MRI
Edited by J. Thomas Vaughan and John R. Griffiths
 ISBN: 978-0-470-77076-4

matrix is addressed in a similar manner as reported in Ref. 5.

For a complete coil analysis, it is important to determine the specific absorption rate (SAR) of the transmit coil. Rojas *et al.*[7] use FEMLAB to compute both the SNR and SAR of a coil. Even though the details are not shown, the numerical method they developed can be used to study the performance of phased arrays.

Jiao and Jin[8] used the MoM approach to simulate a birdcage RF coil. They demonstrated that an asymptotic waveform evaluation (AWE) method can be developed which yields solutions for a range of frequencies near the resonance point. This saves valuable resources since a full scale MoM simulation has to be performed only at a single frequency.

Among recent contributions to quantify SNR and SAR, we should also mention Paska *et al.*[9] and Zhang *et al.*[10] These authors prove that lumped components can be introduced into the coil *after* the full-wave analysis is performed. Tuning and matching of the coil is then accomplished as a post-processing step. Again, this saves significant amounts of time and computation resources because full-wave simulations are performed only once. Furthermore, the electric and magnetic fields can be computed as linear combinations of fields that are calculated during the full-wave simulation.

In a comprehensive article, Kozlov and Turner[11] describe in detail the process of simulating an RF coil. They state that full-wave simulations are to be performed before lumped elements are introduced into the coil model for tuning and matching. They establish a two-way link between 3D electromagnetic (full-wave) simulations and an RF circuit simulator. Figure 26.1, in their article, provides a basic work flow diagram that describes how an RF coil is simulated.

Finally, Lemdiasov *et al.*[12–13] outline a standard procedure for simulating RF coils based on the MoM method. As an example, they use a four-channel breast coil to demonstrate the steps involved in the simulation.

In this chapter, we expand upon the approach laid out in the previous study[12–13] by systematically developing a numerical design approach for RF coils. To make the procedure tractable, we focus on a two-channel coil as an example. The goal of this chapter is therefore to provide the reader with an in-depth understanding of the design process. Although we use the MoM method as the full-wave numerical modeling approach, other methods (FEM, FDTD) could be substituted just as efficiently.

26.2 STRUCTURE

As mentioned above, we consider as a generic example an array of two rectangular loops that share a detuning capacitor. Figure 26.1 depicts the coil geometry in air and over a dielectric load.

The loops are positioned on a cylindrical surface. Each of the loops contains one break to accommodate tuning capacitors, one break for a matching capacitor and cable, and one shared break for a decoupling capacitor. In total, there are five breaks in the structure and consequently we define $N_{\text{structure}} = 5$ to denote the number of ports. In the following, the structure is simulated at a frequency of 63.65 MHz corresponding to proton imaging at 1.5 T. We set the surface conductivity to $\sigma = 7.95 \cdot 10^7$ S m^{-1} (copper). And we assume that each capacitor has a series resistance that is estimated based on the quality factor provided by manufacturers such as Voltronics or ATC. The coil is loaded by a cylindrical load (diameter 5″, height 6″) having properties of human muscle.

In the following, we outline the coil design flow as a sequence of well-defined steps that render the entire approach suitable for computerized evaluation. As a first step, we need to generate a triangular mesh of the coil surface and a tetrahedral mesh for the volumetric load (Figure 26.1). Since meshing is nowadays a standard process that can be performed with a host of software packages, we will not go into further details.

26.3 S-MATRIX

As a second step, we are required to compute the scattering, or S-matrix of the structure. The full-wave software (FEM, FDTD, MoM) needs to solve the system of linear equations five times. The reason for this is the fact that we have to drive in turn each port, while the remaining ports are terminated by a 50 Ω load. Besides obtaining a [5 × 5] S-matrix of the system, we obtain five individual solutions, or solution vectors, associated with the corresponding columns of the S-matrix. Depending on the full-wave method employed, these individual solutions may contain values of currents in the current elements, or values of electric/magnetic fields in the corresponding elements.

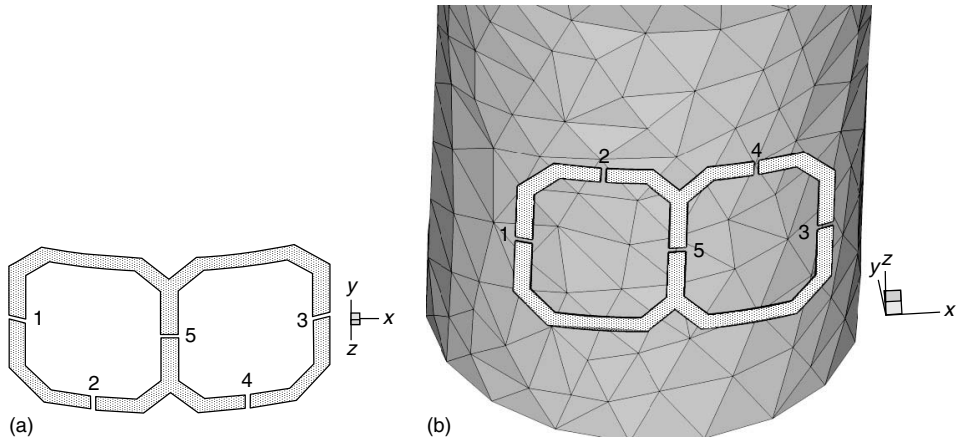

Figure 26.1. Mesh of a two-channel coil. (a) Unloaded and (b) loaded.

These individual solutions are often calculated under the assumption that the incident power wave a is $a = \sqrt{2}A\sqrt{\Omega}$, which corresponds to 1 W power wave incident into the ports of the structure.

26.4 TUNING, MATCHING, AND DECOUPLING

After the S-matrix of the coil arrangement is established, we need to terminate the ports of the structure by lumped elements/circuits. In our particular case, we have three one-port networks (tuning capacitors and a decoupling capacitor) and two two-port networks (matching capacitors).

26.4.1 Expanding S-matrix

We can regard the entire coil structure with its lumped elements as the system that is generically depicted in Figure 26.2. Specifically, the original five-port coil is shown in Figure 26.2(a) with the needed lumped elements. The actual coil system configuration with its lumped element terminations results in a 12-port network and is displayed in Figure 26.2(b).

The size of the total S-matrix is

$$N = N_{\text{structure}} + N_{\text{lumped}} \tag{26.1}$$

where $N_{\text{structure}} = 5$ and $N_{\text{lumped}} = 7$.

The expanded S-matrix S_{exp} of the 12-port device contains the original $[N_{\text{structure}} \times N_{\text{structure}}]$ or $[5 \times 5]$ S-matrix of the structure in the upper left corner; it also contains the S-matrices of lumped elements along the diagonal, as shown in Figure 26.3.

We next need to interconnect certain ports of S_{exp}. In particular, port pairs 1 and 6, 2 and 7, 3 and 9, 4 and 10, and 5 and 12 are interconnected. This implies that the following relationships are valid:

$$\begin{aligned} a_1 &= b_6, \quad a_6 = b_1 \\ a_2 &= b_7, \quad a_7 = b_2 \\ a_3 &= b_9, \quad a_9 = b_3 \\ a_4 &= b_{10}, \quad a_{10} = b_4 \\ a_5 &= b_{12}, \quad a_{12} = b_5 \end{aligned}$$

where a and b are incident and reflected power waves. Ports 8 and 11 are not interconnected. Since they remain free, we call them free ports. The number of free ports is then $N_{\text{freeports}} = 2$. The following system of linear equations is true:

$$S_{\text{exp}}\, a = b$$

Performing several simple linear operations with this system of equations we reduce it to $[N_{\text{freeports}} \times N_{\text{freeports}}] = [2 \times 2]$ form:

$$S_{\text{reduced}} \begin{pmatrix} a_8 \\ a_{11} \end{pmatrix} = \begin{pmatrix} b_8 \\ b_{11} \end{pmatrix}$$

Here, S_{reduced} is now a matrix of the two-channel RF coil at the center frequency of interest.

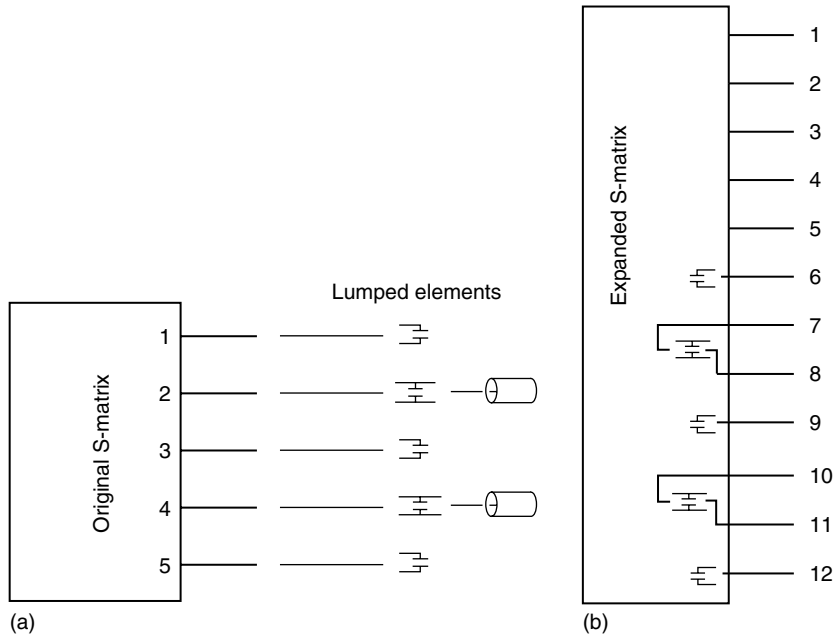

Figure 26.2. (a) Terminating the coil structure by lumped elements and (b) expanded structure.

$$S_{\text{exp}} = \begin{pmatrix} [5\times 5] & & & & \\ & [1\times 1] & & 0 & \\ & & [2\times 2] & & \\ & & & [1\times 1] & \\ & 0 & & & [2\times 2] \\ & & & & & [1\times 1] \end{pmatrix}$$

Figure 26.3. Expanded S-matrix structure of the 12-port coil system.

26.4.2 S-matrix Extrapolation

To be able to tune and match the coil, we need to know the S-matrix in the neighborhood of the center frequency. One way to accomplish this is to perform full-wave simulations at a number of frequency points neighboring the center frequency, a very time-consuming task. Another option is to use an extrapolation technique to find the S-matrix for neighboring frequencies.

We outline how the extrapolation is done for the example of a single loop with one break. The loop can originally be characterized by its S-matrix at a center frequency of ω_0. The admittance of the loop is then $Y(\omega_0) = \frac{1}{Z_0}\frac{1-s(\omega_0)}{1+s(\omega_0)}$. Inductance L and resistance R are calculated as $L = \frac{1}{\omega_0}\text{Im}(\frac{1}{Y(\omega_0)})$ and $R = \text{Re}(\frac{1}{Y(\omega_0)})$. It is assumed that inductance and resistance are weak functions of frequency in close proximity to ω_0. In fact, for our purposes we can consider them to be constants. We next compute the admittance of the loop at frequency ω as $Y(\omega) = \frac{1}{R+j\omega L}$ and the S-parameter as $S(\omega) = \frac{1/Y(\omega)-Z_0}{1/Y(\omega)+Z_0}$.

The interpolation procedure can be modified to be applicable for structures with multiple breaks (ports), see, for instance, Ref. 12. It is important to mention that this interpolation procedure works for structures exhibiting "inductive behavior", such as an MRI coil. Care needs to be exercised when using this procedure at high frequencies, as it may not produce accurate results.

26.4.3 Tuning and Matching

We now select initial values for tuning, matching, and decoupling capacitors and plot the S-parameters in the frequency range containing the center frequency. On the basis of these plots we can then adjust the values of the capacitors and arrive at their final values. The values are summarized in Table 26.1.

The corresponding S-parameter plots are shown in Figure 26.4, where the magnitude and phase of the

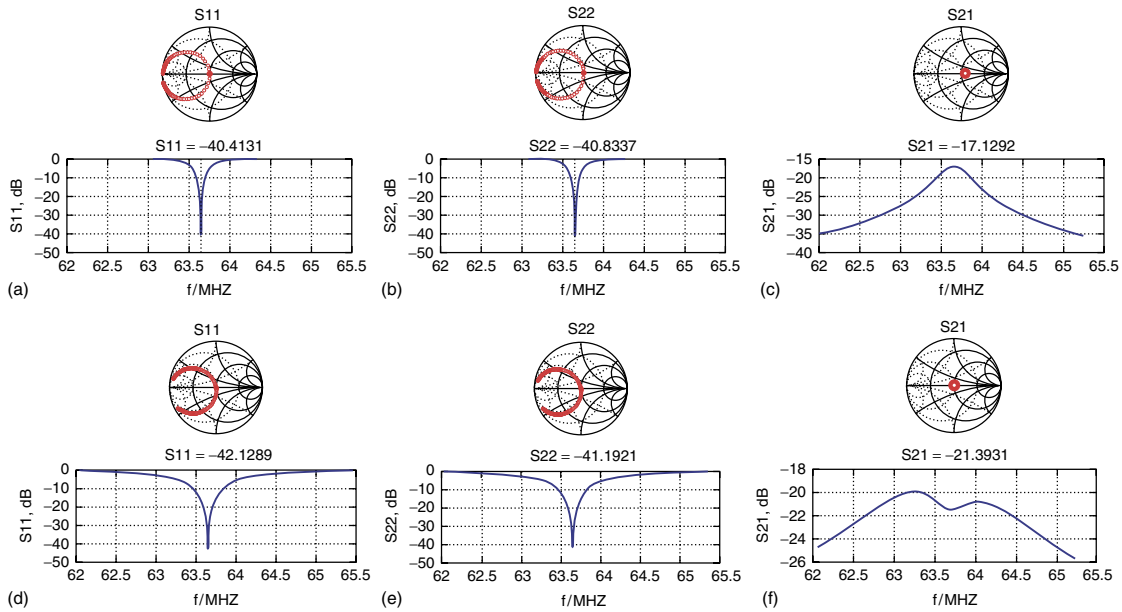

Figure 26.4. (a) Unloaded S_{11}, (b) unloaded S_{22}, (c) unloaded S_{21}, (d) loaded S_{11}, (e) loaded S_{22}, and (f) loaded S_{21}.

Table 26.1. Values of tuning, matching, and decoupling capacitors

	C_{tune}, pF	C_{match}, pF	C_{det}, pF
Unloaded coil	77.5	1105	357.7
Loaded coil	82.5	580	358

individual S-parameters are displayed in the Smith Chart format (a–c) and magnitude only (d–f) format.

In Figure 26.4, points at the center frequency are calculated by the full-wave method. The S-parameters at every other frequency point are extrapolated using the technique described in Section 26.4.2.

26.5 VOLTAGES, CURRENTS, AND POWER

When tuning an RF coil, we deal with two vectors of incident power waves a_1 and a_2 that describe power flow into every port of the expanded structure. These vectors correspond to the case when the first free port and then the second free port are driven. From these power waves we can find the reflected power waves b_1, b_2; currents I_1, I_2; voltages V_1, V_2; and power transfers P_1, P_2 for every port of the expanded structure according to equations (2)–(5). From this point onward, we omit subscripts "1" and "2", keeping in mind that the values in the following expressions need to be calculated for both free ports.

$$b = S_{\text{expanded}} \times a \tag{26.2}$$

$$V = \sqrt{Z_0}(a + b) \tag{26.3}$$

$$I = \frac{1}{\sqrt{z_0}}(a - b) \tag{26.4}$$

$$P = \frac{1}{2}\text{Re}(V \times I^*) \tag{26.5}$$

The power expression [equation (5)] describes the time-averaged RF power flow in and out of the ports of the structure and its lumped components. Using equation (5) we can calculate the power dissipation in every lumped component of the coil. For instance, the power loss P_{lumped} in all lumped elements can be calculated by adding the power flow into all lumped ports, that is,

$$P_{\text{lumped}} = \Sigma_{n=N_{\text{structure}+1}}^{N} P_n \tag{26.6}$$

To obtain more complete information about the total power flow, we also need to calculate the power loss inside the conductors, the load, as well as the power loss due to radiation. Specifically, the power

loss inside the conductors and the load is calculated according to:

$$P_{\text{conductor}} = \frac{1}{2}\int_{V_{\text{conductor}}} \sigma |E|^2 \mathrm{d}V \qquad (26.7)$$

$$P_{\text{load}} = \frac{1}{2}\int_{V_{\text{load}}} \sigma |E|^2 \mathrm{d}V \qquad (26.8)$$

The total power inflow into the system is

$$P_{\text{total}} = \Sigma_n^N \delta_{\text{nis free port}} P_n. \qquad (26.9)$$

where $\delta_{\text{nis free port}}$ is unity if n is a free port and zero otherwise. Typically, when we transmit power into a particular port (for instance, port 8), we have a small amount of power flowing out of the remaining free ports (port 11 in our case) due to nonideal decoupling of the coil channels. The radiation loss can then be calculated as a difference between the total power P_{total} and the other losses quantified in equations (6)–(8):

$$P_{\text{radiation}} = P_{\text{total}} - P_{\text{lumped}} - P_{\text{conductor}} - P_{\text{load}} \qquad (26.10)$$

On the basis of these calculations we can thus reconstruct a complete picture of the power flow in the system. The diagram in Figure 26.5 depicts the detailed power flow behavior for the unloaded and loaded coil.

The input power is slightly lower than 1 W due to imperfect matching. Power transfer into the second port is not zero because of imperfect decoupling. We summarize the results in Table 26.2.

Obviously, absorption by a biological load is the only desired loss mechanism in the RF coil system. Ideally, 100% of the input power should be dissipating in the load. Looking at the percentage of power dissipated in the load, we can draw conclusions about the coil efficiency. We are also able to see what needs to be improved in the coil design. For instance, from Table 26.2 we see that 18.5% of the power is dissipated in the lumped elements. Therefore, higher-Q capacitors would improve the coil performance. Conductor resistance is responsible for dissipating about 12% of the power. Consequently, measures taken to reduce the conductor resistance will also have a positive effect on the coil performance. Interestingly, radiation loss is not a problem in the design since it is negligible at only 0.1%.

The percentages of power dissipated through the various loss mechanisms (conductor, load, lumped elements, radiation) heavily depend on frequency. For instance, it is common knowledge[14] that the resistances grow with frequency, as summarized in Table 26.3.

As we see from Table 26.3, a large portion of the power will be dissipated in the load and through radiation. The actual percentages depend on the size and shape of the coil and its load, as well as on the operating frequency. To demonstrate this dependency,

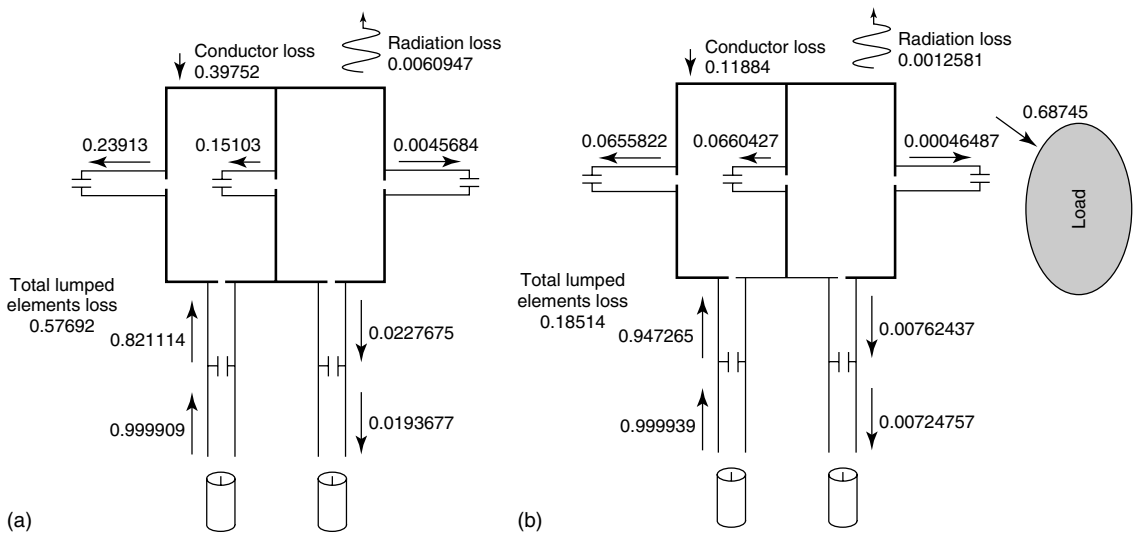

Figure 26.5. Power flow measured in Watts for a frequency of 63.65 MHz. (a) First channel of the unloaded coil is excited and (b) first channel of the loaded coil excited.

Table 26.2. Power flow in the system at 63.65 MHz

	Conductor loss, W	Absorbed by load, W	Lumped element loss, W	Radiation loss, W	Absorbed by a 50 Ω termination of the second channel
Unloaded coil	0.39752	0	0.57692	0.0060947	0.0193677
Loaded coil	0.11884	0.68745	0.18514	0.0012581	0.00724757

Table 26.3. Frequency dependence of loss mechanisms

Resistance associated with conductors	Resistance associated with load	Resistance associated with lumped elements	Resistance associated with radiation
$\sqrt{\omega}$	ω^2	$\omega^{0.45a}$	ω^4

[a]The dependence is estimated from the quality factor data provided by Voltronics Corporation (www.voltronicscorp.com).

we simulate the system for frequencies in the range of 10–500 MHz (Figure 26.6).

As noted in Figure 26.6(a) for the unloaded coil we observe that the radiation loss exceeds the conductor and lumped element losses at frequencies of approximately 300 MHz (or 7 T for proton imaging). For the loaded coil in Figure 26.6(b), we notice that the load resistance is comparable with the conductor and lumped element resistances at a frequency of approximately 20 MHz. The influence of the load begins to increase significantly with frequency, while the losses associated with conductor and lumped elements decrease. In this particular example, the radiation loss does not enter as a major loss mechanism even at high frequencies. However, one can design coil geometries, where radiation loss will dominate at high frequency.

26.6 MAGNETIC FIELD

After the coil is tuned and matched, we can calculate the electromagnetic fields generated by the coil. When working with the expanded S-matrix, we can calculate the power waves a_i flowing into each port of the original structure. These power waves serve as weights, which we use to find combined solution vectors

$$V_{\text{free port1}} = \Sigma_i (a_{1,i}/\sqrt{2}) V_i \quad \text{and}$$
$$V_{\text{free port2}} = \Sigma_i (a_{2,i}/\sqrt{2}) V_i \qquad (26.11)$$

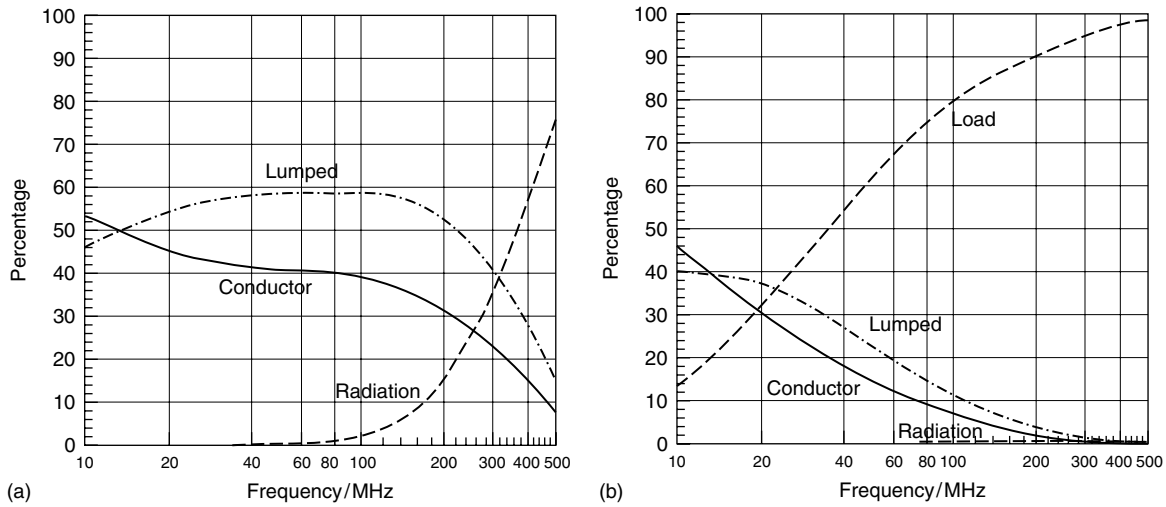

Figure 26.6. Dependence of various loss mechanisms on frequency, (a) unloaded and (b) loaded coil.

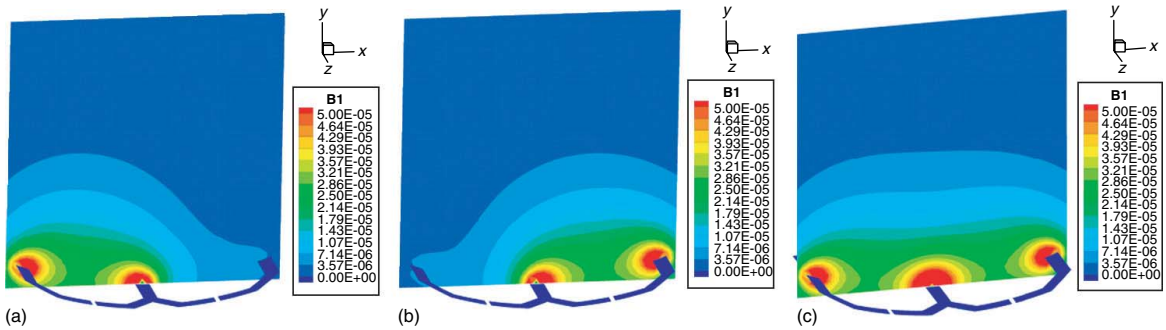

Figure 26.7. Qualitative B_1 field distribution for (a) the first channel, (b) the second channel, and (c) both channels combined.

Scaling coefficient $1/\sqrt{2}$ comes from the fact that each of the solution vectors V_i was calculated based on the $a = \sqrt{2}$ power wave. From these solution vectors, we calculate the B_1 magnetic field for each channel:

$$B_1 = \frac{1}{2}(B_x - jB_y) \tag{26.12}$$

Specifically, we calculate the B_1 fields for every individual channel provided all other channels are terminated by 50 Ω. The combined B_1 field for the coil array may be calculated as the square root of the sum-of-squares (Figure 26.7).

26.7 QUALITY FACTOR AND FILLING FACTOR

From the S-parameters, the quality factor for each channel can be calculated; the results at resonance are reported in Table 26.4. Many generic resonator parameters are estimated from a reflection coefficient (S_{11}) sweep near the resonance frequency.

Knowledge of the unloaded and loaded quality factors gives us an alternative tool to estimate the percentage of power consumed by a load. To this end, we write the power balance in terms of the quality factors as

$$\frac{1}{Q_{\text{loaded coil}}} = \frac{1}{Q_{\text{load}}} + \frac{1}{Q_{\text{unloaded coil}}} \tag{26.13}$$

Here, $Q_{\text{unloaded coil}}$ is responsible for all loss mechanisms except for the load loss. The percentage of load loss can be estimated as

$$\text{Percentage} = \frac{1/Q_{\text{load}}}{1/Q_{\text{loaded coil}}} = 1 - \frac{Q_{\text{loaded coil}}}{Q_{\text{unloaded coil}}} \tag{26.14}$$

For our example, we obtain a number of 69.7%, which is slightly different from the 68.7% reported in Table 26.2. There are several reasons for this slight disagreement: (i) the estimate of the quality factors is obtained from the S_{11} sweep which, in turn, is found by extrapolation of the S-parameters at the center frequency, and (ii) the resonator theory may not be exactly accurate at RF frequencies when wave phenomena play a role.

For a particular load, the quality factor Q_{load} cannot generally be manipulated. A way to improve the coil performance is to enhance $Q_{\text{unloaded coil}}$, which combines the effects associated with conductor, lumped element, and radiation losses.

The filling factor is a ratio of the magnetic energy stored inside a load to the total magnetic energy stored in the coil. This can be expanded as

$$\eta_{\text{f}} = \frac{\int_{V_{\text{load}}} |B|^2 \, dV}{\int_V |B|^2 \, dV} \sim \frac{B_1^2}{QP} \tag{26.15}$$

where B_1 is the magnetic field in a particular point in space, Q is the quality factor of the coil, and P is the input power. $B_1/\sqrt{QP}$ can be considered as an additional figure of merit. It is largely independent of

Table 26.4. Quality factor comparison between loaded and unloaded coils

	Q
Unloaded coil[a]	382.1
Loaded coil	115.5

[a] Unloaded coil with capacitor values corresponding to the loaded coil; the coil cannot be tuned and matched to 50 Ω.

loading and we can approximate $B_1 \sim \sqrt{Q}$ for a wide range of loads. The introduction of a load decreases the quality factor of the coil and also decreases the magnetic field.

26.8 SNR CALCULATION

It is helpful to establish a figure of merit which enables us to compare coils and coil arrays with each other. We use a particular figure of merit that is proportional to SNR as defined in[6]:

$$SNR^2 \sim \frac{[\mathbf{I}^*]^T[B_1^*][B_1]^T[\mathbf{I}]}{\frac{1}{2}[\mathbf{I}^*]^T[R][\mathbf{I}]} \tag{26.16}$$

where $\mathbf{B}_1$ is a vector of the B_1 magnetic field at a specific point in space for all individual channels, based on the fact that we supply 1 A of current into the corresponding channels. $\mathbf{I}$ is a vector of weights, which can be chosen to maximize SNR. The optimal weights are calculated as

$$\mathbf{I} \sim R^{-1}B_1^* \tag{26.17}$$

26.8.1 Resistance Matrix

Calculating the resistance matrix is an important step when calculating SNR. Roemer[5] suggests a method that required integrating over the load to compute the resistance matrix. However, a more straightforward approach is possible; we note that Figure 26.8 is similar to Figure 26.2, except there are no matching capacitors present.

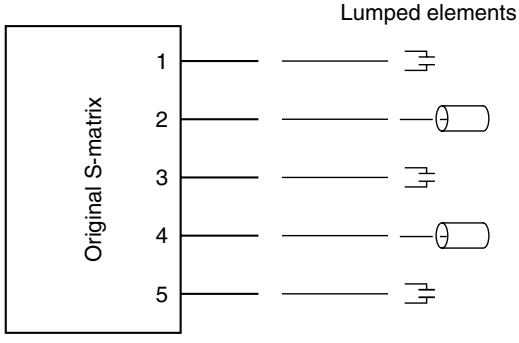

Figure 26.8. Terminating the structure by lumped elements.

The power cables are directly connected to the two channels without any matching capacitors. A [2 × 2] S-matrix of this network can then be calculated, and this S-matrix is converted to the R-matrix according to Ludwig and Bogdanov[14]:

$$R = \mathrm{Re}(Z) = \mathrm{Re}(Z_0(U+S)(U-S)^{-1}) \tag{26.18}$$

The resistance calculated this way takes into account not only losses in the load but also the remaining losses (conductors, lumped elements, radiation). For our example, the resistance matrix is

$$R = \begin{pmatrix} 0.386 & 0.043 \\ 0.043 & 0.386 \end{pmatrix}$$

26.8.2 Unit Currents

To calculate the $\mathbf{B}_1$ vector, we need to supply a 1 A current into each channel consecutively, and 0 A into the remaining channels (Figure 26.9). This is done by sending a $a = \frac{\sqrt{z_0}\times 1\mathrm{A}}{1-S}$ power wave into the first free port and terminating the remaining free ports by open circuits. In this case, S is a [1 × 1] matrix when the remaining free ports are terminated by open circuits.

When solving the system for every free port, we can find the power waves a_i flowing into each of the five ports of the original coil structure. These power waves serve as weights that are used to find the combined solution vectors $V_{\text{free port1}} = \Sigma_i(a_{1,i}/\sqrt{2})V_i$ and $V_{\text{free port2}} = \Sigma_i(a_{2,i}/\sqrt{2})V_i$. On the basis of these solution vectors, it is straightforward to calculate the B_1 magnetic field for each channel.

26.8.3 Signal to Noise Ratio (SNR)

Once the resistance matrix and the magnetic fields for each channel are established, we can use equations (16) and (17) to calculate the SNR and the figure of merit proportional to SNR (Figure 26.10).

The value of the SNR can be used as a basis for comparison with other coils/coil arrays.

In case of one-channel or quadrature coils (birdcage coil, transmission electron microscope (TEM) resonator, etc.), it is not necessary to calculate SNR according to the outlined procedure: in these cases, SNR is proportional to the value of magnetic field B_1.

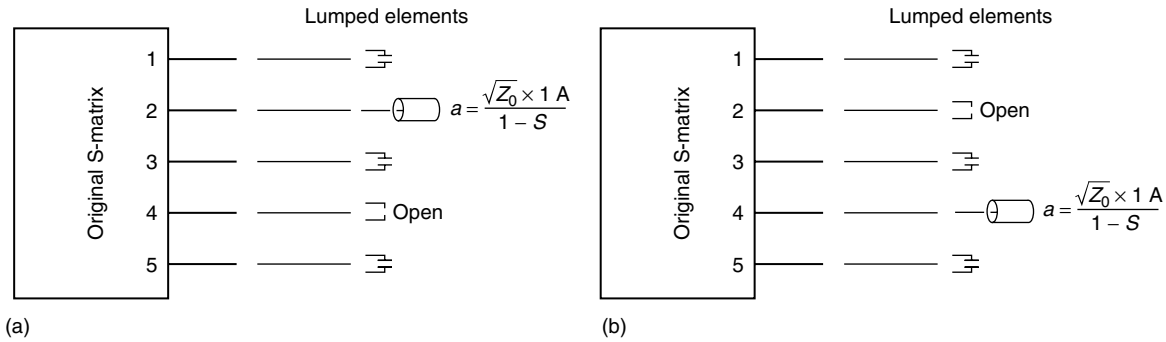

Figure 26.9. (a) Transmitting a current of 1 A into the first channel and (b) transmitting a current of 1 A into the second channel.

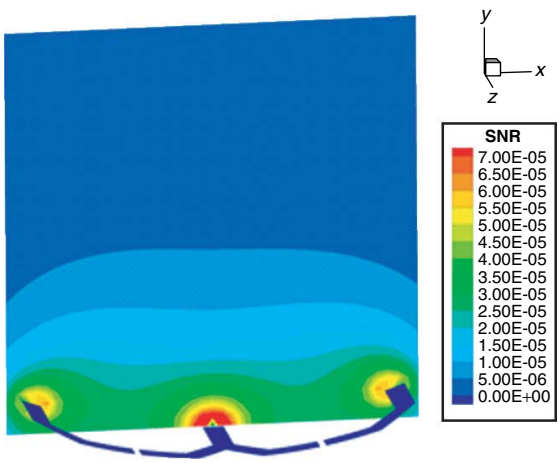

Figure 26.10. SNR plot in a cross-sectional coil plane based on equation 26.16.

26.9 SPECIFIC ABSORPTION RATE CALCULATION

To calculate the SAR, we use the following expression

$$SAR = \frac{\sigma |E|^2}{2\rho} \tag{26.19}$$

The maximum value of SAR in the load may be calculated based on 1 W of input power. There is direct proportionality of SAR and input power.[15] On the basis of the Food and Drug Administration (FDA) limit on SAR for a particular body part (tissue), maximum continuous power P_{cont} of the transmit pulse can be calculated. Product of duty cycle and power of transmit pulse should not then exceed the value of maximum continuous power:

$$\tau P_{\text{pulse}} = P_{\text{cont}} \tag{26.20}$$

26.10 DISCUSSION

Within the context of the above-outlined theoretical design steps, we would like to point out that numerical simulations serve as indispensable tools in the coil analysis, performance assessment, and as a test-bed when reviewing competing coil architectures. However, its accuracy should not be overestimated. There are a number of simulation uncertainties that cannot be eliminated:

1. Copper conductivity may not be ideal. The actual value may depend on the copper manufacturing method and on the amount of impurities in the copper.
2. Properties like the resistances of lumped elements, primarily in the capacitors, are not strictly controlled by the manufacturers. We have little choice but to rely upon the datasheets provided by manufacturers.
3. If microstrip designs are considered, the current density along the edges of a strip is much higher than in the middle of the strip. To account for this effect, a very dense mesh needs to be generated. This is often impossible because of memory and time limitations. Typical mesh densities use 3–5

triangles across the width of a copper strip. Because of this effect, resistances and inductances of the strip coils are underestimated.

4. The inclusion of a simulated biological load is probably the biggest uncertainty when conducting a simulation. Even though dielectric properties of different tissues are listed (e.g., http://niremf.ifac.cnr.it/tissprop/), they may vary noticeably for realistic biological loads. In addition, size and shape of the biological load can fluctuate widely.
5. The coil comparison is conducted on the basis of SNR (or a figure of merit which is proportional to SNR). Here, the resistance matrix is an important part of the SNR formula. Its accurate estimation is a critical step in the successful comparison procedure.

It is interesting to note that on the one hand we desire to minimize the resistance to arrive at a more efficient coil design, and on the other hand, it is the precise estimation of the already small coil resistance that becomes crucial for an accurate comparison of the various designs.

26.11 CONCLUSIONS

In this chapter, we outline a systematic computational approach that enables the analysis and optimization of any clinical and preclinical RF coil or coil array. Although the simulation steps are discussed in the context of the MoM software, the procedure lends itself to other full-wave computational methods.

The presented computational approach helps identify key bottleneck areas associated with conductors, lumped tuning, and matching elements, as well as radiation effects when designing a coil. Depending on the outcome of this analysis, we are in a better position to decide on appropriate measures to improve the coil performance for a particular application.

Our studies show that at low frequencies most of the coil resistance come from conductor resistance and lumped components. These measures may include using copper tube instead of copper strips, using silver-plated copper to improve conductor conductivity, using very high-Q capacitors, and placing several capacitors in parallel.

At a higher frequency, loading typically overwhelms the contributions from conductors and lumped elements. This is obviously desirable, and coil designs based on copper strips are acceptable. One has to be careful about the radiation resistance, in particular, when its contribution increases at a faster rate than the load resistance. To limit radiation effects, shielded coil designs become a necessity.[16]

REFERENCES

1. F. D. Doty, *Probe Design and construction*. The Encyclopedia of Magnetic Resonance, (eds D. M. Grant and R. K. Harris), John Wiley & Sons: Chichester, UK, Published Online: 15 Mar, 2007. DOI: 10.1002/9780470034590.emrstm0414.
2. H. D. W. Hill, *Probes for High Resolution*. The Encyclopedia of Magnetic Resonance, (eds D. M. Grant and R. K. Harris), John Wiley & Sons: Chichester, UK, Published Online: 15 Mar, 2007. DOI: 10.1002/9780470034590.emrstm0415.
3. J. Murphy-Boesch, *Multifrequency Coils for Whole Body Studies*. The Encyclopedia of Magnetic Resonance, (eds D. M. Grant and R. K. Harris), John Wiley & Sons: Chichester, UK, Published Online: 15 Mar, 2007. DOI: 10.1002/9780470034590.emrstm0329.
4. J. Chen, Z. Feng, and Jian.-Ming. Jin, *IEEE Trans. Biomed. Eng.*, 1998, **45**, 949.
5. P. B. Roemer, W. A. Edelstein, C. E. Hayes, S. P. Souza, and O. M. Mueller, *Magn. Reson. Med.*, 1990, **16**, 192.
6. S. M. Wright and L. L. Wald, *NMR Biomed.*, 1997, **10**, 394.
7. R. Rojas and A. O. Rodríguez, *Proceedings of the 29th Annual International Conference of the IEEE EMBS Cité Internationale*, Lyon, France, August 23–26, 2007.
8. D. Jiao and J.-M. Jin, *IEEE Trans. Biomed. Eng.*, 1999, **46**, 1387.
9. J. Paska, J. Froehlich, D. O. Brunner, K. P. Pruessmann, and R. Vahldieck, *Proc. Int. Soc. Magn. Reson. Med.*, 2009, **17**, 3038.
10. R. Zhang, Y. Xing, J. Nistler, and J. Wang, *Proc. Int. Soc. Magn. Reson. Med.*, 2009, **17**, 3040.
11. M. Kozlov, R. Turner, *J. Magn. Reson.*, 2009, **200**(1), 147.
12. R. Lemdiasov, R. Ludwig, G. Bogdanov, *Proc. Int. Soc. Magn. Reson. Med.*, 2009, **17**, 2977.
13. A. A. Obi, R. Lemdiasov, R. Ludwig, G. Bogdanov, *Proc. Int. Soc. Magn. Reson. Med.*, 2009, **17**, 2978.

14. R. Ludwig and G. Bogdanov, *RF Circuit Design, Theory and Practice*, 2nd ed., Prentice Hall: Upper Saddle River, NJ, 2009.

15. T. S Ibrahim, A. M. Abduljalil, B. A. Baertlein, R. Lee, and P.-M.-L. Robitaille, *Phys. Med. Biol.*, 2001, **46**(1), 2545.

16. T. Vaughan, M. Ganvood, K. Ugurbil, *Antennas and Propagation Society International Symposium*, vol. 1, 8–13 July 2001.

Chapter 27
Practical Electromagnetic Modeling Methods

Jian-Ming Jin

Department of Electrical and Computer Engineering, University of Illinois, 1406 West Green Street, Urbana, IL 61801, USA

27.1 INTRODUCTION

Electromagnetic modeling plays an important role in the analysis and design of radiofrequency (RF) coils for magnetic resonance imaging (MRI) applications. For low-field MRI systems, the frequency of the RF field is very low and the corresponding wavelength is very large compared to the size of the RF coils. In such cases, RF coils can be designed as low-frequency circuits based on Kirchhoff's current and voltage laws.[1] Once the electric current in an RF coil is determined, the RF magnetic field can be calculated using Biot–Savart's law since the effect of the imaging subject on the field distribution is negligible. For high-field MRI systems,[2] the frequency of the RF field increases and the corresponding wavelength becomes comparable to the size of the RF coils. In this situation, an RF coil can no longer be modeled by an equivalent circuit because of the distributive and retardation effects, and the RF magnetic field can no longer be calculated using Biot–Savart's law because of the significant contribution of the displacement current to the magnetic field and the strong interaction between the electromagnetic fields and the imaging subject. For an accurate quantitative analysis, we have to solve a boundary-value problem governed by Maxwell's equations. This boundary-value problem has to include the RF coil, its surrounding structures, and the imaging subject. Unfortunately, such a problem is very difficult to solve either analytically or numerically. In this chapter, we describe a few practical methods for electromagnetic modeling of RF coils and RF fields for high-field MRI applications. We focus on the basic principles, advantages, and limitations of these methods and also describe the basic procedure to use these methods. Applications of these methods to specific MRI problems are addressed in other chapters.

27.2 DESCRIPTION OF THE BOUNDARY-VALUE PROBLEM

The physical problem that we intend to analyze is the electromagnetic fields excited by an RF coil, which

RF Coils for MRI
Edited by J. Thomas Vaughan and John R. Griffiths

ISBN: 978-0-470-77076-4

may be loaded with an imaging subject such as a human body and placed inside an MRI scanner. The boundary-value problem involved in this analysis is to solve Maxwell's equations:

$$\nabla \times \boldsymbol{E}(\boldsymbol{r},t) = -\mu \frac{\partial \boldsymbol{H}(\boldsymbol{r},t)}{\partial t} \tag{27.1}$$

$$\nabla \times \boldsymbol{H}(\boldsymbol{r},t) = \varepsilon(\boldsymbol{r}) \frac{\partial \boldsymbol{E}(\boldsymbol{r},t)}{\partial t} + \sigma(\boldsymbol{r})\boldsymbol{E}(\boldsymbol{r},t) + \boldsymbol{J}_{\text{imp}}(\boldsymbol{r},t) \tag{27.2}$$

subject to certain boundary conditions. Here μ, ε, and σ denote, respectively, the permeability, permittivity, and conductivity of the medium where the fields are computed, and $\boldsymbol{J}_{\text{imp}}$ denotes the impressed current density, which is the source of the fields. When the MRI scanner is loaded with a human body, ε and σ are position dependent because different human tissues have different permittivity and conductivity values. However, μ is approximately the same as its free-space value μ_0 since the human body is nonmagnetic. The position dependence of ε and σ makes the solution of equations (27.1) and (27.2) very challenging. The impressed current can be the current flowing through the RF coil or the current that excites the RF coil.

The time-dependent problem described above can also be solved in the frequency domain via the Fourier transform, where equations (27.1) and (27.2) become

$$\nabla \times \boldsymbol{E}(\boldsymbol{r}) = -\mathrm{j}\omega\mu \boldsymbol{H}(\boldsymbol{r}) \tag{27.3}$$

$$\nabla \times \boldsymbol{H}(\boldsymbol{r}) = \mathrm{j}\omega\varepsilon(\boldsymbol{r})\boldsymbol{E}(\boldsymbol{r}) + \sigma(\boldsymbol{r})\boldsymbol{E}(\boldsymbol{r}) + \boldsymbol{J}_{\text{imp}}(\boldsymbol{r}) \tag{27.4}$$

where ω denotes the angular frequency. Although both the electric and magnetic fields can be calculated simultaneously by solving equations (27.3) and (27.4) together, it is also possible to solve for one of the two fields first and then calculate the other. By eliminating $\boldsymbol{H}$ in equations (27.3) and (27.4), we obtain the equation for $\boldsymbol{E}$ as

$$\nabla \times [\nabla \times \boldsymbol{E}(\boldsymbol{r})] - k_0^2 \varepsilon_{\text{r}}(\boldsymbol{r})\boldsymbol{E}(\boldsymbol{r}) = -\mathrm{j}k_0 Z_0 \boldsymbol{J}_{\text{imp}}(\boldsymbol{r}) \tag{27.5}$$

where $\varepsilon_{\text{r}}(\boldsymbol{r}) = \varepsilon(\boldsymbol{r})/\varepsilon_0 - \mathrm{j}\sigma(\boldsymbol{r})/\omega\varepsilon_0$ with ε_0 being the free-space permittivity, and $k_0 = \omega\sqrt{\mu_0\varepsilon_0}$ and $Z_0 = \sqrt{\mu_0/\varepsilon_0}$ are the free-space wavenumber and intrinsic impedance, respectively.

Equations (27.1) and (27.2) or (27.3) and (27.4) have a unique solution only after the boundary conditions are specified. The boundary conditions involved are

$$\hat{n} \times \boldsymbol{E}(\boldsymbol{r}) = 0, \quad \hat{n} \cdot \boldsymbol{H}(\boldsymbol{r}) = 0, \quad \boldsymbol{r} \in S_{\text{PEC}} \tag{27.6}$$

where S_{PEC} denotes the perfect electrically conducting (PEC) surface, which can be the surfaces of the conductors in the RF coil, the surface of the RF shield, or the surface of any other conductors in the MRI scanner. If the fields are not completely confined, the fields far away from the source have to satisfy the Sommerfeld radiation condition:

$$\hat{n} \times \left[\nabla \times \begin{pmatrix} \boldsymbol{E} \\ \boldsymbol{H} \end{pmatrix}\right] + \mathrm{j}k_0 \hat{n} \times \left[\hat{n} \times \begin{pmatrix} \boldsymbol{E} \\ \boldsymbol{H} \end{pmatrix}\right] \approx 0 \tag{27.7}$$

which dictates that the fields should propagate away from the source. In this equation, $\hat{n}$ denotes a normal unit vector pointing away from the source.

27.3 CONSTRUCTION OF ELECTROMAGNETIC MODELS

To solve the boundary-value problem described in the preceding section, we need to build an electromagnetic model for the problem under consideration. An electromagnetic model consists of two parts: one is the geometric model and the other is the specification of the electromagnetic property of the media in the geometric model. The electromagnetic model of an RF coil and its surrounding structures such as an RF shield can be constructed in a straightforward manner because their dimensions can be measured accurately and their electromagnetic properties (permittivity and conductivity) can be found readily in their material specifications. A simplified model of the imaging subject (usually a human body) that approximates a human body as a circular or an elliptical cylinder and a human head as a sphere or a spheroid can also be constructed easily. The most challenging part is to construct an anatomically accurate electromagnetic model of a human body or a human head since such an object consists of many irregularly shaped tissues having very different electromagnetic properties.

To construct an anatomically accurate electromagnetic model of a human body or a human head, one can first collect a set of tomographic images using either MRI- or X-ray-computed tomography and can segment each image using either an automatic segmentation and classification software or any other manual or semiautomatic approach. The

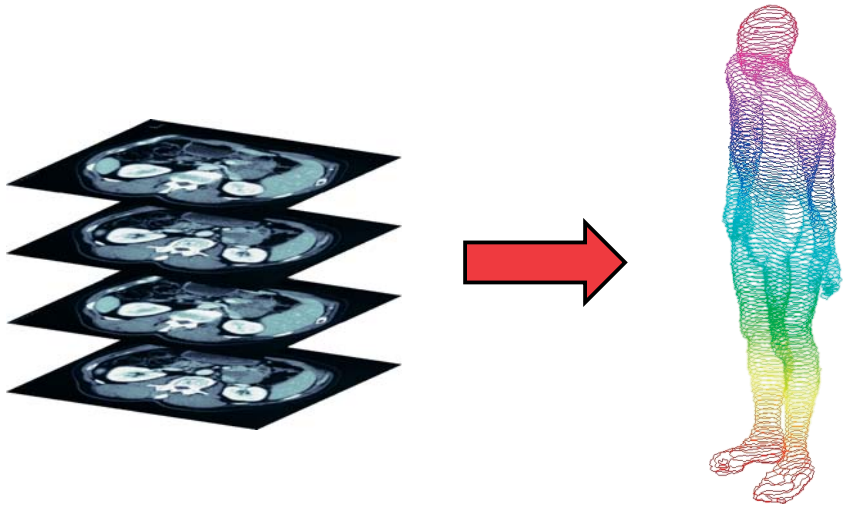

Figure 27.1. Construction of an anatomically accurate human model from a set of tomographic images.

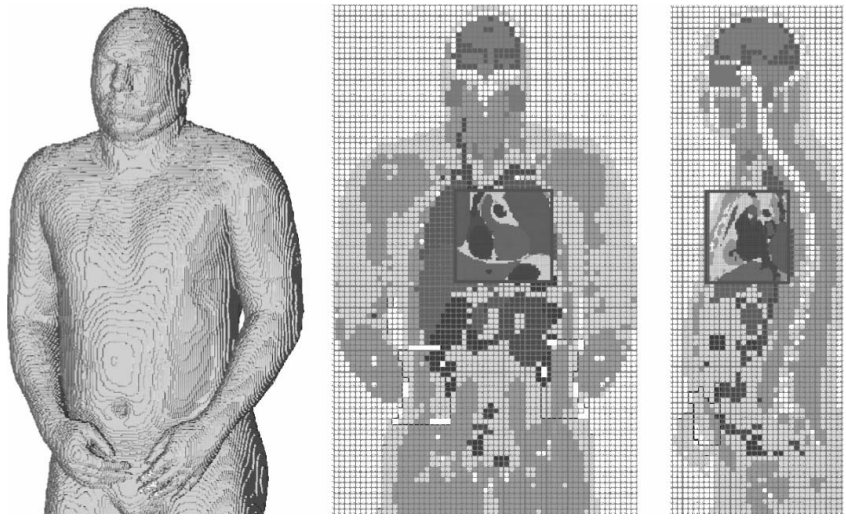

Figure 27.2. A 3D voxel model of a human body and its coronal and sagittal slices. (Reproduced from Ref. 8. © Emerald Group Publishing Limited, 2005.)

segmented images are then stacked and interpolated in the third dimension to form a 3D geometric model of the human body (Figure 27.1). As can be expected, this process is very time consuming and tedious and is difficult, if not impossible, to carry out for each individual study. A more practical approach is to use one of the models that has been constructed[3–7] and to scale it to the appropriate size of the specific human body. Such a model, although not highly accurate, can provide a good approximation since the anatomical structures are similar for most individuals. The voxel model created based on the procedure described above usually has too fine a resolution to be used directly for numerical computation. In such a case, one can combine voxels to form a model with larger voxels until the size of each voxel is on the order of a few millimeters. One such model is shown in

Table 27.1. Relative permittivities (ε_r), conductivities (σ), and densities (ρ) of various tissues in a human head

		64 MHz		128 MHz		171 MHz		256 MHz		299 MHz		341 MHz	
Tissue	ρ(g/cm^3)	ε_r	σ(s/m)	ε_r	σ(s/m)	ε_r	σ(s/m)	ε_r	σ(s/m)	ε_r	σ(s/m)	ε_r	σ(s/m)
Sinus	0	1.0	0.0	1.0	0.0	1.0	0.0	1.0	0.0	1.0	0.0	1.0	0.0
Lens	1.05	55.4	0.44	47.9	0.46	46.1	0.47	44.2	0.49	43.7	0.50	43.3	0.50
Humor	1.01	69.1	1.50	69.1	1.50	69.0	1.50	69.0	1.51	69.0	1.51	69.0	1.52
Blood	1.06	86.5	1.20	73.2	1.25	69.9	1.27	66.6	1.30	65.7	1.31	65.0	1.33
Cartilage	1.10	62.9	0.45	52.9	0.49	50.3	0.51	47.6	0.54	46.8	0.55	46.2	0.57
Bone	1.85	16.7	0.06	14.7	0.07	14.2	0.07	13.6	0.08	13.4	0.08	13.3	0.09
Brain	1.03	82.6	0.40	63.0	0.46	58.2	0.49	53.3	0.53	51.9	0.55	50.9	0.57
Skin	1.10	92.2	0.44	65.4	0.52	58.7	0.56	51.9	0.62	49.9	0.64	48.4	0.66
CSF	1.06	97.3	2.07	84.0	2.14	79.0	2.17	74.1	2.21	72.8	2.22	71.9	2.24
Muscle	1.04	72.0	0.71	63.9	0.74	61.8	0.76	59.6	0.77	59.0	0.79	58.5	0.80

Figure 27.2, together with its coronal and sagittal sectional views.[8]

Once the geometric model of a human body is constructed, one needs to specify the electromagnetic properties for each tissue. Without a reasonably accurate specification of the electromagnetic properties of the tissues, the geometric model is practically useless. The electromagnetic properties are reflected in the values of permittivity, permeability, and conductivity. As mentioned earlier, the value of the permeability is approximately the same as that of free space since human tissues are nonmagnetic. The values of permittivity and conductivity, however, are significantly different from their free-space values and, moreover, they are different for different tissues and their values also change with change in the frequency. Unfortunately, the permittivities and conductivities of human tissues are difficult to measure accurately because the results vary with the mode of tissue collection and measurement. Consequently, there are some discrepancies among the published data.[9–13] Table 27.1 lists, at several frequencies, the relative permittivities and conductivities of various tissues in a human head, which are adapted from Ref. 10.

27.4 ANALYTICAL METHOD

The boundary-value problem described in Section 27.2 is difficult to solve analytically except for a few simple configurations.[14–21] Here, we consider two problems whose solutions are useful for field analysis in MRI. One problem is illustrated in Figure 27.3, where a lossy dielectric cylinder of radius a and relative permittivity ε_r is placed concentrically inside

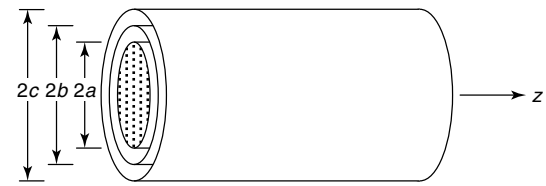

Figure 27.3. A lossy dielectric cylinder placed inside a cylindrical surface current enclosed in a conducting shell.

a cylindrical surface current of radius b, which, in turn, is enclosed in a cylindrical conducting shell of radius c. This configuration is a very rough approximation of a shielded whole-body birdcage coil loaded with a human body. The dielectric cylinder approximates the human body, the cylindrical surface current approximates the birdcage coil, and the cylindrical conducting shell represents the RF shield. If the birdcage coil operates in a linear mode, the z-component of the electric current can be approximated by the surface current with density given by

$$J_z(\phi) = I_0 \cos\phi \tag{27.8}$$

where I_0 is a constant. By expanding the fields inside the dielectric cylinder ($\rho < a$), outside the dielectric cylinder but inside the surface current ($a < \rho < b$), and outside the surface current but inside the RF shield ($b < \rho < c$) as a superposition of cylindrical harmonics, and then applying the boundary conditions at the surface of the dielectric cylinder ($\rho = a$), across the surface current ($\rho = b$), and at the surface of the RF shield ($\rho = c$), we find that the fields inside

the dielectric cylinder are given by Jin[1]

$$\boldsymbol{E}(\rho,\phi) = \hat{z} A J_1(k_\mathrm{d}\rho)\cos\phi \tag{27.9}$$

$$\boldsymbol{H}(\rho,\phi) = \frac{A}{\mathrm{j}\omega\mu_0}\left[\hat{\rho}\frac{J_1(k_\mathrm{d}\rho)}{\rho}\sin\phi + \hat{\phi}\frac{\partial J_1(k_\mathrm{d}\rho)}{\partial\rho}\cos\phi\right] \tag{27.10}$$

where $k_\mathrm{d} = k_0\sqrt{\varepsilon_\mathrm{r}}$ and

$$A = I_0\frac{b}{a}\frac{J_1(k_0 b)Y_1(k_0 c) - J_1(k_0 c)Y_1(k_0 b)}{k_\mathrm{d}J_1'(k_\mathrm{d}a)F(k_0,a,c) - k_0 J_1(k_\mathrm{d}a)G(k_0,a,c)} \tag{27.11}$$

in which

$$F(k_0,a,c) = J_1(k_0 a)Y_1(k_0 c) - J_1(k_0 c)Y_1(k_0 a) \tag{27.12}$$

$$G(k_0,a,c) = J_1'(k_0 a)Y_1(k_0 c) - J_1(k_0 c)Y_1'(k_0 a) \tag{27.13}$$

In the above expressions, J_1 and Y_1 denote the first-order Bessel functions of the first and second kind, respectively. At a low frequency or close to the center of the cylinder such that $k_\mathrm{d}\rho \ll 1$, equation (27.10) is reduced to $\boldsymbol{H}(\rho,\phi) = \hat{y}Ak_\mathrm{d}/2\mathrm{j}\omega\mu_0$, which represents a linearly polarized uniform magnetic field. Despite a very rough approximation, this solution can be used to investigate the field penetration into the dielectric cylinder and the resulting signal-to-noise ratio as the frequency increases, the power dissipation due to the dielectric and conduction losses, the B1-field inhomogeneity due to the increased displacement current, and the effect of the RF shield on the field attenuation and distribution. The investigation can help to develop a qualitative understanding of the problems that might be encountered in the design of RF whole-body coils for high-frequency MRI applications. The solution can also be extended to model a multilayered dielectric cylinder, a birdcage coil with a quadrature excitation, and a birdcage coil with discrete current elements. In the last case, the discrete currents can be expanded into a Fourier series, from which the fields excited can be solved in the form of a Fourier series as well.

The second useful problem is illustrated in Figure 27.4, where a circular current loop of radius b carrying a uniform current I is placed adjacent to a lossy dielectric sphere of radius a and relative permittivity ε_r. This configuration approximates roughly a surface RF coil placed near a human body. The solution can be obtained using the Debye potential in conjunction with a spherical harmonic expansion. The fields inside the dielectric sphere are given by Jin[1]

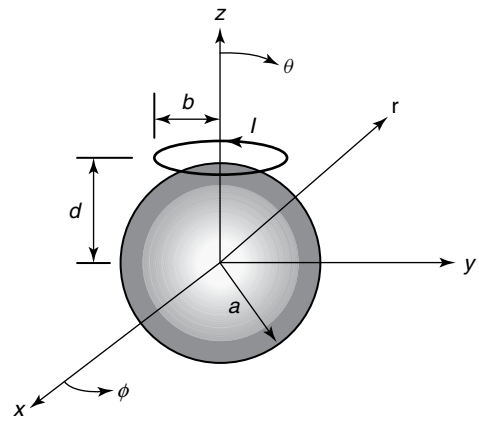

Figure 27.4. A circular current loop placed adjacent to a lossy dielectric sphere.

$$\boldsymbol{E}(r,\phi,\theta) = \hat{\phi}\mathrm{j}\omega\mu_0\sum_{n=1}^{\infty} a_n j_n(k_\mathrm{d}r)\frac{\partial P_n(\cos\theta)}{\partial\theta} \tag{27.14}$$

$$\boldsymbol{H}(r,\phi,\theta) = \frac{1}{r}\sum_{n=1}^{\infty} a_n\left\{\hat{r}n(n+1)j_n(k_\mathrm{d}r)P_n(\cos\theta) + \hat{\theta}\frac{\partial[r j_n(k_\mathrm{d}r)]}{\partial r}\frac{\partial P_n(\cos\theta)}{\partial\theta}\right\} \tag{27.15}$$

where

$$a_n = \frac{Ib^2}{a^2 c}\frac{2n+1}{2n(n+1)} \times \frac{h_n^{(2)}(k_0 c)P_n'(\cos\theta_0)}{k_\mathrm{d}j_n'(k_\mathrm{d}a)h_n^{(2)}(k_0 a) - k_\mathrm{d}j_n(k_\mathrm{d}a)h_n'^{(2)}(k_0 a)} \tag{27.16}$$

In these expressions, $c = \sqrt{b^2+d^2}$, $\theta_0 = \tan^{-1}(b/d)$, j_n denotes the nth-order spherical Bessel function of the first kind, $h_n^{(2)}$ denotes the nth-order spherical Hankel function of the second kind, and P_n denotes the nth-order Legendre polynomial. Along the z-axis, equation (27.15) is reduced to $\boldsymbol{H}(z) = \hat{z}\sum_{n=1}^{\infty} a_n n(n+1)j_n(k_\mathrm{d}z)/z$, which is rather uniform at a low frequency with $k_\mathrm{d}z \ll 1$. The solution given above can be used to study the general characteristics of surface coils, such as the

field penetration depth versus the coil size and the variation of the field as the frequency increases. The solution can also be extended to the case of a multilayered dielectric sphere,[21] which may provide a better approximation to the actual anatomical structure, and to the case where the entire sphere and the coil are enclosed by a concentric spherical conducting shell, which can be used to study the effect of an RF shield.

27.5 FINITE-DIFFERENCE TIME-DOMAIN METHOD

The analytical method described in the preceding section is applicable to a few very simple geometries. For a more complicated problem that involves a realistic RF coil loaded with a complicated imaging subject, we have to resort to numerical methods to solve the boundary-value problem defined in the Section 27.2. Among many numerical methods developed so far, the three most powerful and popular are the finite-difference time-domain (FDTD) method, the finite-element method (FEM), and the method of moments (MoM). The FDTD solves the time-dependent Maxwell's equations directly and the FEM usually solves the vector wave equation derived from Maxwell's equations, whereas the MoM solves an integral equation formulated using the fundamental solution of the problem.

To solve the boundary-value problem defined in Section 27.2 by using the FDTD,[22,23] we first enclose the computational domain, denoted as volume V, in a rectangular box and then subdivide the box uniformly into many small rectangular cells until each cell is smaller than one-twentieth of the shortest wavelength in the computational domain, as shown in Figure 27.5(a). If we denote the dimension of a cell as $\Delta x \times \Delta y \times \Delta z$ and the maximum relative permittivity in volume V as $\varepsilon_{r,\max}$, the condition on the cell size can be expressed as $\max(\Delta x, \Delta y, \Delta z) < \lambda/20\sqrt{\varepsilon_{r,\max}}$, where λ denotes the free-space wavelength. The object to be analyzed is then modeled by a collection of these small rectangular cells. To discretize the fields, we assign the electric field components at the center of each edge of the cells and the magnetic field components at the center of each face of the cells, as illustrated in Figure 27.5(b). If the entire grid is offset by one half of a cell in each direction, then on this dual grid, the magnetic field components would reside at the center of each edge of the cells and the electric field components would reside at the center of each face of the cells. We further divide the time axis uniformly into many small intervals such that the time interval Δt satisfies the condition

$$\Delta t \leq \frac{\sqrt{\mu\varepsilon_{\max}}}{\sqrt{\frac{1}{(\Delta x)^2} + \frac{1}{(\Delta y)^2} + \frac{1}{(\Delta z)^2}}} \tag{27.17}$$

The FDTD method is designed to calculate the spatially discretized electric field at time instants $t = n\Delta t$ and the spatially discretized magnetic field at time instants $t = (n + 1/2)\Delta t$ in a very efficient manner, starting from $n = 1$ and proceeding until the field either vanishes or reaches steady state. This process is called *leap-frog time stepping* or

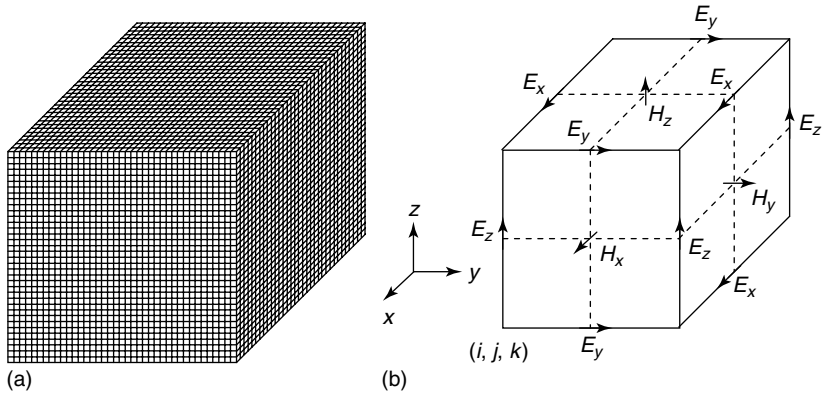

Figure 27.5. (a) A computational domain is discretized into many small rectangular cells. (b) Assignment of the field components on an FDTD cell for Yee's algorithm.

time marching, and the condition in equation (27.17) ensures the stability of the time-stepping process. Equation (27.17) simply dictates that the wave cannot propagate faster than the speed of light in the medium.

By using the central differencing formula to approximate both the spatial and time derivatives based on the discretization scheme depicted in Figure 27.5(b), equation (27.1) can be discretized into

$$\begin{aligned} H_x^{n+\frac{1}{2}}\left(i, j+\frac{1}{2}, k+\frac{1}{2}\right) &= H_x^{n-\frac{1}{2}}\left(i, j+\frac{1}{2}, k+\frac{1}{2}\right) \\ &- \frac{\Delta t}{\mu \Delta y}\left[E_z^n\left(i, j+1, k+\frac{1}{2}\right)\right. \\ &\left. - E_z^n\left(i, j, k+\frac{1}{2}\right)\right] \\ &+ \frac{\Delta t}{\mu \Delta z}\left[E_y^n\left(i, j+\frac{1}{2}, k+1\right)\right. \\ &\left. - E_y^n\left(i, j+\frac{1}{2}, k\right)\right] \end{aligned} \tag{27.18}$$

$$\begin{aligned} H_y^{n+\frac{1}{2}}\left(i+\frac{1}{2}, j, k+\frac{1}{2}\right) &= H_y^{n-\frac{1}{2}}\left(i+\frac{1}{2}, j, k+\frac{1}{2}\right) \\ &- \frac{\Delta t}{\mu \Delta z}\left[E_x^n\left(i+\frac{1}{2}, j, k+1\right)\right. \\ &\left. - E_x^n\left(i+\frac{1}{2}, j, k\right)\right] \\ &+ \frac{\Delta t}{\mu \Delta x}\left[E_z^n\left(i+1, j, k+\frac{1}{2}\right)\right. \\ &\left. - E_z^n\left(i, j, k+\frac{1}{2}\right)\right] \end{aligned} \tag{27.19}$$

$$\begin{aligned} H_z^{n+\frac{1}{2}}\left(i+\frac{1}{2}, j+\frac{1}{2}, k\right) &= H_z^{n-\frac{1}{2}}\left(i+\frac{1}{2}, j+\frac{1}{2}, k\right) \\ &- \frac{\Delta t}{\mu \Delta x}\left[E_y^n\left(i+1, j+\frac{1}{2}, k\right)\right. \\ &\left. - E_y^n\left(i, j+\frac{1}{2}, k\right)\right] \\ &+ \frac{\Delta t}{\mu \Delta y}\left[E_x^n\left(i+\frac{1}{2}, j+1, k\right)\right. \\ &\left. - E_x^n\left(i+\frac{1}{2}, j, k\right)\right] \end{aligned} \tag{27.20}$$

where i, j, and k represent the x, y, and z coordinates of a specific cell ($x = i\Delta x$, $y = j\Delta y$, $z = k\Delta z$). Similarly, equation (27.2) can be discretized to yield

$$\begin{aligned} E_x^{n+1}\left(i+\frac{1}{2}, j, k\right) &= \frac{1}{\beta\left(i+\frac{1}{2}, j, k\right)} \\ &\times \left\{\alpha\left(i+\frac{1}{2}, j, k\right) E_x^n\left(i+\frac{1}{2}, j, k\right)\right. \\ &+ \frac{1}{\Delta y}\left[H_z^{n+\frac{1}{2}}\left(i+\frac{1}{2}, j+\frac{1}{2}, k\right)\right. \\ &\left. - H_z^{n+\frac{1}{2}}\left(i+\frac{1}{2}, j-\frac{1}{2}, k\right)\right] \\ &- \frac{1}{\Delta z}\left[H_y^{n+\frac{1}{2}}\left(i+\frac{1}{2}, j, k+\frac{1}{2}\right)\right. \\ &\left. - H_y^{n+\frac{1}{2}}\left(i+\frac{1}{2}, j, k-\frac{1}{2}\right)\right] \\ &\left. - J_{\text{imp},x}^{n+\frac{1}{2}}\left(i+\frac{1}{2}, j, k\right)\right\} \end{aligned} \tag{27.21}$$

$$\begin{aligned} E_y^{n+1}\left(i, j+\frac{1}{2}, k\right) &= \frac{1}{\beta\left(i, j+\frac{1}{2}, k\right)} \\ &\times \left\{\alpha\left(i, j+\frac{1}{2}, k\right) E_y^n\left(i, j+\frac{1}{2}, k\right)\right. \\ &+ \frac{1}{\Delta z}\left[H_x^{n+\frac{1}{2}}\left(i, j+\frac{1}{2}, k+\frac{1}{2}\right)\right. \\ &\left. - H_x^{n+\frac{1}{2}}\left(i, j+\frac{1}{2}, k-\frac{1}{2}\right)\right] \\ &- \frac{1}{\Delta x}\left[H_z^{n+\frac{1}{2}}\left(i+\frac{1}{2}, j+\frac{1}{2}, k\right)\right. \\ &\left. - H_z^{n+\frac{1}{2}}\left(i-\frac{1}{2}, j+\frac{1}{2}, k\right)\right] \\ &\left. - J_{\text{imp},y}^{n+\frac{1}{2}}\left(i, j+\frac{1}{2}, k\right)\right\} \end{aligned} \tag{27.22}$$

$$\begin{aligned} E_z^{n+1}\left(i, j, k+\frac{1}{2}\right) &= \frac{1}{\beta\left(i, j, k+\frac{1}{2}\right)} \\ &\times \left\{\alpha\left(i, j, k+\frac{1}{2}\right) E_z^n\left(i, j, k+\frac{1}{2}\right)\right. \\ &+ \frac{1}{\Delta x}\left[H_y^{n+\frac{1}{2}}\left(i+\frac{1}{2}, j, k+\frac{1}{2}\right)\right. \\ &\left. - H_y^{n+\frac{1}{2}}\left(i-\frac{1}{2}, j, k+\frac{1}{2}\right)\right] \\ &- \frac{1}{\Delta y}\left[H_x^{n+\frac{1}{2}}\left(i, j+\frac{1}{2}, k+\frac{1}{2}\right)\right. \\ &\left. - H_x^{n+\frac{1}{2}}\left(i, j-\frac{1}{2}, k+\frac{1}{2}\right)\right] \\ &\left. - J_{\text{imp},z}^{n+\frac{1}{2}}\left(i, j, k+\frac{1}{2}\right)\right\} \end{aligned} \tag{27.23}$$

where $\alpha = \varepsilon/\Delta t - \sigma/2$ and $\beta = \varepsilon/\Delta t + \sigma/2$. Clearly, given the source current, the initial values for the electric and magnetic fields at $n = 0$ (which can all be assumed to be zero), and the boundary conditions, we can use equations (27.18)–(27.20) to calculate the discrete magnetic fields and equations (27.21)–(27.23) to calculate the discrete electric fields at $n = 1, n = 2$, and so on. The discretization above, known as *Yee's FDTD scheme*, is of second order in accuracy in terms of the cell size and the time-step size.

Because the FDTD algorithm described above applies to rectangular cells, the human model constructed in Section 27.3 can be employed directly. In that case, each voxel becomes a rectangular FDTD cell. Any conductors, such as the RF shield, can be modeled by forcing the tangential electric field and normal magnetic field to zero along a "staircase" approximation to the surfaces of the conductors. If the currents on the RF coil are known either through measurements or by any other analysis, the coil is then replaced by the currents, which can be imposed directly onto the calculation through $\boldsymbol{J}_{\text{imp}}$. This modeling is relatively simple, but it ignores the effect of the imaging subject on the current distribution in the coil. If the currents on the RF coil are unknown (which is usually the case), the coil has to be modeled as conductors by the aforementioned staircase approximation and then excited by either a current or voltage source. In either case, a gap is created at the feed point of the coil. A current probe can then be inserted into the gap and this current can again be modeled in the FDTD calculation through $\boldsymbol{J}_{\text{imp}}$. In the case of a voltage excitation, we can set $\boldsymbol{J}_{\text{imp}} = 0$ and simply enforce the electric field across the gap as $E = V_0/d$, where V_0 denotes the excitation voltage and d denotes the width of the gap. The temporal profile of the excitation can be chosen on the basis of the type of analysis. If a single-frequency analysis is desired, the temporal profile can be chosen as an exponentially tapered sinusoid. The exponential tapering increases the amplitude of the sinusoid gradually to its full value after a few periods, which reduces the numerical error caused by a large increase in the value of the excitation current over a time step. If a broadband analysis is desired, the temporal profile can be chosen as a modulated Gaussian pulse, whose modulation determines the central frequency and whose width determines the bandwidth. However, the frequency dependence of the permittivity and conductivity must be modeled carefully for an accurate analysis using either the recursive convolution method or the auxiliary differential equation method.[23]

If the computational domain V is not entirely enclosed by a conducting surface, the fields will then extend beyond the exterior surface of the computational domain. In that case, we have to treat this surface carefully to ensure that the exterior surface would not artificially reflect the outgoing fields back into the computational domain to corrupt the correct solution. One approach is to apply an absorbing boundary condition at the exterior surface. Another approach is to place a layer of absorbing material at the exterior surface to absorb the power incident from the inside of the computational domain. The second approach has become very popular since the invention of the perfectly matched layer (PML),[24–26] which is a nonphysical material with an excellent absorption capability. It has been shown[26] that the PML is equivalent to an anisotropic dispersive absorber whose permittivity and permeability are given by

$$\bar{\varepsilon} = \varepsilon \begin{bmatrix} \frac{s_y s_z}{s_x} & 0 & 0 \\ 0 & \frac{s_z s_x}{s_y} & 0 \\ 0 & 0 & \frac{s_x s_y}{s_z} \end{bmatrix}, \qquad \bar{\mu} = \mu \begin{bmatrix} \frac{s_y s_z}{s_x} & 0 & 0 \\ 0 & \frac{s_z s_x}{s_y} & 0 \\ 0 & 0 & \frac{s_x s_y}{s_z} \end{bmatrix} \tag{27.24}$$

where ε and μ denote the permittivity and permeability of the medium terminated by the PML and

$$s_x = 1 - \mathrm{j}\frac{\sigma_x}{\omega\varepsilon}, \quad s_y = 1 - \mathrm{j}\frac{\sigma_y}{\omega\varepsilon}, \quad s_z = 1 - \mathrm{j}\frac{\sigma_z}{\omega\varepsilon} \tag{27.25}$$

It can be shown that for a PML placed perpendicular to the x-axis, if one sets $\sigma_y = \sigma_z = 0$, the surface of the PML will not cause any reflection regardless of (i) the value of σ_x, (ii) the incident angle, and (iii) the frequency. Instead, all the power will enter the PML and will be attenuated because of σ_x. However, since the PML has a finite thickness in order to be used to terminate the computational domain, a small amount of power will eventually be reflected at the back of the PML and reenter the computational domain after being attenuated one more time. For a PML having a thickness of L, the final reflection coefficient is given by

$$|R(\theta)| = \mathrm{e}^{-2\eta\sigma_x L\cos\theta} \tag{27.26}$$

where $\eta = \sqrt{\mu/\varepsilon}$ and θ denotes the incident angle. Therefore, for a specified reflection coefficient $R(0)$, the value of σ_x can be determined via

$$\sigma_x = -\frac{\ln|R(0)|}{2\eta L} \tag{27.27}$$

Note that a better performance can often be achieved by setting a quadratic profile for σ_x such that its value increases quadratically from zero at the surface of the PML and reaches a maximum value at the back of the PML. The maximum value of σ_x can be determined in a similar manner.

To model the PML in the FDTD calculation, we first rewrite equations (27.3) and (27.4) in the PML as

$$\nabla \times \boldsymbol{E}(\boldsymbol{r}) = -\mathrm{j}\omega \begin{bmatrix} s_y & 0 & 0 \\ 0 & s_z & 0 \\ 0 & 0 & s_x \end{bmatrix} \cdot \boldsymbol{B}(\boldsymbol{r}) \tag{27.28}$$

$$\nabla \times \boldsymbol{H}(\boldsymbol{r}) = \mathrm{j}\omega \begin{bmatrix} s_y & 0 & 0 \\ 0 & s_z & 0 \\ 0 & 0 & s_x \end{bmatrix} \cdot \boldsymbol{D}(\boldsymbol{r}) \tag{27.29}$$

where

$$\boldsymbol{D}(\boldsymbol{r}) = \varepsilon \begin{bmatrix} s_z/s_x & 0 & 0 \\ 0 & s_x/s_y & 0 \\ 0 & 0 & s_y/s_z \end{bmatrix} \cdot \boldsymbol{E}(\boldsymbol{r}) \tag{27.30}$$

$$\boldsymbol{B}(\boldsymbol{r}) = \mu \begin{bmatrix} s_z/s_x & 0 & 0 \\ 0 & s_x/s_y & 0 \\ 0 & 0 & s_y/s_z \end{bmatrix} \cdot \boldsymbol{H}(\boldsymbol{r}) \tag{27.31}$$

The x-components of equations (27.28) and (27.29) can be transformed into the time domain as

$$[\nabla \times \boldsymbol{E}]_x = -\frac{\partial B_x}{\partial t} - \frac{\sigma_y}{\varepsilon} B_x \tag{27.32}$$

$$[\nabla \times \boldsymbol{H}]_x = \frac{\partial D_x}{\partial t} + \frac{\sigma_y}{\varepsilon} D_x \tag{27.33}$$

Their FDTD discretization based on Yee's scheme yields

$$\begin{aligned} B_x^{n+\frac{1}{2}}\left(i, j+\frac{1}{2}, k+\frac{1}{2}\right) &= \frac{1}{\beta_y\left(i, j+\frac{1}{2}, k+\frac{1}{2}\right)} \\ &\times \left\{\alpha_y\left(i, j+\frac{1}{2}, k+\frac{1}{2}\right)\right. \\ &\times B_x^{n-\frac{1}{2}}\left(i, j+\frac{1}{2}, k+\frac{1}{2}\right) \\ &- \frac{\varepsilon}{\Delta y}\left[E_z^n\left(i, j+1, k+\frac{1}{2}\right)\right. \\ &\left.-E_z^n\left(i, j, k+\frac{1}{2}\right)\right] \\ &+ \frac{\varepsilon}{\Delta z}\left[E_y^n\left(i, j+\frac{1}{2}, k+1\right)\right. \\ &\left.\left.-E_y^n\left(i, j+\frac{1}{2}, k\right)\right]\right\} \end{aligned} \tag{27.34}$$

$$\begin{aligned} D_x^{n+1}\left(i+\frac{1}{2}, j, k\right) &= \frac{1}{\beta_y\left(i+\frac{1}{2}, j, k\right)} \\ &\times \left\{\alpha_y\left(i+\frac{1}{2}, j, k\right) D_x^n\left(i+\frac{1}{2}, j, k\right)\right. \\ &+ \frac{\varepsilon}{\Delta y}\left[H_z^{n+\frac{1}{2}}\left(i+\frac{1}{2}, j+\frac{1}{2}, k\right)\right. \\ &\left.- H_z^{n+\frac{1}{2}}\left(i+\frac{1}{2}, j-\frac{1}{2}, k\right)\right] \\ &- \frac{\varepsilon}{\Delta z}\left[H_y^{n+\frac{1}{2}}\left(i+\frac{1}{2}, j, k+\frac{1}{2}\right)\right. \\ &\left.\left.- H_y^{n+\frac{1}{2}}\left(i+\frac{1}{2}, j, k-\frac{1}{2}\right)\right]\right\} \end{aligned} \tag{27.35}$$

where $\alpha_y = \varepsilon/\Delta t - \sigma_y/2$ and $\beta_y = \varepsilon/\Delta t + \sigma_y/2$. The x-components of equations (27.30) and (27.31) can also be transformed into the time domain as

$$\frac{\partial D_x}{\partial t} + \frac{\sigma_x}{\varepsilon} D_x = \varepsilon \frac{\partial E_x}{\partial t} + \sigma_z E_x \tag{27.36}$$

$$\frac{\partial B_x}{\partial t} + \frac{\sigma_x}{\varepsilon} B_x = \mu \frac{\partial H_x}{\partial t} + \mu \frac{\sigma_z}{\varepsilon} H_x \tag{27.37}$$

They can be discretized to yield

$$E_x^{n+1} = \frac{1}{\beta_z}\left[\alpha_z E_x^n + \frac{1}{\varepsilon}\beta_x D_x^{n+1} - \frac{1}{\varepsilon}\alpha_x D_x^n\right] \tag{27.38}$$

$$H_x^{n+\frac{1}{2}} = \frac{1}{\beta_z}\left[\alpha_z H_x^{n-\frac{1}{2}} + \frac{1}{\mu}\beta_x B_x^{n+\frac{1}{2}} - \frac{1}{\mu}\alpha_x B_x^{n-\frac{1}{2}}\right] \tag{27.39}$$

where $\alpha_{x,z}$ and $\beta_{x,z}$ are defined similarly to α_y and β_y. In these two equations, the location indexes are omitted because they are the same in each term. Note that

outside the PML, equations (27.38) and (27.39) simply reduce to $E_x^{n+1} = D_x^{n+1}/\varepsilon$ and $H_x^{n+\frac{1}{2}} = B_x^{n+\frac{1}{2}}/\mu$, as expected.

Equations (27.34), (27.35), (27.38), and (27.39) are obtained from the x-components of equations (27.28)–(27.31). Another eight equations can be obtained from their y- and z-components. The resulting 12 equations can be used to calculate all the fields step by step. Given the field values at time steps n and $n - \frac{1}{2}$, we first use the equations such as equation (27.34) to calculate $\boldsymbol{B}^{n+\frac{1}{2}}$, which can then be used in the equations such as equation (27.39) to calculate $\boldsymbol{H}^{n+\frac{1}{2}}$. The values of $\boldsymbol{H}^{n+\frac{1}{2}}$ are then used in the equations such as equation (27.35) to calculate $\boldsymbol{D}^{n+1}$, which are then used in the equations similar to equation (27.38) to calculate $\boldsymbol{E}^{n+1}$. This completes one time stepping, and the process then continues. This PML implementation has been found to be very robust and accurate for terminating the FDTD computational grids.

Because the FDTD method is simple to implement, easy to set up, and highly efficient to calculate as it does not require solving any matrix equations, it has been widely used for numerical simulation of a number of electromagnetic problems, including problems related to RF fields for MRI applications.[27–41] The two most widely used commercial computer codes based on the FDTD method are XFDTD by Remcom[42] and MWS (Microwave Studio) by CST Computer Simulation Technology.[43] In addition to these two codes, there are many other in-house developed codes that can be adapted for the modeling and simulation of RF coils and interactions between RF fields and the human body. To demonstrate the application of the FDTD in conjunction with the PML, we consider the computation of the electric and magnetic fields inside a human head placed in a shielded RF birdcage coil.[28] The electromagnetic model of the human head is highly inhomogeneous and consists of 14 different tissues, some of which are listed in Table 27.1. Three slices of this model are shown in Figure 27.6. The birdcage coil has a diameter of 26 cm, a length of 26 cm, and consists of 16 elements. The coil is excited in a quadrature mode and the maximum electric current in the elements is assumed to be 1 A. The coil is placed inside a cylindrical shield having a diameter of 32 cm and a length of 32 cm. The entire structure is enclosed by a rectangular PML box, which truncates the computational domain. The computed electric field is displayed in terms of the SAR defined by $\text{SAR} = \sigma|\boldsymbol{E}|^2/\rho$, where σ denotes the electric conductivity and ρ denotes the density of the tissue. Figure 27.7 displays the distribution of SAR in the three slices at 256 MHz, and Figure 27.8 shows the corresponding magnetic B1-field distribution.

27.6 FINITE-ELEMENT METHOD

Although the FDTD method is highly efficient, its geometrical modeling capability is limited by the staircase approximation. Although the staircase approximation of a dielectric object does not significantly affect the accuracy of the solution, a staircase modeling of small or thin conductors in RF coils can be technically challenging and may introduce undesirable errors. The FEM overcomes this limitation by using an unstructured tetrahedral mesh to model the computational domain. The FEM is often used in the frequency domain, although it can also be formulated to carry out a time-domain analysis.

Figure 27.6. Axial (a), sagittal (b), and coronal (c) slices of the head model used in the FDTD calculation. (Reproduced from Ref. 28. © IEEE, 1998.)

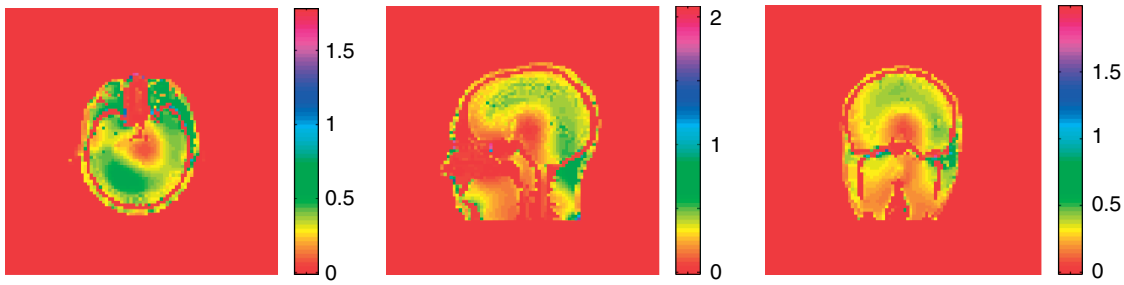

Figure 27.7. SAR (watts per kilogram) distribution in the axial (a), sagittal (b), and coronal (c) slices at 256 MHz. (Reproduced from Ref. 28. © IEEE, 1998.)

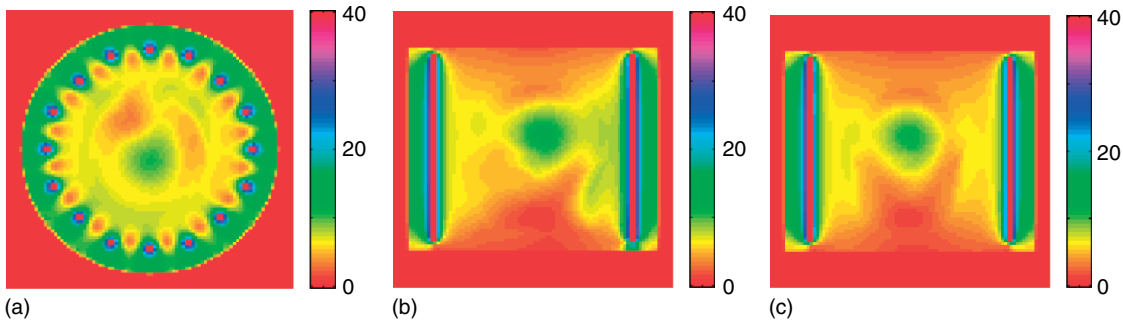

Figure 27.8. Magnetic field (amperes per meter) distribution in the axial (a), sagittal (b), and coronal (c) slices at 256 MHz. (Reproduced from Ref. 28. © IEEE, 1998.)

To solve the boundary-value problem defined by the partial differential equation (27.5) in conjunction with the boundary conditions (27.6) and (27.7) using the FEM,[44,45] we first choose a set of testing functions whose combination fully covers the range of the solution to equation (27.5). We then test equation (27.5) by taking its scalar product with each testing function and integrating over the entire computational domain. This yields

$$\iiint_V [\boldsymbol{W}_i \cdot \nabla \times (\nabla \times \boldsymbol{E}) - k_0^2 \varepsilon_r \boldsymbol{W}_i \cdot \boldsymbol{E}] \mathrm{d}V = -jk_0 Z_0 \iiint_V \boldsymbol{W}_i \cdot \boldsymbol{J}_{\mathrm{imp}} \mathrm{d}V \tag{27.40}$$

where V denotes the volume where the fields are to be computed and $\boldsymbol{W}_i$ denotes a testing or weighting function that satisfies the same boundary condition as $\boldsymbol{E}$. By invoking a vector identity and Gauss's divergence theorem and then applying the boundary condition (27.7) to the field on S that encloses volume V, we obtain

$$\iiint_V \left[(\nabla \times \boldsymbol{W}_i) \cdot (\nabla \times \boldsymbol{E}) - k_0^2 \varepsilon_r \boldsymbol{W}_i \cdot \boldsymbol{E}\right] \mathrm{d}V + jk_0 \iint_S (\hat{n} \times \boldsymbol{W}_i) \cdot (\hat{n} \times \boldsymbol{E}) \mathrm{d}S = -jk_0 Z_0 \iiint_V \boldsymbol{W}_i \cdot \boldsymbol{J}_{\mathrm{imp}} \mathrm{d}V \tag{27.41}$$

which is called the *weak-form representation* of the boundary-value problem defined by equations (27.5) and (27.7).

To discretize equation (27.41) using the FEM, the entire computational domain V is first divided into small elements such as tetrahedral elements and rectangular brick elements. An example of a tetrahedral mesh is given in Figure 27.9, where only the surface of the mesh is shown for the sake of clarity. Within each small element, $\boldsymbol{E}$ can be interpolated using a set

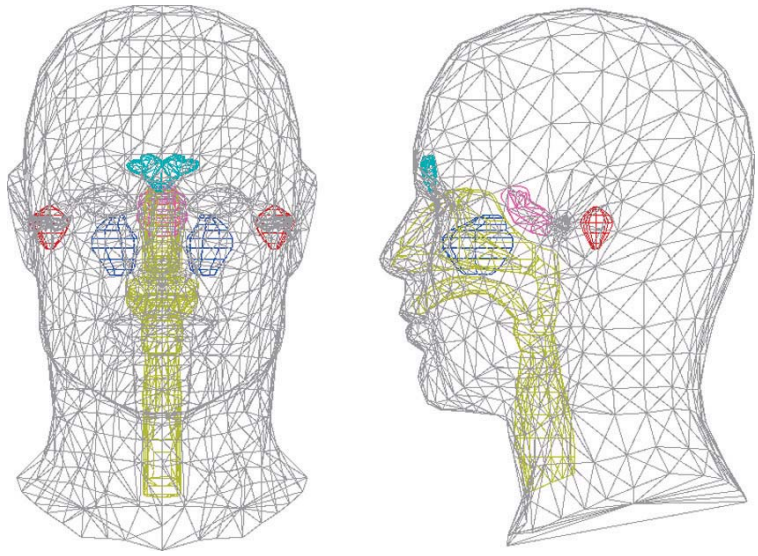

Figure 27.9. A finite-element mesh with tetrahedral elements (only the surface mesh is shown here for clarity). (Reproduced from Ref. 46. © Elsevier, 2002.)

of discrete values. By assigning the tangential component of $\boldsymbol{E}$ at each edge of a tetrahedral element and then interpolating $\boldsymbol{E}$ elsewhere using a set of vector basis functions, the field can be expanded as

$$\boldsymbol{E}^e(\boldsymbol{r}) = \sum_{i=1}^{6} \boldsymbol{N}_i^e(\boldsymbol{r}) E_i^e \tag{27.42}$$

where E_i^e denotes the tangential component of $\boldsymbol{E}$ at edge i of element e, and $\boldsymbol{N}_i^e$ is the corresponding interpolation or basis function. Denoting the simplex coordinates of a tetrahedron as $\lambda_l (l = 1, 2, 3, 4)$,[45] the vector basis function associated with the edge that connects vertices l and k is given by

$$\boldsymbol{N}_{lk}^e(\boldsymbol{r}) = \ell_{lk}(\lambda_l \nabla\lambda_k - \lambda_k \nabla\lambda_l) \tag{27.43}$$

where ℓ_{lk} denotes the length of the edge and $l, k = 1, 2, 3, 4$ with $l < k$. Figure 27.10 shows one of the six first-order vector basis functions for a tetrahedral element. Clearly, such basis functions have a tangential component only along the associated edge, and as such they ensure the tangential continuity of the interpolated field while allowing the normal component to be discontinuous at a material discontinuity. Hence, they accurately model the nature of the vector field $\boldsymbol{E}$. The field in a rectangular brick element can be interpolated as

$$\boldsymbol{E}^e(\boldsymbol{r}) = \sum_{i=1}^{12} \boldsymbol{N}_i^e(\boldsymbol{r}) E_i^e \tag{27.44}$$

since the element has 12 edges. The first-order vector basis functions have a very simple form and are given by

$$\boldsymbol{N}_i^e(\boldsymbol{r}) = \hat{x}\left(1 - \frac{|y - y_i|}{\Delta y}\right)\left(1 - \frac{|z - z_i|}{\Delta z}\right), \quad i = 1, 2, 3, 4 \tag{27.45}$$

for edges parallel to the x-axis,

$$\boldsymbol{N}_i^e(\boldsymbol{r}) = \hat{y}\left(1 - \frac{|x - x_i|}{\Delta x}\right)\left(1 - \frac{|z - z_i|}{\Delta z}\right), \quad i = 5, 6, 7, 8 \tag{27.46}$$

for edges parallel to the y-axis, and

$$\boldsymbol{N}_i^e(\boldsymbol{r}) = \hat{z}\left(1 - \frac{|x - x_i|}{\Delta x}\right)\left(1 - \frac{|y - y_i|}{\Delta y}\right), \quad i = 9, 10, 11, 12 \tag{27.47}$$

for edges parallel to the z-axis, where (x_i, y_i, z_i) denotes the middle point of the edge. The reason that we discuss the rectangular brick elements specifically here is that with this type of element, we can apply

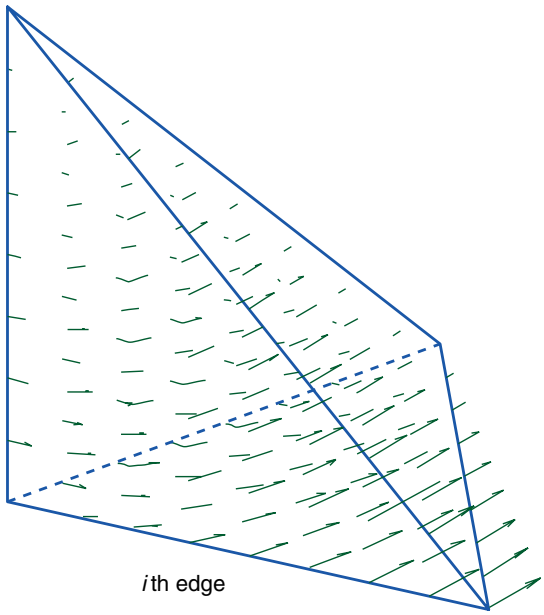

Figure 27.10. One of the six first-order vector basis functions for a tetrahedral element.

the FEM directly to the voxel model described in Section 27.3.

When the $\boldsymbol{E}$-field is interpolated in each element using its tangential values at the edges of the element, the $\boldsymbol{E}$-field in the entire volume V can be expressed as

$$\boldsymbol{E}(\boldsymbol{r}) = \sum_{i=1}^{N_{\text{edge}}} \boldsymbol{N}_i(\boldsymbol{r}) E_i \tag{27.48}$$

where N_{edge} denotes the total number of edges excluding those residing on conducting surfaces, E_i denotes the tangential component of $\boldsymbol{E}$ at the ith edge, and $\boldsymbol{N}_i$ is the corresponding basis function. Obviously, for an edge inside V, $\boldsymbol{N}_i$ spans several neighboring elements that share the common edge. Also note that by excluding the edges on conducting surfaces, the interpolated field satisfies the required boundary condition in equation (27.6).

By substituting equation (27.48) into equation (27.41) and using the same $\boldsymbol{N}_i$ as the testing function $\boldsymbol{W}_i$, we obtain

$$\sum_{j=1}^{N_{\text{edge}}} K_{ij} E_j = b_i, \quad i = 1, 2, \ldots, N_{\text{edge}} \tag{27.49}$$

where

$$K_{ij} = \iiint_V [(\nabla \times \boldsymbol{N}_i) \cdot (\nabla \times \boldsymbol{N}_j) - k_0^2 \varepsilon_r \boldsymbol{N}_i \cdot \boldsymbol{N}_j] \mathrm{d}V + jk_0 \iint_S (\hat{n} \times \boldsymbol{N}_i) \cdot (\hat{n} \times \boldsymbol{N}_j) \mathrm{d}S \tag{27.50}$$

$$b_i = -jk_0 Z_0 \iiint_V \boldsymbol{N}_i \cdot \boldsymbol{J}_{\text{imp}} \mathrm{d}V \tag{27.51}$$

The integrals involved can be evaluated either analytically or numerically using a Gaussian quadrature since the integrands are simple linear or quadratic functions. The results of analytical integration can be found in Ref. 45. Equation (27.49) can be written compactly as

$$[K]\{E\} = \{b\} \tag{27.52}$$

which can be solved for the vector $\{E\}$. Because the elemental interactions in equation (27.50) are local in nature, $[K]$ is a sparse and symmetric matrix that can be computed and solved efficiently using a sparse matrix solver. Once $\{E\}$ is obtained, the field everywhere in V can be calculated using equation (27.48), from which other parameters such as the B1 magnetic field and the specific absorption rate can be computed.

The FEM is probably the most popular numerical method used in a number of engineering and science studies because it can be adapted easily to solve different boundary-value problems and its geometrical modeling capability is unmatched by any other numerical method. However, the method is not as popular as the FDTD in computational electromagnetics and, in particular, for modeling and simulation of RF coils and RF fields in MRI. The main reason is the requirement to generate an FEM mesh, usually with tetrahedral elements, for the problem to be modeled. Although it is no longer difficult to create a model and generate a mesh even for a complicated RF coil, it is still highly challenging to create an anatomically accurate solid model and generate a tetrahedral mesh for a human body or a human head. Since most FEM-based computer codes use tetrahedral elements and there is no tetrahedral mesh readily available for a human body or a human head, the FEM has not been as widely used as the FDTD. However, by incorporating rectangular brick elements into the FEM, we can use the voxel model directly. This may partially alleviate the difficulty of mesh generation for using the FEM for MRI applications.

The second reason that the FEM is less popular is the need to solve the matrix equation (27.52). Even though the matrix is symmetric and sparse, its dimension can be very large when it is used on an accurate human model. Its efficient solution requires a special solver that can exploit the sparsity of the matrix with a minimum computational cost. The best approach is to precondition the matrix equation using an incomplete LU decomposition first and then solve the preconditioned matrix equation iteratively using a Krylov subspace algorithm such as GMRES and BiCGStab.[47] Similar to the case with the FDTD, the excitation of an RF coil can be modeled using either a current probe, which amounts to specifying $\boldsymbol{J}_{\text{imp}}$, or a voltage gap, which can be realized by enforcing the electric field across the gap.[48] The incorporation of lumped circuit elements such as resistors, inductors, and capacitors in the FEM is also straightforward.[45]

The FEM has found some applications in the modeling of RF coils and the interactions between the RF fields and the human body in MRI.[49–60] The most widely used FEM-based computer code for full-wave electromagnetic analysis is HFSS from ANSYS/Ansoft.[61] Another computer code is Multiphysics® from COMSOL.[62] There are several other computer codes that are aimed at the quasi-static analysis of electromagnetic problems. As a simple application example, Figure 27.11 shows a 2D model of a shielded birdcage coil loaded with a human head.[57] This model consists of a cylindrical conducting shell of diameter 30 cm and 16 conducting wires equally spaced on a cylindrical surface of diameter 26 cm. The coil is excited in a quadrature mode and the human head is placed inside the coil with its surface about 3.6 cm away from the wires. The electromagnetic model of the head consists of nine different tissues with different material properties. This problem can be analyzed by solving equation (27.52) for the electric field, from which the magnetic field can be calculated using equation (27.3). Figure 27.12 displays the magnitude of the magnetic field at 64, 128, 171, and 256 MHz. The field inhomogeneity is mainly due to the presence of the human head and is much more pronounced at higher frequencies.

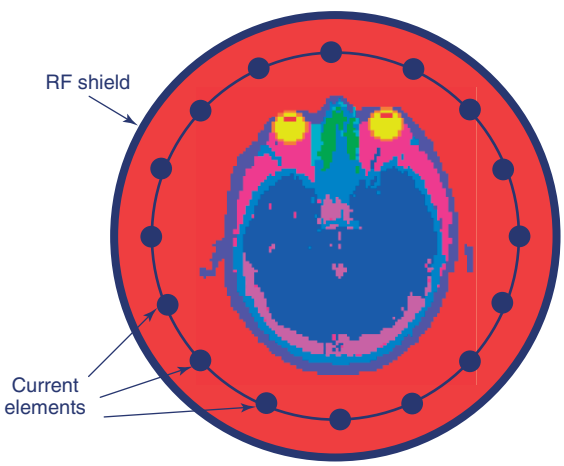

Figure 27.11. A shielded 16-element birdcage coil loaded with a human head. (Reproduced from Ref. 57. © Wiley-Liss, Inc, 1997.)

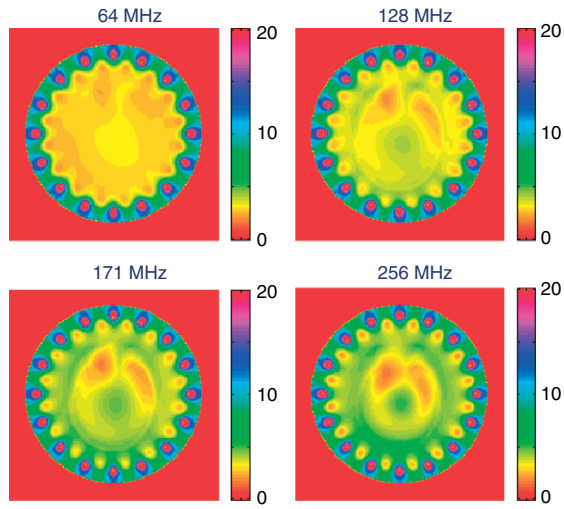

Figure 27.12. Magnitude of the magnetic field inside the loaded birdcage coil at four different frequencies. (Reproduced from Ref. 57. © Wiley-Liss, Inc, 1997.)

27.7 METHOD OF MOMENTS

Both the FDTD and FEM solve Maxwell's equations or the equivalent vector wave equation directly. As such, they require a discretization of the entire computational domain including the surrounding environment and they have to truncate the computational domain using either a perfectly matched layer or

an absorbing boundary condition. Another fundamentally different approach to solving an electromagnetic problem is to find a fundamental solution or the response to a point source first and convert the partial differential equation into an integral equation, which can then be discretized and solved numerically. In the community of computational electromagnetics, this method is known as the *method of moments* (*MoM*) or the *moment method*,[63–69] and the fundamental solution is called *Green's function*.

To illustrate the MoM formulation, we consider a shielded RF coil loaded with a nonmagnetic imaging subject. The excitation to the coil induces a surface electric current in the coil and its shield, which is denoted as $\boldsymbol{J}_{\mathrm{s}}$. For this case, Maxwell's equations (27.3) and (27.4) can be written as

$$\nabla \times \boldsymbol{E}(\boldsymbol{r}) = -\mathrm{j}\omega\mu_0 \boldsymbol{H}(\boldsymbol{r}) \tag{27.53}$$

$$\begin{aligned}\nabla \times \boldsymbol{H}(\boldsymbol{r}) &= \mathrm{j}\omega\varepsilon(\boldsymbol{r})\boldsymbol{E}(\boldsymbol{r}) + \sigma(\boldsymbol{r})\boldsymbol{E}(\boldsymbol{r}) + \boldsymbol{J}_{\mathrm{s}}(\boldsymbol{r}) \\ &= \mathrm{j}\omega\varepsilon_0 \boldsymbol{E}(\boldsymbol{r}) + \boldsymbol{J}_{\mathrm{eq}}(\boldsymbol{r}) + \boldsymbol{J}_{\mathrm{s}}(\boldsymbol{r})\end{aligned} \tag{27.54}$$

in which $\boldsymbol{J}_{\mathrm{eq}}(\boldsymbol{r}) = \mathrm{j}\omega\varepsilon_0[\varepsilon_{\mathrm{r}}(\boldsymbol{r}) - 1]\boldsymbol{E}(\boldsymbol{r})$, where $\varepsilon_{\mathrm{r}}(\boldsymbol{r})$ is defined after equation (27.5). These two equations indicate that the fields produced by the shielded coil loaded with an imaging subject can be expressed as the superposition of the fields radiated by $\boldsymbol{J}_{\mathrm{s}}$ and $\boldsymbol{J}_{\mathrm{eq}}$ in free space. On the basis of the well-known free-space field–source relation,[70] the total field is given by

$$\begin{aligned}\boldsymbol{E}(\boldsymbol{r}) = &-\mathrm{j}\omega\mu_0 \iint_{S_{\mathrm{PEC}}} \overleftrightarrow{\boldsymbol{G}}_{\mathrm{e0}}(\boldsymbol{r}, \boldsymbol{r}') \cdot \boldsymbol{J}_{\mathrm{s}}(\boldsymbol{r}')\mathrm{d}S' \\ &- \mathrm{j}\omega\mu_0 \iiint_{V_{\mathrm{d}}} \overleftrightarrow{\boldsymbol{G}}_{\mathrm{e0}}(\boldsymbol{r}, \boldsymbol{r}') \cdot \boldsymbol{J}_{\mathrm{eq}}(\boldsymbol{r}')\mathrm{d}V'\end{aligned} \tag{27.55}$$

where S_{PEC} denotes the conducting surfaces of the RF coil and the RF shield, V_{d} denotes the volume of the imaging subject, and $\overleftrightarrow{\boldsymbol{G}}_{\mathrm{e0}}(\boldsymbol{r}, \boldsymbol{r}')$ denotes the free-space dyadic Green's function of the electric type[70]

$$\overleftrightarrow{\boldsymbol{G}}_{\mathrm{e0}}(\boldsymbol{r}, \boldsymbol{r}') = \left(\overleftrightarrow{\boldsymbol{I}} + \frac{1}{k_0^2}\nabla\nabla\right) \frac{\exp(-jk_0|\boldsymbol{r} - \boldsymbol{r}'|)}{4\pi|\boldsymbol{r} - \boldsymbol{r}'|} \tag{27.56}$$

where $\overleftrightarrow{\boldsymbol{I}}$ is a unit dyad defined as $\overleftrightarrow{\boldsymbol{I}} = \hat{x}\hat{x} + \hat{y}\hat{y} + \hat{z}\hat{z}$. The first term in equation (27.55) is the field radiated by the shielded coil without the imaging subject and the second term is the field disturbance due to the presence of the imaging subject. Equation (27.55) can be rewritten as

$$\begin{aligned}\frac{\boldsymbol{D}(\boldsymbol{r})}{\varepsilon_0\varepsilon_{\mathrm{r}}(\boldsymbol{r})} = &-\mathrm{j}\omega\mu_0 \iint_{S_{\mathrm{PEC}}} \overleftrightarrow{\boldsymbol{G}}_{\mathrm{e0}}(\boldsymbol{r}, \boldsymbol{r}') \cdot \boldsymbol{J}_{\mathrm{s}}(\boldsymbol{r}')\mathrm{d}S' \\ &- \mathrm{j}\omega\mu_0 \iiint_{V_{\mathrm{d}}} \overleftrightarrow{\boldsymbol{G}}_{\mathrm{e0}}(\boldsymbol{r}, \boldsymbol{r}') \cdot \chi(\boldsymbol{r}')\boldsymbol{D}(\boldsymbol{r}')\mathrm{d}V'\end{aligned} \tag{27.57}$$

where $\chi(\boldsymbol{r}') = \mathrm{j}\omega[\varepsilon_{\mathrm{r}}(\boldsymbol{r}) - 1]/\varepsilon_{\mathrm{r}}(\boldsymbol{r})$. To solve for the unknown surface current density $\boldsymbol{J}_{\mathrm{s}}$ on the coil and shield and the unknown electric flux density $\boldsymbol{D}$ inside the imaging object, we apply the first boundary condition in equation (27.6) to have

$$\begin{aligned}&\hat{n}(\boldsymbol{r}) \times \iint_{S_{\mathrm{PEC}}} \overleftrightarrow{\boldsymbol{G}}_{\mathrm{e0}}(\boldsymbol{r}, \boldsymbol{r}') \cdot \boldsymbol{J}_{\mathrm{s}}(\boldsymbol{r}')\mathrm{d}S' + \hat{n}(\boldsymbol{r}) \\ &\times \iiint_{V_{\mathrm{d}}} \overleftrightarrow{\boldsymbol{G}}_{\mathrm{e0}}(\boldsymbol{r}, \boldsymbol{r}') \cdot \chi(\boldsymbol{r}')\boldsymbol{D}(\boldsymbol{r}')\mathrm{d}V' = 0, \quad \boldsymbol{r} \in S_{\mathrm{PEC}}\end{aligned} \tag{27.58}$$

where $\hat{n}$ denotes the unit normal on S_{PEC}. We then apply equation (27.57) to V_{d} to obtain

$$\begin{aligned}&\frac{\boldsymbol{D}(\boldsymbol{r})}{j\omega\mu_0\varepsilon_0\varepsilon_{\mathrm{r}}(\boldsymbol{r})} + \iint_{S_{\mathrm{PEC}}} \overleftrightarrow{\boldsymbol{G}}_{\mathrm{e0}}(\boldsymbol{r}, \boldsymbol{r}') \cdot \boldsymbol{J}_{\mathrm{s}}(\boldsymbol{r}')\mathrm{d}S' \\ &+ \iiint_{V_{\mathrm{d}}} \overleftrightarrow{\boldsymbol{G}}_{\mathrm{e0}}(\boldsymbol{r}, \boldsymbol{r}') \cdot \chi(\boldsymbol{r}')\boldsymbol{D}(\boldsymbol{r}')\mathrm{d}V' = 0, \quad \boldsymbol{r} \in V_{\mathrm{d}}\end{aligned} \tag{27.59}$$

which can be solved together with equation (27.58) for $\boldsymbol{J}_{\mathrm{s}}$ and $\boldsymbol{D}$.

To solve equations (27.58) and (27.59) numerically, we first discretize S_{PEC} into small surface elements such as triangular and quadrilateral elements and then discretize V_{d} into small volume elements such as tetrahedral and rectangular brick elements. Figure 27.13 shows a surface triangular discretization of a birdcage coil made of conducting strips.[71] Next, we need to expand $\boldsymbol{J}_{\mathrm{s}}$ and $\boldsymbol{D}$ in terms of basis functions. By recognizing the fact that the normal component of $\boldsymbol{J}_{\mathrm{s}}$ should be continuous across an edge shared by two surface elements and should vanish at the edges residing on the edge of a conducting surface, we can expand $\boldsymbol{J}_{\mathrm{s}}$ using the divergence-conforming Rao–Wilton–Glisson (RWG) basis functions[67]

$$\boldsymbol{J}_{\mathrm{s}}(\boldsymbol{r}') = \sum_{n=1}^{N_{\mathrm{s}}} I_n \boldsymbol{f}_n^{(\mathrm{s})}(\boldsymbol{r}') \tag{27.60}$$

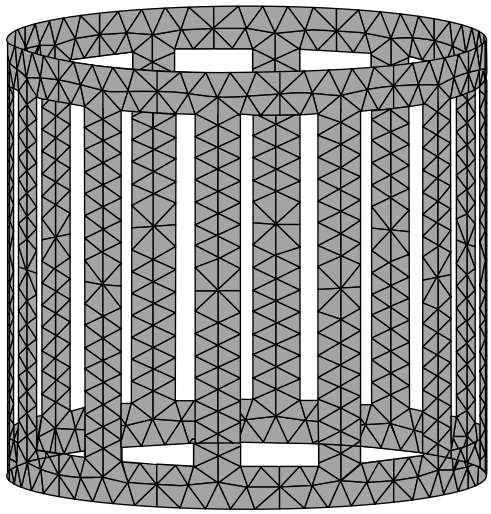

Figure 27.13. A birdcage coil modeled with triangular patches.

where N_s denotes the total number of edges in the surface meshes of the coil and shield except for those residing on the edges of the conducting surfaces, and $\boldsymbol{f}_n^{(s)}(\boldsymbol{r}')$ is the RWG basis function associated with edge n. For a triangular mesh, $\boldsymbol{f}_n^{(s)}(\boldsymbol{r}')$ is defined over two triangular elements joined at edge n:

$$\boldsymbol{f}_n^{(s)}(\boldsymbol{r}') = \begin{cases} \frac{l_n}{2A_n^+}\boldsymbol{\rho}_n^+ & \boldsymbol{r}' \in T_n^+ \\ \frac{l_n}{2A_n^-}\boldsymbol{\rho}_n^- & \boldsymbol{r}' \in T_n^- \end{cases} \tag{27.61}$$

where $T_n^{\pm}$ denote the two triangles associated with the edge, $A_n^{\pm}$ are the areas of triangles $T_n^{\pm}$, l_n is the length of the edge, and $\boldsymbol{\rho}_n^{\pm}$ are the vectors defined in Figure 27.14(a). The vector plot of $\boldsymbol{f}_n^{(s)}(\boldsymbol{r}')$ is illustrated in Figure 27.14(b). The most important feature of this basis function is that its component normal to edge n is a constant (normalized to 1), whereas the components normal to other edges are zero. This feature guarantees the continuity of the current flow over all edges. Similarly, since the normal component of $\boldsymbol{D}$ should be continuous across a facet shared by two volume elements, we can expand $\boldsymbol{D}$ using the divergence-conforming volumetric RWG basis functions[69]:

$$\boldsymbol{D}(\boldsymbol{r}') = \sum_{n=1}^{N_v} D_n \boldsymbol{f}_n^{(v)}(\boldsymbol{r}') \tag{27.62}$$

where N_v denotes the total number of facets in the volume mesh. The volumetric RWG basis functions $\boldsymbol{f}_n^{(v)}(\boldsymbol{r}')$ are very similar to the surface function illustrated in Figure 27.14: it spans two volumetric elements and its normal component is a constant (normalized to 1) at the facet shared by the two elements, whereas the components normal to other facets vanish so that the normal continuity of $\boldsymbol{D}$ across each facet is guaranteed.

Substituting the expansions in equations (27.60) and (27.62) into equations (27.58) and (27.59) and using $\hat{n}(\boldsymbol{r}) \times \boldsymbol{f}_m^{(s)}(\boldsymbol{r})$ to test equation (27.58) and $\boldsymbol{f}_m^{(v)}(\boldsymbol{r})$ to test equation (27.59), we obtain two matrix equations

$$\sum_{n=1}^{N_s} Z_{mn}^{(ss)} I_n + \sum_{n=1}^{N_v} Z_{mn}^{(sv)} D_n = 0, \quad m = 1, 2, \ldots, N_s \tag{27.63}$$

$$\sum_{n=1}^{N_s} Z_{mn}^{(vs)} I_n + \sum_{n=1}^{N_v} Z_{mn}^{(vv)} D_n = 0, \quad m = 1, 2, \ldots, N_v \tag{27.64}$$

where

$$Z_{mn}^{(ss)} = \int\!\!\int_{S_{PEC}} \boldsymbol{f}_m^{(s)}(\boldsymbol{r}) \cdot \int\!\!\int_{S_{PEC}} \overleftrightarrow{\boldsymbol{G}}_{e0}(\boldsymbol{r}, \boldsymbol{r}') \cdot \boldsymbol{f}_n^{(s)}(\boldsymbol{r}') \mathrm{d}S' \mathrm{d}S \tag{27.65}$$

$$Z_{mn}^{(sv)} = \int\!\!\int_{S_{PEC}} \boldsymbol{f}_m^{(s)}(\boldsymbol{r}) \cdot \iiint_{V_d} \overleftrightarrow{\boldsymbol{G}}_{e0}(\boldsymbol{r}, \boldsymbol{r}') \cdot \chi(\boldsymbol{r}') \boldsymbol{f}_n^{(v)}(\boldsymbol{r}') \mathrm{d}V' \mathrm{d}S \tag{27.66}$$

$$Z_{mn}^{(vs)} = \iiint_{V_d} \boldsymbol{f}_m^{(v)}(\boldsymbol{r}) \cdot \int\!\!\int_{S_{PEC}} \overleftrightarrow{\boldsymbol{G}}_{e0}(\boldsymbol{r}, \boldsymbol{r}') \cdot \boldsymbol{f}_n^{(s)}(\boldsymbol{r}') \mathrm{d}S' \mathrm{d}V \tag{27.67}$$

$$Z_{mn}^{(vv)} = \frac{1}{j\omega\mu_0\varepsilon_0} \iiint_{V_d} \frac{\boldsymbol{f}_m^{(v)}(\boldsymbol{r}) \cdot \boldsymbol{f}_n^{(v)}(\boldsymbol{r})}{\varepsilon_r(\boldsymbol{r})} \mathrm{d}V + \iiint_{V_d} \boldsymbol{f}_m^{(v)}(\boldsymbol{r}) \cdot \iiint_{V_d} \overleftrightarrow{\boldsymbol{G}}_{e0}(\boldsymbol{r}, \boldsymbol{r}') \cdot \chi(\boldsymbol{r}') \boldsymbol{f}_n^{(v)}(\boldsymbol{r}') \mathrm{d}V' \mathrm{d}V \tag{27.68}$$

The evaluation of the integrals in the expressions above is certainly nontrivial because their integrands can be singular when $|\boldsymbol{r} - \boldsymbol{r}'|$ approaches zero. Fortunately, the evaluation of these singular integrals has been studied extensively and many accurate schemes have been developed in the past.[64–69]

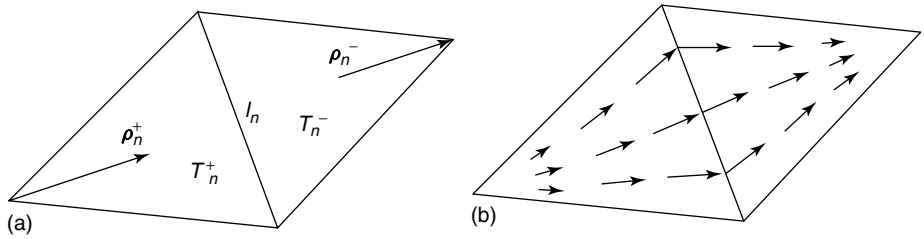

Figure 27.14. (a) Two triangles joined at a common edge. (b) Vector plot of the RWG function.

Before we solve equations (27.63) and (27.64), we have to apply the excitation to the coil. If the excitation is a current probe I_0 placed across edge m', we can simply replace the equation corresponding to $m = m'$ in equation (27.63) with $I_{m'} = I_0$. If the excitation is a voltage source V_0 applied across edge m', the right-hand side of the equation corresponding to $m = m'$ in equation (27.63) is no longer zero because of the applied voltage. Instead, it becomes $V'_m = l'_m V_0$, where l'_m denotes the length of the edge m'. Using a similar approach, we can incorporate capacitors and inductors into the MoM analysis.[1,71] Now, we can solve equations (27.63) and (27.64) for I_n and D_n, from which the field everywhere else can be found from equation (27.55) or (27.57) together with equations (27.60) and (27.62). In particular, the magnetic field can be calculated accurately from its free-space field–source relation[1]:

$$\boldsymbol{H}(\boldsymbol{r}) = \nabla \times \iint_{S_{\mathrm{PEC}}} G_0(\boldsymbol{r}, \boldsymbol{r}')\boldsymbol{J}_{\mathrm{s}}(\boldsymbol{r}')\mathrm{d}S' + \nabla \times \iiint_{V_{\mathrm{d}}} G_0(\boldsymbol{r}, \boldsymbol{r}')\boldsymbol{J}_{\mathrm{eq}}(\boldsymbol{r}')\mathrm{d}V' \tag{27.69}$$

where $G_0(\boldsymbol{r}, \boldsymbol{r}')$ denotes the free-space scalar Green's function

$$G_0(\boldsymbol{r}, \boldsymbol{r}') = \frac{\exp(-jk_0|\boldsymbol{r} - \boldsymbol{r}'|)}{4\pi|\boldsymbol{r} - \boldsymbol{r}'|} \tag{27.70}$$

Similar to the FDTD and FEM, the MoM has been employed for the analysis and design of RF coils in the past two decades.[71–79] In most of these applications, the coils are either unloaded or loaded with simple dielectric objects for the reason discussed below.

On the basis of the formulation described above, we can see that the MoM has two important advantages over the FDTD and FEM. First, the MoM discretization is limited to the conducting surfaces and dielectric volumes. It is not necessary to discretize the free-space region surrounding the coil and the imaging subject. This type of discretization reduces the number of unknowns significantly compared with the FDTD and FEM. Second, because of the use of the free-space Green's function, the MoM does not require any mesh truncation using absorbing boundary conditions or perfectly matched layers. Therefore, it is free of any truncation errors that often appear in the FDTD and FEM solutions. Unfortunately, the coefficient matrix in equations (27.63) and (27.64) is fully populated because of Green's function. Even though the number of unknowns is smaller than those in the FDTD and FEM, the computation associated with the generation of the MoM matrix and its solution is significantly more expensive than the computation of the FDTD and FEM. Therefore, a direct solution of equations (27.63) and (27.64) is computationally intensive and requires a tremendous amount of computer memory. Note that since $N_{\mathrm{v}} \gg N_{\mathrm{s}}$, the main cause of the intensive computation is the second term in equation (27.64), the term associated with the volumetric discretization of the imaging subject. Consequently, an MoM analysis of an RF coil loaded with a practical imaging subject is very time consuming, although the analysis of an unloaded coil can be done quite efficiently. In the following, we briefly discuss two approaches for overcoming this difficulty.

The first approach to alleviating the time-consuming computation of the MoM is to employ a fast algorithm to generate and solve the coefficient matrix in equations (27.63) and (27.64). The most efficient and general algorithms for this case are those based on the fast multipole method[80,81] and the adaptive integral method.[45,82] Both algorithms can reduce the computational cost (computation time and memory requirements) for evaluating a matrix–vector product from $O(N^2)$ to $O(N \log N)$, where N denotes the total number of unknowns. However, the implementation of the two algorithms,

especially the fast multipole algorithm, requires a significant effort. In the case that the imaging subject is modeled by a uniform regular grid as described in Section 27.3 the most efficient algorithm is the fast Fourier transform (FFT) method.[76,83] In this algorithm, the matrix associated with D_n in equation (27.64) can be reformulated as a circulant matrix, whose product with a vector can be evaluated very efficiently via the FFT. This algorithm, especially its modified weak-form version,[84,85] can be implemented relatively easily. To facilitate the use of this algorithm, we can first ignore the second term in equation (27.63) and carry out the analysis of an unloaded coil by solving the remaining equation:

$$\sum_{n=1}^{N_s} Z_{mn}^{(ss)} I_n^{(0)} = 0, \quad m = 1, 2, \ldots, N_s \quad (27.71)$$

Once $I_n^{(0)}$ is solved, we use it as I_n in the first term of equation (27.64) and solve the following equation for $D_n^{(0)}$:

$$\sum_{n=1}^{N_v} Z_{mn}^{(vv)} D_n^{(0)} = -\sum_{n=1}^{N_s} Z_{mn}^{(vs)} I_n^{(0)}, \quad m = 1, 2, \ldots, N_v \quad (27.72)$$

This solution neglects the effect of the imaging subject on the coil; hence, the calculated $I_n^{(0)}$ and $D_n^{(0)}$ can be considered as the zeroth-order approximation to the exact solution. The accuracy of the approximation can then be improved through an iterative process. For example, the first-order approximation can be obtained by first solving the following equation for $I_n^{(1)}$:

$$\sum_{n=1}^{N_s} Z_{mn}^{(ss)} I_n^{(1)} = -\sum_{n=1}^{N_v} Z_{mn}^{(sv)} D_n^{(0)}, \quad m = 1, 2, \ldots, N_s \quad (27.73)$$

and then solving the following equation for $D_n^{(1)}$:

$$\sum_{n=1}^{N_v} Z_{mn}^{(vv)} D_n^{(1)} = -\sum_{n=1}^{N_s} Z_{mn}^{(vs)} I_n^{(1)}, \quad m = 1, 2, \ldots, N_v \quad (27.74)$$

This approximate solution is usually sufficient for practical applications, although the accuracy can be improved continually by the second and third iterations. In this iterative process, equations (27.71) and (27.73) can be solved directly using either a Gaussian elimination or an LU decomposition or an iterative algorithm since N_s is usually quite small, whereas equations (27.72) and (27.74) can be solved using the FFT method because a direct solution would have been very time consuming since N_v can be very large.

The second approach for alleviating the time-consuming computation associated with the second term in equation (27.64) is to calculate the fields inside the imaging subject using either the FDTD or the FEM or, in other words, to replace equation (27.64) with the corresponding equations from the FDTD or FEM. In this approach, we first perform the analysis of an unloaded RF coil by solving equation (27.71). Using this solution, we can calculate an incident field due to the coil on the imaging subject or construct equivalent surface currents on the Huygens' surface that encloses the imaging subject. Using this incident field or Huygens' surface, we can compute the fields inside the imaging subject using either FDTD or FEM, as described in Sections 27.5 and 27.6. This yields the zeroth-order approximation that neglects the effect of the imaging subject on the RF coil. However, as mentioned above, the accuracy of this solution can be improved systematically via an iterative process to include the mutual interactions between the coil and the imaging subject. The calculated fields inside the imaging subject can be used to calculate the right-hand side of equation (27.73), which can be solved for a more accurate solution to the induced currents in the coil and shield. This solution can then be used to calculate a new and more accurate incident field or construct a new and more accurate Huygens' surface to produce a more accurate calculation of the fields inside the imaging subject using either the FDTD or the FEM. This approach, often referred to as the *hybrid MoM/FDTD* or *MoM/FEM* technique, has been employed successfully for the analysis of RF coils loaded with a dielectric object.[86–88] It utilizes the strength of the MoM for modeling an RF coil and takes full advantage of the FDTD and FEM for calculating the fields inside a complicated dielectric object.

Finally, both the FEM and MoM described here solve Maxwell's equations in the frequency domain and, as such, the computations have to be repeated at each frequency if one intends to compute the solution over a frequency band; however, efficient approaches have been developed to perform a fast frequency sweep by computing the fields at only a few frequency points.[45,71] Furthermore, commercial computer codes have been developed based on the

Table 27.2. Comparison between calculated and measured resonant frequencies of a flat low-pass ladder coil

Resonant mode	Calculated (MHz)	Measured (MHz)	Relative error (%)
1	47.6	48.2	1.2
2	75.2	75.5	0.4
3	93.8	93.8	0.0
4	107.2	107.2	0.0
5	117.6	117.5	0.1
6	125.4	125.1	0.2
7	130.6	130.2	0.3
8	133.8	133.7	0.1

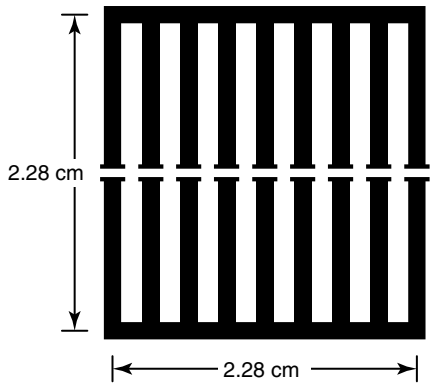

Figure 27.15. A flat low-pass ladder coil made of 0.143-cm wide conducting strips and 200-pF capacitors.

MoM and are available for RF coil analysis. One such code is FEKO from EM Software & Systems.[89] In fact, in addition to the MoM, the MoM/FEM hybrid is also implemented in FEKO to deal with RF coils loaded with a dielectric object. As a simple example, Table 27.2 gives the MoM-calculated results of the resonant frequencies of a flat low-pass ladder coil as compared with the measured data.[1] The specific configuration of the ladder coil is sketched in Figure 27.15. Note that a very good agreement between the calculated and measured data is obtained here because the coil is very simple and can be described very accurately. For more complicated coils, especially when they are loaded with a dielectric object, such an agreement is difficult, if not impossible, to obtain. However, as discussed in the next section, for a practical coil design, it is not necessary to predict resonant frequencies very accurately. Instead, it is more important to understand the current and the resulting field distributions of each resonant mode so that the right resonant mode can be chosen and shifted to the desired frequency.

An excellent example to demonstrate the application of the hybrid techniques is given by Li *et al.*[87] Figure 27.16(a) shows a 3D view of a shielded phased-array head coil loaded with a seven-layer dielectric sphere of diameter 140 mm. The material properties of the sphere are similar to those of a human head. The phased-array coil consists of four 120 mm × 120 mm individual coils placed on a cylindrical surface of diameter 204 mm, which, in

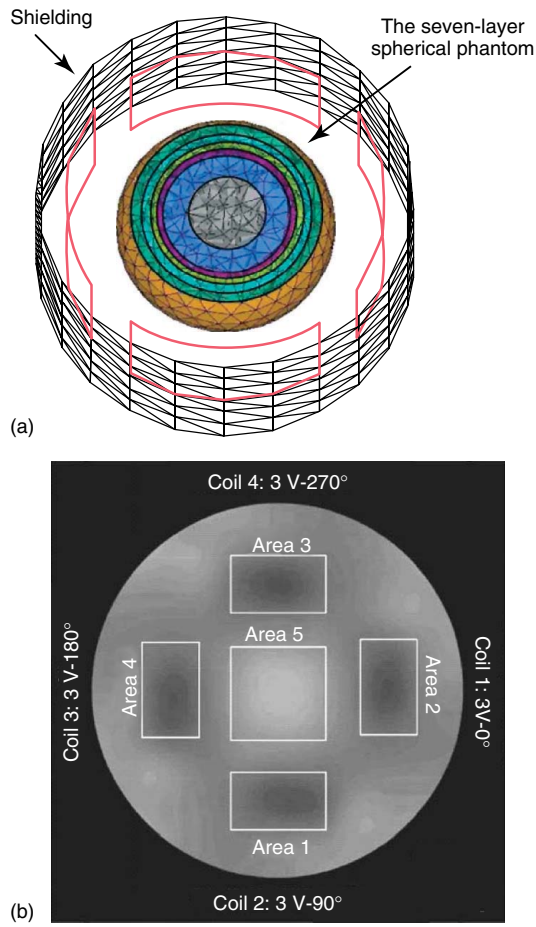

Figure 27.16. (a) A 3D view of a shielded phased-array head coil loaded with a seven-layer stratified sphere model with a diameter of 140 mm. (b) Transmitted B1 field when the phased-array head coil is excited with quadrature excitation. (Reproduced from Ref. 87. © IEEE, 2006.)

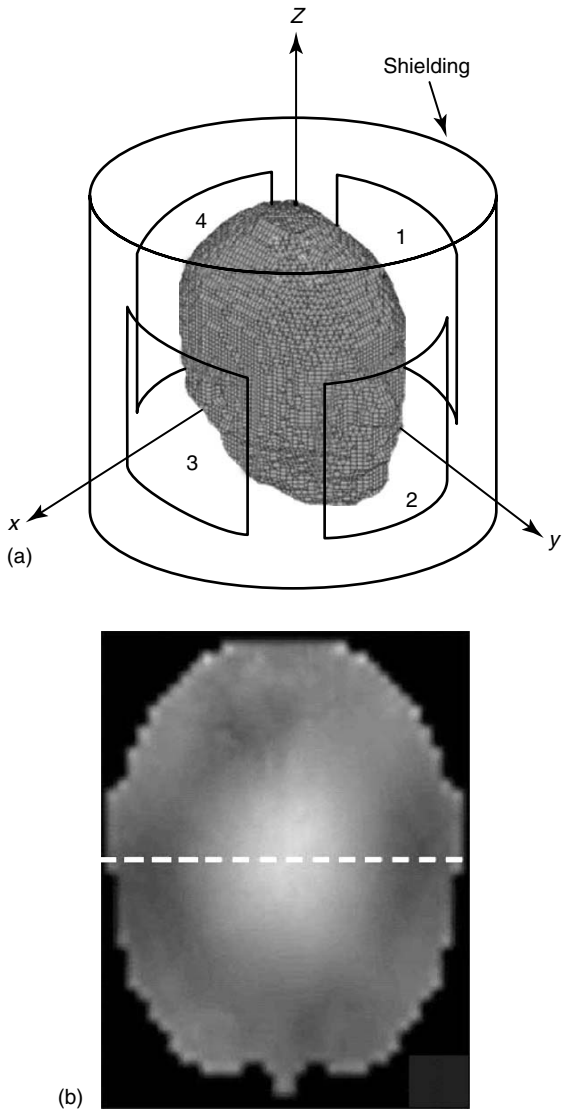

Figure 27.17. (a) A shielded four-element phased-array head coil loaded with the voxel-based human head model. (b) FDTD calculated signal intensity map when the phased-array head coil is excited with quadrature excitation. (Reproduced from Ref. 87. © IEEE, 2006.)

turn, is placed inside a cylindrical RF shield with a diameter of 242 mm and a height of 160 mm. The figure also shows the surface discretization of the RF shield and the volume discretization of the sphere. This problem was simulated using FEKO based on the hybrid MoM/FEM, where the MoM was used to model the currents on the coils and shield and the FEM was used to calculate the fields inside the sphere. Figure 27.16(b) shows the transmitted B1 field in the middle slice of the sphere when the phased-array head coil is excited with quadrature excitation at 470 MHz.[87] It is obvious that the B1 field exhibits a bright spot in area 5 and dark spots in areas 1–4 because of the strong interaction between the RF field and the dielectric sphere. The computed currents on the coils and shield were then impressed into the FDTD calculation using a voxel-based human head model, illustrated in Figure 27.17(a). The calculated B1 field inside the head model was subsequently used to evaluate the signal intensity map. The result in the middle axial slice is shown in Figure 27.17(b), which shows a similar pattern to that of the B1 field in the sphere model.[87] The problem shown in Figure 27.17(a) can also be simulated by using the FDTD method alone with the coils and the shield modeled as conductors and excited by voltage sources. However, an efficient MoM/FEM simulation would allow one to optimize the excitations (amplitudes and phases) of the four coils to produce another B1 field to compensate the field inhomogeneity obtained with quadrature excitation. The image obtained with the optimized excitation can then be combined with the image obtained with quadrature excitation to obtain an improved image, which was demonstrated successfully for brain imaging at 11 T by Li *et al.*[87]

27.8 SUMMARY

In this chapter, we discussed several practical methods for electromagnetic modeling of RF coils and RF fields for MRI applications. We first defined the boundary-value problem, which consists of Maxwell's equations and relevant boundary conditions. We then described the process required to build an electromagnetic model for the analysis of loaded RF coils, which consists of geometrical discretization and specification of electrical properties of the media involved. Next, we described the analytical solution of two simplified problems, whose results allow a quick qualitative examination of critical issues such as the field penetration into a dielectric object versus frequency, the achievable signal-to-noise ratio versus frequency, the magnetic field inhomogeneity due to the increased displacement current at higher frequencies, the level of the specific absorption rate due to the dielectric and conduction losses, the

effects of an RF shield, and the field penetration depth of a surface coil. For a more accurate quantitative analysis of these issues, we described three numerical methods, which are most suited for the modeling of RF coils loaded with a dielectric object. The first method is the FDTD, which is simple to implement and efficient to calculate. However, its geometric modeling capability for RF coils is limited by the staircase approximation. The second method is the FEM, which has an excellent geometric modeling capability. However, its application has been hindered by the necessity to generate an FEM mesh for the geometry to be discretized. The third method is the MoM, which is highly accurate and efficient for the analysis of unloaded coils. However, the method becomes very time consuming when the MoM is applied to the modeling of a dielectric object. For each method, we discussed solutions to overcome its limitations, such as the use of a voxel model directly in the FEM via the use of brick elements, the use of fast algorithms to speed up the MoM analysis of the dielectric object, and the hybridization of the MoM with either the FDTD or the FEM to perform a practical analysis of loaded RF coils.

It should be noted that the main objective of an electromagnetic modeling of RF coils is to understand how a specific RF coil design works (its resonant modes, and the electric current and the magnetic field distributions for each resonant mode) and then how the RF field interacts with the imaging subject (the electric and magnetic field distributions, and the resultant specific absorption rate and signal-to-noise ratio). This understanding can guide one to design a better RF coil for a specific application. The quantitative results of the field distribution can also be incorporated in the design of pulse sequences and image-processing algorithms to compensate for the field inhomogeneity and enhance the image quality. With respect to the coil design, it is rarely the case that one can use the result of a simulation to construct an RF coil that works on the first try. This is due in part to the use of inaccurate parameters such as the permittivity and conductivity values of human tissues because the accurate values are simply not available and in part to some necessary simplification of the problem such as neglecting the effect of the MRI system outside the RF coil (gradient coils, shim coils, magnets, and the supporting structures) for a practical numerical modeling. Therefore, the resonant frequency of an initial design is always shifted from the desired frequency. This is actually not a serious problem and there is no need to deal with it through a more accurate and more complicated analysis. One can simply scale the values of the capacitors based on the measured resonant frequency and the desired value to make the coil resonate at the desired frequency with only one iteration. The important thing is to pick up the right resonant mode to scale the capacitors and that requires a good understanding of the resonance of the RF coil, which can be gained through a numerical modeling using the methods described in this chapter. Finally, we note that since the objective of this chapter is to describe a few practical methods for electromagnetic modeling of RF coils and their interactions with the imaging subject, no attempt was made to use any of these methods to solve specific problems or to design specific coils for MRI applications. The examples given here were simply to demonstrate the use and capabilities of the numerical methods. Specific applications of these methods are addressed in other chapters.

REFERENCES

1. J. M. Jin, *Electromagnetic Analysis and Design in Magnetic Resonance Imaging*, CRC Press: Boca Raton, FL, 1998.
2. P. M. Robitaille and L. J. Berliner, *Ultra High Field Magnetic Resonance Imaging*, Springer: New York, 2006.
3. I. G. Zubal, C. R. Harrell, E. O. Smith, Z. Rattner, G. Gindi, and P. B. Hoffer, *Med. Phys.*, 1994, **21**, 299–302.
4. P. J. Dimbylow, The development of realistic voxel phantoms for electromagnetic field dosimetry, in *Voxel Phantom Development*, *Proceedings of An International Workshop*, ed. P. J. Dimbylow, National Radiological Protection Board: Chilton, 1995, pp. 1–7.
5. X. G. Xu, T. C. Chao, and A. Bozkurt, *Health Phys.*, 2000, **78**, 476–486.
6. K. Saito, A. Wittmann, S. Koga, Y. Ida, K. Kamei, and M. Zankl, *Radiat. Environ. Biophys.*, 2001, **40**, 69–76.
7. M. Zankl and A. Wittmann, *Radiat. Environ. Biophys.*, 2001, **40**, 153–162.
8. A. Barchanski, M. Clemens, H. De Gersem, T. Steiner, and T. Weiland, *COMPEL: Int. J. Comput. Math. Electr. Electron. Eng.*, 2005, **24**, 458–467.

9. M. A. Stuchly and S. S. Stuchly, *J. Microw. Power*, 1980, **15**, 19–26.
10. C. Gabriel, Compilation of the dielectric properties of body tissues at RF and microwave frequencies, Occupational and Environmental Health Directorate, Radio-frequency Radiation Division, Brooks Air Force Base, TX, Tech. Rep. ALOE-TR-1996-0037, 1996.
11. C. Gabriel, S. Gabriel, and E. Corthout, *Phys. Med. Biol.*, 1996, **41**, 2231–2249.
12. S. Gabriel, R. W. Lau, and C. Gabriel, *Phys. Med. Biol.*, 1996, **41**, 2271–2293.
13. F. A. Duck, *Physical Properties of Tissue: A Comprehensive Reference Book*, Academic: London, 1990.
14. P. A. Bottomley and E. R. Andrew, *Phys. Med. Biol.*, 1978, **23**, 630–643.
15. P. Mansfield and P. G. Morris, Advances in magnetic resonance, *NMR Imaging in Biomedicine*, Academic: New York, 1982, Suppl. 2.
16. G. H. Glover, C. E. Hayes, N. J. Pelc, W. A. Edelstein, O. M. Mueller, H. R. Hart, C. J. Hardy, M. O'Donnell, and W. D. Barber, *J. Magn. Reson.*, 1985, **64**, 255–270.
17. P. A. Bottomley, R. W. Redington, W. A. Edlestein, and J. F. Schenck, *Magn. Reson. Med.*, 1985, **2**, 336–349.
18. T. K. Foo, C. E. Hayes, and Y. W. Kang, *Magn. Reson. Med.*, 1991, **21**, 165–177.
19. J. R. Keltner, J. W. Carlson, M. S. Roos, S. T. S. Wong, T. L. Wong, and T. F. Budinger, *Magn. Reson. Med.*, 1991, **22**, 467–480.
20. H. Vesselle and R. E. Collin, *IEEE Trans. Biomed. Eng.*, 1995, **42**, 497–506.
21. F. Liu and S. Crozier, *Phys. Med. Biol.*, 2004, **49**(10), 1835–1851.
22. K. S. Yee, *IEEE Trans. Antennas Propag.*, 1966, **14**, 302–307.
23. A. Taflove and S. C. Hagness, *Computational Electrodynamics: The Finite Difference Time Domain Method*, 3rd edn., Artech House: Boston, MA, 2005.
24. J.-P. Berenger, *J. Comput. Phys.*, 1994, **114**(2), 185–200.
25. W. C. Chew and W. H. Weedon, *Microw. Opt. Tech. Lett.*, 1994, **7**, 599–604.
26. Z. S. Sacks, D. M. Kingsland, R. Lee, and J. F. Lee, *IEEE Trans. Antennas Propag.*, 1995, **43**, 1460–1463.
27. Y. Han and S. M. Wright, Analysis of RF penetration effects in MRI using finite-difference time-domain method, *Proceedings 12th Annual Meeting*, SMRM: New York, 1993, p. 1327.
28. J. Chen, Z. Feng, and J. M. Jin, *IEEE Trans. Biomed. Eng.*, 1998, **45**, 650–659.
29. C. M. Collins, S. Li, and M. B. Smith, *Magn. Reson. Med.*, **1998**, **40**, 847–856.
30. O. P. Gandhi and X. B. Chen, *Magn. Reson. Med.*, 1999, **41**, 816–823.
31. M. Kowalski, J. M. Jin, and J. Chen, *IEEE Trans. Biomed. Eng.*, 2000, **47**(11), 1525–1533.
32. T. S. Ibrahim, R. Lee, B. A. Baertlein, A. Kangarlu, and P. M. L. Robitaille, *Magn. Reson. Imaging*, 2000, **18**, 733–742.
33. C. M. Collins and M. B. Smith, *Magn. Reson. Med.*, 2001, **45**(4), 692–699.
34. T. S. Ibrahim, R. Lee, B. A. Baertlein, and P. M. L. Robitaille, *Phys. Med. Biol.*, 2001, **46**, 609–619.
35. C. M. Collins and M. B. Smith, *J. Magn. Reson. Imaging*, 2003, **18**(3), 383–388.
36. C. M. Collins, W. Liu, J. Wang, R. Gruetter, J. T. Vaughan, K. Ugurbil, and M. B. Smith, *J. Magn. Reson. Imaging*, 2004, **19**(5), 650–656.
37. X. Hanus, M. Luong, and F. Lethimonnier, Electromagnetic fields and SAR computations in a human head with a multi-port driven RF coil at 11.7 Tesla, *Proceedings 13th Annual Meeting ISMRM.*, Miami Beach, FL, 2005.
38. T. S. Ibrahim, A. Kangarlu, and D. W. Chakeres, *IEEE Trans. Biomed. Eng.*, 2005, **52**(7), 1278–1284.
39. T. S. Ibrahim and L. Tang, *J. Magn. Reson. Imaging*, 2007, **25**, 1235–1247.
40. R. Abraham and T. S. Ibrahim, *Magn. Reson. Med.*, 2007, **57**, 235–242.
41. H. Wang, A. Trakic, L. Xia, F. Liu, and S. Crozier, *Concepts Magn. Reson. Part B Magn. Reson. Eng.*, 2007, **31**(3), 147–161.
42. C. Penny, *Microw. J.*, 2007, **50**(12), 118–122. http://www.remcom.com/xf7.
43. EM field distribution and SAR in a human head with MRI coil, http://www.cst.com.
44. P. P. Silvester and R. L. Ferrari, *Finite Elements for Electrical Engineers*, 3rd edn, Cambridge University Press: Cambridge, 1996.
45. J. M. Jin, *The Finite Element Method in Electromagnetics*, 2nd edn, Wiley: Hoboken, NJ, 2002.

46. C. M. Collins, B. Yang, Q. X. Yang, and M. B. Smith, *Magn. Reson. Imaging*, 2002, **20**(5), 413–424.
47. Y. Saad, *Iterative Methods for Sparse Linear Systems*, 2nd edn, SIAM: Philadelphia, PA, 2003.
48. J. M. Jin and D. J. Riley, *Finite Element Analysis of Antennas and Arrays*, Wiley: Hoboken, NJ, 2009.
49. L. S. Petropoulos, E. M. Haacke, R. W. Brown, and E. Boerner, *Magn. Reson. Med.*, 1993, **30**(3), 366–372.
50. Q. X. Yang, C. S. Li, and M. B. Smith, The effect of sample loading on the radio frequency magnetic field distribution in high field: Contributions of dielectric resonance, *Proceedings 12th Annual Meeting*, SMRM, New York, 1993, p. 1367.
51. J. T. Vaughn, H. P. Hetherington, J. O. Otu, J. W. Pan, and G. M. Pohost, *Magn. Reson. Med.*, 1994, **32**, 206–218.
52. Q. X. Yang, H. Maramis, C. S. Li, and M. B. Smith, Three-dimensional full-wave solution of MRI radio frequency resonator, *Proceedings 2nd Meeting*, SMR: San Francisco, CA, 1994, p. 1110.
53. S. Li, Q. X. Yang, and M. B. Smith, *Magn. Reson. Imaging*, 1994, **12**(7), 1079–1087.
54. D. Simunic, P. Wach, W. Renhart, and R. Stollberger, *IEEE Trans. Biomed. Eng.*, 1996, **43**, 88–94.
55. J. G. Harrison and J. T. Vaughan, *12th Annual Review of Progress in Applied Computational Electromagnetics*, Monterey, CA, 1996, Vol. 2, pp 1220–1226.
56. C. Guclu, G. Kashmar, A. Hacinliyan, and O. Nalcioglu, *Magn. Reson. Med.*, 1997, **37**(1), 76–83.
57. J. M. Jin and J. Chen, *Magn. Reson. Med.*, 1997, **38**(6), 953–963.
58. B. J. Dardzinski, S. Z. Li, C. M. Collins, G. D. Williams, and M. B. Smith, *J. Magn. Reson.*, 1998, **131**(1), 32–38.
59. J. F. Vazquez and A. O. Rodriguez, *10th Mexican Symposium on Medical Physics AIP Conference Proceedings*, Mexico City, Mexico, 2008, Vol. 1032, pp 172–175.
60. M. Kozlov and R. Turner, *J. Magn. Reson.*, 2009, **200**(1), 147–152.
61. R. P. Kleihorst and M. H. Vogel, Analysis of MRI Systems Including a Human-body Model, http://www.ansoft.com/products/hf/hfss.
62. MRI Bird-cage Coil, http://www.comsol.com/showroom/gallery/ 4101/.
63. R. F. Harrington, *Field Computation by Moment Methods*, Macmillan: New York, 1968.
64. E. K. Miller, L. Medgyesi-Mitschang, and E. H. Newman, eds, *Computational Electromagnetics: Frequency-domain Method of Moments*, IEEE Press: New York, 1992.
65. J. J. H. Wang, *Generalized Moment Methods in Electromagnetics*, Wiley: New York, 1991.
66. A. F. Peterson, S. L. Ray, and R. Mittra, *Computational Methods for Electromagnetics*, IEEE Press: New York, 1997.
67. S. M. Rao, D. R. Wilton, and A. W. Glisson, *IEEE Trans. Antennas Propag.*, 1982, **30**, 409–418.
68. D. E. Livesay and K. M. Chen, *IEEE Trans. Microw. Theory Tech.*, 1974, **22**, 1273–1280.
69. D. H. Schaubert, D. R. Wilton, and A. W. Glisson, *IEEE Trans. Antennas Propag.*, 1984, **32**, 77–85.
70. C. T. Tai, *Dyadic Green Functions in Electromagnetic Theory*, 2nd edn, IEEE Press: Piscataway, NJ, 1994.
71. D. Jiao and J. M. Jin, *IEEE Trans. Biomed. Eng.*, 1999, **46**, 1387–1390.
72. S. M. Wright and M. F. Lee, Full-wave moment of method analysis of RF coils on lossy media, *Proceedings 10th Annual Meeting*, SMRM: San Francisco, CA, 1991, p. 730.
73. S. M. Wright, Moment method analysis of coupled RF coils, *Proceedings 11th Annual Meeting*, SMRM: Berlin, 1992, p. 4008.
74. H. Ochi, E. Yamamoto, K. Sawaya, and S. Adachi, Calculation of electromagnetic field of an MRI antenna loaded by a body, *Proceedings 11th Annual Meeting*, SMRM: Berlin, 1992, p. 4021.
75. H. Ochi, E. Yamamoto, K. Sawaya, and S. Adachi, *Electron. Commun. Jpn. Part I Commun.*, 1994, **77**(1), 37–45.
76. J. M. Jin, J. Chen, H. Gan, W. C. Chew, R. L. Magin, and P. J. Dimbylow, *Phys. Med. Biol.*, 1996, **41**, 2719–2738.
77. F. H. Lin, W. P. Kuan, S. K. Jeng, and J. H. Chen, *IEEE Trans. Med. Imaging*, 1999, **18**(12), 1129–1137.
78. J. H. Chen, S. K. Jeng, F. H. Lin, and W. P. Kuan, *IEEE Trans. Magn.*, 1999, **35**(4), 2118–2127.
79. J. Fang, M. S. Chow, K. C. Chan, K. K. Wong, G. X. Shen, E. Gao, E. S. Yang, and Q. Y. Ma, *IEEE Trans. Appl. Supercond.*, 2002, **12**(2), 1823–1827.
80. R. Coifman, V. Rokhlin, and S. Wandzura, *IEEE Antennas Propag. Mag.*, 1993, **35**, 7–12.

81. W. C. Chew, J. M. Jin, E. Michielssen, and J. M. Song, eds, *Fast and Efficient Algorithms in Computational Electromagnetics*, Norwood, MA: Artech House, 2001.

82. E. Bleszynski, M. Bleszynski, and T. Jaroszewicz, *Radio Sci.*, 1996, **31**, 1225–1251.

83. D. T. Borup and O. P. Gandhi, *IEEE Trans. Microw. Theory Tech.*, 1984, **32**, 355–360.

84. A. P. M. Zwamborn, P. M. van den Berg, J. Mooibroek, and F. T. C. Koenis, *ACES J.*, 1992, **7**, 26–42.

85. C. F. Wang and J. M. Jin, *IEEE Trans. Microw. Theory Tech.*, 1998, **46**, 553–558.

86. F. Liu, B. L. Beck, B. Xu, J. R. Fitzsimmons, S. J. Blackband, and S. Crozier, *Concepts Magn. Reson. Part B Magn. Reson. Eng.*, 2005, **24B**(1), 28–38.

87. B. K. Li, F. Liu, and S. Crozier, *IEEE Trans. Electromagn. Compat.*, 2006, **48**(4), 628–633.

88. B. K. Li, F. Liu, E. Weber, and S. Crozier, *NMR Biomed.*, 2008, **22**(9), 937–951.

89. Modeling Magnetic Resonance Imaging (MRI) in FEKO, http://www.feko.info/applications/white-papers/mri-modelling/modelling-magnetic-resonance-imaging-mri-in-feko.html.

Chapter 28

Radiofrequency Fields and SAR for Bird Cages

Tamer S. Ibrahim

Departments of Bioengineering and Radiology, University of Pittsburgh, Pittsburgh, PA 15213, USA

28.1 INTRODUCTION

Until recently, the design of RF coils in MRI has been predominantly based on the use of circuit concepts and transmission line theory.[1,2] These analytical models invoke quasistatic field approximations.[3] At relatively smaller electrical sizes, which typically occur at lower MRI Larmor frequencies (<3 T) and smaller coil loads, the quasistatic approximations are valid for head coils because the RF coil and human head are small compared to the wavelength of the RF field. For instance, many 1.5 T (Larmor frequency = 64 MHz) MRI systems use RF head coils such as the birdcage resonator,[2] which is usually driven in quadrature (two ports).[1] At this frequency, circuit/transmission line models can be applied to predict the resonance frequency and to determine the magnetic field distribution, by assuming that the currents on the coil structure are uniform and then using the Biot–Savart Law to determine the magnetic field produced by these currents. While circuit/transmission line models are 0D approximations for the 3D near-field electromagnetic behavior in the coil, they can be very accurate for modeling relatively complex coil geometries.

As the electrical sizes of the RF coil and/or the load become larger, the circuit/transmission models start to fail to describe the electromagnetic behavior of the RF coil.[4–21] While circuit/transmission line models start to break down with increasing operating frequency,[20,22,23] they fail at a much faster rate with the presence of tissue. Tissue distorts the "ideal", easily modeled (from an analytical point of view) transverse electromagnetic (TEM) field structures[6,24,25] leading to more complex hybrid electromagnetic modes that are extremely challenging to analytical model. In this chapter, we examine full-wave computational electromagnetic modeling, using the birdcage coil as an example.

RF Coils for MRI
Edited by J. Thomas Vaughan and John R. Griffiths
 ISBN: 978-0-470-77076-4

28.2 BACKGROUND

Since the inception of MRI, the goal of a Tx/Rx RF volume coil design, such as a birdcage coil, has been to produce a uniform circularly polarized component of the transverse magnetic field, both excitation (B_1^+) and reception (B_1^-), and acceptable specific absorption rate (SAR) values in the imaged subject. These qualities have been typically attainable at 64 MHz. As the resonant frequency increases with field strength, however, not only does the quasistatic approximation begin to fail, but also the homogeneity of the B_1^+/B_1^- field deteriorates, and the tissues become more prone to localized heating (hot-spots) due to electromagnetic absorption. With the failure of quasistatic approximations as the MRI operational frequency increases, a computational tool based on full-wave electromagnetics becomes essential in conducting feasibility studies and in designing and evaluating the performance of high-field RF coils.

Until the early mid 90s, full-wave numerical methods were seldom used to model the fields in RF coils for MRI systems. Before that, there was not much need for such an approach because most of the systems were at magnetic field strengths of 1.5 T and below. In the last decade, however, there have been numerous applications of full-wave numerical methods to analyze a variety of MRI RF coils.[15,26–33] Within the context of birdcage designs, in 1996, Jin *et al*. employed the conjugate gradient method with the fast Fourier transform (FFT) to study the birdcage coil.[34] A 2D finite elements model (FEM) model has also been used to study the field and the SAR in a birdcage coil loaded with a human head model.[35] Later, the finite difference time domain (FDTD) method was also used to analyze the same coil.[7,9,30,36–47] In addition, simulations have also made advances in the prediction of temperature distributions by thermal modeling.[48–51]

28.3 MODELING BIRDCAGE RESONATORS: POTENTIAL COMPUTATIONAL ELECTROMAGNETICS OPTIONS

There are three major numerical methods used in electromagnetics: the FEM, the FDTD method, and the integral equation method, method of moments (MM). Although MM and FEM can be solved in the time domain, they are rarely used in this way; FEM and MM are usually associated with the frequency domain. MM is different from FEM and FDTD in that MM can be formulated in terms of unknown surface currents on perfect conductors and unknown volume currents in materials, whereas the unknowns in FEM and FDTD are the field values everywhere within the volume of interest. Because of this, MM has great advantages over FDTD and FEM when it is applied to geometries consisting of only perfect conductors since the number of unknowns in MM is much less than the other two methods.

For problems where large portions of the geometry are non-perfectly conducting, the number of unknowns for all three methods is comparable; however, the computation times are very different. Both MM and FEM require the solution of matrix equation. Since the number of unknowns required to model the coil is very large, iterative methods offer the only viable way to solve the matrix equation. Assuming the number of unknowns in the problem as N, the computation time is proportional to N^θ, where θ is 2 for MM and 1.5 for FEM. It should be noted that when there are large permittivity and conductivity contrasts in the geometry, which occur when human tissue is present, the values of θ may be significantly larger than the nominal given values. On the other hand, the FDTD method does not require a matrix solution, and its computation time is proportional to $N^{4/3}$.

There is also a wide disparity in terms of memory requirements between the three methods. The memory needed to solve an MM problem with 50 000 unknowns can be used to solve an FEM problem with 5 000 000 unknowns and an FDTD problem with 100 000 000 unknowns. The one disadvantage of FDTD relative to FEM is that it is less flexible for modeling arbitrary geometries because FEM can be applied to an unstructured grid. However, for the electrically large geometries, one can argue that it is better to use FDTD than FEM because, in many cases, the number of unknowns needed to solve the problem is relatively very large. In addition, many other tailored algorithms can also be utilized to optimize the standard FDTD scheme. In fact, many such algorithms have been successfully applied for MRI simulations.[25,37,52] It is noted however that with current advances in computational hardware such as GPUs, matrix solution methods such as FEM, hybrid FEM/FDTD, and/or hybrid MOM/FDTD methods[53–55] may become more computationally affordable, rendering more accurate

results when compared to a standalone method such as the FDTD method.

28.4 MODELING BIRDCAGE RESONATORS USING THE FDTD METHOD

The FDTD technique introduced by Kane[56] is used to give a direct solution to Maxwell's time-dependent curl equations. The FDTD method is essentially based on replacing the spatial and time domain derivatives of Maxwell's equations with finite difference approximations. An excellent source for the FDTD formulation can be obtained from Ref. 57.

28.4.1 Grid and Absorbing Boundaries

3D FDTD models of a high pass birdcage coil can be developed with different coil conductor widths. For the results shown in this chapter, the width of the coil conductors was set to infinitesimal[36,37,58] or to 0.3 in Refs 38, 39. In order to obtain accurate electromagnetic field calculations with the FDTD algorithm, an octagonal geometry can be utilized in which the lumped capacitive elements could be properly modeled. Figure 28.1 shows the FDTD grid and the human head, where eightfold symmetry is maintained. The different color points on the grid correspond to different algorithms utilized to describe the desired geometry. For instance, a lumped element FDTD algorithm was used to model the tuning capacitors.[59] This algorithm requires that the capacitive lumped elements be positioned along the Cartesian axes, namely, x or y. Thus, in order to maintain symmetry, the orientation of the capacitors along the eight slanted edges of the rings may change. Another example is an FDTD algorithm that was utilized to account for the curvatures of the rings and strips, which results in removing stair-stepping errors from these critical coil components. For some of the examples shown in this chapter, a total of 4 000 000 cells were utilized in the case of the thin conductor model and 25 000 000 cells in the case of 0.3 in conductor model to generate the complete grid. Note that the magnet shield was modeled in the 25 000 000 cell system. The perfectly matched layer (PML) absorbing boundary condition can be used to absorb the RF radiation from the coil.[57,60–63]

28.4.2 Developing a Code

FDTD codes typically start by dynamically allocating the memory requirements for the birdcage coil

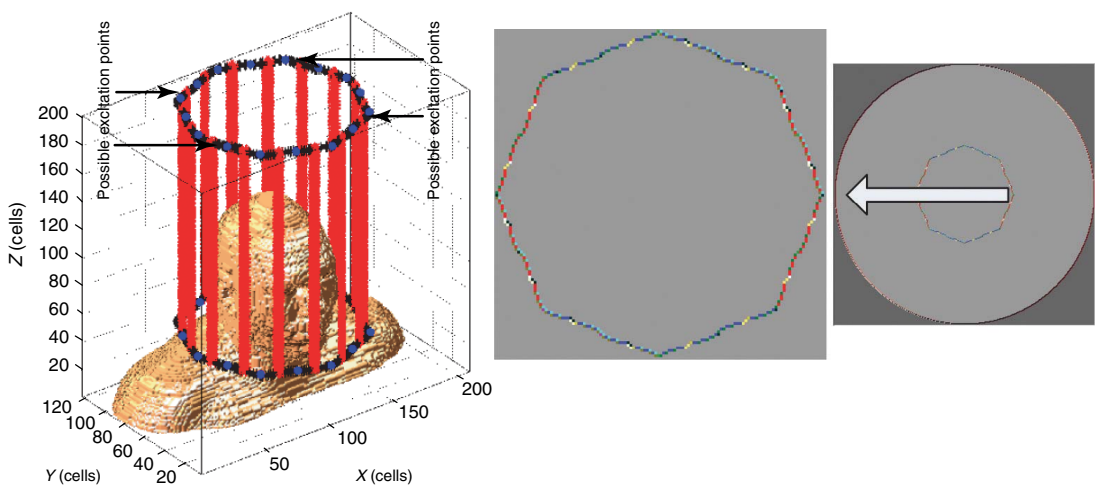

Figure 28.1. FDTD grid (ref) of a 16-end ring high pass birdcage coil loaded with the anatomically detailed visible human project model. The different shadings (top right) on the grid correspond to different nonstandard FDTD algorithms used to achieve an accurate representation of the physical performance of the coil. These include lumped capacitors and slanted noncubical cells for the curvatures of the ring as well as the struts. (Adapted from Ref. 64. © Springer, 2006.)

including electric field vectors, magnetic field vectors, permittivity, conductivity, and capacitance. With different coil geometries, cell sizes, and coil loading (unloaded, phantoms, or human head models), dynamic allocations provide convenience and conservation of memory. The next step is assigning the electrical properties to the desired portions of the grid including the phantom or the biological tissues of the human head model. The time loop then starts with no coil excitations, so the initial field values are set to zero. The time is incremented by a time step. The excitation is turned on in the specified excitation location. The shape of the excitation is unimportant as long as its frequency spectrum contains the frequencies of interest. The electric field values are then updated everywhere in the grid. A lumped element FDTD algorithm is used to model the tuning capacitors at their corresponding positions on the coil. The electric field components that are tangent to a perfectly conducting surface (coil structure) are forced to zero. To avoid stair-stepping errors, algorithms can be used to create slanted perfect conductors. Using the calculated electric field values, the magnetic field values are then updated over the entire grid. This is the end of the time step. The time step procedure is repeated until the simulation has run a prescribed number of time steps. Because the updated field values are only functions of the previous field

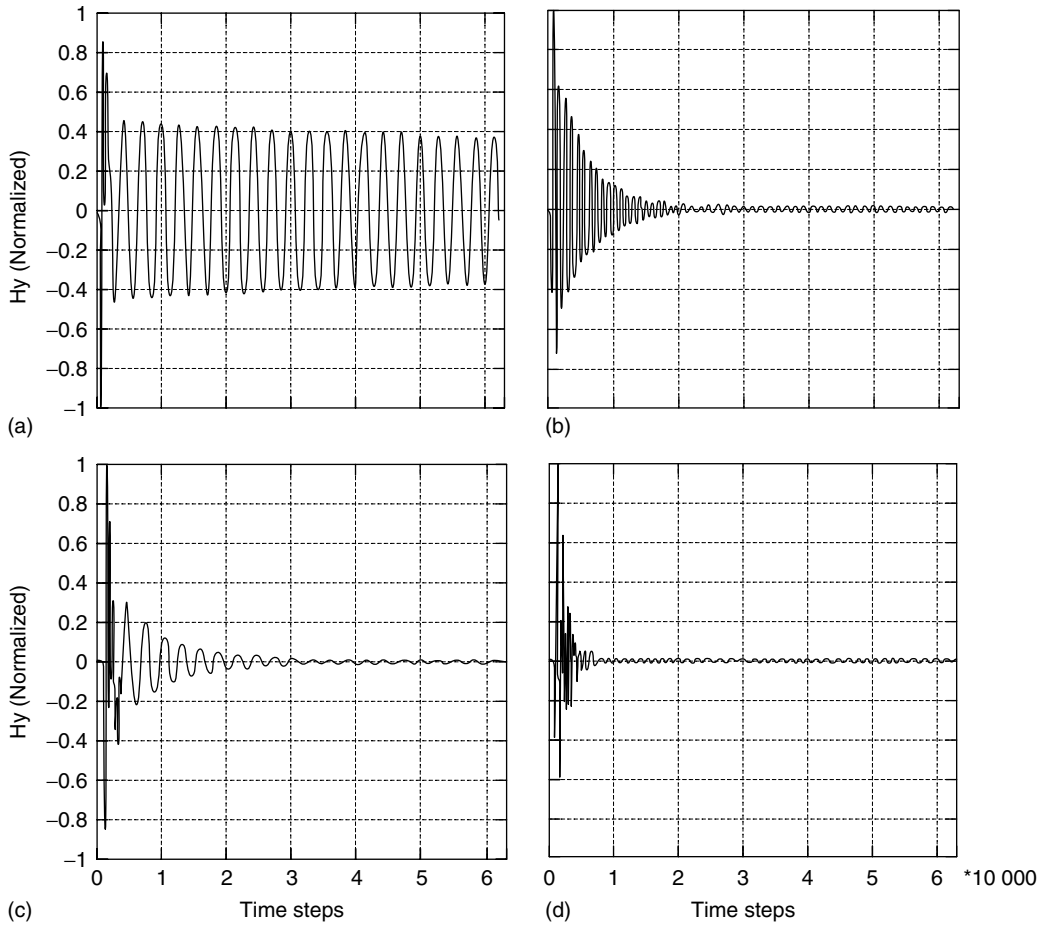

Figure 28.2. Sample time responses inside the birdcage resonator for an unloaded coil (a, c), and a coil numerically loaded with a large octagonal phantom with dielectric properties similar to muscle (b, d). The coil's mode of interest is tuned to 64 MHz (a, b) and 200 MHz (c, d). (Adapted from Ref. 36. © Elsevier, 2000.)

values, memory is conserved. At any cell, memory conservation is accomplished by overwriting the updated field value into the same memory location, which contains the previous value at the same cell.

Typically, the goal is to obtain the field distribution within the coil at the resonance frequency where the lumped capacitors must be tuned to set the resonance at the Larmor frequency. From the magnetic field distribution, one can extract the B_1 field distribution. From the electric field distribution, one can find the SAR as well as the total power absorbed by the phantom or the human head. Finding the field distribution is a two-step process. In the first step, an initial guess is made for the capacitor values. An FFT is then applied to the FDTD solution at a few points within the grid to obtain the frequency response of the coil, or if transmission line excitation is used, S11/coil input impedance can be obtained.[25,65,66] If the calculated resonance frequency of the coil is not at the desired location, the capacitor values are changed and the FDTD program is rerun. This step is repeated until the desired resonance frequency is obtained. In Figure 28.2(a)–(d), time domain data is displayed for the birdcage coil (legs and end rings that are modeled with infinitesimal width), which demonstrate that the signal has significantly decayed or reached steady state within a prescribed number of time steps (in unloaded or loaded coils). In the second step, the FDTD solution is run with the correct capacitor values, and a discrete Fourier transform (DFT) is applied on-the-fly

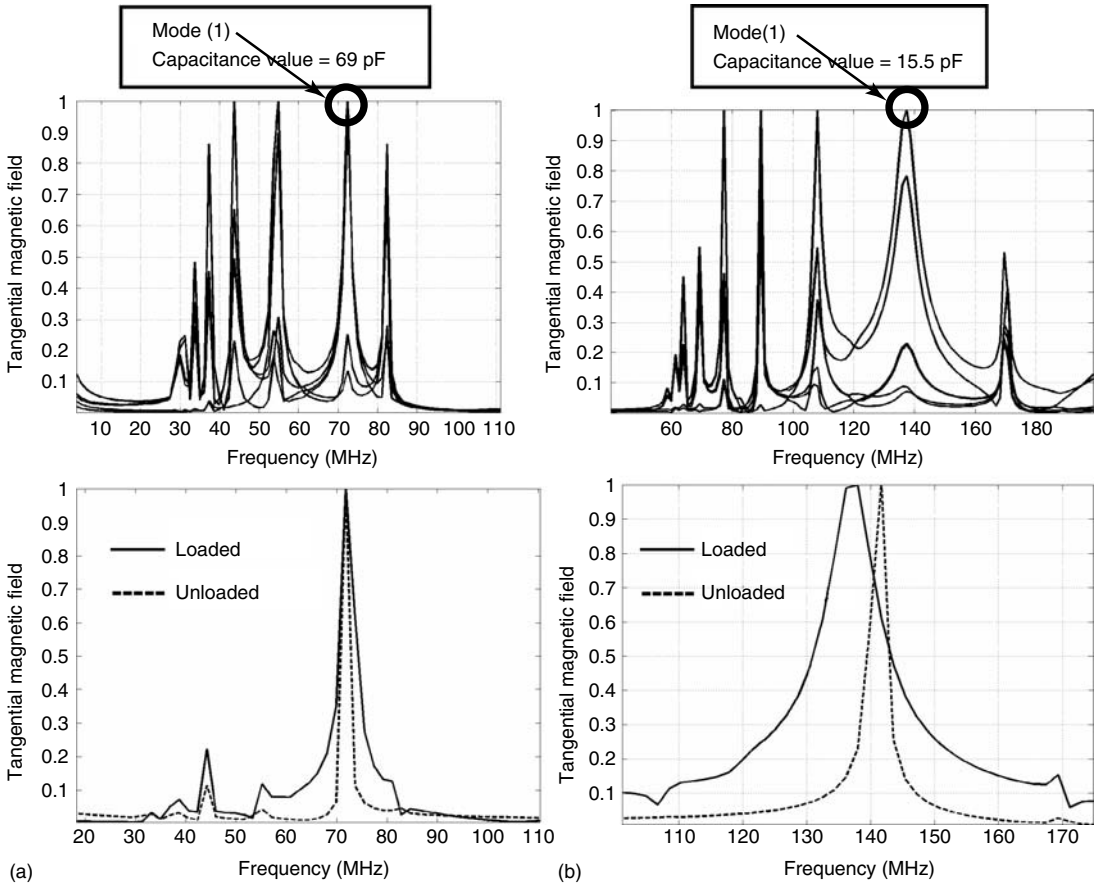

Figure 28.3. FDTD-calculated frequency spectrum of the unloaded and loaded with the anatomically detailed human head/shoulder model (ref) birdcage coils at 1.5 T (a) and 3 T (b). The capacitance values used in the FDTD model resemble the actual capacitance values utilized in the MR system. With this intricate 3D FDTD modeling approach, mode (1) was obtained near the expected frequencies with less than 9% error. (Adapted from Ref. 64. © Springer, 2006.)

at all points within the grid at the resonant frequency. Thus, the time data does not need to be stored, and the field distribution is known at the resonant frequency.

28.4.3 Validation of Modeling through Tuning and Field Distribution

The electrical performance of the coil can be well maintained since the modeled geometry does not deviate too far from the circular shape. Figure 28.3 clearly demonstrates this issue where FDTD-calculated frequency spectra[38,39] of 1.5 and 3 T high pass birdcage coils (width of the coil conductors is 0.3 in.) that are numerically loaded with the visible human project head/shoulder anatomical mesh (ftp://starview.brooks.af.mil/EMF/dosimetry models) are shown. Note that the dielectric properties of the mesh are assigned from Ref. 67. The capacitor values used along the end rings are the values of the actual lumped capacitors used in the GE birdcage coil in a clinical scanner (15.5 pF for 3 T and 69 pF for 1.5 T). The spectra show 9 modes corresponding to the 16 struts in the coil. Also, the resonance frequency of mode 1, the mode of operation, differs only by less than 9% from what is actually obtained in the real coil (128 and 64 MHz). This is the case even though perfect conductors and octagonal coil shape are utilized.

In terms of distributions of electromagnetic fields, Figure 28.4 displays the circularly polarized component of the B_1 (B_1^+) field as a function of anterior–posterior direction in the center of a high pass birdcage coil (Figure 28.4a) and as a function of the median–lateral direction 10 cm down from the center plane of the coil (Figure 28.4b).[36] The numerical FDTD solution (dashed curve) is compared to the experimental 1.5 T extracted B_1^+ field measurements (solid curve). The coil is operating at 64 MHz with quadrature excitation and is loaded with a cylindrical phantom, which is numerically and experimentally filled with material with muscle-like dielectric properties.[68] The sharp variations (spikes) in signal intensity in the MRI curve were due to the presence of air bubbles in the phantom. The results show excellent agreement between the numerical FDTD solution and the experimental MRI measurements.

28.5 ELECTROMAGNETIC OBSERVATIONS FROM MODELING BIRDCAGE RESONATORS USING THE FDTD METHOD

28.5.1 Tuning Behavior

The resonance frequency of the birdcage head coil is strongly dependent on the lumped capacitor values used in the coil. In order to better understand this dependence, simulations for capacitor values varying from 0 to 70 pF in steps of 1 pF for the birdcage

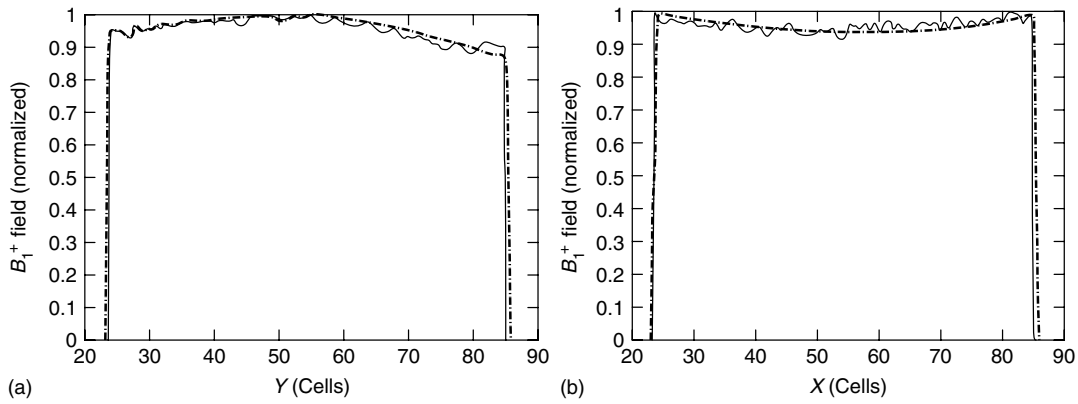

Figure 28.4. The B_1^+ field as a function of anterior–posterior direction in the center of a high pass birdcage coil (a) and as a function of the median–lateral direction, 10 cm down from the center (b). The FDTD solution (dashed curve) is compared to experimental MRI measurements (solid curve) at 1.5 T inside a head sized phantom filled with muscle-like (in terms of dielectric properties) material. (Adapted from Ref. 36. © Elsevier, 2000 and Ref. 64. © Springer, 2006.)

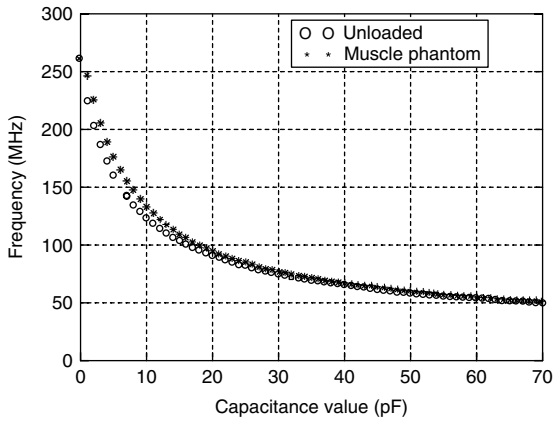

Figure 28.5. FDTD-calculated resonance frequencies of the mode of interest for a high pass birdcage coil as a function of the lumped capacitance value for different loadings. (Adapted from Ref. 36. © Elsevier, 2000.)

coil (legs and end rings that are modeled with infinitesimal width) are shown in Figure 28.5. This corresponds to a total of 71 simulations for the unloaded case and 71 simulations for the phantom case. From this figure, it can be noted that a relatively linear relationship exists between the resonance frequency and the capacitor values up to about 75 MHz. In addition, no significant differences are observed between the unloaded and loaded cases in this range. Above this frequency (100–270 MHz), however, an increasingly nonlinear relationship begins to hold, and the frequency shift caused by the loading of the phantom widens with increasing the tuning frequency.

28.5.2 Current Distribution on Coil Legs

Many of the modeling approaches utilized for birdcage coil simulations have used idealized current distributions that do not fully consider the coupling between the coil and the sample where the common assumption is that birdcage coil functions as an azimuthal transmission line. For instance, this is done by determining the current distribution on the coil legs/end rings without the head being present, using the MM, or by replacing the lumped capacitors with voltage sources in which magnitudes vary sinusoidally. As a result, the currents on the coil elements are required to have a sinusoidal distribution; i.e., the coil is assumed to operate solely in the TEM mode of interest, the ideal mode of operation for the birdcage coil. Therefore, the currents on the coil elements were assumed to vary as

$$I_i = I_{\max} \cos\left(\frac{i2\pi}{N}\right) \tag{28.1}$$

where I_i is the current in the ith element, $I_{\max}$ is the maximum current, and N is the number of coil elements. Another approach would be the rigorous FDTD modeling approach where the effects of the load on the birdcage coil are captured in the modeling approach.[36–38,58,69] In Figure 28.6, the current on each wire (birdcage coil element) is calculated using the latter approach (in-house FDTD package) at 64 MHz for (i) an unloaded coil, (ii) a coil (legs and end rings that are modeled with infinitesimal width) loaded with a head sized cylindrical phantom with circular cross section called *small phantom*, and (iii) a coil loaded with a coil-sized cylindrical phantom with octagonal cross section called *large phantom*.[36] Both of the phantoms were filled with muscle-like dielectric properties. The ideal sinusoidal coil current is also plotted for comparison. As expected, the unloaded coil current is close to the ideal case. When the coil is loaded by a phantom, the interaction between the coil and the phantom can induce additional currents on the wires. At 64 MHz, the induced currents are not too significant for the small phantom, but for the octagonal phantom, the induced currents can be significant. The interaction is stronger for the octagonal phantom because it is electrically larger and thus closer to the coil elements and the excitation port. Also, the phantom does not have circular symmetry, which produces greater asymmetries in the induced currents.

In Figure 28.6(b), the currents on the wires are once again plotted for the case where the unshielded birdcage coil (legs and end rings that are modeled with infinitesimal width) has been retuned to resonate at 200 MHz.[36] The results show that the currents do not follow the ideal sinusoidal curve. At 200 MHz, each leg of the coil is one quarter wavelength long, which means that the coil acts more like an antenna rather than a resonator. To demonstrate this point, Figure 28.6(c) displays the current on one of the coil elements along its length at both 64 and 200 MHz. It is observed that at 64 MHz, the current is relatively constant. At 200 MHz, a standing wave has formed on the wire.

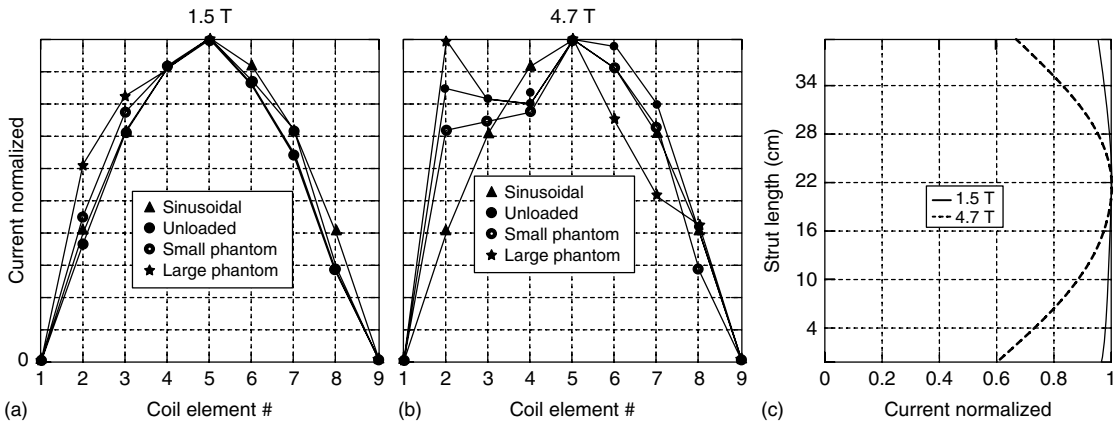

Figure 28.6. (a) and (b): The FDTD-calculated current distribution on the birdcage coil elements for different loadings at 64 and 200 MHz. The sub-figure in (c) corresponds to the absolute value of the current as a function of distance on one of the unloaded coil elements at 64 and 200 MHz. (Adapted from Ref. 36. © Elsevier, 2000 and Ref. 64. © Springer, 2006.)

28.5.3 Effects of Feeding on SAR

By exciting the coil in one point (on the top ring) and allowing the coil currents to be properly calculated with Maxwell's equations, one can properly account for the coupling between the drive port and the object to be imaged. At high frequency, it is expected for this coupling to have a significant effect on the SAR values, especially near the source. To demonstrate this point, Figure 28.7 shows a volumetric 3D view of the SAR inside the "small" and "large" muscle phantoms for linear excitation at 64 and 200 MHz for the unshielded birdcage coil (legs and end rings that are modeled with infinitesimal width). While the drive port does not have much of an effect on the SAR values at 64 MHz (except minimally for the large phantom), the maximum SAR values are located near the source for both the cylindrical and octagonal phantoms at 200 MHz. Because the "large" phantom is present along the length of the coil and is larger than the cylindrical phantom, the source is much closer to the "large" phantom, and consequently, a high local hot spot is observed near the source (see Figure 28.7).[37,69,70]

For the large phantom, the SAR values near source are about 20% higher than those for the small phantom. This is despite the fact that these calculations are given for 1 W CW absorption and the volume of the "large" phantom is about 2.5 times that of the "small" one so that, on average, the SAR values should be 2.5 times lower than the "small" phantom case. Hence, the interaction between the excitation source(s) and the object to be imaged is critical at high frequency; it depends on the size and the shape of the object and its placement inside the coil. From a full-wave analysis point of view, this physical observation associated with high frequency operation and/or electrically large loads cannot be accounted for by utilizing ideal current distributions on the coil elements or by calculating the currents on the coil elements without the load and then forcing these currents on the elements when the load is present. Therefore, (i) rigorous modeling of the excitation source(s) and the lumped capacitors, (ii) accurate consideration of their spatial positioning on the coil, and (iii) numerical tuning, as is done in an experiment, must all be computationally

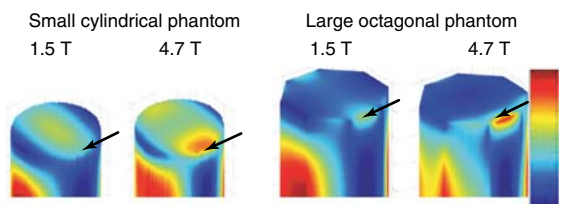

Figure 28.7. Specific absorption rate calculated using the FDTD method inside loaded high pass birdcage coil. The phantoms contain material with muscle-like dielectric properties. The coil is operating under linear excitation where the drive port is positioned near the top of the phantom. (Adapted from Ref. 64. © Springer, 2006.)

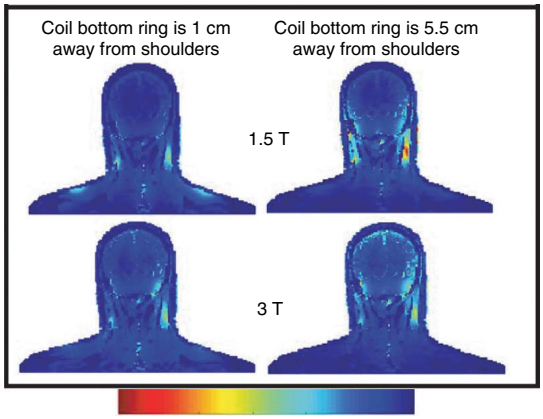

Figure 28.8. SAR calculations inside the head/shoulder model (loaded in birdcage coils) at 1.5 and 3 T. The coronal slices correspond to a case where the excitation locations are positioned behind the head (see Figure 28.1.)

carried out in order to accurately describe the electromagnetic interactions between the birdcage coil and the tissues, most especially at high field operation.

28.5.4 Effects of End Rings on SAR

The effect of birdcage coil end rings has been evaluated extensively at different field strengths.[30,39,71–73] In Figure 28.8, for high pass birdcage coils (width of the coil conductors is 0.3 in.), the SAR distribution is shown for a coronal slice at 1.5 and 3 T for two different head positions. In the first case, the coil is placed such that the end rings are 1 cm away from the shoulder. In this case, the SAR values on the shoulder are high. As the coil is moved away from the shoulder (5.5 cm away from shoulder), the SAR value decreases (most profoundly for the 1.5 T case); however, it appears that high SAR values are generated in the neck region.

28.5.5 Effects of Excitation Mechanism on SAR and the B_1^+ Field Distribution

In this section, we will examine the effect of the excitation mechanism, number of drive ports and quadrature vs RF shimming on the B_1^+ field distribution, and SAR during low and high field operation. It is noted here that the coil tested at 200 MHz was not optimized geometrically for this frequency. It was simply tested by reducing the lumped capacitor values such that the mode of operation was tuned to 200 MHz.

28.5.5.1 Phantom Observations

Figure 28.9 displays B_1^+ field inside the "small" phantom for axial slices at 64 MHz for linear and quadrature excitations. For linear excitation, B_1^+ field distribution is approximately 60% homogeneous (the difference between the maximum and the minimum values of the B_1^+ field in this slice is 40% of the maximum value). A better overall homogeneity (90%) is obtained from linear to quadrature excitation. The results at 200 MHz, however, are quite different. Unlike the 64 MHz case, there is not much improvement in the homogeneity of the fields from linear to quadrature (29% homogeneity) drive. This is due to the fact that the ideal current distribution predicted from circuit analysis is no longer present, rendering the conventional quadrature excitation ineffective. In other words, linear excitation does not produce adequate linear polarization; thus, quadrature excitation does not produce adequate circular polarization.

The corresponding SAR values for 1 W absorption are also shown in Figure 28.9. The two-port quadrature excitation for the unloaded coil (or for the birdcage coil loaded with the "small" phantom) produces fields that are approximately circularly polarized at low frequency. For the "small" phantom, simulations and experiments show that at 64 MHz, the polarization of the tangential electric fields is almost circular when the excitation is applied in quadrature. Because the SAR is an indication of the electric field for the homogeneous medium, Figure 28.9 shows that the SAR distribution is symmetric around the azimuthal direction. It is also well documented that quadrature excitation reduces the transmitting power and consequently the absorbed power by approximately a factor of 2 at 64 MHz (the ratio of the absorbed and radiated power is independent of the source at the same frequency). As the absorbed RF power deposition in the phantom is an indication of the SAR, Figure 28.9 shows that at 64 MHz, by applying quadrature excitation, the SAR peak values have decreased by approximately a factor of 2 compared to the case when the coil is linearly excited.

At 200 MHz (4.7 T), the situation is quite different, however. Because linear excitation does not give a sinusoidal current distribution on the coil elements or

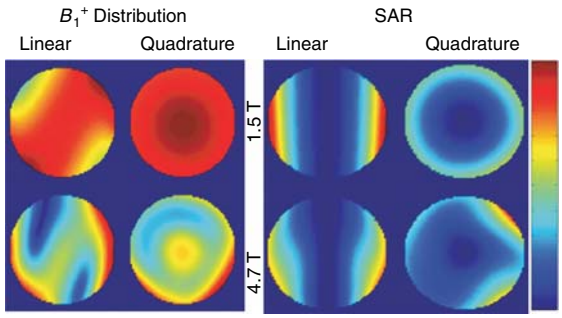

Figure 28.9. Axial slices displaying the calculated normalized B_1^+ field and SAR of a high pass birdcage coil loaded with the "small" phantom at 64 and 200 MHz using linear and quadrature excitations. (Adapted from Ref. 36. © Elsevier, 2000 and Ref. 64. © Springer, 2006.)

linear polarization for the loaded case at 200 MHz, it is impossible to obtain predominantly circularly polarized fields using the conventional (two-port) quadrature drive. This can be clearly seen from Figure 28.9 where the azimuthal symmetry is lost at the 4.7 T case. In addition, the fields induced by each of the two drive ports can now add up either constructively or destructively, depending on the geometrical shape and material properties of the head or phantom. As a result, it can be quite possible for the peak SAR value to increase when switching from linear to the conventional two-port quadrature excitation (unlike that at 64 MHz). This is also demonstrated in Figure 28.9.

28.5.5.2 Human Head Observations

Figure 28.10(a) shows an axial slice of the B_1^+ field in the human head model at 64 MHz for quadrature excitation. Within the brain region, where the axial slice is taken, the homogeneity of the B_1^+ field is around 90%. A better overall homogeneity with quadrature drive is achieved when compared to the linear drive. The same axial slice of the B_1^+ field is shown at 200 MHz in Figure 28.10(b) for quadrature excitation. The field homogeneity has dropped to 37%, making it much less homogeneous than the 64 MHz case.

Four-port quadrature drive (a fixed integer increment of $\pi/2$ phase shifts on each of the four drive ports) and the phase-optimized four-port excitation (RF shimming) are tested for the 200 MHz case. The phase shifts used to produce the phase-optimized four-port excitation results of this figure are 0, 0.714π, π, and 1.52π. Figure 28.10(c) and (d) show axial slices of the B_1^+ field distribution at 200 MHz using four-port quadrature drive (52% homogeneity) and the phase-optimized four-port excitation (63% homogeneity), respectively.

Figure 28.10(e) shows the SAR values in the aforementioned axial slice for quadrature excitation at 64 MHz. Compared to the linear excitation case, it is observed that SAR peak values have dropped by approximately 30% when the excitation is done in quadrature. Note that this value is less than that with the cylindrical phantom. This is because the human head model is heterogeneous and asymmetric; hence, the fields inside it are less circularly polarized (not necessarily homogenous) than with the symmetric and homogeneous cylindrical phantom. Figure 28.10(f) shows the same slice at 200 MHz; no reduction in the SAR peak values was observed for the human head from linear (results not shown) to quadrature excitation. At 200 MHz, Figure 28.10(g) demonstrates that the SAR peak values have dropped by about 50% using a four-port quadrature drive when compared to the conventional quadrature excitation (Figure 28.10f). As previously demonstrated, the four-port quadrature drive reduces effects due to the head-coil interactions leading to more uniform currents on the coil legs. As the optimized phased array drive was used to obtain the most homogenous B_1^+ field distribution at 200 MHz without taking into account SAR in this particular case, the electric field components can add up constructively in some spots and consequently lead to higher peak SARs compared to that obtained with the four-port quadrature excitation case. Figure 28.10(h) shows that the phase-optimized four-port excitation provides SAR peak values higher than those with the four-port quadrature drive; they are however still less than what was obtained with the linear or the conventional quadrature excitations at 200 MHz. Recent computational studies have shown that local SAR can still be constrained as a part of the homogenization of B_1^+ field distribution.[14,15,51]

28.6 CONCLUDING REMARKS

This work is presented as a guide for modeling the electromagnetic interactions of birdcage coils. Some of the results shown and many other works throughout the MRI community indeed show that the

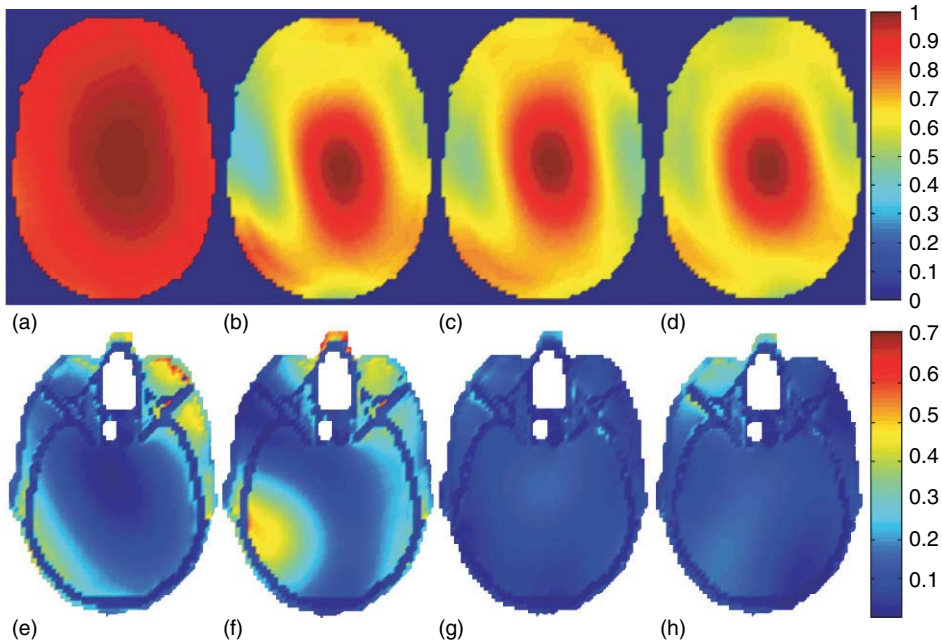

Figure 28.10. Axial slices displaying B_1^+ field and the SAR inside the human head model. Figure (a, e) correspond to the B_1^+ field and the SAR at 64 MHz using quadrature excitation, respectively. Figure (b, f), (c, g), and (d, h) correspond to the B_1^+ field and the SAR at 200 MHz for quadrature, four-port, and phase-optimized (B_1 shimming) four-port excitation, respectively. The color scale for the SAR values is in watts per kilogram for 1 W CW absorption. (Adapted from Ref. 37. © Elsevier, 2000.)

field of computational electromagnetics has become a vital foundation in not only understanding but also advancing MRI systems.

REFERENCES

1. G. H. Glover, C. E. Hayes, N. J. Pelc, W. A. Edelstein, O. M. Mueller, H. R. Hart, C. J. Hardy, M. O'Donnell, and W. D. Barber, *J. Magn. Reson. (1969)*, 1985, **64**, 255–270.
2. C. E. Hayes, W. A. Edelstein, J. F. Schenck, O. M. Mueller, and M. Eash, *J. Magn. Reson. (1969)*, 1985, **63**, 622–628.
3. J. Tropp, *J. Magn. Reson. (1969)*, 1989, **82**, 51–62.
4. T. S. Ibrahim, R. Lee, B. A. Baertlein, A. Kangarlu, and P. M. L. Robitaille, Dielectric Resonance in Ultra High Field MRI, in *International Society for Magnetic Resonance in Medicine Annual Meeting*, ISMRM: Denver (CO), 2000, p. 1681.
5. T. S. Ibrahim, *IEEE Trans. Microw. Theory Tech.*, 2004, **52**, 1999–2003.
6. T. S. Ibrahim, C. Mitchell, R. Abraham, and P. Schmalbrock, *NMR Biomed.*, 2007, **20**, 58–68.
7. C. M. Collins, S. Li, and M. B. Smith, *Magn. Reson. Med.*, 1998, **40**, 847–856.
8. J. T. Vaughan, M. Garwood, C. M. Collins, W. Liu, L. DelaBarre, G. Adriany, P. Andersen, H. Merkle, R. Goebel, M. B. Smith, and K. Ugurbil, *Magn. Reson. Med.*, 2001, **46**, 24–30.
9. C. M. Collins and M. B. Smith, *Magn. Reson. Med.*, 2001, **45**, 684–691.
10. C. M. Collins and M. B. Smith, *Magn. Reson. Med.*, 2001, **45**, 692–699.
11. S. Crozier, I. M. Brereton, F. O. Zelaya, W. U. Roffmann, and D. M. Doddrell, *J. Magn. Reson.*, 1997, **126**, 39–47.
12. B. Xu, Q. Wei, F. Liu, and S. Crozier, *IEEE Trans. Biomed. Eng.*, 2005, **52**, 1582–1587.
13. F. Liu, B. L. Beck, B. Xu, J. R. Fitzsimmons, S. J. Blackband, and S. Crozier, *Concepts Magn. Reson. Part B Magn. Reson. Eng.*, 2005, **24B**, 28–38.

14. C. A. Van den Berg, B. van den Bergen, J. B. Van de Kamer, B. W. Raaymakers, H. Kroeze, L. W. Bartels, and J. J. Lagendijk, *Magn. Reson. Med.*, 2007, **57**, 577–586.
15. B. van den Bergen, C. A. T. van den Berg, L. W. Bartels, and J. J. W. Lagendijk, *Phys. Med. Biol.*, 2007, **52**, 5429–5441.
16. L. L. Wald, G. C. Wiggins, A. Potthast, C. J. Wiggins, and C. Triantafyllou, *Appl. Magn. Reson.*, 2005, **29**, 19–37.
17. B. L. Beck, K. Jenkins, J. Caserta, K. Padgett, J. Fitzsimmons, and S. J. Blackband, *Magn. Reson. Med.*, 2004, **51**, 1103–1107.
18. A. Kangarlu, T. S. Ibrahim, and F. G. Shellock, *Magn. Reson. Imaging*, 2005, **23**, 53–60.
19. G. Adriany, P. F. Van de Moortele, F. Wiesinger, S. Moeller, J. P. Strupp, P. Andersen, C. Snyder, X. Zhang, W. Chen, K. P. Pruessmann, P. Boesiger, T. Vaughan, and K. Ugurbil, *Magn. Reson. Med.*, 2005, **53**, 434–445.
20. D. I. Hoult, *J. Magn. Reson. Imaging*, 2000, **12**, 46–67.
21. D. I. Hoult, *Concepts Magn. Reson.*, 2000, **12**, 173–187.
22. T. S. Ibrahim and L. Tang, *J. Magn. Reson. Imaging*, 2007, **25**, 1235–1247.
23. J. T. Vaughan, H. P. Hetherington, J. G. Harrison, J. O. Otu, J. W. Pan, P. J. Noa, and G. M. Pohost, *Phys. Med. IX*, 1993, **147**, 147–153.
24. B. A. Baertlein, O. Ozbay, T. Ibrahim, R. Lee, Y. Yu, A. Kangarlu, and P. M. Robitaille, *IEEE Trans. Biomed. Eng.*, 2000, **47**, 535–546.
25. T. S. Ibrahim, Y. K. Hue, and L. Tang, *NMR Biomed.*, 2009, **22**, 927–936.
26. J. M. Jin, *IEEE Antennas Propag. Mag.*, 1998, **40**, 7–22.
27. Q. X. Yang, J. Wang, X. Zhang, C. M. Collins, M. B. Smith, H. Liu, X. H. Zhu, J. T. Vaughan, K. Ugurbil, and W. Chen, *Magn. Reson. Med.*, 2002, **47**, 982–989.
28. S. M. Wright, *Concepts Magn. Reson.*, 2002, **15**, 2–14.
29. T. Ibrahim, 7 Tesla Whole-Slice and Localized Excitation Everywhere in the Human head, In *Proceedings 14th Scientific Meeting, International Society for Magnetic Resonance in Medicine*, Seattle (WA), 2006, p. 700.
30. W. Liu, C. M. Collins, P. J. Delp, and M. B. Smith, *Magn. Reson. Med.*, 2004, **51**, 217–221.
31. F. Liu and S. Crozier, *Phys. Med. Biol.*, 2004, **49**, 1835–1851.
32. Q. Wei, F. Liu, L. Xia, and S. Crozier, *J. Magn. Reson.*, 2005, **172**, 222–230.
33. U. Katscher, T. Voigt, C. Findeklee, P. Vernickel, K. Nehrke, and O. Dossel, *IEEE Trans. Med. Imaging*, 2009, **28**, 1365–1374.
34. J. M. Jin, J. Chen, W. C. Chew, H. Gan, R. L. Magin, and P. J. Dimbylow, *Phys. Med. Biol.*, 1996, **41**, 2719–2738.
35. J. M. Jin and J. Chen, *Magn. Reson. Med.*, 1997, **38**, 953–963.
36. T. S. Ibrahim, R. Lee, B. A. Baertlein, Y. Yu, and P. M. Robitaille, *Magn. Reson. Imaging*, 2000, **18**, 835–843.
37. T. S. Ibrahim, R. Lee, B. A. Baertlein, A. Kangarlu, and P. L. Robitaille, *Magn. Reson. Imaging*, 2000, **18**, 733–742.
38. Ibrahim, T. S. and R. Lee, Effects of Geometry, Excitation and Spatial Positioning on the Birdcage Coil Performance, In *International Society for Magnetic Resonance in Medicine Annual Meeting*, ISMRM: Toronto, Canada, 2003, p. 2518.
39. Ibrahim, T. S. and R. Lee, Specific Absorption Rate at 1.5 T and 3 T: A Numerical Study of the Birdcage Coil, In *International Society for Magnetic Resonance in Medicine Annual Meeting*, ISMRM: Toronto, Canada, 2003, p. 2602.
40. S. Li, C. M. Collins, B. J. Dardzinski, C. L. Chin, and M. B. Smith, *Magn. Reson. Med.*, 1997, **37**, 600–608.
41. B. J. Dardzinski, S. Li, C. M. Collins, G. D. Williams, and M. B. Smith, *J. Magn. Reson.*, 1998, **131**, 32–38.
42. M. Alecci, C. M. Collins, J. Wilson, W. Liu, M. B. Smith, and P. Jezzard, *Magn. Reson. Med.*, 2003, **49**, 363–370.
43. F. Liu, B. L. Beck, J. R. Fitzsimmons, S. J. Blackband, and S. Crozier, *Phys. Med. Biol.*, 2005, **50**, 5281–5291.
44. O. P. Gandhi and X. Bin Chen, *Magn. Reson. Med.*, 1999, **41**, 816–823.
45. C. Wang and G. Shen, Optimization of a Multi-Channel Transmit, Quadrature Receive Birdcage Coil, In *Proceedings 14th Scientific Meeting, International Society for Magnetic Resonance in Medicine*, Seattle (WA), 2006, p. 3539.

46. C. Wang, P. Qu, and G. X. Shen, *J. Magn. Reson.*, 2006, **182**, 160–167.
47. C. Wang and G. X. Shen, *J. Magn. Reson. Imaging*, 2006, **24**, 439–443.
48. C. M. Collins, M. B. Smith, and R. Turner, *J. Appl. Physiol.*, 2004, **97**, 2051–2055.
49. A. Trakic, S. Crozier, and F. Liu, *Phys. Med. Biol.*, 2004, **49**, 5547–5558.
50. J. W. Hand, J. J. W. Lagendijk, J. V. Hajnal, R. W. Lau, and I. R. Young, *J. Magn. Reson. Imaging*, 2000, **12**, 68–74.
51. L. Tang, Y. K. Hue, and T. S. Ibrahim, *Concepts Magn. Reson. Part B*, 2011, **39**B(1), 11–25.
52. Ibrahim, T. S., A. Kangarlu, and R. Abraham, FDTD Simulations of Implantable Devices at 3 and 7 Tesla, In *International Society for Magnetic Resonance in Medicine Annual Meeting*, ISMRM: Berlin, Germany, 2007, p. 1097.
53. F. J. Meyer, D. B. Davidson, U. Jakobus, and M. A. Stuchly, *IEEE Trans. Biomed. Eng.*, 2003, **50**, 224–233.
54. T. Grosges, A. Vial, and D. Barchiesi, *Opt. Express*, 2005, **13**, 8483–8497.
55. B. K. Li, F. Liu, E. Weber, and S. Crozier, *NMR Biomed.*, 2009, **22**, 937–951.
56. K. S. Yee, *IEEE Trans. Antennas Propag.*, 1966, **14**, 302–317.
57. A. Taflove and S. C. Hagness, *Computational Electrodynamics The Finite Difference Time Domain Method*, Artech House: Boston, MA, 2000.
58. T. S. Ibrahim, R. Lee, B. A. Baertlein, and P. M. Robitaille, *Phys. Med. Biol.*, 2001, **46**, 609–619.
59. A. Cangellaris and P. Russer, *Int. J. Appl. Electromagnet. Mech.*, 2003, **17**, 19–30.
60. J. P. Berenger, *J. Comput. Phys.*, 1994, **114**, 185–200.
61. J. P. Berenger, *J. Comput. Phys.*, 1996, **127**, 363–379.
62. D. S. Katz, E. T. Thiele, and A. Taflove, *IEEE Microw. Wirel. Compon. Lett.*, 1994, **4**, 268–270.
63. V. Anantha and A. Taflove, *IEEE Trans. Antennas Propag.*, 2002, **50**, 1337–1349.
64. Ibrahim, T. S., A Perspective into Ultra High Field MRI RF Coils, In *Ultra High Field Magnetic Resonance Imaging (Biological Magnetic Resonance)*, eds P. M. Robitaille and L. Berliner, Springer: New York, 2006.
65. T. S. Ibrahim, D. Abraham, R. Abraham, and R. Gilbert, 3D Simulation Technique to Obtain Input Impedance and Frequency Response of Empty/Biologically Loaded RF Coils with Experimental Verifications, In *International Society for Magnetic Resonance in Medicine Annual Meeting*, ISMRM: Seattle (WA), 2006, p. 1384.
66. T. S. Ibrahim, Y.-K. Hue, R. Gilbert, and F. E. Boada, Tic Tac Toe: Highly-Coupled, Load Insensitive Tx/Rx Array and a Quadrature Coil Without Lumped Capacitors, In *International Society for Magnetic Resonance in Medicine Annual Meeting*, ISMRM: Toronto, Canada, 2008.
67. C. Gabriel, *Compilation of Dielectric Properties of Body Tissues at RF and Microwave Frequencies*, http://www.brooks.af.mil/AFRL/HED/hedr/reports/home.htm, AL/OETR-1996-0037, 1996.
68. S. Field and C. Francon, *Physics and technology of hyperthermia*, Martinus Nijhoff Publishers: Dordrech/Boston/Lancaster, 1987.
69. T. S. Ibrahim, R. Lee, B. A. Baertlein, A. Kangarlu, and P. M. L. Robitaille, On the Physical Feasibility of Achieving Linear Polarization at High-field: A Study of the Birdcage Coil, In *International Society for Magnetic Resonance in Medicine Annual Meeting*, ISMRM: Philadelphia (PA), 1999, p. 2058.
70. T. S. Ibrahim, C. Mitchell, P. Schmalbrock, R. Lee, and D. W. Chakeres, *Magn. Reson. Med.*, 2005, **54**, 683–690.
71. C. Collins, W. Liu, and M. Smith, Comparison of Four Different Birdcage Type Coils, In *Proceedings 14th Scientific Meeting, International Society for Magnetic Resonance in Medicine*, Seattle (WA), 2006, p. 3550.
72. A. Novikov, *Magn. Reson. Imaging*, 2011, **29**(2), 260–271.
73. H. Fujita, W. O. Braum, and M. A. Morich, *Magn. Reson. Med.*, 2000, **44**, 633–640.

Chapter 29

RF Field Modeling for Double-Tuned Volume Coils

Wanzhan Liu

Medtronic Inc., Minneapolis, MN 55126, USA

29.1 INTRODUCTION

29.1.1 Why Double-Tuned Volume Coils?

Double-tuned coils are coils simultaneously tuned to two different Larmor frequencies, thus allowing simultaneously acquisition of magnetic resonance (MR) signals from two different nuclei. One of the two nuclei is usually the proton (^{1}H), which has a strong signal compared to other nuclei in the human body and is used to acquire magnetic resonance images (MRIs). The other nucleus that is most widely used is phosphate 31 (^{31}P) although any nucleus with an MR signal can be investigated. Magnetic resonance spectroscopy (MRS) of the non-proton nucleus such as ^{31}P is a well-established method to study physiology such as muscle function. Proton MRI provides an anatomical reference for the MRS, since signal from the non-proton nucleus is generally not high enough to form images. The B_0 shimming is also done using the high signal from the proton resonance. Although the excitation of the two nuclei can be done with two separate coils, simultaneously exciting RF fields at both frequencies speeds up the experiments and minimizes the error associated with switching coils. Volume coils are typically used as transmit coils since they provide homogeneous excitation over a large region of interest. They can also be used as receive coils if the signal-to-noise ratio (SNR) is not a pressing issue.

29.1.2 Why Numerical Methods?

Numerical modeling helps RF coil design by (i) gaining information that cannot be obtained empirically such as the E field and SAR maps inside the human body; (ii) speeding the iterative design process with tools such as field optimization.

Table 29.1 lists the strengths and weaknesses of the numerical method for all the coil design activities. In many areas, the numerical method is complementary to the empirical method.

RF Coils for MRI
Edited by J. Thomas Vaughan and John R. Griffiths

ISBN: 978-0-470-77076-4

Table 29.1. Comparison of experimental and numerical approaches to RF coils' design activities

	Experimental	Numerical
B_1 field mapping	Medium	Easy
E field/SAR mapping	Very difficult	Easy
Receive sensitivity	Medium to difficult	Easy
Optimization	Difficult	Easy
Tuning	Easy	Medium to difficult
Matching	Easy	Irrelevant[a]
Decoupling	Medium	Difficult

[a]The input power in numerical computation can be scaled to any arbitrary levels so matching is not required.

29.1.3 Why Finite Different Time Domain Method?

The finite difference time domain (FDTD) method,[1] the finite element method (FEM),[2] and the method of moments (MoM)[2] are among the most popular numerical methods for full wave electromagnetic modeling. FDTD is recommended by IEEE as the preferred method for performing electromagnetic simulations for biological effects.[3] The FDTD method has been shown to be the most efficient approach and provides accurate predictions of the field penetration into biological tissues.[4]

29.1.4 Outline

This chapter provides readers with a tutorial on how to model RF fields in double-tuned volume coils. First, the two commonly used double-tuned coil designs: the four-ring resonator of the birdcage type[5] and the transverse electromagnetic (TEM) coil are introduced.[6] Then, the fundamentals of the FDTD methods including formula, boundary conditions, and stability and accuracy are reviewed. Section 29.5 shows how to model a head-size four-ring resonator at 3 T, step by step.

29.2 DOUBLE-TUNED BIRDCAGE AND TEM COILS

This section very briefly introduces the two most commonly used double-tuned volume coils – the

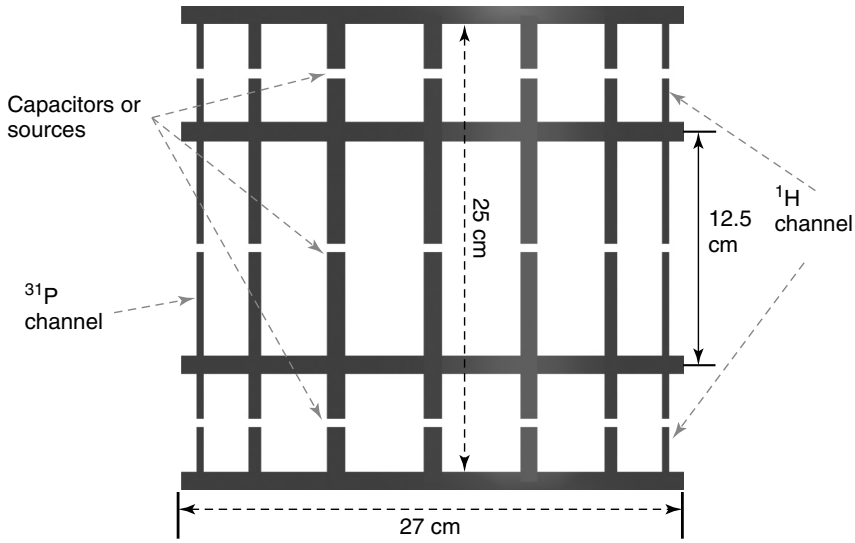

Figure 29.1. Scheme of the LP–LP ^{31}P/^{1}H four-ring birdcage resonator. Capacitors and driving sources, which would be placed at the gaps, are not shown. The coil has a diameter of 27 cm. The distance between the two outer rings is 25 cm and that between the inner rings 12.5 cm.

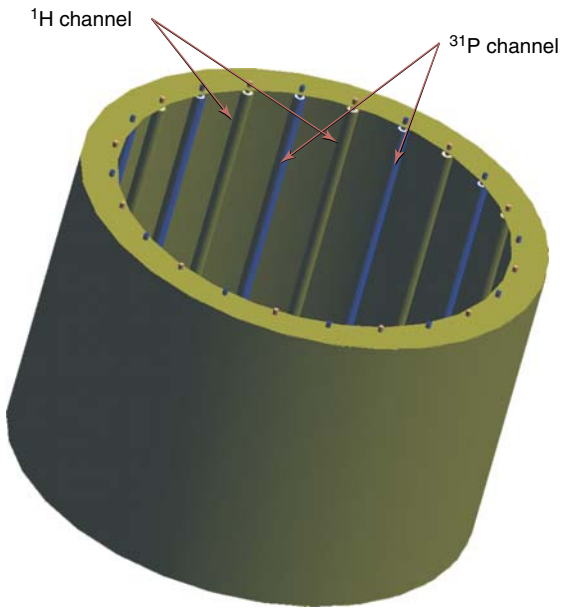

Figure 29.2. Structure of a double-tuned TEM coil.

birdcage coil and the TEM coil. Birdcage-type designs have been widely used for human head-size double-tuned coils at 1.5 and 3 T. Head-size double-tuned TEM coils have been used at 4 and 7 T.

The four-ring resonator is chosen as the birdcage example for this study. Four-ring double-tuned resonators were introduced by Murphy-Boesch *et al*. in 1994. They are constructed by stacking three same diameter birdcage coils together and fusing the two end-rings in the middle so there are four rings in the final structure; thus the name (Figure 29.1). The middle coil is a low-pass (LP) type, tuned for phosphorus or a nucleus other than protons. The two coils at the ends are tuned for protons. They can be LP or high-pass (HP) types. The LP type has all the capacitors on the rungs and the HP type has the capacitors in the end-rings. In both cases, no capacitors are placed in the two middle rings. The LP–LP configuration suits lower fields or smaller coil dimensions and the LP–HP suits higher fields and larger dimensions. The four-ring resonator geometrically decouples the two frequencies and provides excellent homogeneity and sensitivity for the non-proton nucleus and sufficient homogeneity and sensitivity for the proton.

Since they were introduced by Vaughan *et al*. in 1994, TEM double-tuned coils have been used in ultrahigh field MRI/MRS. The alternate rungs in a TEM coil are tuned to two different frequencies by adjusting the length of the inner conductor of the coaxial transmission line elements (Figure 29.2). In the original TEM design, the rungs were coaxial transmission line elements and in the later design multi-strips are also used. These elements can be adjusted individually, either passively by changing the capacitor values or actively by driving with different magnitudes and phases to achieve optimal B_1 homogeneity for different frequencies in human bodies at high fields.[7] Although this type of optimization is a great application for numerical simulations, it is not included in this chapter due to limited space.

29.3 FINITE DIFFERENT TIME DOMAIN METHOD FOR ELECTROMAGNETICS

Numerical methods for electromagnetics solve Maxwell's equations numerically with a set of formulas. Certain boundary conditions are needed since the computational domain cannot be infinite. The formulas also have to meet certain criteria to be numerically stable. The three aspects of the FDTD method: the formula, the boundary conditions, and the stability criteria will be covered in this section.

29.3.1 Formula

The FDTD method uses the finite difference approximations to replace the derivatives in space and time in Maxwell's curl equations so they can be solved directly on a computer in the time domain for arbitrary geometries and material electrical properties. In linear, isotropic, nondispersive materials, Maxwell's curl equations can be written as

$$\frac{\partial \mathbf{B}}{\partial t} = -\nabla \times \mathbf{E} \frac{\partial \varepsilon \mathbf{E}}{\partial t} = -\sigma \mathbf{E} + \frac{\nabla \times \mathbf{B}}{\mu} \quad (29.1)$$

where $\mathbf{B}$ is magnetic flux density, t is time, $\mathbf{E}$ is electrical field intensity, ε is electrical permittivity, σ is electrical conductivity, and μ is magnetic permeability. In a Cartesian coordinates system, the equations can be written as the following:

$$\frac{\partial}{\partial t}(B_x i + B_y j + B_z k) = -\left[\left(\frac{\partial E_z}{\partial y} - \frac{\partial E_y}{\partial z}\right) i + \left(\frac{\partial E_x}{\partial z} - \frac{\partial E_z}{\partial x}\right) j + \left(\frac{\partial E_y}{\partial x} - \frac{\partial E_x}{\partial y}\right) k\right]$$

$$\frac{\partial}{\partial t}\varepsilon(E_x i + E_y j + E_z k) = -\sigma(E_x i + E_y j + E_z k) + \frac{1}{\mu}\left[\left(\frac{\partial B_z}{\partial y} - \frac{\partial B_y}{\partial z}\right) i + \left(\frac{\partial B_x}{\partial z} - \frac{\partial B_z}{\partial x}\right) j + \left(\frac{\partial B_y}{\partial x} - \frac{\partial B_x}{\partial y}\right) k\right] \tag{29.2}$$

The FDTD method simply substitutes finite difference approximations for the partial derivative with respect to time

$$\frac{\partial f}{\partial t} = \frac{f^{(i,j,k,n+1)} - f^{(i,j,k,n-1)}}{2\Delta_t} \tag{29.3}$$

and to space

$$\frac{\partial f}{\partial x} = \frac{f^{(i+1,j,k,n)} - f^{(i-1,j,k,n)}}{2\Delta_x}$$

$$\frac{\partial f}{\partial y} = \frac{f^{(i,j+1,k,n)} - f^{(i,j-1,k,n)}}{2\Delta_y}$$

$$\frac{\partial f}{\partial z} = \frac{f^{(i,j,k+1,n)} - f^{(i,j,k-1,n)}}{2\Delta_z} \tag{29.4}$$

where f is one of **B** or **E** field components, i, j, and k are indices for positions on the 3D grid in the x, y, and z directions; n is the number of time steps; Δ_t is the size of time step; and Δ_x, Δ_y, and Δ_z are the spatial grid cell size in the x, y, and z directions, respectively. The actual algorithm used in electromagnetism computation, the Yee algorithm, is more efficient by staggering the field components in space by half a cell size and in time by half a time step.[1] The positions of the **E** and **B** components in a Yee cell are shown in Figure 29.3. The **E** components are located in the middle of the edges and the **B** components are located at the center of the faces. Every **E** component is surrounded by four circulating **B** components and every **B** component is surrounded by four circulating **E** components (Figure 29.3). With this leapfrog approach, if all **E** and **B** components at or before time $t = 0$ are assumed zero, with appropriately set **E** components at drive sources at each time step and proper boundary conditions, any field component at any spatial point at any future time point can be solved. The FDTD method is straightforward to realize on the computer and the electric properties of media can be easily included into the calculation by assigning proper values to the conductivity σ and permittivity ε to spatial points. This feature is very useful for the modeling of human tissues exposed to RF fields in MR.

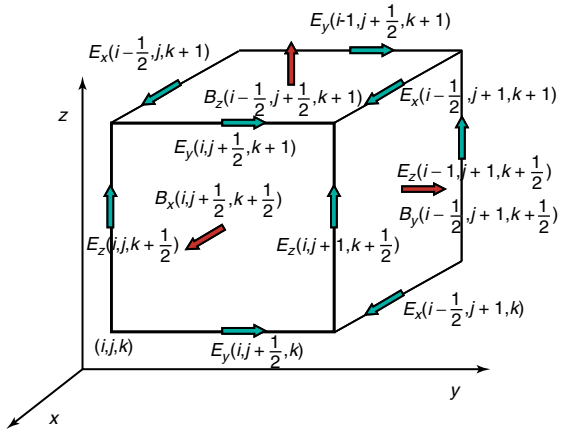

Figure 29.3. Structure of a Yee cell.

29.3.2 Boundary Conditions

A boundary condition is needed for the formulation developed in Section 29.3.1, since any computer can handle only limited space. Most commonly used boundary conditions for FDTD fall into three categories: perfectly electrical conductive (PECs) or perfectly magnetic boundary conditions (PMCs), periodic boundary conditions, and absorbing boundary conditions (ABCs). The PECs and PMCs terminate the computational space with perfectly conducting and perfectly magnetic planes, respectively. They can be used to model structures where no electromagnetic energy can escape outside. The periodic boundary conditions mirror the geometry in computational space periodically into infinite space. They can be used to model structures with periodic characteristics such as waveguides. The ABCs simulate the infinite space by absorbing all the electromagnetic waves at

the boundary. They are the most widely used boundary conditions in MRI RF simulations. Two major implementations of ABC are analytical ABCs and perfectly matched layers (PML) ABCs. The analytical ABCs use fields close to the boundary to update the fields at the boundary such that no waves are reflected back into computational space. The PML ABCs literally patch the computational space with layers of material that perfectly absorbs the outgoing waves. The analytical ABCs are of less computational burden but PML ABCs can be put much closer to the structures in the computational domain. The PML ABC is used in all the simulations in this chapter. Interested readers can find detailed treatment of boundary conditions in Taflove's book.

29.3.3 Stability and Accuracy

Computational stability of FDTD requires that

$$\Delta_t < \frac{1}{c_{\max}\sqrt{(1/\Delta_x)^2 + (1/\Delta_y)^2 + (1/\Delta_z)^2}} \tag{29.5}$$

where $c_{\max}$ is the maximum light velocity in the region concerned and Δ_x, Δ_y, and Δ_z are the sizes of the smallest Yee cell in the x, y, and z directions. The central-difference approach in space and time used in the Yee algorithm has second-order accuracy, or the error of the approximation is proportional to the square of Δ_t or Δ_x. Since Δ_t is restricted by the size of the Yee cell because of the stability requirement, the accuracy of the calculations can be mainly controlled by the Yee cell size. Normally, the Yee cell dimensions are chosen to be equal to or less than 0.1 of the wavelength, to achieve the desired accuracy. Doubling spatial resolution in all three directions increases the computation burden by 16 times because the time step has also to be cut into half to ensure stability. A balance between accuracy and speed has to be made for almost any simulation.

29.4 FDTD MODELING OF A ^{31}P/^{1}H FOUR-RING RESONATOR AT 3T

Typical steps to model RF fields for an RF coil are the following:

1. Create a 3D model of the coil and sample.
2. Mesh the 3D model into Yee cells with sufficient resolution.
3. Choose the minimum time-step size to ensure numerical stability.
4. Excite the coil with an appropriate drive method and boundaries.
5. Save the results.

Commercial FDTD software packages such as SEMCAD X (SPEAG, Switzerland, www.semcad.com) or XFDTD (Remcom, USA, www.remcom.com) provide an integrated environment for all the steps. Step 3 is normally chosen by the software to guarantee stability. For the double-tuned RF volume coil, the whole process needs to be repeated to tune the coil to different frequencies. The effect of coupling between the two channels on the B_1 field is studied by exciting one coil with the other tuned and then examining the B_1 field distribution.

29.4.1 3D Structure

A 16 rung head-size LP–LP four-ring resonator is modeled to have ^{31}P/^{1}H double resonances at 3 T (Figure 29.1). The diameter of the resonator is 27 cm and the distance is 25 cm between the two outer rings and 12.5 cm between the two inner rings. The inner LP birdcage coil is tuned to the phosphate resonant frequency (52 MHz) and the two outer LP birdcage coils are tuned to the proton resonant frequency (128 MHz). The width of the rungs and the rings is 1 cm. One capacitor is placed across a 1 cm gap in the middle of each rung in all three coils. More than one capacitor can be distributed in series evenly along the rung if the capacitor value becomes too small. The coil is loaded with a cylindrical brain phantom (diameter of 24 cm, 30 cm long) that has average electric properties of gray matter and white matter at 3 T. Parameterized 3D models of the structure and phantom are constructed within the software package (SEMCAD X, Switzerland) and then meshed into Yee cells.

29.4.2 FDTD Meshes

The coil and phantom models are placed in an 88.5 cm × 88.5 cm × 90 cm space where the coil is at least 10 cm away from the boundaries. A total of 5.6 million isotropic 5 mm Yee cells are used

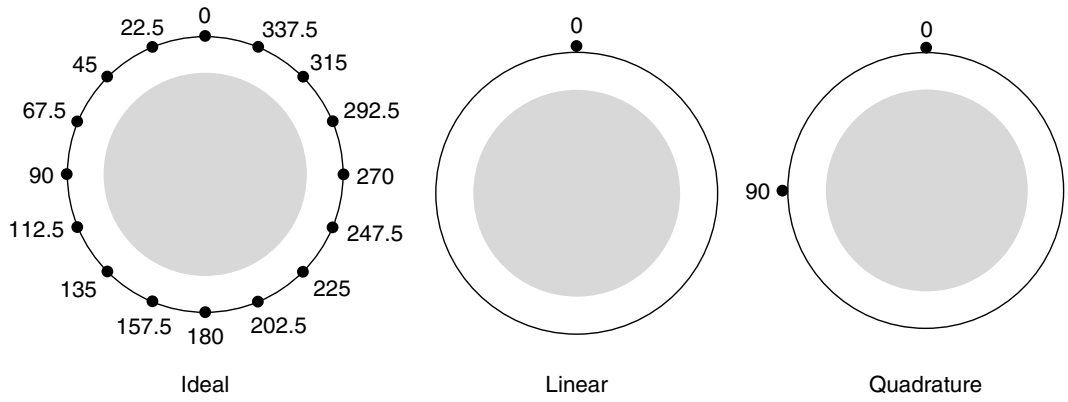

Figure 29.4. Three coil drive methods shown with top view (looking along the axis of the coil). The dots indicate the source locations. The numbers next to the dots are the phase angles (degrees) of the sources. The shaded area is the brain phantom. The ideal drive method uses ideal sources to replace the capacitors to produce the desired current and field pattern. Capacitors are modeled in the linear and quadrature drives.

to mesh the whole computational space. A time step of 9.6 e^{-12} s is chosen by the software to guarantee the stability of the computation. PML boundaries are used in all three directions. In the studies presented here, all computations were accelerated on a graphic card running on a Dell precision workstation with 2.66 GHz Intel X5355 CPU and 8 GB RAM. All simulations converged in several hours.

29.4.3 Source Type

Two types of excitation sources are used in most FDTD simulations: broadband excitation and single frequency excitation.

A broadband excitation is typically a Gaussian pulse containing a band of frequencies of interest. Fast Fourier transform (FFT) can then be applied to field components to reveal the coil's resonant spectrum. All the frequency components have to decay to zero before the FFT can apply. This could take a long time in the resonance condition. The RF fields at discrete frequencies can also be saved from a broadband simulation.

Single frequency excitations are used to compute the RF field distribution at the resonant frequency. Simulations need to reach a steady state to ensure accurate results. An artificial low-loss free space can be used to accelerate the convergence of the simulations in very high-Q resonators as long as the added loss does not change the solution significantly.[8]

29.4.4 Coil Drive Methods

29.4.4.1 Ideal Drive

This section defines the ideal drive, a method to achieve targeted current patterns in an RF coil by replacing the capacitors with ideal current or voltage sources, whose magnitudes and phases can be freely adjusted (Figure 29.4). Ideal drive is a great way to have a quick assessment of the RF field distribution, since the internal impedance of the sources can be adjusted to converge the computations faster without affecting the field distribution. Although by forcing the current pattern, the effect of sample loading on the coil tuning is not modeled, the ideal drive method has been shown to generate useful results for a birdcage body coil at 128 MHz.[9] The ideal drive can also be used to calculate the capacitor values to tune an RF coil. The method will be explained in detail in Section 29.4.5.

29.4.4.2 Linear Drive

In linear drive, the RF coil is excited with one source and the resulting B_1 field is linearly polarized (Figure 29.4). Since the linear drive requires twice as much power as the quadrature drive, it is rarely used in volume coils anymore. In numerical modeling, however, it is a good way to verify the resonant mode of a volume coil since the field pattern of the MR useful mode in a birdcage or TEM coil

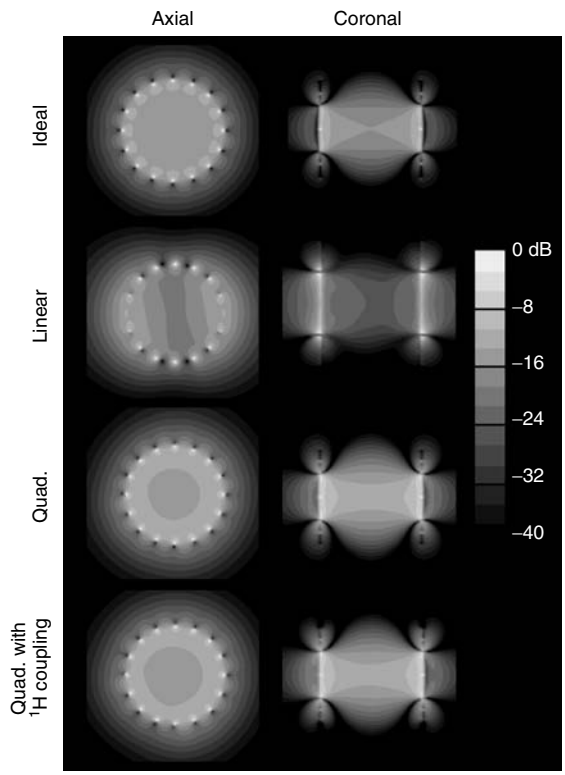

Figure 29.5. B_1^+ maps for the ^{31}P channel with different coil drive methods. The maximum value of each slice is normalized to 0 dB individually; Quad. = quadrature.

is very distinguishable. RF field distribution in the four-ring coil driven linearly is shown in Figures 29.5 and 29.6.

29.4.4.3 Quadrature Drive

In the quadrature drive, the RF coil is excited with two equal-magnitude sources that are 90° separated, both spatially in azimuthal angle and electrically in phase angle (Figure 29.4). The quadrature drive produces a circularly polarized B_1 field that is more homogeneous than that with the linear drive and requires only half of the power. It is the most commonly used drive method for RF volume coils. In a double-tuned birdcage or TEM coil, both proton and non-proton channels can be driven in quadrature, an advantage due to the symmetric structure found in both designs.

29.4.5 Coil Tuning

29.4.5.1 Empirical Coil Tuning

Tuning an RF coil is an iterative process. One starts with initial capacitor values either known from experience or calculated for well-studied structures such as birdcage coils. The capacitor values are then adjusted, usually together with the variable capacitors in the matching circuits, until the coil is resonating at the desired mode and frequency. During the process, the coil is also matched to the characteristic impedance of the driving RF cable, which is typically 50 Ω. The $|S_{11}|$ at the driving port shows the frequencies for the resonant modes. A pickup coil is used to interrogate the B_1 field inside the coil to confirm that the desired field distribution has been reached. MRI images acquired with the coil serve as the final check of the tuning.

29.4.5.2 Numerical Coil Tuning

In numerical simulations, the RF coils are generally tuned but not matched. There are two reasons for that: (i) matching is a tedious process. Anytime a capacitor value is changed, a simulation needs to be rerun and (ii) matching is not as important in simulation as in experiments. In experiments, coils are matched to receive maximum power from the RF amplifiers but in modeling the power is not limited at all. Also, matching does not affect the RF field distribution in the same way as the tuning does. The only downside of not matching the coil to the drive source impedance in modeling is that the resonant modes are not always shown clearly on the $|S_{11}|$ plot. An alternative is to record the field inside the coil during a broadband excitation and run FFT on the field to get the spectrum. This gives the same result as using a pickup coil inside the coil and looking at the $|S_{12}|$ spectrum between the drive port and the pickup coil.

For coils that use lumped capacitors, one can directly determine the capacitor values for a known current pattern of a resonant mode as presented by McKinnon and Wang in the International Society of Magnetic Resonance in Medicine conference in 2003. The idea is to produce the desired current pattern at the desired resonant frequency with ideal sources replacing the capacitors and compute the inductance seen by the sources. The capacitors are then put back into the coil with values that cancel the inductance.

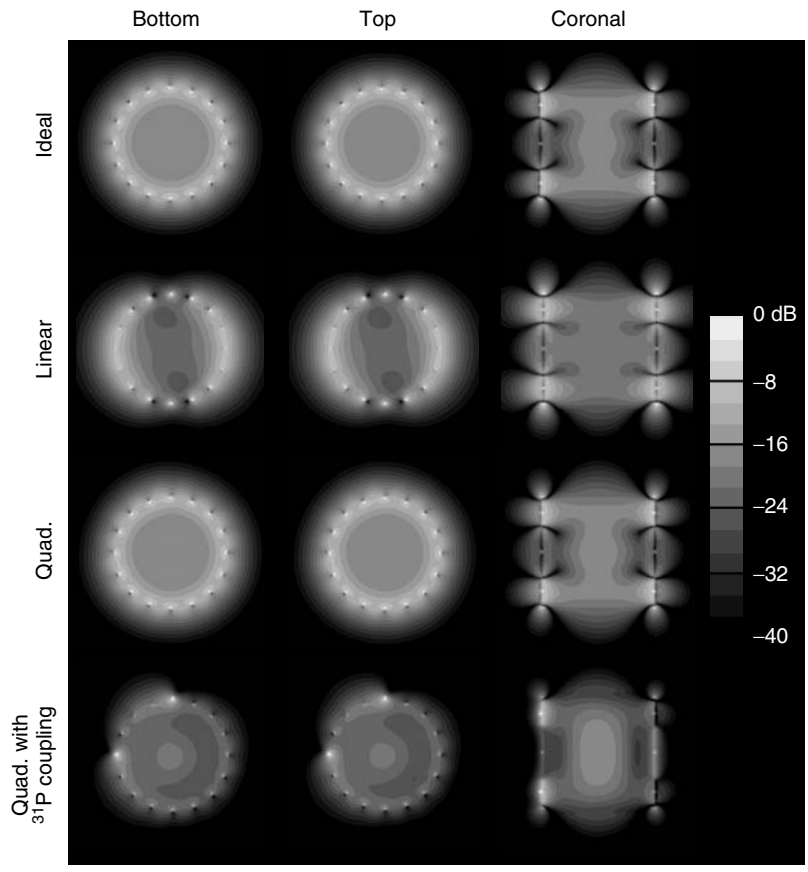

Figure 29.6. B_1^+ maps for the ^{1}H channel with different coil drive methods. The maximum value of each slice is normalized to 0 dB individually. Quad. = quadrature. The impact on the fields of coupling to the ^{31}P channel can be seen in the last row.

This method is used to tune the four-ring resonator in Section 29.4.6.

To tune the phosphate coil in the middle to 52 MHz, the first 16 current sources are placed at the gaps in the middle of the rungs. The sources have the same amplitude and incremental phase change of 22.5° (Figure 29.4 Ideal) – the current pattern for mode 1 in an LP birdcage coil. The simulation is then run at 52 MHz. The average reactance seen at the sources is 235 Ω, which requires capacitor value of 13 pF to resonate at 52 MHz. The 16 current sources are then replaced with sixteen 13 pF capacitors and the coil is driven either linearly with one current source parallel to one capacitor or in quadrature with two current sources at 90° phase apart (Figure 29.4). The ^{1}H is detuned during this process, meaning no capacitors are placed in the two ^{1}H coils.

The tune process is repeated for the proton channel, which consists of two outer LP structures. The corotating mode of the coupled outer structures produces the desired B_1 field at the center of the coils. In the corotating model, the current pattern is the same in the two structures. Sixteen current sources are placed at the gaps in the middle of each coil to produce the same current and B_1 field pattern. The magnitudes and phases of each set of 16 sources are set the same as the ones used for the phosphate channel except that the excitation frequency is now set to 128 MHz, the proton resonant frequency at 3 T. The B_1 field patterns (Figure 29.6) in both coils (top and bottom) are checked to make sure the corotating mode is excited. The average reactance seen at the sources is 490 Ω, which requires capacitor value of 2.54 pF to resonate at 128 MHz. The 16 current sources in each coil are

then replaced by sixteen 2.54 pF capacitors and each coil is driven either linearly or in quadrature in the same manner as the phosphate channel. The ^{31}P is detuned during this process, meaning no capacitors are placed in the middle ^{31}P coils.

After the capacitor values for both channels are determined, each channel is driven in quadrature with the other channel tuned, meaning that all the capacitors are in place. The effect of the coupling from the other channel on the B_1 field distribution can then be observed.

29.4.6 $\mathbf{B_1}^+$ Maps

After the simulation reaches steady state, the vector **B** fields are saved. The magnitude of $\mathbf{B}_1{}^+$, the component of $\mathbf{B}_1$ that is rotating with the spin and exciting the spins, is computed using the following equation:

$$\mathbf{B}_1{}^+ = \left| \frac{(B_x + i \times B_y)}{2} \right| \tag{29.6}$$

where B_x and B_y are the complex $\mathbf{B}_1$ fields in the x and y directions and i is $\sqrt{-1}$.

The $\mathbf{B}_1{}^+$ field map at the central axial and coronal slices in the ^{31} P coil are shown in Figure 29.5 for different drive methods. The field produced by the linear drive is less homogeneous than the ideal drive and the quadrature drive, which both yield homogeneous field distribution. The top three rows in Figure 29.5 are the maps generated with the ^{1}H channel detuned. The last row shows the field distribution driven in quadrature with the ^{1}H channel in tune. One can see that the ^{1}H channel has little effect on the ^{31}P – a phenomenon also observed by Murphy-Boesch *et al*. in their experiments.

The $\mathbf{B}_1^+$ field map at the central axial and coronal slices in the ^{1}H coils is shown in Figure 29.6 for different drive methods. The top three rows are the maps generated with the ^{31}P channel detuned. The last row shows the field distribution with the coils driven in quadrature with the ^{31}P channel in tune. One can see the coupling from ^{31}P channel has changed the field distribution of ^{1}H significantly.

29.4.7 SAR Maps and Power

After the simulation reaches steady state, the vector **E** fields are saved and the total power absorbed in the sample is computed as

$$P_{\text{abs}} = \frac{1}{2} \sum_N \left(\sigma_n E_{xn}^2 + \sigma_n E_{yn}^2 + \sigma_n E_{zn}^2 \right) \Delta_{xn} \Delta_{yn} \Delta_{zn} \tag{29.7}$$

where N is the total number of voxels in the sample, σ_n is the conductivity at cell n, E_{xn}, E_{yn}, and E_{zn} is the magnitude of the **E** field at the nth cell in the x, y, z directions. Δ_{xn}, Δ_{yn}, and Δ_{zn} are the size of the nth cell. Table 29.2 lists the total absorbed power in the sample to produce an average of 11.7 μT $\mathbf{B}_1{}^+$ at the center point of the two ^{1}H coils. The SAR is computed as

$$\text{SAR} = \frac{\sigma E^2}{2\rho} \tag{29.8}$$

where E is the magnitude of the **E** vector and ρ is the mass density. The unit for SAR is W kg^{-1}. Figure 29.7 shows the 10 g average SAR maps at the central axial slices and sagittal slice in the phantom with ^{1}H coils driven. We only list the power and SAR at the proton frequency since the power and SAR increase with square of the frequency, and it is the higher frequency in the double-tuned coil that might reach SAR limits first. The ideal drive has high power efficiency since it forces circular polarization in the coil. The quadrature drive with the ^{31}P coil detuned has almost the same efficiency as the ideal drive, indicating that highly circular polarization is also achieved. The coupling from the ^{31}P in the quadrature drive disturbs the circular polarization and yields higher power consumption. The linear coil consumes twice as much power as the quadrature drive, as expected.

Table 29.2. The power required to produce an average of 11.7 μT $B_1{}^+$ at the center of the ^{1}H coils for different drive methods

	Ideal	Linear	Quad.	Quad. with ^{31}P
Absorbed power (W)	506	1125	511	674

The coil loss is ignored.

29.5 SUMMARY

This chapter covers the basic theory of the double-tuned four-ring resonator and TEM RF volume coils, the fundamentals of the FDTD numerical

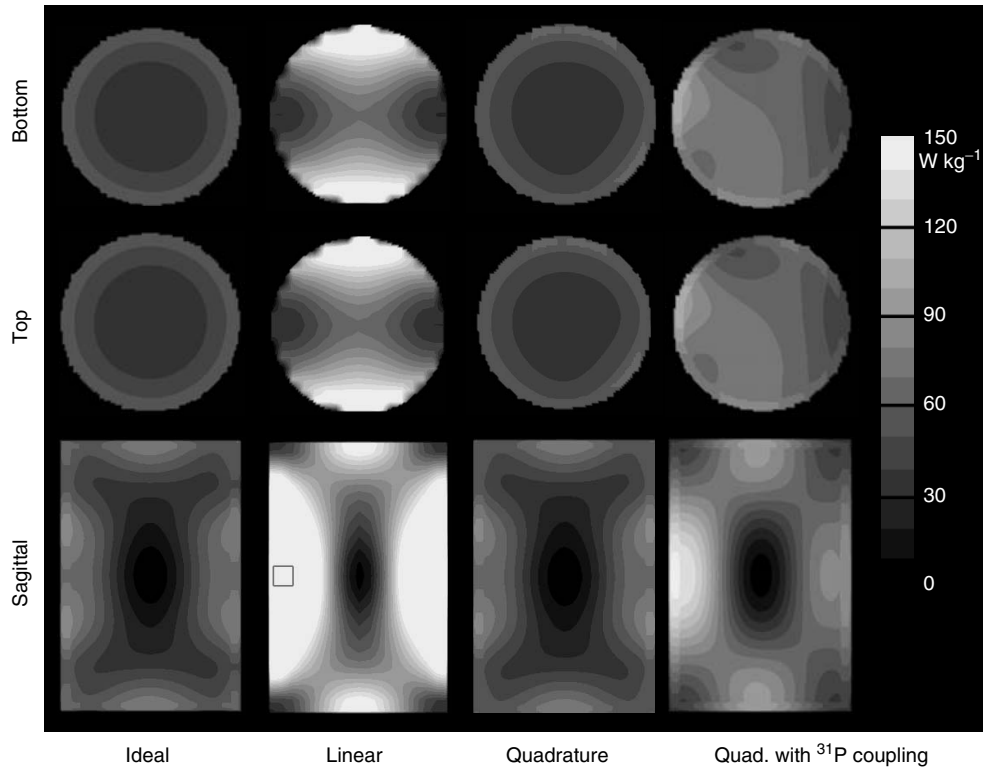

Figure 29.7. The 10 g average SAR maps in the phantom with ^{1}H channel driven. The SAR is normalized to total power that produces average of 11.7 μT B_1^+ at the center point of each ^{1}H coil. The SAR is higher than it would be in a head since the phantom is bigger (diameter of 20 cm, 30 cm long).

method, and the step-by-step process of using FDTD to model RF fields in a double-tuned four-ring resonator. The principle and process for coil tuning and driving, B_1^+ field mapping, and E field and SAR mapping can also be applied to general purpose coils. Once the basic maps of RF fields are obtained, further optimization can be done for more complex structures such as RF coil arrays.

REFERENCES

1. A. Taflove, S. C. Hagness, *Computational electrodynamics: the finite-difference time-domain method*, 2nd edn., Artech House: Boston, 2000, p. 852.
2. J.-M. Jin, *Electromagnetic analysis and design in magnetic resonance imaging*, CRC Press: Boca Raton, FL, 1999, p. xiv.
3. IEEE C95.3–2002 (Revision of IEEE Std C95.3–1991). *IEEE Recommended Practice for Measurements and Computations of Radio Frequency Electromagnetic Fields With Respect to Human Exposure to Such Fields,100 kHz-300 GHz*, 2002, The Institute of Electrical and Electronics Engineers, Inc: New York, p. 126.
4. J. W. Hand, *Phys. Med. Biol.,* 2008, **53**, R243.
5. J. Murphy-Boesch, R. Srinivasan, L. Carvajal, and T. R. Brown, *J. Magn. Reson. B,* 1994, **103**, 103.
6. J. T. Vaughan, H. P. Hetherington, J. O. Otu, J. W. Pan, and G. M. Pohost, *Magn. Reson. Med.,* 1994, **32**, 206.
7. C. J. Snyder, L. DelaBarre, G. J. Metzger, P. F. van de Moortele, C. Akgun, K. Ugurbil, and J. T. Vaughan, *Magn. Reson. Med.,* 2009, **61**, 517.
8. A. Taflove, *IEEE Trans. Electro. Comp.*, 1980, **EMC-22**, 191.
9. W. Liu, C. Collins, and M. Smith, *Appl. Magn. Reson.*, 2005, **29**, 5.

Chapter 30

Radiofrequency Fields and SAR for Transverse Electromagnetic (TEM) Surface Coils

Can Eyup Akgun

Center for Magnetic Resonance Research, University of Minnesota, Minneapolis, MN 55455, USA

30.1 INTRODUCTION

In magnetic resonance imaging (MRI) systems, radiofrequency (RF) coils are integral parts of the imaging system. RF coils are the devices used in MRI to inductively excite and receive the nuclear magnetic resonance (NMR) signal from the anatomy. This nuclear magnetic induction is most efficient at the field-strength-dependent Larmor frequency for a nuclear species. RF coils must resonate at Larmor frequencies of 42.58 MHz/tesla(T)$^{-1}$ to take advantage of the signal-to-noise ratio (SNR) benefits of MRI systems of varying field strengths (e.g., 1.5 T = 63.86 MHz, 7 T = 298.06 MHz, etc.).

To capture the benefits of SNR and spectral resolution with increasing magnetic field strength, in clinical settings, traditional 1.5 T magnets are being replaced by 3 T magnets, which are currently the highest field strength used for clinical systems. High-field MRI magnets (7 T and higher) are being investigated for their "clinical" potential.[1–4] The highest field for "standard" factory-supported systems is 7 T, with approximately 35 of these systems installed. Above this, four 9.4 T systems exist, and one 11.7 T, 68 cm bore (head only) system is being installed at the National Institutes of Health (NIH), while whole-body 10.5 and 11.7 T magnets are being installed at the University of Minnesota Center for Magnetic Resonance Research (CMRR) and at the Atomic Energy Commission (CEA) in France.

As MRI field strengths increase, there are various RF challenges that need to be overcome in coil design strategy. One obstacle at high fields is that RF wavelengths become shorter than the dimensions of the object to be imaged. This leads to significant B_1 (magnetic field component of the RF field) distortions, which are dependent on the tissue electromagnetic properties and geometry.[5,6] One approach toward overcoming these obstacles is combining surface coils in multi-element coil

RF Coils for MRI
Edited by J. Thomas Vaughan and John R. Griffiths

ISBN: 978-0-470-77076-4

phased-array configurations.[7–9] Resonant elements with small electrical lengths, preferably less than $\lambda/10$, can greatly reduce the coil's losses[10,12] when compared to larger RF coils. The ability to control the magnitude and phase parameters in these individual current-carrying elements allows the utilization of techniques like B_1 shimming,[13–15] which can greatly reduce distortion in images.

Another issue at high field strengths is, as the wavelengths decrease, RF wave penetration depths in tissues decrease,[3,16–18] consequently a homogeneous RF coil can no longer generate a uniform B_1^+ field (transmit RF magnetic field component) in the head at higher magnetic field strengths.[6] Hence, more RF power is required to attain the same flip angles in an imaging protocol than at low fields, which leads to greater electrical fields deposited in the tissue. RF losses in the tissue loading the coil also become even more significant. Losses due to the B_1-induced eddy current density and electrical field displacement current density both increase with increasing field strength.[19]

Measurements or estimates of these high field issues are not trivial, particularly in human subjects. Bench testing of coils and circuits cannot predict electromagnetic behavior during an MRI experiment, and an MRI experiment cannot predict losses in the circuit or the electric fields and subsequent specific absorption rate (SAR) values to which the subject will be exposed. Also, SAR that is produced during an MR experiment is a complex function of numerous variables including the frequency, the type of RF pulse sequences used, the repetition time, the type of transmit RF coil used, the volume of tissue contained within the transmit RF coil, and the configuration of the anatomical region exposed, as well as other factors.

The development and safety verification of multi-element surface coils and RF field optimization schemes at ultrahigh magnetic fields (7 T and above) require the ability to predict transmit characteristics in vivo. Accurate simulation permits the estimation of B-fields and E-fields (as mentioned, these are not measured by MR scanners) and consequent SAR values. Numerical simulation provides an accurate tool for the extraction of information including element-specific B_1 and electric fields to evaluate B_1^+ performance and the impact of SAR.

In this chapter, an electromagnetic solver, finite difference time domain (FDTD), is illustrated as a tool to calculate magnetic field patterns produced by multi-element surface coils, as well as a means to determine SAR in human anatomy with these coil configurations. The basics of RF surface coils, surface coil combinations, and FDTD formulations of RF coils will be discussed. The remainder of this chapter illustrates examples of electromagnetic verification of coil designs and approaches that have been used to control RF loss and penetration for human biomedical applications.

30.2 RF COILS

RF coils in high-field MRI systems must efficiently couple magnetic energy to human anatomy at Larmor frequencies of up to 500 MHz (11.7 T) to make these systems useful. RF coil efficiency (defined here as magnetic energy versus localized electric field energy or simply B_1^+ versus SAR) decreases as wavelength decreases, which includes both the wavelength of the coil circuit itself and the wavelengths of the media (air, plastic, anatomy, etc.) through which the RF field propagates. To produce homogeneous images, it is generally desirable to have a homogeneous RF magnetic field that covers the portion of the subject being imaged in order to both excite a uniform distribution of flip angles in this portion and to receive signals equally well from the portion of the subject being imaged.

In high-field MRI, additional challenges occur, as the RF wavelength in tissue decreases and coils that produce homogeneous fields at lower frequencies do so less effectively. At these high RF frequencies, the wavelengths become shorter than the dimensions of the subject to be imaged. This leads to significant B_1 field distortions that occur as a result of the tissue electromagnetic properties and geometry.

30.2.1 Multi-element Surface Coils (Transceive Arrays)

One approach to reduce the RF losses and to control the RF fields in high-frequency MRI systems is to limit the electrical length of the coil, preferably to less than $\lambda/10$. The electrical length of a coil can be limited by reducing its physical dimensions or by distributing capacitors along the length of the resonator. This reduction in size reduces the coil's losses, and the low inductance of a small coil also extends the upper frequency limit at which the

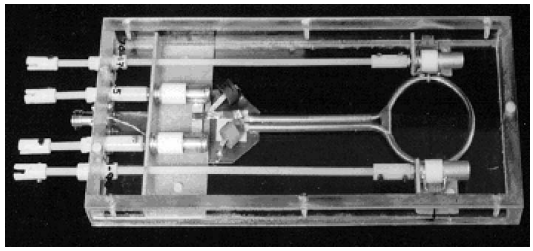

Figure 30.1. Coaxial transmission line loop surface coil.

coil resonates (see Chapter 1). The most common small coil is exemplified by a simple LC circuit loop whose current generates an RF magnetic dipole which inductively couples to a nuclear spin system for excitation and reception of the free induction decay (FID) signal. This coil is generally known as a "surface coil" (Figure 30.1). While small loop coils are efficient at high frequencies, they couple only to limited depths in the sample.

An important development in MRI that may have particularly promising potential at high fields is the use of multiple coils. Multi-element transceiver coils comprised of individual current-carrying surface coils have become a popular means for signal transmission and reception at high magnetic fields. The multi-element coil consists of an array of transmission line (transverse electromagnetic, TEM) elements that are mutually decoupled and operated as independent coils in typically multiple-element transmit and receive configurations. Although an individual surface coil gives the highest possible SNR up to a field of view (FOV) comparable to the diameter of the coil,[7] a single surface coil can only effectively image a limited region. Thus, by combining these noninteracting surface coils into a phased array coil, an image of a larger area can be obtained with uniform sensitivity and higher SNR as compared to large volume coils (e.g., Helmholtz or birdcage resonators). One choice to be made in coil design is whether to use microstrip line elements or loop elements (see Chapters 9 and 10) in the coil construction (Figures 30.2 and 30.3). While both element choices can be made more efficient by transmission line design, the microstrip element is electrically the shortest and can provide a deeper FOV then loops, whereas the loops have stronger SNR performance in the periphery of the imaged object. However, microstrip elements have the additional benefit that optimization schemes can be simplified because of the bi-directional currents on the line elements.[20]

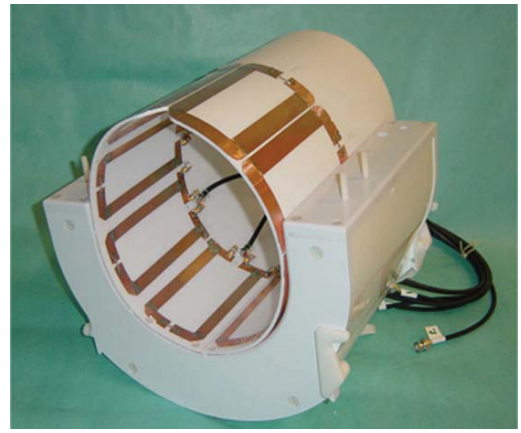

Figure 30.2. Multi-element (7 T) head coil with an array of loops.[20]

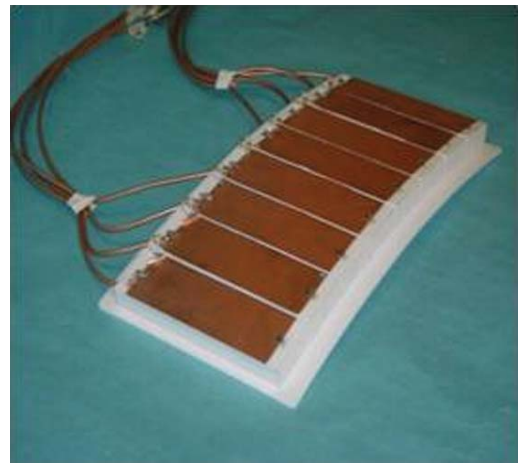

Figure 30.3. Eight-element multi-element body coil array with microstrip segments.[13]

30.3 FINITE DIFFERENCE TIME DOMAIN

First introduced by Yee,[21] the FDTD[22–24] method is the most widely used full-wave electromagnetic technique in MRI (see Chapter 27). This method is based on Maxwell's curl equations

$$\frac{\partial \mathbf{B}}{\partial t} = -\nabla \times \mathbf{E} \tag{30.1}$$

$$\varepsilon \frac{\partial \mathbf{E}}{\partial t} = \frac{\nabla \times \mathbf{B}}{\mu} - \sigma \mathbf{E} \tag{30.2}$$

where **B** (T) is magnetic flux density, **E** (V m^{-1}) is electrical field, t is time, σ (S m^{-1}) is electrical conductivity, ε is electrical permittivity ($\varepsilon = \varepsilon r^{*}\varepsilon_0$) (F m^{-1}), and μ_0 is magnetic permeability (for the purposes of this example, μ in all materials is equal to that of air).

In FDTD, the problem space is initially created by a 3D box referred to as the Yee cell (Figure 30.4). This cell is small compared to the wavelength and is further defined as a "mesh" when many FDTD cells are combined to create a 3D volume. In this mesh, the edges represent the electrical fields while the faces of the box represent the magnetic field components that need to be solved by Maxwell's equations (Figure 30.4).

In these cells, time is quantized into increments where each increment represents the time required for a wave to propagate from one cell node to the next. In all directions, reference nodes for electric and magnetic fields are offset from each other by one-half of grid spacing and one-half of a step in time. Moving forward in time, the electric and magnetic fields are updated using a "leapfrog" scheme where first the electric fields, and then the magnetic fields are computed at each step in time. Equation (30.3) illustrates the computation of electric field (**E**) (x-component) by using the surrounding the magnetic field (**B**) components (y and z components).

$$\varepsilon \frac{\mathbf{E}_x{}^{n+1}\left(i+\frac{1}{2},j,k\right)-\mathbf{E}_x{}^{n}\left(i+\frac{1}{2},j,k\right)}{\Delta t} = \frac{1}{\mu}\left\{\left[\frac{\mathbf{B}_z{}^{n+\frac{1}{2}}\left(i+\frac{1}{2},j+\frac{1}{2},k\right)-\mathbf{B}_z{}^{n+\frac{1}{2}}\left(i+\frac{1}{2},j-\frac{1}{2},k\right)}{\Delta y}\right] + \left[\frac{\mathbf{B}_y{}^{n+\frac{1}{2}}\left(i+\frac{1}{2},j,k-\frac{1}{2}\right)-\mathbf{B}_y{}^{n+\frac{1}{2}}\left(i+\frac{1}{2},j,k+\frac{1}{2}\right)}{\Delta z}\right]\right\} - \sigma \mathbf{E}_x{}^{n}\left(i+\frac{1}{2},j,k\right) \tag{30.3}$$

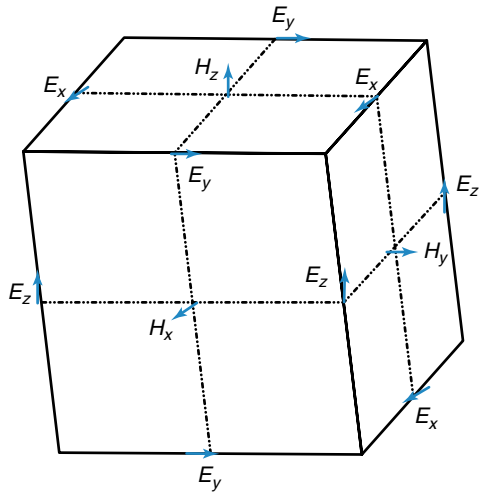

Figure 30.4. Yee cell illustrating offset of E and H field modeled by FDTD.

The x-component of the magnetic field can be calculated from the surrounding electric field components (y and z):

$$\mathbf{B}_x{}^{n+\frac{1}{2}}\left(i,j+\frac{1}{2},k+\frac{1}{2}\right) = \mathbf{B}_x{}^{n-\frac{1}{2}}\left(i,j+\frac{1}{2},k+\frac{1}{2}\right) + \Delta t\left\{\left[\frac{\mathbf{E}_y{}^{n}\left(i,j+\frac{1}{2},k+1\right)-\mathbf{E}_y{}^{n}\left(i,j+\frac{1}{2},k\right)}{\Delta z}\right] + \left[\frac{\mathbf{E}_z{}^{n}\left(i,j,k+\frac{1}{2}\right)-\mathbf{E}_z{}^{n}\left(i,j+1,k+\frac{1}{2}\right)}{\Delta y}\right]\right\} \tag{30.4}$$

Similarly, the y and z components of the electric and magnetic field can also be calculated. Provided that the grid spacing and steps forward in time are small enough to ensure stability and accuracy (there also needs to be computer resources available to complete the calculation in a reasonable time), the fields in the entire problem region can be calculated for any future point in time. By applying appropriate initial boundary equations, these two equations can be alternately applied to simulate the propagation of an electromagnetic wave throughout the model.

In FDTD calculations, the frequency limits and time increment are determined by the cell dimension. In general, it is recommended that the minimum resolution, which also determines the upper frequency limit, should be set at 10 cells per wavelength.[23] In practice, the cell size will often be set by the dimensions and features of the structure to be simulated (e.g., length of a wire or thickness of dielectric); hence, the smaller the feature, the smaller the cell size. There are some limitations to the FDTD method as distinct features or discrete elements such as capacitors are not always fitted well in the mesh. Also, stair-step approximations are needed for diagonal dimensions such as angled conductor plates and long wires. To improve model accuracy for either of these features, a finer mesh has to be used, which increases the memory requirements and computation time.

Remcom's XFdtd (State College, PA) is one of many software packages that incorporate a model of the human body with the FDTD. This 3D mesh was created by first segmenting the digital photographic data of the National Library of Medicine's Visible Male Project, and then a 3D grid of Yee cells was created from the segmented data. Values for material density were taken from the literature[25] and values for electrical properties were derived at each frequency by linear interpolation from measurements by Gabriel *et al.*[26–28] in each tissue.

30.4 TRANSMIT B_1^+

In MRI RF coils, a time-varying magnetic field B_1 ($B_1 = \mu H_1$), which is generated by a unit current in an RF coil with angular frequency ω and phase angle θ, may be represented as a phasor:

$$B_1 = B_{1x}\exp(j\theta_x), B_{1y}\exp(j\theta_y), B_{1z}\exp(j\theta_z) \tag{30.5}$$

Time-domain field quantities are then obtained after multiplying equation (30.5) by e^{jwt} (t = time) and taking the real part. The z-component of the RF field does not influence the MR signal; hence, we will not consider it further. For the subsequent discussion, it is convenient to decompose the RF field into two rotating fields, a circularly polarized component (B_1^+) rotating counterclockwise with respect to the direction of the main magnetic field B_0 [equation (30.6)], and a circularly polarized component rotating in the opposite direction (B_1^-) [equation (30.7)]. The asterisk denotes a complex conjugate in equation (30.7). B_1^+ is denoted as the transmit component of the magnetic field and B_1^- as the receive magnetic field. This chapter focuses on the transmit component B_1^+, since SAR is directly related to the electrical fields produced by coils and, if applicable, RF field combination techniques during the transmit stage of the MR acquisition.

$$B_1^+ = \frac{B_x + iB_y}{2} \tag{30.6}$$

$$B_1^- = \frac{(B_x - iB_y)^*}{2} \tag{30.7}$$

In order to quantify RF coils in an MRI experiment, a map of the B_1^+ field map must be obtained. A conventional approach to B_1^+ mapping is to collect two scans, one of which uses twice the RF amplitude of the other. By taking a ratio of pixels of the two images with the same imaging parameters (except for flip angle), the effects of T_2 relaxation, proton density, and receiver coil sensitivity are cancelled out and therefore not present in the ratio of the two images. This method is commonly referred to as the "double angle mapping" method.[29,30] It can be used to determine the driving voltage necessary to obtain the desired flip angle in addition to obtaining the B_1^+. Other popular methods are the "absolute flip imaging" method[31] and the "Bloch–Siegert" method.[32]

In Remcom's XFdtd, steady-state B_1^+ results in a simulation that can be normalized to 1 W of net input power by the Remcom post-processing tool. Alongside the input power, also the radiated power, dissipated power, and other discrete frequency outputs measured on the coil are scaled. By normalizing the input powers to the same value, experimental and simulated results can be compared. There is, however, some discrepancy; in MRI experiments, power delivered by the coil is not measured on the RF coil. MRI systems typically provide these voltage values from power monitors (directional couplers) established at the back of the magnet, hence there are additional cable losses associated with MRI experiments when compared to simulations (between 10% and 20%). Also, component (capacitor, inductor, etc.) and cable losses and impedance mismatches to the coil are not incorporated in FDTD calculations. To accurately compare experimental and simulated results, one must accurately quantify the experimental losses mentioned above and incorporate them in the final calculations.

30.5 SPECIFIC ABSORPTION RATE

Although high B_0 field strengths and correspondingly high B_1 field frequencies (300 MHz and above) improve the SNR, this improvement comes at a price; RF power deposition in tissue becomes more evident with increase in field strength, leading to safety concerns. A time-varying magnetic field B_1 induces a time-varying electrical field and consequently RF energy is dissipated in the human body resulting in unwanted heating[33–35] (see Chapter 33). The SAR is an approximation for this temperature change and can be defined as

$$SAR = \frac{\text{RF energy absorbed in sample}}{\text{Exposure time} \times \text{weight of sample}} \quad (30.8)$$

Since the E-fields and subsequent SAR fields cannot be measured by an MRI scanner, numerical calculations of SAR become necessary. In FDTD, at every location, SAR can be calculated from the following equation:

$$\begin{aligned} SAR &= \frac{\sigma_x}{2\rho_x}|E_x|^2 + \frac{\sigma_y}{2\rho_y}|E_y|^2 + \frac{\sigma_z}{2\rho_z}|E_z|^2 \\ &= SAR_x + SAR_y + SAR_z \end{aligned} \quad (30.9)$$

where E, σ, and ρ are the electric field magnitude, material conductivity, and material density, respectively, for Yee cell elements in the x, y, and z directions (as indicated by the subscripts) at the specific locations.

In order to reduce the risk of local tissue damage in the patient, the International Electrotechnical Commission (IEC) has issued guidelines for the safe operation of MRI, suggesting limits for the SAR (watts of RF power per kilogram of tissue) allowable over the whole body, averaged over the head, and in any 10 g of tissue. The current IEC normal operating mode limits are 2 W kg^{-1} over the whole body, 3.2 W kg^{-1} over the head, and 10 W kg^{-1} over any 10 g sample of tissue. All of these limits are averaged over a 6 min period. There is also a peak limit of not more than two times the above values over any 10 s period.[36]

30.6 SURFACE COIL

A simple example of an RF coil is the loop resonator. In MRI applications, single surface coils (see Chapter 2) can still be utilized at high fields in ways similar to those at lower field, sharing with the latter a stronger B_1 field magnitude within the vicinity of the RF coil. The loop resonator can be used to image small objects or to localize imaging to a small region in the anatomy. In Figure 30.5, a loop resonator is designed to have four equidistant capacitors tuned to 298 MHz (Figure 30.5a). This resonant surface coil is placed inside a phantom that has the same electrical properties as the average human body at the same frequency. The placement of the loop is intended to represent the placement of a surface coil within human anatomy, much like an endo-rectal RF coil used to image the prostate.[37] The FDTD solver can be used to visualize the magnetic fields of the loop with the sample. Along the plane of the coil, there is equal propagation of the B_1^+ field (Figure 30.5b). The impact of the circuitry and its proximity are seen in the SAR maps in Figure 30.5(c). The SAR distribution is uniform along the loop and peaks above the capacitors. The B_1^+ and SAR values can provide a benchmark for the loop design, as well as a means to limit the RF transmit power in an experiment.

30.7 TRANSCEIVE ARRAYS

As RF wavelengths become shorter than the dimensions of the object to be imaged, significant B_1 field

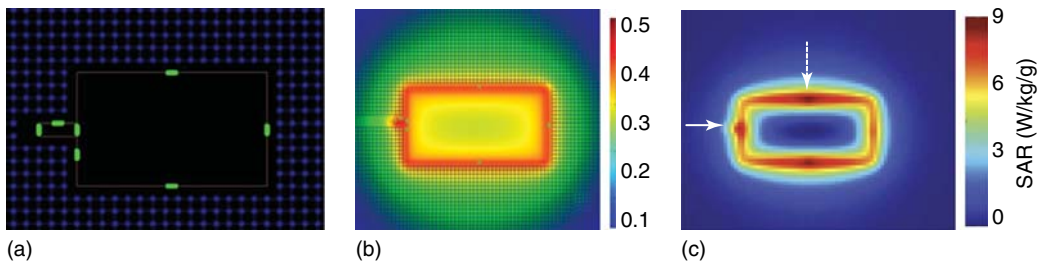

Figure 30.5. (a) RF loop resonator embedded in phantom. (b) **B**-field magnitude profile (μT). (c) SAR profile (W kg^{-1}).

distortions occur, which are dependent on tissue electromagnetic properties and geometry. To image larger objects such as the human head, numerous surface coils can be combined in an array configuration to "focus" the RF field in large regions of interest such as the heart, kidneys, or even the human head. As an example, multiple microstrip TEM surface coils consisting of microstrip transmission line elements can be used to transmit and receive signals in the head (see Chapter 26). In XFdtd, an eight-element stripline transceiver array is modeled (Figure 30.6a) about an anatomically correct head for numerical verification. In both experiment and simulation, the phase angles on the array elements are incrementally phased over 360° to generate a theoretically uniform transverse field through the coil volume (Figure 30.6b). In Figure 30.6(c), experimental $B_1{}^+$ maps acquired from a coil with exactly the same dimensions as the model in Figure 30.6(a) are illustrated. The combined experimental RF field profile in the brain is illustrated in Figure 30.6(c), while the simulated coil's $B_1{}^+$ profile and the resulting SAR profile are illustrated in Figures 30.6(d) and (e), respectively.

When normalized to 1 W of total input power to the coil, the coil produces an average $B_1{}^+$ of 0.332 $\mu T\,W^{-0.5}$ in the center of the brain. In Remcom simulations, an average $B_1{}^+$ value of 0.409 $\mu T\,W^{-0.5}$ is seen at the center of the brain for the combined coil performance. Simulation results having greater $B_1{}^+$ than experimental results are not surprising; the exclusion of cable losses and mismatches at the coil front end (discussed earlier) explain the differences in the values. However, the results give us confidence to determine the SAR values; the unaveraged peak SAR value from this coil in simulation was 1.466 W kg^{-1} (Figure 30.6d) for the same input power.

As seen in Figure 30.6(b) and (c), the B_1 profiles of transceiver RF coils at high field exhibit a feature often described as a "bright center". This is the result of a complicated combination of destructive and constructive interferences.[5,6] This high-field effect can be used to our advantage; a more homogeneous B_1 field can be obtained at a specific location in a slice and suppressed in other regions of the same image by

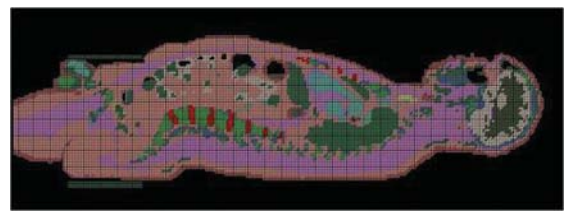

Figure 30.7. Remcom's hi-fi human body mesh (5 × 5 × 5 mm resolution) in sagittal direction with transceiver elements centered on the prostate.

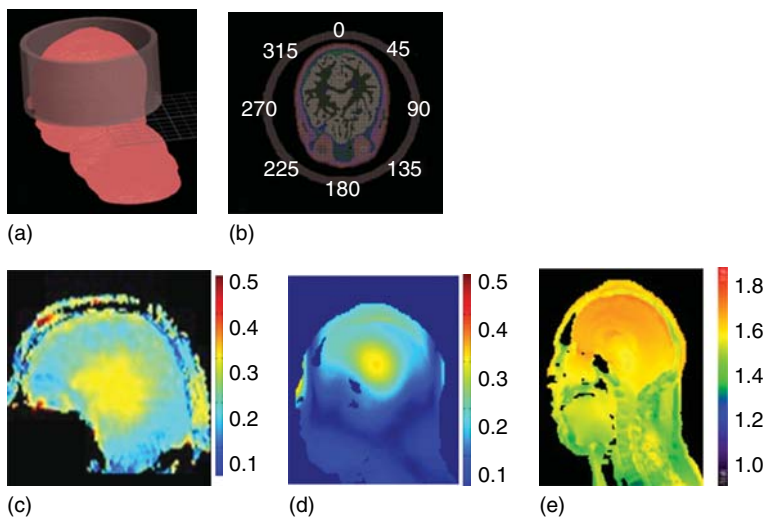

Figure 30.6. (a) Remcom illustrations of head coil around the human head. (b) Geometric phase distribution of elements in volume coil. (c) Experimental $B_1{}^+$ map of eight-element head coil excited in head ($\mu T\ W^{-0.5}$). (d) Simulated $B_1{}^+$ of eight-element volume coil in (c) ($\mu T\ W^{-0.5}$). (e) SAR profile from the eight-element head coil (W kg^{-1}).

adjusting individual current-carrying elements within a transceiver coil at high field (also referred to as "B_1 shimming" or "field focusing").[13,14] Modeling the B_1^+ and E-fields in this field optimization technique is important for understanding and developing methods to manage local SAR.

B_1^+ phase shimming can be performed by determining a set of transmit phases that will maximize the B_1^+ phase coherence at the center of the object being imaged. This can be graphically prescribed in a custom GUI (graphic user interface) tool such as Matlab (MathWorks, Natick, MA). These phases are calculated by averaging the relative transmit phase over the chosen region of interest (ROI) (center of the object being imaged) and subtracting these phases from each transmit element's initial drive phase in simulation (in an experiment, computer-controlled phase shifters would be used to change initial drive phase of coil elements), for subsequent acquisitions when transmitting with all elements simultaneously.

To illustrate this B_1^+ shimming technique, as an example, an eight-element, flexible TEM transceiver array[38] was investigated experimentally and further validated by simulation (illustrated in Figure 30.7). In the experiment, the coil elements were evenly distributed between two identical plates (similar to that in Figure 30.3) which were placed anteriorly and posteriorly on the body, and centered above the prostate. Each element was driven by one voltage source and tuned to the Larmor frequency at 7 T for the prostate. The current phase angles on the array elements were determined to create a uniform transverse field at the prostate. Once the B_1^+ profiles and the phases at the ROI of each element are known, the phases for B_1^+ shimming at the prostate can be employed to optimize the transmit phase for each element on the array.

Figure 30.8(a) shows the fractional available B_1^+ maps for simulated data at an axial slice of the prostate before B_1^+ shimming (the yellow

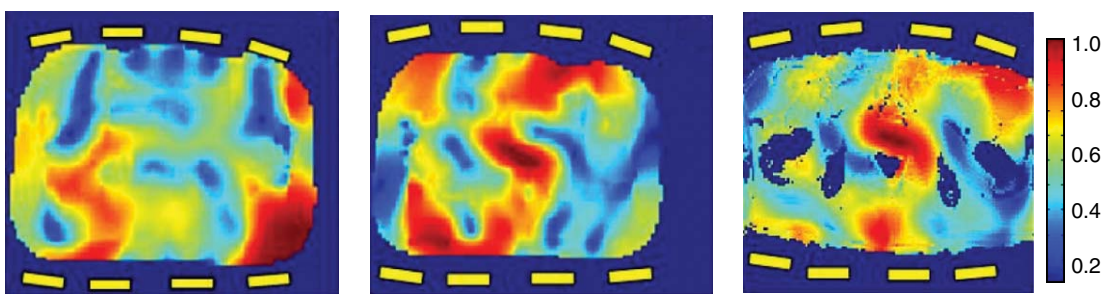

Figure 30.8. XFdtd simulation illustrating (a) fractional B_1^+ map (transaxial view), (b) fractional available B_1 maps determined for the prostate from simulation, and (c) 7 T experimental results with the same phases the simulation in (b).[13]

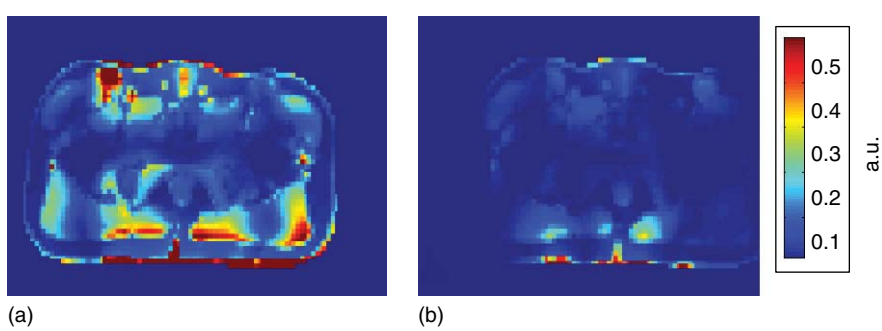

Figure 30.9. Theoretical SAR values for the prostate demonstrating local SAR (a) before and (b) after shimming for an equal B_1^+ within the prostate.[13]

bars indicate the placement of the coil elements). Figure 30.8(b) shows the B_1^+ maps after correct phases are incorporated into the coil in simulation and Figure 30.8(c) illustrates the experimental 7 T results for a subject with the corrected phases (same phase values as simulation). The "S"-shaped pattern observed in the experimental data is also observed in the simulated data with similar transmit B_1^+ values (Figure 30.8b and c). This data gives confidence that the simulated E-fields and the SAR values calculated from them are also correct. The impact of B_1 shimming on SAR levels is illustrated in Figure 30.9. The optimal phase values for a region (Figure 30.9b) of interest produce lower SAR values throughout the slice when compared to the simulation with geometric phase values (Figure 30.9a).

30.8 CONCLUSIONS

The age of high-field MRI presents new challenges to the RF coil builder. Shorter wavelengths and greater power deposition in tissues are obstacles that must be overcome as more applications are being developed to capture the benefits of high fields. Multiple-element surface arrays have been shown as a successful RF coil strategy, along with techniques such as B_1^+ shimming, when trying to tackle these obstacles. Numerical techniques such as FDTD have provided a means to predict transmit characteristics in vivo for development and safety verification in these strategies and undoubtedly will be relied on more as new RF coil designs and optimization techniques surface.

REFERENCES

1. K. Ugurbil, M. Garwood, K. Hendrich, R. Hinke, X. Hu, R. S. Menon, H. Merkle, S. Ogawa, and R. Salmi, *Magn. Reson. Q.*, 1993, **9**, 259–277.
2. J. W. Pan, J. T. Vaughan, R. I. Kuzniecky, G. Pohost, and H. Hetherington, *Magn. Reson. Imaging*, 1995, **13**, 915–921.
3. J. T. Vaughan, M. Garwood, C. M. Collins, W. Liu, L. DelaBarre, G. Adriany, P. Andersen, H. Merkle, R. Goebel, M. B. Smith, and K. Ugurbil, *Magn. Reson. Med.*, 2001, **46**, 24–30.
4. J. T. Vaughan, L. DelaBarre, C. Snyder, J. Tian, C. Akgun, D. Shrivastava, W. Liu, C. Olson, G. Adriany, J. Strupp, P. Andersen, A. Gopinath, P. F. Van de Moortele, M. Garwood, and K. Ugurbil, *Magn. Reson. Med.*, 2006, **56**, 1274–1282.
5. C. M. Collins, W. Liu, W. Schreiber, Q. X. Yang, and M. B. Smith, *J. Magn. Reson. Imaging*, 2005, **21**, 192–196.
6. P. F. Van de Moortele, C. Akgun, G. Adriany, S. Moeller, J. Ritter, C. M. Collins, M. B. Smith, J. T. Vaughan, and K. Ugurbil, *Magn. Reson. Med.*, 2005, **54**, 1503–1518.
7. P. B. Roemer, W. A. Edelstein, C. E. Hayes, S. P. Souza, and O. M. Mueller, *Magn. Reson. Med.*, 1990, **16**, 192–225.
8. C. Hayes, N. Hattes, and P. B. Roemer, *Magn. Reson. Med.*, 1991, **18**, 309–319.
9. J. T. Vaughan, H. P. Hetherington, J. O. Otu, J. W. Pan, and G. M. Pohost, *Magn. Reson. Med.*, 1994, **32**, 206–218.
10. W. L. Stutzman and G. A. Thiele, *Antenna Theory and Design*, 2nd edn, John Wiley & Sons, New York, 1981.
11. D. Pozar, *Microwave Engineering*, 2nd edn, Addison Wesley, New York, 1998.
12. L. L. Libby, *Proc. IRE*, 1946, **34**, 641–646.
13. G. J. Metzger, C. Snyder, C. Akgun, T. Vaughan, K. Ugurbil, and P. F. Van de Moortele, *Magn. Reson. Med.*, 2008, **59**, 396–409.
14. P. Van de Moortele, E. Auerbach, K. Ugurbil, and J. Ritter, *Multiple Area B1 Shimming: An efficient, low SAR approach for T2-weighted fMRI acquired in the Visual and Motor Cortices of the Human Brain at Ultra-High Field*, p. 1548, 2009.
15. G. J. Metzger, L. J. DelaBarre, X. Bi, S. Shah, S. Zuehlsdorff, T. Vaughan, K. Ugurbil, and P-F. van de Moortele, *Left Coronary Artery Imaging at 7 T: Initial Results using Multiple B_1^+ Shimming Algorithms and Targets*, this work was presented in ISMRM 2011.
16. C. N. Chen, V. J. Sank, S. M. Cohen, and D. I. Hoult, *Magn. Reson. Med.*, 1986, **3**, 722–729.
17. C. M. Collins and M. B. Smith, *Magn. Reson. Med.*, 2001, **45**, 684–691.
18. T. S. Ibrahim, *IEEE Trans. Microw. Theory Tech.*, 2004, **52**, 1999–2003.
19. J. T. Vaughan, in *Ultra High Field Magnetic Resonance Imaging*, eds P. Robitaille and L. Berliner, Springer: New York, 2006, pp. 127–161.

20. G. Adriany, P-F. Van de Moortele, F. Wiesinger, S. Moeller, J. P. Strupp, P. Andersen, C. Snyder, X. Zhang, W. Chen, K. P. Pruessmann, P. Boesiger, T. Vaughan, and K. Ugurbil, *Magn. Reson. Med.*, 2005, **53**, 434–445.
21. K. Yee *IEEE Trans. Antennas Propag.*, 1966, **14**, 302–307.
22. J. L. Young, *Antenn. Propag., IEEE Trans.*, 1995, **43**, 422–426.
23. A. Taflove, *Electromagn. Compat., IEEE Trans.*, 1980, **EMC-22**, 191–202.
24. K. S. Kunz and R. J. Luebbers, *The Finite Difference Time Domain Method for Electromagnetics*, CRC Press: Boca Raton, FL, 1993.
25. C. E. Clauser and J. W. Young, *Weight, Volume, and Center of Mass of Segments of the Human Body*, AMRL Technical Report, Wright Patterson Air Force Base: Ohio, 1969.
26. C. Gabriel, S. Gabriel, and E. Corthout, *Phys. Med. Biol.*, 1996, **41**, 2231–2249.
27. S. Gabriel, R. W. Lau, and C. Gabriel, *Phys. Med. Biol.*, 1996, **41**, 2251–2269.
28. S. Gabriel, R. W. Lau, and C. Gabriel, *Phys. Med. Biol.*, 1996, **41**, 2271–2293.
29. C. H. Cunningham, J. M. Pauly, and K. S. Nayak, *Magn. Reson. Med.*, 2006, **55**, 1326–1333.
30. E. Insko and L. Bolinger, *J. Magn. Reson., Ser. A*, 1993, **102**, 82–85.
31. V. L. Yarnykh, *Magn. Reson. Med.*, 2007, **57**, 192–200.
32. L. I. Sacolick, F. Wiesinger, I. Hancu, and M. W. Vogel, *Magn. Reson. Med.*, 2010, **63**, 1315–1322.
33. R. W. Brown, E. M. Haacke, M. A. Martens, J. L. Patrick, and F. R. Zypman, *J. Magn. Reson.*, 1988, **80**(2), 225–248.
34. R. Dickenson, *J. Comput. Assist. Tomogr.*, 1986, **10**, 468.
35. H. P. Schwan and K. R. Foster, in *Proc. IEEE*, 1980, 104–113.
36. IEC, *IEC International standard, medical equipment—part 2: particular requirements for the safety of magnetic resonance equipment for medical diagnosis, 2nd revision*, International Electrotechnical Commission: Geneva, Switzerland, 2002.
37. G. J. Metzger, P. F. Van de Moortele, C. Akgun, C. J. Snyder, S. Moeller, J. Strupp, P. Andersen, D. Shrivastava, T. Vaughan, K. Ugurbil, and G. Adriany, *Magn. Reson. Med.*, 2010, **64**, 1625–1639.
38. C. J. Snyder, L. DelaBarre, P-F. Van De Moortele, A. L. Snyder, C. Akgun, J. Tian, G. Metzger, K. Ugurbil, and J. T. Vaughan, *ISMRM* , 2007, 164.

Chapter 31
TEM Coil Fields and SAR

Jinfeng Tian

Center for Magnetic Resonance Research, University of Minnesota, Minneapolis, MN 55455, USA

31.1 INTRODUCTION

High-frequency MRI scanners, with a main magnetic field of 3 T or above, have many advantages over their lower frequency counterparts, but they also demand more complicated and elaborate RF coil design to make use of these advantages. In short, at high frequency (i) RF coils are harder to tune to the required Larmor frequency, (ii) RF $\mathbf{B}_1$ fields at the Larmor frequency become less uniform, and (iii) RF losses, including coil ohmic losses, coil radiative losses, and the RF power losses within human tissues, increase with frequency. Without solutions to the limitations of RF loss and self-resonance for high-frequency coils, the benefits of high-frequency MRI will be lost.

To meet these high-frequency RF coil design challenges, Dr. Vaughan suggested in the early 1990s that lumped element circuit theory should be replaced by distributed circuit theory for high-frequency MRI RF coil design.[1] Therefore, transmission line coils were proposed for high-frequency MRI. These coils support transverse electromagnetic (TEM) or quasi-TEM modes, and are therefore called TEM coils. Since then, TEM coils have been the most widely used coils for MRI at or above 128 MHz.

A TEM coil comprises N-transmission line elements that can be coaxial elements, microstrip elements, or strip-line elements (Figure 31.1).[1,2] Each element is connected to a section of RF shielding to form an LC resonance loop through a section of end-ring. Depending on the coupling among the resonance loops, TEM coils can be classified as inductively coupled TEM coils and independently driven decoupled TEM coil. *Only inductively coupled TEM coils will be discussed, and by default, the term TEM coil will refer to coupled TEM coil in this chapter.*

One TEM resonance loop is an LC resonator: L is the inductance of the resonance loop and C is the capacitance in the resonance loop. As an LC resonant circuit, capacitance is usually varied to tune the resonant frequency to the required Larmor frequency. The TEM coaxial element comprises two sections of center conductors and one outer conductor, which form two variable cylinder capacitors. By adjusting the overlapping length, the cylinder capacitance can be varied to tune the element or the whole TEM coil to the required Larmor frequency. Additional variable lumped capacitors can also be applied between the TEM coaxial element and the shielding section to increase the frequency tuning range. For TEM coils with microstrip or strip-line elements, elements are usually terminated with lumped capacitors for frequency tuning.

RF Coils for MRI
Edited by J. Thomas Vaughan and John R. Griffiths

ISBN: 978-0-470-77076-4

The resonant theory of a TEM coil with N elements was developed in the mid-1990s.[1] In short, for a TEM coil with N symmetric elements, there are $(N/2 + 1)$ modes that can be seen in a tuned TEM resonator. Separation of modes depends on the strength of the mutual inductive coupling between the elements. When mutual inductance increases, mode separation increases. As the mutual inductive coupling between the tuning elements decreases, the modal resonances converge toward a single frequency, determined by one single element's self-inductance and capacitance. Of all the modes, mode 1 produces the most uniform and the most efficient RF $\mathbf{B}_1$ field. Mode 1 is therefore the most commonly used mode for TEM coils. In reality, to increase the image field of view (FOV) and to improve the transmission efficiency and reception sensitivity of the MRI RF coil, a TEM resonator is usually driven in quadrature at mode 1 frequency.

The resonant frequency of a TEM coil is largely determined by the inductance and the capacitance of its resonance loop, only slightly modified by the mutual inductance of the other elements. This brings additional advantages to a TEM coil: (i) compared with birdcage coils, a TEM coil of the same size has a much shorter resonance loop path and can thus resonate at much higher frequency, (ii) a TEM coil can be tuned such that alternating (odd and even) elements resonate at different frequencies to get MR information from multiple nuclei,[1] and (iii) the amplitude and phase of the elements can be modulated to effect corrective RF field shimming or volume selection.[3]

RF magnetic field $\mathbf{B}_1$ consists of two parts rotating in opposite directions: $\mathbf{B}_1{}^+$ for transmission and $\mathbf{B}_1{}^-$ for receipt. For quadrature-driven inductively coupled TEM coils, $\mathbf{B}_1{}^+$ and $\mathbf{B}_1{}^-$ are similar and symmetric. Descriptions of $\mathbf{B}_1{}^+$ are usually valid for $\mathbf{B}_1{}^-$. Therefore $\mathbf{B}_1$ is used to represent the general RF magnetic field in this chapter, though the RF magnetic field plots and values within tissues are based on $\mathbf{B}_1{}^+$.

In this chapter, RF magnetic field $\mathbf{B}_1$, together with the specific absorption rate (SAR) within the human body, for the inductively coupled TEM coil is introduced. At high frequency, the $\mathbf{B}_1$ fields have very different patterns in free space and within human tissues, owing to the short wave effects and $\mathbf{B}_1$ phase interactions at high frequency and within human tissues. At 300 MHz, the wavelength within the brain is only about 12 cm, which is less than half of a head-size coil diameter. Therefore, a $\mathbf{B}_1$ field within human tissues cannot be approximated by the DC Biot–Savart method, but rather a full wave time-dependent numerical method, such as finite difference time domain (FDTD), should be adopted. By default, $\mathbf{B}_1$ fields and SAR were numerically calculated by XFDTD (Remcom, Inc., State College, PA), a commercially available software employing FDTD (see Chapter 27).

Two different sizes of TEM coil are used for $\mathbf{B}_1$ and SAR calculations. The 16-rung head-size TEM coils are 20 cm long, with a coil diameter of 28.8 cm. The body-size TEM coil under test has the following dimensions: 24-rung, inductively coupled, 58-cm coil diameter, 33-cm coil length, 63-cm cavity diameter, and 100-cm cavity length. The head and body models loaded into TEM coils for $\mathbf{B}_1$ and SAR prediction are based on the male head and body from the National Library of Medicine Visual Human Project.

31.2 TEM $\mathbf{B}_1$ FIELD

31.2.1 TEM $\mathbf{B}_1$ with or without RF Mirror

Besides the basic structures in Figure 31.1, an RF mirror may be attached at the service end of the TEM coil to electrically increase coil length, and therefore improve $\mathbf{B}_1$ field homogeneity along the coil axis direction. This is demonstrated in Figure 31.2 with $\mathbf{B}_1$ fields of head-size TEM coils tuned to 170 MHz, with and without RF mirror. It is apparent that an RF mirror helps improve TEM $\mathbf{B}_1$ homogeneity within the top half coil, with or without a human head loaded in the TEM coils.

31.2.2 TEM $\mathbf{B}_1$ within Human Head Tissues

$\mathbf{B}_1$ fields, for the head-size TEM coils tuned to 170 and 300 MHz respectively, are provided in Figure 31.3. In contrast to what is observed in free space, the $\mathbf{B}_1$ field homogeneity drops within the brain as frequency goes higher. At 170 MHz, $\mathbf{B}_1$ strength in the brain periphery is down 35% from the center value, whereas this $\mathbf{B}_1$ drop is 52% at 300 MHz. An average of 17% less homogeneity is seen at 300 MHz than at 170 MHz in this comparison. Here, $\mathbf{B}_1$ homogeneity is defined as the $\mathbf{B}_1$ field drop within human tissues, divided by the

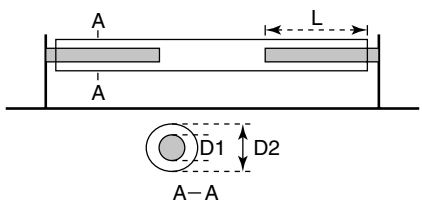

(a) TEM coaxial element

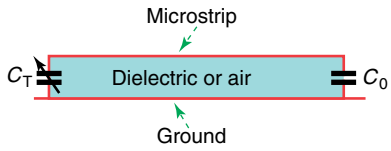

(b) TEM microstrip element

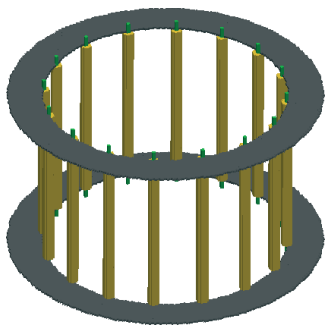

(c) TEM coil with RF shielding removed

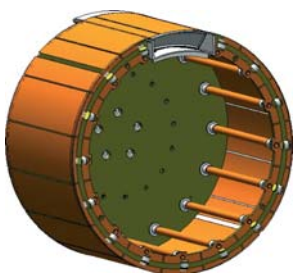

(d) A whole 15-rung coaxial TEM coil

Figure 31.1. TEM coil structures: (a) coaxial TEM element, (b) microstrip element, (c) a 16-rung coaxial TEM coil, in which RF shielding was removed to better demonstrate the inside structure, and (d) a whole 15-rung coaxial TEM coil.

maximum field. Varying coil dimensions, loading coils with head of a different size, or attaching an RF mirror may change field homogeneity.

In another calculation and MR image experiments, the $\mathbf{B}_1$ field homogeneity with a head-size TEM coil is 23.5% at 170 MHz and 42.5% at 300 MHz. The transmission $\mathbf{B}_1$ magnitude is 19.6 μT in the center of the brain and 14.1 μT per 1 kW RF power into the head-size TEM coil.[4]

By observing the $\mathbf{B}_1$ field along three central axes, it is obvious that the $\mathbf{B}_1$ homogeneity drops with frequency, resulting in a relatively higher $\mathbf{B}_1$ at the center and a weaker $\mathbf{B}_1$ at the periphery at higher frequency within the human brain. This is a $\mathbf{B}_1$ field phenomenon commonly seen in high-frequency human MRI images with coupled head coils or array coils driven as described in mode 1. Referred to as "dielectric resonance" in some earlier references, recent numerical modeling and image experiments show that this "center brightness" is a superposition of $\mathbf{B}_1$ fields from all rungs/channels of TEM coils.[5] At the brain center, the $\mathbf{B}_1$ fields from each of the rungs have relatively close phases and tend to add to each other, but at the periphery, the phases vary greatly and $\mathbf{B}_1$ fields near the certain rungs tend to cancel each other. These two kinds of RF field interactions due to relative phases are called *constructive and destructive phase interferences*. Compared with the central transverse slices, the field inhomogeneity in sagittal and coronal slices is even worse, owing to the much lower $\mathbf{B}_1$ fields within facial muscles (Figures 31.3 and 31.4).

Although the center brightness caused by destructive phase interference seriously reduces $\mathbf{B}_1$ field homogeneity and image FOV, efforts are being taken to take advantage of this to achieve images of uniform intensity by using a TEM coil for transmission and a separate surface coil array for receive. In contrast to the transmission $\mathbf{B}_1$ fields within a head-size TEM coil, surface coils generate stronger $\mathbf{B}_1$ fields in the periphery and weaker $\mathbf{B}_1$ fields in the center. When used in receive mode, surface coil arrays have more sensitivity at the periphery and less at the center. Since the final image intensity is a function of the transmission $\mathbf{B}_1$ of the TEM volume coil and the receive sensitivity of the surface array, more uniform image intensities are expected from the combination of TEM transmission and surface array receive.

31.2.3 TEM $\mathbf{B}_1$ Field within a Body Coil

A body coil is favored for homogeneous excitation, but body coil design is challenging at 3 T or above, since such a coil is required to produce a uniform and efficient transmission $\mathbf{B}_1$ field across an FOV

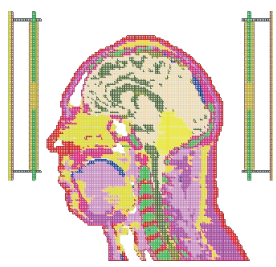

(a) TEM head coil without RF mirror

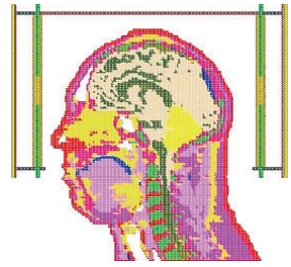

(b) TEM head coil with RF mirror

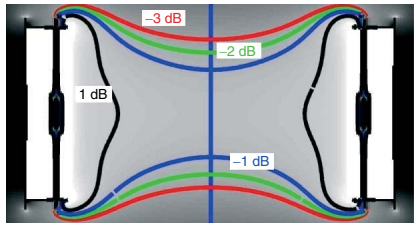

(c) Unloaded $\mathbf{B}_1$ field without RF mirror

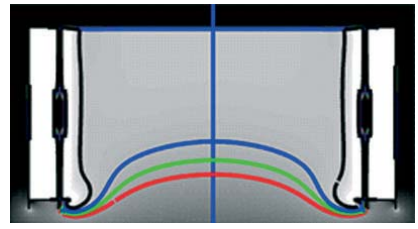

(d) Unloaded $\mathbf{B}_1$ field with RF mirror

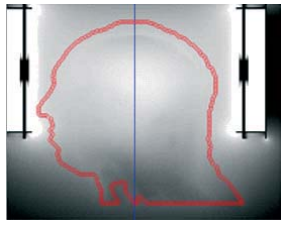

(e) Loaded $\mathbf{B}_1$ field without RF mirror

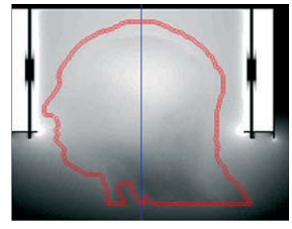

(f) Loaded $\mathbf{B}_1$ field with RF mirror

(g) Colorbar for both unloaded and loaded $\mathbf{B}_1$ field

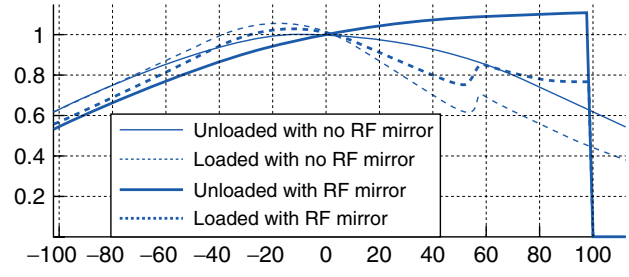

(h) Loaded $\mathbf{B}_1$ along coil axis with and without RF mirror

Figure 31.2. TEM $\mathbf{B}_1$ field at 170 MHz, without (a, c, e) and with (b, d, f) an RF mirror/end-cap at the service end. All $\mathbf{B}_1$ fields are normalized to center $\mathbf{B}_1$ and the same color scale (color-bar) is used (g). $\mathbf{B}_1$ field along the coil axis (vertical lines in c–f) shows that $\mathbf{B}_1$ field homogeneity within the top half of the coil or the human brain can be improved with an RF mirror.

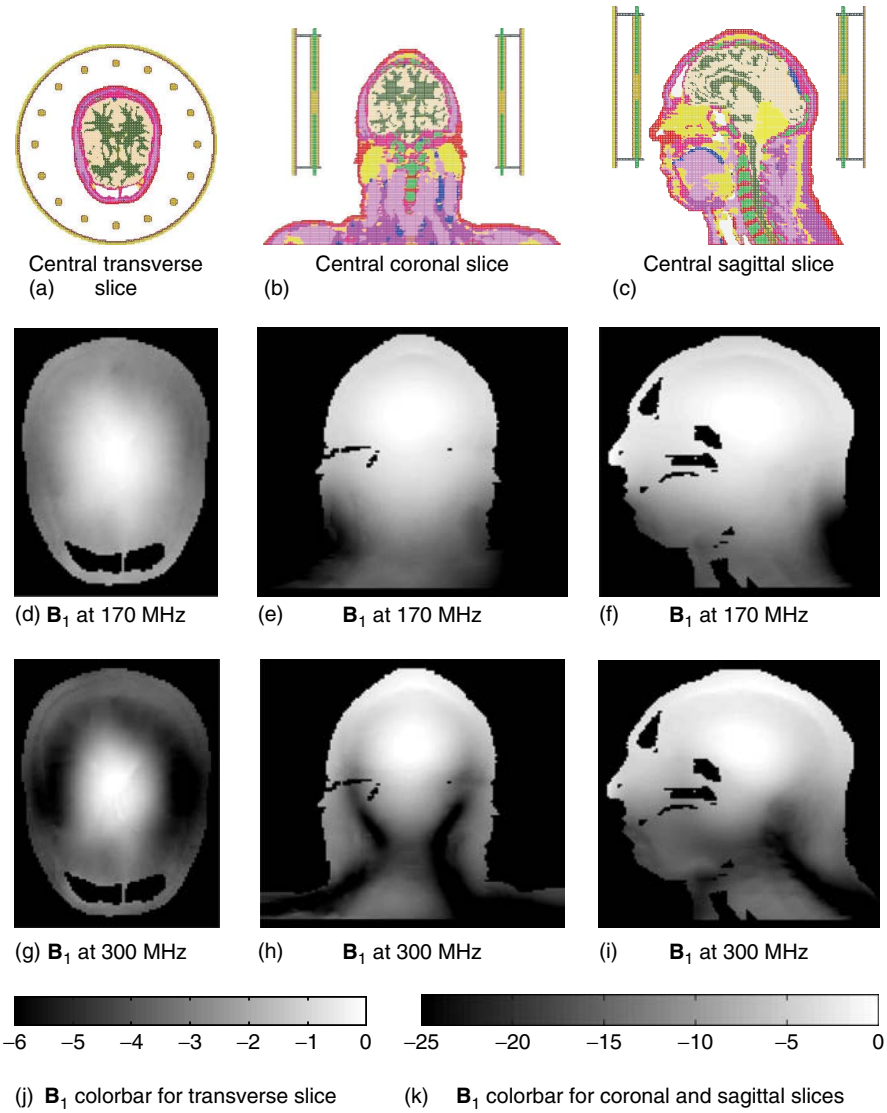

Figure 31.3. TEM $\mathbf{B}_1$ distribution within the human head on three central slices at 170 MHz (d–f) and 300 MHz (g–i).

comparable or bigger than the wavelength and the dimensions of a human being.

Birdcage coils are the most used body coils for low-frequency MRI, but their use in high-frequency MRI is limited by their resonance, field homogeneity, and efficiency, owing to the long resonant circuit and its end-ring effects.

The resonant frequency of a TEM coil is dependent on the resonant frequency of the independent line element, modified slightly by its reactive coupling with neighboring elements in the coil, and it can be tuned to resonate at a high MRI frequency. Bench tests with the body-size TEM coil show that it can resonate at up to 348 MHz.[2] TEM coils produce uniform $\mathbf{B}_1$ field efficiently without end-ring currents at the two coil ends (Figure 31.5). At 170 MHz, the unloaded central transverse $\mathbf{B}_1$ field is highly homogeneous and does not vary by more than 1 dB over a 46-cm-diameter FOV, and the RF field falls by less than 3 dB from its peak value at the coil center to

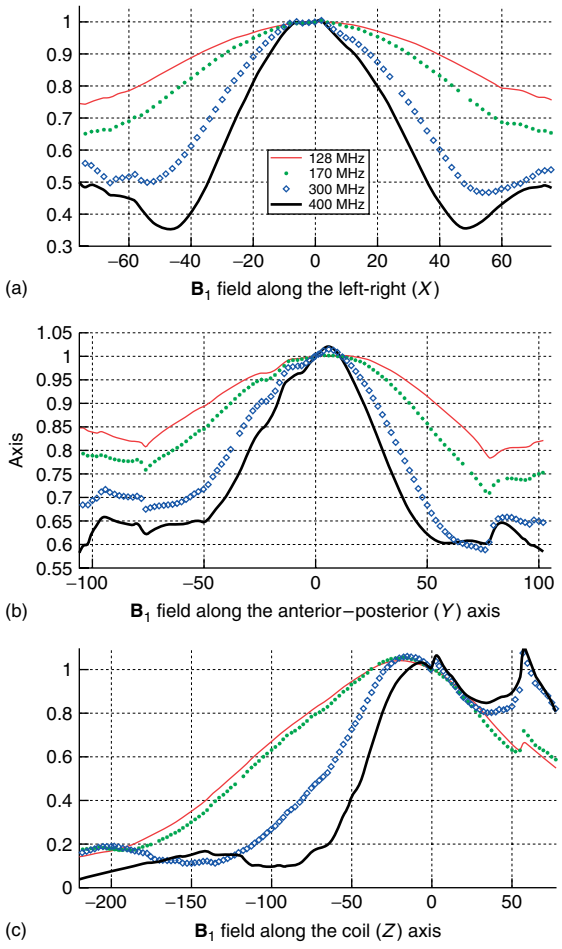

Figure 31.4. TEM $\mathbf{B}_1$ distribution over three central axes within human head at 128, 170, 300, and 400 MHz. Center brightness and $\mathbf{B}_1$ field homogeneity degradation with frequency are apparent.

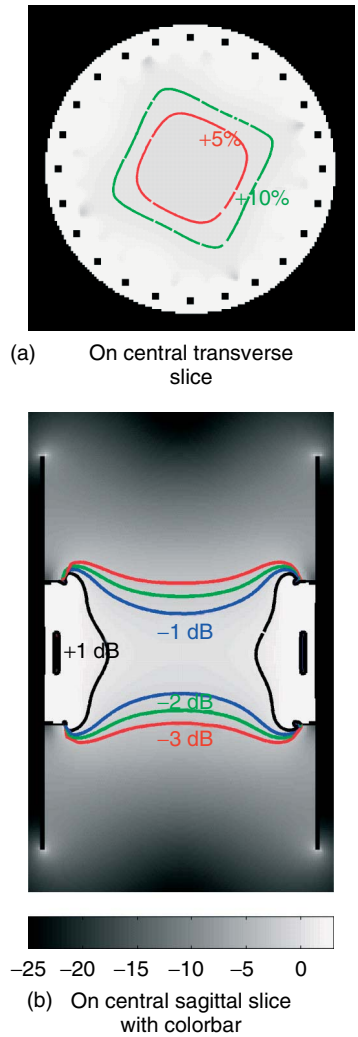

Figure 31.5. Body TEM $\mathbf{B}_1$ field distribution and its contour lines on central transverse (a) and sagittal slices (b) in air at 170 MHz. For an unloaded TEM coil, the $\mathbf{B}_1$ field is homogeneous within the coil.

the lowest value at the coil ends along the coil axis, suggesting that for a TEM coil, the axial 3-dB FOV is dependent on coil length. In agreement with the simulation, the test coil has a ±1.5-dB homogeneity over a cylindrical volume (36 cm long and 46 cm in diameter), but outside the coil there is a 7-dB drop over 10 cm. The slow field drop within the coil and the relatively steep drop outside it indicate both high field homogeneity and high transmission efficiency.[2]

The RF field has been modeled by the FDTD method for the body coil loaded with human body at 128 MHz, 170 MHz, and 300 MHz (Figure 31.6). In general, the $\mathbf{B}_1$ field homogeneities within the human body look acceptable at 128 and 170 MHz for MR images with most parts of the human body. For example, at 170 MHz, the RF field homogeneity and MR images are still good within the head and breast, which agrees with the spin-echo images, but $\mathbf{B}_1$ artifacts are evident within the human heart[6]; RF shimming could be used as a solution. Owing to RF power limits and the heavy loading

Table 31.1. RF power requirements for whole body imaging at 4 T

1-ms inversion block pulse	Weight/ kg	Power/ kW	Flip angle
Abdomen = 10.9 kW for 95 kg human	60	3.1	120
	75	3.1	114
	95	3.0	96
Thorax = 6.7 kW for 95 kg human	60	3.1	150
	75	3.1	135
	95	3.0	120
Head = 6.7 kW For 95 kg human	60	3.1	178
	75	3.1	169
	95	3.0	139

of the human body, RF power requirements for spin-echo imaging were estimated and reproduced in Table 31.1.[2]

Destructive interference patterns are shown to increase with frequency and create high non-uniformities in the $\mathbf{B}_1$ field within the body at 300 MHz. In the body, the $\mathbf{B}_1$ spans 40 dB, with the lowest level regions running longitudinally in the body center and the highest $\mathbf{B}_1$ magnitude in the periphery of the body. The numerical modeling predicted significant RF artifacts in at least one sharp line running longitudinally through the body, primarily because of destructive interference of the short (12 cm) wavelengths in the high water content tissue dielectrics at 300 MHz. The central black lines of RF destructive interference in the figure were also observed in the body images.[6,7] Interestingly, the head, which is outside of the coil, experiences some of the highest $\mathbf{B}_1$ values due to the traveling waves. The severe $\mathbf{B}_1$ artifacts within the human body at 300 MHz suggest that conventional MRI methods employing a homogeneous, circularly polarized body coil with quadrature excitation do not produce uniform enough RF fields within the area of interest for 7 T proton imaging.

31.3 TEM SAR WITHIN HUMAN HEAD AND BODY TISSUES

In the assessment of SAR levels for MRI, numerical simulation has been an important option for evaluating the maximum 1-g-averaged and 10-g-averaged local SAR within human head and torso tissues.

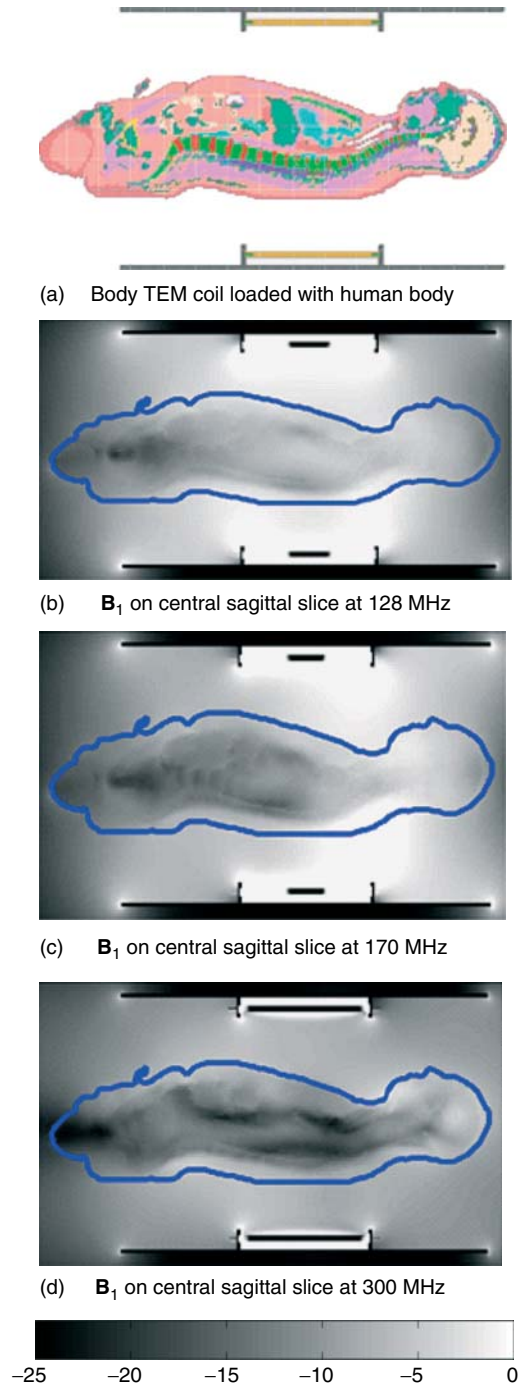

Figure 31.6. Body TEM $\mathbf{B}_1$ on the central sagittal slice at 128 MHz (b), 170 MHz (c), and 300 MHz (d). The body-size TEM coil is loaded with the human body (a).

Table 31.2. Ratio of maximum local to whole head average SAR for a human head model in the head TEM coil at 170 and 300 MHz, compared to the regulatory limits

Frequency	SAR_{1g}/SAR_w	SAR_{10g}/SAR_w
170	6.7	4.6
300	8.3	6.4
FDA limit	2.7	—
IEC limit	—	3.12

To guarantee patient safety, the US Food and Drug Administration (FDA) and the International Electro-technical Commission (IEC) have published local maximum 1 gram SAR (SAR_{1g}) guidance, maximum SAR requirements over any 10 gram volume (SAR_{10g}), and global SAR limits averaged (SAR_W) over the whole head or body.[8,9]

Ratios of calculated maximum SAR_{1g} and SAR_{10g} to SAR_W are compared with ratios in the regulatory limits, and results are listed in Table 31.2. For this simulation setup, the calculated ratios are much higher than those in the regulatory limits, suggesting that the local maximum 1 g and 10 g SAR limits would be reached first, and that tighter SAR_W limits are therefore required to guarantee patient or subject RF safety.[10] Since SAR_W can be easily monitored during MRI scans, maximum RF power without exceeding SAR_{1g} and SAR_{10g} limits can be calculated with these ratios. At 300 MHz, the maximum 1 g SAR within the head occurs within CSF and blood tissues in the top of the head, right below the skull, with a value of 24.9 W kg^{-1} for a head SAR_W of 3.0 W kg^{-1} Figure 31.7.

More RF energy deposits within brain or top head as frequency goes higher, i.e., brain SAR_{1g} increases with frequency for same RF power deposition. From 170 to 300 MHz, the averaged SAR_{1g} over the central transverse slice goes from 0.18 W kg^{-1} to 0.2572 W kg^{-1} for a total of 1 W RF power deposition

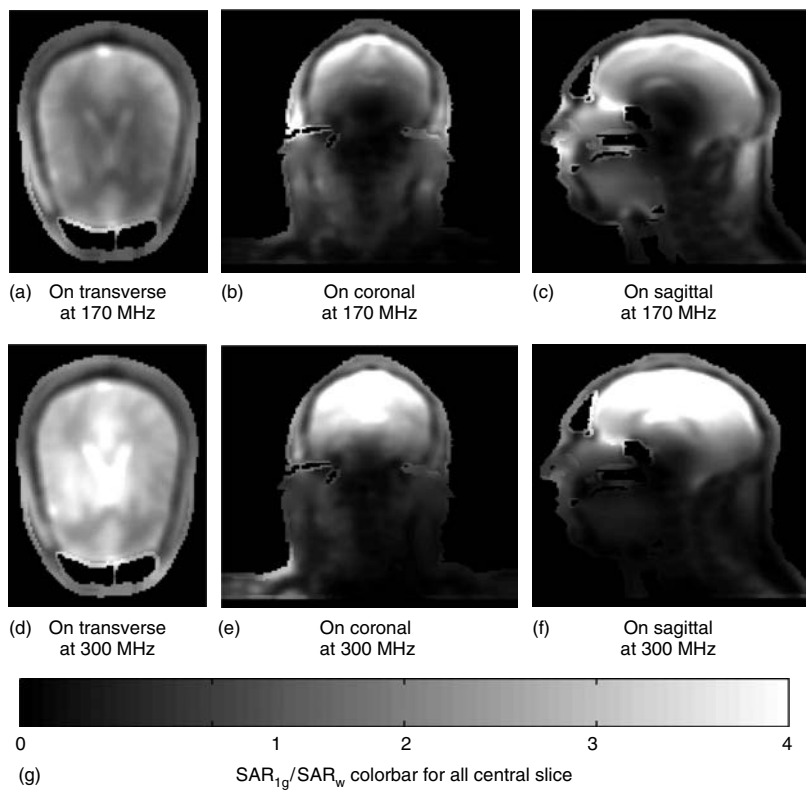

Figure 31.7. TEM SAR_{1g}/SAR_w ratio distributions within the human head on the three central slices at 170 MHz (a–c) and 300 MHz (d–f).

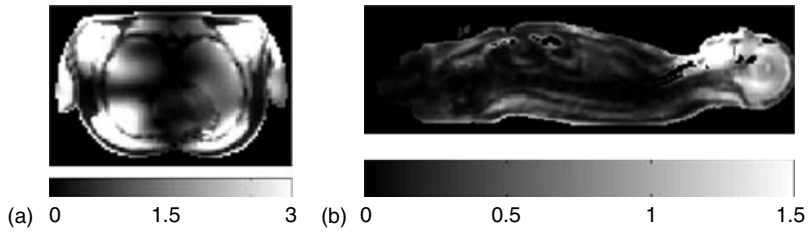

Figure 31.8. TEM SAR_{1g}/SAR_w on central sagittal (a) and transverse (b) planes for a body-size TEM coil tuned to 300 MHz. Note that different decibel gray scales are applied to the two planes.

within the human head. This is a 43% jump for same RF power deposition within human tissues. In reality, more RF energy at higher frequency is required at 300 MHz because of the higher RF losses. For example, to achieve an averaged $\mathbf{B}_1$ magnitude of 1 μT on the central transverse slice, the averaged SAR_{1g} in the same slice is 0.4272 W kg^{-1} at 170 MHz and 1.2156 W kg^{-1} at 300 MHz, resulting in a 185% increase.

Dr. Collins performed SAR calculations for a head-size birdcage coil at 64 MHz and a head-size TEM coil at 300 MHz. For the birdcage coils at 64 MHz, a maximum SAR_{1g} of 16.2 W kg^{-1} within the *head* was seen within the skin and facial muscles, and a maximum SAR_{1g} of 13.7 W kg^{-1} within the *brain* was located in the superior cerebrum and superior sagittal sinus. The TEM coil at 300 MHz has a maximum 16.1 W kg^{-1} SAR_{1g} in the muscle tissue in the masticator space. The TEM coil at 300 MHz has less local maximum SAR than the birdcage coil at 64 MHz.[11]

The SAR was also estimated by the FDTD method for a human body-loaded coil at 7 T.[7] The SAR contours span a 50 dB range, with maximum SAR experienced in the tissues nearest to the drive elements of the coil, and the lowest SAR values found near the center-line of the body. To better compare with the regulatory limits, the ratio of SAR_{1g}/SAR_w in the sagittal body plane is presented (Figure 31.8).

During 7-T MR body imaging with the body-size TEM coil, the RF power used to acquire the images was estimated as 996 W peak power, which, when imaging parameters were taken into consideration, resulted in an average body SAR of less than the 1.0 W kg^{-1} FDA guideline for human torso imaging with most adults.[6]

SAR is determined by multiple factors, including frequency, head or body size, coil dimension, the human body loading position in the coil, and the biological conditions of the patient being imaged.[12] To guarantee patient safety, SAR should be revisited when any of the above factors varies significantly.

Correlations between SAR and $\mathbf{B}_1$ fields are observed for both head and body TEM coils. In general, SAR is usually high wherever a high $\mathbf{B}_1$ field exists. For example, the top head, including brain and the CSF and blood above the brain, has the highest $\mathbf{B}_1$ and the highest SAR for head TEM coils. For body TEM coils, the area that has both high $\mathbf{B}_1$ and SAR is the body periphery close to the drive elements. Caution should be taken when a relatively high $\mathbf{B}_1$ is seen in an area of MR images.

ACKNOWLEDGMENTS

NIH-R01 EB000895, NIH-R01 EB006835, NIH-R01 EB007327, NIH-P41 RR08079

REFERENCES

1. J. T. Vaughan, H. P. Hetherington, J. O. Otu, W. Pan Jullie, and G. M. Pohost, *Magn. Reson. Med.*, 1994, **32**, 206–218.
2. J. T. Vaughan, G. Adriany, C. J. Snyder, J. Tian, T. Thiel, L. Bolinger, H. Liu, L. Delabarre, and K. Ugruibil, *Reson. Med.*, 2004, **52**, 851–859.
3. J. T. Vaughan, C. Snyder, G. Adriany, L. Bolinger, H. Liu, A. Stolper, and K. Ugruibil. In *Proceedings of the 11th Annual Meeting of ISMRM* , Toronto, Canada, 2003, 425.
4. J. T. Vaughan, M. Garwood, C. M. Collins, W. Liu, L. Delabarre, G. Adriany, P. Andersen, H. Merkel, R. Goebel, M. B. Smith, and K. Urgurbil, *Magn. Reson. Med.*, 2001, **46**, 24–30.
5. P. F. V. D. Moortele, C. Akgun, G. Adriany, S. Moeller, J. Ritter, C. M. Collins, M. B. Smith, J. T.

Vaughan, and K. Ugurbil, *Magn. Reson. Med.*, 2005, **54**, 1503–1518.

6. J. T. Vaughan, C. Snyder, L. Delabarre, L. Bolinger, J. Tian, P. Andersen, J. Strupp, G. Adriany, and K. Ugruibil, *Proc. Intl. Soc. Mag. Reson. Med.*, 2006, **14**, 213.
7. J. T. Vaughan, C. Snyder, L. Delabarre, J. B. L. Patric, J. Tian, L. Bolinger, G. Adriany, P. Andersen, J. Strupp, and K. Ugruibil, *Magn. Reson. Med.*, 2009, **61**, 244–248.
8. International Electrotechnical Commission. *International standard, medical equipement-part 2: particular requirements for the safety of magnetic resonance equipment for medical diagnosis*, 2nd revision, International Electrotechnical Commission 601-2-33: Geneva; 2002, pp. 29–31.
9. U.S. Department of Health and Human Services, Food and Drug Administration Document 793. Criteria for Significant Risk Investigations of Magnetic Resonance Diagnostic Devices, July 14, 2003.
10. Z. Wang, J. Lin, W. Mao, W. Liu, M. B. Smith, and C. M. Collins, *J. Magn. Reson. Imaging*, 2007, **26**, 437–441.
11. C. M. Collins, W. Liu, J. Wang, R. Gruetter, J. T. Vaughan, K. Urguibil, and M. B. Smith, *J. Magn. Reson. Imaging*, 2004, **19**, 650–656.
12. J. Tian, C. J. Snyder, L. Delabarre, C. Akgun, W. Liu, C. M. Collins, A. Gopinath, and J. T. Vaugan, *Proc. Intl. Soc. Mag. Reson. Med.*, 2007, **15**, 10–11.

PART G
RF Safety

Chapter 32
RF Device Safety and Compatibility

John Nyenhuis

School of Electrical and Computer Engineering, Purdue University, West Lafayette, IN 47907, USA

32.1 INTRODUCTION

While it is the magnetic component of the RF field that produces the desired torque on the nuclei in NMR and MRI, the accompanying electric field is the source of bioeffects. The immediate bioeffects of electromagnetic fields are, principally, the stimulation of nerves and tissue heating.[1] Tissue heating is the dominant bioeffect for frequencies greater than 100 kHz. Thus, safety considerations in NMR and MRI are focused on limiting in vivo temperature rises to safe limits. This chapter deals with power deposited in the body due to interaction with the RF coil. This results in core and local temperature elevation. Potential bioeffects due to long-term exposure to power deposition in the body are not addressed.

RF Coils for MRI
Edited by J. Thomas Vaughan and John R. Griffiths

ISBN: 978-0-470-77076-4

In this chapter, MRI/MR will mean both NMR (which generally refers to *laboratory instrumentation*) and MRI (which generally refers to *medical imaging equipment*).

Safety considerations for MR coils may be broadly categorized as follows:

- Safety of the electronic instrumentation that powers the coils: Instantaneous and average power is applied to an MR coil. It is essential that MR workers and patients do not come in contact with the high voltages in the amplifier electronics, the cabling, and the metal of the coil. For instance, the Siemens Verio 3 T produces a peak RF power of 35 kW.[2] This power presents 1333 V rms across a 50 Ω load. Working with this level of power requires appropriate training, protection equipment, and caution. Further discussion on this topic is beyond the scope of this article.
- Power deposition in the body of the MR workers and patients: This thermal power comes from the electric fields that are induced in the patient by the time-varying RF magnetic field and capacitively coupled by the high voltages of the coil. The local power deposition is quantified by the specific absorption rate (SAR, with typical units of $W\,kg^{-1}$). The local SAR is strongly influenced by the different electrical properties of tissues in the body and thus there has been concern over "hot spots" in critical tissues such as the eyes. A comprehensive review of RF-induced heating during MR procedures, with an emphasis on clinical and physiological issues, has been presented by Shellock.[3]

- Localized concentration of SAR due to the interaction of metallic structures with the RF electric fields: The presence of an implant alters the distribution of the electric field in its vicinity. Significant temperature elevation near the electrodes has been measured during in vitro tests on pacemaker and neurostimulator leads. Significant attention has recently been devoted to measurement and computational methods for assessment of implant heating. External conductors, such as guidewires and electrodes connected to conductors may lead to burns where they come into contact with the patient.

In this chapter, we provide background information on the safety of MR coils and present results of our recent calculations relevant to MR safety. Regulatory requirements for MR safety are summarized. SAR distributions in the patient without implants are presented. High-resolution (1 mm) calculations of local SAR in the eyes and the heart are shown. Interactions of implants with the electric field in the patient are discussed and calculations related to patient safety are presented. We provide an overview of test methods for in vitro measurements of implant heating by the RF magnetic field in MR. An introduction is given on the calculation of the in vivo temperature rise and safe limits for temperature elevation are calculated using CEM 43 analysis.

32.2 SAFETY STANDARDS FOR SAR IN MRI

Safety and standards organizations have developed limits on SAR for safe MRI. The National Radiological Protection Board has determined that a whole-body temperature rise of 1°C can be safely withstood by healthy people.[4] Experiments and calculations have projected that a whole-body SAR of approximately $4\,\mathrm{W\,kg^{-1}}$ would produce this temperature elevation. The International Commission of Non-Ionizing Radiation Protection (ICNIRP) has published guidelines[5] for limits on whole-body average SAR for occupational and general public exposure. For occupational exposure, the limits are $0.4\,\mathrm{W\,kg^{-1}}$ for whole-body average SAR, $10\,\mathrm{W\,kg^{-1}}$ for localized SAR in the head and trunk, and $20\,\mathrm{W\,kg^{-1}}$ for localized SAR in the limbs. The corresponding limits for general public exposure are 0.08, 2, and $4\,\mathrm{W\,kg^{-1}}$, respectively. The SAR values are to be averaged for 6 min and the local SAR is evaluated in any 10 g of contiguous tissue.

In 2005, ICNIRP published a statement on the protection of patients during MRI.[6] SAR levels for whole-body, partial-body SAR, and local SAR were presented. These levels are for a running average of 6 min. The objective of the SAR levels in normal mode is to limit the core temperature rise to 0.5 °C and to limit temperatures in the head, trunk, and extremities to 38, 39, and 40 °C, respectively. The temperature limits are the same for controlled mode, but a core rise of 1 °C is permitted.

Since the original ICNIRP statement, there have been numerous scientific studies on bioeffects of high-frequency electromagnetic fields. Numerical modeling has yielded significant additional information on current and SAR distribution in the body, including elevation of local SAR due to the resonances in the body. Nonetheless, in a recent follow-up statement,[7] ICNIRP concluded as follows:

However, it is the opinion of ICNIRP that the scientific literature published since the 1998 guidelines has provided no evidence of any adverse effects below the basic restrictions and does not necessitate an immediate revision of its guidance on limiting exposure to high frequency electromagnetic fields.

The standard IEC 60601-2-33[8] lists the SAR limits for the different operating modes of the MR system in Table 105. A summary of these limits for volume transmit coils is presented in Table 32.1. The normal mode is the default mode of the MR system in which the system outputs will not cause physiological stress. The first-level controlled mode requires operator approval prior to the start of the scan. There is also the second-level controlled mode with higher SAR limits; this level requires the approval of a review board.

The partial-body specific absorption rate (PB-SAR) limit is calculated as

$$\mathrm{PB-SAR} = 10\ \mathrm{W\ kg^{-1}} - K \times (\text{exposed patient mass}/\text{patient mass}) \tag{32.1}$$

where $K = 8\ \mathrm{W\ kg^{-1}}$ in normal mode and $6\,\mathrm{W\,kg^{-1}}$ in first-level controlled mode. The exposed patient mass is the mass of the patient that is within the effective volume of the RF transmit coil. The effective volume is defined to be the volume of a homogeneous

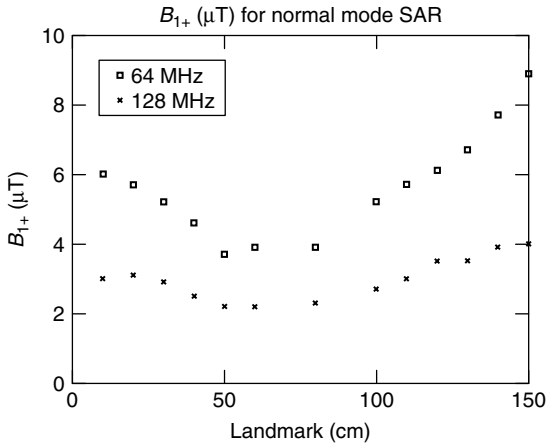

Figure 32.1. Calculated RF magnetic field B_1^+ in the rotating frame for the Hugo model at IEC normal operating mode limits. The coils are whole-body cylindrical with circular polarization. Landmark is the distance from the top of the head to the coil center. B_1^+ is averaged over the slice at landmark.

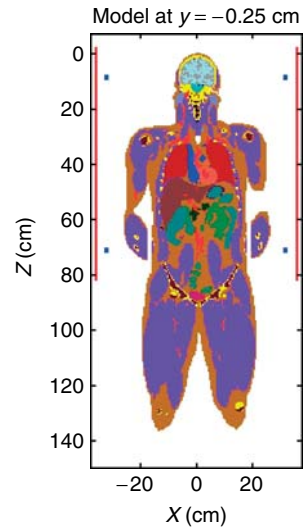

Figure 32.2. Hugo model in the MRI coil with landmark (center of coil) being 40 cm below the top of the head. The red lines on the side represent the shield of the RF coil, which extends about 10 cm beyond either end of the coil.

material that absorbs less than 95% of the total RF power.

IEC 60601-2-33 specifies the local SAR to be averaged over a mass of 10 g. For both normal and first-level controlled operating mode, the local SAR limits are 10 W kg^{-1} in the head and trunk and 20 W kg^{-1} in the extremities.

Figure 32.1 shows a calculation of the RF magnetic field B_1^+ in the rotating frame versus position in the coil for the Hugo model at IEC normal operating mode limits. (The Hugo model is derived from the Visible Human Project at the National Library of Medicine and has frequently been used in calculations of SAR. The model is shown in Figure 32.2.)

The B_1^+ limits in Figure 32.1 were calculated as the values that meet the head, whole-body, and partial-body limits in Table 32.1. For landmarks (distances between top of head and center of RF coil) 10 and 20 cm below the head, B_1^+ is set by the head SAR restriction. For landmarks 30–140 cm, B_1^+ is set by the whole-body SAR. At the landmark of 150 cm, which is in the center of the lower leg, the partial-body and whole-body SAR restrictions set similar values for B_1^+. For landmarks beyond 150 cm, such as for an ankle scan, partial-body SAR will presumably set the B_1^+ limit. It is not clear, however, whether current MR systems exceed the maximal B_1^+ values of 9 μT at 64 MHz and 4 μT at 128 MHz in Figure 32.1.

The American College of Radiology (ACR) has published guidance for safe MR practices.[9] Guidance pertaining to thermal issues with RF include (i) removal of electrically conductive materials that are not needed, prior to the scan; (ii) placing of thermal insulation (including air, pads etc.) between the patient and conductive materials; (iii) where appropriate, avoiding contact between the patient and the inner bore of the MR system; and (iv) avoiding loops made by the patient's arms and legs. In the document,

Table 32.1. IEC 60601-2-33 limits on SAR for volume transmit coil. These limits are valid for environmental temperatures of 24 °C and below

Operating mode	Whole-body SAR (W/kg)	Partial-body SAR (W/kg)	Head SAR (W/kg)
Normal	2	2–10	3.2
First-level controlled	4	4–10	3.2

ACR describes precautions for patients with skin staples, superficial metallic sutures, and dark tattoos. Long conductive wires and leads are identified as a potential source of burns, with temperatures at the tips of wires or leads potentially reaching 90 °C in a few seconds. A brief discussion is made of thermal hazards associated with implants, which depend on several factors.

32.3 CALCULATION OF SAR IN THE BODY

The SAR, in units of $W\,kg^{-1}$, at some location inside the body is calculated as

$$\mathrm{SAR} = \frac{\sigma E^2}{\rho} \tag{32.2}$$

where σ is the electrical conductivity, E is the rms electric field in $V\,m^{-1}$, and ρ is the mass density in $W\,kg^{-1}$.

For the patient in an MRI coil, the SAR is usually calculated with the finite difference time domain (FDTD) method, in which Maxwell's equations are numerically integrated in time. Figure 32.2 shows the Hugo model inside the MRI coil at a landmark of 40 cm. The hands have been removed to reflect the clinical recommendation[9] to avoid loops that may result in RF burns.

Figure 32.3 shows the calculated RF magnetic field intensity B_1^+ with the patient in the coil. (The calculations in this chapter were made with custom programs developed by the author and his collaborators. Computer resources of the Purdue University Rosen Center for Advanced Computing were used for several of the calculations.) The field is relatively uniform over the cross section of the patient, though there is some nonuniformity as a consequence of the currents induced in the patient. Figure 32.3 also shows the electric field pattern inside and outside the patient. It is worth noting that the electric field intensity is greatest outside the patient, as the external electric field is screened by the dielectric properties of the body.

The electric field $\mathbf{E}$ may, in general, be written as

$$\mathbf{E} = -\frac{\partial \mathbf{A}}{\partial t} - \nabla \Phi \tag{32.3}$$

where $\mathbf{A}$ is the magnetic vector potential and Φ is the electrostatic potential. The sources of $\mathbf{A}$ are the current in the coil and the induced eddy currents in the body. The sources of Φ are electric charge on the metal of the coil, electric charge on the surface of the patient, and electric charge within the patient at the interfaces between tissues with different dielectric

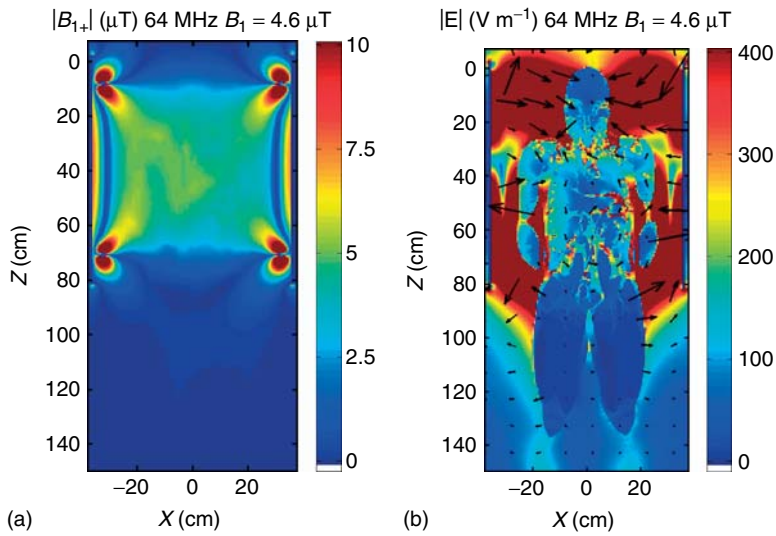

Figure 32.3. Map of B_1^+ (a) and electric field pattern (b) at 64 MHz, landmark of 40 cm, and whole-body average SAR of 2 W kg^{-1}. The arrows indicate the direction and relative magnitude of the electric field. The coil is high pass and rotation direction is clockwise (CW).

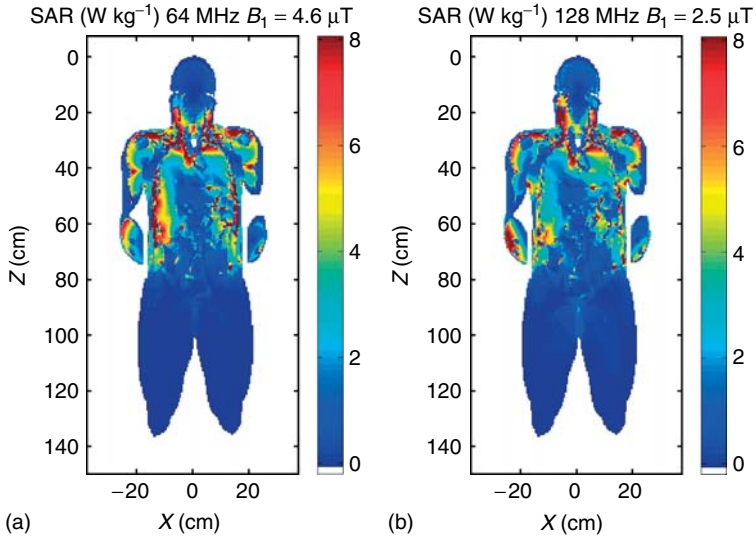

Figure 32.4. SAR distributions in Hugo at 64 MHz (a) and 128 MHz (b) at a landmark of 40 cm, CW rotation, and B_1^+ at the value that produces a whole-body SAR of 2 W kg^{-1}. The coronal section is through the middle of the body.

properties. The charge distribution on the coil is different for different coil types, i.e., high pass versus low pass versus band pass. However, due to the screening effects of the body, the internal electric fields is mostly sourced by $\partial \mathbf{A}/\partial t$. The charges on the coil, however, contribute to the internal electric field. There is the potential for patient burns,[10] especially if there is RF current through the relatively poorly conducting skin. Hence, it has been recommended[9,11] that at least a centimeter of foam or similar insulating material is placed between the patient's skin and the RF transmit coil. The foam, with its relatively small dielectric constant, should form a significant impedance that limits the capacitive current between the patient and the coil.

Figure 32.4 shows a calculated SAR in the patient at 64 MHz and 128 MHz. Features of the SAR in Figure 32.4 that apply in general are the following: (i) the greatest SAR tends to be concentrated at the periphery of the body and (ii) there are local "hot spots" of SAR concentration due to different electrical conductivity of the various tissues. The SAR patterns in Figure 32.4 are calculated at an RF intensity that produces a whole-body average SAR of 2 W kg^{-1}. With this normalization, the intensity and distributions of the two SAR patterns for 64 MHz and 128 MHz in Figure 32.4 are similar, although there are some differences in the details of the hot spots.

The SAR patterns in Figure 32.4 are calculated for a model with a 5-mm voxel resolution. For evaluating the global SAR parameters such as that presented in Table 32.1, this resolution has been found to be adequate.[12] Arbitrarily fine resolution is possible in FDTD, but the computer time to model a uniformly meshed volume scales as the inverse fourth power of the cell size. Thus, assuming the computer memory capacity does not become the limiting factor, a model with 1-mm resolution requires a factor of 625 more computer time than does a 5-mm model. One approach to accomplish a finer resolution is to use the Hugyen's box approach, which, for this application, involved two FDTD simulations.

- FDTD simulation 1: The electric (E) and magnetic (H) fields are calculated with Hugo model and MRI coil of relatively coarse resolution equal to 5 mm.
- FDTD simulation 2: A rectangular portion (Huygen's box) of the 1-mm Hugo model is selected. The electric and magnetic fields from the whole-body simulation set the boundary conditions on the box. These boundary conditions are updated for each time step of the FDTD simulation.

The boundary conditions for E and H on the surface of the Huygen's box have been presented by

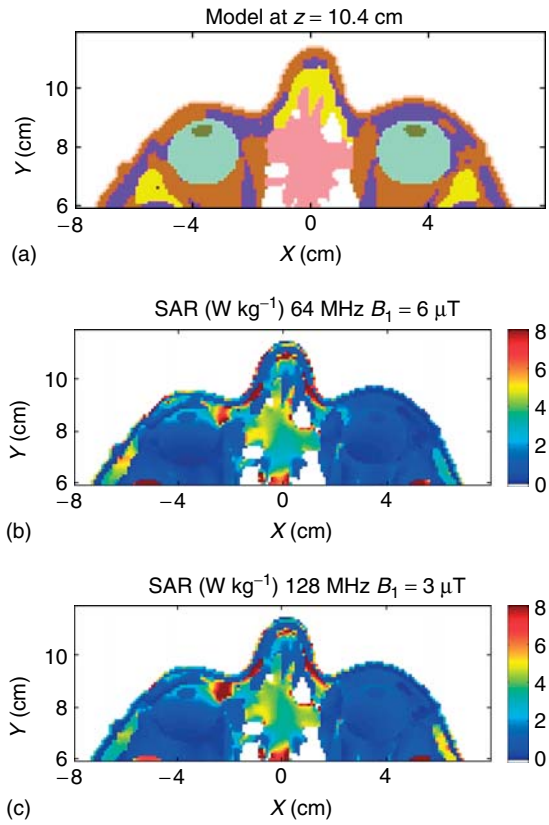

Figure 32.5. (a) Axial section through the eyes of the Hugo model at 1-mm resolution with the SAR distribution for (b) 64 MHz and (c) 128 MHz). The head-average SAR is 3.2. W kg^{-1} and the landmark is 10 cm.

Merewether *et al*.[13] Neufeld *et al*. recently described the use of this method to calculate RF-induced temperature rises model implants in the form of an insulated wire and a spiral.[14]

We present two examples of the assessment of local SAR at 1-mm resolution. In Figure 32.5, the SAR distribution in the eyes of the human model is calculated. At a head-average SAR equal to the IEC limit of 3.2 W kg^{-1}, the local SAR in the eyes is generally less than 2 W kg^{-1}. There is a region of greater SAR in the right eye, which may be a consequence of current from two adjacent muscles flowing through the eye. A calculation with a finer resolution model would yield more detail. The low SAR values calculated here are consistent with the modest temperature rises of the cornea that were measured in clinical investigations with head and body transmit MR coils.[15]

In Figure 32.6, the electric field intensity is shown for a coronal section of the heart. The greatest intensity occurs at the lower part of the ventricle. When scaled to the same whole body SAR of 2 W/kg, the electric field intensity is similar for 64 MHz and 128 MHz.

32.4 SAR FOR OTHER COIL TYPES

The SAR calculations presented above are specific for a circularly polarized whole-body coil, in part, because this type of coil is used in most clinical MR systems. The FDTD method can be used to calculate the SAR for essentially any MRI coil. The crucial step is setting up the coil model in the program and achieving the correct current distribution.

The SAR distribution for a birdcage coil operating in linear mode would depend on the direction of the incident RF field. Since a linearly polarized RF wave is equivalent to two oppositely circulating polarizing waves, only one of which is effective for MRI, the average SAR for the linear coil will be approximately twice that for a quadrature coil.

Wang *et al*.[16] calculated the average SAR and the 1 and 10 g local SAR in a head coil. The ratio of the local SAR to the average SAR was greater than the ratio in the regulatory limits. The ratio of 10 g average SAR to head-average SAR ranged from 3.4 to 5.0 over a frequency range of 64–400 MHz. This compares to the ratio of 3.12 in the IEC standard, for which the head-average SAR limit is 3.2 W kg^{-1} and the local SAR limit is 10 W kg^{-1}. For the body coil, the ratio of 10 g local SAR to whole-body SAR with two subjects and frequencies of 64 and 128 MHz ranged from 10 to 13, compared to the ratio of 5 in the IEC limit. Thus regulatory limits on local SAR limit would be exceeded before limits on body-average or head-average SAR are reached.

Figure 32.7 shows SAR patterns in the coronal plane for the Hugo model in a head coil. The head-average SAR is 3.2 W kg^{-1} for the calculations at 64 and 128 MHz.

In the birdcage resonator, the currents in the arms are of equal magnitude and have a constant phase difference between each of the arms. In a transmit array coil,[17] the magnitude and phase of the current in each conductor is variable. This flexibility allows a reduction of B_1^+ inhomogeneity that is associated

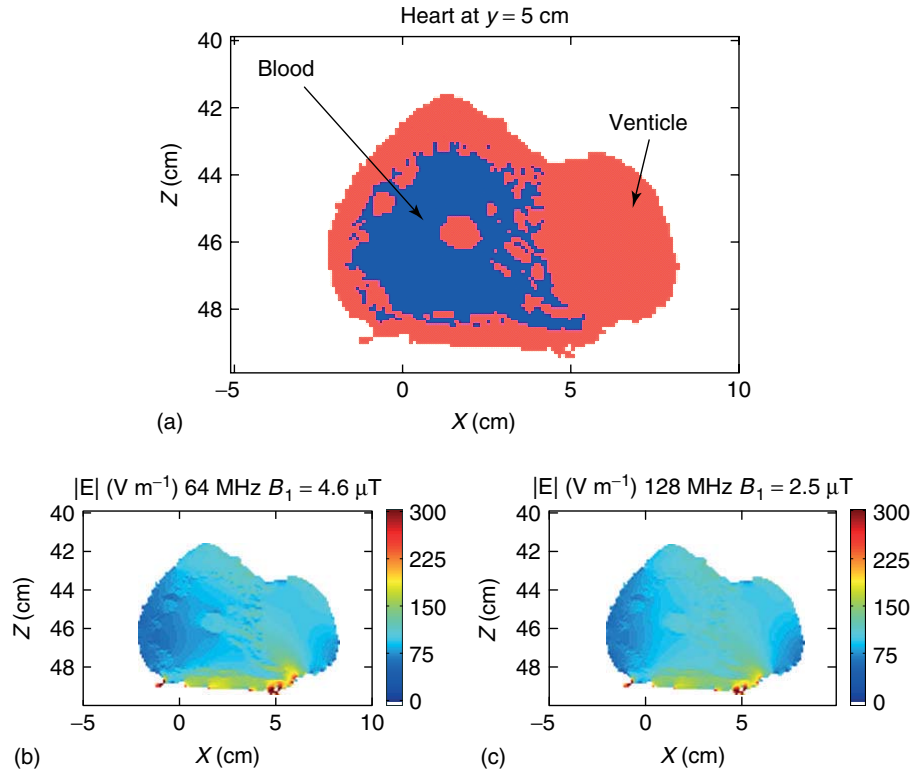

Figure 32.6. (a) Coronal slice of the heart of the Hugo model showing the ventricle and venous blood. Plots (b) and (c) show the electric field intensity on the slice for 64 MHz (b) and 128 MHz (c). The whole-body SAR is 2 W kg^{-1} and the landmark is 40 cm.

with higher frequencies. The change in B_1^+ also causes a change in the SAR distribution. Modeling will, in general, be required to ensure that regulatory limits on SAR are not exceeded.

Ibrahim *et al*. calculated SAR for an 8-T transverse electromagnetic (TEM) head coil with a 2-mm resolution human head model.[18] SAR was found to be affected by the local conditions in the coil, such as coil geometry and the number of drive points, as well as the head to coil interaction.

A rather different method for applying B_1 at high field has recently been described.[19] The patient is placed inside a conducting bore. An antenna at the end of the core launches traveling waves, i.e., the MR bore becomes a waveguide. The magnetic part of the wave excites the nuclear magnetization. Magnetic gradient fields are applied and an antenna receives the signal from the precessing protons. An image of a human leg obtained with this method was superior to the one obtained with a traditional resonant probe. The same thermal safety considerations discussed earlier would apply to traveling wave coils. Presumably, FDTD or similar modeling could be used to determine the SAR distributions. It is noted that a traveling wave MRI is suitable only for higher frequencies that exceed the cutoff frequency of the bore.

Surface or local coils may be of the transmit or receive type. The electric and magnetic fields from the local coil will be most intense in its proximity. Collins and Smith calculated SAR for a surface coil adjacent to a human model.[20] SAR limits were approached for some imaging sequences at frequencies above 175 MHz. Schaefer calculated SAR for a generalized model of a surface coil.[21] SAR was found to fall off much more rapidly than B_1 for increasing distance into the patient. For receive-only coils, the blocking network may become warm.[21]

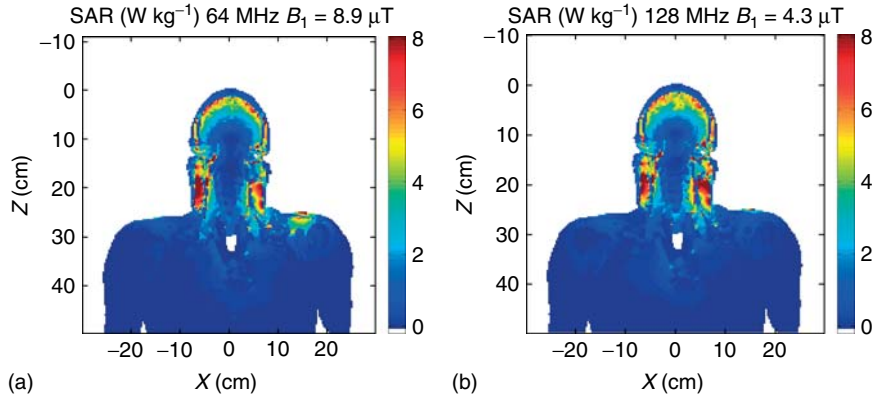

Figure 32.7. SAR distribution for a head transmit coil for 64 MHz (a) and 128 MHz (b). The RF field amplitude produces a head-average SAR of approximately 3.2 W kg^{-1}.

32.5 RF SAFETY WITH IMPLANTS

Patients with implants, especially complex ones such as cardiac pacemakers and neurostimulators, are generally contraindicated for MRI. However, there is increasing interest in qualifying implants for MRI. The US Food and Drug Administration (FDA) has recently released guidance for establishing safety and compatibility of implants in the MRI environment.[22] ASTM International has developed standards for the testing of passive implants with MRI. An ISO/IEC (International Organization for Standarization/International Electrotechnical Commission) joint working group is developing test methods for assessing MRI interactions with active implants.

A review of MRI safety from a clinical perspective that includes a discussion of implant safety has been presented by Shellock and Crues.[23]

Metallic implants concentrate on the RF electric field inside the body, producing locally elevated SAR. Note that the SAR within the metal of the implant will be essentially zero. However, the implant will heat due to the transference of heat from the surrounding tissue.

The greatest heating of implants occurs for elongated structures, such as catheters, leads, and guidewires. A review of the heating of implants by MRI has been presented by Nyenhuis *et al.*[24] Some of the significant rises reported in in vitro measurements have been 30 °C for guidewires,[25] 30–60 °C for electrodes on cardiac pacemaker leads,[26,27] and 25 °C for electrodes on deep brain stimulation leads.[28]

Implants with smaller dimensions tend to exhibit lower in vitro rises. For example, the Bion microstimulator was found to exhibit minimal heating in in vitro tests.[29] Implants that are made from electrically insulating materials[30] are candidates for being designated as MR safe, as defined in ASTM F2503.[31]

Physically, the implant can be viewed as an antenna in a lossy media. The RF electric field induces waves of current on the metal surface. These current waves[32] propagate along the length of the implant. At the end of the implant, part of the current is reflected and part of the current flows into the surrounding tissue. The current that flows into the tissue will produce a local SAR according to equation (32.2).

As described by Park *et al.*,[33] the temperature rise ΔT of an electrode may be expressed as

$$\Delta T = A \left| \int_0^L S(z) E_{\tan}(z) \mathrm{d}z \right|^2 \qquad (32.4)$$

where A is a constant, S is the electric field sensitivity function of the lead, $E_{\tan}$ is the tangential electric component of the incident electric field, z is the distance along the lead, which has a length L and $z = 0$ is at the electrode. Both $E_{\tan}$ and S are complex quantities, having magnitude and phase. The sensitivity function S will depend on the construction of the lead, the conductivity of the surrounding tissue, and whether or not the pulse generator is present. To a first approximation, S should not be influenced by slight curvature of the lead, but significant curvature

such as that which is present with loops will affect S.

The lead wire for an implant has a length of the order of tens of centimeters and a minimal dimension that is less than 0.1 mm. This large aspect ratio makes numerical calculation of lead heating challenging. Recently, however, calculations were made of the heating of model leads during MRI with FDTD[14] and of the heating of the electrodes of a vagus nerve simulator with finite element analysis (FEA).[34] Improvements in computer hardware and algorithms for lead modeling should make accurate calculation of electrode heating feasible in the future.

ASTM Standard F2182-09[35] describes an in vitro measurement method for evaluating RF heating of an implant. A rectangular phantom with dimensions $65 \times 42 \times 9$ cm^3 is presented in this document. The phantom is to be centered inside the MRI coil and the conductivity of the material is about 0.45 S m^{-1}. Figure 32.8 shows the calculated SAR patterns inside the phantom at 64 and 128 MHz. The arrows in the coronal images indicate the direction of the electric field. As expected, the electric field near the edges is parallel to the wall. The SAR, and hence electric field, is the most intense near the sidewall section at the coil center. There is significant nonuniformity in the SAR in the vertical direction, with the same skewing pattern that has been described by Amjad *et al*.[36] for the previous ASTM phantom. The vertical variation in heating is particularly strong at 128 MHz, with SAR near the sidewalls differing by a factor of nearly 4 between top and bottom. Thus, the in vitro temperature increase of an implant will be sensitive to its location in the phantom, especially at 128 MHz.

The implant to be tested for heating is to be placed close to the wall at the longitudinal midline. The measured temperature rise will be the "worst case" rise for any location in the phantom. Fiber-optic temperature probes are placed on parts of the implant that are expected to exhibit the greatest temperature rise. The phantom and implant are inserted in the MRI coil and an RF pulse sequence is applied.

The new F2182-09 specifies that the background or local SAR at the site of the implant be measured. This measurement is made by removing the implant and measuring the SAR at the site where the implant was during the tests. (It is assumed that the power applied to the RF coil for the SAR test is the same as that applied for the tests with implants.) A reference implant for the assessment of the local SAR has recently been introduced and F2182-09 has an appendix on the use of the implant. This implant is a 3.175 mm diameter by 10-cm-long rod made from Grade 5 titanium. Holes are drilled in the ends of the rod and the fiber-optic temperature probes are placed in the rod for the SAR run. Figure 32.9(a) shows the standard implant with the fiber-optic temperature probes placed in the end. Figure 32.9(b) shows an MR image of the rod in the phantom. There is a distortion that extends about 5 cm from the rod that is a result of the induced current.

The reference implant heats by the interaction with the tangential electric field. The temperature rise will thus be proportional to the tangential SAR, which is obtained by replacing E by $E_{\tan}$ in equation (32.2). We have calculated the temperature rises of the Ti reference rod scaled to the local tangential SAR.[37] For a tangential electric field producing a local tangential SAR of 1 W kg^{-1} and medium conductivity of 0.46 S m^{-1}, the temperature rise at the end of the rod will be approximately 1.30 °C at 64 MHz and 1.45 °C at 128 MHz. By comparing the local measured and calculated temperature rises, the tangential SAR is determined. Figure 32.10 shows an example of calculation and measurement. The measured temperature rise versus time for the two probes at the end of the rod is plotted and superimposed on the plot of calculated temperature rise versus time. A local tangential SAR of 8.95 W kg^{-1} provides a nearly exact fit between the measured and calculated temperature rises.

The titanium rod can be viewed as an SAR amplifier, yielding a temperature rise much greater than would be the rise of the gel. For example, in Figure 32.10, the local SAR of 8.9 W kg^{-1} would produce a background rise in the gel of just 0.77 °C. The error in local SAR assessment will be less with the rod. Nonetheless, we have generally found agreement to within 10–20% for SAR determined by temperature rise of the gel and by temperature rise of the rod.

Another application of the Huygen's box FDTD technique has been to calculate the electric field scattering by the rod and the consequent temperature rise. In FDTD simulations, the rod was embedded in a lossy background with conductivity 0.46 S m^{-1} and relative dielectric constant of 80. It was exposed to two plane waves propagating perpendicularly to its axis in opposite directions, which yield a standing wave with rather uniform electric field in the vicinity of the rod. The E-field component of the plane wave

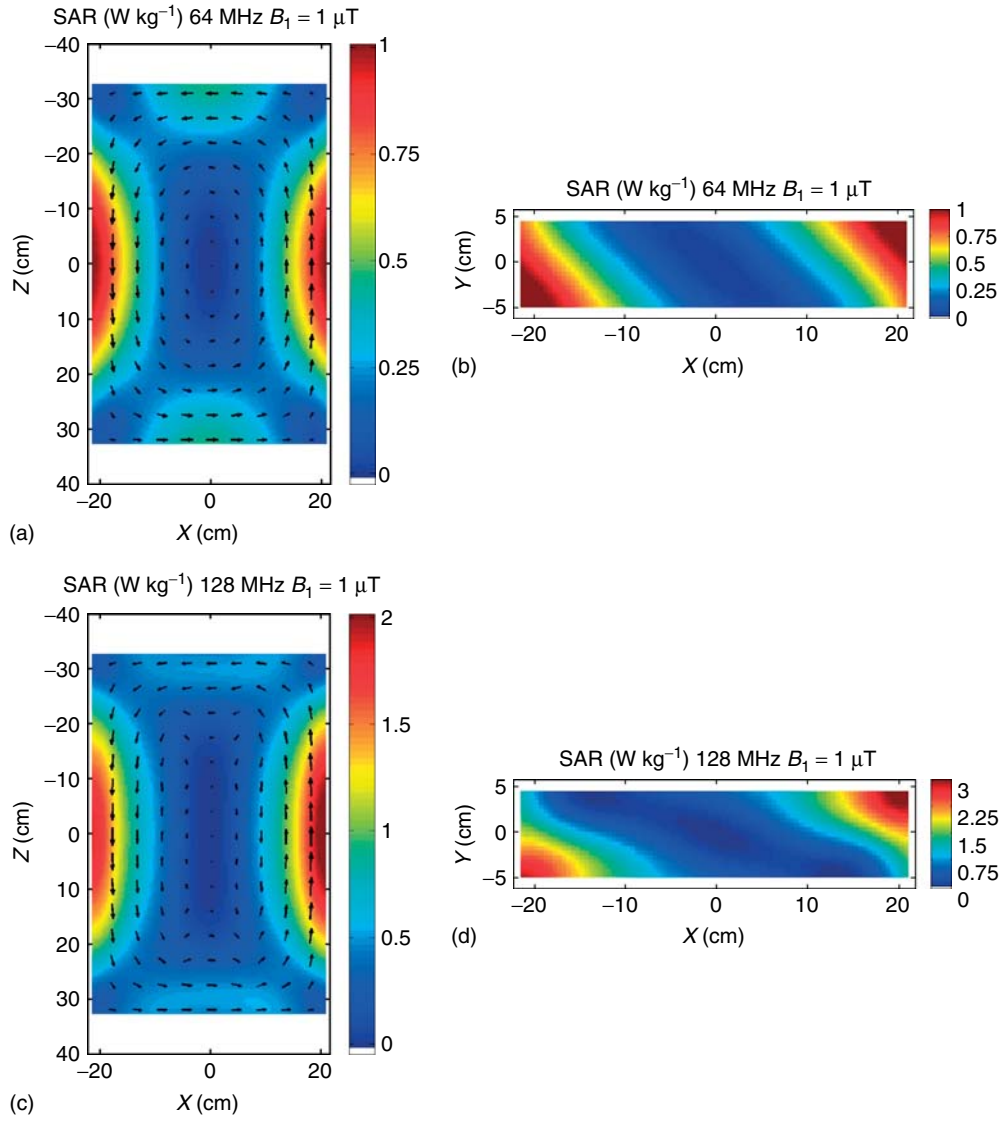

Figure 32.8. SAR distribution for the ASTM phantom in the coronal (a,c) and axial (b,d) midplanes in circularly polarized birdcage coils. The rotation sense is CW. Plots (a and b) are for 64 MHz and plots (c and d) are for 128 MHz. Medium conductivity is 0.47 S m^{-1}. Phantom average SAR is 0.32 W kg^{-1} at 64 MHz and 0.63 W kg^{-1} at 128 MHz. The arrows in the coronal plots indicate the direction and relative magnitude of the electric field.

is aligned with the wire. An FDTD grid with variable size was used, with a minimal grid size equal to 0.1 mm in the vicinity of the rod.

Figure 32.11(a) shows the SAR distribution surrounding the rod. Near the surface, the SAR is more than 100 times greater than the background rise. Figure 32.11(b) shows the temperature distribution after 6 min. The region of maximal SAR is concentrated to within about 2 mm from the edge of the rod and the temperature rise is concentrated to within 3 mm or so from the end of the rod. Thus variations in temperature probe placement of approximately 1 mm will not result in significant in measured differences in temperature rise.

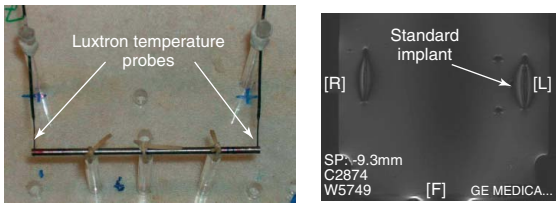

(a) (b)

Figure 32.9. (a) Temperature probe placement on the 3.175 mm diameter ×10 cm long standard implant. The tips of the probes are placed in 1-mm diameter holes centered 1 mm from the end of the rod. (b) Image of the rod in a 3-T MR system.

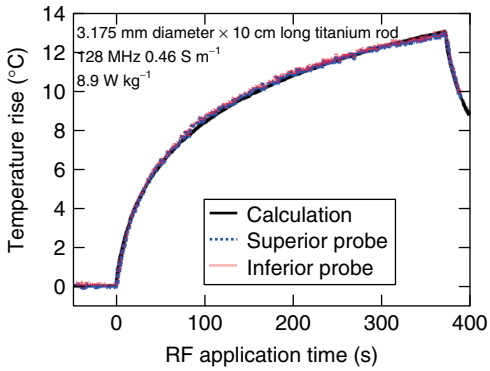

Figure 32.10. Calculated and measured temperature rises versus time for the Ti rod at 128 MHz. The measured rises match the calculated rises for a local tangential SAR of 8.9 W kg^{-1}.

As demonstrated by the MR image in Figure 32.9(b), the incident electric field induces current in the rod. Figure 32.12 shows the current induced in the rod by the incident electric field. As is expected, the current has the shape of a half-sinusoid and is maximal at the center of the rod. MRI could, in principle, be used to determine the induced currents. The measurement of current in the titanium reference rod and the calculated currents in Figure 32.12 could be used as a validation for the use of MRI to determine induced currents.

The relationship between the temperature rise of the reference rod and the local SAR described here is valid for a uniform tangential electric field. This condition is satisfied if

1. the rod is parallel to the wall of the phantom and longitudinally centered at mid-torso;
2. the center of the rod is at the longitudinal center of the RF coil. Calculation confirmed by measurement shows that for a nonuniform electric field, the average rise at the two ends provides a good indication of the average SAR along the length.

32.5.1 Heating with Externalized Lead Wires

While considerable attention has been devoted to thermal safety of implants, a perusal of the FDA MAUDE database reveals that device-related burns in MRI are largely related to external cabling. In one case,[38] failure to remove a pulse oximeter sensor and cable resulted in a burn so severe that it was necessary to amputate the forearm of the infant patient. In another case, a pressure transducer adhered to the patients scalp after MRI and 3 days thereafter, there was 3.5 × 6 cm necrotic area on the right temporal aspect of the head, suggestive of a burn.

The mechanism for the heating of an external conductor is essentially the same as that for the heating of an implant. Assume that a conducting wire is connected to an electrode on the skin. The tangential component of the electric field induces current waves on the surface of the wire. Part of the current will be transmitted through the electrode, heating the skin. If the impedance between the skin and the electrode is appropriate, the power dissipation will be large, producing a burn. Since the external wire is in the air, the wavelength of the RF field will be nearly nine times longer than in the tissue. The longer wavelength will permit efficient coupling of the electric field over a long distance, resulting in potentially massive power deposition. Note that closed loops are not required for heating; dangerous heating can occur under an electrode that is connected to a straight wire.

Heating with external conductors touching the patient wire may be decreased by reducing the induced voltage. This can be seen by the examination of equation (32.4). For simplicity, assume that S is uniform along the length of the wire. The temperature rise at the electrode is then

$$\Delta T = A|S|^2 \left| \int_0^L E_{\tan}(z)\mathrm{d}z \right|^2 = A|S|^2|\Delta V|^2 \quad (32.5)$$

ΔV is the line integral of the electric field along the path of the wire. By running the lead to minimize the induced voltage ΔV, heating at the electrode or

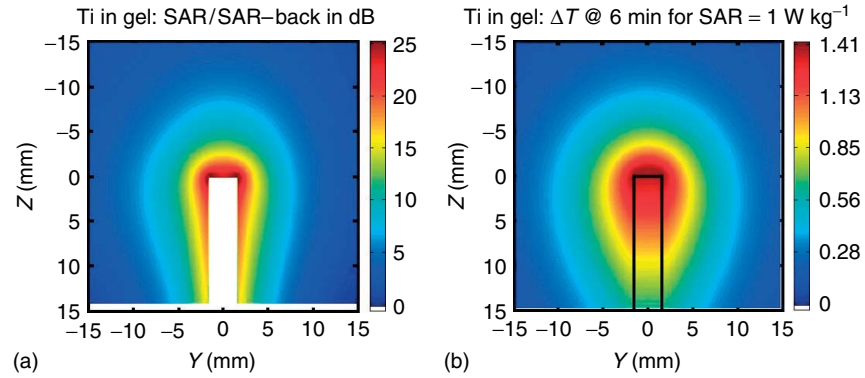

Figure 32.11. (a) Calculated SAR distribution in decibels relative to the background surrounding the end of the 3.175 mm diameter ×10 cm long rod. (b) Calculated temperature distribution at the end of the titanium rod. The temperature is calculated for 6 min power application with an electric field that produces a background SAR of 1 W kg^{-1}. Both calculations are for 64 MHz and medium conductivity of 0.46 S m^{-1}.

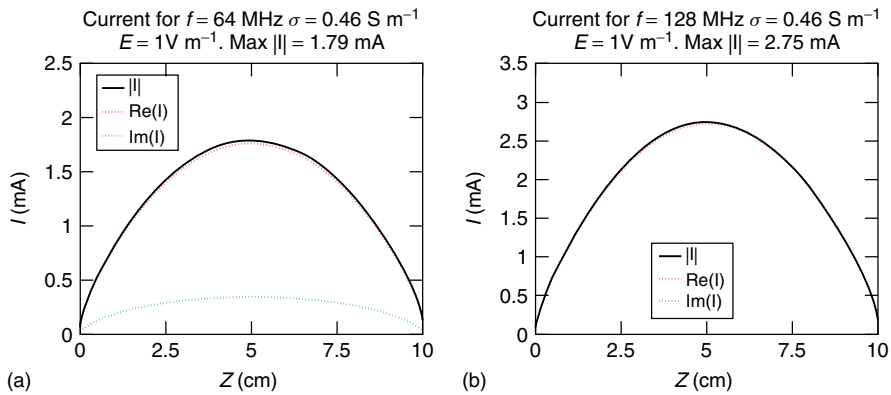

Figure 32.12. Calculated currents along the length of the 3.175 mm diameter ×10 cm long titanium rod at 64 MHz (a) and 128 MHz (b). The incident tangential electric field has an amplitude of 1 V m^{-1} and the medium conductivity is 0.46 S m^{-1}. The current maxima are 1.79 mA at 64 MHz and 2.75 mA at 128 MHz.

other structure under the skin is reduced. By reference to a plot of the external electric field, such as in Figure 32.3, a strategy for safe placement of the lead can be devised. In general, it is best to run the wires near the center of the bore, where the electric field intensity is lowest.

The Codman ICP is an intracranial pressure transducer that is connected to a long lead wire. From testing and physical considerations, conditions for safe MRI at 1.5 T with the Codman ICP were identified. The labeling[39] specifies that the lead wire be bundled on top of the head, on top of an insulating pad. Owing to the central position of the head in the bore, the electric field intensity at the lead bundle will be small. Furthermore, the impedance from the inductance of the loops will restrict the current flow. Added safety is provided in the labeling by the requirement that whole-body and head SAR do not exceed 1 W kg^{-1}.

32.6 IN VIVO TEMPERATURE RISE

In the absence of cooling, the temperature rise ΔT induced by the SAR will be

$$\Delta T = \frac{\text{SAR} \times t}{C} \tag{32.6}$$

where t is the time and C is the heat capacity. For most tissues, C does not differ much from the value for water, 4186 J $(\text{kg}^{\circ}\text{C})^{-1}$. In the absence of cooling, the temperature rise would increase without limit. For example, a local SAR of 10 W kg^{-1} would produce a temperature rise of 2.15 °C after 15 min.

In the presence of blood flow, the bioheat equation is

$$\frac{\mathrm{d}\Delta T}{\mathrm{d}t} = \alpha\nabla^2 T - \frac{1}{\tau}\Delta T + \frac{1}{c}\text{SAR} \qquad (32.7)$$

where ΔT is the temperature rise, c is the heat capacity, α is the thermal diffusivity, and τ is the perfusion time constant. The thermal diffusivity α is expressed as

$$\alpha = \frac{k}{\rho c} \qquad (32.8)$$

where k is the thermal conductivity (in W $(\text{m}^{\circ}\text{C})^{-1}$) and ρ is the mass density (in kg m^{-3}). The units of α are $\text{m}^2\ \text{s}^{-1}$ and its value for tissue is approximately $1.4 \times 10^{-7}\ \text{m}^2\ \text{s}^{-1}$. The perfusion time constant is

$$\tau = \frac{c}{c_\text{b}\rho_\text{b} m} \qquad (32.9)$$

where c_b is the heat capacity of the blood, ρ_b is the mass density of the perfusing blood, and m is the volumetric flow rate of the blood per unit mass of tissue.

As an example, consider the maximum perfusion rate m for muscle, which is about 2.5 l $(\text{kg}^{-1}\ \text{min}^{-1})$, which is equivalent to $4.17 \times 10^{-5}\ \text{m}^3\ (\text{kg}^{-1}\ \text{s}^{-1})$. Assume that $c = c_b$ and $\rho_b = 1000$ kg m^{-3}. The perfusion time constant τ is then calculated to be 24 s.

With blood perfusion, the approximate maximum of the local temperature rise is obtained by setting $t = \tau$ in equation (32.6). A more sophisticated analysis has been used by Athey[40] to model temperature rise in the head during MRI.

Figure 32.13 shows a numerical calculation on how perfusion may influence the temperature rise of an implant. The temperature rise has been calculated for the 3.175 mm diameter × 10-cm titanium rod without perfusion and with a perfusion time constant of 150 s. The temperature rise after 6 min with perfusion is about 40% less than the rise with no perfusion. The curve with perfusion follows the trend shown by Aksa *et al.*,[41] with the temperature rise saturating at a time approximately equal to the perfusion time constant.

There is also an overall rise in core temperature due to power deposition in the body. In response to temperature elevation, the body will dissipate heat through the skin. The amount of power dissipation will depend on factors such as ambient temperature, air flow, and clothing. A comprehensive analysis of patient response to the power deposition during MRI, which includes much clinical data, has been presented by Shellock and Schaefer.[15]

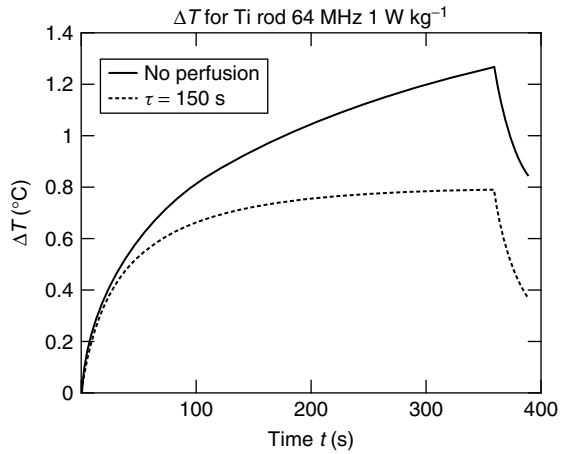

Figure 32.13. Calculated temperature versus time for the 3.175 mm diameter ×10 cm long titanium rod, with no perfusion and with a perfusion time constant of 150 ms. The RF field is turned off at $t = 360$ s.

An important question is how much temperature rise may be safely experienced by tissue in the vicinity of an implant. The CEM 43 thermal analysis described by Goldstein[42] is used here to project the relationship between temperature elevation and risk for tissue damage. The allowable time t_D for thermal damage at a given tissue temperature T can be expressed as

$$t_\text{D} = t_{43} 2^{(43-T)} \qquad \text{For } T > 43\ ^{\circ}\text{C} \quad (32.10)$$

$$t_\text{D} = t_{43} 4^{(43-T)} \qquad \text{For } T < 43\ ^{\circ}\text{C} \quad (32.11)$$

where t_{43} is the CEM 43 thermal time. The CEM 43 value will depend on the type of tissue. For example, brain tissue and testes are reported by Goldstein to be the organs most sensitive to acute damage with damage seen at <20 CEM 43 °C. Assume an MRI procedure that lasts 15 min. Then $t_D = 15$ min and $t_{43} = 20$ min in equations (32.10 and 32.11). The allowable temperature T over a 15-min duration then is

$$T = 43 - \log_2\left(\frac{15}{20}\right) = 43.4\ ^{\circ}\text{C} \qquad (32.12)$$

Given that body temperature is 37 °C, equation (32.12) predicts that tissue can withstand a temperature rise of at least 6.4 °C over a period of 15 min. Pearce has recently presented a detailed exposition of the relationship between Arrhenius models of thermal damage and the CEM 43 thermal dose.[43]

32.7 SUMMARY AND CONCLUSIONS

This chapter has reviewed the safety of MR coils. The principle safety consideration is that the patient or worker in the vicinity of the coil does not experience unsafe temperature elevation. Regulatory agencies and standards organizations have developed limits for SAR and safe in vivo temperature rises. Modeling techniques are now robust enough to calculate the SAR in the model with local resolution of less than 1 mm, assuming that the incident electromagnetic field is accurately known.

The electromagnetic field distributions produced by standard birdcage coils are well known and calculation of the various SAR values (whole body, head, partial body, and local) is rather straightforward. Other transmitter coils may expose the patient to electromagnetic fields that depend on patient characteristics and the region that is imaged. It is necessary to ensure that these coils are safe for all patient exposures.

Medical implants will concentrate the electric field in the body and may result in SAR averaged over a few cubic millimeters that is more than 100 times the background value. Standards organizations have developed and are developing test methods for assessing thermal safety of implants. It is anticipated that improvements in numerical simulation will enhance the understanding of interactions of medical implants with MRI.

ACKNOWLEDGMENTS

NIH-R01 EB000895, NIH-R01 EB006835, NIH-R01 EB007327, NIH-P41 RR08079

REFERENCES

1. J. P. Reilly, *Health Phys.*, 2002, **83**, 341–355.
2. A. G. Siemens, Medical Solutions, Verio MR Compatibility Data Sheet, March 2008.
3. F. G. Shellock, *J. Magn. Reson. Imag.*, 2000, **12**, 30–36.
4. National Radiological Protection Board (NRPB), 'Electromagnetic Fields and the Risk of Cancer'. Technical Report Documents of the NRPB 3(1). Report of an Advisory Group on Nonionising Radiation, 1992.
5. International Commission on Non-Ionizing Radiation Protection, *Health Phys.*, 1998, **74**, 494–522.
6. International Commission on Non-Ionizing Radiation Protection, *Health Phys.*, 2004, **87**, 197–216.
7. International Commission on Non-Ionizing Radiation Protection, *Health Phys.*, 2009, 257–258.
8. International Electrotechnical Commission (IEC), *Diagnostic Imaging Equipment, Publication IEC 60601-2-33 Ed. 3.0, Medical Electrical Equipment, Part 2, International Electrotechnology Commission International Electrotechnical Commission (IEC), 3, rue de Varemb, P.O. Box 131, CH - 1211 Geneva 20*, Switzerland.
9. American College of Radiology, *Am. J. Radiol.* 2007, **188**, 1447–1474.
10. Event 988411, 2008. http://www.accessdata.fda.gov/scripts/cdrh/cfdocs/cfMAUDE/TextSearch.cfm
11. Institute for Magnetic Resonance, Safety, Education, and Research 2010, 'Guidelines to Prevent Excessive Heating and Burns Associated with Magnetic Resonance Procedures', http://www.imrser.org/.
12. C. M. Collins and M. B. Smith, In *Proceedings of the 7th Annual Meeting of ISMRM*, Philadelphia, 1999, p 2051.
13. D. E. Merewether, R. Fisher, and F. W. Smith, *IEEE Trans. Nucl. Sci.*, 1980, **NS-27**, 1829–1833.
14. E. Neufeld, S. Kuehn, G. Szekely, and N. Kuster, *Phys. Med. Biol.*, 2009, **54**, 4151–4169.
15. F. G. Shellock and D. J. Schaefer, in *Health Effects and Safety of Radiofrequency Power Deposition Associated with Magnetic Resonance Procedures, in Magnetic Resonance Procedures: Health Effects and Safety*, ed F. G. Shellock, CRC Press, 2001.
16. Z. Wang, J. C. Lin, W. Mao, W. Liu, M. B. Smith, and C. M. Collins, *J. Mag. Reson. Imag.*, 2007, **26**, 437–441.
17. J. Nistler, R. Kurth, and M. Vester, *et al.*, *Proc. Intl. Soc. Magn. Reson. Med.*, 2006, **14**, 2471.
18. T. S. Ibrahim, A. M. Abduljahil, B. A. Baertlein, R. Lee, and P.-M.-L. Rotitaille, *Phys. Med. Biol.*, 2001, **46**, 2545–2555.

19. D. O. Brunner, N. DeZanche, J. Froelich, J. Paska, and K. P. Pruessmann, *Nature*, 2009, **457**, 994–998.
20. C. M. Collins and M. B. Smith, *Mag. Reson. Med.*, 2001, **45**, 692–699.
21. D. J. Schaefer, in *Health Effects and Safety of Radiofrequency Power Deposition Associated with Magnetic Resonance Procedures, in Magnetic Resonance Procedures: Health Effects and Safety*, ed F. G. Shellock, CRC Press, 2001.
22. FDA Center for Devices and Radiological Health, 'Guidance for Industry and Staff, Establishing Safety and Compatibility of Passive Implants in the Magnetic Resonance (MR) Environment', http://www.fda.gov/downloads/MedicalDevices/DeviceRegulationandGuidance/GuidanceDocuments/UCM107708.pdf, 2008.
23. F. G. Shellock and J. V. Crues, *Radiology*, 2004, **232**, 635–652.
24. J. A. Nyenhuis, S. M. Park, R. Kamondetdacha, A. Amjad, F. G. Shellock, and A. Rezai, *IEEE Trans. On Devices Mater. Reliab.*, 2005, **5**, 467–480.
25. M. K. Konings, L. W. Bartels, H. F. M. Smits, and C. J. G. Bakker, *J. Magn. Reson. Imag.*, 2000, **12**, 79–85.
26. S. Achenbach, W. Moshage, B. Diem, V. Schibgilla, and K. Bachmann, *Am. Heart J.*, 1997, **134**, 467–474.
27. R. C. Luechinger, 'Safety Aspects of Cardiac Pacemakers in Magnetic Resonance Imaging', Ph.D. Thesis, Swiss Federal Institute of Technology: Zurich, 2002.
28. A. R. Rezai, D. Finelli, J. A. Nyenhuis, G. Hrdlicka, J. Tkach, A. Sharan, P. Rugieri, P. H. Stypulkowski, and F. G. Shellock, *J. Magn. Res. Imag.*, 2002, **15**, 241–250.
29. F. G. Shellock, G. Cosendai, S. M. Park, and J. A. Nyenhuis, *Invest. Radiol.*, 2004, **39**, 591–599.
30. J. A. Nyenhuis and L. Duan, *J. Am. Coll. Radiol.*, 2009, **6**, 500–505.
31. ASTM International, 'Standard Practice for Marking Medical Devices and other Items for Safety in the Magnetic Resonance Environment', Standard 2503-05, ASTM International, 2005.
32. M. E. Ladd, H. H. Quick, P. Boesinger, and G. C. McKinnon, *Proc. Intl. Soc. Magn. Reson. Med.*, 1998, **6**, 473.
33. S. M. Park, R. Kamondetdacha, and J. A. Nyenhuis, *J. Mag. Reson. Imag.*, 2007, **26**, 1278–1285.
34. S. A. Mohsin, U. Saeed, J. Nyenhuis, and N. M. Shekih, *Antennas and Propagation Society International Symposium, 2008. AP-S*, 2008. San Diego, California, USA.
35. ASTM International, 'Standard Test Method for Measurement of Radio Frequency Induced Heating Near Passive Implants During Magnetic Resonance Imaging', Standard F2182-09, ASTM International, 2009.
36. A. Amjad, R. Kamondetdacha, A. V. Kildishev, S. M. Park, and J. A. Nyenhuis, *IEEE Trans. Magn.*, 2005, **41**, 4185–4187.
37. J. A. Jallal, J. A. Nyenhuis, and S. M. Park, *Proceedings 17th Scientific Meeting, International Society for Magnetic Resonance in Medicine*, Honolulu, 2009.
38. Event 770624, 2007, http://www.accessdata.fda.gov/scripts/cdrh/ cfdocs/cfMAUDE/TextSearch.cfm.
39. Codman, A Johnson & Johnson Company, 'MRI Safety of the Codman® Microsensor Transducer at 1.5 Tesla', 2004.
40. T. W. Athey, *Magn. Reson. Med.*, 1989, **9**, 177–184.
41. I. Aksa, O. Fernonogle, C. Yeung, S. Guney, T. Tasci, and E. Atalar, *J. Mag. Reson. Imag.*, 2007, **26**, 1228–1235.
42. L.S. Goldstein, M. W. Dewhirst, M. Repaholi, and L. Kheifets, *Int. J. Hyperthermia*, 2003, **199**, 373–384.
43. J. A. Pierce, *Proceedings of SPIE*, 2009, vol. 7181.

Chapter 33

Radiofrequency Heating Models and Measurements

Devashish Shrivastava and J. Thomas Vaughan

Center for Magnetic Resonance Research, University of Minnesota, Minneapolis, MN 55455, USA

33.1 INTRODUCTION

Significant progress has been made over the past years in an effort to determine radiofrequency (RF) heating during magnetic resonance (MR) imaging and spectroscopy applications, using both numerical and experimental models, and MR thermometry. A brief overview of the capabilities and limitations of these models and MR thermometry methods in determining the RF heating is presented below. Additionally, RF heating results obtained using the models are discussed in the context of the capabilities and limitations of the models. Modeling and measuring RF heating are of utmost importance to safeguard humans since thermogenic cellular and systemic hazards are directly related to in vivo temperatures—and not to RF power.

Specifically, Section 33.2 discusses the thermal models to determine RF heating. The exact thermal model (the convective energy equation (CEE)), the artificially generated discrete blood-vasculature-based thermal model, and two potentially most useful bioheat thermal models are discussed. Section 33.3 discusses various experimental models to measure RF heating. Section 33.4 discusses MR thermometry methods to measure RF heating. Finally, Section 33.5 summarizes the chapter and makes suggestions about predicting and measuring RF heating with relevance to human safety.

33.2 NUMERICAL MODELS TO DETERMINE RF HEATING

A numerical model with sub-degree Celsius accuracy is needed to develop fundamental understanding, to predict and minimize RF heating during MR imaging and spectroscopy applications, and to assure human safety. This is because US and international safety guidelines limit the maximum temperatures developed during an MR application to 38 °C in the head, 39 °C in the trunk, and 40 °C in the periphery.[1,2] Assuming a human core temperature of ∼37 °C, the limits allow maximum temperature changes of ∼1 °C

RF Coils for MRI
Edited by J. Thomas Vaughan and John R. Griffiths
 ISBN: 978-0-470-77076-4

in the head, ~2 °C in the trunk, and ~3 °C in the periphery. Nonuniform temperatures may result, with the possibility of local hot spots due to the nonhomogeneous geometry and composition of an imaged tissue, and nonuniform RF power deposition and blood flow.[3–7]

33.2.1 Convective Energy Equation (CEE)

The convective energy equation (CEE equation (33.1)) is an exact, continuum thermal model that can predict pointwise true, in vivo temperatures. The CEE is derived by satisfying conservation of energy at a continuum point in a perfused tissue.[8]

$$(\rho C_p)\left[\frac{\partial T}{\mathrm{d}t} + u \cdot \nabla T\right] = \nabla \cdot k \nabla T + Q \quad (33.1)$$

where ρ is density (kg m^{-3}), C_p is specific heat (J (kg K)$^{-1}$), T is temperature (K), t is time (s), u is blood velocity (m s^{-1}), k is thermal conductivity (W (m K)$^{-1}$), Q is net source term (W m^{-3}; metabolic heat generation + RF power).

The full implementation of the CEE to predict pointwise temperatures in vivo is computationally demanding and has not been achieved yet for any vascularized organ. This is because implementing the CEE requires knowledge of the complete blood vasculature and the associated local blood velocity field down to the capillary level (equation (33.1), second term on the left hand side). The large variation in the blood vessel diameters (8 μm–3 cm) and the multitude of vessels make the task of determining the in vivo blood velocity field challenging. Additionally, at least 20 nodes are required along the diameter of a vessel to accurately solve for the pointwise true blood temperature field.[9]

33.2.2 Artificially Generated Discrete Blood-vasculature-based Thermal Model

An artificial blood vessel network is generated in a tissue volume of interest to simulate a physiologically realistic spatial and temporal distribution of the blood–tissue heat transfer rate and tissue temperatures due to a source term (Figure 33.1); e.g., RF power.[10–18] Temperatures in the tissue are modeled using the CEE with $u = 0$. Temperatures in the blood vessels are modeled by solving an area-averaged CEE along the blood vessels, using a constant blood to blood vessel wall heat transfer coefficient.[8,19] The models clearly depict the effect of discrete, nonuniform vasculature on the resultant nonuniform tissue temperature distribution. Further, the models buttress the fact that MR-related RF heating should be determined in physiologically realistic geometries embedded with physiologically real blood vasculature[10,18] to best assure human safety.

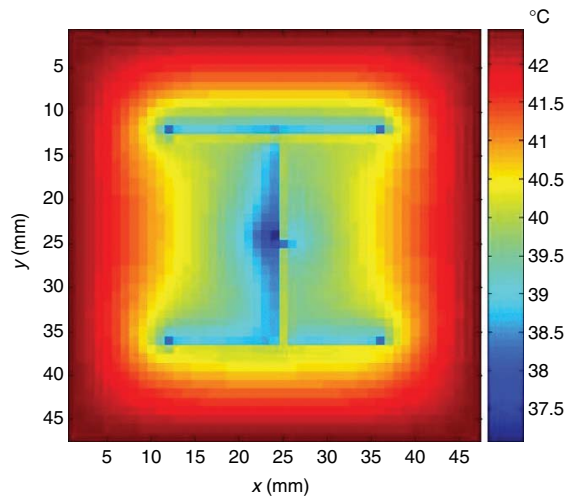

Figure 33.1. Effect of blood vessels on the temperatures is shown in a lateral cross section of a cuboidal tissue. The tissue volume was embedded with more than 8000 countercurrent blood vessels.[10] The tissue surface was heated to 42.5 °C. Blood inlet temperature was 37 °C.

33.2.3 Bioheat Transfer Thermal Models

Bioheat transfer models (BHTMs) are employed to determine in vivo temperatures with significantly reduced computational costs.[20–32] BHTMs are developed by conserving energy in a finite, perfused tissue volume (as opposed to the CEE, where energy is conserved at a point).[32] The volume averaging allows the BHTMs to have at the maximum two unknowns (one for the blood temperature, another for the tissue temperature) per finite averaging volume (compared to at least 20 unknowns along a blood vessel diameter in the CEE). Owing to the averaging, BHTMs predict volume-averaged temperatures. BHTMs differ from one another in the simplifications made to quantify

the thermal effects of blood vessels on the surrounding tissue.[32]

A BHTM may be employed alone or together with the CEE[13] to determine in vivo temperatures. The use of a BHTM alone neglects the thermal effects on the temperatures of those blood vessels (mostly large and infrequently occurring blood vessels) that were not included in the original derivation of the BHTM. The CEE may be used separately to include the effect of those blood vessels, if desired. It should be noted that BHTMs and CEE predict volume-averaged and pointwise true temperatures, respectively. Therefore, matching temperature boundary conditions need to be developed and employed at the interface between the blood vessels modeled using the CEE and the rest of the tissues modeled using a BHTM.

33.2.3.1 Pennes' Bioheat Transfer Equation (BHTE)

Pennes' BHTE (equation (33.2)) is the simplest and the most widely employed BHTM.[33–41] The equation was first proposed in 1948 by H. H. Pennes to determine in vivo temperatures in the resting human forearm.[20]

$$(\rho C_{\mathrm{p}})_{\mathrm{T}}\frac{\partial T_{\mathrm{T}}}{\partial t} = \nabla \cdot k_{\mathrm{T}}\nabla T_{\mathrm{T}} + wC_{\mathrm{p,Bl}}(1-\varepsilon)(T_{\mathrm{Bl}} - T_{\mathrm{T}}) + Q_{\mathrm{T}} \tag{33.2}$$

where w stands for blood perfusion ($\mathrm{kg\,m^{-3}\ s^{-1}}$), ε stands for blood thermal equilibration constant, and subscripts T and Bl stand for tissue and blood, respectively.

Traditionally, Pennes' BHTE was assumed to be a pointwise true differential equation owing to the lack of a rigorous theoretical derivation. However, assigning two pointwise true temperatures (i.e., the tissue temperature and the blood temperature in equation (33.2)) simultaneously to a physical point is physically as well as mathematically inappropriate for a pointwise true differential equation. Thus, the validity of Pennes' BHTE as a pointwise true differential equation has been questioned on physical as well as theoretical grounds.[22] The volume-averaged nature of the Pennes' equation was suggested and demonstrated by several previous researchers to provide the Pennes' equation with physical and theoretical validity; e.g.,[23,28,32] As it is a volume-averaged equation, T_{T} and T_{Bl} of Pennes' BHTE represent a volume-averaged tissue temperature and a volume-averaged blood temperature, respectively.[32] Conventionally, both volume-averaged temperatures are assigned to the centroid of the finite averaging volume.

The simplicity of the Pennes' BHTE originates from the assumptions of the thermal equilibration constant $\varepsilon = 0$, and uniform and constant T_{Bl} in the blood–tissue heat transfer rate term (second term on the right hand side in equation (33.2)). Pennes introduced a thermal equilibration constant ε into his equation to appropriately quantify the spatial and temporal variation of the blood–tissue heat transfer rate in a vascularized, heated/unheated tissue. However, in practice, no determination of ε has been available, and ε has always been assumed to be zero. The assumptions of $\varepsilon = 0$, and uniform and constant T_{Bl} make the blood act as an imaginary and ideal heat sink.[42] In other words, the finite heat transfer rate between the blood and surrounding tissue does not change the blood temperature in the equation, and no energy is convected with the blood flow to spatially redistribute the deposited energy—a physical impossibility. The assumptions make the equation overestimate the cooling and heating effects of the blood when the assigned blood temperature T_{Bl} is lower and higher than the local tissue temperature, respectively. Thus, in general, the simplifying features of the Pennes' equation result in an inaccurate estimation of the spatial and temporal blood–tissue heat transfer rate in a 3D, vascularized, heated tissue. Statistically, significant errors may result in predicting tissue temperatures.[32,43,44]

Nevertheless, in applications where blood temperature does not vary significantly along the blood flow direction, Pennes' BHTE predicts accurate volume-averaged tissue temperature distributions. In applications where blood temperature varies appreciably along the blood flow direction, use of an "average" blood temperature may provide useful indications about the general nature of volume-averaged tissue temperature distributions.

Regarding the use of Pennes' BHTE for RF heating predictions, Nguyen *et al.* used Pennes' BHTE to determine RF heating in a physiologically realistic human head due to a birdcage coil excited at frequencies ranging from 63 to 500 MHz[45] Collins *et al.* used Pennes' BHTE to determine RF heating in a human head due to a 64 MHz birdcage head coil, and a 300 MHz surface and volume coils.[34]

Hand *et al*. used Pennes' BHTE to determine RF heating due to a 64 MHz surface coil in a human leg.[46,47] Trakic *et al*. used Pennes' BHTE to determine RF heating in rats due to a birdcage coil excited at frequencies ranging from 500 to 1000 MHz.[38] As mentioned above, Pennes' BHTE with $\varepsilon = 0$, and uniform and constant T_{Bl} = initial core temperature, overestimates the blood–tissue heat transfer rate in deep tissues. Therefore, the tissue temperatures predicted using the BHTE are expected to underestimate the tissue RF heating in deep tissues when blood cools the RF-heated tissue.

To qualitatively study RF heating during MRI and the effect of various parameters of Pennes' BHTE on the RF heating in a nonuniform tissue with nonuniform blood flow and RF power, an exact, steady state, analytical solution to the Pennes' BHTE is presented below, in the radial direction, for a sphere and an infinitely long cylinder, respectively. The two analytical solutions were obtained by assuming that a uniform RF power was deposited in a uniformly perfused, and uniform and isotropic tissue. An insulated boundary condition and a convective boundary condition were employed, respectively, at the center and the outer boundary of the sphere/cylinder. Numerical solution schemes such as the finite difference time domain (FDTD) or finite element methods (FEMs) need to be employed in a real, nonuniform geometry with nonuniform blood flow and RF power deposition to obtain quantitative results for RF heating.

Nondimensional, steady-state Pennes' equation and the boundary conditions for a sphere in the radial direction are presented below in equations (33.3) and (33.4), respectively.

$$\frac{1}{\xi^2}\frac{\partial}{\partial \xi}\left[\xi^2 \frac{\partial \theta}{\partial \xi}\right] + \alpha[1-\theta] + \beta = 0 \qquad (33.3)$$

$$\left.\frac{\partial \theta}{\partial \xi}\right|_{\xi=0} = 0 \quad \text{and} \quad \left.\frac{\partial \theta}{\partial \xi}\right|_{\xi=1} = -3Bi(\theta|_{\xi=1}) \qquad (33.4)$$

The nondimensional parameters used in equations (33.3) and (33.4) are defined below.

$$\theta = \frac{T - T_{\mathrm{Bl}}}{T_{\mathrm{Bl}} - T_{\mathrm{amb}}}, \quad \xi = \frac{r}{R_0}, \quad \alpha = \frac{wC_{\mathrm{p}}R_0^2}{k},$$
$$\beta = \frac{QR_0^2}{k[T_{\mathrm{Bl}} - T_{\mathrm{amb}}]}, \quad Bi = \frac{hR_0}{3k}$$

where T_{amb} (K) is the ambient temperature, R_0 (m) is the radius of a sphere, and h (W m^{-2} K^{-1}) is the heat transfer coefficient between the outer boundary of the sphere and the ambient.

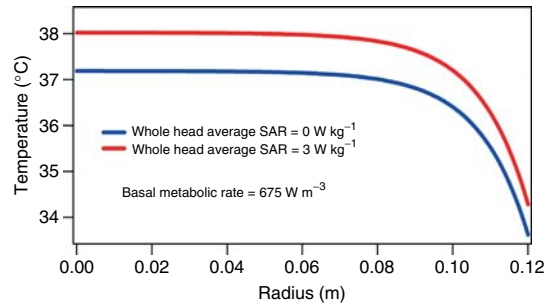

Figure 33.2. Radial temperature distributions in a uniform spherical head as predicted by the Pennes' BHTE.

The analytical solution to equation (33.3) with boundary conditions from equation (33.4) is as follows

$$\theta = \sum_{n=0}^{\infty} a_{2n}\xi^{2n} \qquad (33.5)$$

with

$$a_0 = \frac{(\alpha+\beta)\sum_{n=1}^{\infty}\frac{\left(n+\frac{3Bi}{2}\right)\alpha^{n-1}}{(2n+1)!}}{\frac{3Bi}{2} + \sum_{n=1}^{\infty}\frac{\left(n+\frac{3Bi}{2}\right)\alpha^{n}}{(2n+1)!}}$$

and

$$a_{2n} = \frac{\alpha^n a_0 - \alpha^{n-1}(\alpha+\beta)}{(2n+1)!}, \quad n \geq 1$$

Using the above solution, Figure 33.2 presents radial temperature profiles in approximately a human-head-sized sphere using the basal metabolic rate of 675 W m^{-3} and uniformly deposited RF power of 0–3 W kg^{-1}. The other parameters used were $\rho = 1000$ kg m^{-3}, $C_{\mathrm{p}} = 3600$ J kg^{-1} K^{-1}, $k = 0.5$ W m^{-1} K^{-1}, $R_0 = 0.12$ m, $w = 1.0$ kg m^{-3} s^{-1}, $T_{\mathrm{Bl}} = 37$ °C, $T_{\mathrm{amb}} = 20$ °C, and $h = 10$ W m^{-2} K^{-1}. Note that the uniform whole head average specific absorption rate (SAR) of 3 W kg^{-1} produced a temperature change of ~0.83 °C in the deep tissue and ~0.66 °C at the skin, respectively. As explained above, the deep tissue temperature changes and the skin temperature changes might be under- and overestimated, respectively, due to the heat sink assumption of the Pennes' BHTE. Shrivastava *et al*.[6,7] measured maximum RF-induced in vivo temperature changes varying between ~0.5–1.4 °C in the brain and ~0.3–1.0 °C in the subcutaneous layer of

the scalp of porcine models. The RF heating was measured with a volume head coil due to $3\,\mathrm{W\,kg^{-1}}$ whole head average SAR at ~400 MHz (9.4 T).

A nondimensional, steady-state Pennes' equation and the boundary conditions for a cylinder in the radial direction are presented in equations (33.6) and (33.7), respectively.

$$\frac{1}{\xi}\frac{\partial}{\partial\xi}\left[\xi\frac{\partial\theta}{\partial\xi}\right]+\alpha[1-\theta]+\beta=0 \qquad (33.6)$$

$$\left.\frac{\partial\theta}{\partial\xi}\right|_{\xi=0}=0 \quad \text{and} \quad \left.\frac{\partial\theta}{\partial\xi}\right|_{\xi=1}=-2Bi(\theta|_{\xi=1}) \qquad (33.7)$$

The nondimensional parameters used in equations (33.6) and (33.7) are defined below.

$$\theta=\frac{T-T_{\mathrm{Bl}}}{T_{\mathrm{Bl}}-T_{\mathrm{amb}}},\quad \xi=\frac{r}{R_0},\quad \alpha=\frac{wC_{\mathrm{p}}R_0^2}{k},$$
$$\beta=\frac{QR_0^2}{k[T_{\mathrm{Bl}}-T_{\mathrm{amb}}]},\quad Bi=\frac{hR_0}{2k}$$

The analytical solution for equation (33.6) with the boundary conditions from equation (33.7) is as follows

$$\theta=\sum_{n=0}^{\infty}a_{2n}\xi^{2n} \qquad (33.8)$$

with

$$a_0=\frac{(\alpha+\beta)\sum_{n=1}^{\infty}\frac{(n+Bi)\alpha^{n-1}}{2^{2n}(n!)^2}}{Bi+\sum_{n=1}^{\infty}\frac{(n+Bi)\alpha^{n}}{2^{2n}(n!)^2}}$$

and

$$a_{2n}=\frac{\alpha^n a_0-\alpha^{n-1}(\alpha+\beta)}{2^{2n}(n!)^2},\quad n\geq 1$$

Using the above solutions, Figure 33.3 presents radial temperature profiles in approximately a human-torso-sized cylinder using the basal metabolic rate of $675\,\mathrm{W\,m^{-3}}$ and uniformly deposited RF power of 0 and $4\,\mathrm{W\,kg^{-1}}$. The other parameters used were $\rho=1000\,\mathrm{kg\,m^{-3}}$, $C_{\mathrm{p}}=3600\,\mathrm{J\,kg^{-1}\,K^{-1}}$, $k=0.5\,\mathrm{W\,m^{-1}\,K^{-1}}$, $R_0=0.275$ m, $w=1.0\,\mathrm{kg\,m^{-3}\,s^{-1}}$, $T_{\mathrm{Bl}}=37\,^{\circ}\mathrm{C}$, $T_{\mathrm{amb}}=20\,^{\circ}\mathrm{C}$, and $h=10\,\mathrm{W\,m^{-2}\,K^{-1}}$. Note that the uniform whole body average SAR of $4\,\mathrm{W\,kg^{-1}}$ produced a temperature change of ~1.11 °C in the deep tissue and ~0.90 °C at the skin. Again, as explained above, the deep tissue temperature changes and the skin temperature changes might be under- and overestimated, respectively, owing to the heat sink assumption of the Pennes' BHTE.

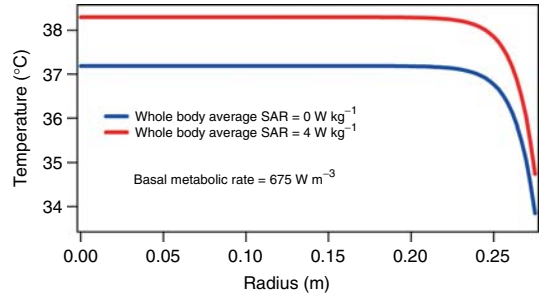

Figure 33.3. Radial temperature distributions in a uniform cylindrical torso as predicted by the Pennes' BHTE.

33.2.3.2 The Generic Bioheat Transfer Model (GBHTM)

The generic bioheat transfer model (GBHTM, equation (33.9a)) is the most general and potentially most accurate bioheat transfer thermal model. The model was derived by Shrivastava and Vaughan in 2009 to predict temperatures in a vascularized tissue volume due to a source term (e.g., RF power deposition during MR imaging). The GBHTM takes into account the spatial and temporal blood temperature variation due to a 3D source term (e.g., RF heating). In other words, the general equation models the nonuniform blood–tissue heat transfer rate and the nonuniform redistribution of the deposited source term due to the blood flow in a 3D space.[32] This relatively more complex BHTM has the potential to predict tissue temperatures more accurately than the Pennes' BHTE. The GBHTM reduces to the Pennes' BHTE in the special case of blood being an ideal heat sink.[32]

$$\langle(\rho C_{\mathrm{p}})_{\mathrm{T}}\rangle^{T}\frac{\partial\langle T_{\mathrm{T}}\rangle^{T}}{\partial t}=C_{\mathrm{T1}}\nabla\cdot k_{\mathrm{T}}\nabla\langle T_{\mathrm{T}}\rangle^{T}+\frac{(US)_{\mathrm{Bl-T}}}{(1-\chi)}\times(\langle T_{\mathrm{Bl}}\rangle^{Bl}-\langle T_{\mathrm{T}}\rangle^{T})+\langle Q_{\mathrm{T}}\rangle^{T} \qquad (33.9a)$$

$$\langle(\rho C_{\mathrm{p}})_{\mathrm{Bl}}\rangle^{Bl}\frac{\partial\langle T_{\mathrm{Bl}}\rangle^{Bl}}{\partial t}=C_{\mathrm{Bl2}}\nabla\cdot(PC_{\mathrm{p}}\langle T_{\mathrm{Bl}}\rangle^{Bl})+\frac{(US)_{\mathrm{Bl-T}}}{\chi}\times(\langle T_{\mathrm{T}}\rangle^{T}-\langle T_{\mathrm{Bl}}\rangle^{Bl})+\langle Q_{\mathrm{Bl}}\rangle^{Bl} \qquad (33.9b)$$

where, $\langle A \rangle^Z$ stands for a volume-averaged quantity A over a subvolume Z, superscript T stands for the tissue subvolume, superscript Bl stands for the blood subvolume, C_{T1} is a nondimensional tissue specific conduction constant, $(US)_{Bl-T}$ is volume-averaged blood–tissue heat transfer rate coefficient $(W\,K^{-1})$, C_{Bl2} is a nondimensional perfusion related constant, and $P(\frac{1}{V_{Bl}}\int_{V_{Bl}}(\rho u)_{Bl}dV)$ is perfusion vector $(kg\,m^{-2}\,s^{-1})$.

Various parameters of the new GBHTM are currently being identified to determine subject-specific, in vivo RF heating in an MR application. The GBHTM requires as input the thermal properties of the tissue and blood (density, specific heat, and thermal conductivity), the blood–tissue heat transfer coefficient, the RF power deposition, the perfusion vector, and the nondimensional conduction and perfusion constants. Thermal properties of various tissue types and blood are available in the literature, but the blood–tissue heat transfer coefficient is only partially available. The blood–tissue heat transfer coefficient is a function of the blood to blood vessel wall heat transfer coefficient and the blood vessel wall to tissue heat transfer coefficient. The blood to blood vessel wall heat transfer coefficient, defined on the basis of the volume-averaged blood temperature and the average vessel wall temperature, is currently under development. The vessel wall to tissue heat transfer coefficient, defined on the basis of the average vessel wall temperature and the volume-averaged tissue temperature, is available for one or more thermally important vessels arbitrarily embedded in a heated tissue.[48–52] The RF power deposition can be obtained by solving 3D Maxwell equations in segmented, realistic tissue geometries. The perfusion vector needs to be quantified and validated using MRI. The nondimensional conduction and perfusion constants need to be developed using realistic blood vessel networks.

Superior performance of the GBHTM over the Pennes' BHTE was demonstrated by Shrivastava and Vaughan[32] by taking a simple, 1D case of a perfused, unheated tissue. The superior performance of the GBHTM originated from its ability to model the nonuniform blood–tissue heat transfer rates and the redistribution of a source term due to the blood flow.

Another example showing superior performance of the GBHTM over the Pennes' BHTE in predicting temperatures in vivo was presented by Shrivastava *et al.* for the case of RF heating in swine with a large 31.75 cm internal diameter, 8 channel, TEM, volume head coil. The GBHTM was implemented by neglecting the spatial distribution of the thermal energy transport by blood[53] (Figure 33.4).

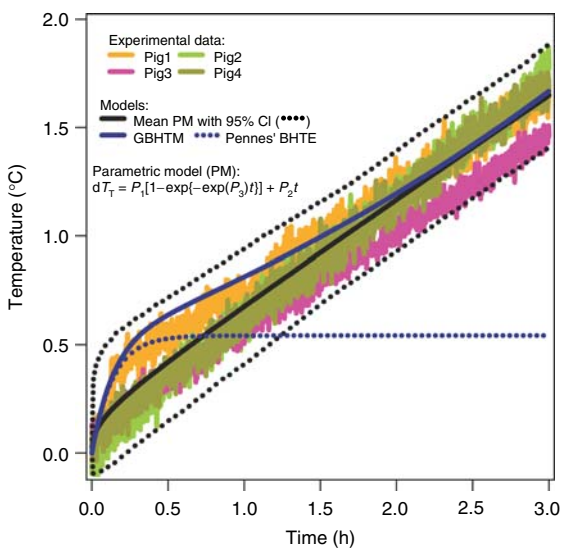

Figure 33.4. RF-power-induced temperature change in the swine brain with an 8 channel, 31.75 cm internal diameter volume head coil. The whole head average SAR was $\sim 3\,W\,kg^{-1}$.

33.3 EXPERIMENTAL MODELS TO DETERMINE RF HEATING

Experimental models are required to realistically measure RF heating and study its thermophysiological consequences. Thermophysiological consequences of the nonuniform RF heating of the brain and body in the range of 38–40 °C are yet to be studied.[54] Exact temperature thresholds after which irreversible cellular and systemic thermophysiological incidences occur are yet to be ascertained for various brain tissues.

33.3.1 Phantom Models

Phantom models are useful for obtaining approximate, qualitative estimates of RF heating and are easy to build. Uniform[55–61] and nonuniform[61] gel phantoms have been extensively used to measure RF heating due to MRI. Electrical and thermal conductivity

of the gel are modified to simulate a real tissue at a given Larmor frequency. Human-head-shaped plastic mannequins filled with ground turkey breast tissue or gel have also been employed to study RF heating.[62–65] The RF heating is a function of the geometry, tissue electrical and thermal properties, and blood flow. Thus, physiologically realistic geometry, tissue composition, and blood flow are required to measure RF heating accurately. Additionally, it should be stressed that the absence of blood flow in geometrically and tissue distributionwise unrealistic/realistic phantom models may not present a worst-case scenario for measuring the RF heating distribution. Blood flow convects the deposited RF energy and thus, cools as well as heats the tissue.

33.3.2 Cadaver Models

Fresh, perfused cadaver models are appropriate models for measuring RF heating during an MR application, because of the presence of a human-relevant geometry, tissue distribution, and fluid flow. However, no such studies have yet been reported. Cadaver models lack metabolism and thermophysiologic control mechanisms. The effect of the absence of metabolism on tissue temperatures can be countered by perfusing a cadaver with a fluid maintained at the normal core temperature of 37 °C. Saline or blood mixed with anticoagulant agents such as sodium citrate or heparin can be used as the circulating fluid. The effect of the thermophysiological control mechanisms such as vasodilation and vasoconstriction on the temperatures can be studied by increasing and decreasing the fluid flow. The effect of the absence of metabolism on the temperature changes induced owing to the RF power is negligible, as is mathematically shown below.

Temperature distribution in the tissue and blood due to a metabolic source term can be given as follows

$$\langle(\rho C_{\mathrm{p}})_{\mathrm{T}}\rangle^{T}\frac{\partial\langle T_{T1}\rangle^{T}}{\partial t}=C_{\mathrm{T1}}\nabla\cdot k_{\mathrm{T}}\nabla\langle T_{T1}\rangle^{T}+\frac{(US)_{\mathrm{Bl-T}}}{V_{\mathrm{T}}}\times\left(\langle T_{\mathrm{Bl1}}\rangle^{Bl}-\langle T_{\mathrm{T1}}\rangle^{T}\right)+\langle Q_{\mathrm{T,met}}\rangle^{T} \tag{33.10a}$$

$$\langle(\rho C_{\mathrm{p}})_{\mathrm{Bl}}\rangle^{Bl}\frac{\partial\langle T_{Bl1}\rangle^{Bl}}{\partial t}=C_{\mathrm{Bl2}}\nabla\cdot(PC_{\mathrm{p}}\langle T_{\mathrm{Bl1}}\rangle^{Bl})+\frac{(US)_{\mathrm{Bl-T}}}{V_{\mathrm{Bl}}}\times\left(\langle T_{\mathrm{T1}}\rangle^{T}-\langle T_{\mathrm{Bl1}}\rangle^{Bl}\right)+\langle Q_{\mathrm{Bl,met}}\rangle^{Bl} \tag{33.10b}$$

Temperature distribution in the tissue and blood due to the metabolism and RF power can be presented as given below.

$$\langle(\rho C_{\mathrm{p}})_{\mathrm{T}}\rangle^{T}\frac{\partial\langle T_{\mathrm{T2}}\rangle^{T}}{\partial t}=C_{\mathrm{T1}}\nabla\cdot k_{\mathrm{T}}\nabla\langle T_{\mathrm{T2}}\rangle^{T}+\frac{(US)_{\mathrm{Bl-T}}}{V_{\mathrm{T}}}\times\left(\langle T_{\mathrm{Bl2}}\rangle^{Bl}-\langle T_{\mathrm{T2}}\rangle^{T}\right)+\langle Q_{\mathrm{T,met}}\rangle^{T}+\langle Q_{\mathrm{T,RF}}\rangle^{T} \tag{33.11a}$$

$$\langle(\rho C_{\mathrm{p}})_{\mathrm{Bl}}\rangle^{Bl}\frac{\partial\langle T_{\mathrm{Bl2}}\rangle^{Bl}}{\partial t}=C_{\mathrm{Bl2}}\nabla\cdot(PC_{\mathrm{p}}\langle T_{\mathrm{Bl2}}\rangle^{Bl})+\frac{(US)_{\mathrm{Bl-T}}}{V_{\mathrm{Bl}}}\times\left(\langle T_{\mathrm{T2}}\rangle^{T}-\langle T_{\mathrm{Bl2}}\rangle^{Bl}\right)+\langle Q_{\mathrm{Bl,met}}\rangle^{Bl}+\langle Q_{\mathrm{Bl,RF}}\rangle^{Bl} \tag{33.11b}$$

Subtracting equation (33.10a) from equation (33.11a) and equation (33.10b) from equation (33.11b) provides RF power-deposition-induced temperature changes in the tissue and blood, respectively. Note that the RF-induced temperature changes in equation (33.12) are functions of geometry, tissue type, and fluid flow alone, which can be readily measured in fresh, perfused cadavers.

$$\langle(\rho C_{\mathrm{p}})_{\mathrm{T}}\rangle^{T}\frac{\partial\langle T_{\mathrm{T,RF}}\rangle^{T}}{\partial t}=C_{\mathrm{T1}}\nabla\cdot k_{\mathrm{T}}\nabla\langle T_{\mathrm{T,RF}}\rangle^{T}+\frac{(US)_{\mathrm{Bl-T}}}{V_{\mathrm{T}}}\left(\langle T_{\mathrm{Bl,RF}}\rangle^{Bl}-\langle T_{\mathrm{T,RF}}\rangle^{T}\right)+\langle Q_{\mathrm{T,RF}}\rangle^{T} \tag{33.12a}$$

$$\langle(\rho C_{\mathrm{p}})_{\mathrm{Bl}}\rangle^{Bl}\frac{\partial\langle T_{\mathrm{Bl,RF}}\rangle^{Bl}}{\partial t}=C_{\mathrm{Bl2}}\nabla\cdot\left(PC_{\mathrm{p}}\langle T_{\mathrm{Bl,RF}}\rangle^{Bl}\right)+\frac{(US)_{\mathrm{Bl-T}}}{V_{\mathrm{Bl}}}\left(\langle T_{\mathrm{T,RF}}\rangle^{T}-\langle T_{\mathrm{Bl,RF}}\rangle^{Bl}\right)+\langle Q_{\mathrm{Bl,RF}}\rangle^{Bl} \tag{33.12b}$$

where, $T_{\mathrm{T,RF}}=T_{\mathrm{T2}}-T_{\mathrm{T1}}$ and $T_{\mathrm{Bl,RF}}=T_{\mathrm{Bl2}}-T_{\mathrm{Bl1}}$.

Subject-specific, absolute RF heating can be determined in a cadaver or a live human by solving equation (33.10) first and later equation (33.12). Solution to equation (33.10) gives the baseline temperature distribution. Solution to equation (33.12) gives the RF-induced temperature changes over the baseline temperatures. Spatially unique correlations between the whole head/body average SAR and RF heating can be developed using direct fluoroptic temperature measurements to estimate RF heating in humans.[6]

33.3.3 Animal Models

Large animal models, with thermal mass and thermophysiology comparable to humans, are appropriate models to study the thermophysiological consequences of MR-related RF heating. The intact tissue electrical and thermal properties, blood flow, and thermophysiology in anesthetized animal models help obtain reasonable estimates of the RF heating. Lack of similarity between the tissue geometry and distribution of human and animal models prevents the direct application of these RF heating measurements to humans. Possible alterations in absolute temperature thresholds of vasoconstriction and vasodilation due to anesthesia may complicate the interpretation of the observed thermophysiological consequences.

RF heating can be measured very accurately ($\pm 0.2\ ^{\circ}C$) in vivo using invasive fluoroptic temperature probes. Multiple fluoroptic temperature probes can be placed in an RF-heated tissue to map the RF heating. The invasive nature of the fluoroptic temperature probe placement excludes the possibility of using humans. Canine,[66] ovine,[67] and swine[6,7] models have been employed to study RF heating due to MRI. Spatially unique correlations can be obtained between the whole head or body average SAR and the RF-induced temperature changes. These empirical correlations are extremely useful since they provide good estimates of the RF heating in vivo.

Shrivastava *et al.*[6] obtained spatially unique correlations between the whole head average SAR and in vivo brain temperatures in porcine models with a volume head coil at 9.4 T (400 MHz). Figure 33.5

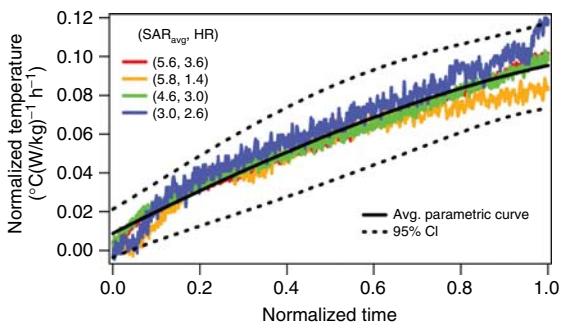

Figure 33.5. Normalized temperature change vs normalized RF heating duration at 10 mm in the brain with corresponding average parametric curve and 95% confidence interval (CI) curves.

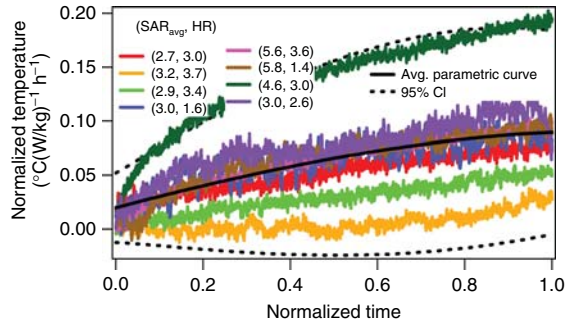

Figure 33.6. Normalized temperature change vs normalized RF heating duration at the head skin with corresponding average parametric curve and 95% confidence interval (CI) curves.

shows that the RF-induced in vivo brain temperatures, when normalized by the whole head average SAR and heating duration, produced a spatially unique temperature distribution ($N = 4$). The unique correlations in porcine models suggest that the effect of subject to subject variability on the normalized RF heating may be minimal. The average SAR was varied between 3.0 and 5.8 W kg^{-1}. The heating duration was varied between 1.4 and 3.6 h. Note that the in vivo temperature change at this location is easily estimated by multiplying the obtained statistical average temperature curve with the average SAR and heating duration. Further, no unique normalized temperature was obtained for the head skin (Figure 33.6). Also, the temperature variation in the head skin varied significantly, suggesting that the RF-induced head skin temperature changes might vary significantly from one subject to another. Thus, the skin temperature change should not be used to gauge in vivo temperature change.[6]

33.3.4 Human Models

Human-relevant RF heating and its thermophysiological consequences can be best studied in live human models with appropriate clinical conditions and predispositions. RF safety can be best assured by developing accurate bioheat transfer models with subject-specific inputs and accurate MR thermometry methods. This is because human models have the necessary and appropriate geometry, tissue distribution, fluid flow, and thermophysiology. Unavailability of a suitable BHTM and an MR thermometry approach

with subdegree Celcius accuracy and the invasive nature of fluoroptic temperature probes make it difficult to determine local, deep tissue RF heating in humans with appropriate accuracy and sensitivity.

Studies have been conducted on unanesthetized human volunteers to monitor MR-related RF heating in 1.5 T and lower fields.[68–78] Temperatures in the skin, esophagus, cornea, and rectum were measured to quantify RF heating. More studies to measure/determine local RF heating distribution on the body surface and in deep tissue are urgently needed to develop a fundamental understanding of RF heating in humans, of the thermophysiological consequences of the RF heating, and ultimately to assure human safety.

33.4 MR THERMOMETRY TO DETERMINE RF HEATING

An absolute temperature MR thermometry method is desired with subdegree Celcius accuracy and sensitivity in order to reliably measure RF heating in humans and assure safety. Proton resonance frequency (PRF) shift based MR thermometry method is the most accurate and widely applied MR thermometry method available. Generally, the PRF shift coefficient of $-0.01\,\text{ppm}/^{\circ}\text{C}$ is used for all tissue types,[79–89] which is equal to the PRF shift coefficient due to the change in the molecular screening constant of water protons with temperature.[90] However, a wide range of the PRF shift coefficients has been reported in the literature; e.g., $-0.0067\,\text{ppm}/^{\circ}\text{C}$ for a canine brain, $-0.0097\,\text{ppm}/^{\circ}\text{C}$ for a porcine muscle, $-0.0135\,\text{ppm}/^{\circ}\text{C}$ for a porcine liver, $-0.0146\,\text{ppm}/^{\circ}\text{C}$ for a rat thigh, etc.[91–94] The PRF, to the first approximation, linearly changes with temperature due to the change in the local magnetic field. The local magnetic field changes with temperature due to the change in molecular arrangement and thus, molecular screening of the water proton, volume magnetic susceptibility, and the macroscopic magnetic field distribution.[92] The total PRF shift coefficient, which includes all the effects, needs to be measured and validated to detect RF heating with subdegree Celcius accuracy.[95,96]

The PRF-based MR thermometry method measures temperature changes over a baseline temperature. A combination of a bioheat thermal model and PRF-based thermometry may provide an absolute estimate of RF heating, with appropriate accuracy and sensitivity to assure human safety in MR applications.

33.5 SUMMARY

RF heating and its thermophysiologic consequences can be best understood by developing subject-specific thermal transport models and measuring RF heating directly in humans. The newly derived GBHTM has the potential to determine accurate RF heating in perfused tissues. This model needs to be developed further for human applications in high field MR. Fresh, perfused cadaver models seem best to provide direct measurements of human-relevant RF-power-induced temperature changes. Animal models with thermophysiology similar to humans may provide human-relevant and conservative in vivo thermal thresholds of various tissue types for irreversible cellular and/or systemic alterations. PRF shift-based MR thermometry method needs to be further developed and validated in humans to measure temperature changes due to RF heating with sufficient accuracy and sensitivity. The PRF thermometry method together with the newly developed GBHTM may provide the absolute RF heating predictions in humans necessary to assure human safety at the highest fields.

ACKNOWLEDGMENTS

NIH-R01 EB000895, NIH-R01 EB006835, NIH-R01 EB007327, NIH-P41 RR08079

REFERENCES

1. CDRH-FDA, Guidance for Industry and FDA Staff-Criteria for Significant Risk Investigations of Magnetic Resonance Diagnostic Devices, 2003, pp. 1–3.
2. ICNIRP, *Health Phys.*, 2004, **87**(2), 197–216.
3. O. P. Gandhi and X. B. Chen, *Magn. Reson. Med.*, 1999, **41**(4), 816–823.
4. O. P. Gandhi, *Annu. Rev. Biomed. Eng.*, 2002, **4**, 211–234.
5. J. T. Vaughan, M. Garwood, C. M. Collins, W. Liu, L. DelaBarre, G. Adriany, P. Andersen, H. Merkle, R. Goebel, M. B. Smith, and K. Ugurbil, *Magn. Reson. Med.*, 2001, **46**(1), 24–30.

6. D. Shrivastava, T. Hanson, R. Schlentz, W. Gallaghar, C. Snyder, L. Delabarre, S. Prakash, P. Iaizzo, and J. T. Vaughan, *Magn. Reson. Med.*, 2008, **59**(1), 73–78.
7. D. Shrivastava, T. Hanson, J. Kulesa, L. DelaBarre, C. Snyder, and J. T. Vaughan, *Magn. Reson. Med.*, 2009, **62**(4), 888–895.
8. W. M. Kays and M. E. Crawford, *Convective Heat and Mass Transfer*, McGraw-Hill, Inc.: New York, 1993.
9. J. A. White, A. W. Dutton, J. A. Schmidt, and R. B. Roemer, *Int. J. Hyperthermia*, 2000, **16**(2), 145–158.
10. D. Shrivastava and R. B. Roemer, *J. Biomech. Eng.*, 2006, **128**(2), 210–216.
11. V. M. Flyckt, B. W. Raaymakers, and J. J. Lagendijk, *Phys. Med. Biol.*, 2006, **51**(19), 5007–5021.
12. B. W. Raaymakers, M. Van Vulpen, J. J. Lagendijk, A. A. De Leeuw, J. Crezee, and J. J. Battermann, *Phys. Med. Biol.*, 2001, **46**(12), 3115–3131.
13. O. I. Craciunescu, B. W. Raaymakers, A. N. Kotte, S. K. Das, T. V. Samulski, and J. J. Lagendijk, *Med. Phys.*, 2001, **28**(11), 2289–2296.
14. B. W. Raaymakers, A. N. Kotte, and J. J. Lagendijk, *Phys. Med. Biol.*, 2000, **45**(11), 3385–3401.
15. G. M. Van Leeuwen, A. N. Kotte, B. W. Raaymakers, and J. J. Lagendijk, *Phys. Med. Biol.*, 2000, **45**(4), 1035–1049.
16. A. N. Kotte, G. M. van Leeuwen, and J. J. Lagendijk, *Phys. Med. Biol.*, 1999, **44**(1), 57–74.
17. A. Kotte, G. van Leeuwen, J. de Bree, J. van der Koijk, H. Crezee, and J. Lagendijk, *Phys. Med. Biol.*, 1996, **41**(5), 865–884.
18. D. Shrivastava and R. Roemer, Evaluation of tissue convective energy balance equation in unheated tissue region with a realistic vessel network. In *ASME Heat Transfer Division, (Publication) HTD, Proceedings of the ASME Heat Transfer Division - 2004*, 2004, pp. 695–697. (ASME Heat Transfer Division, (Publication) HTD, Proceedings of the ASME Heat Transfer Division - 2004).
19. A. K. Cousins, *J. Biomech. Eng.*, 1997, **119**(1), 127–129.
20. H. H. Pennes, *J. Appl. Physiol.*, 1998, **85**(1), 5–34.
21. K. H. Keller and L. Seiler Jr, *J. Appl. Physiol.*, 1971, **30**(5), 779–786.
22. W. Wulff, *IEEE Trans. Biomed. Eng.*, 1974, **BME-21** (6), 494–495.
23. M. M. Chen and K. R. Holmes, *Ann. N. Y. Acad. Sci.*, 1980, **335**, 137–150.
24. M. M. Osman and E. M. Afify, *J. Biomech. Eng.*, 1984, **106**(2), 123–130.
25. S. Weinbaum and L. M. Jiji, *J. Biomech. Eng.*, 1985, **107**(2), 131–139.
26. H. Brinck and J. Werner, *J. Appl. Physiol.*, 1994, **77**(4), 1617–1622.
27. S. Weinbaum, L. X. Xu, L. Zhu, and A. Ekpene, *J. Biomech. Eng.*, 1997, **119**(3), 278–288.
28. R. B. Roemer and A. W. Dutton, *J. Biomech. Eng.*, 1998, **120**(3), 395–404.
29. J. W. Baish, *J. Biomech. Eng.*, 1994, **116**(4), 521–527.
30. J. Wren, M. Karlsson, and D. Loyd, *Int. J. Hyperthermia*, 2001, **17**(6), 483–498.
31. H. S. Kou, T. C. Shih, and W. L. Lin, *Phys. Med. Biol.*, 2003, **48**(11), 1577–1589.
32. D. Shrivastava and J. Vaugahn, *ASME J. Biomech. Eng.*, 2009, **131**(7), 074506.
33. C. M. Collins, M. B. Smith, and R. Turner, *J. Appl. Physiol.*, 2004, **97**(6), 2051–2055.
34. C. M. Collins, W. Liu, J. Wang, R. Gruetter, J. T. Vaughan, K. Ugurbil, and M. B. Smith, *J. Magn. Reson. Imaging*, 2004, **19**(5), 650–656.
35. V. M. Flyckt, B. W. Raaymakers, H. Kroeze, and J. J. Lagendijk, *Phys. Med. Biol.*, 2007, **52**(10), 2691–2701.
36. J. M. Huttunen, T. Huttunen, M. Malinen, and J. P. Kaipio, *Phys. Med. Biol.*, 2006, **51**(4), 1011–1032.
37. S. C. Jiang and X. X. Zhang, *Lasers Med. Sci.*, 2005, **19**(4), 197–202.
38. A. Trakic, S. Crozier, and F. Liu, *Phys. Med. Biol.*, 2004, **49**(24), 5547–5558.
39. C. Diao, L. Zhu, and H. Wang, *Ann. Biomed. Eng.*, 2003, **31**(3), 346–353.
40. J. H. Niu, H. Z. Wang, H. X. Zhang, J. Y. Yan, and Y. S. Zhu, *Med. Biol. Eng. Comput.*, 2001, **39**(5), 601–604.
41. L. Zhu and C. Diao, *Med. Biol. Eng. Comput.*, 2001, **39**(6), 681–687.
42. Y. A. Cengel and M. A. Boles, *Thermodynamics: An Engineering Approach*, McGraw-Hill Companies, Inc.: New York, 1998, p. 1010.
43. H. Brinck and J. Werner, *J. Biomech. Eng.*, 1994, **116**(3), 324–330.

44. H. Brinck and J. Werner, *Int. J. Hyperthermia*, 1995, **11**(5), 615–626.
45. U. D. Nguyen, J. S. Brown, I. A. Chang, J. Krycia, and M. S. Mirotznik, *IEEE Trans. Biomed. Eng.*, 2004, **51**(8), 1301–1309.
46. J. W. Hand, R. W. Lau, J. J. Lagendijk, J. Ling, M. Burl, and I. R. Young, *Magn. Reson. Med.*, 1999, **42**(1), 183–192.
47. J. Hand, J. Lagendijk, J. Hajnal, R. Lau, and I. Young, *J. Magn. Reson. Imaging*, 2000, **12**(1), 68–74.
48. D. Shrivastava and R. B. Roemer, *Phys. Med. Biol.*, 2005, **50**(15), 3627–3641.
49. D. Shrivastava, R. Roemer, and B. McKay, *J. Heat Transfer*, 2005, **127**(2), 179–188.
50. D. Shrivastava and R. Roemer, *Int. J. Heat Mass Transfer*, 2005, **48**(19–20), 4090–4102.
51. D. Shrivastava and R. Roemer, Poisson conduction shape factors' for 'mixed case' counter-current heat transfer applications, Advances in Bioengineering, BED, Advances in Bioengineering - 2004, 2004. pp. 79–82. (Advances in Bioengineering, BED, Advances in Bioengineering - 2004).
52. D. Shrivastava and R. Roemer, *Int. J. Heat Mass Transfer*, 2004, **47**(19–20), 4293–4300.
53. D. Shrivastava, T. Hanson, J. Kulesa, J. Tian, A. Gregor, and J. T. Vaugahn, *Magn. Reson. Med.*, 2011, **66**(1), 255–263.
54. M. W. Dewhirst, B. L. Viglianti, M. Lora-Michiels, M. Hanson, and P. J. Hoopes, *Int. J. Hyperthermia*, 2003, **19**(3), 267–294.
55. T. Hess, B. Stepanow, and M. V. Knopp, *Eur. Radiol.*, 1996, **6**(1), 66–68.
56. F. G. Shellock, *J. Magn. Reson. Imaging*, 2001, **13**(1), 152–157.
57. H. Cline, R. Mallozzi, Z. Li, G. McKinnon, and W. Barber, *Magn. Reson. Med.*, 2004, **51**(6), 1129–1137.
58. K. B. Baker, J. Tkach, J. D. Hall, J. A. Nyenhuis, F. G. Shellock, and A. R. Rezai, *Neurosurgery*, 2005, **57**(4 Suppl), 392–397; discussion 392–397.
59. R. W. Gray, W. T. Bibens, and F. G. Shellock, *Magn. Reson. Imaging*, 2005, **23**(8), 887–891.
60. H. Bassen, W. Kainz, G. Mendoza, and T. Kellom, *Minim. Invasive Ther. Allied Technol.*, 2006, **15**(2), 76–84.
61. P. L. Davis, C. Shang, L. Talagala, and A. W. Pasculle, *IEEE Trans. Biomed. Eng.*, 1993, **40**(12), 1324–1327.
62. A. Kangarlu, F. G. Shellock, and D. W. Chakeres, *J. Magn. Reson. Imaging*, 2003, **17**(2), 220–226.
63. A. Kangarlu, T. S. Ibrahim, and F. G. Shellock, *Magn. Reson. Imaging*, 2005, **23**(1), 53–60.
64. C. K. Chou, J. A. McDougall, and K. W. Can, *Bioelectromagnetics*, 1995, **16**(5), 307–316.
65. C. K. Chou, J. A. McDougall, and K. W. Chan, *IEEE Trans. Biomed. Eng.*, 1997, **44**(5), 367–373.
66. W. P. Shuman, D. R. Haynor, A. W. Guy, G. E. Wesbey, D. J. Schaefer, and A. A. Moss, *Radiology*, 1988, **167**(2), 551–554.
67. B. J. Barber, D. J. Schaefer, C. J. Gordon, D. C. Zawieja, and J. Hecker, *AJR Am. J. Roentgenol.*, 1990, **155**(5), 1105–1110.
68. F. G. Shellock, D. J. Schaefer, W. Grundfest, and J. V. Crues, *Acta Radiol. Suppl.*, 1986, **369**, 514–516.
69. F. G. Shellock and J. V. Crues, *AJNR Am. J. Neuroradiol.*, 1988, **9**(2), 287–291.
70. F. G. Shellock, D. J. Schaefer, and J. V. Crues, *Br. J. Radiol.*, 1989, **62**(742), 904–909.
71. D. Morvan, A. Leroy-Willig, P. Jehenson, C. A. Cuenod, and A. Syrota, *Radiology*, 1992, **185**(3), 871–874.
72. F. G. Shellock, C. J. Gordon, and D. J. Schaefer, *Acta Radiol. Suppl.*, 1986, **369**, 512–513.
73. F. G. Shellock and J. V. Crues, *Radiology*, 1987, **163**(1), 259–262.
74. F. G. Shellock and J. V. Crues, *Radiology*, 1988, **167**(3), 809–811.
75. F. G. Shellock, D. J. Schaefer, and J. V. Crues, *Magn. Reson. Med.*, 1989, **11**(3), 371–375.
76. F. G. Shellock, B. Rothman, and D. Sarti, *AJR Am. J. Roentgenol.*, 1990, **154**(6), 1229–1232.
77. F. G. Shellock and C. J. Schatz, *Radiology*, 1992, **185**(3), 697–699.
78. F. G. Shellock, D. J. Schaefer, and E. Kanal, *Radiology*, 1994, **192**(3), 865–868.
79. A. V. Shmatukha, P. R. Harvey, and C. J. Bakker, *J. Magn. Reson. Imaging*, 2007, **25**(3), 579–587.
80. D. Meister, F. Hubner, M. Mack, and T. J. Vogl, *Rofo*, 2007, **179**(5), 497–505.
81. P. Wust, C. H. Cho, B. Hildebrandt, and J. Gellermann, *Int. J. Hyperthermia*, 2006, **22**(3), 255–262.
82. M. Lepetit-Coiffe, B. Quesson, O. Seror, E. Dumont, B. Le Bail, C. T. Moonen, and H. Trillaud, *J. Magn. Reson. Imaging*, 2006, **24**(1), 152–159.

83. A. Boss, H. Graf, B. Muller-Bierl, S. Clasen, D. Schmidt, P. L. Pereira, and F. Schick, *J. Magn. Reson. Imaging*, 2005, **22**(6), 813–820.

84. V. Rieke, K. K. Vigen, G. Sommer, B. L. Daniel, J. M. Pauly, and K. Butts, *Magn. Reson. Med.*, 2004, **51**(6), 1223–1231.

85. V. Paliwal, A. M. El-Sharkawy, X. Du, X. Yang, and E. Atalar, *Magn. Reson. Med.*, 2004, **52**(4), 704–708.

86. M. W. Vogel, P. M. Pattynama, F. L. Lethimonnier, and P. Le Roux, *J. Magn. Reson. Imaging*, 2003, **18**(4), 507–512.

87. C. Weidensteiner, B. Quesson, B. Caire-Gana, N. Kerioui, A. Rullier, H. Trillaud, and C. T. Moonen, *Magn. Reson. Med.*, 2003, **50**(2), 322–330.

88. J. A. de Zwart, F. C. Vimeux, C. Delalande, P. Canioni, and C. T. Moonen, *Magn. Reson. Med.*, 1999, **42**(1), 53–59.

89. R. D. Peters, R. S. Hinks, and R. M. Henkelman, *Magn. Reson. Med.*, 1998, **40**(3), 454–459.

90. J. C. Hindman, *J. Chem. Phys.*, 1966, **44**, 4582–4592.

91. J. R. MacFall, D. M. Prescott, H. C. Charles, and T. V. Samulski, *Med. Phys.*, 1996, **23**(10), 1775–1782.

92. J. De Poorter, *Magn. Reson. Med.*, 1995, **34**(3), 359–367.

93. K. Kuroda, R. V. Mulkern, K. Oshio, L. P. Panych, T. Nakai, T. Moriya, S. Okuda, K. Hynynen, and F. A. Jolesz, *Magn. Reson. Med.*, 2000, **43**(2), 220–225.

94. K. Kuroda, Y. Suzuki, Y. Ishihara, K. Okamoto, and Y. Suzuki, *Magn. Reson. Med.*, 1996, **35**(1), 20–29.

95. J. Weis, L. Covaciu, S. Rubertsson, M. Allers, A. Lunderquist, and H. Ahlstrom, *Magn. Reson. Imaging*, 2009, **27**(7), 923–932.

96. S. M. Sprinkhuizen, M. K. Konings, M. J. van der Bom, M. A. Viergever, C. J. Bakker, L. W. Bartels, *Magn. Reson. Med.*, 2010, **64**(5), 1360–1372.

Index

Abbreviations and Acronyms

1Q	Single-Quantum
2D	Two Dimensional
2QF-COSY	Double-Quantum-Filtered Correlation Spectroscopy
AAG	Ala-Ala-Gly
ABCs	Absorbing Boundary Conditions
ABMS	Anisotropy of the Bulk Magnetic Susceptibility
ACR	American College of Radiology
ADC	Analog-to-digital Converter
ADF	Amsterdam Density Functional
ADRF	Adiabatic Demagnetization in the Rotating Frame
AlN	Aluminum Nitride
AP	Anterior–Posterior
APW	Augmented Plane Wave Method
ARP	Adiabatic Rapid Passage
ARRL	American Radio Relay League
ATC	American Technical Ceramic
AWE	Asymptotic Waveform Evaluation
BCS	Bardeen–Cooper–Schrieffer
BeO	Beryllium Oxide
BHP	Balanced High Pass
BHTMs	Bioheat Transfer Models
BLEW	Burum, Linder & Ernst (Windowless pulse sequence)
BLP	Balanced Low Pass
BLYP	Becke, Lee, Yang, Parr
BO	Bridging Oxygen
BOM	Bond Orbital Model
BPP	Bloembergen–Purcell–Pound
BR-24	Burum & Rhim (pulse sequence)
CAS	Crystal Axis System
CB	Conduction Band
CEA	Atomic Energy Commission
CEE	Convective Energy Equation
CF1T	Center-fed One-turn
CG	Conjugate
CH	Choline
CI	Confidence Interval
cLC	Capillary Liquid Chromatography
CMRR	Center for Magnetic Resonance Research
CODEX	Centerband-only Detection of Exchange Experiment
COSY	Correlation Spectroscopy
CP	Circular Polarization
CP	Cross Polarization
CPMAS	Cross Polarization and Magic Angle Spinning
CPMG	Carr–Purcell–Meiboom–Gill
Cr	Creatine
CRAMPS	Combined Rotation and Multiple-Pulse Spectroscopy
CRC	Counter-rotating Current
CS	Chemical Shift
CSA	Chemical Shift Anisotropy
CST	Chemical Shift Tensor
CST	Computer Simulation Technology
CT	Central Transition
CT	Contact Time
CTMAS	Central Transition Magic Angle Spinning
CW	Continuous Wave
CYCLOPS	Cyclically Ordered Phase Sequence
D	Dipolar
DAH	Dynamic Angle Hopping
DANTE	Delays Alternating with Nutations for Tailored Excitation
DAS	Dynamic Angle Spinning
DD	Dipole-Dipole
DDC	Dual Directional Coupler
DEAR	Dipolar Exchange-Assisted Recoupling
DEISM	Direct Enhancement of Integer-Spin Magnetization
DEPT	Distortionless Enhancement by Polarization Transfer
DFS	Double Frequency Sweeps
DFT	Density Functional Theory
DFT	Discrete Fourier Transform
DMS	Dilute Magnetic Semiconductors
DNP	Dynamic Nuclear Polarization
DOR	Double Rotation
DOS	Density of States
DPPC	Dipalmitoylphosphatidylcholine
DQ	Double-Quantum
DQC	Double-Quantum Coherence
DQF	Double-Quantum Filter
DR-NQR	Double-Resonance Nuclear Quadrupole Resonance
DRESS	Depth-resolved Surface Coil Spectroscopy
DRSE	Dipolar-Rotational Spin Echoes
DSPC	Distearoyl-*sn*-Glycero-3-Phosphatidylcholine

EFG	Electric Field Gradient
EM	Electromagnetic
EMC	Electromagnetic Compatibility
EMF	Electromotive Force
EMI	Electromagnetic Interference
ENDOR	Electron-Nucleus Double Resonance
EP	Electrophysiology
EPI	Echo Planar Images
EPR	Electron Paramagnetic Resonance
ER	End-ring Mode
EXAFS	Extended X-Ray Absorption Fine Structure
FAM	Fast Amplitude Modulation
FC	Fermi-Contact
FDA	Food and Drug Administration
FDTD	Finite Difference Time Domain
FEA	Finite Element Analysis
FEM	Finite Element Method
FFLO	Fulde–Ferrell–Larkin–Ovchinnikov
FFT	Fast Fourier Transform
FID	Free Induction Decay
FIR	Finite Impulse Response
FIT	Finite Integration Technique
FLASH	Fast Low Angle SHot
FML	Fast Motion Limit
fMRI	Functional Magnetic Resonance Imaging
FOQI	First-Order Quadrupolar Interaction
FOV	Field of View
FSLG	Frequency-Switched Lee Goldburg
FSW	Fourier Series Window
FT	Fourier Transform
FWD	Forward
FWHM	Full-width Half-maximum
GBHTM	Generic Bioheat Transfer Model
GGA	Generalized Gradient Approximation
GIPAW	Gauge Including Projector Augmented Waves
GRAPPA	Generalized Auto-calibrating Partially Parallel Acquisition
GRE	Gradient Echo
GRP	Glass-reinforced Plastic
HDOR	Heteronuclear Dipolar-Order Rotor-Encoding
HETCOR	Heteronuclear Correlation
HF	Hartree–Fock
HLW	High-Level Waste
HMQC	Heteronuclear Multiple Quantum Correlation
HMQC	Heteronuclear Multiple-Quantum Coherence
HMT	Hexamethylenetetramine
HOHAHA	Homonuclear Hartman-Hahn
HORROR	Homonuclear Rotary Resonance
HP	High-pass
HPBC	High Pass Birdcage
HS	Hyperbolic Secant
HSQC	Heteronuclear Single-Quantum Coherence
HTS	High-temperature Superconducting
IBMS	Isotropic Bulk Magnetic Susceptibility
ICNIRP	International Commission of Non-Ionizing Radiation Protection
ICRF	Inductively Coupled RF
ID	Inside Diameter
IEC	International Electro-technical Commission
INADEQUATE	Incredible Natural Abundance Double Quantum Transfer Experiment
INEPT	Insensitive Nuclei Enhanced by Polarization Transfer
INEPT-HSQC	Insensitive Nuclei Enhanced by Polarization Transfer-Heteronuclear Single-Quantum Correlation
IR	Infrared
ISIS	Image-selected In Vivo Spectroscopy
ISMRM	International Society of Magnetic Resonance in Medicine
ISNR	Intrinsic Signal-to-noise Ratio
KSAs	Knight Shifts and Associated Anisotropies
LG-CP	Lee–Goldberg CP
LMTO	Linear Muffin Tin Orbital
LO	Local Oscillator
LP	Low-pass
LR	Left–Right
LT	Low Temperature
MAH	Magic Angle Hopping
MAS	Magic Angle Spinning
MAS-J-HMQC	Magic Angle Spinning-J-Heteronuclear Multiple Quantum Coherence
MAS-J-HSQC	Magic Angle Spinning-J-Single Quantum Coherence
MD	Molecular Dynamics
MGH	Massachusetts General Hospital
MIL	Materials of the Institute Lavoisier
MIT	Metal–Insulator Transition

Continued on the back end papers

MLEV-4	A broadband decoupling sequence
MM	Method of Moments
MOM	Method of Moments
MOSFETs	Metal-oxide-semiconductor Field-effect Transistor
MPB	Morphotropic Phase Boundary
MQ	Multiple-Quantum
MQDOR	Multiple-Quantum Double Rotation
MQMAS	Multiple-Quantum Magic Angle Spinning
MQW	Multiple Quantum Well
MR	Magnetic Resonance
MR	Modern Magnetic Resonance
MREV	Mansfield, Rhim, Elleman, & Vaughan (pulse sequence)
MRFM	Magnetic Resonance Force Microscopy
MRI	Magnetic Resonance Imaging
MRI/MRS	MR Imaging and Spectroscopy
MRI/S	Magnetic Resonance Imaging and Spectroscopy
MRIs	Magnetic Resonance Images
MRIS	MRI Scanner
MRS	Magnetic Resonance Spectroscopy
MTLR	Multi-transmission Line Resonator
MWS	Microwave Studio
NA	Natural Abundance
NAA	*N*-acetyl Aspartate
NAR	Nuclear Acoustic Resonance
NBO	Non-Bridging Oxygen
NEXAFS	Near-Edge X-Ray a Fine Structure
NIH	National Institutes of Health
NMR	Nuclear Magnetic Resonance
NMRS	NMR Spectrometer
NOE	Nuclear Overhauser Effect
NOESY	NOE Spectroscopy
NQCC	Nuclear Quadrupole Coupling Constant
NQR	Nuclear Quadrupole Resonance
OCT	Optimal Control Theory
OD	Outer Diameter
ODESSA	One-Dimensional Exchange Spectroscopy by Sideband Alternation
ODNMR	Optically Detected NMR
OTf	Ovotransferrin
PAC	Perturbed Angular Correlation
PAS	Principal Axis System
PAW	Projector Augmented Wave
PB-SAR	Partial-body Specific Absorption Rate
PBE	Perdew–Burke–Ernzerhof
PCB	Printed Circuit Board
PDSD	Proton-Driven Spin Diffusion
PEC	Perfect Electrically Conducting
PFG	Pulse Field Gradient
PIN	Positive-intrinsic-negative
PL	Photoluminescence
PLM	Phospholemman Transmembrane
PMCs	Perfectly Magnetic Boundary Conditions
PML	Perfectly Matched Layers
PMLG	Phase-Modulated Lee Goldburg
PRF	Proton Resonance Frequency
PSD	Proton Spin-Diffusion
PSII	Photosystem II
PTFE	Polytetrafluoroethylene
PVC	Polyvinyl Chloride
Q	Quadrupolar
QC	Quadrupole Coupling
QCPMG	Quadrupolar Carr–Purcell–Meiboom–Gill
QF	Quadrupole Moment/Field Gradient (interaction or relaxation mechanism)
QI	Quadrupolar Interaction
QIS	Quadrupole-Induced Shift
QW	Quantum Well
R-INEPT	Refocused INEPT
RAPT	Rotor Assisted Population Transfer
RARE	Rapid Acquisition with Relaxation Enhancement
RDC	Residual Dipolar Coupling
RDS	Residual Dipolar Splitting
REAPDOR	Rotational Echo Adiabatic Passage Double Resonance
REDOR	Rotational Echo Double Resonance
REF	Reflected
RELM	Rotor-Encoding of Longitudinal Magnetization
REPT-HMQC	Recoupled Polarization-Transfer Heteronuclear Multiple-Quantum Coherence
REREDOR	Rotor-Encoded Rotational Echo
RF	Radio Frequency
RFDR	Radio Frequency Driven Recoupling
RFPA	Radio Frequency Power Amplifier
RHF	Restricted Hartree–Fock
RIACT	Rotation-Induced Adiabatic Coherence Transfer
RIDER	Relaxation-Induced Dipolar Exchange with Recoupling
rms	Root Mean Square
ROI	Region of Interests
RT	Room Temperature

RVB	Resonant Valence Bond
RWG	Rao–Wilton–Glisson
S-RESPDOR	Symmetry-Based Resonance-Echo Saturation-Pulse Double-Resonance
S/N	Signal to Noise
SA	Shielding Anisotropy
SAM	Smooth Amplitude Modulation
SAR	Specific Absorption Rate
SATRAS	Satellite Transition Spectroscopy
SBU	Structural Building Unit
SBV	Strongly Bound Vanadium
SD	Spin-Dipolar
SEDOR	Spin Echo Double Resonance
SEFT	Spin Echo Fourier Transform
SENSE	Sensitivity Encoding
SF_6	Sulfur Hexafluoride
SFAM	Simultaneous Frequency and Amplitude Modulations
SG	Space Group
SI	Superior–Inferior
SLF	Separate-Local-Field
SMASH	SiMultaneous Acquisition of Spatial Harmonics
SNR	Signal-to-noise Ratio
SOFC	Solid Oxide Fuel Cells
SOQI	Second-Order Quadrupolar Interaction
SPAM	Soft Pulse Added Mixing
SPI	Selective Population Inversion
SPIDER	Saturation-Pulse Induced Dipolar Exchange with Recoupling
SPINAL	Small Phase Increment Alternation
SPT	Selective Population Transfer
SQ	Single-Quantum
SQT	Symmetric Quarter Turn
SR	Spin-Rotation (interactive or relaxation mechanism)
SSB	Single Sideband
ssb	Spinning Sidebands
SSNMR	Solid-State Nuclear Magnetic Resonance
SSTMAS	Selected Transitions in MAS Spectra
ST	Satellite Transition
STARTMAS	Satellite-Transition Acquired In Real Time Magic Angle Spinning
STEAMER	Slow-Turning Echo Amplitude Modulation and Echo Reduction
STMAS	Satellite-Transition Magic Angle Spinning
STO	Slater-Type Orbital
TE	Echo Time
TEDOR	Transferred Echo Double-Resonance
TEM	Transmission Line
TEM	Transverse Eletro-magnetic
THF	Tetrahydrofuran
TIR	Inversion Recovery Time
TLR	Transmission Line Resonators
TMS	Tetramethylsilane
TOSS	Total Suppression of Sidebands
TPA	Tetrapropylammonium
TPPI	Time Proportional Phase Incrementation
TPPM	Two-Pulse Phase Modulation
TQ	Triple-Quantum
TR	Repetition Time
T/R	Transmit/Receive
TRAPDOR	Transfer of Populations in Double Resonance
TRLs	Transmission Lines
TSE	Turbo Spin Echo
TTL	Transistor–Transistor Logic
Tx/Rx	Transmit/Receive
UE	Unpaired Electron relaxation mechanism
UHF	Ultra High Frequency
UHF	Ultra-High Field
uiSNR	Ultimate Intrinsic SNR Ratio
UL	Underwriters Laboratories
USR	Ultra Shield and Refrigerated
UW	Ultra-Wideline
VAS	Variable Angle Spinning
VB	Valence Band
VOCS	Variable-Offset Cumulative Spectrum
VSWR	Voltage Standing Wave Ratio
WAHUHA	Waugh, Huber, & Haeberlen (pulse sequence)
WALTZ-16	A broadband decoupling sequence
WISE	Wide-Line Separation
WURST	Wideband, Uniform Rate, and Smooth Truncation
WZ	Wurtzite
XFDTD	Finite Difference Time Domain
XRD	X-Ray Diffraction
YBaCuO	Yttrium-barium-copper-oxide
ZB	Zincblende
ZORA	Zeroth-Order Regular Approximation
ZQ(C)	Zero Quantum (Coherence)